Inertial Fusion Energy
Reactor Design Studies
Volume III

DOE/ER-54101
MDC 92E0008
March 1992

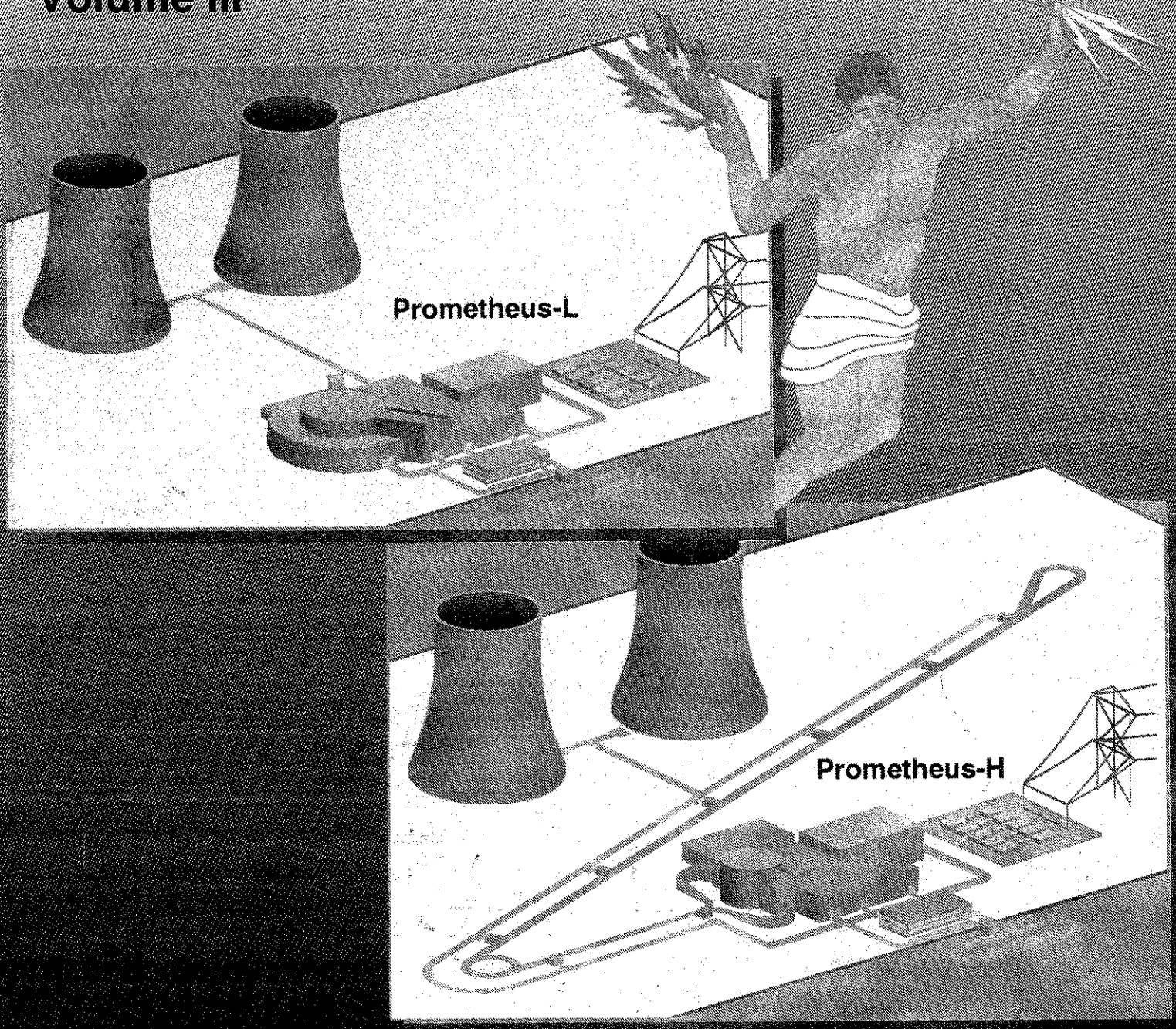

McDonnell Douglas Aerospace Team

Canadian Fusion Fuels Technology Group • Ebasco Services, Inc. • KMS Fusion, Inc.
SPAR Aerospace, Ltd. • TRW Space & Technology Group • University of California at Los Angeles

Final Report

GP33-0272-0001-VC

DOE/ER-54101
MDC 92E0008

INERTIAL FUSION ENERGY REACTOR DESIGN STUDIES

PROMETHEUS-L
PROMETHEUS-H

FINAL REPORT
MARCH 1992

The manuscripts for this document were prepared for publication in March 1992.
The review of the document by DOE delayed publication until July 1993.

Volume III

Copy No. 191

McDonnell Douglas Aerospace
P.O. Box 516
St. Louis, MO 63166-0516

Canadian Fusion Fuels Technology Project
Mississanga, Ontario, Canada

Ebasco Services, Inc.
New York, NY

KMS Fusion, Inc.
Ann Arbor, MI

SPAR Aerospace, Ltd.
Brampton, Ontario, Canada

TRW Space and Electronics Group
Redondo Beach, CA

University of California-Los Angeles
Los Angeles, CA

Copyright Unpublished — 1992. All rights reserved under the copyright laws by McDonnell Douglas Corporation.

Furnished to the U.S. Government with UNLIMITED RIGHTS as defined in Contract DE-AC02-90ER54101, Part II, Section I, Appendix B, Clause No. 6, Rights in Data — General (JUNE 1987) which takes precedence over any restrictive markings herein.

This material may be reproduced by or for the U.S. Government pursuant to the copyright license under Contract DE-AC02-90ER54101, Part II, Section I, Appendix B, Clause No. 6, Rights in Data — General (JUNE 1987).

This work was supported by the US Department of Energy, Office of Fusion Energy, under contract DE-AC02-91ER54101.

DISCLAIMER

This report was prepared as an account of work sponsored by an agency of the United States Government. Neither the United States Government not any agency thereof, nor any of their employees, makes any warranty, express or implied, or assumes any legal liability or responsibility for the accuracy, completeness, or usefulness of any information, apparatus, product, or process disclosed, or represents that its use would not infringe privately owned rights. Reference herein to any specific commercial product, process, or service by trade name, trademark, manufacturer, or otherwise, does not necessarily constitute or imply its endorsement, recommendation, or by the United States Government or any agency thereof. The views and opinions of authors herein do not necessarily state or reflect those of the United States Government or any agency thereof.

CONTRIBUTING AUTHORS

McDONNELL DOUGLAS AEROSPACE

Lester M. Waganer, Daniel E. Driemeyer, V. Dennis Lee

Robert L. Calkins | Henry B. Wald | Forrest R. Williams

CANADIAN FUSION FUELS TECHNOLOGY PROJECT

Ronald S. Matsugu, Otto K. Kveton

K. Kalyanam | Savtantar K. Sood

EBASCO SERVICES, INC.

Stephen L. Ostrow, Stephen F. Marschke

Paul J. Estreich | Marvin J. Parnes

KMS FUSION, INC.

Douglas J. Drake[1]

SPAR AEROSPACE, LTD.

Julian W.F. Millard

John Ballantyne | Terry Haines | Don Perrot
Chris English | Clive Holloway | Andy Turner

TRW SPACE AND ELECTRONICS GROUP

Gary J. Linford | **Steven W. Fornaca** | **Alfred W. Maschke**

UNIVERSITY OF CALIFORNIA, LOS ANGELES

Mohamed A. Abdou, Nasr M. Ghoniem, Mark S. Tillack

James E. Eggleston | Farrokh Issacci | Alice Y. Ying
Anter El-Azab | A. Rene Raffray | Mahmoud Z. Youssef
Zinovy R. Gorbis | Shahram Sharafat | Li Zhang
Insoo Jun

1. Now associated with Interscience, Inc, Germantown, MD

ACKNOWLEDGMENT

The McDonnell Douglas team wishes to thank a great number of people who supported and contributed to this overall effort. Their time and effort are greatly appreciated.

Oversight Committee

Ronald C. Davidson, Chairman	Princeton Plasma Physics Laboratory
Charles C. Baker	Oak Ridge National Laboratory
Roger O. Bangerter	Lawrence Berkeley Laboratory
E. C. Brolin	Princeton Plasma Physics Laboratory
Daniel R. Cohn	Massachusetts Institute of Technology
Donald L. Cook	Sandia National Laboratories
Donald J. Dudziak	North Carolina State University
William Hogan	Lawrence Livermore National Laboratory
David B. Harris	Los Alamos National Laboratory
Robert A. Krakowski	Los Alamos National Laboratory
Thomas E. Shannon	Oak Ridge National Laboratory
Charles P. Verdon	University of Rochester

Target Working Group

Roger O. Bangerter, Chairman	Lawrence Berkeley Laboratory
George Allhouse	Sandia National Laboratories
John Lindl	Lawrence Livermore National Laboratory
William Mead	Los Alamos National Laboratory
Charles P. Verdon	University of Rochester

ARIES Project Staff

Ronald L. Miller	Los Alamos National Laboratory

Lawrence Berkeley Design Staff

Edward Lee	Lawrence Berkeley Laboratory
Andy Faltens	Lawrence Berkeley Laboratory

We would also like to acknowledge the contributions of other people who made this report possible.

David B. Harris, LANL, who facilitated the review process at his facility
Phillip Lang, LANL, Technical Review
Linda M. Merritt, MDA, Principal Text and Graphics Coordinator and Senior Editor
David E. Morgan and J. Warren Stultz, MDA, Technical Editors
Joanne Matheson , SPAR Aerospace, Ltd, Secretarial Support
Bruce Sayer, SPAR Aerospace, Ltd, Graphics Support
Thomas Chao, Alan Chen, Winn Hong, Billy Jimenez, and Faiz Sherman: UCLA Technical Support
Julie Austin, UCLA Secretarial Support
Matt Durkan, UCLA Administrative Support

Use or disclosure of data
subject to title page restriction

TABLE OF CONTENTS

Section	Title	Page
	VOLUME I	
EXECUTIVE SUMMARY		ES-1
CHAPTER 1	INTRODUCTION	1-1
CHAPTER 2	STUDY OVERVIEW	2-1
2.1	INTRODUCTION	2-1
2.2	KEY OBJECTIVES, REQUIREMENTS, AND ASSUMPTIONS	2-2
2.3	SYSTEMS MODELING AND TRADE STUDIES	2-3
2.4	PROMETHEUS-L REACTOR PLANT DESIGN OVERVIEW	2-13
2.5	PROMETHEUS-H REACTOR PLANT DESIGN OVERVIEW	2-29
2.6	KEY TECHNICAL ISSUES AND R&D REQUIREMENTS	2-42
2.7	COMPARISON OF IFE DESIGNS	2-55
2.8	STUDY CONCLUSIONS	2-57
	VOLUME II	
CHAPTER 3	OBJECTIVES, REQUIREMENTS, AND ASSUMPTIONS	3-1
3.1	INTRODUCTION	3-1
3.2	GENERAL GUIDELINES	3-1
3.3	TARGET AND DRIVER GUIDELINES	3-4
3.4	REACTOR SYSTEMS	3-15
3.5	ECONOMIC GUIDELINES	3-16
CHAPTER 4	RATIONALE FOR DESIGN OPTION SELECTION	4-1
4.1	SELECTION OF REACTOR SYSTEM TECHNOLOGY OPTIONS	4-1
4.2	KrF LASER DRIVER OPTIONS	4-16
4.3	RATIONALE FOR HEAVY ION DRIVER OPTIONS	4-38
4.4	CAVITY DESIGN OPTIONS	4-43
4.5	SELECTION CRITERIA FOR SiC/SiC COMPONENTS	4-50
4.6	TARGET SELECTION	4-59
4.7	DESIGN RATIONALE FOR THE GIMM	4-85
CHAPTER 5	KEY TECHNICAL ISSUES AND R&D REQUIREMENTS	5.1-1
5.1	INTRODUCTION	5.1-1
5.2	IDENTIFICATION OF KEY ISSUES	5.2-1
5.3	PROMETHEUS REACTOR DESIGN STUDY CRITICAL ISSUES	5.3-1
5.4	KEY ISSUES DESCRIPTION	5.4-1
5.5	RESEARCH AND DEVELOPMENT ASSESSMENT	5.5-1
CHAPTER 6	CONCEPTUAL DESIGN SELECTION AND DESCRIPTION	6.1-1
6.1	INTRODUCTION	6.1-1
6.2	DESIGN POINT SELECTION	6.2-1
6.3	CONFIGURATION AND MAINTENANCE APPROACH	6.3-1
6.4	TARGET AND TARGET FABRICATION	6.4-1
	VOLUME III	
6.5	**DRIVER SYSTEM DEFINITION**	**6.5-1**
6.6	**VACUUM SYSTEM**	**6.6-1**
6.7	**FUEL PROCESSING SYSTEMS (FPS)**	**6.7-1**
6.8	**CAVITY DESIGN AND ANALYSIS**	**6.8-1**
6.9	**HEAT TRANSPORT AND THERMAL ENERGY CONVERSION**	**6.9-1**
6.10	**BALANCE OF PLANT SYSTEMS**	**6.10-1**
6.11	**REMOTE MAINTENANCE SYSTEMS**	**6.11-1**
6.12	**SAFETY AND ENVIRONMENT**	**6.12-1**
6.13	**ECONOMICS**	**6.13-1**

Use or disclosure of data
subject to title page restriction

TABLE OF CONTENTS

Section	Title	Page
	VOLUME III (CONT.)	
CHAPTER 7	COMPARISON OF IFE DESIGNS	7-1
7.1	INTRODUCTION	7-1
7.2	EVALUATION METHODOLOGY	7-2
7.3	COMPARATIVE EVALUATION RESULTS	7-12
APPENDIX A	PROMETHEUS-L BASELINE PARAMETER LIST	A-1
APPENDIX B	PROMETHEUS-H BASELINE PARAMETER LIST	B-1
APPENDIX C	INERTIAL FUSION ENERGY REACTOR DESIGN STUDIES COST BASIS	C-i
INTRODUCTION		C-1
C.1	DEVELOPED ECONOMIC STUDY GUIDELINES	C-10
C.2	OVERALL COSTING AND ECONOMIC METHODOLOGY	C-14
C.3	CAPITAL COST ACCOUNTS	C-17
C.4	COST OF ELECTRICITY ACCOUNTS	C-37

Use or disclosure of data
subject to title page restriction

LIST OF PAGES – VOL. III

title page
ii through xx
6.5-1 through 6.5-2
6.5.1-1 through 6.5.1-62
6.5.2-1 through 6.5.2-50
6.5.3-1 through 6.5.3-12
6.6-1 through 6.6-10
6.7-1 through 6.7-42
6.8-1 through 6.8-8
6.8.1-1 through 6.8.1-16
6.8.2-1 through 6.8.2-76
6.8.3-1 through 6.8.3-32
6.8.4-1 through 6.8.4-6
6.8.5-1 through 6.8.5-32
6.9-1 through 6.9-22
6.10-1 through 6.10-26
6.11-1 through 6.11-26
6.12-1 through 6.12-20
6.13-1 through 6.13-8
7-1 through 7-24
A-1 through A-6
B-1 through B-6
C-i through C-iv
C-1 through C-42

Use or disclosure of data
subject to title page restriction

LIST OF FIGURES – VOL. III

No.	Title	Page
6.5.1-1	This block diagram illustrates how the Prometheus ELMO pulses are beam-divided, amplified, accumulated, pulse-compressed, and focused onto the DT target	6.5.1-2
6.5.1-2	The 1 J output pulse from the ELMO is divided into 1020 beamlines, amplified by ELPs, ELDs, and ELPAs. The Stokes seeds are generated and injected into the Raman accumulators along with the main output beams.	6.5.1-3
6.5.1-3	Following the conversion of the excimer pump beams in the Raman accumulators, the long 250-ns (for EDELs) or 500-ns (for EBELs) pulses are injected into the SBS pulse compressor cells where ~65% of the energy is converted into a 6-ns pulse using a ramped Stokes SBS seed.	6.5.1-4
6.5.1-4	The output pulse of Prometheus laser driver is initiated at the ELMO, amplified by the EDELs, Raman converted in 60 Accumulator Cells, Pulse Compressed in 60 SBS Cells, and Focused onto the Direct-Drive Target with the Final Focus Mirror and the Grazing Incidence Mirror	6.5.1-6
6.5.1-5	The electric discharge excimer laser (EDEL) excitation geometry provides for direct excitation of the KrF excimer via electric discharges between electrodes immersed in preionized volumes.	6.5.1-9
6.5.1-6	The electron-beam excited excimer laser (EBEL) excitation geometry permits larger volumetric excitation of the KrF excimer via direct e-beam excitation transmitted through a Hibachi and foil vacuum barrier.	6.5.1-11
6.5.1-7	Pulsed power configuration for the EDEL version of the ELPA	6.5.1-16
6.5.1-8	Each Raman accumulator subsystem consists of a local Raman oscillator (LRO), a Raman preamplifier, and a recollimation telescope generating 120x120 cm Raman Stokes seed beam of 30 J to drive the Raman accumulator cells.	6.5.1-17
6.5.1-9	Injection of the Stokes seed into the Raman accumulator cell permits the efficient extraction of the excimer pump beams into a 100 kJ beam having an aperture of 1.2x1.2 m	6.5.1-20
6.5.1-10	The RAC conversion efficiency is dependent upon the CRAM angle, hydrogen gas density, and distance along the accumulator axis assuming a 5 GHz bandwidth, 250 nm pump beam, 100 kJ energy in 250 ns pulse duration	6.5.1-21
6.5.1-11	The complex temporal shape of the direct-drive laser driver pulse consists of a ramped, 80 ns precursor pulse followed by a short, 6 ns main pulse.	6.5.1-24
6.5.1-12	By frequency-"chirping" the leading edge of the SBS pumping pulse and reflecting it back upon the incoming pulse within an SF cell, it is possible to compress the RAC output pulse from 250 ns (or 500 ns) down to short pulse durations	6.5.1-26
6.5.1-13	Pulse compression in the SBS pulse compressor	6.5.1-27
6.5.1-14	By use of a large aperture Pockels cell and a delay line, the short main pulse and long precursor pulses are temporally inverted	6.5.1-28
6.5.1-15	With fast Pockels cells and additional delay lines, additional temporal tailoring of the pulse shape is possible.	6.5.1-29
6.5.1-16	A variety of compressed pulse shapes could be achieved using a 600 ns Raman pump beam, 100 kJ energy, 1 amagat SF_6 density, and the indicated Stokes seed ramp ratios	6.5.1-30
6.5.1-17	Further compressed pulse shapes can be generated using a 250 ns Raman pump beam at 250 nm, 120 kJ of energy, 2 amagat SF_6 density, 1x1 meter aperture and the indicated Stokes seed ramp ratios	6.5.1-30
6.5.1-18	The SBS pulse compressor efficiency for 5 GHz 250 ns 120 kJ Raman pulses at 250 nm decreases as the Stokes seed ramp ratio increases	6.5.1-31
6.5.1-19	Temporal developments of depleted pump pulses emerging from SBS pulse compressor for 5 GHz, 100 kJ, 500 ns RAC pulses in 1 amagat of SF_6, 1x1 m apertures	6.5.1-32
6.5.1-20	Temporal developments of depleted pump pulses from SBS pulse compressor for 5 GHz, 120 kJ, 250 nm pump, 250 ns pulse duration RAC pulses in 2 amagat of SF_6	6.5.1-32

LIST OF FIGURES – VOL. III (CONT.)

No.	Title	Page
6.5.1-21	By utilizing a figured meniscus dichroic focusing mirror, it is possible to image the shine shield onto a highly magnified CCD array	6.5.1-35
6.5.1-22	The incident beam from the E/O Switchyard is focused through and shielding by the collimating mirror, refocused by the focusing mirror, and beam directed onto the target by the grazing incidence mirror	6.5.1-36
6.5.1-23	The single beam Prometheus laser intensity as a function of distance from a 6 mm diameter direct drive target with the beam diameter = target diameter at the target for a 100 kJ beam in a 6 ns pulse	6.5.1-39
6.5.1-24	Schematic of Prompt Radiation for D/T Target Ablating Plasma from Reactor Chamber First Wall	6.5.1-42
6.5.1-25	Schematic of Placement of Final Focusing Optics, Magnetic Deflector, Rotating Mechanical Shutter, and Input Laser Pulse Relative to Target Chamber	6.5.1-43
6.5.1-26	Target Debris Velocity Spectra for Bare D/T Target	6.5.1-45
6.5.1-27	Reflectivities at Normal Incidence	6.5.1-47
6.5.1-28	Reflectivities at Grazing Incidence	6.5.1-47
6.5.1-29	Neutron-Induced Swelling in Aluminum	6.5.1-50
6.5.1-30	Neutron-Induced Swelling in Magnesium	6.5.1-50
6.5.1-31	Void Swelling at High Temperature	6.5.1-51
6.5.1-32	Top View of GIMM with Scaled Measurements	6.5.1-52
6.5.1-33	Cross-Sectional View of GIMM	6.5.1-53
6.5.1-34	Detailed Cross-Section of GIMM	6.5.1-54
6.5.1-35	Section View of Mirror Structure Illustrating Expansion Capability	6.5.1-54
6.5.1-36	Thermal Design of the GIMM	6.5.1-58
6.5.1-37	Surface Deformation of Mirror	6.5.1-60
6.5.2-1	The Prometheus-H Heavy Ion Driver consists of a single beam LINAC operated in a burst mode to generate 18 beamlets, 12 storage rings, focusing magnets, and two channel transport for a 2-sided indirect drive DT target	6.5.2-2
6.5.2-2	Schematic of the Prometheus-H Quadrupole Focusing Channel	6.5.2-3
6.5.2-3	Heavy Ion Trajectories Lie Within this Elliptical Envelope in Phase Space	6.5.2-4
6.5.2-4	Relationships Between Magnetic Fields at Poletips, Walls, and Wires	6.5.2-5
6.5.2-5	Relationship Between Particle Energy, V, and Accelerator Gradient, G, in LINAC	6.5.2-6
6.5.2-6	Heavy Ion beam current as a function of time at a given location in the Prometheus Heavy Ion Driver	6.5.2-6
6.5.2-7	Dependence of accelerator gradient on the displacement along the LINAC axis, z, in the ramp-gradient section of the Prometheus-H heavy ion driver	6.5.2-12
6.5.2-8	Variation of heavy ion beam energy with distance along accelerator axis in ramp-gradient portion of accelerator	6.5.2-12
6.5.2-9	Variation of beam energy with displacement along axis for both ramped gradient and constant gradient accelerators	6.5.2-13
6.5.2-10	Depressed tune, σ, vs. displacement along the LINAC axis	6.5.2-14
6.5.2-11	G_τ as a function of displacement along LINAC axis	6.5.2-14
6.5.2-12	Variations of Displacement between Quads (L), blank space between Quads (space) and Quadrupole Length (q) as functions of displacement along accelerator axis	6.5.2-15
6.5.2-13	Variation of Quad Packing Fraction (η) and Quad Aspect Ratio (a/l) as functions of displacement along LINAC axis (z)	6.5.2-15
6.5.2-14	Dependence of HI beam current (I) and pulse duration (τ) on location along LINAC axis (z)	6.5.2-16
6.5.2-15	Pulse length (τ) of HI beam as a function of displacement along LINAC axis (z)	6.5.2-16
6.5.2-16	Comparison of Multiple Beam LINAC with Single Beam LINAC	6.5.2-18
6.5.2-17	Energy Dissipation for Metglas as a Function of (Square) Pulse Duration	6.5.2-19
6.5.2-18	Metglas Heat as a Function of PRF	6.5.2-20
6.5.2-19	Damping Resistor Circuit on LINAC (Similar to LLNL ATA Design)	6.5.2-21
6.5.2-20	Evolved Pulsed Power Component Configuration to Limit Failures	6.5.2-22

Use or disclosure of data
subject to title page restriction

LIST OF FIGURES – VOL. III (CONT.)

No.	Title	Page
6.5.2-21	Prometheus-H Superconducting cos (2θ) Quadrupole Core Configuration	6.5.2-23
6.5.3-1	Conceptual Design of Neutron Pinhole to Limit Neutron Propagation into Driver Building	6.5.3-3
6.5.3-2	Common Enclosure of Heavy Ion Beams Provides Plenum for Attaining 10^{-5} torr Pressure Level	6.5.3-4
6.5.3-3	Prometheus Instrumentation and Control Methodology	6.5.3-7
6.5.3-4	Shielding of Final Laser Optics Contains Radiation Within the Beamline	6.5.3-9
6.5.3-5	Details of Heavy Ion Beam Final Focus Shielding	6.5.3-10
6.6-1	Hydrogen Pumping Speed Vs. Pump Diameter	6.6-3
6.6-2	Vacuum Ports Required	6.6-4
6.6-3	Total Active Cryogenic Pump Required Vs. Number of Vacuum Ports	6.6-5
6.6-4	Cryopump Hydrogen Capacity Vs. Pump Diameter	6.6-6
6.6-5	Laser-Driven Reactor Vacuum Manifold System Arrangement	6.6-7
6.6-6	Heavy Ion Reactor Vacuum Manifold Systems Arrangement	6.6-10
6.7.1-1	Fuel Processing Systems Arrangement	6.7-2
6.7.3-1	Thermally Coupled Pressure Swing Adsorption for Fuel Treatment	6.7-6
6.7.3-2	Laser-Based Isotope Separation System	6.7-9
6.7.4-1	Chamber Exhaust Purification and Impurity Treatment System	6.7-11
6.7.5-1	PSA Column Pressure Variation with Time	6.7-13
6.7.5-2	PSA HT Adsorbed as Function of Time	6.7-13
6.7.5-3	PSA for Tritium Extraction from Breeder	6.7-15
6.7.6-1	Functional Arrangement of ADS	6.7-17
6.7.6-2	Recombiner-Dryer Based Air Detritiation System	6.7-20
6.7.6-3	Membrane Based Air Detritiation System	6.7-21
6.7.7-1	Getter-Based Inert Gas Detritiation System	6.7-23
6.7.7-2	Recombiner/Dryer Based Inert Gas Detritiation System	6.7-24
6.7.8-1	Fuel Storage and Management System Diagram	6.7-26
6.7.9-1	ISS and Water Detritiation – Flow Diagram	6.7-28
6.7.10-1	Y.YH2 Formation vs. Equilibrium Hydrogen Pressure	6.7-37
6.7.10-2	Recovery of Tritium from Na by Yttrium Gettering	6.7-38
6.8-1	Perspective View of the Cavity with Laser Beams	6.8-3
6.8-2	Perspective View of the Cavity without Laser Beams	6.8-4
6.8-3	Radial Build of the Cavity	6.8-7
6.8.1-1	Material Composition in the 1-D Cavity Model	6.8.1-2
6.8.1-2	Nuclear Heating Rate Profile in the Baseline Design	6.8.1-5
6.8.1-3	Nuclear Heating Rate Profile in the First Wall Design	6.8.1-6
6.8.1-4	Nuclear Heating Rate Profile in the Blanket/Reflector/Plena System	6.8.1-6
6.8.1-5	Nuclear Heating Rate Profile in the Concrete Bulk Shield Case	6.8.1-7
6.8.1-6	Displacement Per Atom Per Full Power Year in Silicon	
6.8.1-7	Tritium Production Rate Profile in the Breeding Zone Per Incident Neutron	6.8.1-12
6.8.1-8	Neutron Flux in the First Wall of the FWS and in the First Wall of the Blanket/ Reflector/Plena System Per Incident Neutron	6.8.1-12
6.8.1-9	Neutron Flux in the FW of the FWS and the FW of the Blanket/Reflector/Plena System	6.8.1-13
6.8.1-10	Neutron Flux Above 0.2 MeV in the FW of the FWS and in the FW of the Blanket/ Reflector/Plena System per Incident Neutron	6.8.1-14
6.8.1-11	Neutron Flux in the FW of the FWS and in the FW of the Blanket/Reflector/Plena System	6.8.1-14
6.8.2-1	First Wall Panel; Cross Sectional View	6.8.2-1
6.8.2-2	Schematic View of Film Supply Systems	6.8.2-3
6.8.2-3	Target X-Ray Spectra Used for Prometheus-L and -H	6.8.2-7

Use or disclosure of data
subject to title page restriction

LIST OF FIGURES – VOL. III (CONT.)

No.	Title	Page
6.8.2-4	Cross Section in Pb as a Function of X-Ray Energy	6.8.2-8
6.8.2-5	Fraction of X-Ray Energy Absorbed by the Lead Vapor	6.8.2-9
6.8.2-6	Energy Deposition Profile in Pb Film	6.8.2-11
6.8.2-7	Integrated Energy Deposition Profile in Pb Film	6.8.2-12
6.8.2-8	Debris Ion Deposition Profiles in Cavity Vapor	6.8.2-13
6.8.2-9	Mathematical Model of the Vapor Flow in the Cavity	6.8.2-16
6.8.2-10	The Staggered Grid and Nodes	6.8.2-18
6.8.2-11	Filtering Process Applied to the CDS Result	6.8.2-21
6.8.2-12a	Instantaneous Uniform Pressure on the Wall with Lithium Vapor	6.8.2-23
6.8.2-12b	Instantaneous Uniform Pressure on the Wall with Lead Vapor	6.8.2-23
6.8.2-13	Energy Transport Pathways and Overall Geometry	6.8.2-25
6.8.2-14	Specific Energy of Pb Vapor vs. Temperature	6.8.2-28
6.8.2-15	Cavity Vapor Pressure and Mass Histories for Prometheus-L	6.8.2-30
6.8.2-16	Cavity Vapor Pressure and Mass Histories for Prometheus-H	6.8.2-31
6.8.2-17	Saturation Pressure of Pb and Saturation Pressure Corrected to 0°C	6.8.2-31
6.8.2-18	Base Case Cavity Vapor Temperature and Pressure Histories for Prometheus-L	6.8.2-32
6.8.2-19	Base Case Cavity Vapor Temperature and Pressure Histories for Prometheus-H	6.8.2-33
6.8.2-20	Base Case Temperatures at the Film Surface and Interface Between the Film and SiC Wall for Prometheus-L	6.8.2-34
6.8.2-21	Effect of Rep. Rate on the Cavity Pressure Following a Blast	6.8.2-35
6.8.2-22	Effect of Increasing the Cavity Size on the Cavity Pressure Following a Blast	6.8.2-35
6.8.2-23	Effect of Changing the Cavity Area with the Volume Fixed	6.8.2-37
6.8.2-24	Effect of Changing the Cavity Volume with the Area Fixed	6.8.2-37
6.8.2-25	Effect of Increasing the Cavity Volume on the Pressure History	6.8.2-38
6.8.2-26	Effect of Non-Condensable Gas Pressure on the Final Cavity Pressure	6.8.2-38
6.8.2-27	Identification of Wave Classes	6.8.2-41
6.8.2-28	Longitudinal Distribution of Maximum and Minimum Film Thickness	6.8.2-42
6.8.2-29	Baseline Pressure Distribution and Seepage Rate Along the First Wall	6.8.2-43
6.8.2-30	Illustration of Force Elements Acting on the Upper Wall Film	6.8.2-44
6.8.2-31	Minimum Required Film Velocity for Attachment on the Upper Hemisphere Wall	6.8.2-46
6.8.2-32	Turbulent Film Thickness and Minimum Volumetric Flow Rate for Attachment	6.8.2-46
6.8.2-33	Film Thickness as a Function of Distance Away fro the Top End Cap	6.8.2-47
6.8.2-34	Average Film Velocity as a Function of Distance from the Top End Cap	6.8.2-47
6.8.2-35	Film Thickness as a Function of Distance Away from the Top End Cap	6.8.2-49
6.8.2-36	Film Velocities as a Function of Distance Away from the Top End Cap	6.8.2-49
6.8.2-37	Cavity and Differential Pressure Histories at the Uppermost Point of the Cavity	6.8.2-51
6.8.2-38	Ultimate Film Thickness and Film Velocity Histories Following the Cavity Pressure Build-Up	6.8.2-52
6.8.2-39	The History of the Pressure Loading on the First Wall Following the Microexplosion	6.8.2-54
6.8.2-40	Instantaneous Velocity and Radial Displacement of the Continuous First Wall	6.8.2-55
6.8.2-41	Hoop Stress History in the Continuous First Wall	6.8.2-56
6.8.2-42	Kinetic Energy of the Vibrating Continuous First Wall	6.8.2-56
6.8.2-43	Schematic of Mechanical Loading of the FW Panels	6.8.2-58
6.8.2-44	Instantaneous Velocity and Displacement at Center of First Wall Plate	6.8.2-59
6.8.2-45	The History of Stresses at Center of FW Plate	6.8.2-60
6.8.2-46	The History of Stresses at Clamped Edge of FW Plate	6.8.2-60
6.8.2-47	The Stress-Strain Diagram for SEP 2D SiC/SiC Composite	6.8.2-61
6.8.3-1	Schematic of a Blanket Module	6.8.3-1
6.8.3-2	Enlarged Breeder Region Cutaway	6.8.3-2
6.8.3-3	Blanket Module Internal Structure Showing Coolant and Purge Manifolds and Reinforcing Ribs	6.8.3-3
6.8.3-4	The Radial-Build of the Prometheus Cavity	6.8.3-6
6.8.3-5	Material Composition in the 1-D Cavity Model	6.8.3-7
6.8.3-6	Nuclear Power Multiplication as a Function of Lead Zone Thickness	6.8.3-9

LIST OF FIGURES – VOL. III (CONT.)

No.	Title	Page
6.8.3-7	Tritium Breeding Ratio and Nuclear Power Multiplication as a Function of Lead Zone Thickness	6.8.3-9
6.8.3-8	Fraction of Nuclear Power Deposited in the First Wall and Blanket/Reflector Systems as a Function of Lead Zone Thickness	6.8.3-10
6.8.3-9	Fraction of Nuclear Power Deposited in the Vacuum Vessel and Shield Systems as a Function of Lead Zone Thickness	6.8.3-10
6.8.3-10	Nuclear Power Density as a Function of the Lead Zone Thickness	6.8.3-11
6.8.3-11	Nuclear Power Density as a Function of the Lead Zone Thickness	6.8.3-11
6.8.3-12	Tritium Production Rate from Li-6 as a Function of Lead Zone Thickness	6.8.3-12
6.8.3-13	Tritium Production Rate from Li-7 as a Function of Lead Zone Thickness	6.8.3-13
6.8.3-14	Nuclear Power Multiplication as a Function of the Breeding Zone Thickness	6.8.3-14
6.8.3-15	Tritium Breeding Ratio as a Function of the Breeding Zone Thickness	6.8.3-14
6.8.3-16	Fraction of Nuclear Power Deposited in the First Wall and Blanket/Reflector Systems	6.8.3-15
6.8.3-17	Fraction of Power Deposited in the Vacuum Vessel and Shield Systems	6.8.3-15
6.8.3-18	Nuclear Power Multiplication as a Function of the Beryllium Zone Thickness	6.8.3-17
6.8.3-19	Tritium Breeding Ratio as a Function of Beryllium Zone Thickness	6.8.3-17
6.8.3-20	Fraction of Nuclear Power Deposited in the First Wall and Blanket/Reflector Systems as a Function of Beryllium Zone Thickness	6.8.3-18
6.8.3-21	Fraction of Nuclear Power Deposited in the Vacuum Vessel and Shield Systems as a Function of Beryllium Zone Thickness	6.8.3-18
6.8.3-22	He Coolant Velocity in the Blanket as a Function of the Inlet Pressure for Different Fractional Flow Areas	6.8.3-19
6.8.3-23	He Coolant Pressure Drop in the Blanket as a Function of the Inlet Pressure for Different Fractional Flow Areas	6.8.3-21
6.8.3-24	He Purge Pressure Drop in the Blanket as a Function of the Li_2O Bed Packing Fraction for Different Purge Inlet Pressures	6.8.3-22
6.8.3-25	Cross-Section of the Module Front Wall Showing the He Cooling Channels	6.8.3-23
6.8.3-26	Thermal Stress in the Module Wall as a Function of the Distance Between the Coolant Channel and the Wall Edge	6.8.3-24
6.8.3-27	Maximum Bending Stress in a Plate with Built-In Edges as a Function of the Plate Width for Different Plate Thicknesses	6.8.3-26
6.8.4-1	Neutrons and Gamma Ray Fluxes in the Concrete Bulk Shield as a Function of Depth Inside the Bulk Shield	6.8.4-3
6.8.4-2	Neutron and Gamma Ray Fluxes in the Composite Bulk Shield as a Function of Depth Inside the Shield	6.8.4-3
6.8.5-1	Cavity Cross-Section and Zone Designation	6.8.5-3
6.8.5-2	Radioactivity Calculational Procedure	6.8.5-4
6.8.5-3	Specific Radioactivity in the First Wall System	6.8.5-9
6.8.5-4	Specific Radioactivity in the Blanket and Reflector	6.8.5-9
6.8.5-5	Specific Radioactivity in the Vacuum Vessel, Shield, and Surrounding Air	6.8.5-10
6.8.5-6	Integrated Radioactivity in Each Component as a Function of Time After Shutdown	6.8.5-12
6.8.5-7	Comparison of Activation Levels Between Prometheus and Conventional Concrete Shield	6.8.5-13
6.8.5-8	Neutron Flux Comparison Between Prometheus and Conventional Concrete Shield	6.8.5-14
6.8.5-9	Photon Flux Comparison Between Prometheus and Conventional Concrete Shield	6.8.5-14
6.8.5-10	Cylindrical Modeling of the Cavity	6.8.5-15
6.8.5-11	Specific BHP in the First Wall System	6.8.5-17
6.8.5-12	Specific BHP in the Blanket and Reflector	6.8.5-18
6.8.5-13	Specific BHP in the Vacuum Vessel, Shield, and Surrounding Air	6.8.5-18
6.8.5-14	Po^{210} Buildup in the Prometheus First Wall System	6.8.5-21
6.8.5-15	Specific Decay Heat Histories at Different Components	6.8.5-23
6.8.5-16	Temperature Histories at SiC FW and Blanket Components Following a Loss of Coolant Accident	6.8.5-24

Use or disclosure of data subject to title page restriction

LIST OF FIGURES – VOL. III (CONT.)

No.	Title	Page
6.8.5-17	Scenarios of Dry Spot Formation Which Lead to a Reactor Shutdown	6.8.5-28
6.8.5-18	The Energy Available for Sublimation Is the Difference Between the Radiative and Conductive Heat Fluxes	6.8.5-29
6.9-1	Prometheus Baseline Power Flow	6.9-2
6.9-2	Prometheus-L Energy Conversion System	6.9-3
6.9-3	Prometheus-H Energy Conversion System	6.9-3
6.9-4	Prometheus-L Turbine Thermal Cycle	6.9-5
6.9-5	Prometheus-H Turbine Thermal Cycle	6.9-6
6.9-6	Coolant Distribution and Steam Generation	6.9-10
6.9-7	Steam Generation Flow Schematic	6.9-10
6.9-8	Helium Heat Exchanger Module	6.9-11
6.9-7	Vessel #1, Helium Steam Generator	6.9-12
6.9-10	Vessel #4, Liquid Lead Steam Generator	6.9-14
6.9-11	Liquid Lead Heat Exchanger - Cross Section	6.9-15
6.9-12	Liquid Lead Steam Generator - Top Tube Sheet Connections	6.9-15
6.9-13	Helium System Cost vs. Circulating Power	6.9-20
6.10-1	Prometheus Control Complex	6.10-9
6.11-1	In-Vessel Vehicular System Represents Current State-of-the-Art in Manipulator Technology	6.11-2
6.11-2	Remote Manipulators Performing Typical Maintenance Tasks of INTER	6.11-3
6.11-3	Maintenance Manipulators and Vehicle at the JET Facility	6.11-4
6.11-4	SPAR 2500 and Schilling Manipulator at the DOE Hanford Facility	6.11-5
6.11-5	MASCOT, a Typical Small Nuclear Manipulator at the JET Fusion Facility	6.11-6
6.11-6	Curved Deployable X-Boom Truss	6.11-8
6.11-9	STEM Mounted Camera	6.11-9
6.11-9	Mobile Folding Crane	6.11-12
6.11-10	Deployable Crane Hoist	6.11-13
6.11-11	Heavy Crane with Removable Drives	6.11-14
6.11-12	Typical Remote Handling Tool (JET Pipe Cutter)	
6.11-13	Upper Reactor Manipulator	6.11-17
6.11-14	Deployable Heavy Duty Manipulator	6.11-19
6.11-15	Mobile Heavy Duty Manipulator	6.11-20
6.11-16	Two-Arm Dexterous Manipulator	6.11-22
6.11-17	Small Power Manipulator	6.11-23
6.11-18	Steam Generator Robot	6.11-24
6.13-1	Unit Cost Reduction Factors for 70, 80, and 90% Learning	6.13-2
6.13-2	Change in Prometheus COE for Different LSA Assumptions	6.13-5
6.13-3	Change in Prometheus COE for Different Plant Electric Power Outputs	6.13-6
7-1	Evaluation Methodology Approach	7-3
7-2	Safety and Environment Evaluation Approach	7-8
C-1	Log Linear Unit Cost Curves	C-11
C-2	Radial Build of the First Wall, Blanket, and Shield Subsystems	C-22

LIST OF TABLES – VOL. III

No.	Title	Page
6.5.1-1	Prometheus ELMO Specifications	6.5.1-7
6.5.1-2	Prometheus ELP Specifications	6.5.1-13
6.5.1-3	Prometheus ELD Specifications	6.5.1-14
6.5.1-4	Prometheus ELPA Specifications	6.5.1-15
6.5.1-5	Common Raman Amplifier Specifications	6.5.1-17
6.5.1-6	Prometheus Local Raman Oscillator Specifications	6.5.1-19
6.5.1-7	Prometheus Raman Preamplifier Specifications	6.5.1-19
6.5.1-8	Prometheus Raman Accumulator Specifications	6.5.1-21
6.5.1-9	Energy Distribution in Excimer Laser Pumping	6.5.1-33
6.5.1-10	Excimer Laser Optical Subsystems	6.5.1-34
6.5.1-11	Potential Damage Sources for Final Turning Optics	6.5.1-39
6.5.1-12	Reflectivity for Materials of Interest (Polished Surfaces)	6.5.1-46
6.5.1-13	Thermal-Hydraulic Parameters for the GIMM	6.5.1-55
6.5.2-1	Summary of Heavy Ion Driver Parameters	6.5.2-8
6.5.2-2	Summary of Injector Parameters	6.5.2-9
6.5.3-1	Pulsed Power Requirements for EDEL	6.5.3-1
6.5.3-2	EDEL Ceramic PFL Design Parameters	6.5.3-2
6.5.3-3	Laser Pulsed Power System Efficiency Summary	6.5.3-2
6.6-1	Laser Driven Reactor Vacuum System Design Requirements	6.6-2
6.6-2	Heavy Ion-Driven Reactor Vacuum System Requirements	6.6-8
6.7.1-1	FPS Design Data-L - Laser Option – Stream Identification is Consistent with Figure 6.7.1-1	6.7-3
6.7.1-2	Fuel Processing Services and Proposed Technologies for Prometheus IFE	6.7-4
6.7.6-1	ADS Design Parameters	6.7-18
6.7.8-1	Tritiated Hydrogen Storage Requirements	6.7-25
6.7.8-2	Tritium Storage Tank Requirements	6.7-26
6.7.9-1	Water Distillation Column Parameters	6.7-31
6.7.9-2	Cryogenic Distillation Column Parameters	6.7-33
6.7.9-3	ISS Liquid Flows, L-Option	6.7-34
6.7.9-4	ISS Gas Flows, L-Option	6.7-34
6.7.9-5	ISS Liquid Flows, H-Option	6.7-34
6.7.9-6	ISS Gas Flows, H-Option	6.7-34
6.7.9-7	Failure Modes and Effects Analysis for the ISS	6.7-36
6.7.9-8	Heat Transfer Media Must Be Processed to Keep Tritium Permeation Within Acceptable Limits	6.7-36
6.8.1-1	Key Neutronics Parameters for Prometheus-L and Prometheus-H	6.8.1-5
6.8.1-2	Nuclear Heating in Prometheus First Wall/Blanket/Shield Systems	6.8.1-9
6.8.1-3	Cavity Energy Balance	6.8.1-10
6.8.2-1	First Wall System Major Parameters	6.8.2-4
6.8.2-2	First Wall Power Balance	6.8.2-4
6.8.2-3	First Wall System Thermal Hydraulic Parameters	6.8.2-6
6.8.2-4	Chamber Parameters (Base Cases)	6.8.2-8
6.8.2-5	Mass and Thickness of Layer Vaporized by X-Rays	6.8.2-11
6.8.2-6	Target Debris Ion Spectra and Masses	6.8.2-13
6.8.2-7	The Function A(Pe) for Different Schemes	6.8.2-20
6.8.2-8	Properties of Liquids Used in Hydrodynamics Calculations	6.8.2-22
6.8.2-9	Base Case Parameters	6.8.2-32
6.8.2-10	Summary of Cases Analyzed	6.8.2-47
6.8.2-11	Properties of SEP-2D SiC-SiC	6.8.2-53
6.8.3-1	Final Blanket Performance Parameters	6.8.3-4
6.8.3-2	Properties of SiC Composite Used in the Stress Calculations	6.8.3-24

LIST OF TABLES – VOL. III (CONT.)

No.	Title	Page
6.8.3-3	Input Used in MISTRAL to Calculate the Blanket Tritium Inventory Results	6.8.3-27
6.8.3-28	Tritium Inventory as a Function of the Activation Energy of Solution for Constant Heat of Adsorption	6.8.3-29
6.8.3-29	Tritium Invetory as a Function of the Heat of Adsorption for Constant Activation Energy of Solution	6.8.3-29
6.8.5-1	Cavity Failure Modes and Consequences	6.8.5-2
6.8.5-2	Zonal Specific Radioactivity as a Function of Post Shutdown Times After 30 Years Full Operation	6.8.5-6
6.8.5-3	Reaction Products Resulting from the Neutron Irradiation of Reactor Materials	6.8.5-8
6.8.5-4	Zone-Averaged ^{14}C Radioactivity Level in Breeding Zone After 30 Years	6.8.5-11
6.8.5-5	Radioactivity of Po^{210} With Other Dominating Nuclides in the Pb Film	6.8.5-20
6.8.5-6	BHP of Po^{210} With Other Dominating Nuclides in the Pb Film	6.8.5-20
6.8.5-7	Summary of Passive Lead Decay Heat Removal Systems	6.8.5-25
6.9-1	Turbine Input Conditions	6.9-4
6.9-2	Auxiliary Power Requirements	6.9-8
6.9-3	Performance	6.9-8
6.9-3	Helium Pipe Costs	6.9-19
6.9-4	Key Helium System Valves	6.9-20
6.10-1	Cooling Tower System Design Parameters	6.10-4
6.12-1	ESECOM Threshold Dose Release	6.12-13
6.12-2	NRC Compliance Parameters	6.12-15
6.13-1	Cost Summaries for Prometheus-L and -H Power Plants	6.13-3
6.13-2	Indirect Cost Factors for Different LSA Values	6.13-5
7-1	Engineering Feasibility Evaluation	7-5
7-2	Scoring System for Engineering Feasibility	7-6
7-3	Safety and Environmental Evaluation Indices and Weights	7-9
7.3.2-1	Physics Feasibilities of Laser and Heavy Ion Drivers	7-15
7.3.3-1	Engineering Feasibility Evaluation	7-17
7.3.5-1	Safety and Environment Comparison	7-22
7.3.6-1	Summary of Key Items of Costs of R&D for Laser and Heavy Ion Reactors	7-24
7.3.7-1	Summary of Scores for the Five Evaluation Areas	
C-1	Economic Requirements and Criteria	C-2
C-2	Commerce Department Gross National Product Implicit Price Level Deflators	C-2
C-3	Prometheus Plant Cost Accounts	C-3
C-4	Application of Learning Curve by Cost Account	C-12
C-5	Site Improvements and Facilities Costs	C-18
C-6	Cost of Materials Used in the FW/B/S Systems	C-23
C-7	First Wall and Blanket Material Costs	C-23
C-8	Cost of Shield Materials Comparison	C-24
C-9	Total Shielding and Vacuum Vessel Costs	C-25
C-10	Primary Structure Weights and Costs	C-26
C-11	Main Heat Transfer and Transport System Costs	C-28
C-12	Reactor Plant Maintenance	C-31
C-13	Turbine Plant Cost Estimating Relationships	C-33
C-14	Target and Target Plant Cost Factors	C-34
C-15	Driver Plant Equipment Costs	C-35
C-16	Prometheus Reactor Plant Cost Factors in Constant 1991 Dollars	C-36
C-17	Cost of Electricity Accounts for the Prometheus Reactor Plants	C-37

Use or disclosure of data
subject to title page restriction

ABBREVIATIONS AND ACRONYMS

ADS	Air Detritiation System
ALARA	As Low As Reasonably Achievable
ANL	Argonne National Laboratory
ARIES	Advanced Reactor Innovations and Evaluation Study
ASE	Amplified Spontaneous Emission
ASWS	Auxiliary Service Water System
ATA	Advanced Test Reactor
AVLIS	Atomic Vapor Laser Isotope Separation
BCSS	Blanket Comparison and Selection Study
BHP	Biological Hazard Potential
BOP	Balance of Plant
BQ	Beam Quality
BRP	Blanket/Reflector/Plena
BW	Bandwidth
CANDU	Canadian Deuterium Uranium (Fission Reactor)
CAS	Compressed Air System
CASCADE	LLNL IFE reactor concept using rotating ceramic-granuale blanket
CCWS	Closed Cooling Water System
CCW	Component Cooling Water
CD	Cryogenic Distallation
CDS	Central Difference Scheme
CEA	Commissariat A L'Energie Atomique
CEBAF	Continuous Electron Beam Accelerator Facility
CECE	Combined Electroysis and Catalytic Exchange
CERN	Centre for European Research, Nuclear
CET	Chemical Equilibrium Thermodynamic Code
CFFTP	Canadian Fusion Fuels Technology Project
CH	Hydro-Carbon based material
COE	Cost Of Electricity
CRAM	(beam) Crossed Raman Accumulator
CTMS	Cooling Tower Makeup System
CS	Constant Spot
CSS	Condensate Storage System
CVD	Chemical Vapor Deposition
CVI	Chemical Vapor Infilteration
CWS	Circulating Water System
DAC	Derived Air Concentrations
DBTT	Ductile-to-Brittle Transition Temperature
DCG	Derived Concentration Guide
DD	Direct Drive (target)
DEMO	Demonstration Power Plant
DESY	Deutsches Elektron-Synchrotron
DOD	Department of Defense
DOE	Department of Energy
DPA	Displacements Per Atom
DPP	Demonstration Power Plant
DRTF	Darlington Tritium Removal Facility
DSTI	Dual-Sided Target Irradiation
DT	Deuterium-Tritium
DTX	Dose-To-Flux
E/O	Electro-Optical
EADS	Exhaust Atmosphere Detritiation System
EBEEL	Electron Beam Excited Excimer Laser
EBEL	Electron Beam Excimer Laser
EBSEDL	Electron Beam Sustained Electric Discharge Laser
EDEL	Electric Discharge Excimer Laser

Use or disclosure of data
subject to title page restriction

ABBREVIATIONS AND ACRONYMS (CONT.)

EDS	Electrical Distribution System
EEDS	Exchaust Effluent Detritiation System
EGDS	Exhaust Gas Detritiation System
ELD	Excimer Driver Laser
ELMO	Excimer Laser Master Oscillator
ELP	Excimer Laser Preamplifier
ELPA	Excimer Laser Power Amplifier
EMRLD	Excimer Mid-range Raman-shifted Laser Device
ENEA	European Nuclear Energy Agency
EP	Exhaust Purfication
EPA	Environmental Protection Agency
EPR	Experimental Power Reactor
EPRI	Electric Power Research Institute
ER	Energy Research
ESECOM	Environmental, Safety, and Economic Aspects of MFE COmmittee
ESCWS	Essential Services Cooling Water System
ETF	Engineering Test Facility
ETHEL	European Tritium Handling and Experimental Laboratory
ETR	Engineering Test Reactor
FCU	Fuel Cleanup Unit
F	Fluence
FEL	Free Electron Laser
FET	Field Effect Transistor
FFTF	Fast Flux Test Facility
FINESSE	Fusion Integrated Nuclear Experiments Strategy Study Effort
FMEA	Failure Modes and Effects Analysis
FODO	Focus-Drift-DeFocus-Drift
FPCCS	Fuel Processing Closed Coolant System
FPS	Freeze Protection System
FPS	Fuel Processing System
FPY	Full Power Year
FRC	Fiber Reinforced Composite
FRRA	Forward Rotational Raman Amplifier
FSMS	Fuel Storage and Management System
FSS	Fuel Storage System
FW/B	First Wall/Blanket
FW	First Wall
FWS	First Wall System
GB	Grain Boundary
GBCS	Glove Box Cleanup System
GBFEL	Ground-Based Free Electron Laser
GC	Gas Chromatographic
GDP	Glow Discharge Polymerization
GIA	Grazing Incidence Angle
GIMM	Grazing Incidence Metal Mirror
HI	Heavy Ion
HIBALL	Heavy Ion Beams and Lithium Lead
HID	Heavy Ion Driver or Driven
HIF	Heavy Ion Fusion
HIFSA	Heavy Ion Fusion Systems Assessment
HIP	Hot Isostatic Pressing
HITEX	High Temperature Isotopic EXchange
HR	High Reflectivity
HVAC	Heating, Ventilation, Air Conditioning
HYLIFE	High-Yield Lithium-Injection Fusion Energy
IADS	Inert Atmospheric Detritiation System

Use or disclosure of data
subject to title page restriction

ABBREVIATIONS AND ACRONYMS (CONT.)

IB	Inverse Bremsstrahlung
ICCOMO	Inertial COfinement systems performance and COst MOdel
ICF	Inertial Confinement Fusion
ICFSS	Inertial Confinement Fusion System Study
ICRP	International Commission on Radiological Protection
ID	Indirect Drive (target)
IDLD	Indirect Drive, Laser Driven (targets)
IDLH	Immediately Dangerous to Life or Health
IDPR	IFE Experimental Power Reactor
IEEE	Institute of Electrical and Electronic Engineers
IEPR	IFE Experimental Power Reactor
IFE	Inertial Fusion Energy
IFERDS	Inertial Fusion Energy Reactor Design Study
ILSE	Induction Linac System Experiment
IS	Inherent Safety
ISI	Induced Spatial Incoherence
ISR	Ion Storage Ring
ISS	Isotope Separation System
IT	Impurity Treatment
ITER	International Thermonuclear Experimental Reactor
IVVS	In-Vessel Vehicle System
JAERI	Japan Atomic Energy Research Institute
JET	Joint European Torus
KfK	Kernforschungszentrum Karlsruhe
LA	Large Aperture
LAM	Large Aperture Module
LANL	Los Alamos National Laboratory
LBL	Lawrence Berkeley Laboratory
LD	Laser Driver or Driven
LIA	Linear Induction Accelerator
LIACEP	Linear Induction Accelerator Cost Evaluation Program
LIBRA	Light Ion Beam Fusion Reactor Conceptual Design Study
LINAC	LINear ACcelerator
LLE	Laboratory for Laser Energetics
LLNL	Lawrence Livermore National Laboratory
LLW	Low Level Radioactive Waste
LMF	Laboratory Microfusion Facility
LOCA	Loss of Coolant Accident
LOE	Level Of Effort
LOFA	Loss of Flow Accident
LRO	Local Raman Oscillator
LSA	Level of Safety Assurance
LTA	Long Term Activation
LTE	Local Thermodylnamic Equilibrium
LV	Low Voltage
M	Blanket or Nuclear Power Multiplication
MARS	Mirror Advanced Reactor Study
MB	Multiple Beam
MBL	Multiple Beam Linac
MCF	Magnetic Confinement Fusion
MD	Molecular Dynamics
MDA	McDonnell Douglas Aerospace
MDESC	McDonnell Douglas Electronic Systems Company
MDMSC	McDonnell Douglas Missile Systems Company
MFE	Magnetic Fusion Energy
MHD	Magneto-Hydromanmic

Use or disclosure of data
subject to title page restriction

ABBREVIATIONS AND ACRONYMS (CONT.)

MINIMARS	Mini-Mirror Advanced Reactor Study
MOPA	Master Oscillator Power Amplifier
MPC_a	Maximum Premissible Concentration in Air
MSM	Master-Slave Manipulator
MTA	Maintainability Task Analysis
MTBF	Mean Time Between Failure
MTTR	Mean Time To Repair
MUF	Mass Utilization Factor
MV	Medium Voltage
NASA	National Aerospace and Space Administration
NECDB	Nuclear Energy Cost Data Base
NET	Next European Torus
NIOSH	National Institute for Occupational Safety and Health
NLO	Non Linear Optical
NMFECC	National Magnetic Fusion Energy Computer Center
NPB	Neutral Particle Beam
NPBIE	Neutral Particle Beam Integrated Experiment
NPR	New Production Reactor
NPRD	Non-electrical Parts Reliability Data
NRC	Nuclear Regulatory Commission
NRF	Neutron Reflection Factor
NRL	Naval Research Laboratory
OEL	Optimized Excimer Laser
OFE	Office of Fusion Energy
ORNL	Oak Ridge National Laboratory
PC	Pulse Compression
PF	Pulse Forming
PFL	Pulse Forming Line
PFN	Pulse Forming Network
PHA	Preliminary Hazards Analysis
PKA	Primary Knock-on Atom
PPPL	Princeton Plasma Physics Laboratory
PRA	Preliminary Risk Analysis
PRF	Pulse Repetition Frequency
PSA	Pressure Swing Adsorption
PWR	Pressurized Water Reactor
PVA	PolyVinyl Acetate
R&D	Research and Development
RA	Resonance Absorption
RA	Resonant Absorption
RAC	Raman Accumulator Cell
RADS	Recirculating Air Detritiation System
RAM	Reliability, Availability, Maintainability
RCRA	Resource, Conservation, and Recovery Act
RCS	Replacement Collision Sequences
RECON	A UCLA Heat and Mass Transfer Computer Model
RF	Radio Frequency
RHR	Reactor Heat Removal
RMCS	Remote Manipulator and Control System
RMS	Remote Monitoring System
RMSD	Remote Manipulator Systems Division (SPAR)
RPE	Reactor Plant Equipment
RPM	Revolutions Per Minute
RR	Repetition Rate
RT	Rayleigh-Taylor (instability)
RT	Room Temperature

Use or disclosure of data
subject to title page restriction

ABBREVIATIONS AND ACRONYMS (CONT.)

SB	Single Beam
SBFEL	Space-Based Free Electron Laser
SBL	Single Beam Linac
SBS	Stimulated Brillouin Scattering
SCR	Silicon Controlled Rectifier
SDI	Strategic Defense Intitative
SDIO	Strategic Defense Intitative Organization
SENRI	A Japanese Fusion Reactor Design Study
SEP	Socie'te' Europeenne de Propulsion
SIRIUS	A Symmetric Direct Drive Laser Fusion Reactor Study (Univ of Wisc)
SLAC	Stanford Linear Accelerator
SNL	Sandia National Laboratories
SOLASE	Experimental Inertial Reactor Study (at Univ of Wisc)
SOW	Statement Of Work
SP	Single Pulse
SPAR	Spar Aerospace, Ltd
SPTF	Single Pulse Test Facility
SRRS	Stimulated Rotational Raman Scattering
SRS	Stimulated Raman Scattering
SSC	Superconducting Super-Collider
SSTI	Single-Sided Target Irradiation
STEM	Storage Tubular Extendible Member
STP	Standard Temperature and Pressure
TARM	Telescoping Articulating Remote Maniupulator
TBCCWS	Turbine Building Closed Cooling Water System
TBR	Tritium Breeding Ratio
TCPSA	Thermally Coupled Pressure Swing Adsorption
TCPSA	Thermally Coupled Pressure Swing Adsroption
TDRF	Threshold Dose Release Fractions
TEXTOR	Tritium Experiment for Technology Oriented Research
TFTR	Tokamak Fusion Test Reactor
TPD	Two Plasmon Decay
TPR	Tritium Production Rate
TRIUMF	Tri-University Meson Facility
TRM	Total Remote Maintenance
TSA	Thermal Swing Adsorption
TSDS	Tritium Storage and Delivery System
TSTA	Tritium System Test Assembly
TVD	Total Variation Diminishing
TWA	Time Weighted Averages
TWI	Target Debris-Wall Interaction
TWG	Target Working Group
UCLA	University of California at Los Angeles
UHS	Ultimate Heat Sink
US	United States
UV	Ultraviolet
VLS	Vapor-Liquid-Solid
VPCE	Vapour Phase Catalytic Exchange
VS	Ventilation System
WD	Water Distillation
WD	Water Detritation System
WJSA	W.J. Schafer Associates
XDL	Times Diffraction Limit
ZS	Zoomed Spot

Use or disclosure of data
subject to title page restriction

TABLE OF CONTENTS – CHAPTER 6.5 through 6.13

Section	Title	Page
6.5	DRIVER SYSTEM DEFINITION	6.5-1
6.5.1	Laser Driver Subsystems	6.5.1-1
6.5.1.1	Excimer Laser Master Oscillator (ELMO)	6.5.1-6
6.5.1.1.1	ELMO Excitation Design	6.5.1-8
6.5.1.1.2	ELMO Performance Characteristics	6.5.1-8
6.5.1.2	Excimer Laser Amplifiers	6.5.1-8
6.5.1.2.1	Electric Discharge Excimer Laser (EDEL) Amplifiers	6.5.1-8
6.5.1.2.2	Electron-Beam Excited Excimer Lasers	6.5.1-10
6.5.1.2.3	Excimer Laser Preamplifier	6.5.1-12
6.5.1.2.4	Excimer Laser Driver	6.5.1-13
6.5.1.2.5	Excimer Laser Power Amplifier	6.5.1-14
6.5.1.3	Raman Accumulator Subsystems	6.5.1-15
6.5.1.3.1	Local Raman Oscillator	6.5.1-18
6.5.1.3.2	Raman Preamplifiers	6.5.1-19
6.5.1.3.3	Raman Accumulator Cells	6.5.1-20
6.5.1.4	SBS Pulse Compressors	6.5.1-23
6.5.1.4.1	Generation of SBS "Seed" Beam	6.5.1-23
6.5.1.4.2	Amplification of Short Duration Stokes "Seed"	6.5.1-23
6.5.1.4.3	Precursor Pulse Generation	6.5.1-26
6.5.1.5	Excimer Laser Gas Flow System	6.5.1-33
6.5.1.6	Laser Driver Optical Subsystems	6.5.1-33
6.5.1.6.1	Laser Beam/Target Alignment System	6.5.1-34
6.5.1.7	Final Optics	6.5.1-36
6.5.1.7.1	Collimating Mirror	6.5.1-36
6.5.1.7.2	Focusing Mirror	6.5.1-37
6.5.1.7.3	Grazing Incidence Metal Mirrors	6.5.1-38
6.5.1.7.4	Laser Beams Propagation Through Target Chamber Atmosphere	6.5.1-38
6.5.1.7.5	Plasma Closure Inside Target Chamber	6.5.1-40
6.5.1.8	Grazing Incidence Metal Mirror	6.5.1-46
6.5.1.8.1	Introduction	6.5.1-46
6.5.1.8.2	Metal Reflectivity and Absorptivity for Laser Light	6.5.1-46
6.5.1.8.3	Radiation Effects on Candidate Materials	6.5.1-48
6.5.1.8.4	Configuration and Material Selection	6.5.1-51
6.5.1.8.5	GIMM Thermal Design	6.5.1-55
6.5.1.8.6	GIMM Mechanical Deformation	6.5.1-56
	References for 6.5.1	6.5.1-61
6.5.2	Heavy Ion (HI) Driver Subsystems	6.5.2-1
6.5.2.1	Single Beam LINAC	6.5.2-9
6.5.2.1.1	Injector	6.5.2-9
6.5.2.2	Acceleration Modules	6.5.1-17
6.5.2.3	Superconducting Magnets	6.5.1-23
6.5.2.4	Cooling and Cryogenics	6.5.1-25
6.5.2.5	Storage Rings	6.5.2-26
	References for 6.5.2	6.5.2-49
6.5.3	Common Driver Subsystems	6.5.3-1
6.5.3.1	Power Supplies	6.5.3-1
6.5.3.2	Vacuum Systems	6.5.3-3
6.5.3.3	Instrumentation and Control	6.5.3-4
6.5.3.4	Driver Maintenance Equipment	6.5.3-7
6.5.3.5	Driver Shielding	6.5.3-8
	Reference for 6.5.3	6.5.3-11
6.6	VACUUM SYSTEM	6.6-1
6.6.1	Laser Driven Reactor Vacuum System	6.6-1
6.6.1.1	General Description	6.6-1
6.6.1.2	System Design	6.6.-2
6.6.2	Heavy Ion-Driven Reactor Vacuum System	6.6-7
6.6.2.1	General Description	6.6-7
6.6.2.2	System Design	6.6-8
	Reference for 6.6	6.6-10

Use or disclosure of data
subject to title page restriction

TABLE OF CONTENTS – CHAPTER 6.5 THROUGH 6.13 (CONT.)

Section	Title	Page
6.7	FUEL PROCESSING SYSTEMS (FPS)	6.7-1
6.7.1	Basic Requirements and Functions	6.7-1
6.7.2	Technology Options	6.7-1
6.7.3	Selection of Reference Process Options – Development Trends	6.7-1
6.7.3.1	Thermally Coupled Pressure Swing Adsorption	6.7-6
6.7.3.2	Laser-Based Hydrogen Isotope Separation	6.7-8
6.7.4	Chamber Exhaust Purification and Impurity Treatment	6.7-10
6.7.4.1	Process Description and Control	6.7-10
6.7.5	Tritium Extraction from Breeder Blanket (PSA)	6.7-12
6.7.5.1	PSA – Functional and Performance Requirements	6.7-12
6.7.5.2	PSA – Process Description and Control	6.7-14
6.7.6	Air Detritiation Systems	6.7-15
6.7.6.1	ADS – Functional and Performance Requirements	6.7-17
6.7.6.2	ADS – Process Description and Control	6.7-19
6.7.7	Inert Atmosphere Detritiation System	6.7-22
6.7.8	Fuel Storage and Management System	6.7-24
6.7.8.1	FSS – Functional and Performance Requirements	6.7-25
6.7.8.2	FSMS – Process Description and Control	6.7-26
6.7.9	Isotope Separation System and Water Detritiated System	6.7-27
6.7.9.1	ISS Functional and Performance Requirements	6.7-28
6.7.9.2	Waste Water Detritiation Options	6.7-29
6.7.9.3	ISS – Process Description	6.7-31
6.7.9.4	Water and Hydrogen Distillation – Control Description	6.7-32
6.7.9.5	Safety Analysis	6.7-35
6.7.10	Heat Transfer Media Detritiation	6.7-35
6.7.10.1	Tritium Extraction from Sodium-Filled Heat Transfer Tube	6.7-37
6.7.10.2	Permeation Through SiC – From Breeder Purge Gas to He Coolant	6.7-38
6.7.11	Solids Removal from First Wall Protection	6.7-39
6.7.12	Tritiated Waste Processing	6.7-40
	References for 6.7	6.7-41
6.8	CAVITY DESIGN AND ANALYSIS	6.8-1
6.8.1	Neutronics Analysis	6.8.1-1
6.8.1.1	Introduction	6.8.1-1
6.8.1.2	Base Case Configuration	6.8.1-1
6.8.1.3	Results	6.8.1-4
	References for 6.8.1	6.8.1-15
6.8.2	First Wall Protection System	6.8.2-1
6.8.2.1	Introduction and Overall Configuration	6.8.2-1
6.8.2.2	Cooling System Thermal-Hydraulics	6.8.2-5
6.8.2.3	X-Ray and Debris Spectra and Energy Deposition	6.8.2-7
	References for 6.8.2.3	6.8.2-14
6.8.2.4	Cavity Hydrodynamics	6.8.2-15
	References for 6.8.2.4	6.8.2-23
6.8.2.5	Cavity Clearing	6.8.2-24
	References for 6.8.2.5	6.8.2-39
6.8.2.6	Film Flow	6.8.2-40
	References for 6.8.2.6	6.8.2-52
6.8.2.7	Mechanical Response and Component Lifetime	6.8.2-53
	References for 6.8.2.7	6.8.2-62
6.8.3	Blanket	6.8.3-1
6.8.3.1	Configuration	6.8.3-1
6.8.3.2	Blanket Neutronics	6.8.3-4
6.8.3.3	Thermal Hydraulics	6.8.3-19
6.8.3.4	Thermo-Mechanics	6.8.3-23
6.8.3.5	Tritium Analysis	6.8.3-26
	References for 6.8.3	6.8.3-30
6.8.4	Primary Shield	6.8.4-1
6.8.4.1	Introduction	6.8.4-1
6.8.4.2	Nuclear Field Attenuation Characteristics of the Shielding Materials Considered	6.8.4-2
	References for 6.8.4	6.8.4-5

Use or disclosure of data
subject to title page restriction

TABLE OF CONTENTS – CHAPTER 6.5 THROUGH 6.13 (CONT.)

Section	Title	Page
6.8.5	Cavity Safety and Environmental Impact	6.8.5-1
6.8.5.1	Introduction	6.8.5-1
6.8.5.2	Radioactivity in the Cavity	6.8.5-2
	References for 6.8.5.2	6.8.5-22
6.8.5.3	Accident Analysis	6.8.5-23
	References for 6.8.5.3	6.8.5-30
6.8.5.4	Summary	6.8.5-31
6.9	HEAT TRANSPORT AND THERMAL ENERGY CONVERSION	6.9-1
6.9.1	Energy Source	6.9-1
6.9.2	Design Rationale	6.9-2
6.9.3	Thermal Cycle	6.9-4
6.9.4	Auxiliary Power	6.9-7
6.9.5	Plant Performance	6.9-8
6.9.6	Steam Generators, Reheaters, and Superheaters	6.9-9
6.9.7	Helium System Piping	6.9-17
6.9.8	Liquid Lead System Piping	6.9-21
	References for 6.9	6.9-21
6.10	BALANCE OF PLANT SYSTEMS	6.10-1
6.10.1	Water Systems	6.10-1
6.10.1.1	Circulating Water System	6.10-1
6.10.1.2	Closed Cooling Water System	6.10-1
6.10.1.3	Auxiliary Service Water System	6.10-2
6.10.1.4	Demineralized Water Makeup System	6.10-2
6.10.1.5	Potable Water System	6.10-2
6.10.1.6	Essential Services Cooling Water System	6.10-2
6.10.1.7	Main Cooling Tower	6.10-3
6.10.1.8	Cooling Tower Water Treatment System	6.10-3
6.10.1.9	Condensate Storage System	6.10-4
6.10.1.10	Chilled Water System	6.10-5
6.10.1.11	Chlorination System	6.10-5
6.10.1.12	Sanitary Waste System	6.10-5
6.10.1.13	Cooling Tower Makeup System	6.10-6
6.10.1.14	Turbine Building Closed Cooling Water System	6.10-7
6.10.1.15	Steam Generator Blowdown System	6.10-7
6.10.1.16	Fresh Water Supply System	6.10-8
6.10.2	HVAC Systems	6.10-8
6.10.2.1	Control Complex Air Conditioning System	6.10-9
6.10.2.2	Containment Cooling System	6.10-10
6.10.2.3	Containment Atmosphere Purification and Cleanup System	6.10-11
6.10.2.4	Auxiliary Building Ventilation System	6.10-12
6.10.2.5	Driver Ventilation System	6.10-12
6.10.2.5.1	Laser Building Ventilation System	6.10-12
6.10.2.5.2	Accelerator Tunnel Ventilation System	6.10-12
6.10.2.6	Turbine Building Ventilation System	6.10-13
6.10.3	Electrical Systems	6.10-13
6.10.3.1	DC Electrical Systems	6.10-13
6.10.3.2	Standby Power Supply Systems	6.10-14
6.10.3.3	120 VAC Systems	6.10-14
6.10.3.4	Medium Voltage and Low Voltage Electrical Distribution Systems	6.10-15
6.10.3.5	Lightning Protection	6.10-15
6.10.3.6	Station Grounding System	6.10-16
6.10.3.7	240 kV System	6.10-17
6.10.4	Auxiliary Systems	6.10-17
6.10.4.1	Fire Protection System	6.10-17
6.10.4.2	Compressed Air System	6.10-18
6.10.4.3	Process Sampling System	6.10-19
6.10.4.4	Equipment and Floor Drainage Systems	6.10-20
6.10.4.5	Communications Systems	6.10-20
6.10.4.6	Lighting Systems	6.10-21

Use or disclosure of data
subject to title page restriction

TABLE OF CONTENTS – CHAPTER 6.5 THROUGH 6.13 (CONT.)

Section	Title	Page
6.10.4.7	Auxiliary Steam System	6.10-22
6.10.4.8	Freeze Protection (Electric Heating) Systems	6.10-23
6.10.4.9	Sanitary Drainage and Vent System	6.10-23
6.10.4.10	Bulk Gas Storage System	6.10-23
6.10.4.11	Decontamination Facilities	6.10-24
6.10.5	Site Preparation	6.10-25
	Reference for 6.10	6.10-25
6.11	REMOTE MAINTENANCE SYSTEMS	6.11-1
6.11.1	Manipulator Technology	6.11-1
6.11.1.1	Master/Slave Telemanipulators	6.11-1
6.11.1.2	Long-Reach Configurations	6.11-7
6.11.1.3	Large Payload Manipulators	6.11-10
6.11.2	Transport/Handling Technology	6.11-10
6.11.2.1	Mobile Platforms	6.11-10
6.11.2.2	Crawlers/Inspection Robots	6.11-10
6.11.2.3	Tracked/Legged Robots	6.11-11
6.11.2.4	Overhead Systems	6.11-11
6.11.2.5	Elevator Systems	6.11-11
6.11.3	Automatic Control Technology	6.11-11
6.11.3.1	Sensing and Control	6.11-11
6.11.3.2	Robot "Intelligence" and Task Level Control	6.11-15
6.11.3.3	Human-Machine Interface Technology	6.11-15
6.11.4	Tools	6.11-15
6.11.5	Principal Plant Manipulators	6.11-15
6.11.5.1	Overhead Bridge-Mounted Manipulator	6.11-15
6.11.5.2	Deployable Heavy Lift Manipulator	6.11-18
6.11.5.3	Mobile Heavy Duty Manipulator	6.11-18
6.11.5.4	Two-Armed Dexterous Manipulator	6.11-21
6.11.5.5	Small Power Manipulator	6.11-21
6.11.5.6	Steam Generator Robot	6.11-24
	References for 6.11	6.11-25
6.12	SAFETY AND ENVIRONMENT	6.12-1
6.12.1	Occupational Radiation Exposures	6.12-2
6.12.1.1	Radiation Zone Definitions	6.12-3
6.12.1.2	In-Plant Radiation Monitoring System	6.12-5
6.12.2	Off-Site Radiation Exposures	6.12-7
6.12.2.1	Normal Operation Release Estimate – HT vs. HTO	6.12-8
6.12.2.2	Effluent Monitoring System	6.12-10
6.12.3	Off-Site Impacts From Accidents	6.12-10
6.12.3.1	LSA Determination	6.12-11
6.12.3.2	NRC Compliance	6.12-14
6.12.4	Waste Disposal	6.12-15
6.12.4.1	Waste Volume Estimates	6.12-17
6.12.5	Non-Radiological Impacts	6.12-17
6.12.6	Safety and Environment Conclusions	6.12-18
	References for 6.12	6.12-19
6.13	ECONOMICS	6.13-1
	References for 6.13	6.13-7

Use or disclosure of data
subject to title page restriction

6.5 Driver System Definition

Two driver designs have been developed for the IFE Reactor Design Studies program: a 4 MJ/pulse KrF Laser driver and a 7.8 MJ/pulse heavy ion driver. These IFE drivers (and their supporting subsystems) are described in this section.

A key element in the Prometheus reactor driver designs was to implement recent advances in high energy laser and heavy ion accelerator technologies. This enhanced performance, reduced risk, and promoted cost-effectiveness.

Prometheus-L – The MDA team selected an economical, reliable KrF laser amplifier design which is compatible with the non-linear optical (NLO) techniques pioneered during the past decade. The NLO techniques include:

(1) Use of stimulated rotational Raman scattering (SRRS) with large aperture beams, high energy beam synthesis, correction of dynamic optical beam distortions, and intensity smoothing to minimize UV optical damage.
(2) Replacing elaborate, multiple beam pulse compression systems with simple stimulated Brillouin scattering (SBS) pulse compressor driven by an electronically-controlled seed generator. This resulted in significant cost savings.

Implementation of NLO beam conditioning technologies has a profound effect on the Prometheus KrF laser driver design. These novel technologies permit the KrF excimer laser amplifiers to be optimized for performance and economy without having to meet simultaneously a very high output energy level (~200 kJ) or ambitious beam quality (BQ ~1) goal. The NLO technologies permit the Prometheus KrF laser driver to have superior operational characteristics at lower cost than conventional KrF laser designs.

Prometheus-H – A new look was taken at previous heavy ion driver design concepts together with some innovative techniques involved with superconducting magnets, auto-neutralization, self-focusing of heavy ion (HI) beams, etc. Key elements of the heavy ion driver include these innovative elements:

(1) A single LINAC operated in the burst mode to generate a series of HI pulses,
(2) Sequential pulses stored in appropriate storage rings,
(3) Triplet focusing magnets to collapse two sets of HI beams into compact beam bundles inside pre-ionized, self-pinched channels for transport to the target.

Use or disclosure of data
subject to title page restriction

The success of this single accelerator/storage ring approach is heavily dependent upon improvements in Metglas to reduce core losses. Further cost reductions are possible by exploring a number of attractive attributes possessed by the Prometheus heavy ion driver design. These attributes may also help reduce costs of other plant elements. For example, the self-focused HI beam channel transport through the reactor target chamber shield, blanket, and wall to the indirect-drive DT target needs only two small entrance apertures. This improvement greatly simplifies the radiation shielding problems and inproves the first wall and blanket design and performance.

Prometheus drivers are designed to minimize the cost of electricity by employing redundancy where feasible in the key driver subsystems. These subsystems are designed in such a manner that the overall Prometheus driver requirements are met by using a multiple number of coordinated subsystems. The subsystems were optimized to maximize performance and cost-effectiveness, resulting in a more reliable and economical driver design.

The interrelationships of these Prometheus driver subsystems are described in detail in the subsequent sections.

Use or disclosure of data
subject to title page restriction

6.5.1 Laser Driver Subsystems - The baseline Prometheus laser driver is composed of the following major subsystems:

(1) Excimer laser master oscillator (ELMO)
(2) Electric discharge excimer laser (EDEL) amplifiers (consisting of the excimer laser preamplifiers (ELPs), excimer laser drivers (ELDs), and excimer laser power amplifiers (ELPAs))
(3) Raman accumulators (together with their Stokes seed generators)
(4) SBS Pulse Compression Cells (together with their "chirper" seed generators)
(5) E/O Switchyard and Delay Lines
(6) Excimer Laser and NLO Cell Gas Flow Subsystems
(7) Beam Coupling Optics, Image Relaying, and Final Optics

A block-diagram of the Prometheus KrF laser driver architecture is provided in Figure 6.5.1-1. This figure also indicates the energy level, and beam pulse length, and number of components in each driver element.

As indicated in Figure 6.5.1-1, the 60 Prometheus KrF laser driver output beams are initiated with a single, carefully timed and synchronized 1 J pulse from the ELMO, followed by division of this initial ELMO beam into 1,020 beamlets by the beamsplitter array, followed by two tiers of ELPs (totaling 1,080 amplifiers) which amplify the beamlet energies up to 4 J, 1,020 ELDs which further increase the beamlet energies to 200 J, 60 ELD beams used to generate sixty 30 J Stokes seed beams, and the 960 ELPAs producing output energies of 6 kJ each. The 60 main beams are dominated by a NLO architecture—the Raman accumulator architecture is repeated 60 times. Arrays of 16 of the ELPA 6 kJ beams are injected into each of the sixty 120x120 cm aperture Raman accumulators prior to introduction into each of the 60 SBS pulse compressors. Following pulse compression and temporal tailoring, these 60 pulse-compressed beams are collimated and focused through the final focusing optics to generate the laser pulses which deliver 4 MJ of total energy on the direct-drive targets. A similar KrF laser driver system could be used for irradiation of indirect-drive targets.

The example illustrated in Figure 6.5.1-1 represents our preferred baseline design choice for the work-horse excimer laser chains; i.e., the case in which 960 moderate energy (~6 kJ), electric-discharge excimer laser (EDEL) amplifiers are used as the pump lasers for the 60 Raman accumulators. As noted above, also assumed in Figure 6.5.1-1 is the Prometheus laser driver configuration appropriate for illumination

Use or disclosure of data
subject to title page restriction

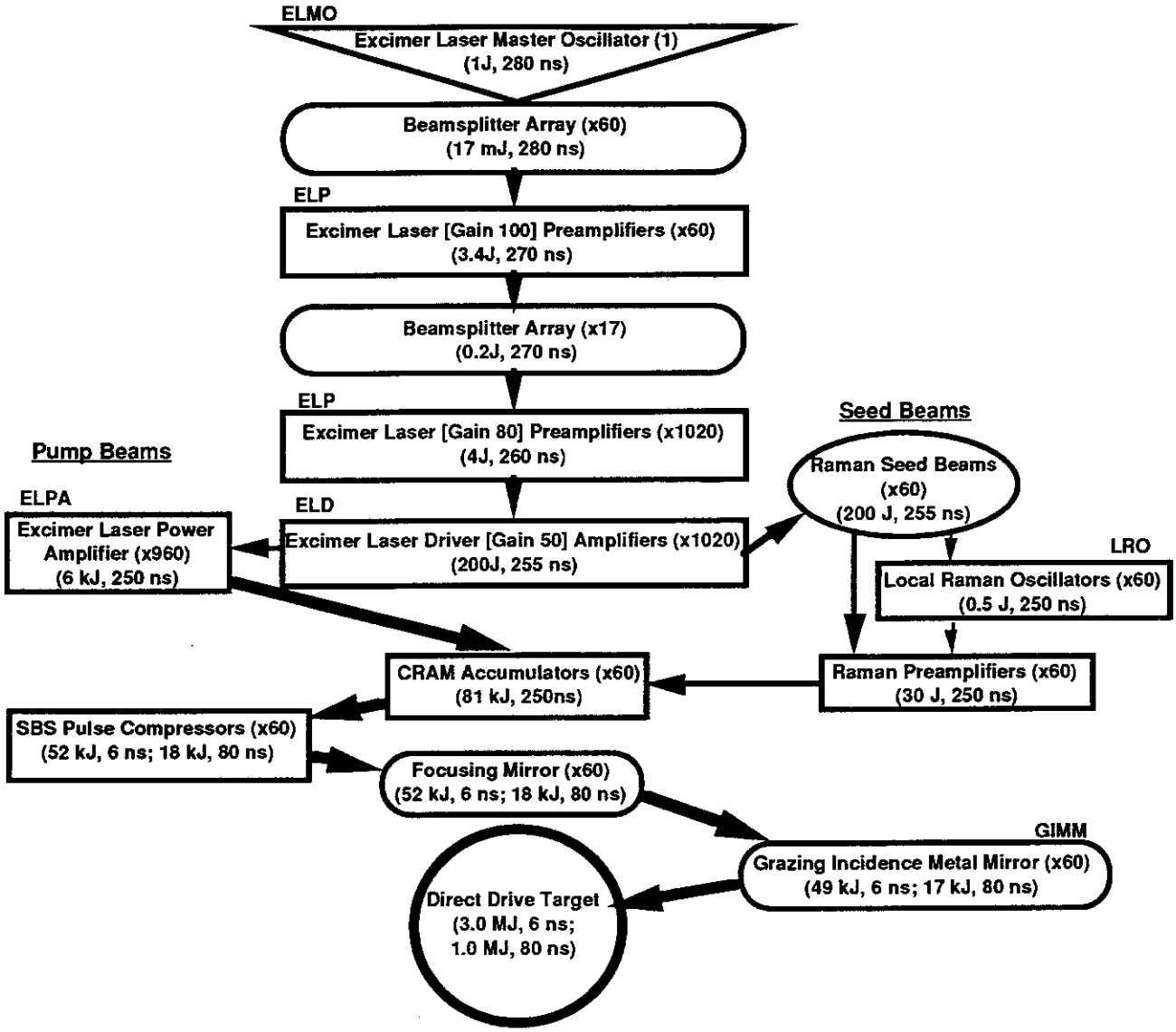

Figure 6.5.1-1 This block diagram illustrates how the PROMETHEUS ELMO pulses are beam-divided, amplified, accumulated, pulse-compressed, and focused onto the DT target.

of a direct-drive DT target (indirectly-driven laser targets require a different final focus laser beam configuration than shown). In order to illustrate the working relationships of these laser driver subsystems relative to each other, an overall simplified schematic of the Prometheus laser driver from the ELMO through the beamsplitter arrays, the ELPs, the ELDs, and the ELPAs to the Raman Accumulator is shown diagramatically in Figure 6.5.1-2.

Use or disclosure of data
subject to title page restriction

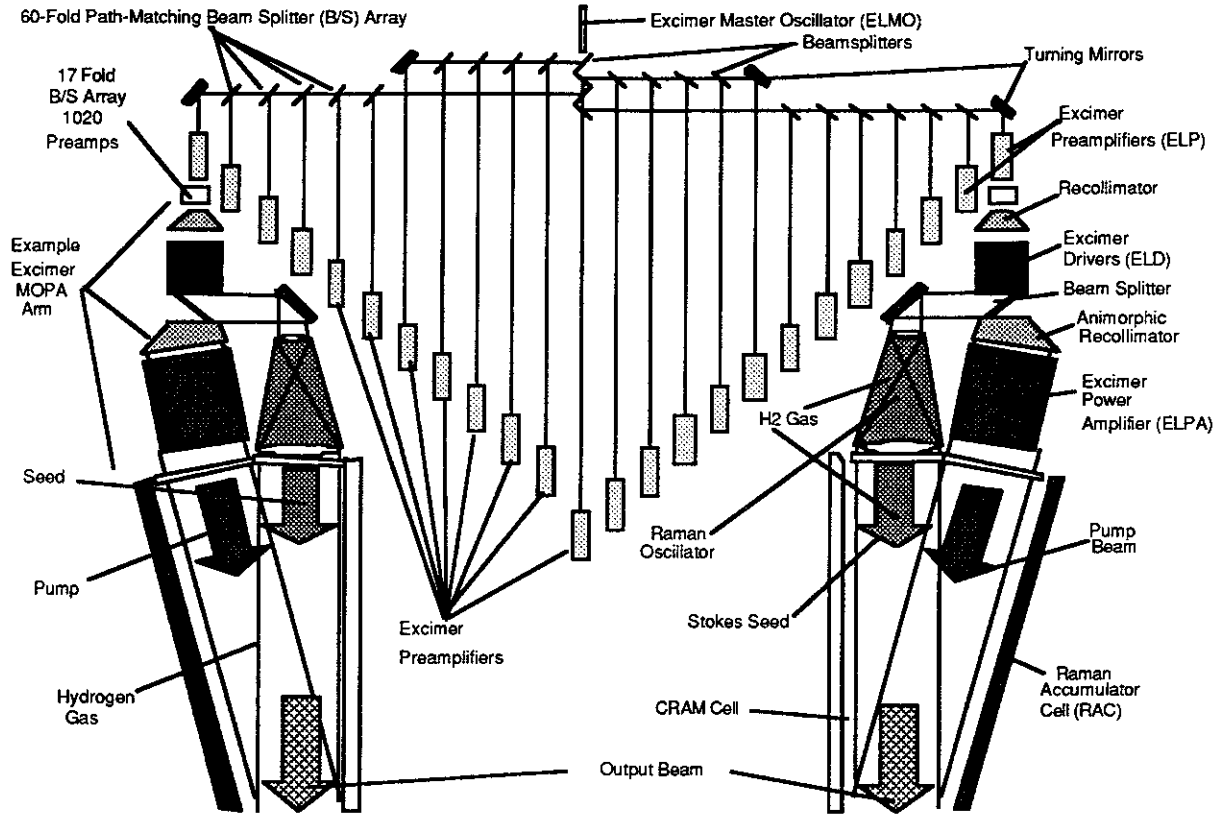

Figure 6.5.1-2 The 1 J output pulse from the ELMO is divided into 1020 beamlines, amplified by ELPs, ELDs, and ELPAs. The Stokes seeds are generated and injected into the Raman accumulators along with the main output beams.

In Figure 6.5.1-2, following division of the original single ELMO beam into 1,020 beamlets, the ELMO output pulse determines the phase, timing, intensity, etc., of the square output beams from the 1,020 ELPs, 1,020 ELDs, and 960 ELPAs. There are 60 additional excimer laser amplifier chains consisting of 60 ELPs and 60 ELDs. A small amount (0.5 J) of energy is split off from the 200 J output beams from each ELD and is fed into a Raman seed generator cell, path-matched with the original output beam from the ELD. This 100 mJ Stokes seed is then spatially filtered to improve beam quality, amplified in a Raman preamplifier having a gain of 300 up to a level of ~30 J, collimated to a 120-cm aperture, and injected into the 120x120-cm square aperture Raman accumulator. The 4x4=16 ELPA pump beams enter the Raman accumulator cell (RAC) at a slight angle, $\theta \sim 5^{o}$, to the RAC axis. In the baseline Prometheus excimer laser driver design, these 16 ELPA beams (each having an energy of ~6 kJ and a pulse duration of 250 ns (for EDEL ELPAs) or 500 ns (for EBEL ELPAs)) have square apertures of approximately 30x30 cm. These beams are combined (or "accumulated") in the large aperture (120 cm) Raman accumulator cells to yield an output beam of ~80 kJ. Note that electron-beam excimer laser (EBEL) amplifiers are an alternative technology which could be employed. This topic is discussed thoroughly in Section 6.5.1.2.2.

Use or disclosure of data
subject to title page restriction

As discussed in Section 6.5.1.4, the beam qualities of the output beams from the ELPAs are not expected to be high, owing to the turbulent flow of gases through the excimer amplifiers, dynamic gas disturbances caused by excimer laser excitation, and other disturbing factors. However, the beam-crossed Raman (or CRAM) accumulator is able to improve the resultant beam quality of the excimer laser pumps considerably, so that the output beams from the Raman accumulators can be of excellent quality.

Following the Raman accumulators, each of the sixty ~80 kJ beams is then injected into each of the 60 SBS pulse compressors, as shown in the schematic diagram in Figure 6.5.1-3.

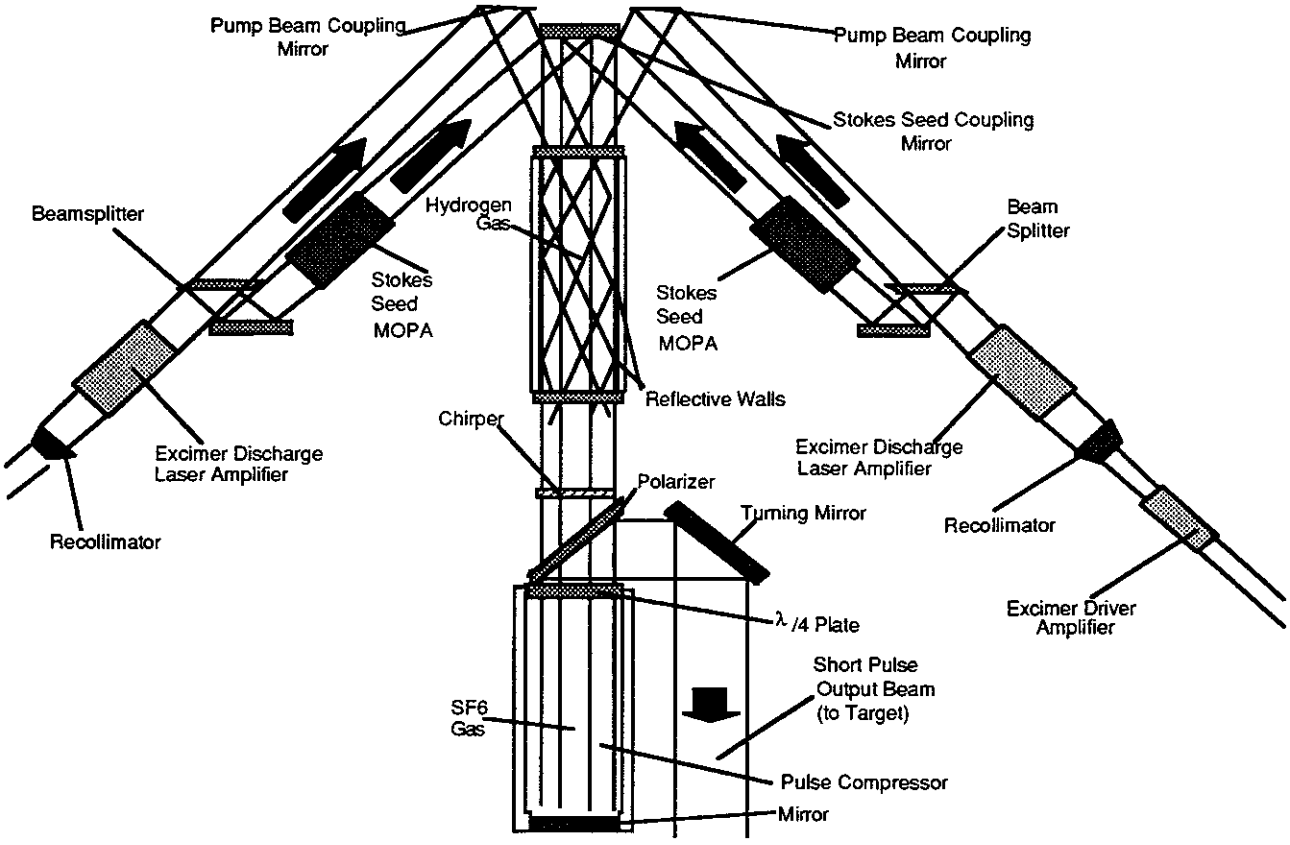

Figure 6.5.1-3 Following the conversion of the excimer pump beams in the Raman accumulators, the long 250-ns (for EDELs) or 500-ns (for EBELs) pulses are injected into the SBS pulse compressor cells where ~65% of the energy is converted into a 6-ns pulse using a ramped Stokes SBS seed.

As shown in Figure 6.5.1-3, the large diameter (~120 cm), high energy square output beams from the Raman accumulators are directed through a time-varying electro-optical modulator "chirper" which places a specific acoustical frequency shift on the leading 6-ns edge of the Raman accumulator pulse. This "chirper" element generates the Stokes seed for the stimulated Brillouin scattering (SBS) pulse compression cell.

Use or disclosure of data subject to title page restriction

The "chirper" is operated in a ramped mode to permit control over the compressed pulse shape (see Section 4.2.1 for a description of the variety of possible output pulse shapes obtained from SBS pulse compressor computer simulations).

Only approximately 70% of the laser energies in the 250 ns (EDEL) or 500 ns (EBEL) Raman accumulator pulses are converted into the short, 6 ns output pulses in the SBS pulse compressor. The remaining 30% of the beam energy remains in a long pulse duration (<250 or <500 ns respectively), is described as the "depleted SBS pump beam," and is available to supply the long, precursor pulse specified for the direct-drive DT target. Details of how this is accomplished can be found in Section 4.2.1. A precursor pulse has been defined as containing 35% of the total laser driver energy in the direct-drive target illumination requirements set forth by the Target Working Group.

Following pulse compression in the SBS cells, each of the 60 square laser beams is directed through an electro-optical switchyard for pulse tailoring, and then directed in 60 beams (assuming direct-drive) onto the DT target. A simplified, end to end diagram of the overall Prometheus laser driver system from master oscillator to DT target is provided in Figure 6.5.1-4.

The schematic diagram, Figure 6.5.1-4, illustrates the approximate optical arrangements of a single arm of the laser driver subsystems. For reasons of clarity, this figure does not illustrate the actual proposed Prometheus configuration of the laser driver subsystems that are described in Section 6.3.

The functions of each of these laser driver subsystems are briefly described in the following sections.

Use or disclosure of data
subject to title page restriction

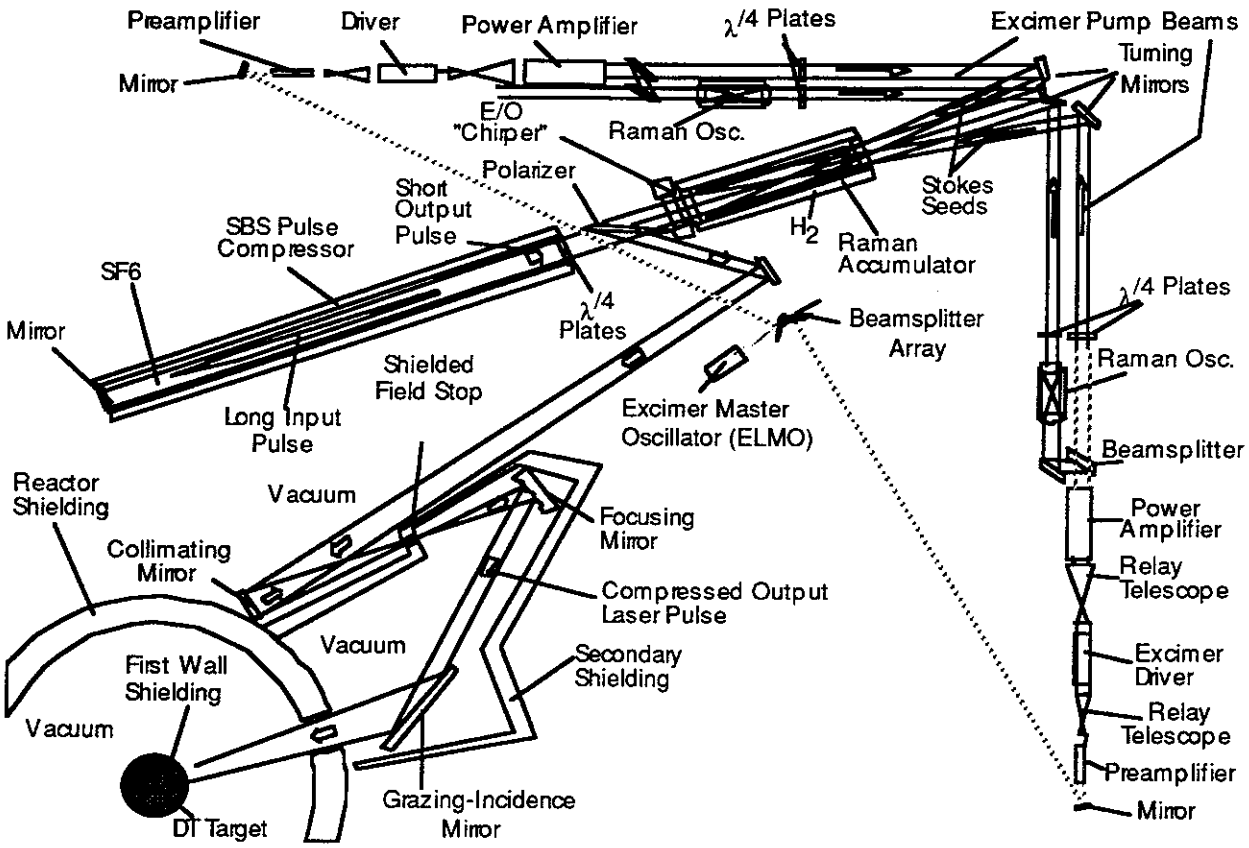

Figure 6.5.1-4 The output pulse of Prometheus laser driver is initiated at the ELMO, amplified by the EDELs, Raman converted in 60 Accumulator Cells, Pulse Compressed in 60 SBS Cells, and Focused onto the Direct-Drive Target with the Final Focus Mirror and the Grazing Incidence Mirror.

6.5.1.1 Excimer Laser Master Oscillator (ELMO) - As indicated in Figure 6.5.1-1, the generation of the Prometheus KrF laser driver's 4 to 6 MJ output pulse begins with the KrF excimer laser master oscillator (ELMO) emitting an initial pulse of ultraviolet (UV) laser light at $\lambda = 248$ nm (for KrF). The use of ArF at $\lambda = 194$ nm could also be used in this application. This pulse is first divided into 16x60 = 960 beam lines by a beamsplitter array, and then is successively amplified by KrF excimer laser preamplifiers (ELPs), excimer laser driver (ELDs), and excimer laser power amplifiers (ELPAs) to deliver output pulses of approximately 6 kJ each (960 beam lines). The output pulse from the ELMO needs to meet a series of requirements as summarized in Table 6.5.1-1.

The ELMO is the crucial timing and synchronizing element in the Prometheus laser driver. Although it can be triggered by signals derived from the DT target launching facility (see Section 6.4.4), the Prometheus laser driver computer control system monitors the output pulse shapes from the ELMO in multiple locations along the beam

Use or disclosure of data subject to title page restriction

lines to assure that the input pulse shapes to the excimer laser amplifiers are appropriate for achieving the desired output pulse shapes and energies.

The ELMO characteristics are carefully selected to permit the excimer laser power amplifiers to be converted efficiently in the Raman accumulators and pulse-compressed in the SBS cells, thereby permitting the laser driver to generate the precise output pulse format required for DT implosion. In general, the spectral, temporal, and power characteristics of the ELMO output pulse will be changed in the process of efficient power extraction from the excimer laser power amplifiers (ELPAs), and thus the ELMO pulse characteristics must be deconvolved in order to produce the desired results at the ELPA output apertures.

Since the laser pulses originate with the ELMO, it is crucial that this subsystem be at least doubly redundant in order to prevent failure of the ELMO from forcing a shutdown of the reactor. Thus, it is recommended that three ELMOs be on line at the same time with one unit active, one unit on standby, and one unit capable of being activated in a matter of seconds.

The general specifications for the ELMO are summarized in Table 6.5.1-1.

Table 6.5.1-1 Prometheus ELMO Specifications

Parameter	Nominal Value	Unit of Measure
Number of Units	3 (for redundancy)	
Wavelength	248	nm
EDEL Mode Pulse Duration	280 (650, EBEL)	ns
Output Energy	1	J
Bandwidth	5	GHz
Polarization State	Linear	
Aperture	1x1	cm
Gain Length	100	cm
Output Fluence	1	J/cm^2
EDEL Mode Output Intensity	3.8 (1.5, EBEL)	MW/cm^2
Repetition Rate	5	Hz
Mean Firings Between Failures	10^{10}	
Number of 50% R Beamsplitters	490	
Number of Output Beamlines	1020	
Number of Diagnostic Beamlines	10	

The specific parameter values listed in Table 6.5.1-1 represent nominal values appropriate for high performance from the Raman and SBS cells. Thus, for example, the bandwidth of the ELMO output pulse can be varied over a wide range, from a minimum of a few GHz to a maximum of more than 1000 GHz (10^{12} Hz). Similar adjustments can be made in the other parameters to support different excimer laser driver design points.

Use or disclosure of data
subject to title page restriction

6.5.1.1.1 ELMO Excitation Design - The ELMO excitation design is similar to that described below for the ELP, ELD, and ELPA units. Depending upon the excimer laser technology, iEDELs or EBELs, each amplifiers will conform to one of these two general categories.

6.5.1.1.2 ELMO Performance Characteristics - The ELMO is designed to be a versatile laser pulse generator with wide bandwidth ranges, output energy, and polarization state. Pulse durations are typically selected for the type of excimer laser chain (EDEL or EBEL) and are corrected for amplifier saturation in the excimer amplifiers, shortening the output pulse durations.

6.5.1.2 Excimer Laser Amplifiers - There are three general types of excimer laser amplifiers proposed for use in the Prometheus KrF laser driver. These are the excimer laser preamplifiers (ELPs), the excimer laser drivers (ELDs), and the excimer laser power amplifiers (ELPAs). In addition to these excimer laser amplifier types, there are also two possible choices of excimer laser excitation: electron beam excimer lasers (EBELs) and electric discharge excimer lasers (EDELs). These two types of excimer laser amplifiers will be described and each of these different excimer laser amplifier sizes will be briefly described below.

6.5.1.2.1 Electric Discharge Excimer Laser (EDEL) Amplifiers - The EDEL amplifiers are a class of amplifier for which the principal excitation technique of the excimer gas is a preionized electric discharge. In this geometry, an ionization mechanism (such as ultraviolet light, an electron beam, etc.) produces a sufficient ion density in the active medium to permit an efficient volumetric discharge to excite the upper laser level of the KrF (or ArF) excimer molecule. The primary source of excitation energy in this geometry is provided by the electric discharge (and its external pulsed power circuit).

A schematic cross-sectional diagram of an EDEL prototype amplifier excitation geometry is shown in Figure 6.5.1-5.

Use or disclosure of data
subject to title page restriction

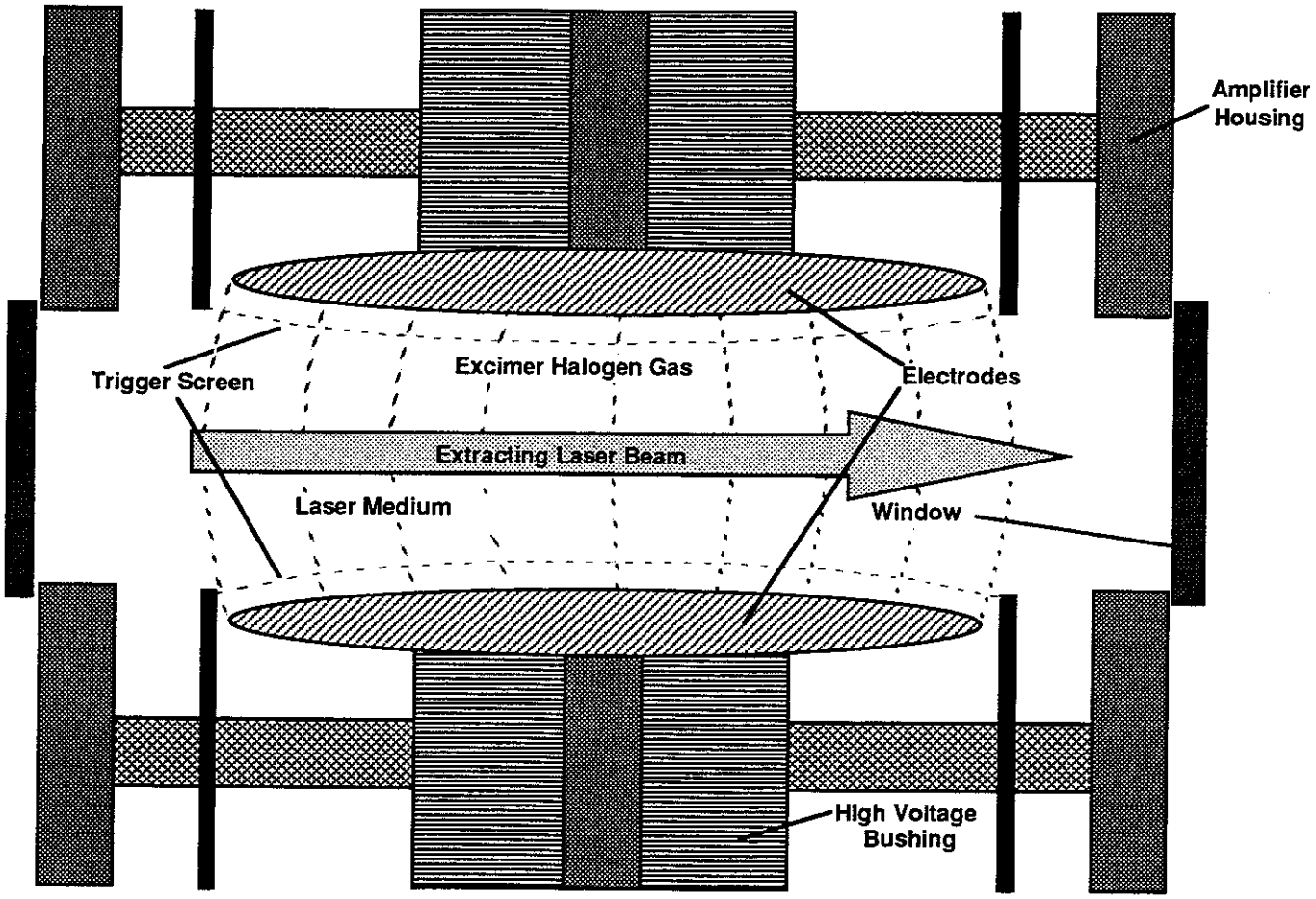

Figure 6.5.1-5 The electric discharge excimer laser (EDEL) excitation geometry provides for direct excitation of the KrF excimer via electric discharges between electrodes immersed in preionized volumes.

Note that the output apertures of these EDEL amplifiers are typically rectangular or square because the excitation geometry is rectangular. Theoretical studies[1,2] of the EDEL have suggested that increased laser amplifier pumping efficiencies could be achieved with direct electric discharge excitation of the excimer fuel. This increased efficiency appears promising for the following reasons:

(1) Excitation of the excimer gas occurs by direct contact with the electric discharge between the electrodes with no electron energy losses in a vacuum barrier (foil, Hibachi, etc.).
(2) Excimer laser excitation in an EDEL is expected to occur along the neutral channel[2] with the discharge optimized to populate the upper laser level of the 248 nm transition, thereby reducing the number of excited states generated in the active medium to only those leading to the appropriate inversion density.

Use or disclosure of data
subject to title page restriction

(3) Reduced heating of the laser gas by the discharge current should occur with excitation along the neutral channel, thereby reducing gas dynamic-induced deterioration of amplifier beam quality.

There are a number of disadvantages associated with direct electric discharge excitation. These include:

(1) Only relatively small cross-sectional diameters (<35 cm) are feasible with electric discharge excitation, thereby limiting the output energies of the laser amplifiers to values of approximately 6 kJ. Optimized EDELs may produce even less energy.
(2) Instabilities arise in the electric discharge owing to temporal impedance changes caused by consumption of fluorine,[2] thereby limiting the pulse duration of the laser and increasing the cost of the pulsed power.

It is important to recognize, however, that the preceding discussion of EDELs is primarily based upon initial theoretical work, and both additional analysis and significant experimental EDEL development is essential if the relative promise of a KrF (or ArF) EDEL is to be properly assessed.

6.5.1.2.2 Electron-Beam Excited Excimer Lasers (EBEL) - Although the baseline Prometheus-L KrF laser driver design does not include the use of e-beam excited excimer lasers, considerable research and development has been carried out on these devices[3,4,5,6] and their inclusion in a future ICF laser driver design may occur if some of the more pressing technological problems with the amplifiers can be solved.

In the case of e-beam excited excimer lasers (EBELs), the entire excitation energy of the amplifier volume is delivered by relatively high energy electrons (<1.5 MeV), delivered at relatively high currents (~1 MA), transmitted through a foil barrier between the excimer fuel and the high vacuum of the electron beam machines.[5,6,7] This geometry is very useful for exciting relatively large volumes of gas (cubic meters) with large amplifier apertures (~1 m). Like the EDEL excitation geometry described above, the output apertures of EBELs tend to be rectangular or square.

Electrons having energies >0.6 MeV can produce serious radiation effects, such as the generation of γ-rays, photo-disintegration of nuclei, formation of color centers in transmissive optics (such as EBEL amplifier windows), etc. In addition, the energetic e-beams may excite excimer and other atomic energy levels which do not lead to the generation of an inversion density at the desired upper laser level of KrF (or ArF). A cross-sectional diagram of an EBEL prototype amplifier excitation geometry is shown in Figure 6.5.1-6.

Use or disclosure of data
subject to title page restriction

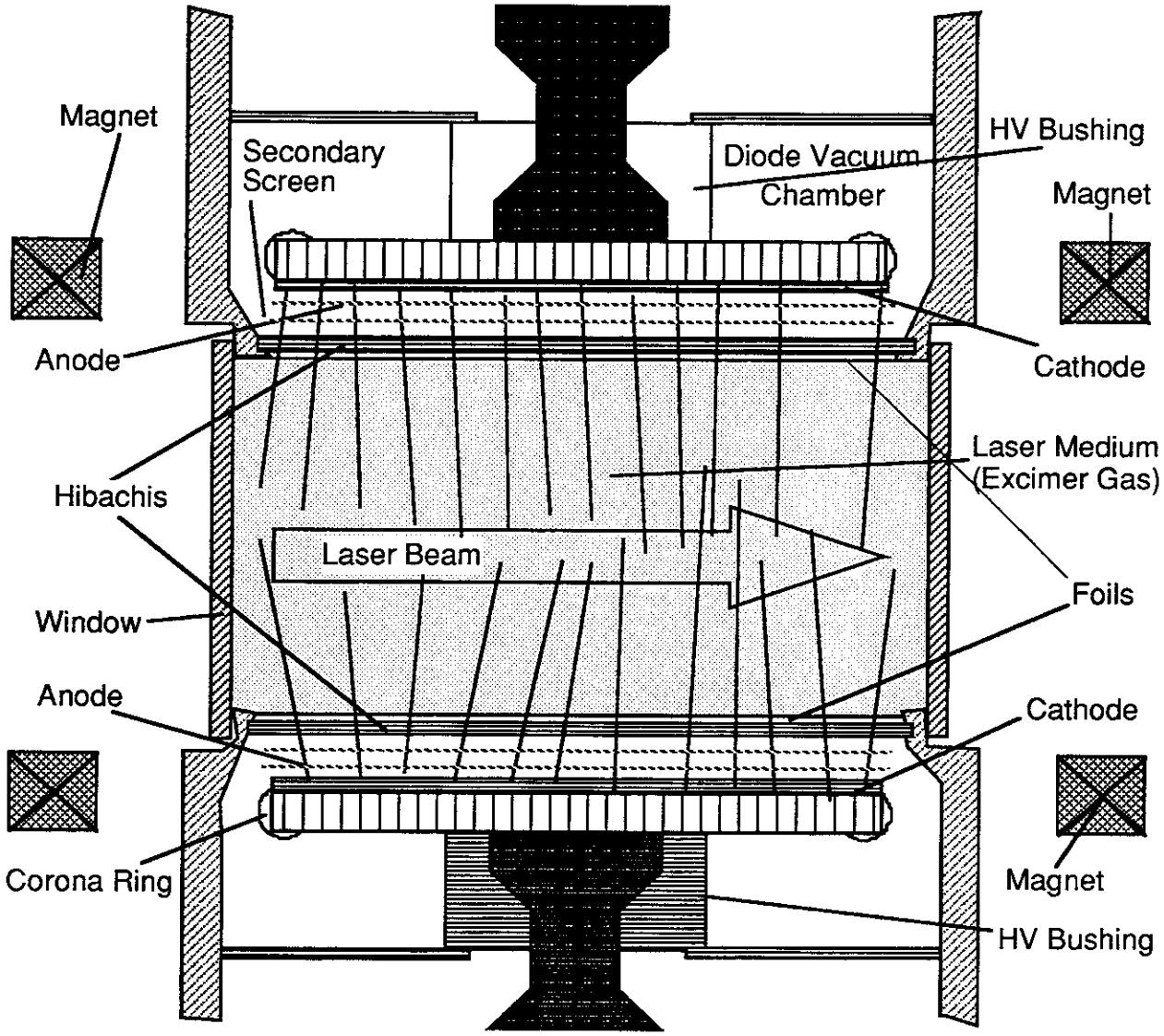

Figure 6.5.1-6 The electron-beam excited excimer laser (EBEL) excitation geometry permits larger volumetric excitation of the KrF excimer via direct e-beam excitation transmitted through a Hibachi and foil vacuum barrier.

As shown in Figure 6.5.1-6, the high energy (~1 MeV), high current (~1 MA) electron beams are generated in a high vacuum diode adjacent to a thin foil supported on a mechanical structure referred to as a Hibachi. These high energy, high current beams must then be transmitted through the thin foils (assuming double-sided illumination, as illustrated) and Hibachi structures where they subsequently interact with the Kr, F_2, Ar, etc., gases located at approximately a total pressure of 1 atm (760 torr). Under these conditions, a large number of excited states are created in the newly formed KrF excimer molecules. Some of these excited states lead to the formation of an inversion density for the desired λ_{laser} = 248 nm (or λ_{laser} = 194 nm) transition(s). Excitation of

Use or disclosure of data subject to title page restriction

other energy levels in the excimer fuel ends up as heat which may cause laser beam quality problems.

Advantages associated with e-beam excitation of excimer laser amplilfiers are:

(1) Large apertures (D ~ 1 m) and large volumes (V ~ 2 m^3) can be excited with relatively high uniformity.
(2) Relatively long pulses can be used (τ ~ 600 ns) to excite the excimer gas, thereby relaxing pulsed power requirements.
(3) A relatively large number of experiments have been carried out demonstrating the efficiency of the excitation technique.

Some disadvantages to the EBEL are:

(1) Transmission of high voltage, high current electron beams through thin foil/Hibachi structures has proven to cause reliability problems.
(2) If foil rupture occurs, the vacuum diode is flooded with hot, fluorine-containing fuel from the gain volume of the laser amplifier. As a consequence, damage can occur to the cathode, high voltage bushing, etc., increasing repair cost and time.
(3) Although the EBEL can theoretically be constructed at large apertures and volumes (Advantage #1), amplified spontaneous emission (ASE) and parasitic oscillations can occur in these larger excimer amplifier volumes, thereby reducing efficiency.
(4) Since the e-beams are transmitted through foil/Hibachi structures and excite numerous energy levels which do not result in achievement of the specific inversion density appropriate for the desired laser transitions (λ_{laser} = 248 nm [or λ_{laser} = 194 nm]), reduced pumping efficiencies and lowered beam qualities can be expected.

The Prometheus-L KrF laser driver baseline design excludes large EBELs because of their catastrophic failure modes, potentially serious impact on reactor operation if a failure occurs (owing to the 1% direct-drive target illumination uniformity requirement), and unproven reliability for a large number of high quality amplifier firings (~10^9).

6.5.1.2.3 Excimer Laser Preamplifier (ELP) - The purpose of the excimer laser preamplifier (ELP) is to amplify the relatively weak beamsplitter-divided beams from the ELMO to a level sufficient to drive the ELDs to their specified output energies. The specifications for the ELP are provided in Table 6.5.1-2 (with a possible future substitution of ArF).

It should be noted that there are 960 excimer laser amplifier chains which generate the ~5.9 MJ of energy directed into the 60 Raman accumulator cells (RACs). In addition, there are 60 excimer laser chains (using 60 ELPs and 60 ELDs) which drive the Stokes seed generators for the RACs.

Table 6.5.1-2 Prometheus ELP Specifications

Parameter	Nominal Value	Unit of Measure
Number of Units	1020	
Wavelength	248	nm
EDEL Mode Pulse Duration	270 (620, EBEL)	ns
Input Energy	0.04	J
Output Energy	4	J
Gain	100	
Polarization State	Linear	
Aperture	1x1	cm
Gain Length	200	cm
Output Fluence	4	J/cm^2
Anode Voltage	100	kV
Beam Current	1.6	kA
Fuel Pressure (Kr, F_2, Ar)	760	torr
Number of Firings between Failures	10^{10}	
EDEL Mode Input Intensity	0.16 (0.08, EBEL)	MW/cm^2
EDEL Mode Output Intensity	16 (8, EBEL)	MW/cm^2
Repetition Rate	5	Hz

ELP Excitation Design - In order for the excimer laser amplifier chains to function efficiently, all types must have similar pumping pulse durations, spectral outputs, etc. Thus the ELP excitation design is similar to that of the ELMO, ELD, and ELPA units. A further consideration which is pending is the substitution of ArF for KrF as possibly being more efficient if corresponding transmissive optics problems can be solved.

Depending upon whether the excimer laser technology is based upon electric discharge or e-beam excited excimer lasers, each of the excimer amplifier types will conform to one of these two general categories.

ELP Performance Characteristics - The ELP is a general purpose excimer laser preamplifier designed to increase power levels in the Prometheus excimer laser chains to levels achieve efficient power extraction from the laser amplifiers. Excitation pulse durations are selected to be appropriate for the type of excimer laser chain (EDEL or EBEL) and are corrected for amplifier saturation effects (associated with efficient energy extraction) in the excimer amplifiers producing a noticeable shortening of the output pulse durations.

6.5.1.2.4 Excimer Laser Driver (ELD) - The excimer laser driver (ELD) subsystems in each of the 960 beamlines amplify the beams from the ELPs to levels sufficient to drive the ELPAs to reach their specified output energies. Schematics of

Use or disclosure of data subject to title page restriction

the locations of the ELDs relative to ELMO and the ELPAs are provided in Figure 6.5.1-3. Specifications for the ELD are provided in Table 6.5.1-3.

Table 6.5.1-3 Prometheus ELD Specifications

Parameter	Nominal Value	Unit of Measure
Number of Units	1020	
Wavelength	248	nm
EDEL Mode Pulse Duration	260 (570, EBEL)	ns
Input Energy	4	J
Output Energy	200	J
Gain	50	
Polarization State	Linear	
Aperture	10x10	cm
Gain Length	200	cm
Output Fluence	2	J/cm^2
Fuel Pressure (Kr, F_2, Ar)	760	torr
Number of Firings between Failures	10^{10}	
Anode Voltage	200	kV
Beam Current	40	kA
EDEL Mode Input Intensity	0.16 (0.08, EBEL)	MW/cm^2
EDEL Mode Output Intensity	8 (4, EBEL)	MW/cm^2
Repetition Rate	5	Hz

6.5.1.2.5 Excimer Laser Power Amplifier (ELPA) - The excimer laser power amplifiers (ELPAs) amplify the ELD beams to levels sufficient to drive the subsequent Raman accumulator cells. These amplifiers are primarily scaled-up versions of the ELDs with apertures increased from 5x5 cm to 30x30 cm and amplification length of 2 m. Schematics of the relative locations of the ELPAs relative to ELDs and the Raman accumulators are provided in Figures 6.5.1-3 and 6.5.1-4. The specifications for the ELPA are provided in Table 6.5.1-4.

Note that by arranging to have the total pressure in the ELPA ~1 atmosphere permits the amplifier windows to be thinner since the differential pressure can be nearly zero for quiescent amplifiers. (The dynamic overpressure is several atmospheres when the amplifiers are fired.) Similar conditions apply to the ELPs and ELDs, although the cost benefits for these smaller amplifiers is less.

Table 6.5.1-4 Prometheus ELPA Specifications

Parameter	Nominal Value	Unit of Measure
Number of Units	960	
Wavelength	248	nm
EDEL Mode Pulse Duration	250 (500, EBEL)	ns
Input Energy	200	J
Output Energy	6000	J
Gain	30	
Polarization State	Linear	
Aperture	30x30	cm
Gain Length	200	cm
Output Fluence	5.5	J/cm^2
Anode Voltage	300	kV
Current	3.3	MA
Fuel Pressure (Kr, F_2, Ar)	760	torr
Number of Firings between Failures	10^{10}	
EDEL Mode Input Intensity	0.7 (0.35, EBEL)	MW/cm^2
EDEL Mode Output Intensity	22 (11, EBEL)	MW/cm^2
Repetition Rate	5	Hz

A schematic of a possible pulsed power configuration for an EDEL version of the ELPA is shown in Figure 6.5.1-7. As indicated in the figure, maximum efficiency can be realized by locating the pulsed power Blumleins adjacent to the EDEL amplifiers. Although UV preionization grids are shown, this configuration could also be used for an e-beam sustained EDEL. Circulation of the hot gases from the ELPA will be discussed in Section 6.5.1.6. The 6 kJ output beams from each of these ELPAs are then directed into the Raman accumulator optical system.

6.5.1.3 Raman Accumulator Subsystems - Using a Raman laser subsystem duplicated 60 times, the ~6 kJ output beams from 4x4=16 ELPAs are directed into a 1.2x1.2 m-square aperture, 5-m long Raman accumulator cell (RAC) filled with ~1 amagat of D_2. For maximum conversion efficiency, the intended stimulated Raman scattering amplification process in the RAC is stimulated rotational Raman scattering (SRRS); more specifically, SRRS from the S(1) transition in H_2 or D_2. (Raman laser operation with D_2 has a slightly higher quantum efficiency than with H_2.) The required Stokes seed is derived from a local SRRS master oscillator, pumped with excimer laser light derived from a particular ELD chain, having identical spectral (and temporal) content as the 16 ELPA pump beams entering the RAC. This spectral matching of the Stokes seed to the 16 ELPA pump beams assures high Raman gain[9] even in the presence of relatively broad-band (~1 GHz) excimer pump beams. This results in efficient conversion of these 16 pump beams to generate the main square 1.2x1.2-m aperture 100 kJ Stokes output beam from the RAC. By injecting the pump beams into the RAC at an angle of 5° with respect to the RAC axis, an acceptable degree of pump[9,10,11] beam intensity averaging is achieved in the 5 m gain length, while not significantly reducing the Raman amplifier gain (see Section 4.2.1).

Use or disclosure of data
subject to title page restriction

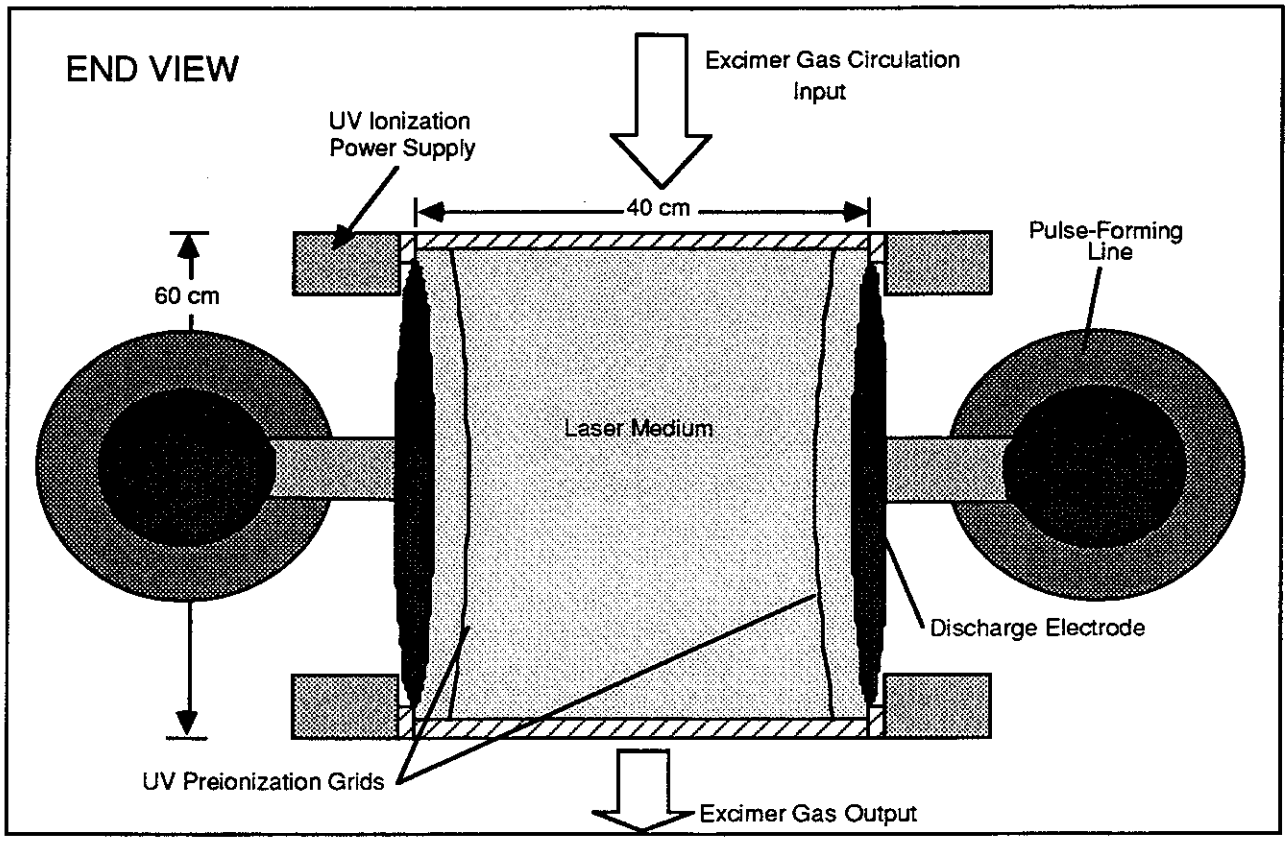

Figure 6.5.1-7 Pulsed power configuration for the EDEL version of the ELPA

A simplified schematic of the Raman Stokes seed generator designed to drive the Raman accumulator cell (RAC) is shown in Figure 6.5.1-8.

The 200 J output beam from the 17th ELD beam line is divided into a small 0.5 J pump beam and main beam (199.5 J). This small beam is directed into a local Raman oscillator with an output Stokes energy of 0.1 J. The beams (Stokes seed and main) rejoined at an angle relative to each other in the Raman preamplifier. The Raman Preamplifier output is a 30 J Raman Stokes seed at a wavelength of 251 nm (for KrF) or 196 nm (for ArF)). It is essential that the Raman seed have excellent beam quality to assure high quality beams on the DT target. The Stokes seed generator would include image-relayed spatial filter telescopes (not illustrated in the figure) to produce essentially diffraction-limited 1.2 m x 1.2 m beams for injection into the Raman accumulator.

Use or disclosure of data
subject to title page restriction

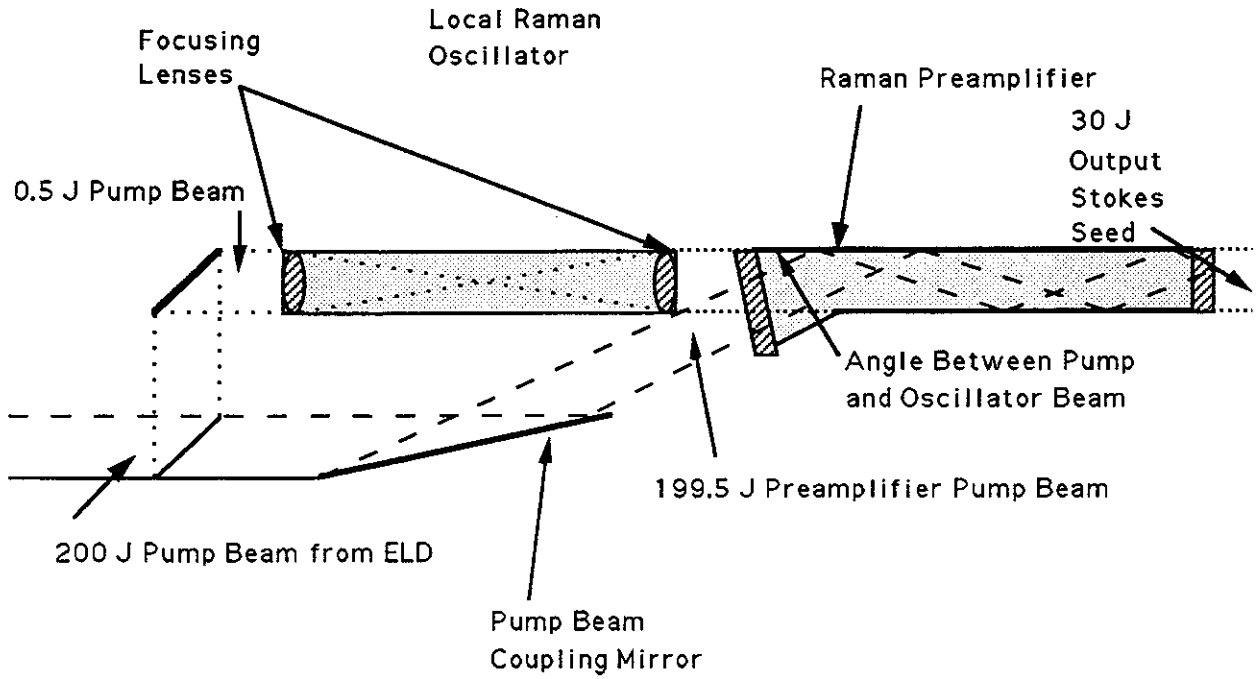

Figure 6.5.1-8. Each Raman accumulator subsystem consists of a local Raman oscillator (LRO), a Raman preamplifier, and a recollimation telescope generating 120x120 cm Raman Stokes seed beam of 30 J to drive the Raman accumulator cells.

To achieve good spectral match among the Raman oscillator and amplifier elements, the entire Raman conversion system operates at the same temperature and pressure. Characteristics of the Raman amplifier cells are summarized in Table 6.5.1-5.

Table 6.5.1-5 Common Raman Amplifier Specifications

Parameter	Nominal Value	Unit of Measure
Pump Laser Type	KrF	λ = 248 nm
Raman Medium	hydrogen	gas
Gas Density	~ 1	amagat
Transition #1	S(2)--S(0)	$\Delta E \sim 354\ cm^{-1}$
Quantum Efficiency #1	99.1 (KrF)	%
First Stokes Wavelength #1	250.2	nm
Transition #2	S(3)--S(1)	$\Delta E \sim 587\ cm^{-1}$
Quantum Efficiency #2	98.5 (KrF)	%
First Stokes Wavelength #2	251.6	nm
Pump Laser Type	ArF	λ = 193 nm
Transition #1	S(2)--S(0)	$\Delta E \sim 354\ cm^{-1}$
Quantum Efficiency #1	99.3 (ArF)	%
First Stokes Wavelength #1	194.3	nm
Transition #2	S(3)--S(1)	$\Delta E \sim 587\ cm^{-1}$
Quantum Efficiency #2	98.9 (ArF)	%
First Stokes Wavelength #2	195.2	nm

Use or disclosure of data
subject to title page restriction

6.5.1.3.1 Local Raman Oscillator - The local Raman oscillator (LRO) generates a high quality Stokes seed that is amplified by the Raman preamplifier prior to injection into the Raman accumulator cell (RAC). The general construction of the LRO is shown in Figure 6.5.1-8. In this geometry, the 0.5 J pump beam is focused into a 200-cm long H_2 cell using a high quality lens of focal length, f ~ 100 cm. The gas pressure in the LRO cell is selected to be similar to the Raman preamplifier and RAC to achieve similar Raman bandwidth and gain coefficients (see Section 4.2.1). For an input pump with wavelength λ_{pump} of diameter d_b, having an energy E_p, a beam quality of ξ, and a pulse duration of τ_p, the intensity, I_{laser} , near the focus of the lens is simply:

$$I_{focus} = \frac{E_p d_b^2 \pi}{4\lambda_{pump}^2 f^2 \tau_p \xi^2} \qquad (6.5.1\text{-}1)$$

Using the values in Eq. 6.5.1-1 produces a pump intensity near the focus is ~3 GW/cm^2. The small angle, forward Raman gain, G_R, in H_2 under these circumstances is described by the expression:

$$G_R(\rho,\theta,\lambda) = \exp\left[g_R(\rho,\theta,\lambda) I_{focus}(\lambda) L(\lambda)\right] \qquad (6.5.1\text{-}2)$$

where $L(\lambda)$ is defined by

$$L(\lambda) = \frac{4\xi f^2 \lambda_{pump}}{\pi d_b^2} \qquad (6.5.1\text{-}3)$$

where g_R is the Raman gain coefficient, L_λ is the depth of focus of the lens, and I_{focus} is the intensity of the laser beam described by Eq. 6.5.1-1 above. Substituting values from Table 6.5.1-6 into Eq. 6.5.1-2 yields a result that the small signal Raman gain, G ~ 30 nepers or approximately 10^{13}. Under these circumstances, the Raman gain is sufficiently high that amplified spontaneous emission (ASE) is sufficient to saturate the Raman medium, yielding a 0.1 J pulse of Stokes radiation. The beam quality of the Stokes seed generated under these conditions is relatively good since the solid angle of the gas in which the seed is generated is relatively small. It is necessary, however, to spatially filter the seed further prior to amplification in the Raman preamplifier in order to improve the Stokes seed beam quality to be close to the diffraction limit. Care must be taken to assure that the LRO only generates the first Stokes order and that generation of all higher order Stokes outputs are strongly suppressed.

Use or disclosure of data
subject to title page restriction

Typical values for the LRO parameters can be found in Table 6.5.1-6.

Table 6.5.1-6 Prometheus Local Raman Oscillator Specifications

Parameter	Nominal Value	Unit of Measure
Number of Units	60	
EDEL Mode Pulse Duration	250 (500, EBEL)	ns
Input Pump Energy	~0.5	J
Output Stokes Energy	~0.1	J
Conversion Efficiency	20%	
Polarization State	Circular	
Aperture	1x1	cm
Oscillator Length	3	m
Output Fluence	0.1	J/cm^2
Number of Conversions/Failures	10^{11}	
EDEL Mode Input Intensity	2 (1, EBEL)	MW/cm^2
EDEL Mode Output Intensity	0.4 (0.2, EBEL)	MW/cm^2
Repetition Rate	5	Hz

6.5.1.3.2 Raman Preamplifiers - The Raman preamplifiers increase the power of the Stokes seed generated in the LRO from 100 mJ to a level ranging from 30 to 50 J prior to injection into the RAC. A schematic of the relation of the Raman preamplifier relative to the LRO is shown in Figure 6.5.1-6. The general specifications of Raman preamplifiers are summarized in Table 6.5.1-7.

Table 6.5.1-7 Prometheus Raman Preamplifier Specifications

Parameter	Nominal Value	Unit of Measure
Number of Units	60	
Wavelength	249	nm
EDEL Mode Pulse Duration	250 (500, EBEL)	ns
Stokes Seed Energy	0.1	J
Input Pump Energy	~200	J
Output Stokes Energy	~30	J
Conversion Efficiency	15%	
Raman Cell Gain	300	
Polarization State	Circular	
Aperture	5x5	cm
Gain Length	3	m
Output Fluence	1.2	J/cm^2
Number of Conversions/Failures	10^{11}	
EDEL Mode Input Intensity	32 (16, EBEL)	MW/cm^2
EDEL Mode Output Intensity	4.8 (2.4, EBEL)	MW/cm^2
Repetition Rate	5	Hz

As indicated, the Raman preamplifiers are pumped with ~200 J pulses delivered by the 17th excimer amplifier chain (composed of an ELP followed by an ELD). The pump pulses are injected into the Raman preamplifiers at an angle in order to permit the intensity inhomogeneities present in the ELD pump beam to be averaged out in the Raman preamplifier, thereby permitting a very smooth Stokes seed to be delivered to the RAC.

6.5.1.3.3 Raman Accumulator Cells (RAC) - The Raman accumulator cells (RACs) perform the important task of combining the output beams from 16 ELP/ELD/ELPA laser chains into a single, 100 kJ beam having an aperture of 1.2 x 1.2 m. A simplified schematic of the Raman accumulator cells (RACs) is shown in Figure 6.5.1-9.

A diagram illustrating in more detail the proposed injection scheme of all 16 ELPA beams into the RAC can be found in Section 2.4. The general performance requirements for the Raman accumulator cells (RACs) are summarized in Table 6.5.1-8.

Many variables influence the conversion efficiency of a Raman accumulator. As shown in Figure 6.5.1-10, even for constant values of excimer laser intensity, variations in hydrogen gas density, angle of injection, and cell length play important roles in determining the cell conversion efficiency.

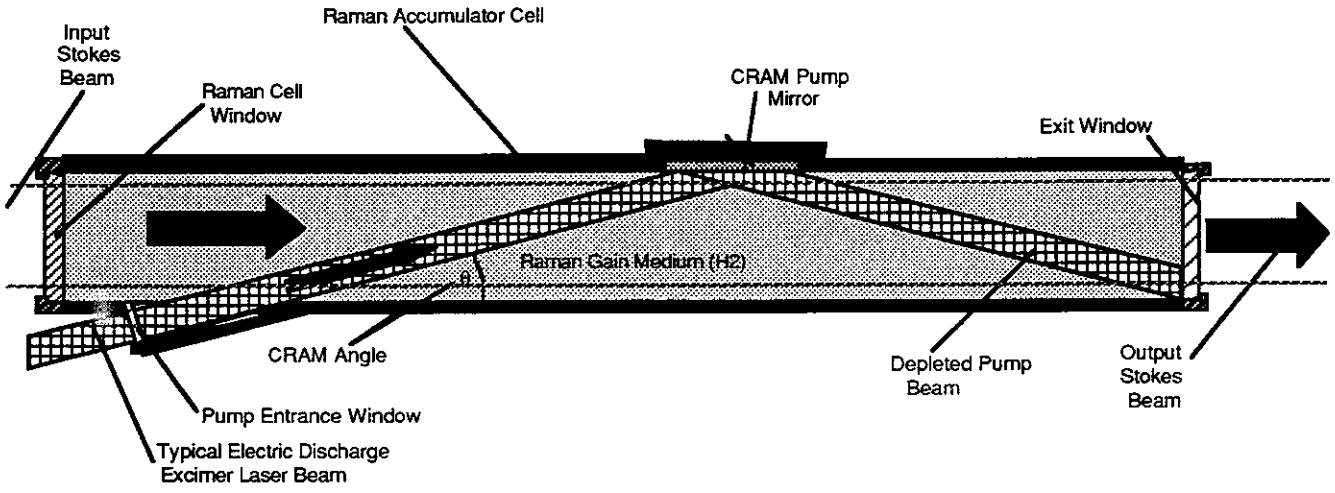

Figure 6.5.1-9 Injection of the Stokes seed into the Raman accumulator cell permits the efficient extraction of the excimer pump beams into a 100 kJ beam having an aperture of 1.2x1.2 m.

Use or disclosure of data subject to title page restriction

Table 6.5.1-8 Prometheus Raman Accumulator Specifications

Parameter	Nominal Value	Unit of Measure
Number of Units	60	
Wavelength	249	nm
EDEL Mode Pulse Duration	250 (500, EBEL)	ns
Stokes Seed Energy	30	J
Input Pump Energy	~96	kJ
Output Stokes Energy	~81	kJ
Conversion Efficiency	84%	
Raman Cell Gain	3000	
Polarization State	Circular	
Aperture	1.2x1.2	m
Beam Quality	1.2	xDL
Gain Length	6	m
Output Fluence	8	J/cm^2
Number of Conversions/Failures	10^{11}	
EDEL Mode Input Intensity	0.16 (0.08, EBEL)	MW/cm^2
EDEL Mode Output Intensity	8 (4, EBEL)	MW/cm^2
Repetition Rate	5	Hz

In order to avoid conversion of the first Stokes output to higher order Stokes components[9,10,11], Raman conversion efficiencies higher than 90% should be avoided. Thus, as indicated in Figure 6.5.1-10, the RAC cell should be ~250 cm in length for a hydrogen density of 1.4 amagat and a CRAM angle of 10° in order to avoid higher order Stokes components from being generated (using the converted first Stokes beam as a pump beam for the second Stokes, etc.).

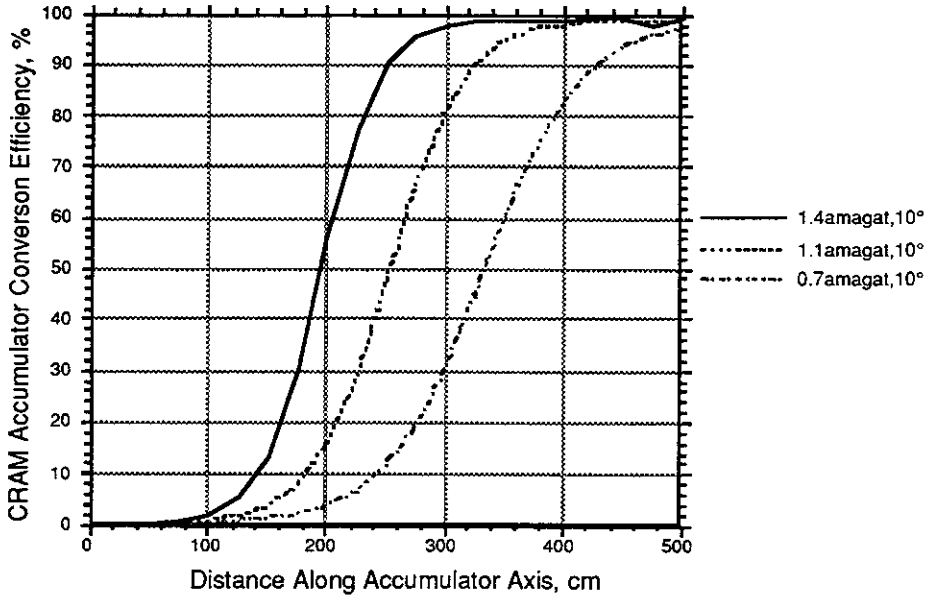

Figure 6.5.1-10 The RAC conversion efficiency is dependent upon the CRAM angle (example shown is 10°), hydrogen gas density (examples shown are 0.7, 1.1, and 1.4 amagats), and distance along the accumulator axis assuming a 5 GHz bandwidth, 250 nm pump beam, 100 kJ energy in 250 ns pulse duration.

Use or disclosure of data
subject to title page restriction

The formal dependencies of the Raman gain on hydrogen density, CRAM angle, pump bandwidth, laser intensity, cell length, etc., were described in Section 4.2.1; the angular dependence of the Raman gain coefficient, g_R, is defined by the expression:

$$g_R(\theta,\lambda,\rho) = \frac{\alpha(\lambda,\rho)}{1+\xi(\lambda,\rho)\left[1+\psi(\lambda,\rho)\sin^2\left\{\frac{\theta}{2}\right\}\right]} \qquad (6.5.1\text{-}4)$$

where θ is the angle between the pump and Stokes seed (α, ξ, ψ) are functions of the laser wavelength, λ, and hydrogen density, ρ. The Raman gain, G_R, on the other hand is given by the expression:

$$G_R(\theta,\lambda,\rho) = \exp\left[g_R(\theta,\lambda,\rho)\, I_{pump}(\lambda)\, L_{cell}(\theta)\right] \qquad (6.5.1\text{-}5)$$

where I_{pump} is the intensity of the excimer pump laser beams, and $L_{cell}(\theta)$ is the length of the Raman cell. It is important to recognize that there are competing processes present in the RAC which must be controlled if the performance described in Figure 6.5.1-10 is to be realized. Some of these processes include higher order Raman conversion or generation of parasitic Raman oscillations parallel to the RAC axis (as discussed in Section 4.2.1 and illustrated in Eq. 6.5.1-1); the Raman gain coefficient for $\theta = 0°$ is significantly higher than for $\theta = 10°$). In general, if $G_R > 10^{10}$ for a Raman process (equivalent to 23 nepers of gain), superfluorescent oscillation may occur, depleting the available pump energy.

6.5.1.4 SBS Pulse Compressors - The SBS pulse compressors transform the relatively long (~250 ns pulses in the case of the EDELs or ~500 ns in the case of the EBELs) laser pulses from the RACs into complex pulse shapes. For direct-drive laser targets, these complex pulse shapes consist of a ramped precursor pulse of ~80 ns duration containing ~30% of the energy, followed by a main pulse having a ~6 ns duration with ~70% of the total pulse energy. Two examples of such a direct-drive pulse scenario are shown in Figure 6.5.1-11.

A SBS pulse compressor subsystem takes the roughly rectangular, 250 ns pulse from the RAC and generates a short, 6 ns main pulse illustrated in Figure 6.5.1-11. A long, 80 ns precursor pulse is derived from temporally inverting the depleted pump beam emanating from the SBS cell. These SBS processes are described below.

6.5.1.4.1 Generation of SBS "Seed" Beam - In a manner analogous to the Raman seed generator described in Section 6.5.1.3.1, the SBS pulse compressor seed is derived from the long duration pulse of the RAC. Henceforth, this long duration pulse from the RAC is referred to as the "SBS pump pulse." Using a method originally suggested by Mak,[12] the leading edge (i.e., the first 10 ns) of this SBS pump pulse is "chirped" or frequency-shifted by an amount equal to the Brillouin shift in the SF_6 gas used as the SBS gain medium. By varying the duration and modulation depth of the "chirped" signal on the leading edge of the SBS pump beam, significant control can be exercised over the shape and pulse duration of resulting compressed pulse.

6.5.1.4.2 Amplification of Short Duration Stokes "Seed" - This long SBS pump beam is then passed through a quarter-wave plate to convert the previously circular polarized light (needed in the rotational Raman accumulators) to linearly polarized light vibrating in the "p" polarization. The beam is then transmitted without loss through a dielectric polarizer, a second quarter-wave plate oriented to return the "p"-polarized beam to circular polarization, and then passed through a gas cell filled with approximately 2 amagat of SF_6. The length of this SF_6 cell is designed to be $L_{cell} = c\,\tau_{pulse}/2$. At the far end of the SBS cell a high reflectivity mirror is located which retro-reflects the incident pump beam directly back into itself. Since the leading edge of the SBS pump beam has been frequency-shifted by the "chirper" by an amount equal to the SBS shift in SF_6, the leading edge of the SBS pumping pulse therefore serves as the SBS Stokes "seed" beam, and the frequency-shifted photons on the leading edge of the pump pulse experience high optical gain[13] as these photons propagate back

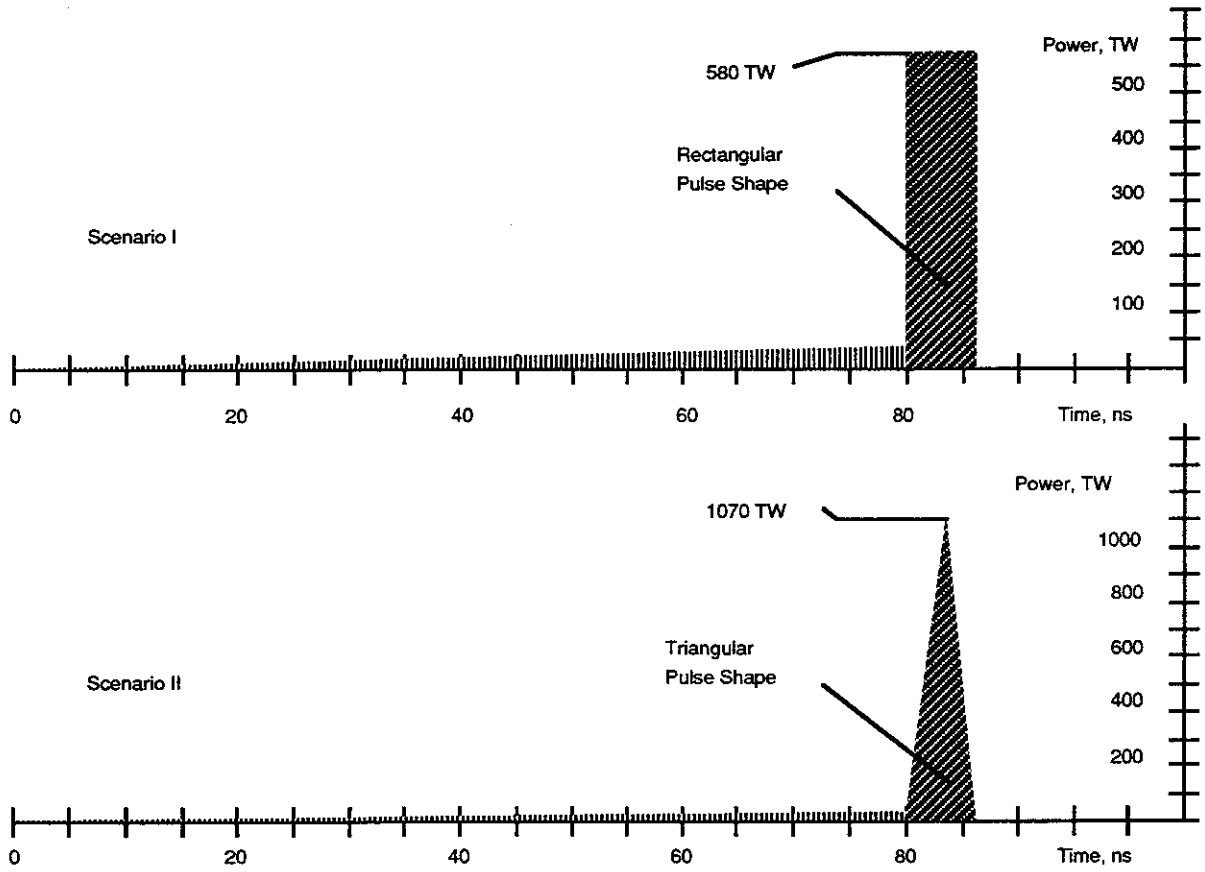

Figure 6.5.1-11 The complex temporal shape of the direct-drive laser driver pulse consists of a ramped, 80 ns precursor pulse followed by a short, 6 ns main pulse.

through the volume of the SF_6 gas "pumped" by the incoming beam. Assuming that the temporal pulse shape of the SBS pump beam is rectangular, the SBS gain, G_{SBS}, of the pulse compressor is given by the expression:

$$G_{SBS}(\rho,\Delta\nu,t) = \exp\left(g_{SBS}\left[\rho,\Delta\nu_{pump}\right]I_{laser}(\Delta\nu,t)L_{cell}\right) \qquad (6.5.1\text{-}6)$$

where g_{SBS} is the Brillouin gain coefficient, I_{laser} is the intensity of the SBS pump beam, and $L_{cell} = c\ \tau_{pulse}/2$ is the effective gain length of the SBS pulse compressor. Typical values for G_{SBS} in SF_6 for 100 kJ RAC pulses of 250 ns duration are 10 nepers, or ~2000. The SBS gain coefficient, $g_{SBS}(\rho,\ \Delta\nu_{pump})$ is primarily a function of the gas density, ρ, and the bandwidth of the pump laser, $\Delta\nu_{pump}$.

The physical process of SBS differs from that of Stimulated Raman Scattering (SRS) in that the scattering of incident laser photons from sound waves in the SBS medium occurs, as compared with the scattering of light from molecular energy states as the

Use or disclosure of data
subject to title page restriction

basis of the SRS process. Since the difference in frequency between the excimer laser, ν_{laser}, and the Stokes seed, ν_{SBS} is simply the Doppler shift, $\Delta\nu_D$, suffered by the pump photons when scattered from the moving density waves in the Brillouin gain medium. Thus, $\Delta\nu_D = 2\nu_{laser}v/c$ (where v is the sound speed in the SBS medium and c is the speed of light), the quantum efficiency for the SBS process defined in Eq. 6.5.1-6 can be very high, $\xi \sim 100\%$.

The Brillouin gain coefficient, g_B, is defined by the relation:[13]

$$g_B = \frac{k_s^2 \gamma_e^2}{ncv_s\rho\Gamma_B} \qquad (6.5.1\text{-}7)$$

where k_s is the wave vector of the Stokes beam, γ_e is the electrostrictive coefficient (of the SF_6 SBS gain medium), n is the refractive index, c is the speed of light, v_s is the speed of sound in the gas, ρ is the density, and Γ_B is the spontaneous Brillouin line width.

Building upon the work of Mak,[12] et al., in Russia, we have analyzed the case in which the leading edge of the long, 250 ns (or 500 ns for an EBEL) excimer laser pulse is electronically chirped in frequency by an amount equal to the SBS seed frequency, $\Delta\nu_{SBS}$, and then ramped in modulation depth to encourage the generation of pulses >1 ns duration, we then have a very flexible method of generating a variety of output compressed pulse shapes in a single non-linear, self-seeding, pulse compressor. A schematic of the SBS pulse compression concept is shown in Figure 4.2.1.2-12.

The short, ~10 ns "chirped" leading edge of the retro-reflected pump beam is amplified by the SBS gain, G, until it extracts most of the pump beam energy. With a second passage through the quarter-wave plate, the "p"-polarized beam is converted to an "s"-polarized beam, and reflected from the large aperture dielectric polarizer to the electro-optical switchyard and delay line. A schematic of this self-seeded SBS pulse compressor geometry is shown in Figure 6.5.1-12.

Details regarding the variety of short pulse shapes that can be generated by varying the shapes of the "chirped" leading edges of the input pump pulses can be found in Section 4.2.1. A diagram of this pulse compression process is shown in Figure 6.5.1-13.

Use or disclosure of data
subject to title page restriction

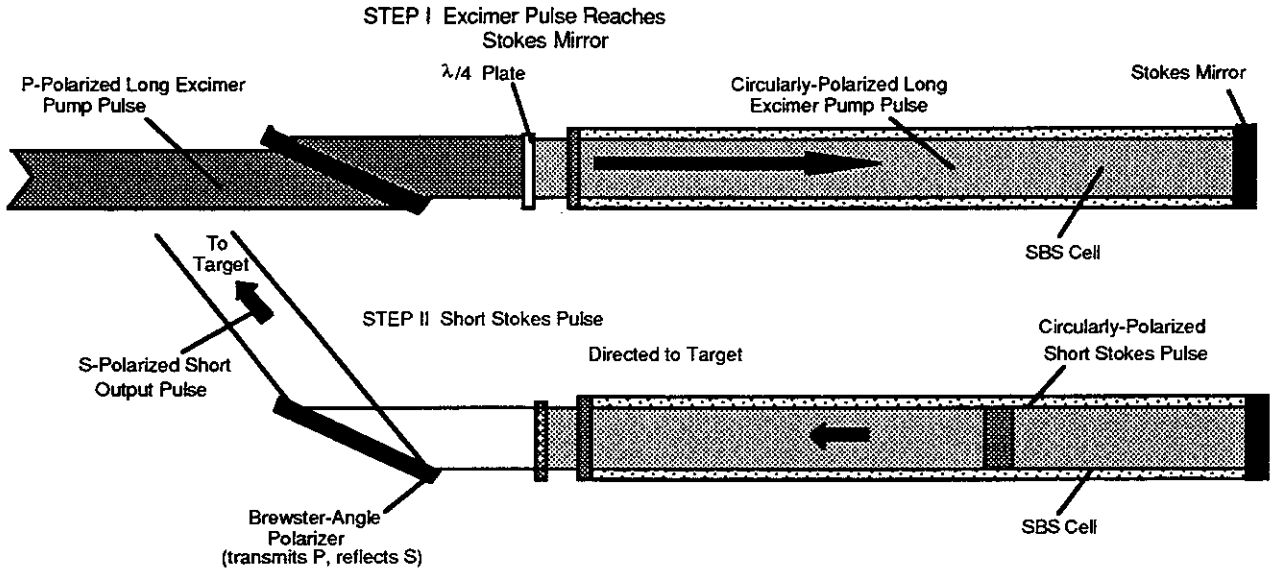

Figure 6.5.1-12 By frequency-"chirping" the leading edge of the SBS pumping pulse and reflecting it back upon the incoming pulse within an SF cell, it is possible to compress the RAC output pulse from 250 ns (or 500 ns) down to short pulse durations.

6.5.1.4.3 Precursor Pulse Generation - As mentioned previously, the SBS cell inefficiently generates compressed pulses as long as 6 ns. As a consequence of this inefficiency, approximately 60 to 70% of the pump beam is converted to the main 6 ns pulse, with 30 to 40% of the pump pulse being unconverted. As it turns out, these energy ratios of the long, depleted pump to the short main pulse are very similar to the required ratios for direct-drive target illumination set forth by the TWG. However as generated in the SBS pulse compressor, the short, 6 ns pulse precedes the long, depleted pump pulse. Accordingly, in order to generate the long duration precursor pulse from the depleted pump beam, it is necessary temporally to invert the short, 6 ns main pulse, from the long pulse. A schematic of how this can be accomplished is illustrated in Figure 6.5.1-14.

As indicated in Figure 6.5.1-14, the combined main short pulse and the long depleted pump beam emanating from the SBS pulse compressor cell enter into the pulse inverter optical system. This system applies a half-wave voltage to the large aperture Pockels cell, thereby changing the polarization of the short pulse from "p" to "s." The dielectric polarizer then reflects the short pulse into an optical delay line of length $L = c\tau_{laser}/4$ bisected with the dielectric polarizer. Immediately after the arrival of the short pulse, the half-wave voltage is removed from the Pockels cell, allowing the long duration, depleted pump beam to pass without loss through the dielectric polarizer. A quarter-wave plate located in the first arm of the delay line then converts the "s"-polarized short pulse into a

Use or disclosure of data subject to title page restriction

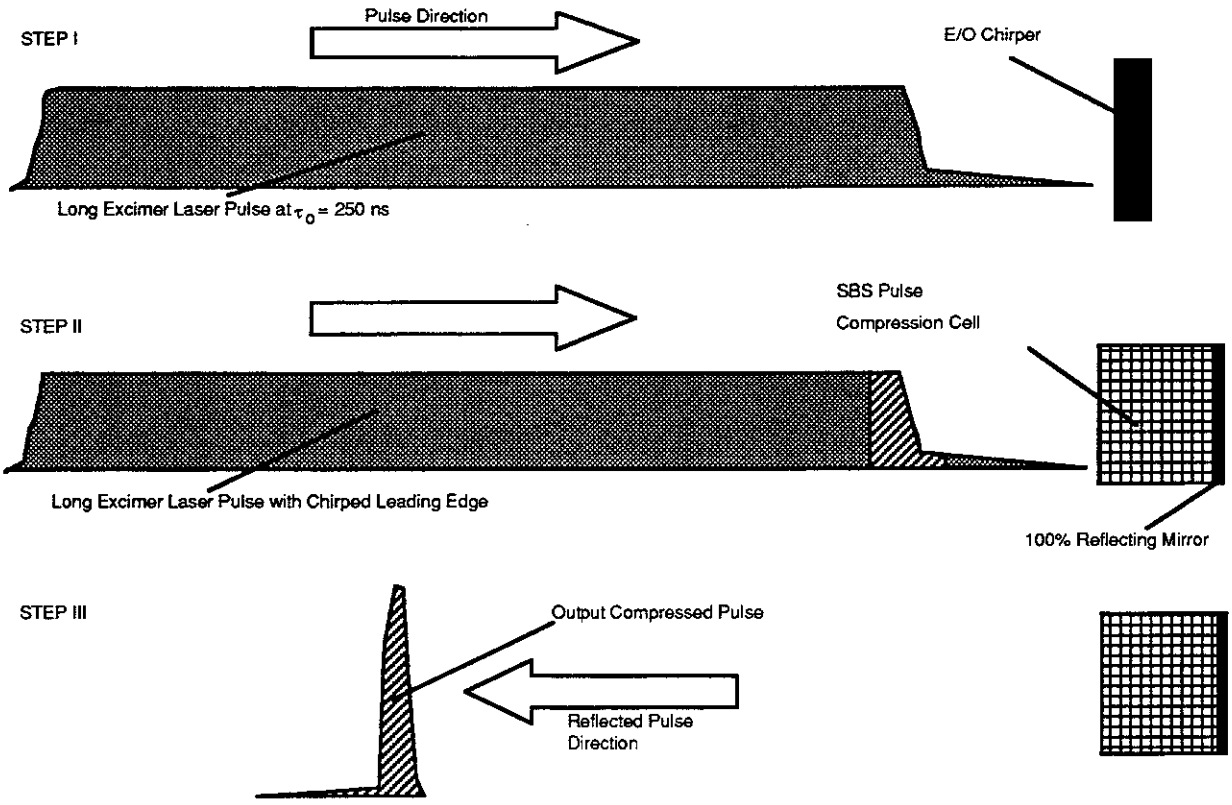

Figure 6.5.1-13 Pulse compression in the SBS pulse compressor.

"p" polarized wave which then transmits through the polarizer to the second delay line arm. Here a second quarter-wave plate converts the "p" -polarization back to "s"-polarization where the short pulse is finally reflected by the dielectric polarizer back into the main beam line, delayed by a time t = τ_{pulse}. The primary problem with this technique is that the pulse shape of the depleted pump beam from the SBS cell starts out at a relatively high level and ramps down (see Section 4.2.1).

An additional precursor pulse-shaping technique could be implemented if fast, large aperture Pockels cells are developed. A schematic of such a sample electro-optical switchyard technique is shown in Figure 6.5.1-15.

As shown in Figure 6.5.1-15, the SBS pulse compressor cell first generates the short, 6 ns main laser pulse, followed by the long, ~150 ns duration depleted pump beam. The first Pockels cell inverts the order of the short and long pulses, and the second (rapid rise-time) Pockels cell inverts the head and tail of the depleted pump beam to achieve a ramped precursor pulse shape.

Use or disclosure of data
subject to title page restriction

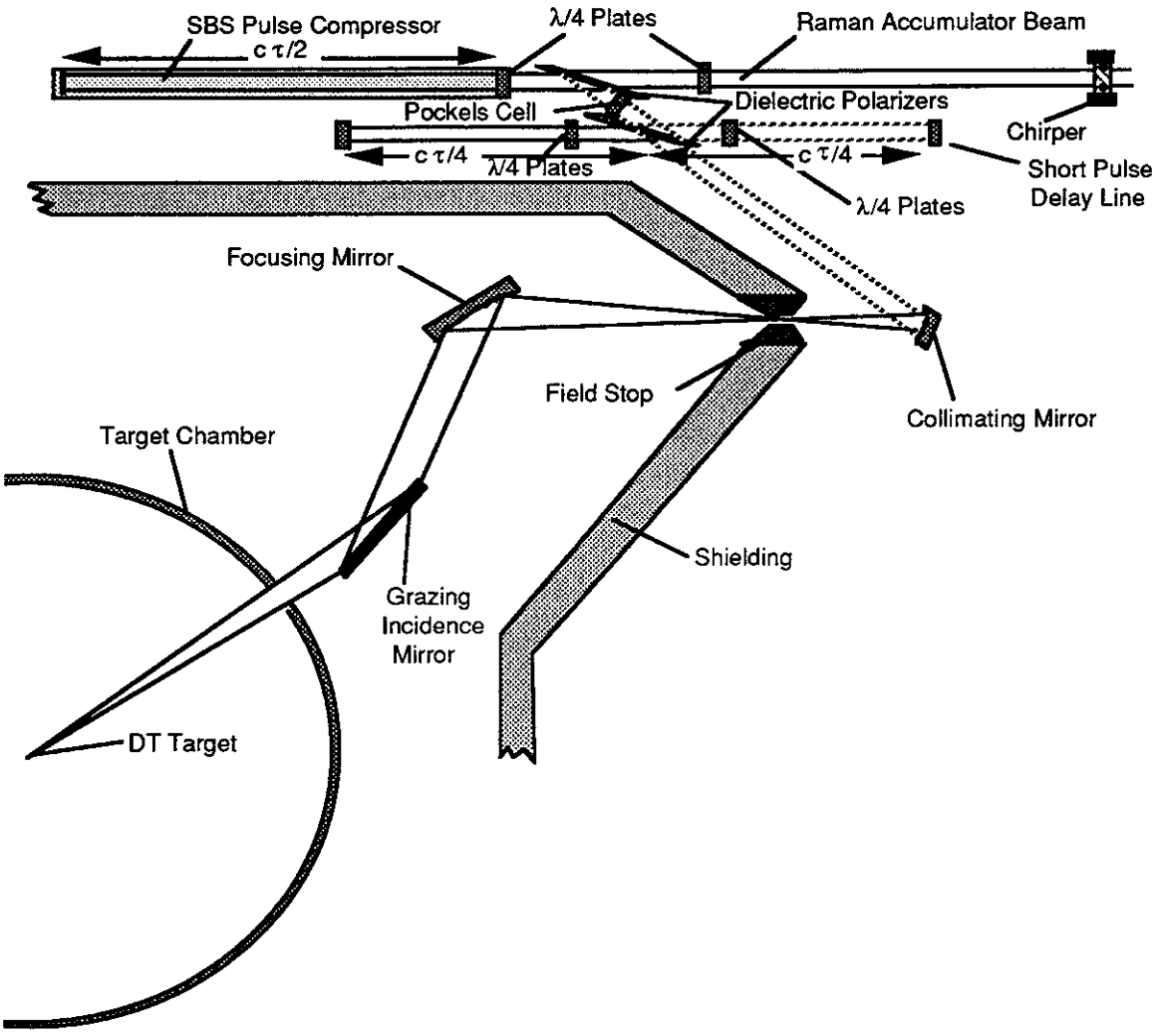

Figure 6.5.1-14 By use of a large aperture Pockels cell and a delay line, the short main pulse and long precursor pulses are temporally inverted.

SBS Pulse Shapes - Calculations were carried out for both EBEL (500-600 ns) and EDEL-pumped (250 ns) NLO pulse accumulator and compressor systems. As discussed above, the longer (~500 ns) EBEL pulses required a proportionally longer SBS cell ($L = c\,\tau_{pulse}/2$) than the shorter EDEL pulses. However, SBS conversion efficiencies >50% could be achieved with the longer EBEL pulses with SF_6 densities of ~1 amagat. An example of the variety of output pulse shapes that could be generated for an EBEL-converted Raman pump beam is shown in Figure 6.5.1-16.

Use or disclosure of data
subject to title page restriction

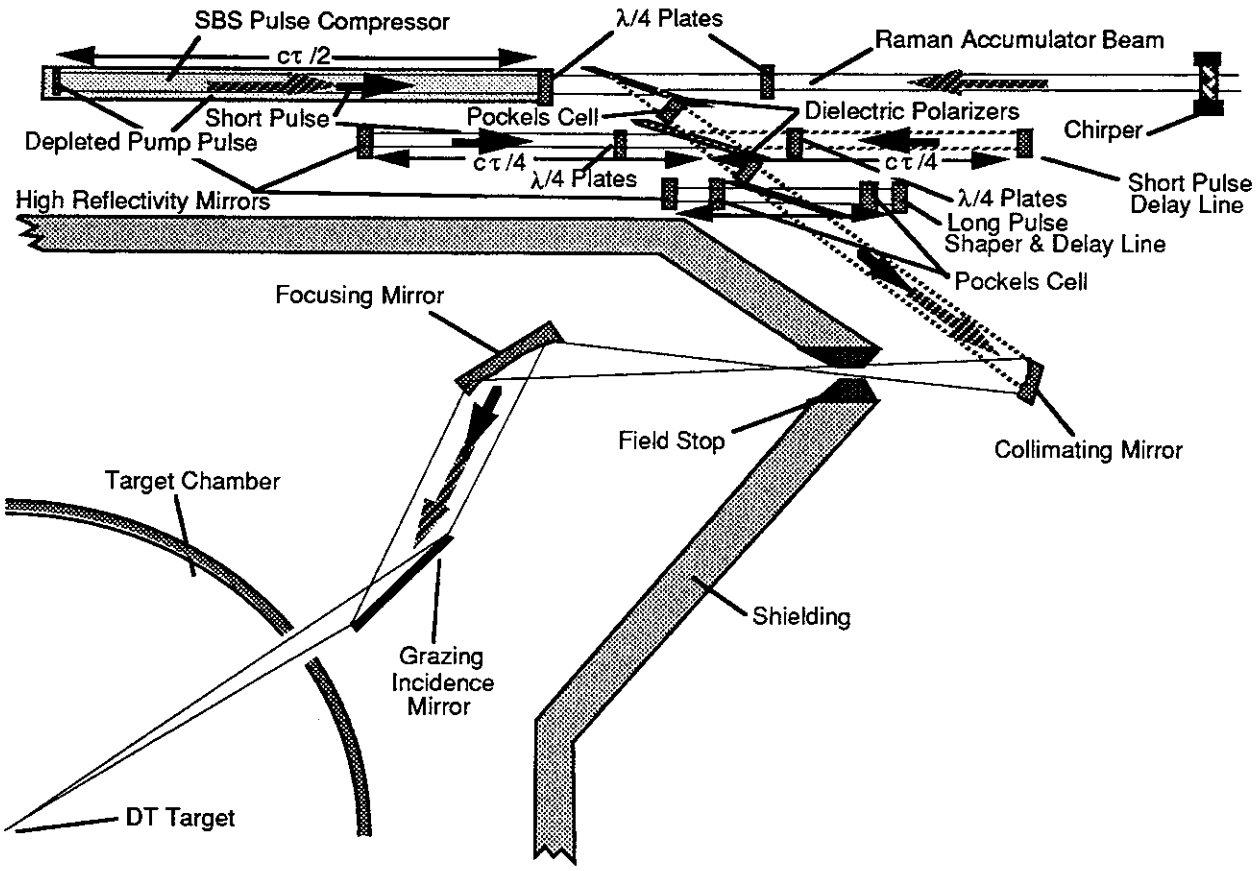

Figure 6.5.1-15 With fast Pockels cells and additional delay lines, additional temporal tailoring of the pulse shape is possible.

Similar results were obtained for the EDEL-pumped RAC case for which the pulse duration was ~250 ns. There was, however, insufficient SBS gain in the SF_6 gain medium to achieve high SBS conversion efficiencies with 1 amagat of SF_6 density. As a consequence, the density of SF_6 was increased to 2 amagat. The resulting pulse shapes as a function of the SBS "chirper" seed ramp ratios (see Section 4.2.1 for a discussion of the SBS "chirper" pulse ramp techniques) were calculated and the results are shown below in Figure 6.5.1-17 for a 248 nm pump, 5 GHz bandwidth, 1 m x 1 m aperture, and a 120 kJ input energy.

A laser designer does not have unlimited freedom in selecting different ramp ratios. The SBS pulse compression efficiency depended upon the ramp ratios, as shown in Figure 6.5.1-18.

Use or disclosure of data
subject to title page restriction

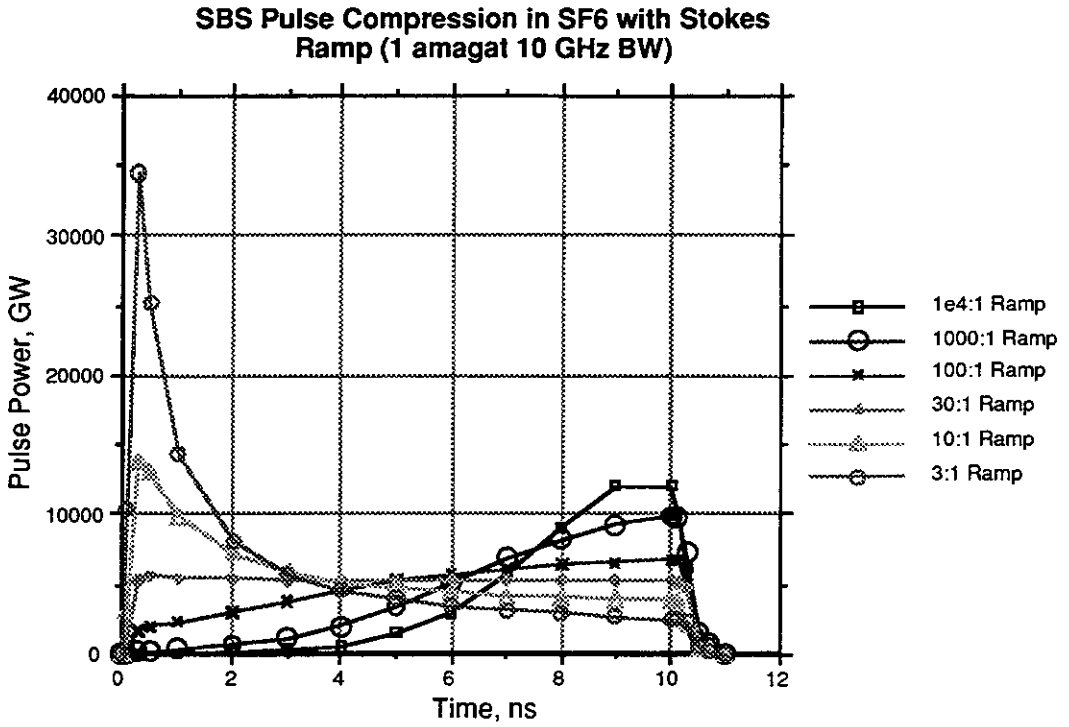

Figure 6.5.1-16 A variety of compressed pulse shapes could be achieved using a 600 ns Raman pump beam, 100 kJ energy, 1 amagat SF_6 density, and the indicated Stokes seed ramp ratios.

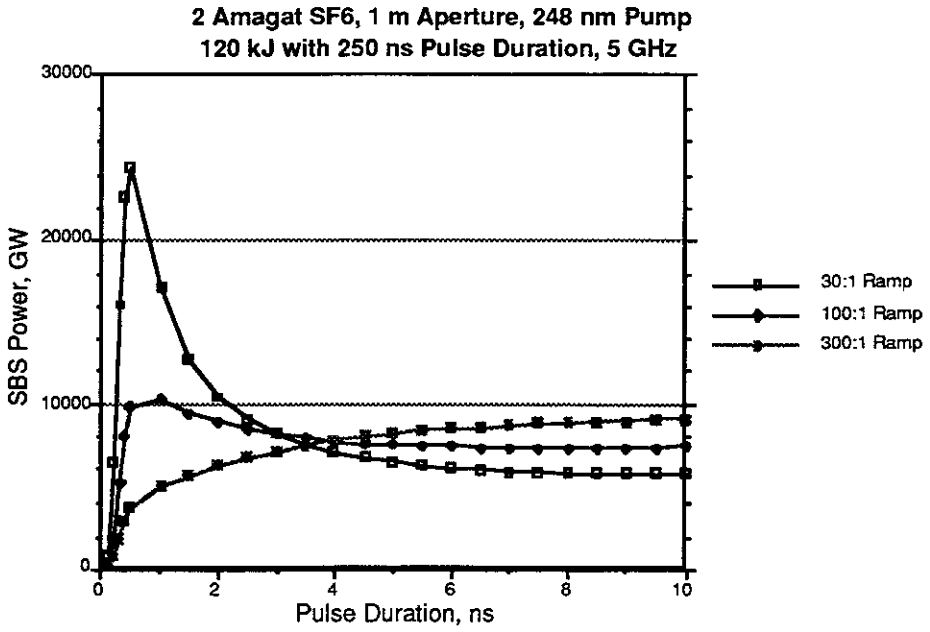

Figure 6.5.1-17 Further compressed pulse shapes can be generated using a 250 ns Raman pump beam at 250 nm, 120 kJ of energy, 2 amagat SF_6 density, 1x1 meter aperture and the indicated Stokes seed ramp ratios.

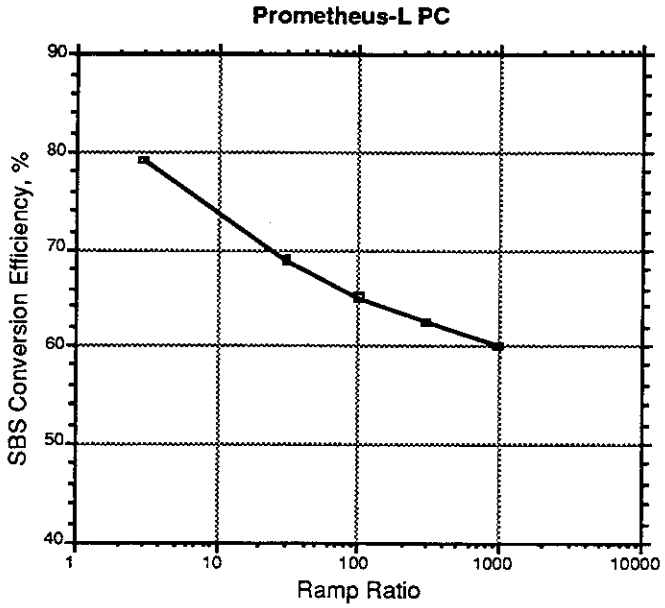

Figure 6.5.1-18 The SBS pulse compressor efficiency for 5 GHz 250 ns 120 kJ Raman pulses at 250 nm decreases as the Stokes seed ramp ratio increases.

As a consequence of design tradeoffs, an optimum pulse shape for the compressed main laser pulse can then lead to an optimization of the SBS pulse compressor conversion efficiency for the conditions necessary to generate the optimum pulse shape.

Temporal shapes of the depleted RAC pump beams emerging from the SBS compressor cells are also of interest since these pulses may be utilized elsewhere in the laser driver optical systems. These depleted pump pulses from the SBS cell remain of long duration and may be used as pump beams in a second SBS pulse compression stage or, if large aperture Pockels cells are developed, the depleted pumps can be electro-optically switched to generate a precursor pulse for the direct-drive target irradiation scheme.

As shown in Figure 6.5.1-19, the long RAC pulses (generated in the case of EBEL pumps) ramp down from ~190 GW to ~5 GW over the ~500 ns duration of the RAC pulse.

Similar results are obtained for the shorter pulse, EDEL-pumped RAC case. As shown in Figure 6.5.1-20, the temporal development of the depleted RAC pulse is illustrated for SBS "chirper" ramp ratios of 300:1 through 30:1.

Use or disclosure of data
subject to title page restriction

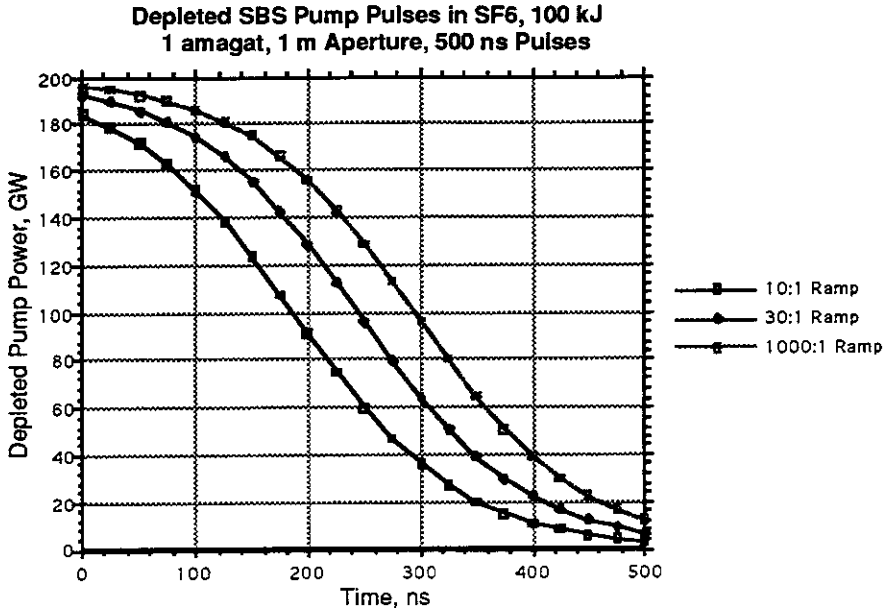

Figure 6.5.1-19 Temporal developments of depleted pump pulses emerging from SBS pulse compressor for 5 GHz, 100 kJ, 500 ns RAC pulses in 1 amagat of SF_6, 1x1 m apertures.

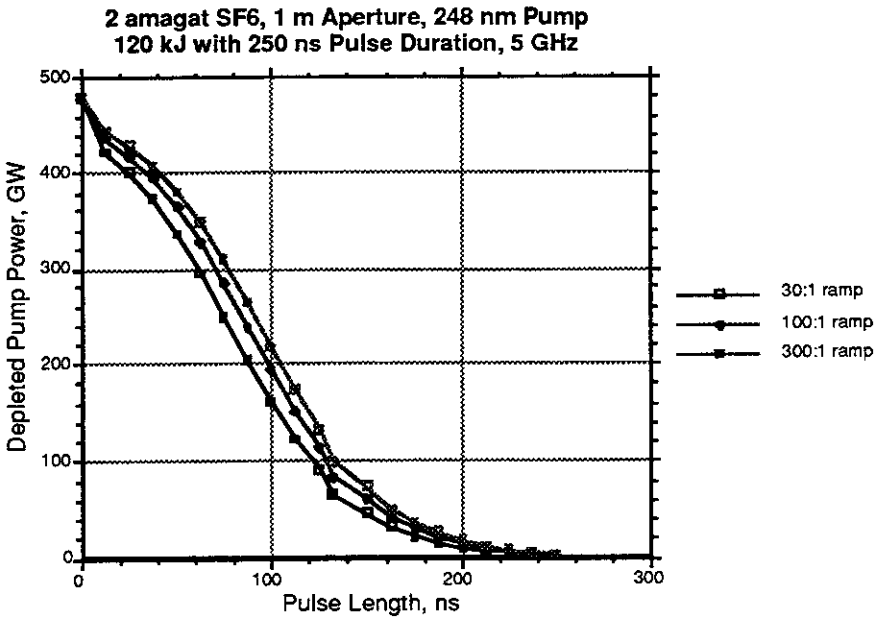

Figure 6.5.1-20 Temporal developments of depleted pump pulses from SBS pulse compressor for 5 GHz, 120 kJ, 250 nm pump, 250 ns pulse duration RAC pulses in 2 amagat of SF_6.

These are the pulse shapes which would need to be manipulated by the electro-optical switchyard depicted in Figures 6.5.1-14 and 6.5.1-15.

6.5.1.5 Excimer Laser Gas Flow System - As noted in Section 6.5.1.1, the overall efficiencies of the excimer laser amplifiers are predicted to be in the range of 12-15%. If the pulsed power efficiency is ~80%, then approximately 60% of the excimer laser pumping power will appear in the form of heat in the excimer laser fuel mixture gas. These estimates are summarized in Table 6.5.1-9, assuming that the power being fed to the laser driver is 250 MW.

Table 6.5.1-9 Energy Distribution in Excimer Laser Pumping

No.	Excimer Amplifier Component	% Power	Power (MW)
1	Output Photons	12-15%	30-40
2	Pulsed Power	20%	50
3	Excimer Gas	60%	150
4	Cooled Electrodes	3%	8
5	Cooled Amplifier Shell	2%	5

Each ELPA produces an average optical power of 30 kW (6 kJ at a 5 Hz rate) and, assuming a 12% efficiency, would be supplied with a power ~240 kW of which 60% (144 kW) would end up as heat in the excimer gas. Since the principal gases in the excimer laser are argon and krypton (the concentration of fluorine is only a few percent), the heat capacity of the excimer fuel is simply $C_V = 3/2$ R. The volume, V_a, of each of the ELPAs is 30x30x200 cm, or V_a ~ 180 liters which corresponds to 8.04 moles at standard temperature and pressure (STP).

6.5.1.6 Laser Driver Optical Subsystems - A wide variety of optical subsystems which are crucial to the operation of the Prometheus laser driver. Several were previously described, such as the beamsplitter array in conjunction with the ELMO and the electro-optical switchyard. A number of these optical subsystems are integrated with the laser driver computer control system to permit real-time adjustments on the performance of the laser system. A summary of the elements comprising the Prometheus laser driver optical subsystems is provided in Table 6.5.1-10.

Table 6.5.1-10 Excimer Laser Optical Subsystems

No.	Optical Subsystem Component	Function	Approximate Quantity
1	Beamsplitter Array Mirrors	Generate Beam Multiplicity	1000
2	Oscillator Beam Detectors	Measures ELMO Power	10
3	Amplifier Coupling Mirrors	Deflects Beam Directions	8000
4	Recollimating Telescopes	Matches Amplifier Diameters	1900
5	Raman Seed Beamsplitters	Feeds Raman Oscillator	100
6	NLO Windows	NLO Cell/Atmosphere Barriers	240
7	Quarter-Wave Plates	Converts Linear Polarized to Circular	120
8	Spatial Filter Telescopes	Improves Seed Beam Quality	60
9	LA Image Relaying Telescopes	Eliminates Egg-Crate Diffraction	120
10	Amplifier AR-Coated Windows	Excimer/Atmosphere Barriers	6000
11	Large Aperture (LA) Mirrors	Deflects Beam Directions	120
12	Segmented NLO Windows	NLO Cell/Atmosphere Barriers	240
13	LA Electro-Optical "Chirper"	Generates SBS Seed	60
14	LA Quarter-Wave Plates	Converts Linear Polarized to Circular	360
15	LA Pockels Cells	Rapidly Changes Polarized State	120
16	LA Delay Line Mirrors	Reflects Beams at Normal Incident	240
17	LA Dielectric Polarizers	Reflects "s"-Polarized Beams	180
18	LA Collimating Mirrors	Focuses Beams Through Shield	60
19	Alignment Detector Array	Tracks Reflection from Target	60
20	Holographic Alignment System	Locates Target Precisely	3
21	Pulse Shape Monitors	Measures Output Pulse Shape	60
22	Back-Reflected Calorimeters	Measures Energy Missing Target	60
23	LA Focusing Mirrors	Focuses Beams on Target	60
24	Plasma Shutters	Blocks Retro-reflected Light	60
25	LA Grazing Incidence Mirrors	Reflects Focused Beams	60

A schematic diagram of the operational layout of the beamsplitter array can be found in Figure 6.5.1-2. Although space does not permit a thorough discussion of each of these optical subsystems here, some of the more important are described in the following sections.

6.5.1.6.1 Laser Beam/Target Alignment System - A key element in the Prometheus-L laser driver system is the laser beam/target alignment system. This system senses the positions of the moving DT target as it moves through the target chamber on its way to the location where all 60 laser beams are pointed. This is a difficult challenge because the laser/target alignment system contains sensitive sensors which can easily be damaged by the thermonuclear burn of the DT fuel pellet. As a consequence, a system of fast shutters will be required to protect the sensitive sensors in the 100 ms time following the DT target implosions. A simplified schematic of one of the target position sensors in the laser beam/target alignment system is shown in Figure 6.5.1-21.

Use or disclosure of data
subject to title page restriction

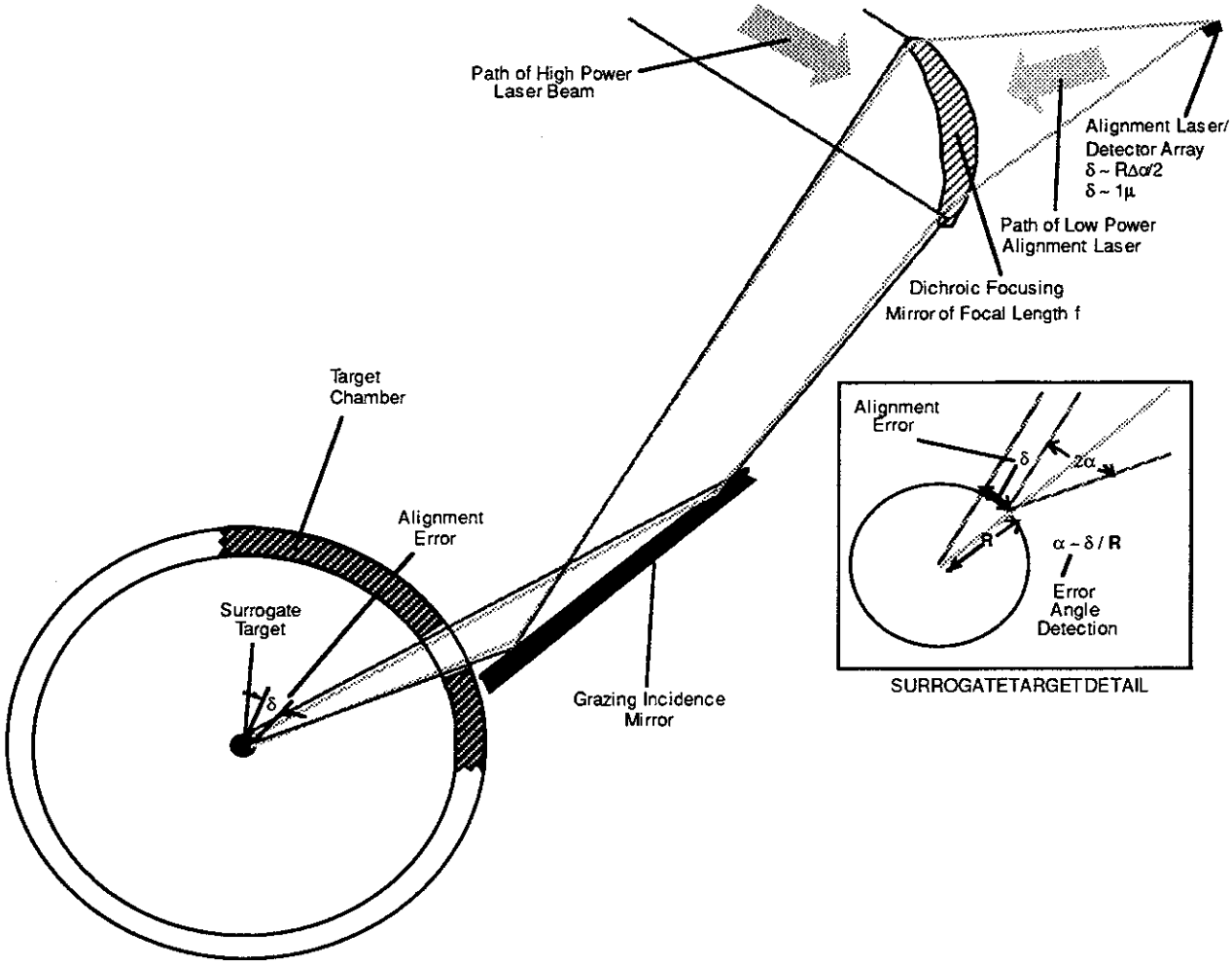

Figure 6.5.1-21 By utilizing a figured meniscus dichroic focusing mirror, it is possible to image the shine shield onto a highly magnified CCD array.

As indicated, it is recommended that the DT target have a "shine-shield" to assist the laser beam alignment system in tracking the target. Use of a holographic alignment system for the target permits very precise measurement of target positions as it moves through the target chamber.

Use or disclosure of data
subject to title page restriction

6.5.1.7 Final Optics - The Prometheus-L target focusing scenario involves 60 beamlines using ~ 1 m diameter optics located 30 m from the target (20 m distance to the GIMM and an additional 10 m to the focusing mirror). A schematic of the three major elements in the Final Optical Train are shown in Figure 6.5.1-22.

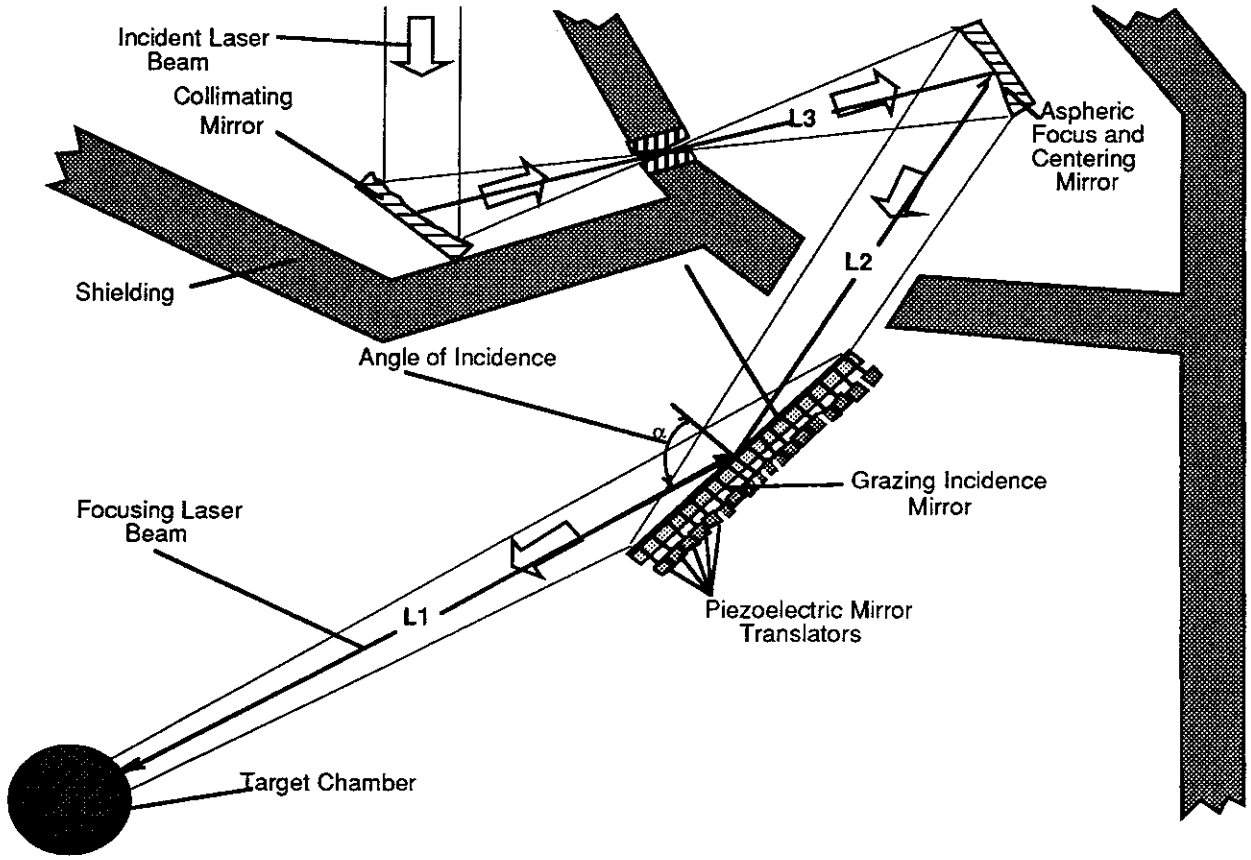

Figure 6.5.1-22 The incident beam from the E/O Switchyard is focused through and shielding by the collimating mirror, refocused by the focusing mirror, and beam directed onto the target by the grazing incidence mirror.

The grazing incidence mirror is shown with piezoelectric mirror translators for correcting neutron-induced neutron swelling. (These mirror adjustment devices are shown for illustration purposes only. Piezoelectric translators often show hysteresis effects and are prone to neutron damage.)

6.5.1.7.1 Collimating Mirror - The collimating mirror focuses the beam through the shielding to the focusing mirror. This permits a significant reduction in neutron fluence leaking through the primary shielding.

Use or disclosure of data subject to title page restriction

6.5.1.7.2 Focusing Mirror - The focusing mirror images the laser beam onto the DT target. Different scenarios are appropriate, depending upon whether the target is a direct-drive (DD) or indirect-drive (ID). The predicted far field focal spot size, d_{focus}, on the target is given by the expression:

$$d_{focus} \frac{4\xi\lambda f_m}{\pi D} \qquad (6.5.1\text{-}8)$$

where λ is the laser wavelength (248 nm), D is the effective aperture of the focusing mirror (~1 m), f_m is the mirror focal length (~20 m), and ξ is the beam quality (~1.1). Substituting these values into Eq. 6.5.1-4 produces a value of d_{focus} 7 μm . Smaller spot sizes can be achieved for smaller values of λ (i. e., ArF at λ = 194 nm), f_m or for larger values of D.

Laser focal spot sizes this small are not of particular interest for direct drive targets with diameters of ~0.6 cm. However, this ability to focus the laser beams down to dimensions on the order of 10 microns is very interesting for indirect drive targets. A somewhat different illumination geometry would be likely—two-sided target irradiation with 30 beams per side arranged in 50° cones or sets of cones.

In addition, this mirror can be constructed to perform alignment tasks if properly figured and equipped with dichroic coatings (see Section 6.5.1.7.4).

A key issue associated with all of the optics in the laser chain is the optical damage threshold, Φ_o. The particular case considered here is that of the optical train consisting of the focusing mirror and the GIMM.

For an assumed total energy delivered to the target, E_{laser} = 5 MJ, each beamline spreads approximately 100 kJ over an area of 1.2 m x 1.2 m or ~ 1.44 x 10^4 cm^2. At normal incidence, the resulting optical fluence Φ ~ 7 J/cm^2. This fluence level is comparable with the current industry definitions for "optimistic" (Φ_{max} = 8 J/cm^2) and "conservative" (Φ_o= 3 J/cm^2) limits used for dielectric-coated high reflectivity (HR) mirrors in the ultraviolet using advanced coating technology. Higher values can be expected in the year 2030 if technological development occurs to improve the damage threshold of UV mirrors. If the angle of incidence of the laser beam is θ, then the effective fluence on the mirror is reduced by a factor of cos θ. If the damage threshold cannot be increased by coating manufacturers and if the cosine factor is insufficient, it may be necessary to increase the mirror aperture somewhat to provide an adequate mirror damage safety margin.

Use or disclosure of data
subject to title page restriction

6.5.1.7.3 Grazing Incidence Metal Mirrors (GIMMs) - As shown in Figure 6.5.1-22, the initial 1.2 m diameter for the laser beam at the focusing mirror decreases geometrically (down to 0.8 m diameter) at the GIMM (for a 10 m separation between the focusing mirror and the GIMM). Significant optical flux reductions are possible if grazing incidence mirrors are used as final turning mirrors since, for $\theta = 80°$, the cosine factor is ~5.75, reducing the fluence to ~3 J/cm^2. The optics designer must be cautious, however, since there are other damage mechanisms which may degrade grazing incidence mirrors. (Especially, particles lying on the optical surface experience the full laser intensity.)

This geometrical factor advantage of GIMMs carries over into reducing neutron fluence (and concomitant damage) as well. Additional work needs to be performed on the coatings for GIMMs to permit them to have damage thresholds higher than 3 J/cm^2 (assuming 6 ns pulse durations). The GIMM will be sized appropriately to assure that it will survive laser irradiation. A schematic illustrating the location of the GIMM is shown in Figure 6.5.1-22.

6.5.1.7.4 Laser Beams Propagation Through Target Chamber Atmosphere - A variety of non-linear processes arising from residual gases in the target chamber can interfere with the delivery of the laser beam to the target. Non-linear processes depend upon the densities and compositions of the residual gases (as well as the laser beam intensity); therefore care must be taken to assure that their collective influences are negligible. Non-linear processes include: (1) laser-induced gas breakdown, (2) stimulated Raman scattering, (3) stimulated Brillouin scattering, and (4) multi-photon scattering. The ranges of laser intensity for each beam line as it propagates from the focusing mirror to the target can readily be calculated. Intensity at the GIMM would be I_{mirror} ~1.3 GW/cm^2. The intensity of the focused laser beam at the target is on the order of 10^{14} W/cm^2. A plot of Prometheus laser intensity, $I_{laser}(z)$ as a function of distance, z, from the final turning mirror to beyond the target focal plane is shown in Figure 6.5.1-23.

Laboratory experiments have shown that laser-induced gas breakdown and plasma formation begins at intensities[14] at or above 10^{10} W/cm^2 (or 10 GW/cm^2). Thus, it is possible to consider placing a high-Z gas cell with pressures higher than a few millitorr at distances from the target greater than 8 m. The high Z gas cell (e.g., Pb or Xe [Xe might cause some gas-pumping problems]) could be used to protect the final optics from the softer x-rays. For neutron protection, a fill of Ne can be considered owing to the relatively large neutron cross-sections of low-Z atoms.

Use or disclosure of data
subject to title page restriction

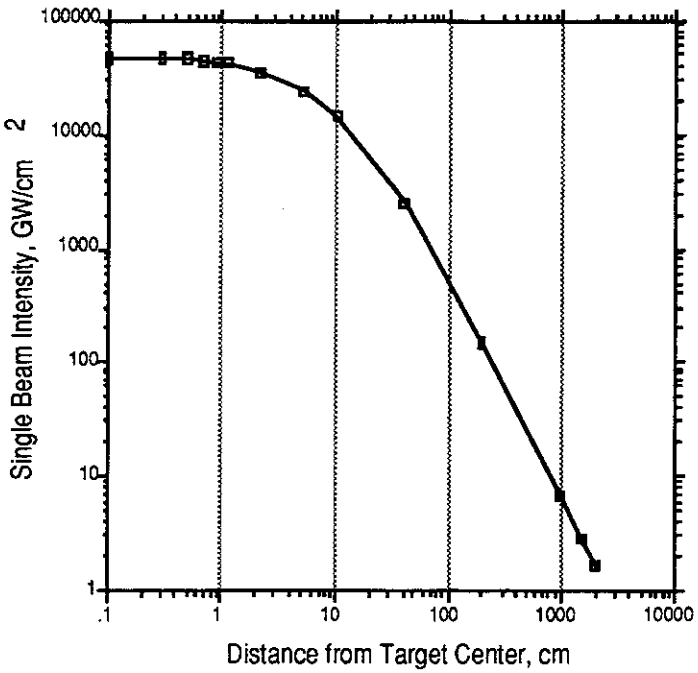

Figure 6.5.1-23 The single beam Prometheus laser intensity as a function of distance from a 6 mm diameter direct drive target with the beam diameter = target diameter at the target for a 100 kJ beam in a 6 ns pulse

Damage issues for the final focusing/turning optics arise from six sources:

(1) x-rays
(2) γ-rays
(3) neutrons
(4) laser radiation
(5) charged particles
(6) debris

Some of the properties of the five sources are summarized in Table 6.5.1-11.

Table 6.5.1-11
Potential Damage Sources for Final Turning Optics

Type of Source	Propagation Speed	Damage Threshold	Proposed Barrier
x-rays	$3x10^{10}$ cm/sec	0.5 MRad	Xe gas
γ-rays	$3x10^{10}$ cm/sec	0.5 MRad	Xe gas
neutrons	$5x10^{9}$ cm/sec	$4x10^{11}$/cm^2 (~1 J/cm^2)	Ne gas
laser light	$3x10^{10}$ cm/sec	8 J/cm^2	none
ions	$1--9x10^{9}$ cm/sec	0.1 J/cm^2	Ne/Xe gas
debris	$0.2--4x10^{7}$ cm/sec	0.5 J/cm^2	mech. shutter

Use or disclosure of data
subject to title page restriction

The optical radiation emanating from the target chamber may move too rapidly for protection schemes to protect the GIMM. As discussed in the following section, since the laser beams enter the target chamber through restricting apertures located approximately 5 meters from the target, a time delay of ~16.7 ns will occur before this "prompt" radiation reaches the target chamber entrance apertures. The "prompt" radiation can ablate a plasma traveling at a speed of ~4×10^5 m/sec which may influence the passage of further optical radiation through the entrance apertures.

6.5.1.7.5 Plasma Closure Inside Target Chamber - Plasma closure of the laser beam entrance ports inside the target chamber were considered in order to evaluate this mechanism as potentially contributing to the protection of the final focusing optics from target radiation. The calculations are based upon the assumption that a complete DT target "burn" occurs; calculations of the expected behavior for "near misses" or "dud" targets (both with no thermonuclear output) may generate some non-charged, relatively large diameter (>1 μm) particles.

Previous work[14] carried out at the Lawrence Livermore National Laboratory on plasma closure of optical apertures revealed that laser induced plasmas reached critical densities (for illumination wavelengths of 1064 nm) at speeds of approximately 4×10^5 m/sec. The threshold for plasma formation was measured for intensities $>5 \times 10^{10}$ W/cm^2. Since the excimer lasers have significantly shorter wavelengths (λ_{KrF} = 248 nm and λ_{ArF} = 193 nm) than the wavelengths at which these measurements were made (λ_{Nd} = 1064 nm), a higher ion density will be required before the plasma critical density is reached for these shorter wavelengths. However, for plasmas generated by the impact of γ-rays, x-rays, and high energy neutrons with the wall material, a hotter (i. e., more energetic) plasma would be expected. Accordingly, it is estimated that the critically-dense portion of the plasma would arrive at a speed of 5×10^5 m/sec. There are four areas of interest:

(1) Plasma closure in the target chamber laser beam entrance ports
(2) Target debris ion speeds for Pb capsule hohlraum designs (for ID targets)
(3) Update of the configuration for SBS pulse compression in the target chamber vicinity
(4) Update of the Raman accumulator geometry for electric discharge excimer lasers.

Each of these areas is briefly described in the sections below.

Plasma Closure from Ablation Products in Target Chamber - The complete thermonuclear burn of the DT fuel capsule will generate roughly 500 to 1000 MJ of

Use or disclosure of data subject to title page restriction

energy primarily in the form of "prompt" radiation, i.e., particles and radiation moving at or near the speed of light, $3x10^8$ m/sec. This "prompt" radiation consists of γ-rays, x-rays, and primarily 14 MeV neutrons. We assume further that the thermonuclear burn occurs over the time period of approximately 5 ns. As discussed in Section 3.0, ionized target debris derived from the explosion of the high-Z capsule moves at a significantly slower speed, $<4x10^5$ m/sec. Thus, for a target chamber of radius R, the time delay, Δt, before the "prompt" radiation strikes the chamber wall is simply:

$$\Delta t = \frac{R}{c} \qquad (6.5.1\text{-}9)$$

For R = 5 m, Δt = 16.7 ns. The X-ray portion of the "prompt" radiation is expected to ablate a plasma from the wetted wall of the chamber. This plasma expands outward from the wetted wall of the target chamber with an estimated speed of $v_p \sim 5x10^5$ m/sec. A portion of this plasma will help stop the ionized debris from the exploded target capsule so that some of this debris may not reach the GIMM located at a distance $R_1 \sim 20$ m from the target.

The γ-rays and neutrons of the "prompt radiation" penetrate deeper into the first wall, and consequently a Pb vapor cloud will be ejected and expand into the target chamber. An expression for the rate of energy loss of an ionized particle of charge Q passing through a cloud of N neutral atoms/cm^3 is given by:

$$\frac{dE}{dr} = \frac{4\pi N Z Q^2 e^2}{m_e v_p^2}\left\{\ln\left[\frac{2m_e v_p^2}{\eta}\right] - \ln\left(1-\beta^2\right) - \beta^2\right\} \qquad (6.5.1\text{-}10)$$

where Z in the atomic number, v_p is the particle velocity, $\beta = v_p/c$ e is the electronic charge, m is the electron mass, and η is the ionization potential of the neutral atoms. The stopping distance, R_s, for the ionized particle can be calculated from:

$$R_s = \int_0^E \frac{dE}{-dE/dr} \approx \xi_p \frac{E_p}{Q^2 N} \qquad (6.5.1\text{-}11)$$

where E_p is the energy of the particle and ξ_p (Z, Ep, N) is a constant. For charged particles passing through a plasma, dE/dis even larger, resulting in increased Bremsstrahlung. For a few hundred millitorr of Pb vapor erupted from the first wall, preliminary calculations show Pb ions of up to 200 keV energy will be stopped in ~1 cm of vapor.

It should also be noted that the low-Z materials (e.g., C, H, D, & T) in the target should be included in these analyses since these elements may be numerically more abundant than the high-Z casing materials. Assuming that the low-Z elements have approximately the same kinetic energy spectrum as the high-Z (and assuming local thermodynamic equilibrium [LTE]), the velocities of the lightest isotopes will be approximately an order of magnitude greater than an element such as Pb. A schematic of this effect is illustrated in Figure 6.5.1-24.

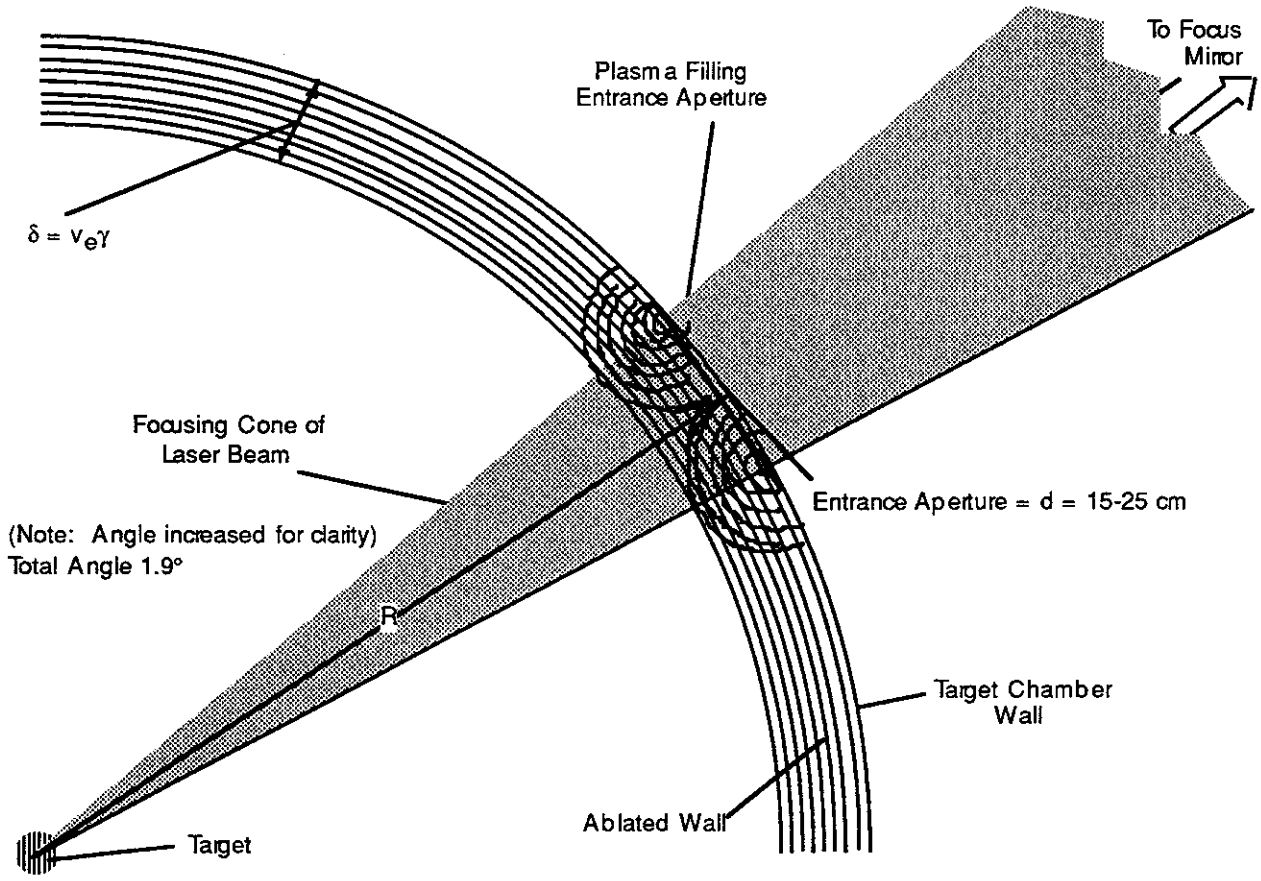

Figure 6.5.1-24 Schematic of Prompt Radiation for D/T Target Ablating Plasma from Reactor Chamber First Wall

As illustrated in Figure 6.5.1-24, the expanding plasma and vapors from the first wall around each of the optical beam entrance ports eventually will fill the beam ports. Although the fast-moving plasma may achieve "critical density" such that it is optically opaque, ions with energies > 100 keV have considerable penetration of the plasma. Assuming that the diameter of the optical beam entrance ports is d, then the length of time needed for the expanding plasma to fill these apertures is simply:

$$\tau = d/2v_p \qquad (6.5.1\text{-}12)$$

Use or disclosure of data subject to title page restriction

where v_p is the plasma expansion speed (v_p ~ 5x10^5 m/sec). A schematic of the arrangement of the ~1 m effective aperture final focusing mirror relative to the target chamber is shown in Figure 6.5.1-25.

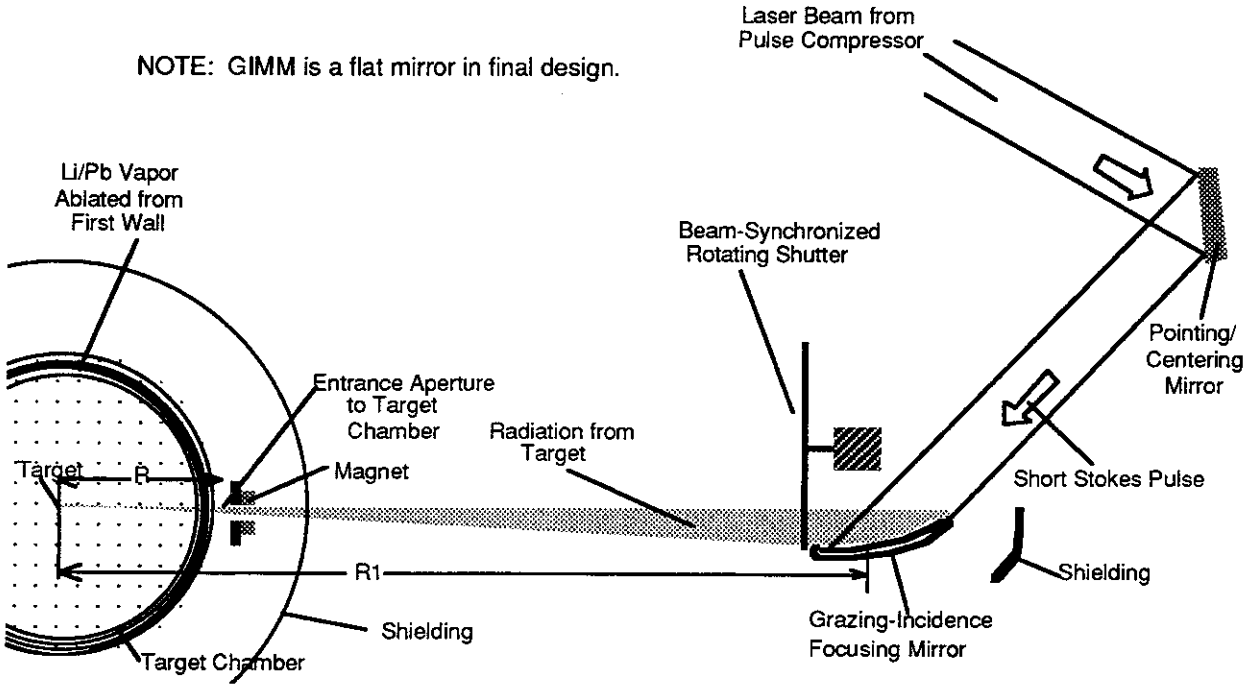

Figure 6.5.1-25 Schematic of Placement of Final Focusing Optics, Magnetic Deflector, Rotating Mechanical Shutter, and Input Laser Pulse Relative to Target Chamber

This geometry illustrates possible placements for an ion deflection magnet and a rotating "slow debris" mechanical shutter, both of which are intended to provide target debris protection for the final focusing mirror. As indicated in Figures 6.5.1-24 and 6.5.1-25, the approximate diameter, d, for the optical entrance port in the target chamber is estimated by

$$d = \xi DR/R_1 \qquad (6.5.1\text{-}13)$$

where D is the effective diameter of the focusing mirror, R_1 is the distance from the target to the grazing incidence focusing mirror, and ξ is an apodizing factor to guarantee that the near field laser beam intensity incident on the perimeter of the entrance port is below 10^{10} W/cm^2. For D =1 m, R_1 = 25 m, R = 5 m, and ξ = 1.2, d ~24 cm.

Calculations of Target Debris Velocity Spectra - Although the adopted target for the laser design is the direct-drive, the indirect-drive laser target was used as a more severe case to assess. Following a review of LLNL calculations of the target debris velocity spectra for different thickness indirect drive capsules, velocity spectra measured[15] by

Use or disclosure of data subject to title page restriction

Charles Orth were considered. In all cases, following the 500 to 1000 MJ burn, the high-Z capsule debris appears to be completely ionized (with many ions in the +3 ionization state) with essentially all heavy ions having energies less than 500 keV. For Pb ions, this energy is not relativistic, so the estimated speed spectra, v_p, of the particles follows the calculated energies (expressed in electron volts) from the expression:

$$v_p = \sqrt{\frac{2E_p e}{m}} \sim 7x10^5 m/s \qquad (6.5.1\text{-}14)$$

where E_p is the particle energy in electron volts, e is the electronic charge in coulombs, and m is the mass of the lead atom in g.

The indirect laser target is assumed to be subjected to two-sided illumination with two cones of approximately 50° each.

Although many of the details of the indirect drive laser target are not defined , the major features include the DT fuel capsule suspended within the high-Z case. Reductions in the required high-Z mass for the case may require more realistic designs for mass-produced targets for which the legacy of recovering large quantities of vaporized high-Z material would not be cost effective.

As mentioned earlier, not considered at this time is the problem of target debris generated when a target misfires, yielding little or no thermonuclear energy. Under these circumstances, non-charged, relatively small (~1 μm) particles could be expelled from the target chamber at relatively low speeds. A possible protection mechanism for this eventuality is illustrated in Figure 6.5.1-25 in which synchronized, high speed, rotating mechanical shutters close off each of the 60 final focusing optical system beamlines shortly after delivery of each laser pulse. With a shutter speed of 1 km/sec, a one-meter beamline could be protected in 1 ms.

By far the most common problem faced by the focusing optics is dealing with the fluence of γ-rays, x-rays, and high energy neutrons. Both the γ-rays and the neutrons will penetrate deeply into the final focusing mirror substrate, whereas the x-rays will be absorbed in the mirror surface (with the x-ray fluence reduced by cos θ). At present our plan is to design the final focusing mirror to survive the "prompt" radiation loading.

The slower debris from the target should be effectively attenuated by ablated plasma (and to a minor extent Pb vapor) from the first wall of the target chamber. Installation of a strong deflecting magnetic field near the target chamber will help keep charged particles away from the focusing optics.

Use or disclosure of data
subject to title page restriction

Charged ion debris velocity spectra for the bare DT target is shown in Figures 6.5.1-26. The spectra for lead should also be included as it was selected for use in the case.

Thus the ions from the target should be effectively stopped in the residual Pb vapor present in the direct line of sight between the GIMM and the center of the target chamber.

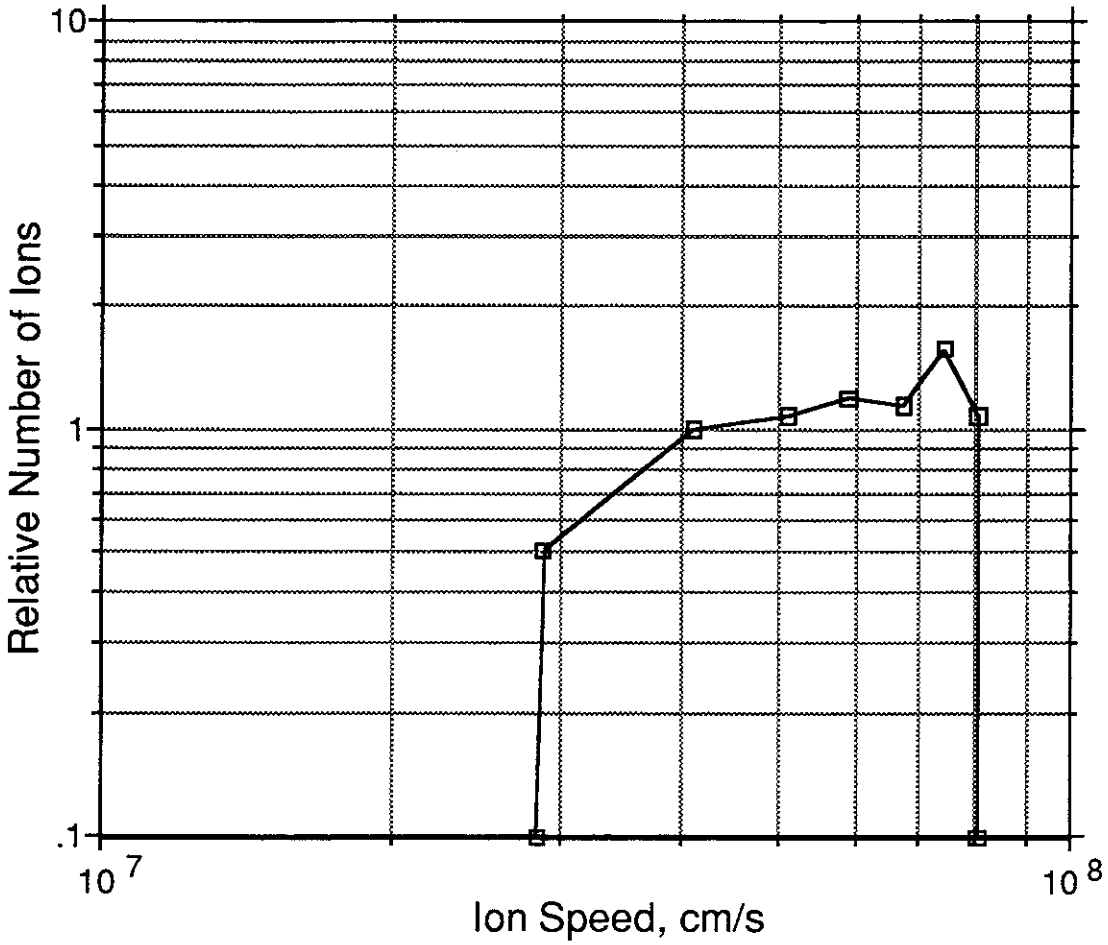

Figure 6.5.1-26 Target Debris Velocity Spectra for Bare D/T Target

Use or disclosure of data
subject to title page restriction

6.5.1.8 Grazing Incidence Metal Mirror

In this section, the data base which is relevant to the material selection of the final Grazing Incidence Metal Mirror (GIMM) is presented. A unique design for the GIMM is then presented and analyzed.

6.5.1.8.1 Introduction - Transmission measurements for conventional dielectrics show that the absorption coefficient of MgF_2 and the optical transmission of ZnS for wavelengths of interest (250-500 mm) both degrade by an order of magnitude after 10^{16} n/cm^2. [16] This is an extremely low fluence limit, and even if most of the color centers are annealed out by periodic heating, residual defects would still remain and lead to an extremely short life time. For these reasons, a metal mirror surface is chosen as the final optical element in our laser system before focused laser light enters the cavity.

6.5.1.8.2 Metal Reflectivity and Absorptivity for Laser Light - The surface material for the GIMM must have the highest reflectivity and lowest absorptivity. This optimum choice is necessary so that the damage to the mirror's surface is minimized. Table 6.5.1-12 gives the room temperature for materials of interest. These values are experimental and are for polished surface reflectivity light of long wavelength (500-10,000 nm).[17]

Table 6.5.1-12. Reflectivity for Materials of Interest (Polished Surfaces)

Element	l (μm)	%R
C	0.5-10	22-59
Mg	0.5-9.0	72-93
Al	1-12	71-98
Si	0.5-10	34-28
Fe	0.5-9.0	55-92
Ag	0.8-9.0	96.8-98.7

In the wavelength of interest (i.e., 200 to 500 nm), metal reflectivities are strong functions of the wavelength (photon energy) and the angle of incidence. It is desirable to select a material which does not exhibit electronic absorption bands close to the operational regime of KrF laser. Figure 6.5.1-27 shows the reflectivity of Ag, Al, and Mg at normal incidence as a function of the wavelength. The strong photon-electron interaction in Ag for wavelength in the vicinity of 320 nm would exclude it from our list since the wavelength of KrF laser is 300 nm. At grazing incidence (q = 85°), the reflectivities of both Al and Mg markedly improve, as can be seen in Figure 6.5.1-28. For KrF laser light, the reflectivity of both Al and Mg is about the same (99.4%).

Use or disclosure of data subject to title page restriction

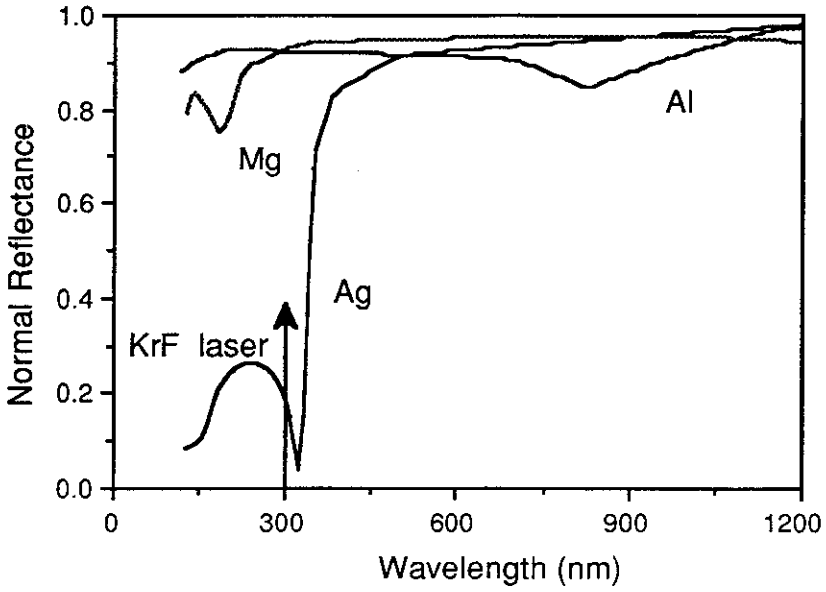

Figure 6.5.1-27 Reflectivities at Normal Incidence

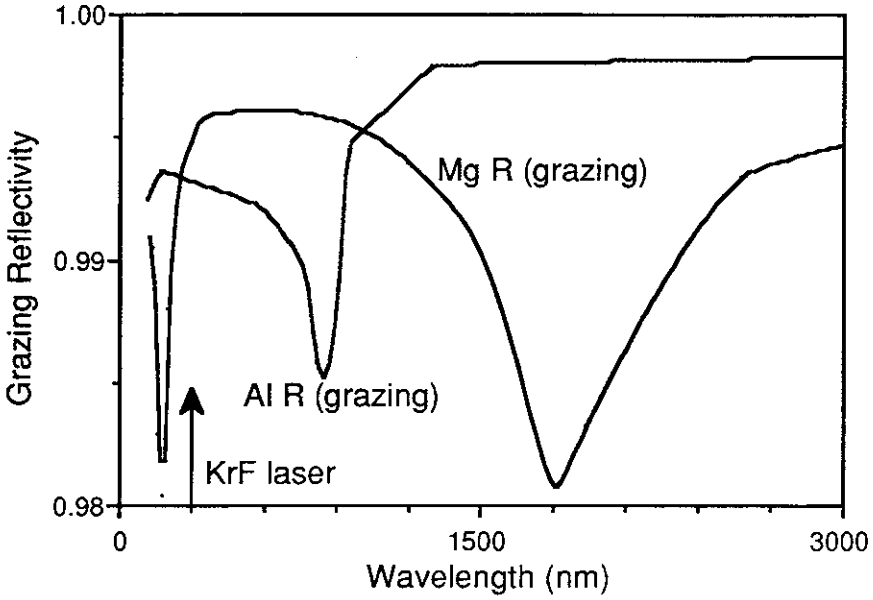

Figure 6.5.1-28. Reflectivities at Grazing Incidence (85°)

Use or disclosure of data
subject to title page restriction

6.5.1.8.3 Radiation Effects on Candidate Materials - Neutron irradiation results in a number of detrimental effects to the mirror's optical performance. Defects, in the form of vacancies, interstitials, transmutations, and subsequent micro-structural changes, lead to deterioration of the focusing quality of the mirror and increase the absorption of incident laser light. The salient effects of neutron irradiation are discussed in the following sections, including how such effects can be accommodated. Main areas of concern are the effects of produced defects on increasing the electrical resistivity (and hence the laser light absorptivity) of the mirror and the deformation of the mirror's surface, leading to defocusing of the laser beam.

Radiation Effects on Resistivity and Surface Absorptivity - The increase in the resistivity of the aluminum layer will occur by the accumulation of point defects and transmutation products. The rate of increase in the resistivity due to point defects must saturate, either by overlap of neighboring collision cascades or by thermal annealing effects. The rate of resistivity change can be written as:

$$\frac{dP}{dt} = k\sigma_d \phi \rho_F - \frac{\rho}{\tau} \qquad (6.5.1\text{-}15)$$

where k is an efficiency factor, σ_d is the displacement cross-section, ϕ is the neutron flux, ρ_F is the measured resistivity increase per Frenkel Pair, and τ is the cascade lifetime in aluminum. The resistivity will saturate at a neutron fluence of $(\phi t)_{sat.} = \phi t$ (Eq. 6.5.1-15). At high temperatures, t is very short and resistivity saturation will occur at a very small fluence (on the order of $x10^{17}$-10^{18} n/cm^2).

At cryogenic temperatures (77 K), the corresponding change in the mirror's absorptivity is reported to be less that 1% at normal incidence and less than 0.5% at grazing incidence.[2] In our design, however, the aluminum surface will run hot, and point defect annealing will result in a further decrease in the magnitude of the irradiation-induced absorptivity.

The contribution of transmutations to the increase in resistivity and, hence, the absorptivity of the surface does not saturate, as is the case with point defects. However, the resistivity increase per transmutation atom is 4-5 orders of magnitude less than that for point defects.[2] For this reason, their contribution during the mirror's lifetime will be negligible.

Sputtering of surface atoms can lead to roughening. It is experimentally estimated that the sputtering yield of 14 MeV neutrons is on the order of $5x10^{-4}$ per neutron.[18] If a gas shield is introduced to protect from x-rays, additional sputtering from argon atoms will contribute by a small amount,[17] on the order of 6% of the neutron sputtering value.

Use or disclosure of data
subject to title page restriction

These sputtering events can lead to surface features which would destroy the quality of the laser beam. Since the aluminum surface temperature will be high, rapid atomic surface diffusion is expected to result in the removal of layer-by-layer from the surface of the mirror.

In conclusion, it is estimated that the total increase in absorptivity of the mirror due to point defects, transmutations, and sputtering is on the order of 0.5% and that it will saturate after few days of operation. For all practical purposes, therefore, the reflectivity for 300 nm laser light will degrade to 99%; i.e., only 1% of the light will be absorbed.

Neutron-Induced Swelling - When non-uniform swelling takes place in the aluminum layer, gradients in surface displacements will occur. Focusing of the laser light may become impossible if surface undulations on the order of 1/4 of the wavelength result. This tolerance (about 75 nm) is very strict and has actually resulted in very short lifetimes for similar mirrors in other conceptual designs.

Neutron swelling data on aluminum and magnesium show strong dependence on the impurity level. Experimental data of Adda[18] are summarized in Figures 6.5.1-29 and 6.5.1-30. The base case for our design (99.994% purity) is replotted in Figure 6.5.1-31, where the swelling is shown as a function of the high energy neutron fluence. It is clear from this figure that aluminum will be a better choice for the mirror's surface than magnesium. The following design equation is used to fit the swelling data of aluminum and magnesium:

$$\frac{\Delta V}{V}\% = k\phi t \qquad (6.5.1\text{-}16)$$

where k is a constant, and $\phi\tau$ is the neutron fluence in n/cm^2. For Mg, $\kappa = 1.29 \times 10^{-21}$ and, for Al, $\kappa = 1.11 \times 10^{-21}$.

Use or disclosure of data subject to title page restriction

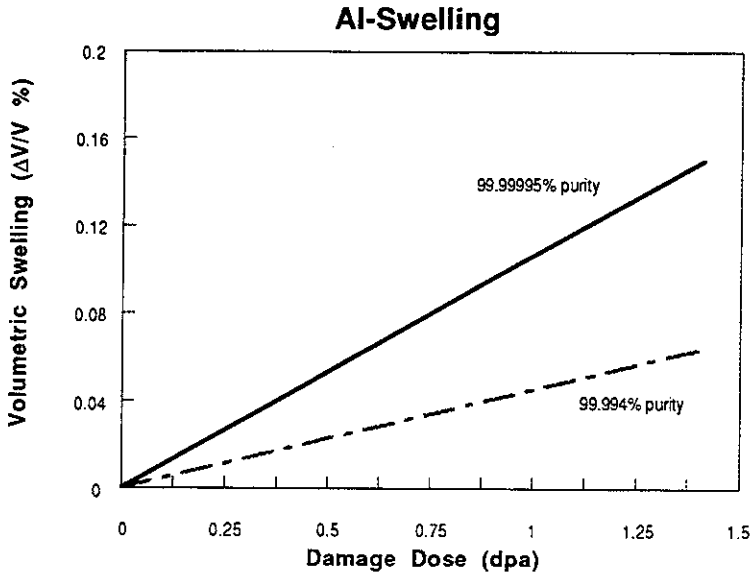

Figure 6.5.1-29 Neutron-Induced Swelling in Aluminum[18]

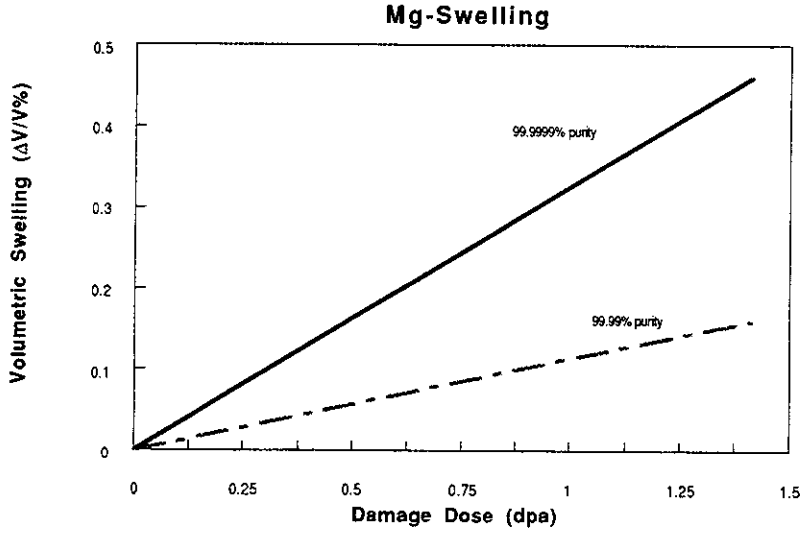

Figure 6.5.1-30 Neutron-Induced Swelling in Magnesium[18]

Use or disclosure of data
subject to title page restriction

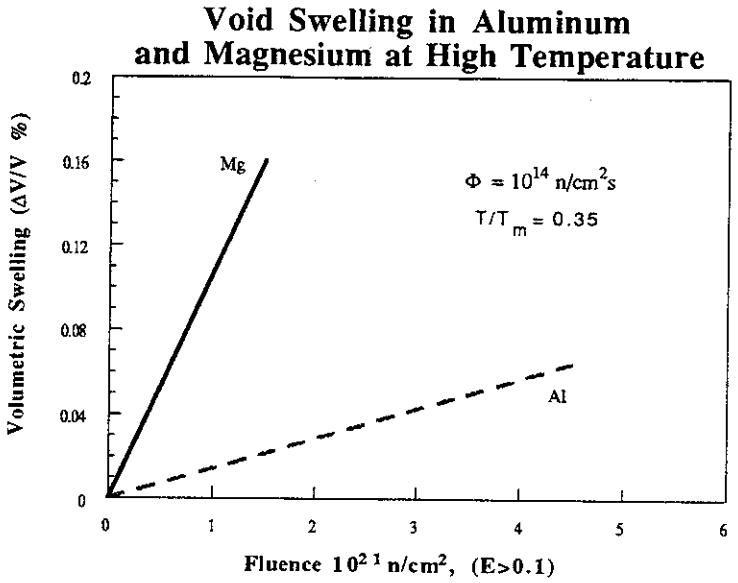

Figure 6.5.1-31 Void Swelling at High Temperature

6.5.1.8.4 Configuration and Material Selection - The basic design philosophy of the mirror is to separate the functions of each material. For this reason, a high reflectivity aluminum surface is created by a CVD process on top of a SiC structure. The SiC structure is stiffened in two transverse directions by two sets of I-beams. The surface is cooled by flowing helium through the coolant channels. A top view of the mirror is shown in Figure 6.5.1-32. Mirror sizing is dictated by two factors:

(a) Maximum temperature rise in the aluminum during the laser pulse should not exceed the re-crystallization temperature.

(b) Induced thermal stress in the aluminum layer should not exceed its fatigue endurance limit.

Design Rationale For The GIMM - The optical properties of the mirror's surface have been decoupled from the mechanical properties of the supporting structure. In this regard, we have achieved a great degree of flexibility in the design. The surface of the GIMM is metallic because dielectric materials show great sensitivity to the effects of ionizing radiation.

The leading high reflectivity candidate metals are aluminum, magnesium, silver, gold, and copper. The following criteria were used to select between these metals:

Use or disclosure of data
subject to title page restriction

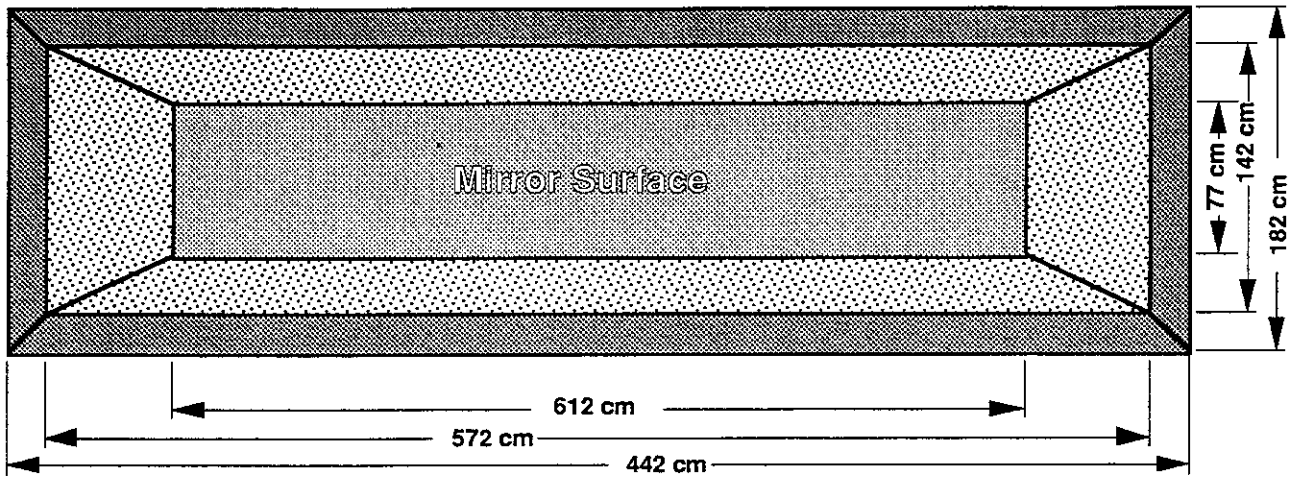

Figure 6.5.1-32. Top View of GIMM with Scaled Measurements.

(1) High reflectivity in the wavelength of interest (i.e., 250 to 500 nm)
(2) Effects of radiation on absorptivity
(3) Surface temperature rise during the laser pulse
(4) Thermal fatigue resistance
(5) Radiation effects on surface deformation

Although silver has excellent reflectivity, neutron-induced micro-craters are expected to distort the mirror's surface. Near-surface collision cascades in silver are very dense because of the high electronic stopping power of silver. Copper was excluded on the basis of its high neutron-induced swelling, particularly when it is pure. The higher fatigue strength of aluminum results in a smaller mirror size when it is compared to magnesium. In addition, the neutron-induced swelling rate of commercial grade aluminum is lower than that of magnesium. For the above reasons, aluminum is selected as the material for the reflective surface of the mirror.

Structural support of the mirror is composed of two parts: a low swelling composite SiC high-rigidity support structure and a concrete support frame for control of thermal deformations. The SiC structure is composed of small helium cooling channels, running along the length of the mirror. Two other layers are attached immediately underneath. Each one of these two layers is stiffened by I-beams. A SiC composite structure was chosen for the following reasons:

Use or disclosure of data
subject to title page restriction

(1) Very low neutron-induced deformations by thermal and irradiation creep mechanisms in the temperature range of 500 to 700 K.
(2) For porosity of approximately 10-15%, no neutron swelling is to be expected; thus, mechanical deformations of the mirror's surface are minimized.
(3) SiC is a low activation material. The choice of SiC will allow passive safety and shallow land burial of the mirror at the end of life.

The SiC structure is surrounded by a concrete frame to provide complete to restrict out-of-plane deformations. A sliding bolt mechanism between the SiC strucure and the concrete frame compensates for all movement.

Since the coefficient of thermal expansion of aluminum is higher than that of SiC, a shear graphitic layer is deposited first on the surface of the SiC composite, and the aluminum is added on top of the graphitic shear layer . With this arrangement, in-plane mismatch thermal expansions of the aluminum can be isolated from the SiC composite structure.

A GIMM cross-section is shown in Figure 6.5.1-33 and the details are illustrated in Figure 6.5.1-34. Thermal expansion gaps are provided around the mirror structure to prevent buckling. The main structure of the mirror (SiC) is surrounded by a rigid concrete frame structure. This mirror support structure is designed to prevent mirror deflections by distributed clamping forces, over a 30 cm distance, as shown in Figure 6.5.1-35. The magnitude of the distributed clamping forces will be calculated in the section on surface deformations.

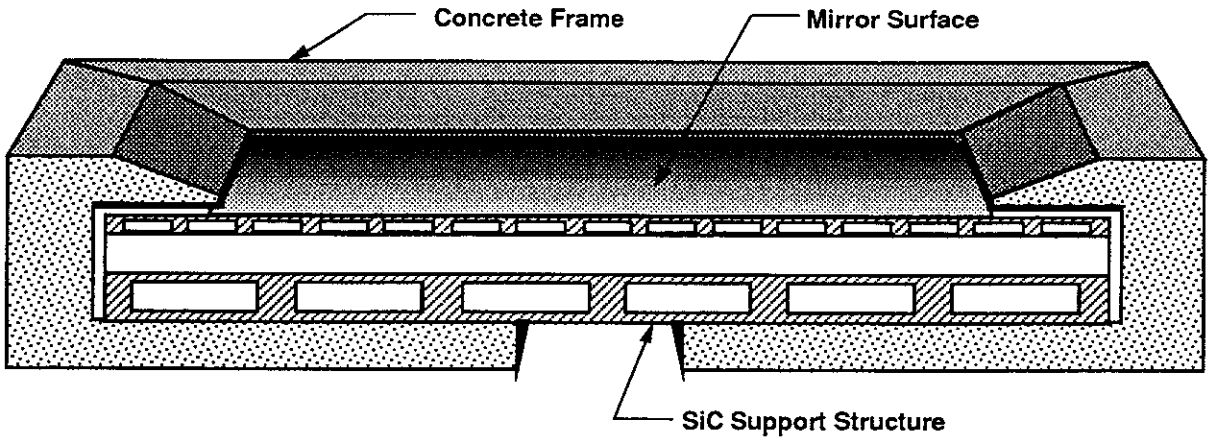

Figure 6.5.1-33. Cross-Sectional View of GIMM

Use or disclosure of data
subject to title page restriction

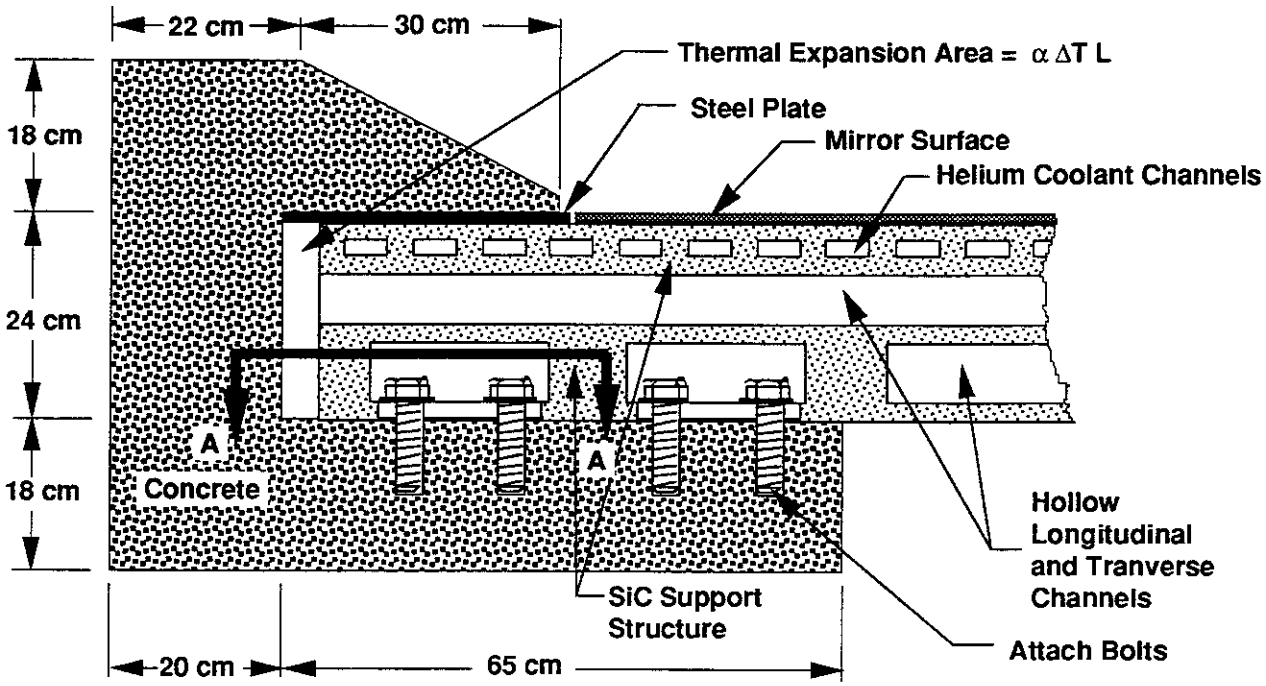

Figure 6.5.1-34. Detailed Cross-Section of GIMM

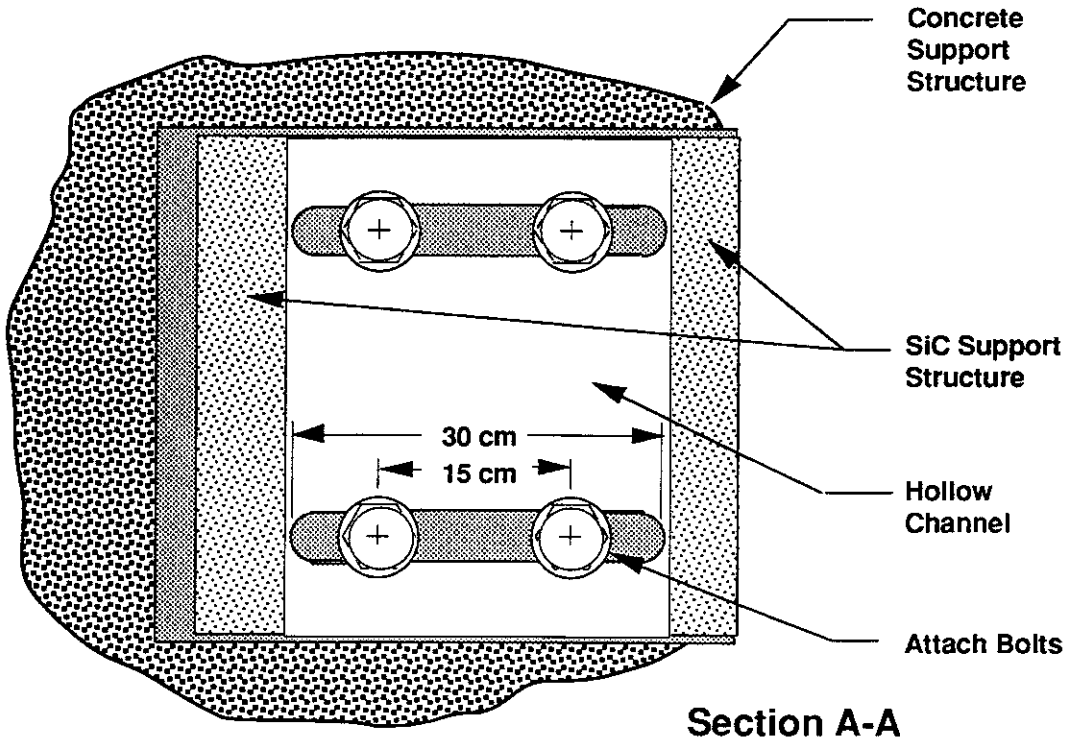

Figure 6.5.1-35. Section View of Mirror Structure Illustrating Expansion Capability

Use or disclosure of data
subject to title page restriction

6.5.1.8.5 GIMM Thermal Design - Steady-state temperature gradients and the instantaneous rise in the mirror's surface temperature are minimized by cooling. Cooling concepts existe to control the steady-state temperature gradients, but the instantaneous surface temperature rise is almost a material property, since the duration of the laser pulse (a few ns) is much shorter than typical thermal diffusion times. The optical penetration distance of the laser light is given by:

$$d = \frac{\lambda}{4\pi k} \qquad (6.5.1\text{-}17)$$

where λ is the wave length, and k is the extinction coefficient. A KrF laser penetrates aluminum only 7 nm for normal incidence, and about 2-3 atomic layers for grazing incidence. Therefore, a good approximation to the surface temperature will be an instantaneous temperature rise given by:

$$\Delta T_s = \frac{2(1-R)q_{beam}}{k}\sqrt{\frac{\alpha t}{\pi}} \qquad (6.5.1\text{-}18)$$

where q_{beam} is the instantaneous surface power density and t is the duration of the laser pulse. k, α, and R are for the aluminum surface.

The mirror is designed with convective helium cooling channels as shown in Figures 6.5.1-32 and 6.5.1-33. Since heat loss from the bottom surface of the mirror is very small, the temperature gradient through the mirror will be slightly greater than across the cooling channel thickness. Temperature and convective heat transfer calculations across the cooling channel are shown in Table 6.5.1-13.

Table 6.5.1-13. Thermal-Hydraulic Parameters for the GIMM

Parameter	Value	Units
Wall Temperature	450	K
Bulk Temperature	350	K
Pressure Exit	1	MPa
Pressure Drop	19.58	Pa/m
Bulk Velocity	20	m/s
Reynolds Number	2.47×10^5	
Heat Transfer Coefficient	261	W/mK

The temperature drop across a 2-cm channel wall at the average heat flux can be computed as follows:

Use or disclosure of data subject to title page restriction

Total mirror surface area = number of mirrors x width x length = 60 x 77 x 442
= 2.04 x 10^6 cm^2

Energy Density per pulse = $\frac{5MJ}{2.04x10^6} = 2.45\,J/cm^2$

Absorbed energy density per pulse = 0.01 x 2.45 = 0.0245 J/cm^2

Average heat flux = 3.5 x 0.0245 = 0.08575 W/cm^2.

If the conductivity of SiC is taken as 0.20 W/cm/K (for irradiated SiC at low temperature), then the temperature drop across the support structure will be on the order of 2 K. The effective coolant channel thickness is taken as 4 cm. This small temperature drop must be taken into account for calculations of the thermal deflections of the mirror's surface.

When the laser energy is delivered in a short pulse (7.3 ns), the instantaneous power is very high. The rise in the surface temperature of the mirror is mainly dictated by the thermal diffusivity of the aluminum. Calculations with Eq. 6.5.1-18 above give the results shown in Table 6.5.1-14. The instantaneous surface temperature rise is 130.6 K. The corresponding thermal stress can simply be found as:

$$\sigma \approx \frac{E}{(1-\nu)}\alpha\Delta T \qquad (6.5.1\text{-}19)$$

Using the properties of aluminum (annealed material), the following is obtained:

$$\sigma = \frac{63.8x10^3}{(1-0.34)} x\ 25x10^{-6} = 130.6\,MPa \qquad (6.5.1\text{-}20)$$

This may exceed the fatigue endurance limit of some aluminum alloys. (It is in the range of 50-390 MPa.) However, if the radiation hardening effects are considered, the endurance limit can be raised by as much as 50 MPa for aluminum.[19]

6.5.1.8.6 GIMM Mechanical Deformation - Out-of-plane deformation of the mirror's surface should be minimized, or eliminated, if high quality laser beams are to be maintained. Two primary sources of deformation must be analyzed.

(1) Thermal deformation
(2) Neutron-induced swelling deformation

The design approach is to isolate these two effects. In this respect, an aluminum metal surface and an SiC backing is used. The temperature of SiC can be kept low enough

Use or disclosure of data
subject to title page restriction

Table 6.5.1-14. Thermo-Physical Properties of High Purity Aluminum

Parameter	Symbol	Value	Units
Thermal Conductivity	k	2.4	W/cm K
Density	ρ	2.7	g/cm^3
Specific Heat	c_p	0.95	J/gm K
Thermal Diffusivity	γ	0.936	cm^2/s
Characteristic Thermal Diffusion Distance	<d>	0.466	μm
Average Energy Density	<E>	2.45	J/cm^2
Average Power Density During Pulse	<q>	3.36E+08	W/cm^2
Average Absorbed Power Density	<q>0	3.36E+05	W/cm^2
Temperature Rise During Pulse	ΔT	130.6	K

that neutron-induced swelling is eliminated. Therefore, the design must eliminate the deformation of the SiC plate as a result of the modest temperature gradient of a few degrees. When this is accomplished, the deformation of the aluminum surface by neutron swelling should be compensated for separately.

The theory of plates and shellsis an appropriate theory for calculating the surface deformations. However, a good approximation is the elementary beam theory applied in the two transverse directions. The influence of in-plane shear is neglected in this case.

Consider the elementary theory of straight beams, as illustrated in Figure 6.5.1-36. The axial strain, ε_z, is given by:

$$\varepsilon_z = \frac{x}{\rho} \tag{6.5.1-21}$$

where x is the distance off the neutral axis, and ρ is the radius of curvature of the mirror's surface. We know, however, that the mirror's curvature is given by:

$$\frac{1}{\rho} = \frac{d^2v}{dz^2} \tag{6.5.1-22}$$

where υ is the deflection of the mirror's surface, which we try to minimize, or better yet, eliminate.

Combining Eqs. 6.5.1-21 and 6.5.1-22, we obtain a relationship between the strain, ε_z, and the deflection of the mirror's surface. This is of the form:

Use or disclosure of data
subject to title page restriction

$$\varepsilon_z = x\frac{d^2v}{dz^2} \qquad (6.5.1\text{-}23)$$

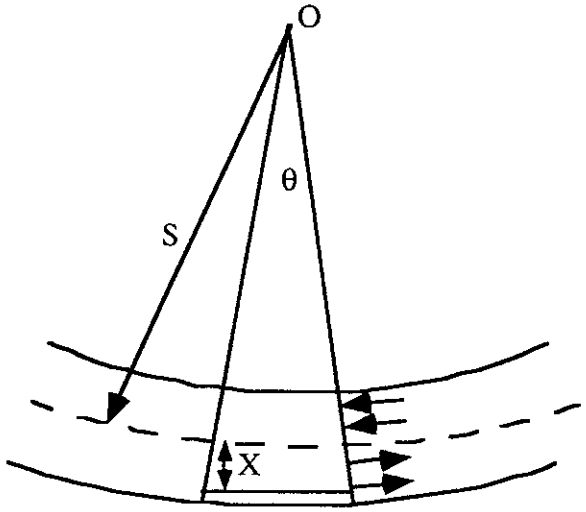

Figure 6.5.1-36. Thermal Design of the GIMM

The total axial strain at any distance, x, off the neutral axis is composed of an elastic component, σ/E, and two other inelastic components, αT and ε^s. αT is the thermal strain, while ε^s is the swelling strain. Now Eq. 6.5.1-23 can be put in the form:

$$x\frac{d^2v}{dz^2} = \frac{\sigma}{E} + \alpha T + \varepsilon^s \qquad (6.5.1\text{-}24)$$

The composite SiC structure is designed to exhibit very low swelling at high temperature by control of its internal porosity. At low temperature, as is the case in the GIMM, neutron irradiation will produce no swelling. The damaging neutron fluence is estimated from the uncollided neutron flux as:

$$\phi_u \approx \frac{S_0}{4\pi R^2} \qquad (6.5.1\text{-}25)$$

where the neutron slowing down and multiple scattering effects are neglected. For example, at the center of the mirror,

$$\phi_u \approx 1.957 x 10^3 \, n/cm^2/s \qquad (6.5.1\text{-}26)$$

with a displacement cross-section of 3140 barns, the flux translates to a defect production rate of:

$$p = \phi_u \sigma_d \approx 2 \, dpa/yr \qquad (6.5.1\text{-}27)$$

Detailed neutronics calculations are costly and are probably not warranted at this stage. Such calculations will lead to more accurate results than those given by

Use or disclosure of data
subject to title page restriction

Eq. 6.5.1-27. However, it is clear that the swelling of SiC will be zero under these conditions and can, therefore, be eliminated from Eq. 6.5.1-24.

Multiplying both sides of Eq. 6.5.1-24 by bx, where b is the mirror's width, and integrating between -h and +h, where h is the mirror's height, the following is obtained:

$$\frac{d^2v}{dz^2} b \int_{-h}^{h} x^2 dx = \frac{1}{E} b \int_{-h}^{h} x\sigma dx + \alpha b \int_{-h}^{h} T x dx \qquad (6.5.1\text{-}28)$$

Assuming a linear temperature variation across the thickness of the mirror yields:

$$T = \frac{\Delta T}{2L} X \qquad (6.5.1\text{-}29)$$

where ΔT is the temperature difference between the top and bottom surfaces of the mirror. Inserting Eq. 6.5.1-29 into Eq. 6.5.1-28 and performing the integrations, the mirror's deflection equation is obtained:

$$\frac{d^2v}{dz^2} = \frac{M}{EI} + \frac{\alpha \Delta T}{2h} \qquad (6.5.1\text{-}30)$$

where M is the acting moment at any specific point in the mirror. The mirror is designed such that v=0 everywhere on the mirror's surface. This can be achieved via Eq. 6.5.1-30 by requiring that:

$$\frac{d^2v}{dz^2} = 0 \qquad (6.5.1\text{-}31)$$

and clamped end condition (i.e., $v(0) = v'(0) = v(l) = v'(l) = 0$). The solution to Eq. 6.5.1-30 will yield identically zero deflection everywhere.

This situation can be realized in one of two ways:

(1) Apply a uniform moment by force couples at distributed locations on the mirror's bottom surface.
(2) Clamp the edges of the mirror to produce a uniform moment everywhere on the mirror's surface. The clamping moment is given by:

$$M = -EI \frac{\alpha \Delta T}{2h} \qquad (6.5.1\text{-}32)$$

The second design approach is adopted. Clamping forces may be applied either as concentrated force couples, or distributed over a clamping distance, 2L. The required clamping force per unit length along the clamp, P, is numerically equal to M/L^2.

Using the properties of SiC and a temperature drop of 2.0°C (as was shown in the previous section), the clamping force per unit length is given by:

Use or disclosure of data
subject to title page restriction

$$P = \frac{M}{L^2} = \pm EI\frac{\alpha\Delta T}{2hL} \qquad (6.5.1\text{-}33)$$

6.5.1.8.7 Neutron-Induced Mirror Surface Swelling - Using only non-collided neutron flux as a first approximation, the displacement rate at any point on the mirror's surface, a distance R away from the cavity center is given by:

$$R = (\phi t)\sigma\ (dpa / fpy) \qquad (6.5.1\text{-}34)$$

It is interesting to note from the above analysis that the surface deformation will be a function of the thickness of the aluminum layer. Figure 6.5.1-37 shows the various locations along the mirror's surface. The deformation is analyzed in the following two cases:

(1) Uniform aluminum layer thickness of 1 mm.
(2) A linearly graded thickness of 2 mm at the leading edge of the mirror, down to 1 mm at the trailing edge.

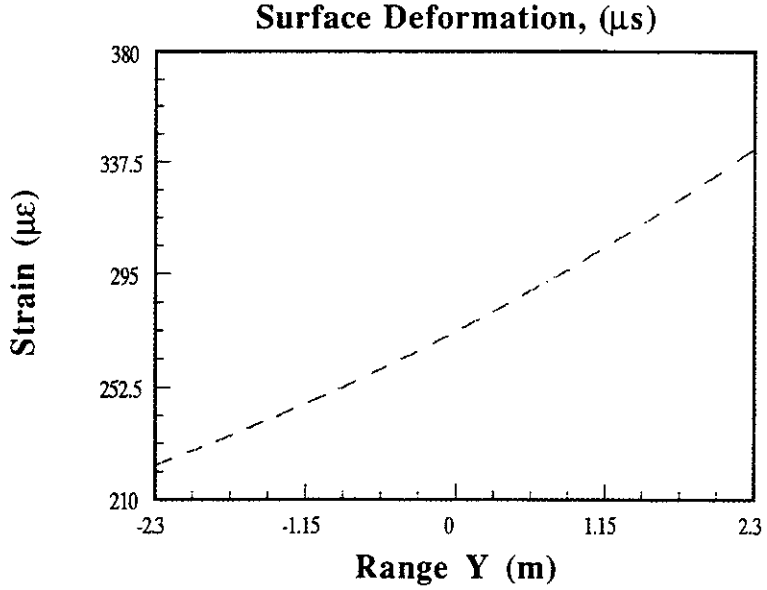

Figure 6.5.1-37. Surface Deformation of Mirror

In the first case, the difference in the normal deformation between the leading and trailing edges is

$$\Delta \approx 112 \text{ nm}$$

which suggests that the lifetime of the mirror will be about one full power year. On the other hand, if the mirror's surface is linearly graded, this difference is given by:

$$\Delta = 332.2 \times 1.0 - 223 \times 1.5 = 2.3 \text{ nm}$$

Use or disclosure of data
subject to title page restriction

It is concluded, therefore, that the GIMM may last for plant lifetime if the present design is adopted.

References for 6.5.1

1. J. M. Auerbach, N. C. Holms, J. T. Hunt, and G. J. Linford, "Closure Phenomena in Pinholes Irradiated by Nd:Laser Pulses," Applied Optics, 18, 510 (1979).

2. TRW IOC from Gary Linford to Les Waganer, "Prometheus Telephone Contact Report: John Lindl/LLNL," K323-L-91-79, 10 May 1991.

3. Charles D. Orth, "Improved Understanding of First-Wall Vaporization-Condensation in Inertial Confinement Fusion Reactors," Fusion Technology, 10, pp. 1245--1250, (1986).

4. TRW IOC from Gary Linford to Les Waganer, "Initial Response to Comments by David Harris: LANL," K323-L-91-80, 12 May 1991.

5. John A. Hanlon and John McLeod, "The Aurora Laser Optical System," Fusion Technology 11, pp. 636-653 (1987).

6. Louis A. Rosocha, et al., "Aurora Multi-kJ KrF Laser System Prototype for Inertial Confinement Fusion," Fusion Technology 11, pp. 497-531 (1987).

7. Louis A. Rosocha and Kenneth B. Riepe, "Electron-Beam Sources for Pumping Large Aperture KrF Lasers," Fusion Technology 11, pp. 576-611 (1987).

8. J. E. Jones, et al., "Performance of the Aurora KrF ICF Laser System," Proceedings of the International Conference on Lasers '89, pp. 88-95, 3-8 December 1989.

9. Shirley J. Pfeifer, K. Allardyce, R. Johnson, G. Linford, H. Injeyan, and J. Betts (TRW Applied Technology Division, Redondo Beach, CA) and H. Komine, G. Lombardi, W. Long, and E. Stappaerts (Northrop Research & Technology Center) "Raman Beam Combining Program," Final Report for Contract #F29601-85-C-0053, prepared for the Air Force Weapons Laboratory, Kirtland Air Force Base, NM, September 1986.

10. Jerry Oldenettel and Michael Terpka, "Raman Oscillator Studies," Final Report for Contract F29601-84-C-0051, prepared for AFCMD, Kirtland AFB, NM, by Western Research Corporation, San Diego, CA, March 1987.

Use or disclosure of data subject to title page restriction

11. Mark Kushner, et al., "New Techniques for KrF Laser Fusion Systems," Interim Report for Los Alamos National Laboratory by Spectra Technology, Inc., Seattle, WA, 1989.

12. Arthur A. Mak and Leonid N. Soms, "Optical Methods for Laser Beam Control," Proceedings of SPIE, Vol. 1415, Modeling and Simulation of Laser Systems II, pp. 110-119, (1991).

13. W. Kaiser, M. Maier, "Stimulated Rayleigh, Brillouin, and Raman Spectroscopy," Laser Handbook, edited by F. T. Arecchi, North-Holland Book Co., pp. 1116-1120.

14. J. M. Auerbach, N. C. Holms, J. T. Hunt, and G. J. Linford, "Closure Phenomena in Pinholes Irradiated by Nd:Laser Pulses," Applied Optics, 18, 510 (1979).

15. Charles D. Oreth, "Improved Understanding of First-Wall Vaporization-Condensation in Inertial Confinement Fusion Reactors," Fusion Technology, 10, 1245 (1986).

16. M. J. Weber, Handbook of Laser Science and Technology, Vol. III, Optical Materials; Part 1, pages 336 and 366, CRC Press. Inc., 1986.

17. Robert Bieri and Michael Guinan, "An Analysis of Grazing Incidence Metal Mirrors in a Laser ICF Reactor Cavity," Lawrence Livermore Report, September 1990.

18. Y. Adda, "Report on the CEA Program of Investigations of Radiation-Induced Cavities in Metals," Proc. of the 1971 International Conference held at Albany, NY, June 1971.

19. D. S. Billington and J. S. Crawford, Jr., "Radiation Damage in Solids," Princeton University Press, Princeton, NJ (1961)

Use or disclosure of data
subject to title page restriction

6.5.2 Heavy Ion (HI) Driver Subsystems

The Prometheus-H heavy ion driver is based on space charge limited acceleration and transport of a heavy ion beam in a simple alternating magnetic quadrupole focussing channel. The channel containing the intense beam is formed by a slowly varying FODO lattice (focus-drift-defocus-drift). The Prometheus-H Heavy Ion Driver illuminates an indirect-drive target from two sides. The major subsystem elements of the heavy ion driver are:

(1) A single-beam induction linear accelerator (LINAC) produces a train of identical current pulses running in a high repetition rate burst mode.

(2) Storage rings accumulate the LINAC current pulses and act as a series of delay lines. Beams generated over microseconds are conditioned to reach the target within hundreds of picoseconds of each other. Storage rings are located where the beams segregate into main and precursor beams. Some of the beamlets become the two precursor beams, which contain roughly 30% of the beam energy and have a duration 4 to 5 times that of the main current pulses. The combination of the single beam LINAC and the storage rings was selected in Prometheus-H as opposed to a multiple beam accelerator usually chosen in earlier studies.

(3) Combination bunching/drift sections are downstream of the LINAC and storage rings. Their function is to compress the beams longitudinally. The precursor and main beams share a common tunnel, but they have different requirements and are handled separately in these subsystems. Following the buncher/drift section, all beamlets are divided into two identical sets and directed toward opposite sides of the target chamber.

(4) Final focus sections on each side of the reactor chamber compress the beamlets radially, coalesces the main beamlets into a main beam, and merges this beam with the end of the precursor beam just inside the target chamber. The merged beams then propagate across the target chamber to opposite sides of the indirect-drive target. The entire Prometheus-H heavy ion driver system is cycled at 3.54 Hz.

Prometheus-H heavy ion driver is composed of subsystems and individual modules which are subject to parallel optimization during the years 1992-2030. Each of these subsystems is described below. A general schematic illustrating the geometrical relationship of the main single beam LINAC to the storage rings, bunchers, final focus, and target chamber is provided below in Figure 6.5.2-1.

Use or disclosure of data
subject to title page restriction

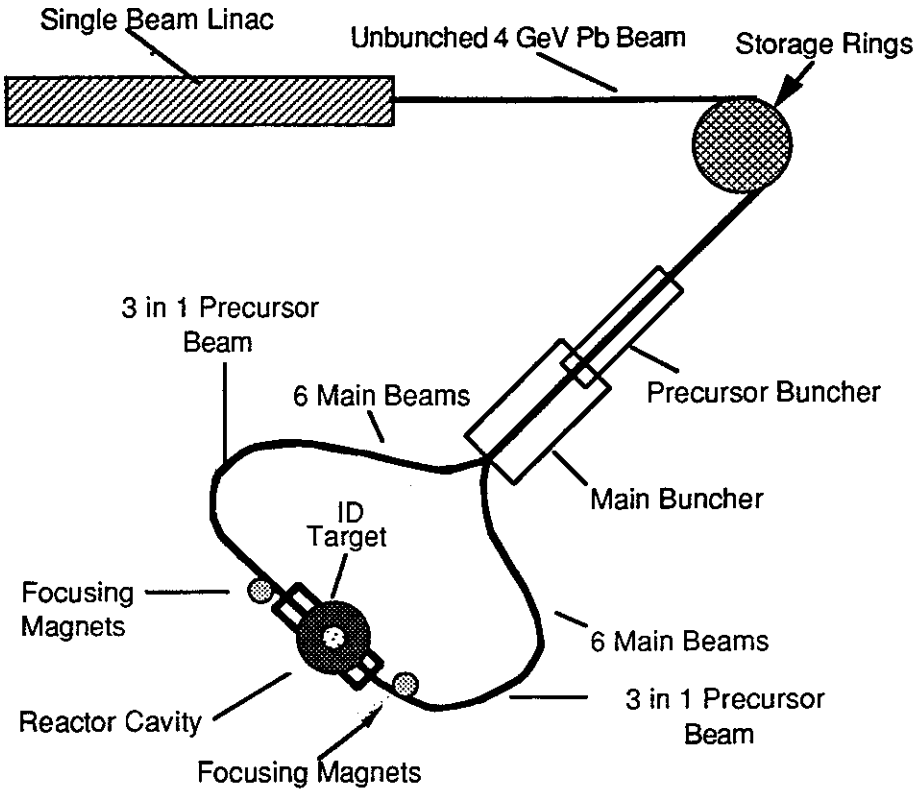

Figure 6.5.2-1 The Prometheus-H Heavy Ion Driver consists of a single beam LINAC (consisting of a high brightness injector, ramp gradient accelerator, and main accelerator) operated in a burst mode to generate 18 beamlets, 12 storage rings, focusing magnets, and two channel transport for a 2-sided indirect drive DT target.

To meet the overall IFE reactor requirements, the overall heavy ion driver is cycled at 3.54 Hz. This driver is based on space charge limited acceleration and transport of a heavy ion beam in a simple alternating magnetic quadrupole focussing channel. As noted previously, the channel containing the intense HI beam is formed by a slowly varying FODO lattice, whose parameters are illustrated in Figure 6.5.2-2.

Figure 6.5.2-2 defines the quadrupole spacing, L, the quadrupole length, $l_q = \eta L$, the space between the quadrupoles, $L(1 - \eta)$, the beam envelope of radius a, the heavy ion beam trajectory, the alternating focus and defocus (FODO) magnets, the betatron wavelength, λ_b, and the phase advance, $\sigma = 2\pi \ 2L/\lambda_b$.

Use or disclosure of data
subject to title page restriction

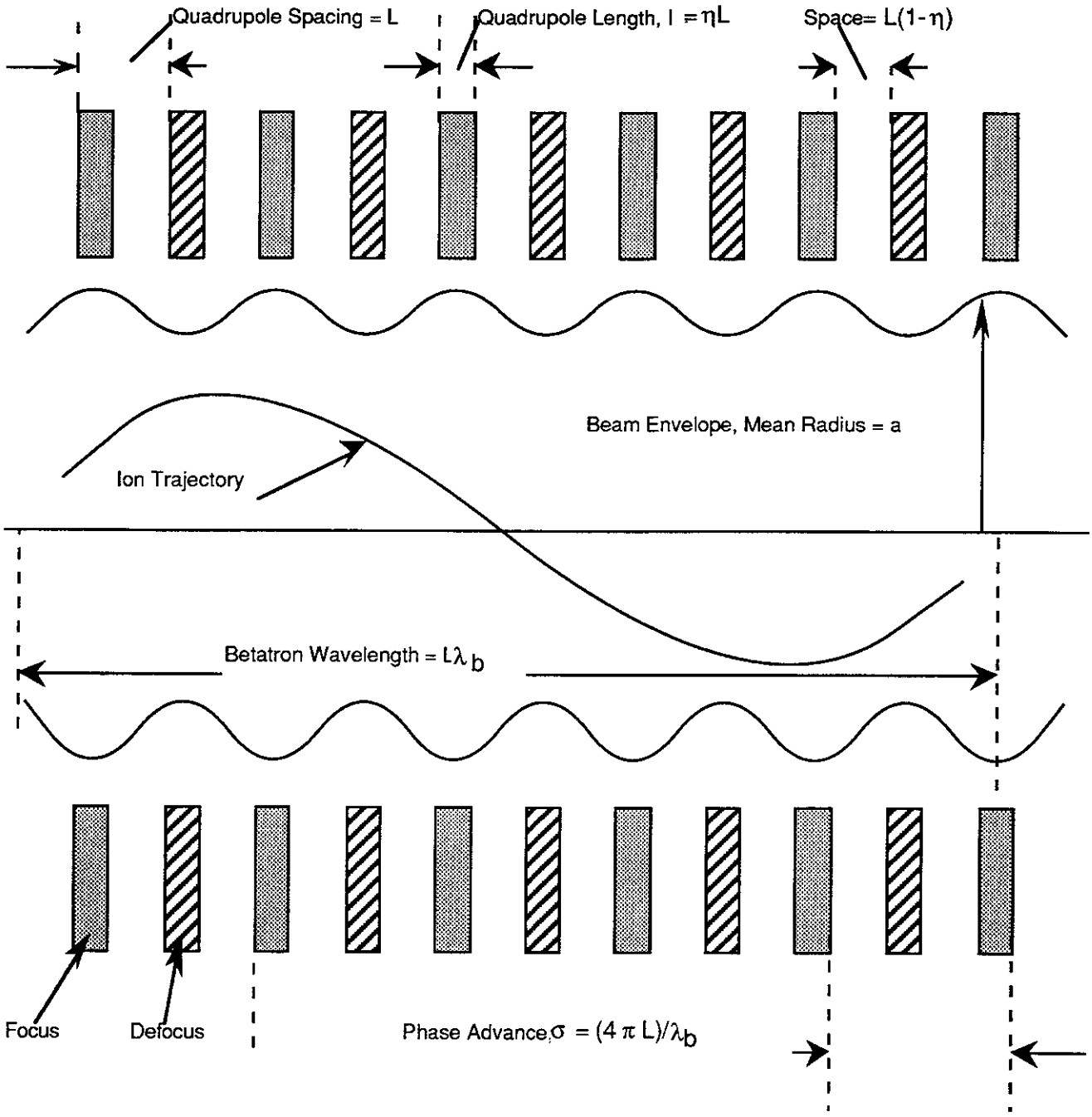

Figure 6.5.2-2 Schematic of the Prometheus-H Quadrupole Focussing Channel

The HI beam envelope has a periodicity equal to that of the quadrupoles, but the trajectory of an individual ion within the channel is characterized by a betatron wavelength. The betatron wavelength, λ_b, is indicative of the balance between the radial space charge forces on the beam and restoring force of the quadrupole channel. The betatron period divided by four, $\lambda_b/4$, is the distance in which the HI

Use or disclosure of data
subject to title page restriction

beam would reach its maximum displacement after receiving an angular kick. An infinite betatron period (or zero phase advance) corresponds to having no net restoring force on the ion.

As indicated in Figure 6.5.2-3, at any location along the beamline, the trajectories of the individual ions fall within an envelope in phase space (x-x'). The area of the envelope is related to $\pi\varepsilon$, where ε is the beam emittance.

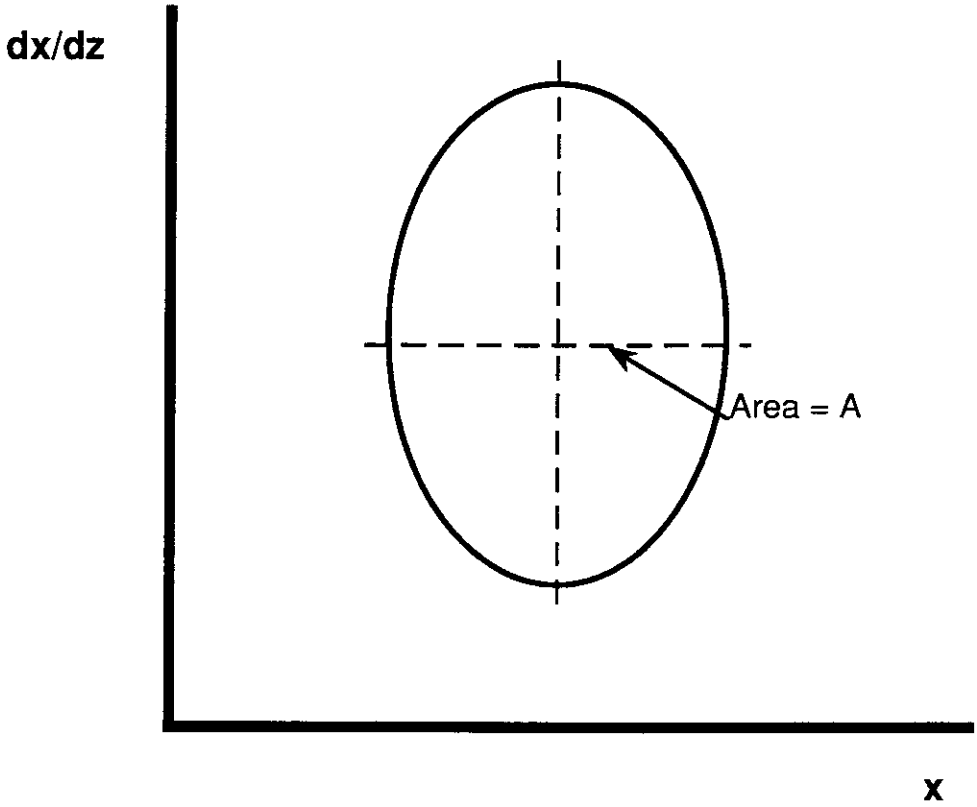

Figure 6.5.2-3 Heavy Ion Trajectories Lie Within this Elliptical Envelope in Phase Space.

For the coasting HI beam, the area is constant, although the aspect ratio changes. As the HI beam accelerates, the area decreases. The normalized emittance defined by the expression:

$$\varepsilon_N = \beta\gamma\varepsilon \qquad (6.5.2\text{-}1)$$

The strength of the FODO channel focussing depends not only on the physical spacing of the magnets but the quadrupole gradient as well; the magnetic parameters are illustrated in Figure 6.5.2-4. (Note: For the type of magnet proposed, "poletip" is a misnomer. The poletip field is defined as the magnetic field at the beam edge.)

Use or disclosure of data
subject to title page restriction

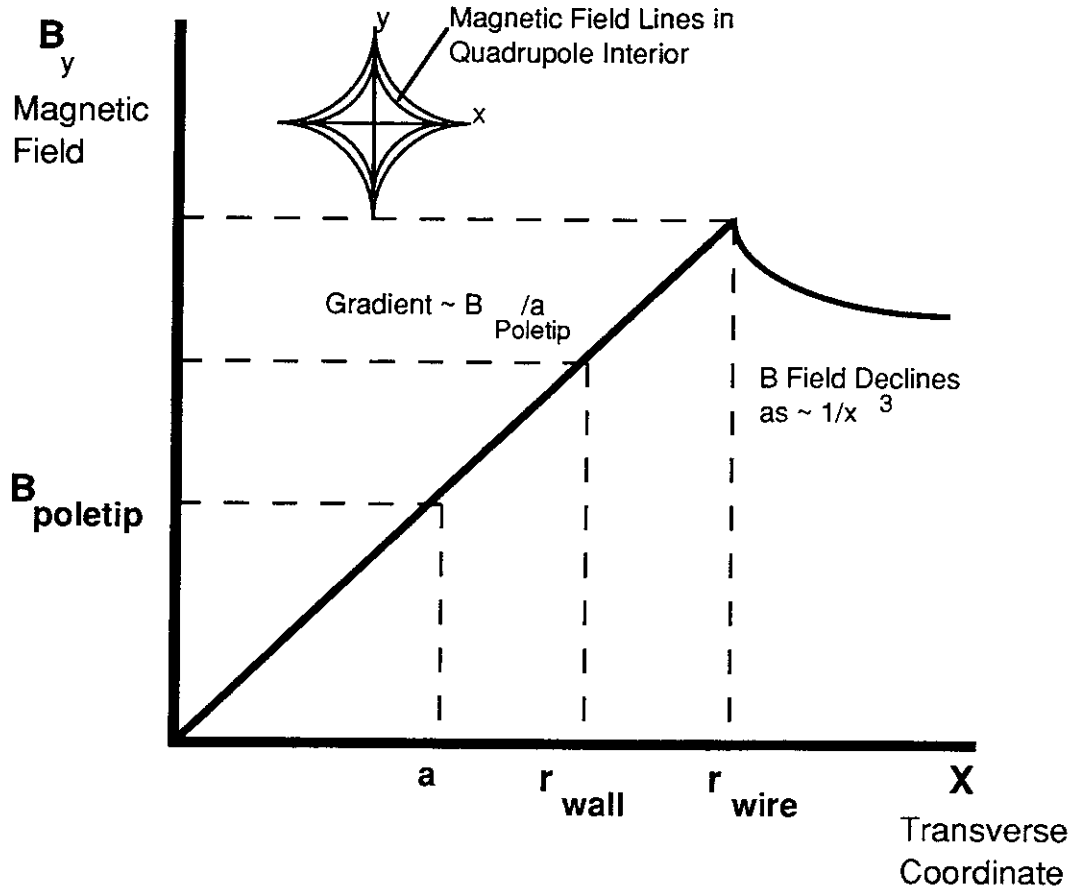

Figure 6.5.2-4 Relationships Between Magnetic Fields at Poletips, Walls, and Wires

The lattice parameters vary along the driver according to the local beam energy and/or current; the acceleration and bunching schedules (see Figures 6.5.2-5 and 6.5.2-6) which determine V(z) and I(z) are free parameters.

Note that the ramp portion of the LINAC commences the prebunching of the HI beams. Beyond the ramp gradient region of the LINAC, bunching continues.

Illustrated in Figure 6.5.2-6 is the heavy ion beam current as a function of time at a given location in the Prometheus-H heavy ion driver. In this case, the HI pulse duration, $\tau = \delta/v$ (where δ is the HI pulse length in m, and v is the bunch velocity in m/s).

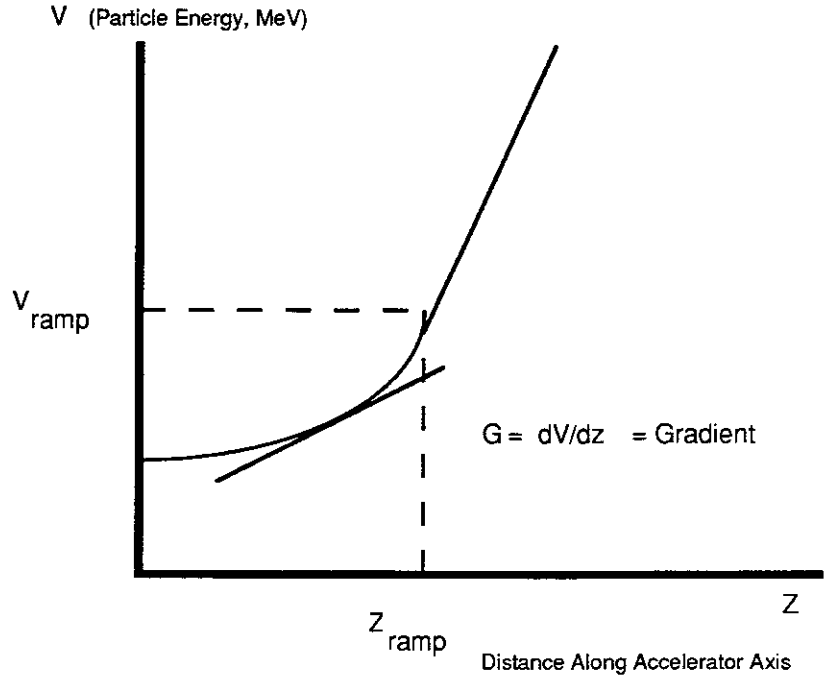

Figure 6.5.2-5 Relationship Between Particle Energy, V, and Accelerator Gradient, G, in LINAC

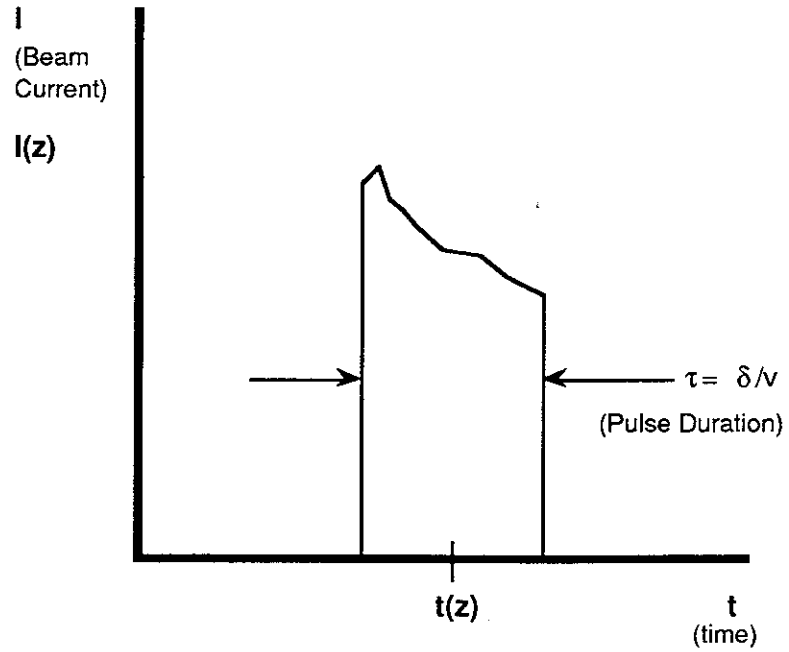

Figure 6.5.2-6 Heavy Ion beam current as a function of time at a given location in the Prometheus Heavy Ion Driver.

Use or disclosure of data
subject to title page restriction

Simple equations for the space charge-limited current, the emittance, and the quadrupole focussing strength were used to derive three scaling parameters. These characterize the driver and lattice variables throughout the bunch acceleration and compression processes in terms of the local beam energy and peak current. Practical limitations on physical parameters (e.g., component access, currents in magnet windings, minimum depressed tune, etc.) were used to constrain the parameters to realizable configurations of the driver. Given a set of basic beam parameters at the target (total beam energy, ion kinetic energy, number of beamlets, pulse length, etc.) the cost of electricity from the plant minimizes at specific values of the three parameters; different values are obtained if the LINAC and buncher costs are considered separately. The scaling laws, practical constraints, and driver variables in terms of the three scaling parameters are given below.

Equations Governing Transport in FODO - To define the space-charge limited current, I_{max}, the following expressions are valid:

$$I_{max} = 1.56\times10^{7}\,\sigma_o^2\left(\frac{a}{2L}\right)^2\frac{A}{Z}(\beta\gamma)^3 \qquad (6.5.2\text{-}2)$$

where $\sigma = 2\pi/\lambda_o$ is the depressed tune (and is λ_o the wavelength of the ion trajectory, a is the beam radius, L is the distance between alternating quadrupoles, A is the atomic weight (which in the case of Pb requires A = 208), Z = 2 is the ion charge state, $\beta = v_i/c$ (where v_i = ion velocity), similarly $\gamma = 1/(1-\beta^2)^{1/2} \sim 1 + \beta^2/2 \sim 1.0029$ for these non-relativistic ions. To define the superconducting quadrupole limitation, the following expression for the poletip magnetic field, $B_{poletip}$, is:

$$B_{poletip} = 3.13\frac{A}{Z}\left(\frac{a}{L^2}\right)(\beta\gamma)\left(\frac{1}{\eta}\right) \qquad (6.5.2\text{-}3)$$

where the constant ($\xi = 3.13$) is based upon recent experience with Superconducting Supercollider (SCC) quadrupoles, η = quadrupole packing fraction = $1_q/L$ (1_q = quadrupole length), and $B_{poletip}$ is the magnetic field at the beam edge. In order to calculate the constant normalized emittance, ε_N, the following equations were used:

$$\varepsilon_N = \frac{2\pi\, a^2\, \beta\, \gamma}{\lambda_\beta}$$

$$\varepsilon_N = \frac{\sigma\, a^2\, \beta\, \gamma}{2\, L}$$

$$\beta\gamma = \frac{v}{c\sqrt{1 - \frac{v^2}{c^2}}}$$

(6.5.2-4)

A summary of the heavy ion driver parameters is provided below in Table 6.5.2-1.

Table 6.5.2-1
Summary of Heavy Ion Driver Parameters

#	Parameter	Symbol	Variable Voltage	Constant Voltage
1	Depressed Tune	σ	V^{κ}	$I^{-\zeta}$
2	Current	I	$V^{1-\alpha}$	I
3	Beam Radius	a	$V^{\alpha/2-\kappa-1/4}$	$I^{\zeta-1/2}$
4	Pulse Duration	τ	$V^{\alpha-1}$	I^{-1}
5	Bunch Length	δ	$V^{\alpha-1/2}$	I^{-1}
6	Quad Spacing	L	$V^{\alpha-\kappa}$	$I^{\zeta-1}$
7	Packing Fraction	η	$V^{-3/2\alpha+\kappa+1/4}$	$I^{3/2-\zeta}$
8	Quad Length	l_q	$V^{1/4-\alpha/2}$	$I^{1/2}$
9	Ion Charge	Q		

Additional constraints include: For adequate access to the HI beamlines, $\eta < 0.8$ everywhere. The control of the final focus magnetic lens aberration requires that the ratio of the beam radius to the quad length satisfy the following inequality:

$$a/l_q < 0.25 \qquad (6.5.2\text{-}5)$$

throughout the HI driver FODO system. For the superconducting magnets, it is necessary that the current density be kept below its local limit; SSC-type conductors are assumed and the limits are never approached in Prometheus-H.

The Prometheus-H driver subsystems generally stay within the bounds of demonstrated or readily extrapolated technologies. There are some exceptions, which are listed here and will be discussed in more detail in the following sections. First, the entire Prometheus-H driver (LINAC, storage ring, and buncher sections) is designed around a very aggressive transport schedule. The current is maintained at the local

Use or disclosure of data
subject to title page restriction

space charge limit of a magnetic quadrupole focussing channel throughout the driver, and the depressed tune is allowed to drop as the beam approaches the target. The ability to transport the current at its space charge limit over long distances is identified as a Critical Issue for the Heavy Ion Driver since it heavily impacts the driver cost.

Second, the ability to maintain the high current heavy ion beams in the storage rings for millisecond time scales is also identified as a Critical Issue, since the use of a cost-effective Single Beam LINAC for this application hinges on the ability to delay the arrival time of successively generated bunches. Last, the final stage of the transport uses an admittedly speculative process, self-pinched transport in a narrow channel; this is not listed as a Critical Issue because there are acceptable (albeit less attractive) workarounds if the process proves to be unrealizable in practice.

6.5.2.1 Single Beam LINAC - The high repetition rate burst mode Single Beam LINAC comprises two portions, the injector and the main LINAC. The injector includes the ion source and whatever preacceleration and beam manipulation is required to produce a suitable beam for the main LINAC. The two sections of the main LINAC, the ramped gradient and the fixed gradient sections, differ in the allowed voltage gradient as a function of position, but are otherwise identical in function: they both accelerate a single space-charge-limited beam at the maximum allowed rate. The main components of the single beam LINAC are the induction modules that accelerate the beam and the superconducting quadrupole magnets that form the transport channel.

6.5.2.1.1 Injector - The baseline Prometheus-H driver design calls for the injector to deliver a beam with specific properties at the injection point. The Prometheus-H heavy ion driver injector parameters are summarized below in Table 6.5.2-2.

Table 6.5.2-2
Summary of Injector Parameters

#	Parameter	Symbol	Choice	Unit
1	Ion Charge State	q	Pb^{+2}	
2	Energy	V	6 .0	MeV
3	Beam Current	I	14	A
4	Pulse Duration	τ	15.5	μs
5	Pulse Shape		Nominally Square	
6	Beam Radius	a	9.4	cm
7	Current Density	$I/\pi a^2$	50	mA/cm^2
8	Normalized Emittance	ε	< .00001	m-rad
9	Pulses in Burst Mode		18	
10	Pulse Repetition Rate		30	kHz
11	Time Between Bursts		200	ms

In defining the injector requirements it is anticipated that the techniques in use today will be extrapolated to meet these requirements. The problems in the injector are the production of the total current, with the required brightness, at a sufficiently high repetition rate and duty factor, without generating an unacceptable gas load for the rest of the LINAC, and to do all this reliably. The development of the injector is identified as one of the key issues for a heavy ion driver.

The beam was assumed to be space charge limited at the injector exit, rather than source limited. Although the current is high, the cross section of the beam is large and the required electrical current density is below 60mA/cm^2. Nearly 600 mA/cm^2 has been demonstrated using high brightness proton sources and the C^{1+} source developed for the ILSE program delivers 30mA/cm^{-2} at 2MeV, but when adjusted for the charge and mass (the space charge-limited current density scales as $(Q/A)^{-1/2}$, where Q is the ion charge and A is the atomic number) the Pb^{2+} beam of Prometheus-H is seen to have a stricter requirement. It is possible that multiple beamlets can be generated and combined before injection into the LINAC, since the brightness of these beams exceeds the driver requirement; excess brightness provides a margin against phase space dilution downstream as the individual beamlets are combined. It would be preferable if the beam could be generated in a single stage.

Source techniques in use today will probably be used in the driver injector. The ions could be extracted from a pulsed lead plasma of number density around 10^{13} cm^{-3}; low ion temperature rf discharge plasmas can approach those densities over large volumes. Plasma control via a pulsed extraction electrode, currently used with the C^+ source mentioned above, can switch the flow of ions from a multi-aperture source on and off. It is possible that the ions generated in the rf discharge plasma will be created in a lower charge state (Pb^{1+}) or in a mixture of states. This would require charge state selection; if the 1+ state is dominant, the beam would require 6 MV of acceleration to reach the ion injection energy, followed by stripping to the 2+ state.

The high voltage techniques used in the driver injector will also probably be similar to today's, with adjustments made for the high duty factor. Burst repetition rate in the driver system is limited by the source duty factor at the high end, and practically by the beam storage time at the other extreme (and ultimately by the 5 Hz target interaction rate). The ~15 μs pulse duration at the injector is sufficiently long that many of the issues of steady state operation must be faced: gas loading, voltage standoff, etc. The repetition rate set by the storage rings is such that during a ~2 ms burst the duty factor of the injector is running at around 10%.

Use or disclosure of data
subject to title page restriction

One option for the voltage source for the injector is a series of induction modules ganged together and applying a large positive potential to the source, which extends through the modules on a stalk. This has an advantage in that it shares a common high voltage technology with the rest of the LINAC. It is not clear that this is desirable, since the core area that is required to provide the 45 V-s for a 3 MV, 15 μs pulse is nearly 30 m^2 for a 1.5 T flux swing. Although core volume is minimized by using long, small diameter cylinders, even a 30 m long cylinder has a minimum volume of over 90 m^3. Even at a low value of 100 J/m^3 loss per pulse in the Metglas, this is nearly a megawatt in heat just in the core. In contrast, the beam power is only 60 kW.

Another option might be a dc high voltage power supply. The ~15 ms pulse duration at the injector is sufficiently long that many of the issues of steady state operation must already be faced: gas loading, voltage standoff, etc. Although the peak current is 14 A, the true average beam current is only 20 mA and the average current during the burst is only 1.5 A. DC power supplies capable of 3 MV at tens of milliamperes are available commercially now, and the design is such that 2 A of average current should be possible.

Source techniques in use today will probably be adapted for use in the driver injector. The ions could be extracted from a pulsed lead plasma of number density around 10^{13} cm^{-3}; low ion temperature rf discharge plasmas can approach those densities over large volumes. The problem of gas loading can be mitigated to some extent by puffing the gas in before each shot; unlike hydrogen, lead is readily pumped. Plasma control via a pulsed extraction electrode, currently used with the carbon arc source mentioned above, can switch the flow of ions from a multi-aperture source on and off.

It is possible that the ions generated in the rf discharge plasma will be created in a lower charge state (Pb^{1+}) or in a mixture of states. This would require charge state selection; if the 1+ state is dominant, the beam would require 6 MV of acceleration to reach the ion injection energy, followed by stripping to the 2+ state for propagation in the rest of the system.

A plot of the acceleration gradient, dV/dz, in the ramp-gradient portion of the Prometheus-H driver LINAC is shown in Figure 6.5.2-7.

The variation of beam energy with distance along the accelerator axis, V(z), for a displacement of up to 500 m is plotted in Figure 6.5.2-8,.

The variation of heavy ion beam energy with distance through the constant gradient portion of the Prometheus-H accelerator is illustrated in Figure 6.5.2-9.

Use or disclosure of data
subject to title page restriction

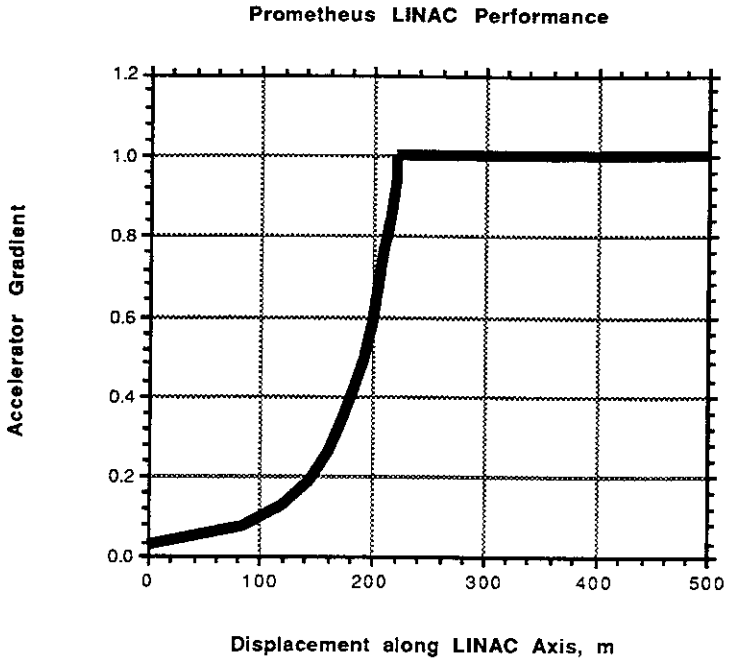

Figure 6.5.2-7 Dependence of accelerator gradient on the displacement along the LINAC axis, z, in the ramp-gradient section of the Prometheus-H heavy ion driver.

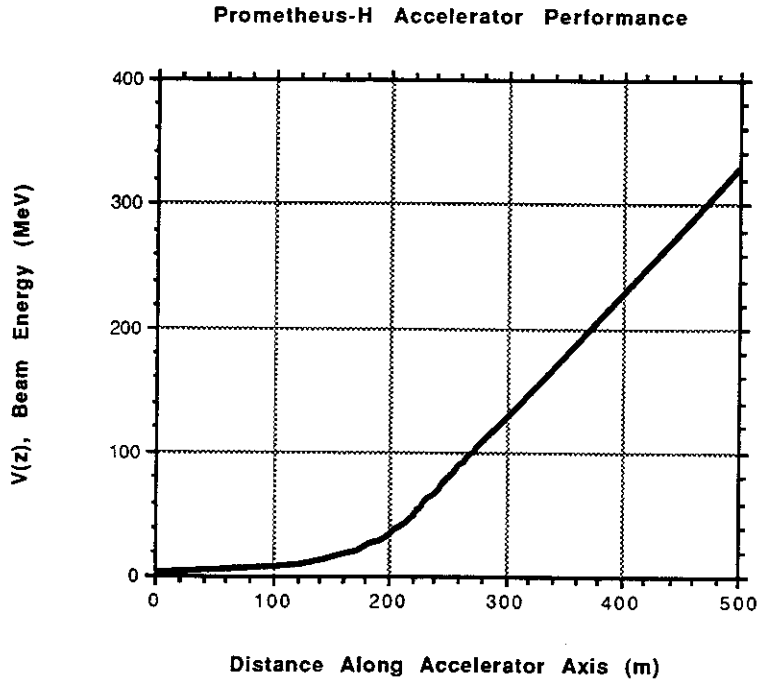

Figure 6.5.2-8 Variation of heavy ion beam energy with distance along accelerator axis in ramp-gradient portion of accelerator.

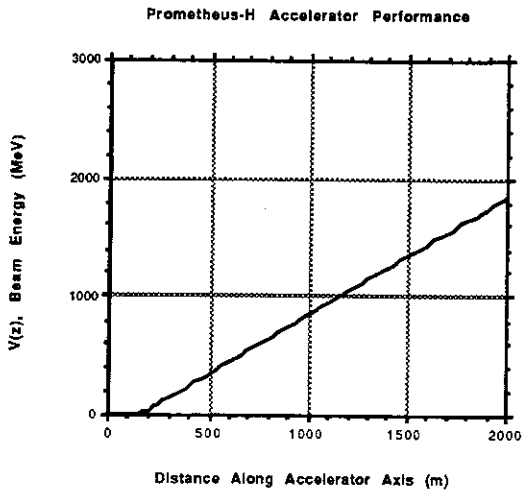

Figure 6.5.2-9 Variation of beam energy with displacement along axis for both ramped gradient and constant gradient accelerators.

Main LINAC - The heavy ion beam is accelerated at the maximum possible rate in the LINAC. In the ramped gradient section, the local voltage gradient is limited to a value proportional to the local ion energy. This is necessary so that the velocity gained at different portions of the beam as it traverses a given gap are sufficient to bunch the beam without grossly affecting the energy gained by the pulse as a whole. The end of the ramped gradient section is defined to be point where the maximum gradient is reached, at the voltage V_{ramp}. The fixed gradient section is just that, and the energy gain is linear with distance from V_{ramp} to the end of the LINAC. The variation in velocity gained as the beam traverses a gap is sufficiently low that the beam can be compressed without limiting the gradient.

The maximum gradient is taken to 1 MV/m, which should be a conservative value for a pulsed system. Graded DC accelerator columns typically run at 22 kV/cm in multi-electrode systems (e.g. Van de Graaf accelerators), and as high as 35 kV/cm in compact few-gap systems such as guns. The limitation is usually insulator flash-over. Presumably a pulsed gradient will perform at least as well.

Based on this choice for maximum gradient, The driver scaling parameters in the LINAC were found to be $\alpha = 0.2$, $\kappa = -0.15$; the resulting acceleration schedule for Prometheus-H is shown in Figure 6.5.2-9. The various accelerator and beam parameters associated with these scaling parameters are shown as a function of distance along the LINAC in the subsequent Figures 6.5.2-10 through 15.

Use or disclosure of data
subject to title page restriction

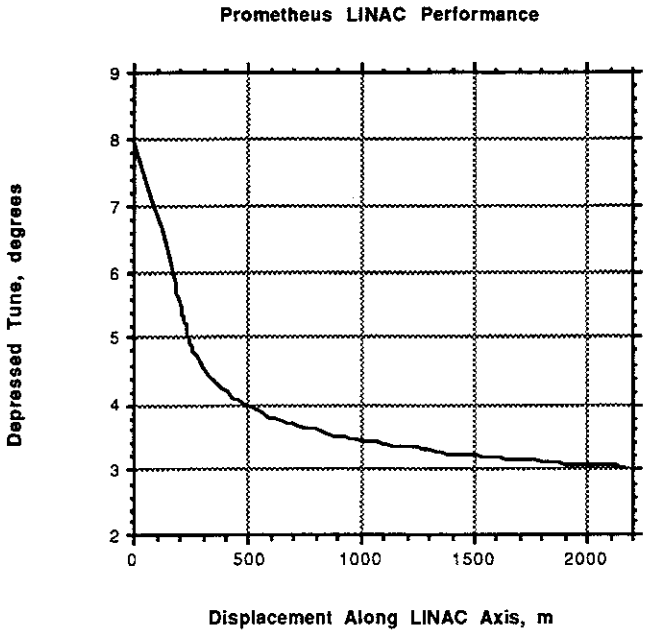

Figure 6.5.2-10 Depressed tune, σ, vs. displacement along the LINAC axis

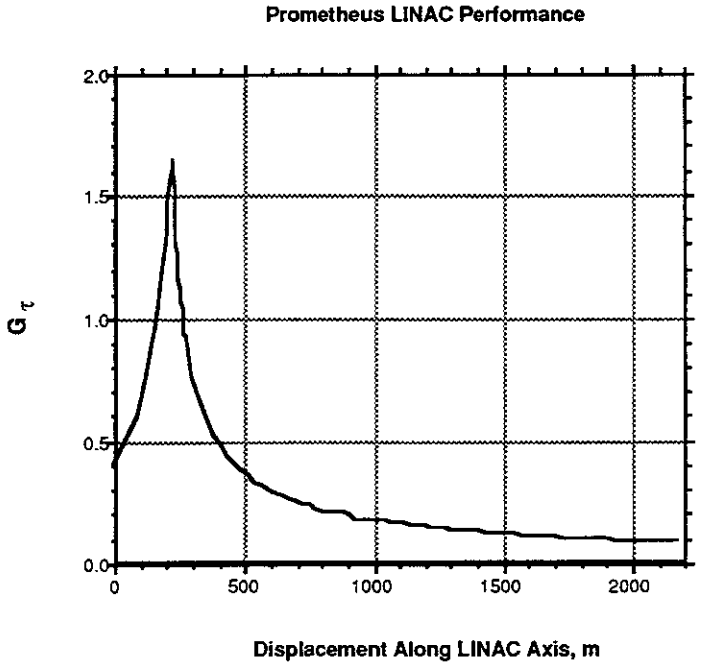

Figure 6.5.2-11 G_τ as a function of displacement along LINAC axis.

Use or disclosure of data
subject to title page restriction

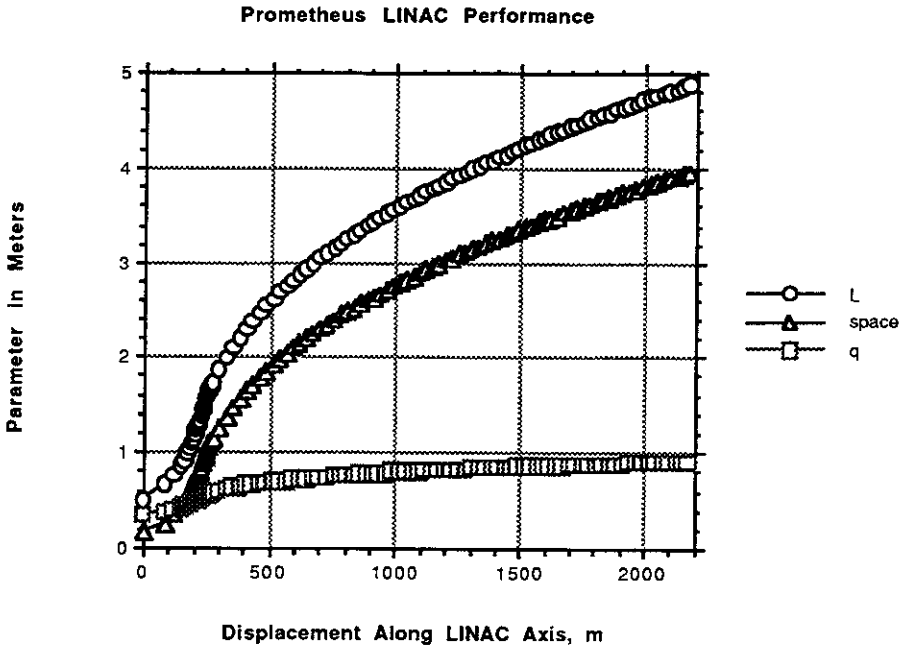

Figure 6.5.2-12 Variations of Displacement between Quads (L), blank space between Quads (space) and Quadrupole Length (q) as functions of displacement along accelerator axis.

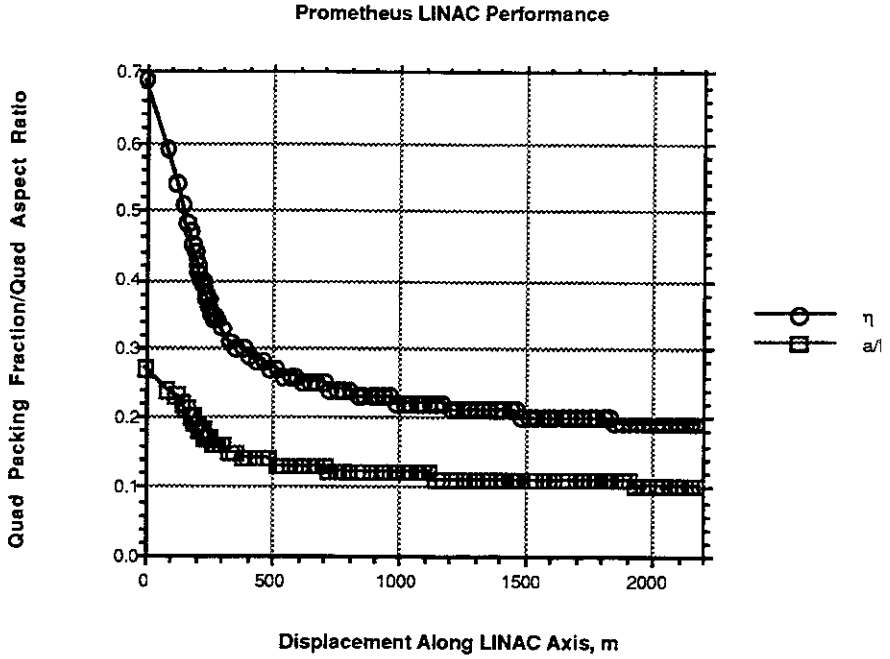

Figure 6.5.2-13 Variation of Quad Packing Fraction (η) and Quad Aspect Ratio (a/l) as functions of displacement along LINAC axis (z).

Use or disclosure of data
subject to title page restriction

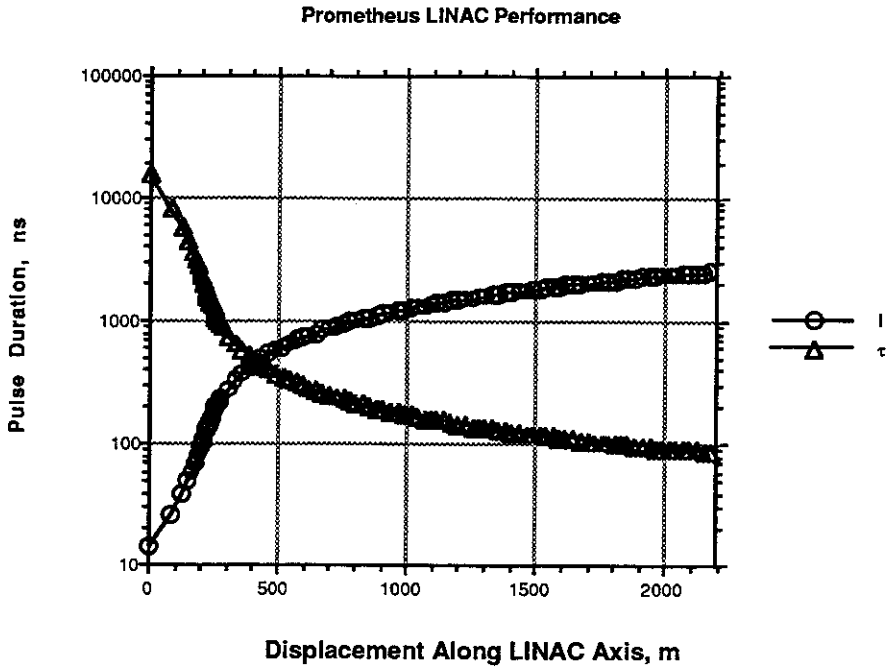

Figure 6.5.2-14 Dependence of HI beam current (I) and pulse duration (τ) on location along LINAC axis (z).

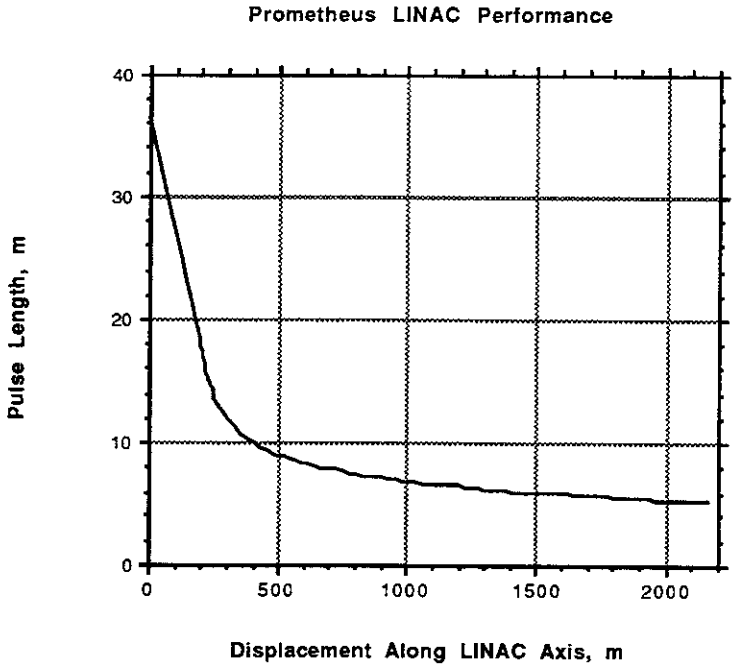

Figure 6.5.2-15 Pulse length (τ) of HI beam as a function of displacement along LINAC axis (z).

Use or disclosure of data
subject to title page restriction

The depressed tune (betatron phase advance per quadrupole pair) decreases from 8 degrees to 3; most of the drop occurs in the first 225 m, i.e., the ramped gradient section. Displayed in Figure 6.5.2-11 is the volt-seconds per meter required to maintain the induction modules; it is a product of the gradient and the pulse duration. This number, when divided by the nominal flux swing in the cores, yields the minimum difference in inner and outer core radii; the actual difference is larger to account for core packing fraction, i.e. the average density of Metglas in the core windings when insulation and other factors are included. The quadrupole center-to-center spacing L, the length lq, and the space available for access between the magnets are shown in Figure 6.5.2-12.

In Figure 6.5.2-13, the quadrupole longitudinal packing fraction η, the ratio of quadrupole length to center-to-center spacing, and a/l_q, the ratio of beam radius to quadrupole length as functions of the distance along the accelerator axis (m). (The beam radius is a constant value of 9.4 cm all along the LINAC.)

The current and pulse duration are shown in Figure 6.5.2-14; because the charge per pulse is fixed, current, and pulse duration are inversely related.

Figure 6.5.2-15 shows the pulse length as a function of displacement along the LINAC.

The total number of quadrupoles in the LINAC, derived from L(Z) and the gradient, is 878. Based on the conservative assumption that the cores surround the focussing magnets all along the LINAC, the total volume of core is 2535 m^3.

6.5.2.2 Acceleration Modules - The acceleration modules occurring in the LINAC are composed of the induction cells and the pulsed power systems that drive them. The induction cells for the single beam LINAC are relatively simple, resembling the cells of electron LINACs more than those of a multiple beam LINAC. The core volume is much smaller, surrounding only a single beamlet and focussing magnet, compared to N beamlets and magnets (see Figure 6.5.2-16).

By using the single beam LINAC, an N-fold reduction in the number of magnets is achieved, and the total core volume is reduced by $N^{1/2}$. In the LINAC the penalty paid for this simplicity is that the single core must be rapidly pulsed N times, since the beamlets are accelerated serially rather than in parallel. This increases the complexity and the cost per joule of the pulsed power.

Use or disclosure of data
subject to title page restriction

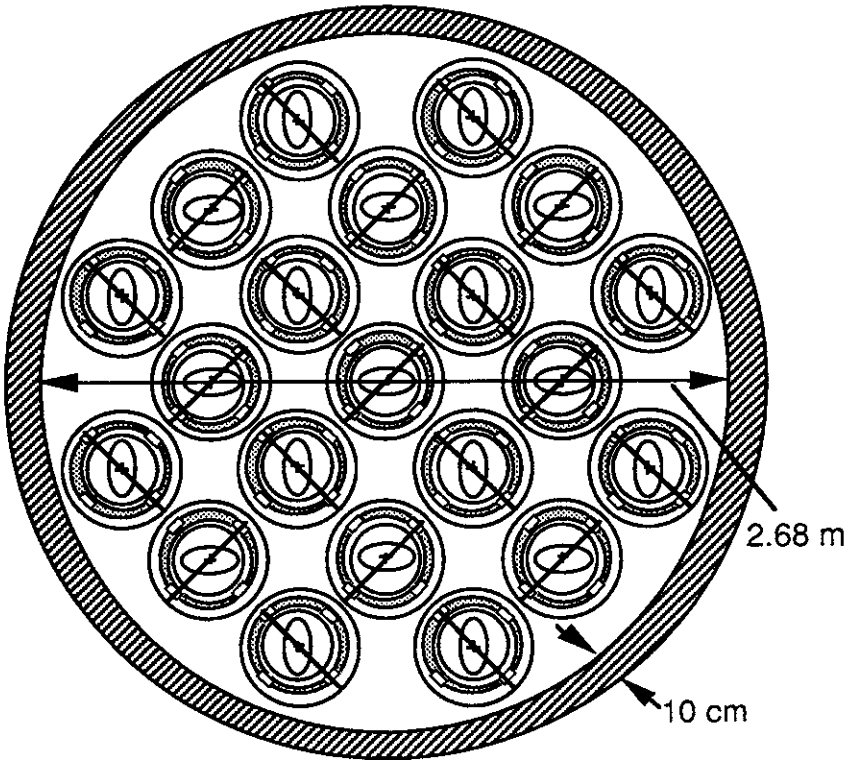

Ratio of Magnets
21:1

Ratio of Core Volumes
48:1

($\sqrt{21}$ = 4.6)

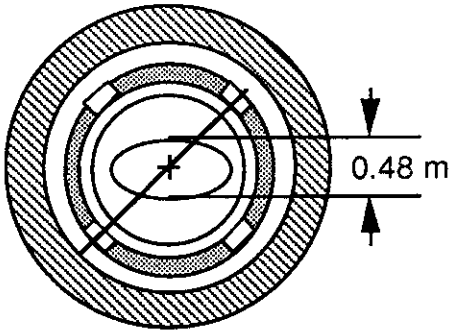

Figure 6.5.2-16 Comparison of Multiple Beam LINAC with Single Beam LINAC

Within the context of the induction cell, there are some issues that need to be addressed. First is the problem of heat generation and removal from the cores. Heat is generated in the cores due to hysteresis losses in the B-H curve and due to eddy currents in the finite resistivity Metglas material. The power loss per unit volume per target interaction is at least a factor of N higher in the case of the SBL than in the corresponding multiple beam LINAC (MBL) case, simply because the cores are being fired N times per target interaction. However, the loss curves for the Metglas core material indicate that the temperature rise caused by a burst of 18 pulses is less than 100 K, so that the ratcheting-up of the induction core temperature is still dominated by the 3.5 Hz repetition rate of the reactor. The total heat dissipated per meter per reactor

Use or disclosure of data
subject to title page restriction

shot is nominally only $N^{1/2}$ higher for the single beam LINAC (SBL), but the cell cooling circuit must be designed to handle the higher density of energy dissipation in the smaller SBL cells.

The primary problem is the eddy current losses, which can be minimized by making the core ribbon thinner so that the skin depth is a larger fraction of the thickness and by adjusting the frequency components of the applied field. The Prometheus-H cores were assumed to be wound from 1 mil thick ribbon, rather than the 1.25 mil ribbon in common use today, and the insulator between layers was assumed to thin proportionally to maintain the same packing fraction. Metglas ribbons as thin as 0.75 mil have been produced, and plasma spraying of magnesium oxide has been suggested as a method of producing a thin insulating layer, so the modest extensions suggested are not far-fetched.

The difficulty in tailoring the waveform to minimize eddy current losses is that the time available to reset the SBL core is limited by the burst repetition rate (which is in turn set by the maximum beamlet lifetime in the downstream storage rings and the total number of beamlets). The energy dissipation for Metglas is shown in Figure 6.5.2-17 as a function of square pulse duration.

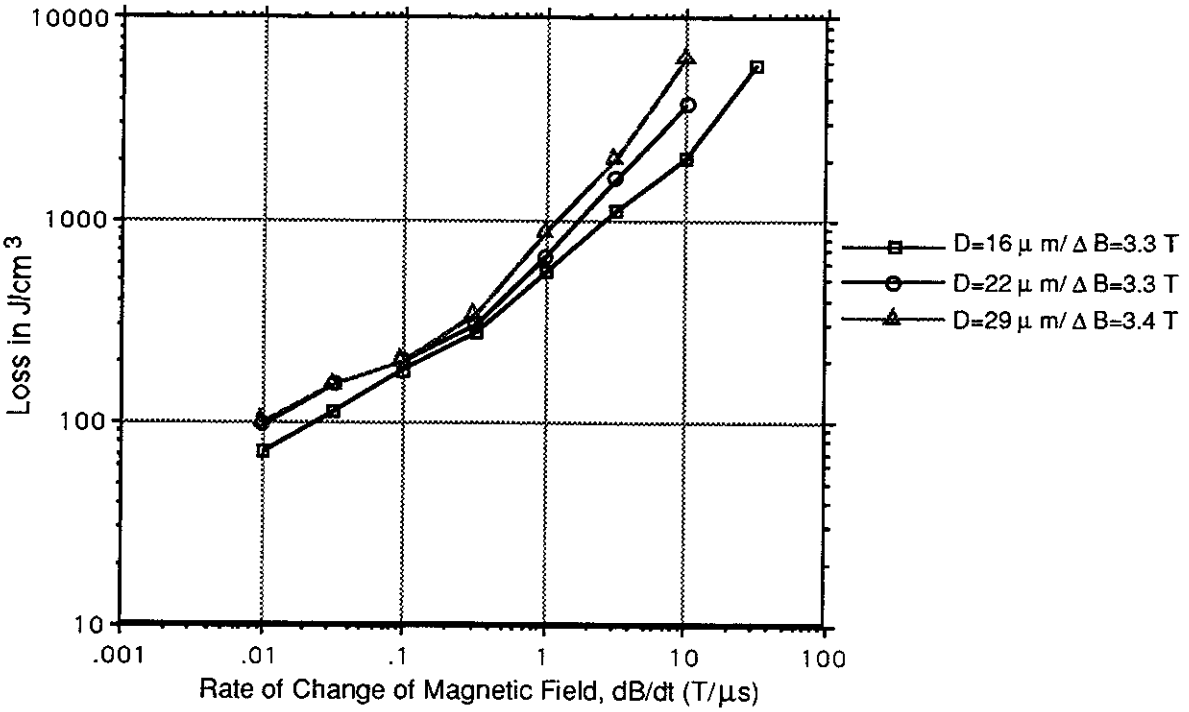

Figure 6.5.2-17 Energy Dissipation for Metglas as a Function of (Square) Pulse Duration

Use or disclosure of data
subject to title page restriction

Real waveforms are not square and both the acceleration time and the reset time come into play, Figure 6.5.2-18 shows the heat as a function of PRF for a (1 cos θ) reset pulse.

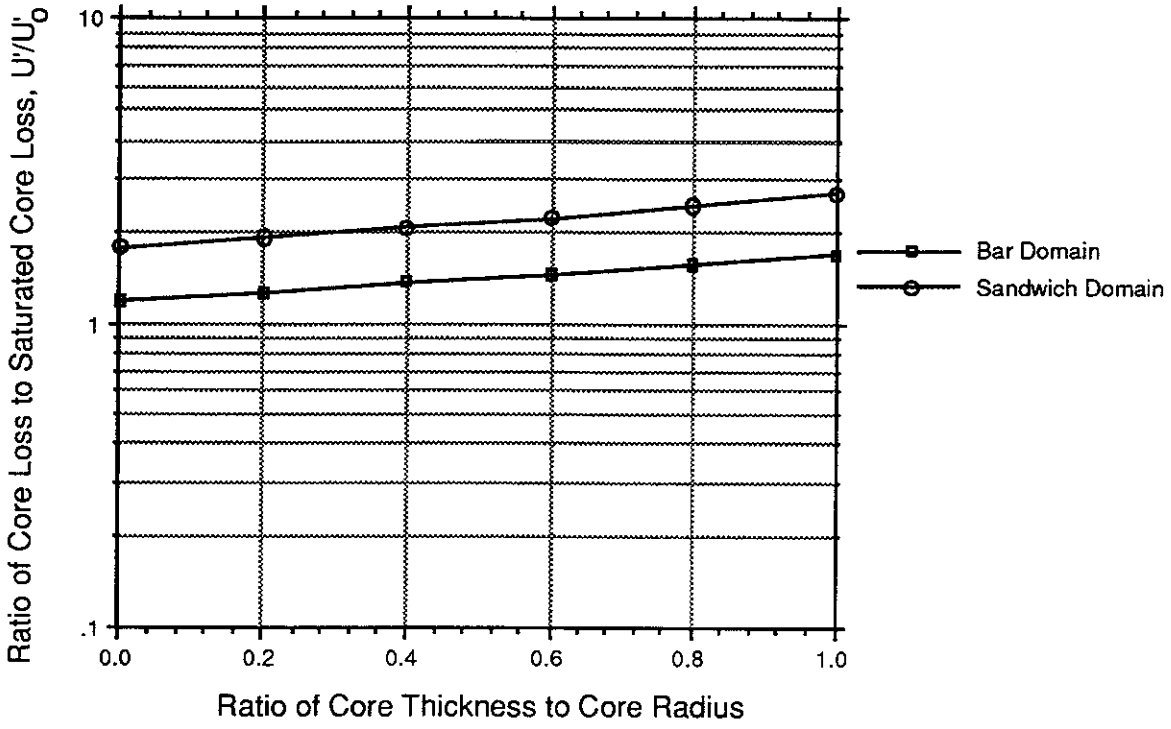

Figure 6.5.2-18 Metglas Heat as a Function of PRF

Because less time is available to reset the cores, the loss (J/cm^3) per shot in the SBL case is necessarily larger than the MBL case. Although not done for the Prometheus-H design, optimization of the waveform with respect to losses should result in lower heat generation in the core and lower installed power costs.

Another issue has to do with lifetime and reliability of the modules, since it concerns protection of the induction cell components against overvoltage in case of a misfire situation. One might think that the induction cells in a multiple beam LINAC would be less sensitive to errors such as late arrival of one of the beamlets since they are more heavily loaded by total beam current. Induction LINACs that have been built to date, including the 10 kA ATA at LLNL, have a damping resistor in parallel with the beam to limit the voltage appearing across the cell and critical components in case the beam arrival time is off (see Figure 6.5.2-19).

Use or disclosure of data
subject to title page restriction

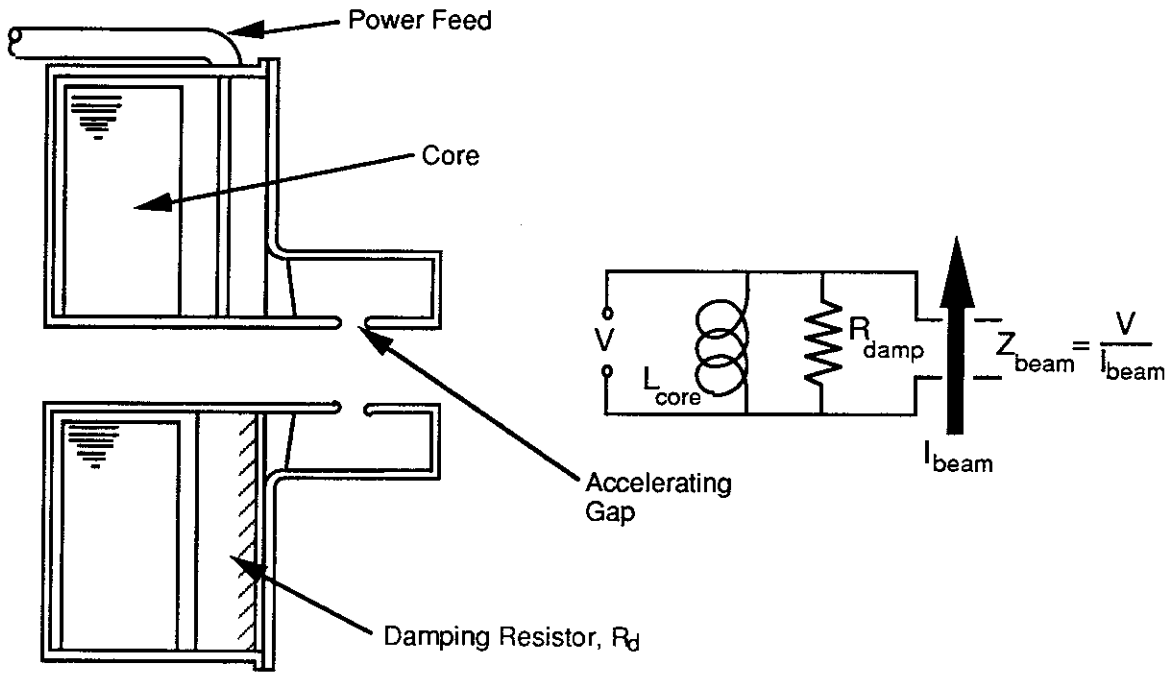

Figure 6.5.2-19 Damping Resistor Circuit on LINAC (Similar to LLNL ATA Design).

This resistor typically has an impedance equal to or even less than the beam load

$$Z_{beam}=V_{gap}/I_{beam},$$

so that the beam is only a minor perturbation to the total load. Most of the pulsed power goes into heating the damping resistor. Although this is an effective, low-cost solution to component protection in a low repetition rate experimental device, it will not be acceptable economically in a power plant simply because the pulsed power systems cost so much. Either steps must be taken to prevent firing a module in a fault condition, or the components of the induction cells in the driver will have to be designed to withstand a 2x overvoltage; similarly the pulsed power systems must be configured so they are able to withstand firing into an open circuit or be prevented from firing.

The pulsed power requirements vary along the LINAC as the pulse length, gap voltage, and current vary. The requirements for the modules are straightforward, but advancements must be made to achieve the high repetition rate burst mode operation. While thyratron switching may be used for low PRF applications such as a multiple beam LINAC, silicon-controlled rectifiers have been proposed for induction LINACs with PRF up to 6 kHz not just for pulse rate enhancement but for improved long-term reliability. The solid state devices have a near-infinite lifetime (>10^{11} shots) if they are run within their specifications, but they are very fault-intolerant: a single out-of-bounds

Use or disclosure of data
subject to title page restriction

shot is capable of destroying the device. As a result, effort has been directed toward arranging the components so that faults in the load do not cause the pulse power components to exceed their allowed range. This evolution in configuration is illustrated in Figure 6.5.2-20.

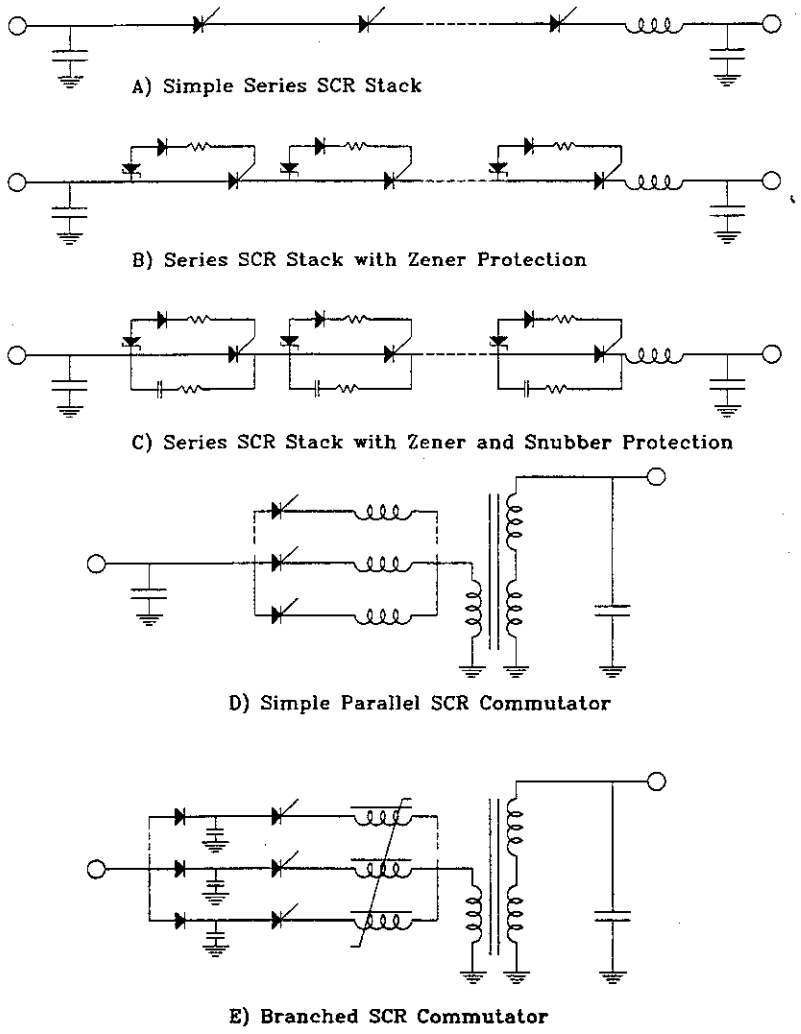

Figure 6.5.2-20 Evolved Pulsed Power Component Configuration to Limit Failures.

Work was done at LLNL and elsewhere to develop essentially cw kilojoule 6 kHz (6 MW average power) pulse compressors for use in the GBFEL and AVLIS programs, so the average power capability is there. For the factor of three higher PRF required for the SBL driver burst mode, even SCRs are probably insufficient and FETs will probably be necessary. The high pulse repetition frequency (PRF) pulsed power for the SBL will be more expensive on a per joule basis than the very low PRF used in the MBL; a value of $100/J was assumed in costing the pulsed power in the Prometheus driver.

Use or disclosure of data
subject to title page restriction

6.5.2.3 Superconducting Magnets - The focussing quadrupoles used to contain the beam radially during acceleration will be superconducting with cos(2θ) windings to provide the quadrupolar magnetic field and covered with iron to provide flux return. These quadrupoles must fit beneath the accelerator cores (at least in the low energy end of the LINAC where the packing fraction is high) as shown in Figure 6.5.2-21.

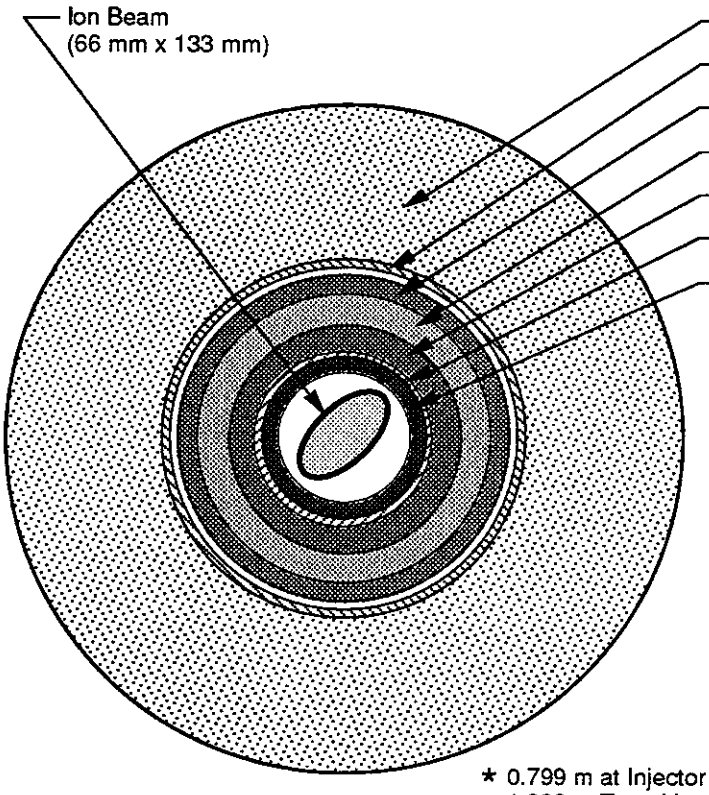

Size of Quadrupole Components

Component	Inner Radius (meters)	Outer Radius (meters)
Accelerator Core	0.43	*
Core Insulator	0.41	0.43
Magnet Cryostat	0.35	0.39
Magnet Quad Iron	0.27	0.35
Magnet Conductor Iron	0.21	0.27
Magnet Wire	0.195	0.21
Magnet Inner Case	0.155	0.195

* 0.799 m at Injector
1.932 at Transition
0.508 at Linac End

Figure 6.5.2-21 Prometheus-H Superconducting cos (2θ) Quadrupole Core Configuration.

The cost of this type of quadrupole is relatively insensitive to the quadrupole size; however, because the induction cores fit over magnets, it was necessary to estimate the quadrupoles radial extent in order to calculate the core volume. The rule of thumb used is as follows: multiply the (circular) beam envelope by 1.65 to account for the effect the envelope ellipticity at the quadrupole location (a difference of ±30% depending on direction) and to provide a margin between the beam edge and the inner bore of the cryostat. Add 4 cm for each of two 4-300 K transitions, plus the thickness of both the superconducting windings to provide the required field and the stainless steel support structure. Finally, add the minimum thickness of laminated steel yoke to avoid saturation. Because the Prometheus-H LINAC system runs at a relatively low quadrupole gradient, the entire structure is compact.

Use or disclosure of data
subject to title page restriction

A specific relation between the scaling law parameters was selected to provide a uniform beam diameter all along the LINAC. A consequence of this choice is that in order to meet the simultaneous constraints on axial packing fraction ($\eta < .8$) and aspect ratio ($a/L_q < 0.25$) everywhere, the ideal length of the quadrupole must vary along the LINAC (Figure 6.5.2-12).

From a spares inventory viewpoint, having unique magnets is undesirable. However, the field strength used in the quadrupoles is nowhere near the limits of the superconductors (the 2T "poletip" field in the Prometheus-H driver LINAC is less than 60% of the maximum allowed by the conservative poletip constraint). Since each magnet acts to provide a transverse momentum impulse the quadrupole length can be fixed at a standard value (or a few values) and the field varied, keeping the impulse (proportional to the product BL_q) constant.

The high allowed aspect ratio of beam radius to quadrupole length in the Prometheus-H design (1/4 versus 1/10 in other studies) is an area of potential concern. The issue is growth in the normalized emittance that is caused by magnetic lens aberrations due to the relatively short length. While there are octupole components to the lens as a result of end effects, these appear to play a significant role only if the beam is not space charge dominated. As part of the Neutral Particle Beam program, experiments have been performed at LANL on the acceleration of high current, high brightness proton beams in a large aperture drift tube LINAC. The short quadrupoles are contained within the drift tubes to keep the high current beam focussed. The beam there is observed to propagate without increasing its emittance significantly.

While it is certain that there will have to be considerable magnet design to optimize the quadrupoles, these first-cut approximations were sufficient to proceed with the Prometheus-H design.

Use or disclosure of data
subject to title page restriction

6.5.2.4 **Cooling and Cryogenics** - Some observations regarding cooling not common to both types of ICF drivers are made here. The induction modules (both the cores and parts of the pulsed power) require special treatment because of the various combinations of high voltage, material corrosion, and dielectric breakdown. By their nature, the superconducting magnets require liquid helium to operate, necessitating a large distributed cryogenics system. A cryogenic system of some sort is required for the target factory as well, but the driver is spread out over a much larger area and needs a distribution system.

Induction Modules. The amount of heat generated per cubic centimeter per pulse in an induction core is small; over time the temperature does build, although it could take several minutes to become a problem. Adequate cooling in the modules and magnetic pulse compressors is a concern because the glass-like structure of Metglas makes it a poor thermal conductor and some of its properties are temperature-dependent. There must be axial gaps between Metglas pancakes for fluid, but because these gaps decrease the axial packing fraction, the core diameter must go up to compensate.

Low conductivity water (a good dielectric) is unacceptable as a cooling fluid in the cores because it will corrode the steel in Metglas. Cooling fluids such as Freon or Fluorinert (non-conductive, non-corrosive, and capable of withstanding the fields inside the module) are probably good choices as coolants. Although these fluorocarbons have other undesirable features that may force their phase-out over the next few years, suitable substitutes might be found. Their relatively low boiling points and high heat of vaporization may provide an additional advantage. For simplicity, it might be desirable to cool the induction modules passively (without forced flow). Under this scenario, the fluorocarbon is maintained at its boiling point and the heat deposited in the cores is transferred from the Metglas via heat of vaporization (forming a very small volume of bubbles). This two-phase cooling process is quite efficient. A heat exchanger then removes the heat from the fluid and deposits it in water.

The magnets in the heavy ion driver are required to be cooled to liquid helium temperature to be superconducting. The magnets are in cryostats that isolate them from room temperature. During the field ramping stage during start up, eddy currents generate a thermal load, but once operating the predominant thermal loading mechanism on the system is static heat leaks through the cryostat penetrations. Liquid helium is brought into the magnet and cold gas exits. Higher temperature gaseous helium from the boil-off is used to thermally anchor the shields at intermediate temperatures (typically 20 K and 80 K), eliminating the need for a separate liquid N2 system.

Large distributed cryogenic systems (refrigerators, cold boxes, distribution lines, etc.) of this scope have been built and operated reliably at various accelerator facilities

Use or disclosure of data
subject to title page restriction

around the world (Fermilab, CERN, DESY, CEBAF, JAERI), and a much larger one will soon be built for the SSC. The cryogenics system is not viewed as an issue for Prometheus-H.

A properly designed cryostat will have mainly axial losses due to supports; for this reason one is driven to make the cryostat as long as possible (consistent with access requirements), minimizing the number of penetrations between 300 K and 4 K. Because the cost of a cryostat is more or less fixed, independent of size, the later portions of the Prometheus-H driver (when the beams are carried in parallel beamlines) have single cryostats containing many magnets.

6.5.2.5 Storage Rings - Each of the 18 beamlets exiting the single beam LINAC is captured and stored in one of 14 identical rings. Twelve beamlets are stored in individual rings, while the remaining six beamlets are divided into the two remaining rings. The two groups of three beamlets form the two precursor beams. The injection timing is such that the three beamlets are sequenced one after another. The precursor beams are then sent to the bunching LINACs, followed by the main beams.

Ring sizing for this study is based on a simple sublattice; focus-drift-bend-drift-defocus-drift-bend-drift. This is replicated twice and then a straight section was added to allow for injection and extraction of the beams; this was repeated four times. The storage ring is illustrated in Figure 6.5.2-22. Thirty-four 1-m long cos(2θ) superconducting quadrupoles, identical in all respects to those at the end of the LINAC, have a spacing of 4.6 m around the ring. Thirty 2-1/4 m long 6T cos(θ) superconducting dipole bending magnets have a 50% packing fraction (the magnetic rigidity of the 4 GeV Pb^{2+} ions is 65 T-m).

The storage rings share common cryostats although the beamlines are separated.

This ring is suggested only as a placeholder. No attempt was made to check the dynamic aperture even for single particles, much less a space-charge dominated beam. Nor were any aberration-correcting elements added to the lattice. Anything more serious than a cursory "reality-check" look at the storage ring is beyond the scope of this study.

Use or disclosure of data
subject to title page restriction

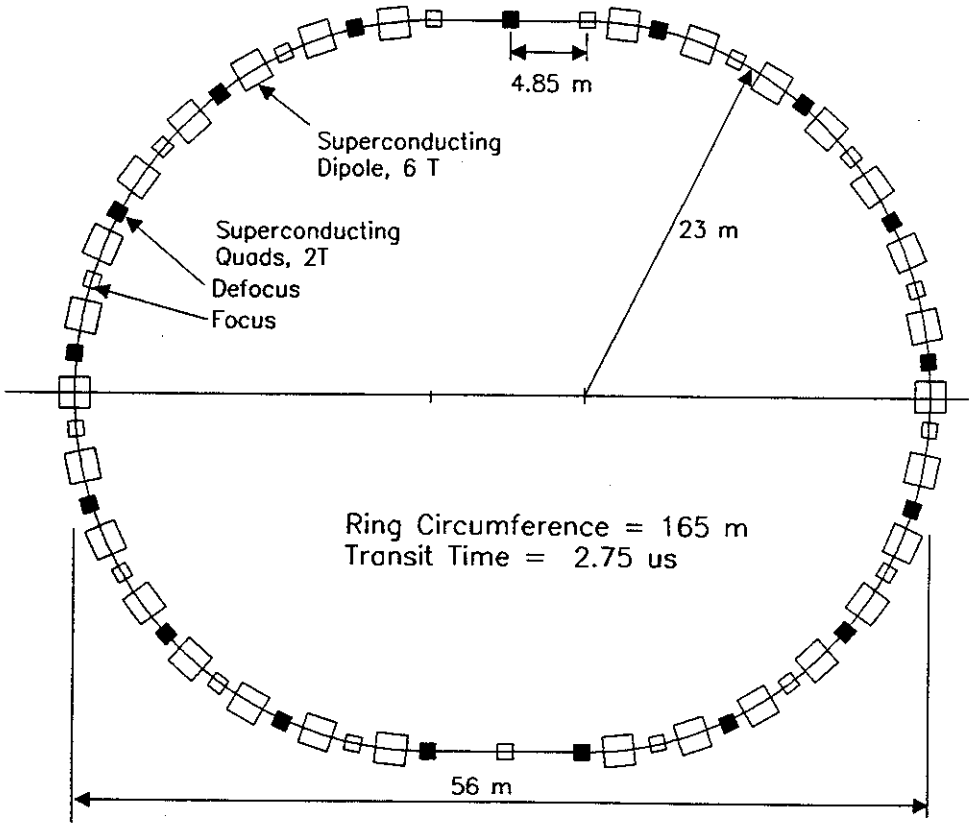

Figure 6.5.2-22 Dipole Magnet Schematic

The maximum storage time in one of these rings is 18 times the interbunch spacing. At a burst rate of 20 kHz (for example), the duration that the first bunch is stored is 50 μs x 18 = 0.9 ms. During this time, the coasting bunch makes nearly 400 revolutions, traveling almost 55 km around the ring. There is a real possibility of the beam coupling to resonances in the circular system, leading to beam degradation (emittance growth) or scrape-off. To help in this regard, the baseline burst rate of 30 kHz was chosen.

The consequences of scrape-off are more serious in a circular machine since the beam passes the same spot over and over. A slight loss of beam to the wall could evolve enough gas to further perturb the beam on a subsequent pass, eventually causing closure of the aperture through this vacuum instability; the ALADDIN storage ring at Wisconsin was plagued for years by this effect. In a linear device the gas has a chance to dissipate before the next beam pulse arrives.

Use or disclosure of data
subject to title page restriction

At this time, all that can be truly said about the detailed dynamics within the ring is that they require a much closer look than could be given here. Storage time in the rings has been identified as a Critical Issue.

Despite the lack of a definitive ring design and ignoring the issue of whether the beam can be stored at all, some points basic to the overall concept can be addressed. Specific issues concern maintaining the longitudinal profile of the beam and coupling into and out of the rings.

First, unless prevented the beam will de-bunch as it coasts around the ring. In the central part of the beam, the axial electric field is nearly zero, but toward the ends the axial forces try to accelerate the head and decelerate the tail. To remain at the space charge limited current, the beam will occasionally have to be "kicked" at its ends to counteract the cumulative effects of the axial space charge force. The beam head must be retarded and the tail accelerated. This can be done with very few cores per ring. Because the kicker voltage is low and the affected portion of the beam is small, there is little stress on the induction modules. The core volume is negligible. This adjustment does not have to be made often, perhaps less than once per revolution. The process is illustrated in Figure 6.5.2-23.

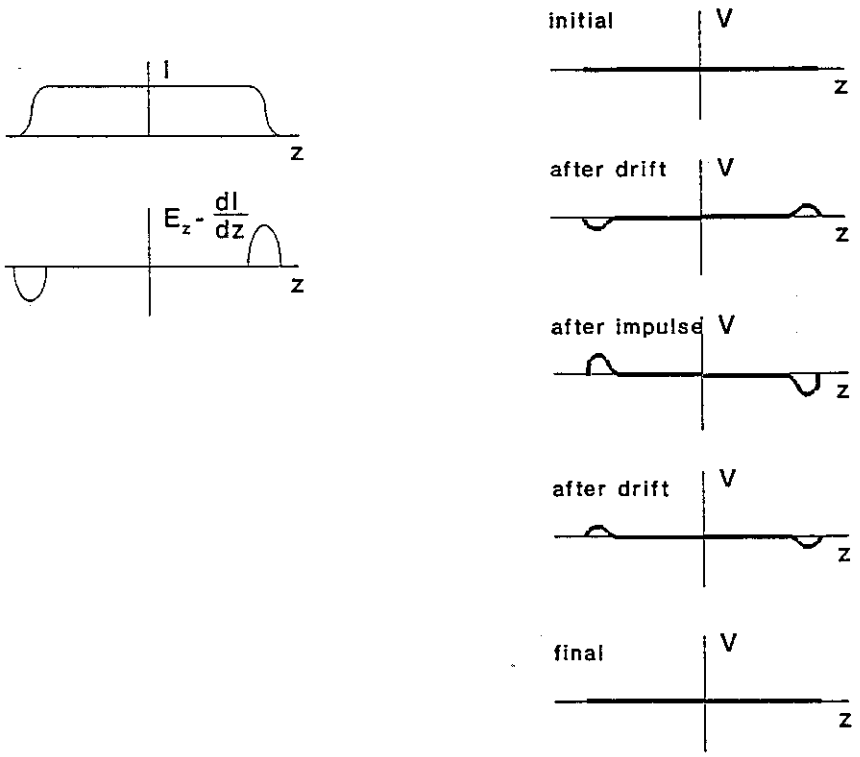

Figure 6.5.2-23. Effects of Drift and Overcorrection on Longitudinal Phase Space

Use or disclosure of data
subject to title page restriction

In fact, this energy adjustment must be made to the heads and tails of the beam throughout the driver. In the main LINAC and the buncher, this voltage can be provided by the induction modules already present. Separate correction modules are required only in the storage rings because the beams coast at constant energy and constant length and there is no need for the main modules. However, the short length of the correction pulse may make it desirable to use separate function kicker modules in the rest of the driver as well.

It has been predicted that a high-current, heavy ion beam will couple to the impedance of gap structures in the LINAC, forming a longitudinal analog of head-to-tail cumulative beam-breakup in electron LINACs. Small-scale variations in beam energy along the pulse (with wavelength long enough that the space charge forces do not reduce them quickly) would be transformed to current variations by the drift, and it is easy to imagine an instability that would grow to some finite level before it saturates. The outcome would be to increase the longitudinal emittance of the pulse and make it more difficult to compress. The problem would presumably be worse in a storage ring, where the total path length is much longer and the possibility of a regenerative instability also exists. Mechanisms for control of the instability include lowering the impedance of the gap and using feedback in the cells to damp the modes.
A method must be provided to assure that the beams in all rings are synchronized so that they are at the correct position when they are ejected from the ring. Small differences in beam energy or ring circumference could otherwise accumulate, leading to a condition in which the beams are separated in time by as much as 2.3 μs due to one beam passing the extraction point before the others. RF storage rings use the principle of phase stability to maintain the particle in the right position; a slight periodic ramp over the pulse would accomplish the same thing in the long-pulse induction systems, accelerating late pulses and retarding early ones. The parameters would have to be controlled carefully.

As an aside, the previous two points serve to illustrate the need for a feedback control system, not just for the storage rings but for the entire driver. Diagnostics to sense the beam and mechanisms to control it must be integrated into the driver. An expert system will probably be required to make Prometheus-H feasible. Interest in model-based systems is increasing at accelerator facilities as the machines become larger and more complex. It is probable that operations knowledge and experience accumulated in the R&D efforts in support of the heavy ion driver will be used in educating an expert system.

Finally, there is the problem of injection and ejection. In the high current ring, the quadrupoles are necessarily close together, leaving very little room to couple into and out of the ring. Consider Figure 6.5.2-24, a detail of the ring described above. There are only 3.7 m of space between quadrupoles with 0.43-m radius. Bringing the beams out between adjacent quadrupoles does not appear to be practical. A pulsed

Use or disclosure of data
subject to title page restriction

dipole magnet producing 10 T would have to be 2.7 meters long in order to allow the beam to clear the quadrupoles. The magnetic field energy alone is on the order of 40 MJ per magnet per pulse; even assuming that the energy is not dissipated, the field would have to be established within 2 μs.

A more practical solution might be to use an approach suggested by the LLNL team working on recirculating induction LINACs. Several large-bore quadrupoles would be inserted into the lattice, and the beam would be slowly extracted through them via multiple kicks. This concept is illustrated schematically in Figure 6.5.2-25.

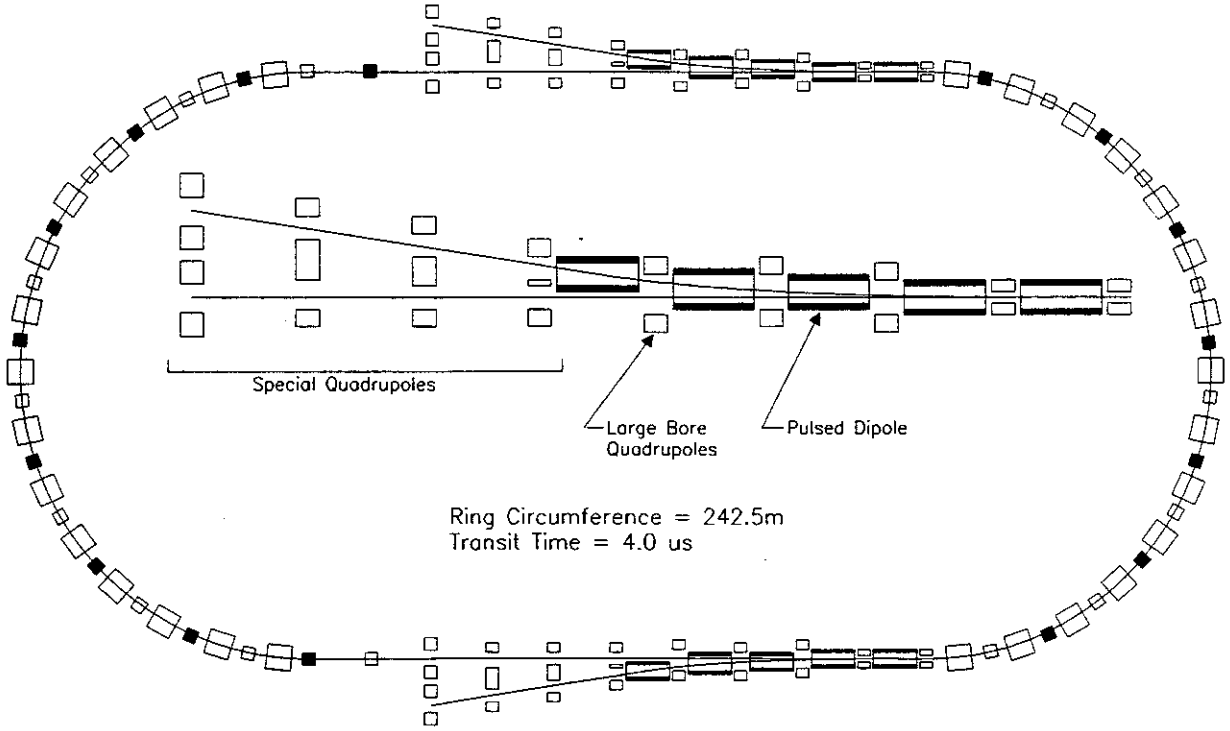

Figure 6.5.2-24. Portion of Ring with Gap

Use or disclosure of data subject to title page restriction

The issue of matching into ring lattice from the LINAC and into the final focus from the rings must still be addressed.

A number of issues may have to be resolved before the community accepts the idea of a single beam LINAC and high current storage rings as a viable alternative to a multiple beam LINAC (MBL). The MBL approach requires the development of very large induction modules and very complex multiple-channel superconducting quadrupoles. The single beam LINAC (SBL) approach shifts the technology onus from the LINAC, which now becomes within reach of demonstrated technology, to the storage rings. However, the potential cost savings achievable with the single beam system may be the factor that determines whether an HIF power plant is eventually built.

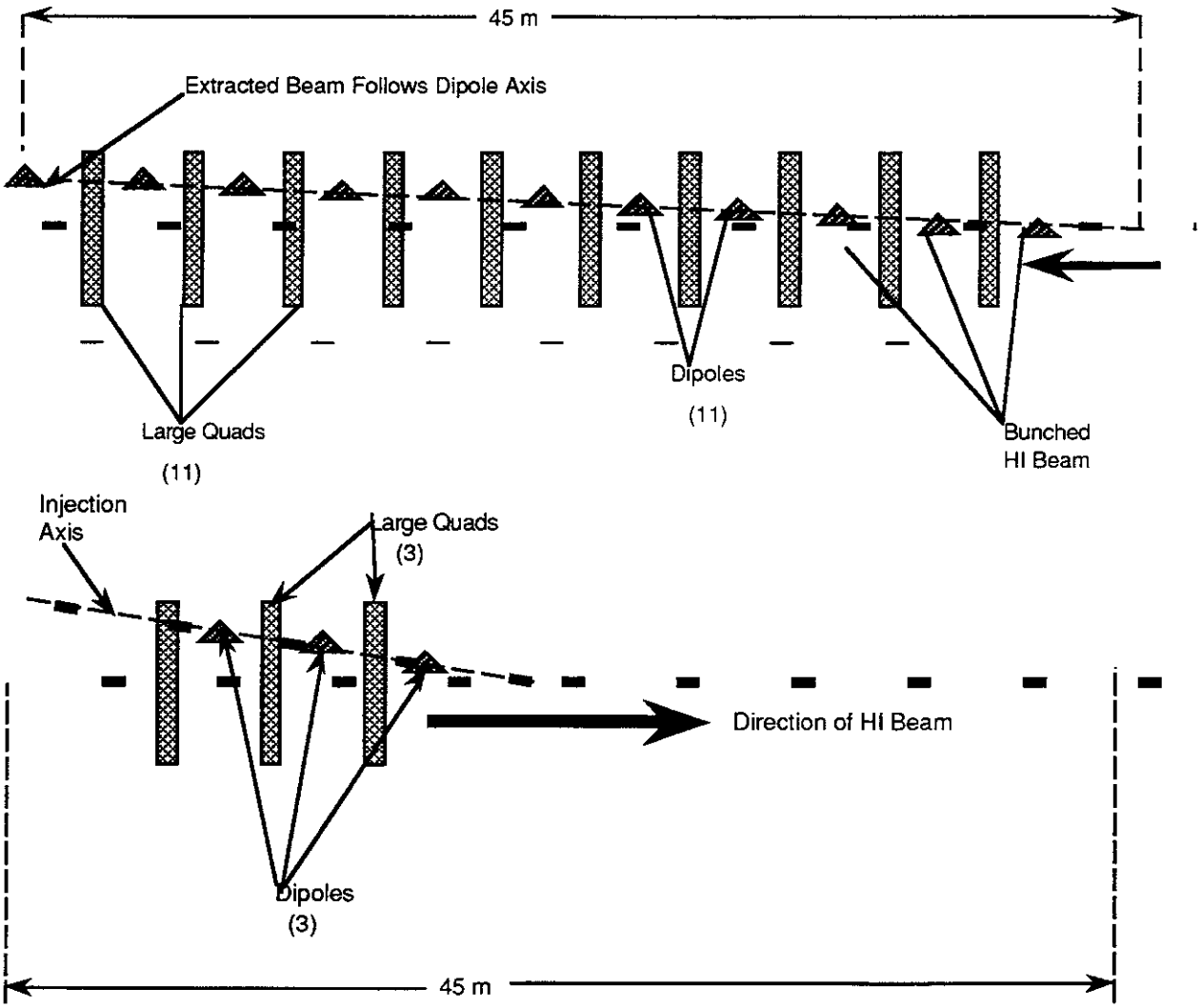

Figure 6.5.2-25. Schematic of Multiple Quads and Beam Ejection Techniques

Use or disclosure of data
subject to title page restriction

6.5.2.6 Final Transport - The final transport of the beams to the target consists of several steps. The majority of the beamlets are bunched, transported to the reactor area in two groups, tightly focused, and finally combined in a small spot just outside of the target chamber. The remaining beamlets are combined before focusing and form the two precursor beams with a longer duration and a lower total energy content. The beam is transported to the target in a self-pinched mode through a preformed channel.

Bunching - When the storage rings eject the 14 pulses, the beamlets are sent to one of two induction-LINAC based bunchers. The first buncher compresses the twelve main beams, the second compresses the two precursor beams. The two bunchers are in close proximity, sharing the same tunnel. Both bunchers are configured with independent beamlines, with superconducting quadrupole focusing magnets sharing common cryostats and the induction module cores surrounding the beamlines between cryostats. The configuration is illustrated in Figure 6.5.2-26.

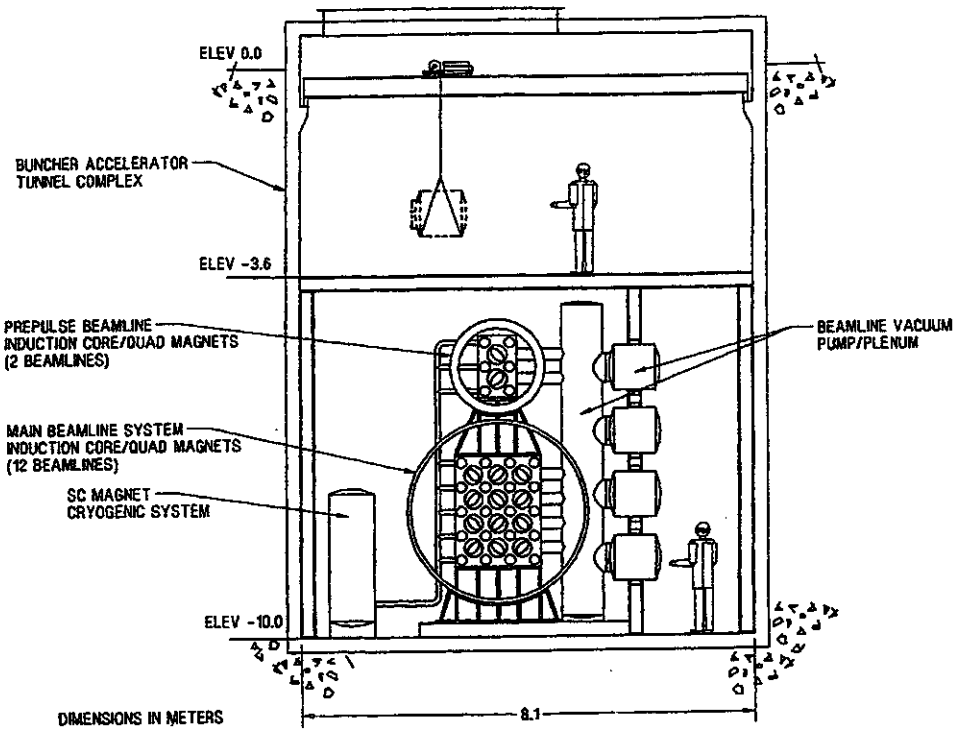

Figure 6.5.2-26. Precursor and Main Pulse Bunchers Equipped with Common Cryostats

The quadrupole lattice parameters at the entrance to each buncher are the same as at the SBL exit.

Use or disclosure of data subject to title page restriction

Each buncher LINAC adds a position-correlated energy across its beam pulse. The buncher cells are ramped in time, adding zero to the front of the pulse and producing the maximum 1 MV/m gain at the end of the pulse. The main (precursor) buncher extends 85 m (180 m), so there is a 4.2% (9%) energy difference from the front to the back of the pulse. The bunchers do add to the total beam energy, but ignore that for the purpose of this discussion and consider the beam to be coasting. In practice the energy of the LINAC would be dropped 2.1% to compensate for the net energy gain in the buncher. The precursor beams would still be 2.1% high in energy and the precursor buncher would be readjusted accordingly.

As the bunches drift, the backs of the pulses begin to catch up with the fronts, increasing the current. This bunch compression process starts within the buncher and continues up to the target. The beam current is shown as a function of distance from the front of the buncher to the target for both the main and precursor beams in Figure 6.5.2-27.

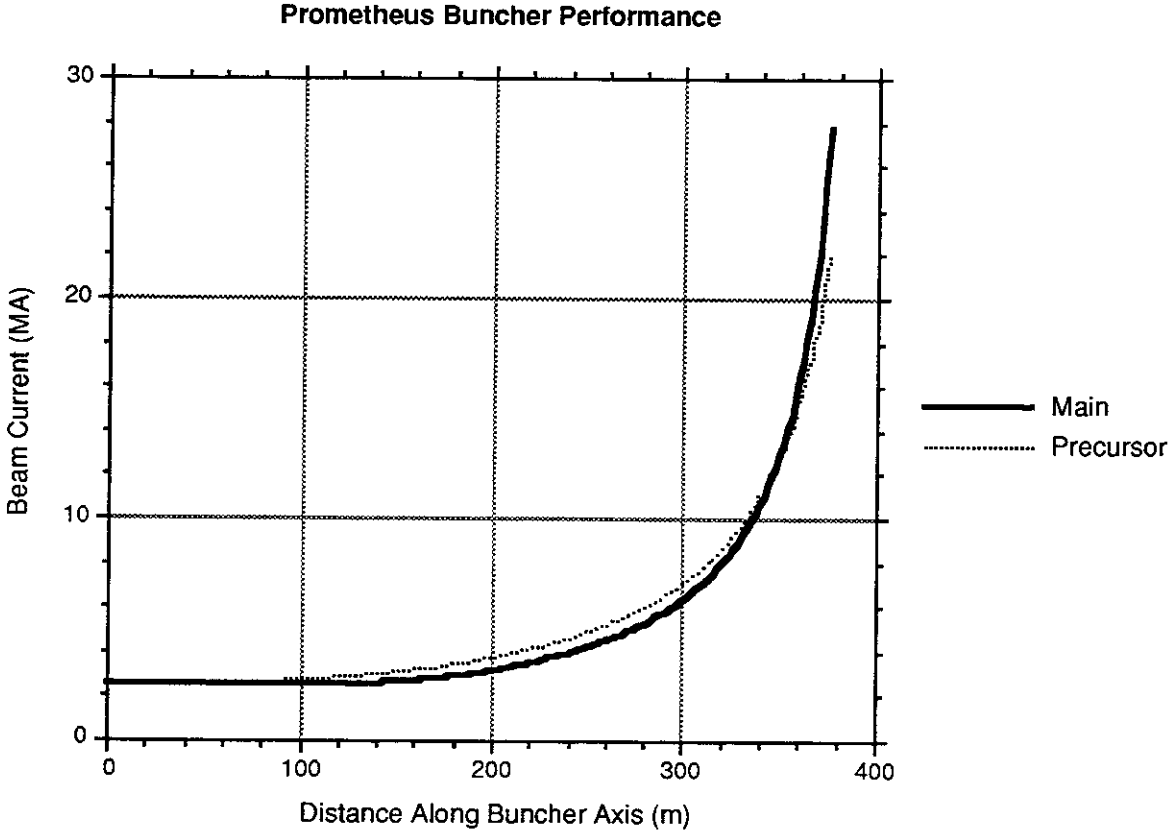

Figure 6.5.2-27. Plots of Beam Current for Precursor and Main Beams vs. Distance Along Accelerator Axis

Use or disclosure of data
subject to title page restriction

Note that the length of the buncher tunnel is dominated by the precursor, not the main pulse; the main pulse actually coasts for 80 m in the tunnel before the bunching begins.

Like the rest of the system, the final transport is adjusted to keep the beam at its space charge limit, even as the current is increasing. The driver scaling parameter used in the constant voltage portion of the accelerator was $\gamma = 0.8$. The focusing lattice parameters are a function of the local current, and the current profile along the final transport was used to produce curves of lattice parameters versus distance shown in Figures 6.5.2-28 through 6.5.2-34.

These curves terminate about 30 m short of the target since, at that point, the focusing channel approach is abandoned and the beams enter the final focus.

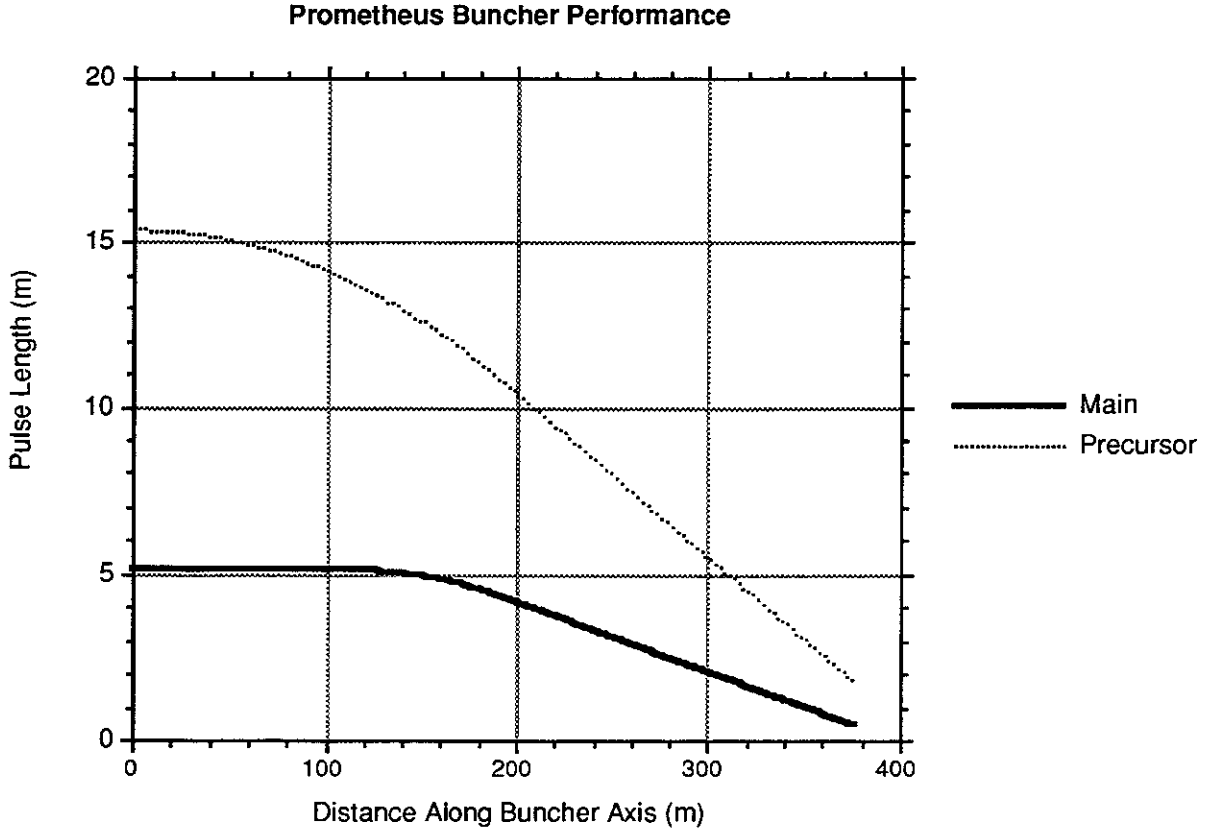

Figure 6.5.2-28 Pulse Lengths of Main and Precursor Pulses vs. Distance Along the Buncher Axis.

Use or disclosure of data
subject to title page restriction

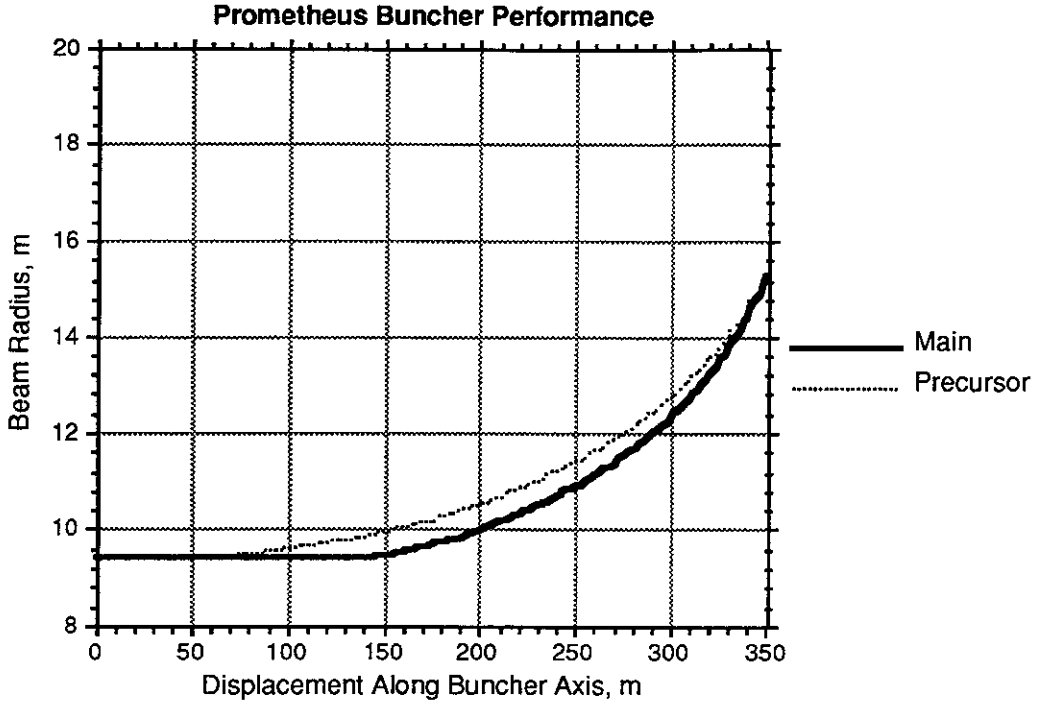

Figure 6.5.2-29 Beam Radii of Main and Precursor Beams vs. Distance Along the Buncher Axis

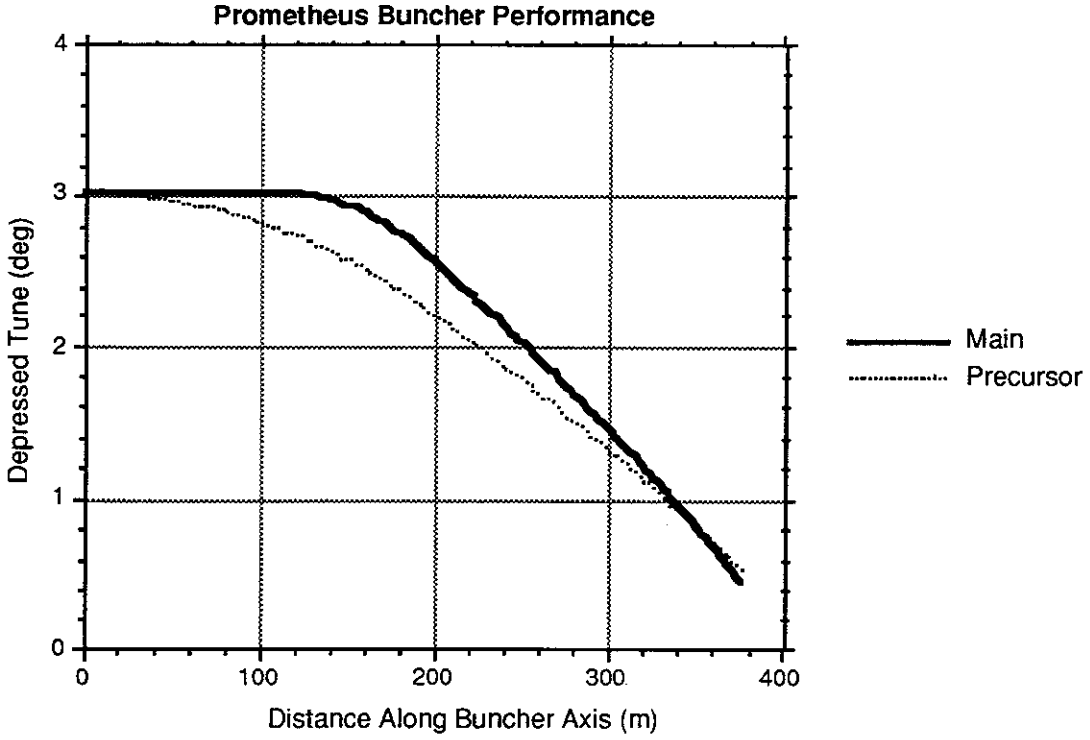

Figure 6.5.2-30 Depressed Tune as a Function of Distance Along the Buncher Axis

Use or disclosure of data
subject to title page restriction

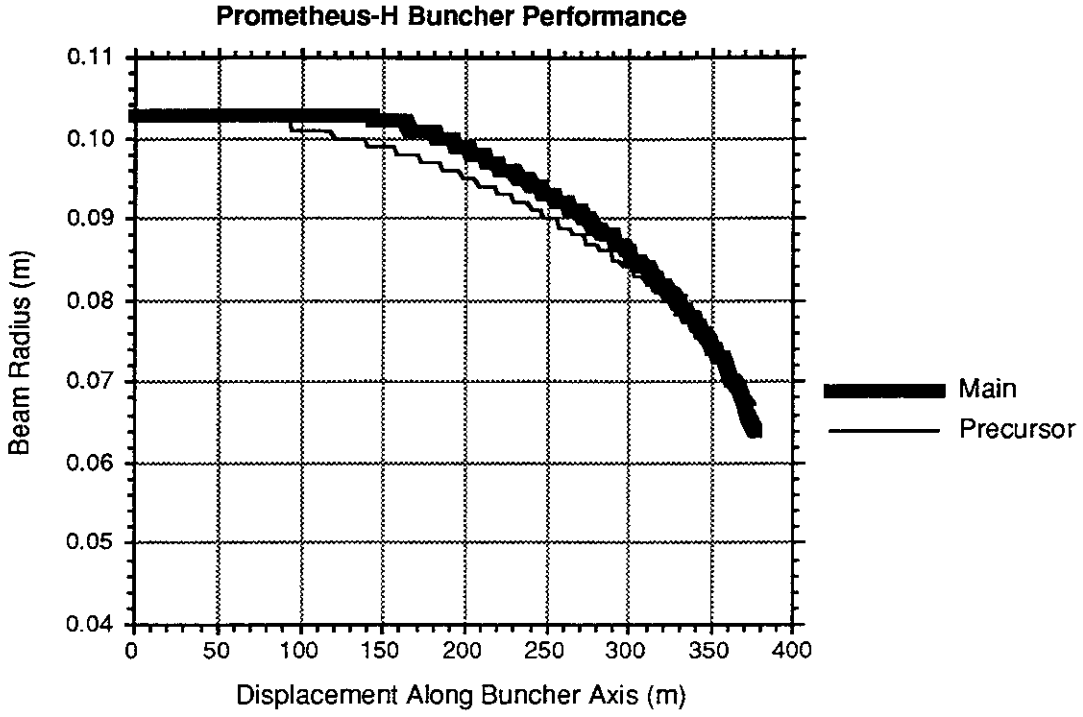

Figure 6.5.2-31 Ratio of Beam Diameter Over Length as a Function of Distance Along the Buncher Axis.

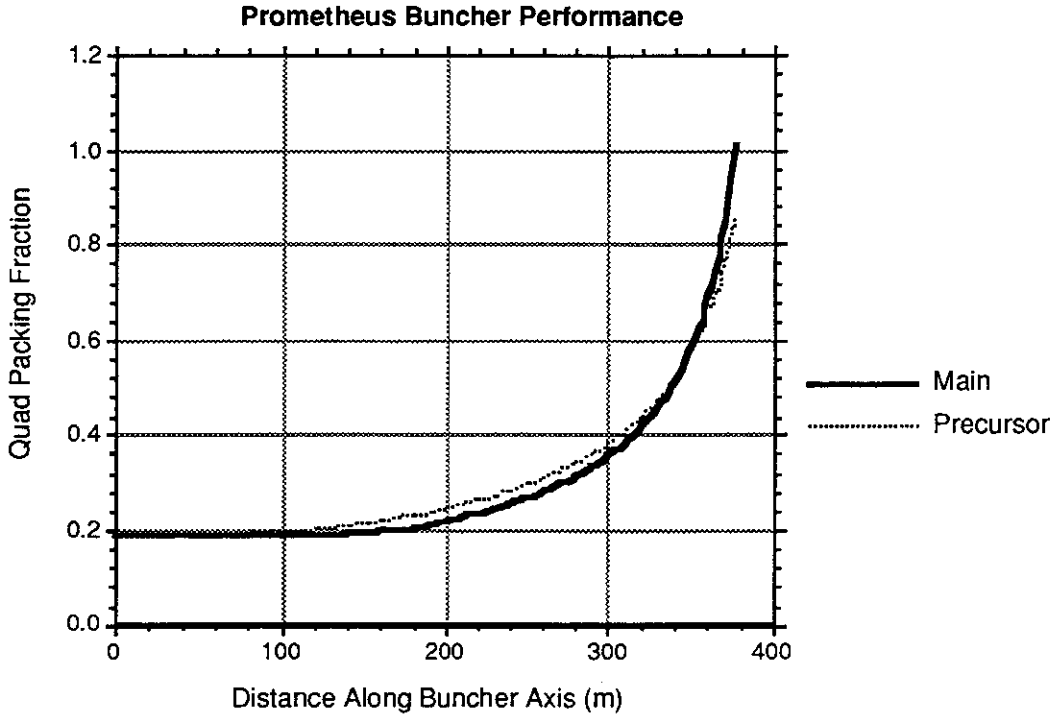

Figure 6.5.2-32 Quad Packing Fractions of Main and Precursor Beams vs. Distance Along the Buncher Axis

Use or disclosure of data
subject to title page restriction

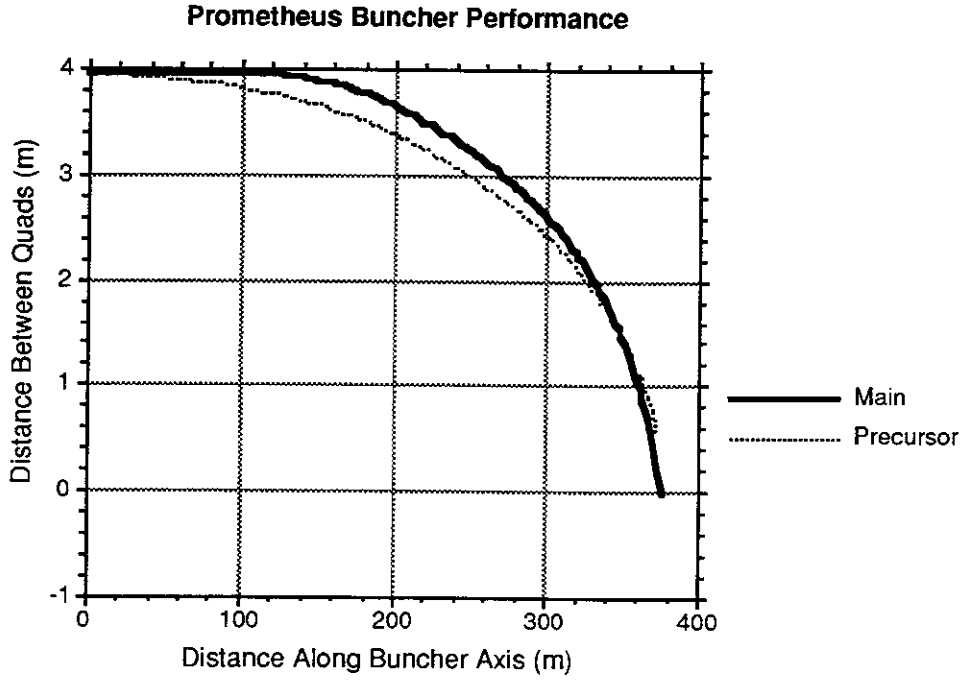

Figure 6.5.2-33 Distance Between Quads for Main and Precursor Beams vs. Distance Along the Buncher Axis.

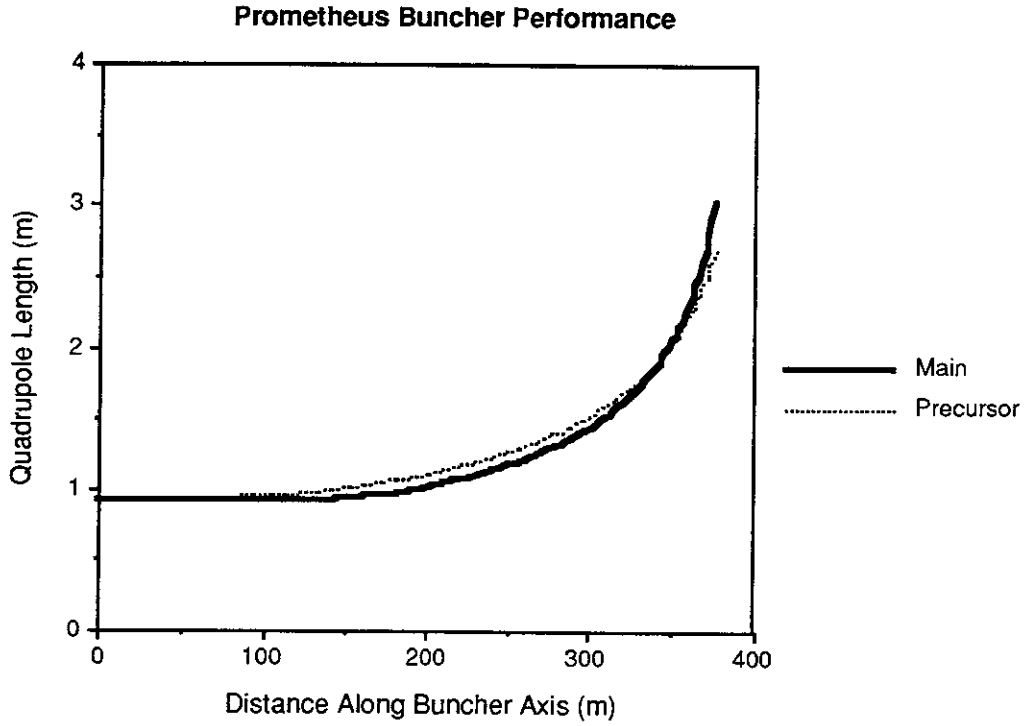

Figure 6.5.2-34 Quad Lengths for Main and Precursor Beams vs. Distance Along the Buncher Axis.

Use or disclosure of data
subject to title page restriction

The same constraints on packing fraction and aspect ratio as used in the rest of the LINAC were used in the final transport calculations. Toward the end of the drift, the beam radius, and hence the model's "ideal" quadrupole radius, increases significantly. As was the case in the LINAC, the quadrupole strength will be adjusted so that a standard quadrupole is used.

At the end of the bunchers, half the beams (six main and one precursor) go to one side of the reaction chamber and half to the other. For most of the distance, the six main beams are bundled to share a common cryostat, but as they approach the reactor chamber building, they first diverge and then regroup as they go into the final focus. On each side, the precursor beam comes in on axis and the six main beams are arrayed symmetrically about it.

As was stated at the outset of this section, the transport schedule is very aggressive. Near the final focus section, the depressed tune has dropped to one degree, one-eighth of its value at the injector. While no instabilities have been identified, the system is on the very edge of stability. The betatron period is longer than the distance from the storage ring to the target. Extreme care must be taken not to significantly perturb the beam since there is virtually no restoring force.

Final Focus - The assumptions made about the lattice concerning packing fraction, etc., are violated before the target is reached. The beamlets are released from their FODO arrays before the limits are reached. The beams expand radially under the influence of their space charge as they drift toward the final focus magnets. The beams are reformatted with quadrupoles before they enter the final lens system. A quadrupole triplet is the simplest lens system that focuses in both planes and is astigmatic to lowest order. The magnets in this quadrupole triplet are low field superconducting cos(2θ) coils, similar in principle to the quadrupoles everywhere else in the driver, but larger and containing shielding against the neutrons from the reactor. The magnets are illustrated in Figure 6.5.2-35.

The triplet is adjusted to focus a monoenergetic, low-charge beam to a 6-mm diameter spot a distance approximately 10 m from beyond the last magnet (Figure 6.5.2-36).

The magnets are sized so that the outer diameter is as small as possible and the magnet closest to the reactor defines the solid angle subtended by the triplet as seen from the focus. All seven lenses are tightly packed (Figure 6.5.2-37).

Use or disclosure of data
subject to title page restriction

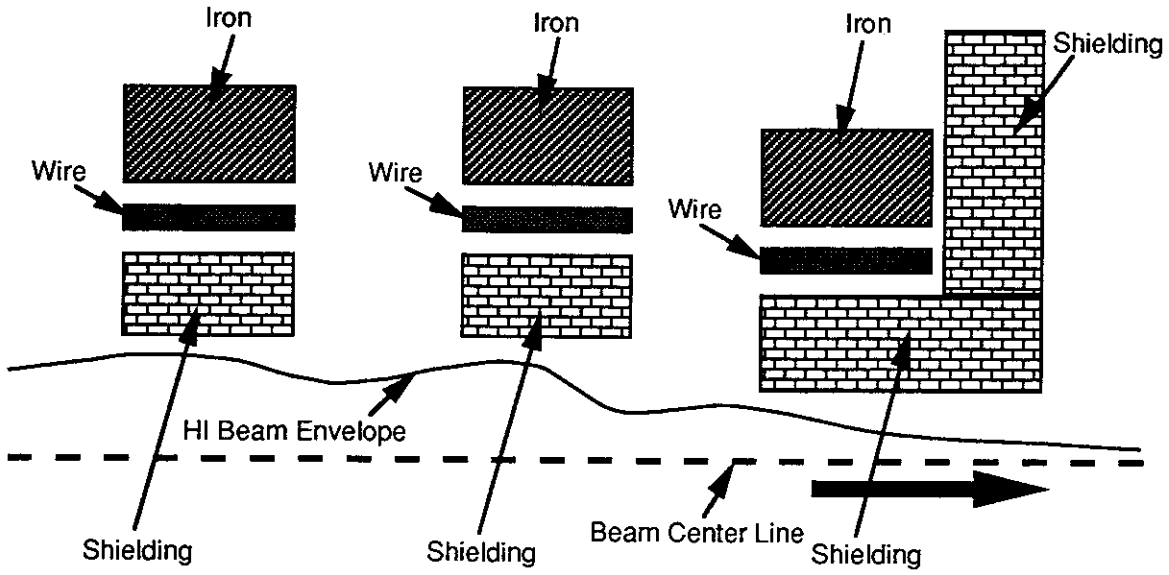

Figure 6.5.2-35 Quadrupole Triplet Magnet Cross-Section.

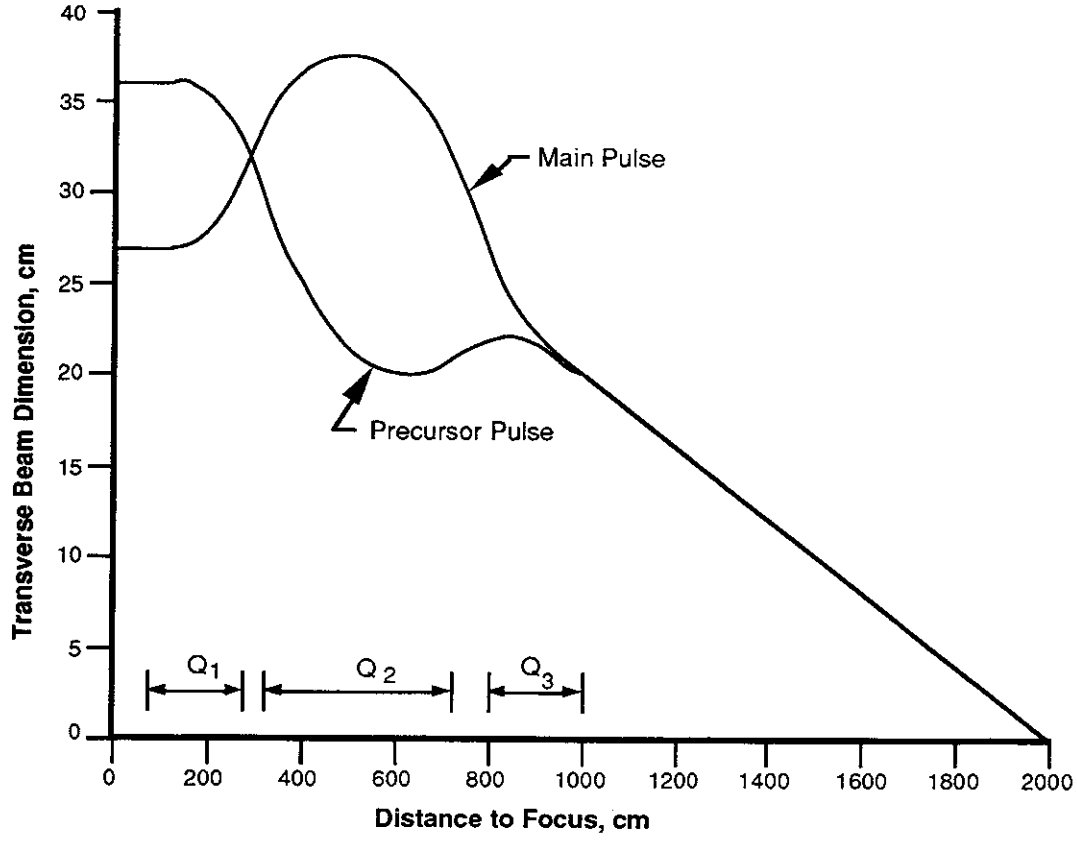

Figure 6.5.2-36. Convergences of Precurser and Main HI Beamlets in Final Focusing

Use or disclosure of data
subject to title page restriction

The allowable f/# of the lens (focal length divided by effective aperture) is limited by geometric aberrations on the low side, and by beam emittance on the high side. However, the incoming beam is neither monoenergetic nor neutral and lens chromaticity and space charge of the beamlet become problems before these limits are approached. The approach taken in the Prometheus-H driver final focus design was to have the final focus dominated by emittance of the beam and work to reduce the effects of space charge and momentum spread on lens performance.

Chromatic Aberration - Even without additional effects related to space charge and high current transport, a simple magnetic lens is not achromatic. The focal length of a quadrupole is proportional to the momentum, and a spread in beam momentum translates directly to a spread in image distances from the lens. In a plane at a fixed distance from the lens, the apparent beam spot size changes with momentum.

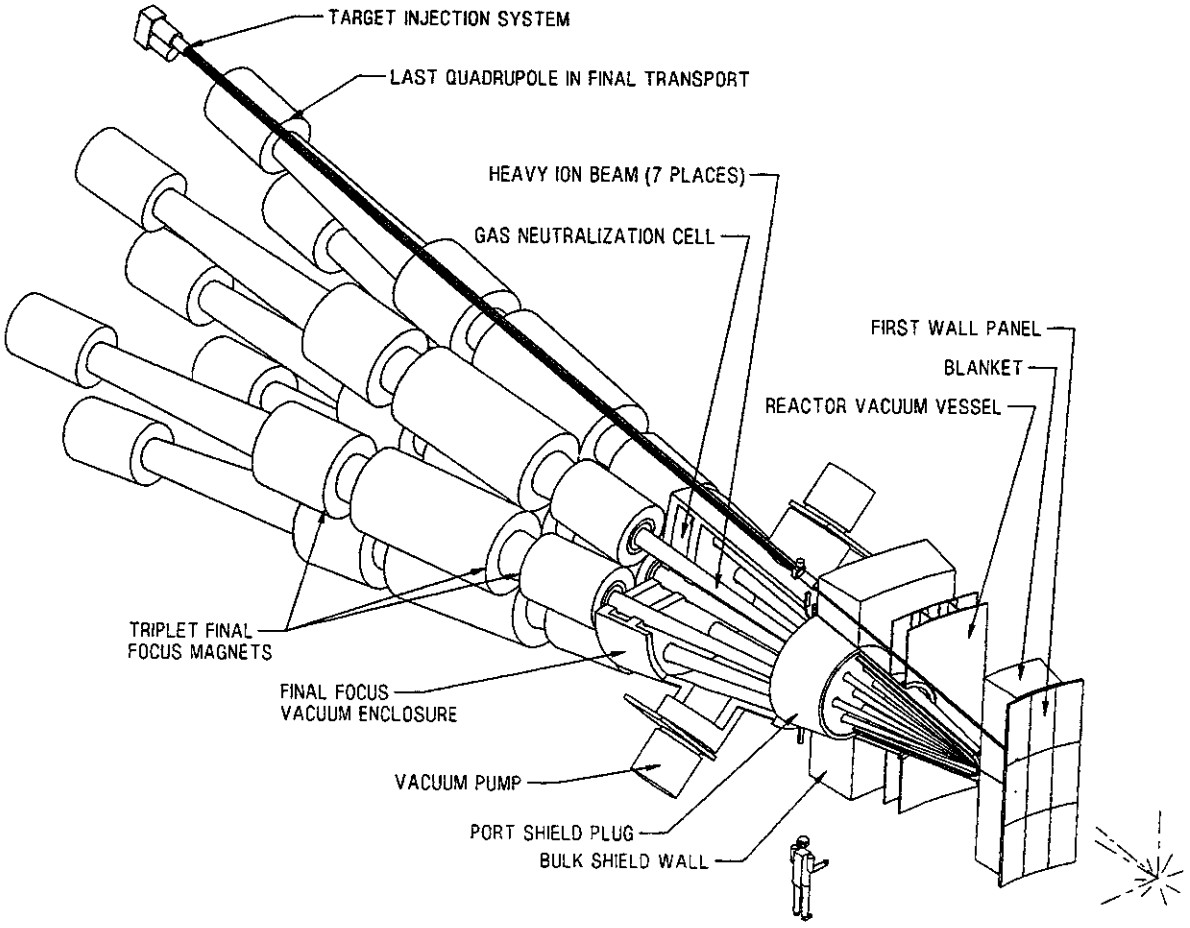

Figure 6.5.2-37. Final Focus Physical Arrangement of Final Focus Triplet Coils, Vacuum Plenum, and Shielding

Use or disclosure of data subject to title page restriction

The inclusion of a pair of dipoles was suggested in the HIBALL-II study to add compensating position-energy dispersion to make the final focus achromatic to first order, as shown in Figure 6.5.2-38. The spot diameter at the target position is then nearly constant. However, the residual dispersion causes the focal spot of a 1% spread beam to sweep across the target in one dimension (as shown in Figure 6.5.2-38). A net improvement is realized by adding the dipoles, but the gain is not all that one would hope.

Longitudinal Tailoring. There have been simulations appearing in the literature showing that, by precisely tailoring the axial spatial and momentum profile upstream, the beam will compress longitudinally in such a way as to completely eliminate energy spread at the lens position (as shown in Figure 6.5.2-39). Residual chromaticity causes beam with 1% energy spread to sweep across target, lowering time-averaged power on target.

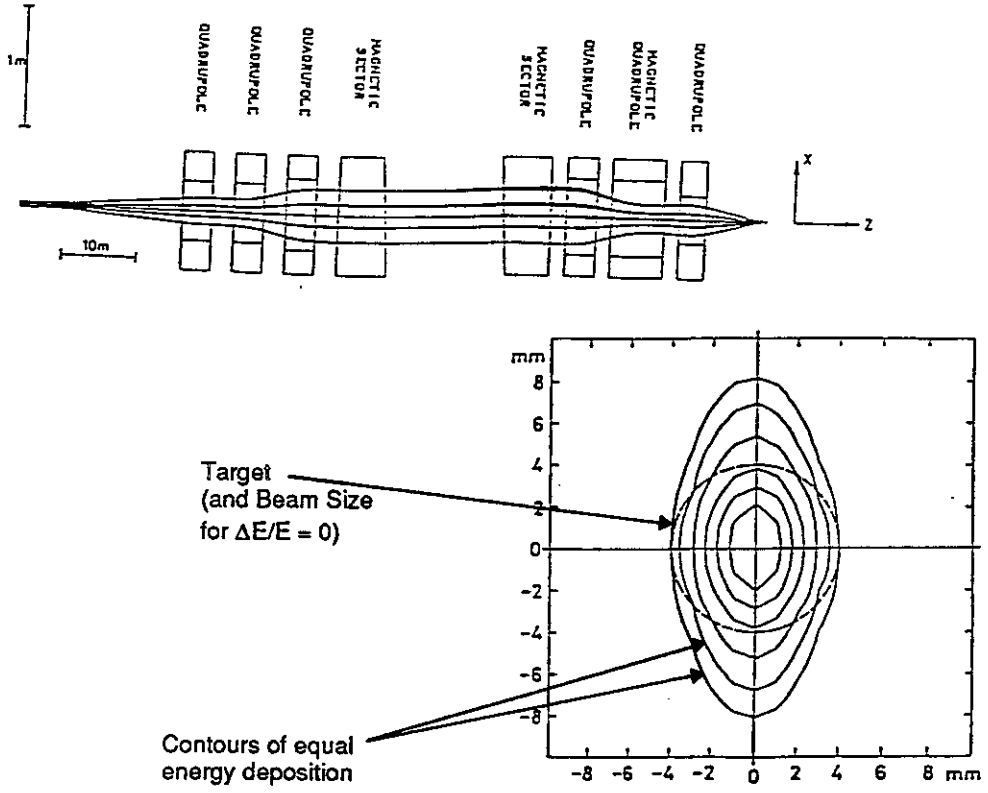

Figure 6.5.2-38. Chromatic Aberration Effects with Magnetic Dipoles.[1]

Use or disclosure of data
subject to title page restriction

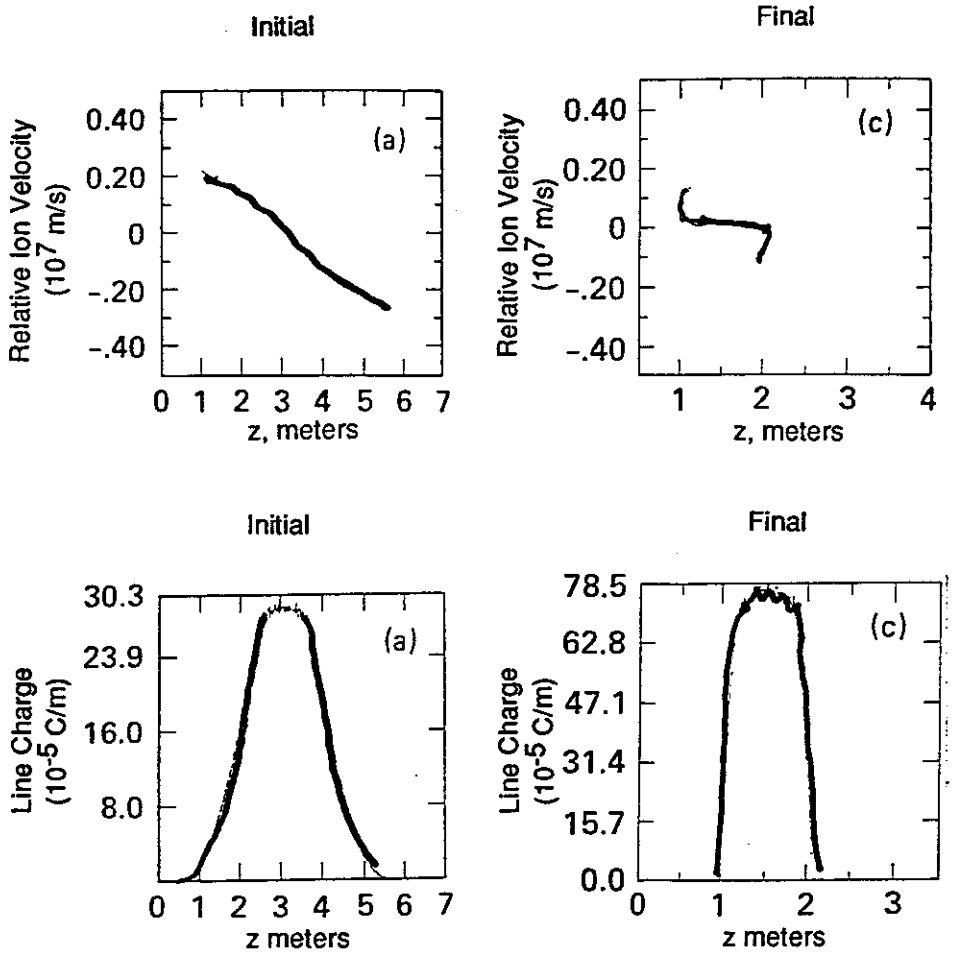

Figure 6.5.2-39 Longitudinal HI Beam Compression of a Monoenergetic HI Beam[2]

The beam reaches its peak current at the final lens; the current then drops on its way to the target as the beam re-expands under space charge forces. In practice, the degree to which the axial momentum spread can be reduced at the lens is uncertain.

Transverse Tailoring. A second approach, developed for use in the Neutral Particle Beam program, is to keep the image point of the lens fixed by altering the apparent object point of the lens to track the changing focal strength. This method relies on correlating the instantaneous transverse properties of the beam with the instantaneous momentum. The place to do this is at the exit of the buncher, where there is a nearly perfect correlation between position in the pulse and the momentum. Relatively low field, slowly varying quadrupole lenses are used to shift the final focus lens object position to compensate for the momentum-correlated focal length shifts of the final focus lens. This is illustrated in Figure 6.5.2-40.

Use or disclosure of data
subject to title page restriction

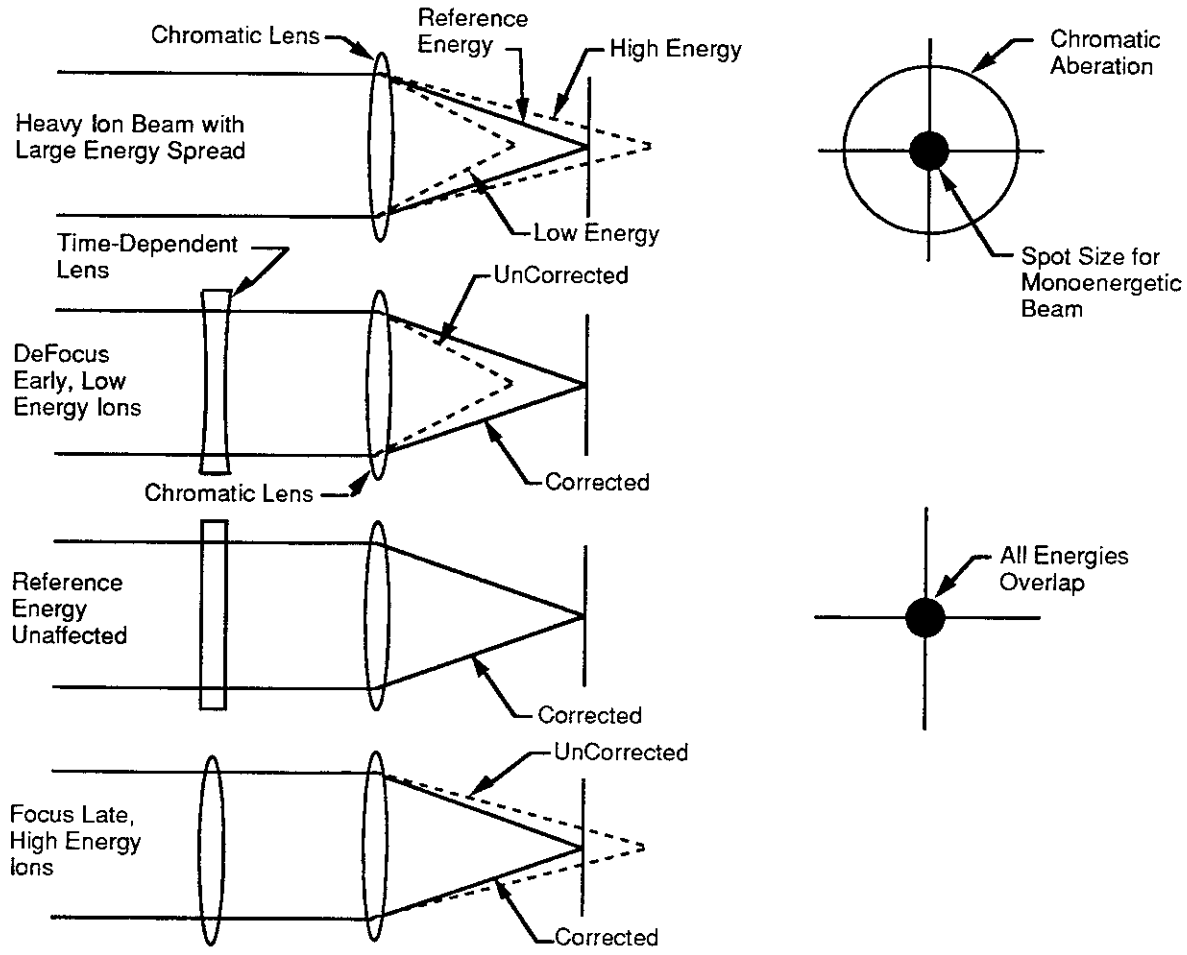

Figure 6.5.2-40 Optical Focusing Analogies for Triplet Quadrupole Focusing of HI Beams.

Simulations show that this approach works as well as the longitudinal tailoring. An additional advantage is that the beam is still contracting when it passes the final focus lens; the current peaks at the target rather than the lens. For this reason it was chosen for the Prometheus-H baseline.

Space Charge Neutralization - Beam space charge is an annoyance within the triplet lens, since it is an additional radial de-focusing force. Note that, because the beam is still contracting at the final triplet, the space charge is a function of position within the lens system, although still much lower than the ultimate current at the target. The individual magnet strengths can be tweaked to compensate, although the degree of adjustment will be larger for the main beam than the precursor.

Past the final lens, space charge is a major problem because it dominates the final spot size. By time-reversing the radial free expansion of a beam (in a manner similar to that discussed under the transverse tailoring section above), we see that the

Use or disclosure of data subject to title page restriction

minimum convergence angle required to reach a 6-mm diameter spot 10 meters away is 0.6 mR. If the beam is to reach its required diameter, the effects of beam space charge must be eliminated soon after it leaves the final lens.

Channel Formation - A number of methods to propagate a high current, high voltage, heavy ion beam to the target have been suggested,[1] as summarized in Figure 6.5.2-41.

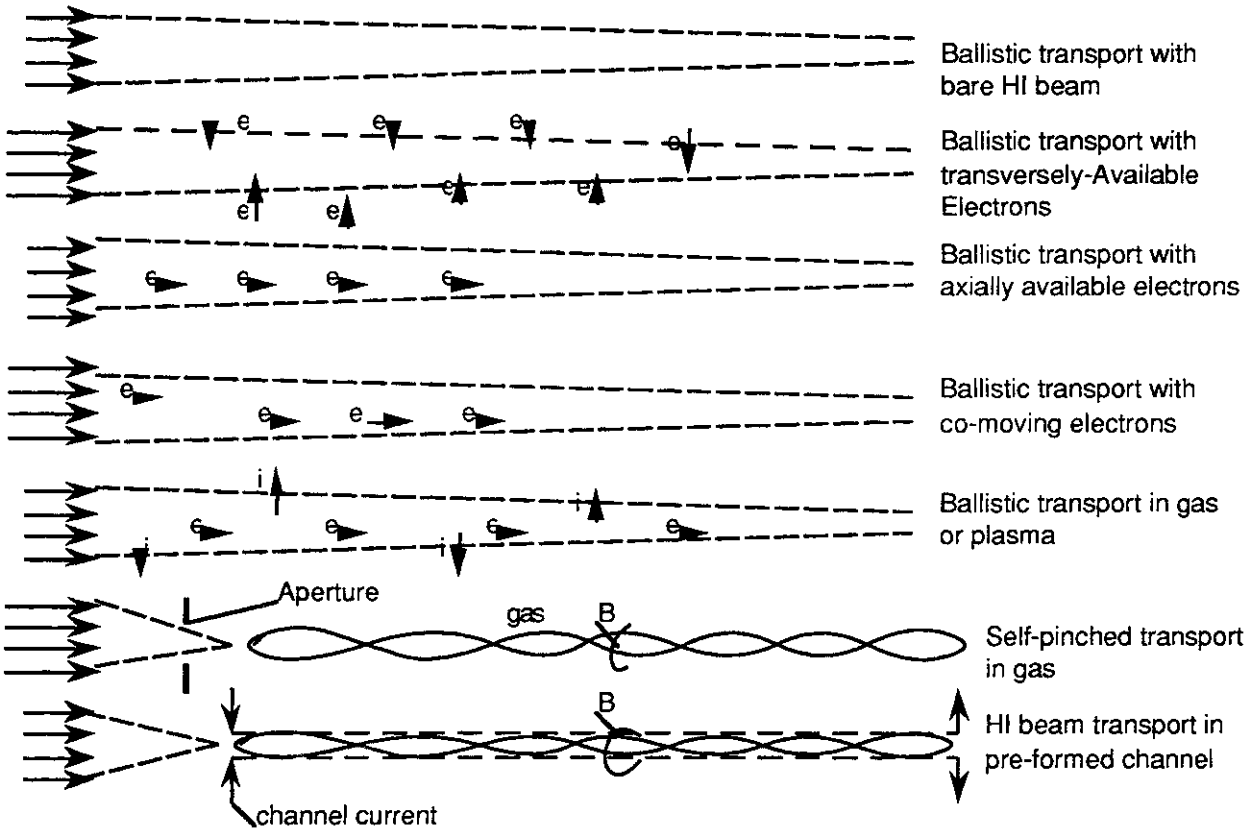

Figure 6.5.2-41 Techniques for Propagating HI Beams to Targets.[1]

With the exception of propagation through hard vacuum, they all rely on plasmas and are all speculative to one degree or another. Detailed mechanisms of propagation, as well as susceptibility to a host of instabilities, depends on the plasma's response to the beam. Most of the guidance as to allowed parameter ranges comes either from analytic models or from computer simulations coupled to atomic physics theories or measurements. Depending on the details of the assumptions, different results are obtained and there is nothing to anchor the codes. Some data comes from experiments with low energy, high current light ion diodes. There appears to be no experimental data on anything approaching a relevant regime for a heavy ion driver, and there won't be any data until a device is built that can approach the required current and energy.

Use or disclosure of data subject to title page restriction

However, given that propagation through hard vacuum does not lead to attractive reactor designs, one is forced to make a choice among the various plasma-propagation methods. The beam can be neutralized by adding bare electrons directly to the beam (e.g. via field emission or thermionic emission) or by adding a plasma whose density is much higher that of the beam. In the former case, it is difficult to imagine a practical scenario (one compatible with a reactor) that injects electrons uniformly into the beam. In the latter case, the beam is not necessarily completely neutralized, but its effective charge is reduced by the ratio of beam density to plasma density since the electrons act to shield the beam ions as well. Due to the inertia of the plasma ions, they can be considered stationary for the duration of the beam pulse. If the electrons remain cold (the DeBye length much smaller than the beam size), the neutralization can be quite effective.

Passive (collisional) ionization of a gas by the beam and other autoneutralizing processes tend to generate co-moving electrons that drift along at about 1±.3 times the beam velocity. Simulations indicate that the electrons heat adiabatically as the beam compresses radially by nearly two orders of magnitude. These heated electrons lose their capacity to shield the beam ions, which then see their own space charge and defocus again. In order to create enough electrons to neutralize, the gas density is fairly high. Some stripping of the beam can occur, raising the ion charge state. As long as the beam ions are neutralized by cold electrons, the electric field within the beam is very nearly zero and the ion charge state does not matter. As the shielding deteriorates, the ions that have higher charge states are defocused more strongly. This is the option adopted in the Prometheus design.

If a lower density gas is preionized, the plasma can provide sufficient electrons to neutralize the beam, without further ionizing the beam to any great extent. With a source of fresh cold electrons available, electrons that begin to be heated by radial compression can escape from the beam, leaving the shielding effective.

In another option, the drift space following the lens is filled with low density gas which is then preionized before the beam arrives. This is a transient process in which a small amount of gas is introduced via a fast valve and then ionized with a pulsed RF burst. From a practical standpoint, pulsing the plasma is necessary to vacuum-isolate this final transport region near the reactor from the UHV region upstream. On the time scale of beam propagation through the region, the gas is stationary; the beam is gone before the gas reaches the magnets. On the time scale of the reactor shots, there is minimal gas loading and the gas is gone before the next pulse 200 ms later. This may also be a viable option.

With each beamlet transported ballistically through the plasma, all eventually converge on a 6-mm diameter spot just outside the blanket, about 5 m from the pellet.

Use or disclosure of data
subject to title page restriction

The precursor beam arrives first, traveling on axis. All main beams overlap spatially at this spot with an 8.5 degree angle between individual beams and the axis.

Transport to Target - At the point where the beams converge, there is a 2-cm diameter cylindrical hole passing through the blanket. The hydrogen partial pressure in the blanket is approximately 100 mtorr (see Table 6.8.2-9 for details) and the hole in the blanket is the major gas load for the final focus region. To lower this load, a thin, high velocity jet of lead vapor is directed across the aperture. This jet forms a gas barrier to the target chamber, entraining the escaping hydrogen in the flow like a diffusion pump. Since the lead is condensible, it does not constitute a vacuum problem even if it escapes the jet. A detail is shown in Figure 6.5.2-42.

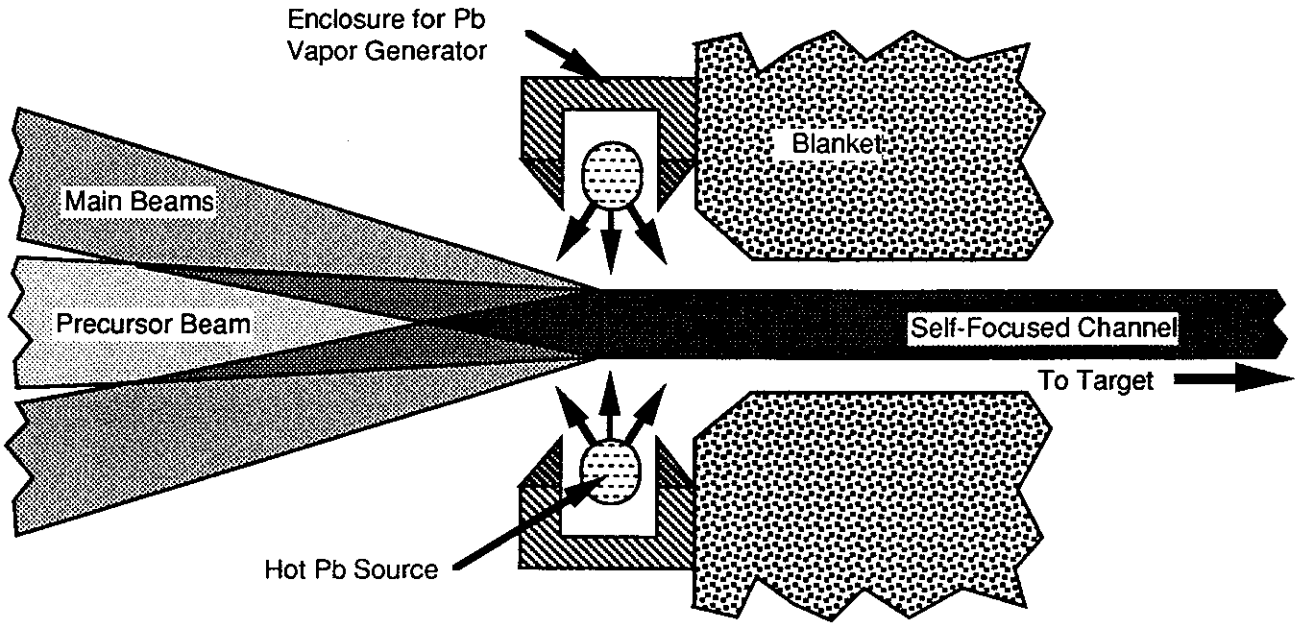

Figure 6.5.2-42. Schematic of Lead Jet System for Stripping Pb Heavy Ions

More importantly, the heavy ion beam is completely stripped in this lead vapor jet. The charge state increases from 2+ to 82+ and vastly multiplies the ion beam current. If it were not for the current multiplication, the beam would diverge into separate beamlets on the other side of the jet and collide with the blanket. Instead the current is high enough that the beam pinches and propagates 5 m to the target without expanding.

The initial direction of pinched beam propagation is presumably defined by its net momentum. The precursor is aimed along the axis and, assuming axisymmetry, it should go where it is meant to. The six main beams are merged and the net momentum, if the beams are perfectly balanced, is directed along the axis as well (see Figure 6.5.2-43).

Use or disclosure of data
subject to title page restriction

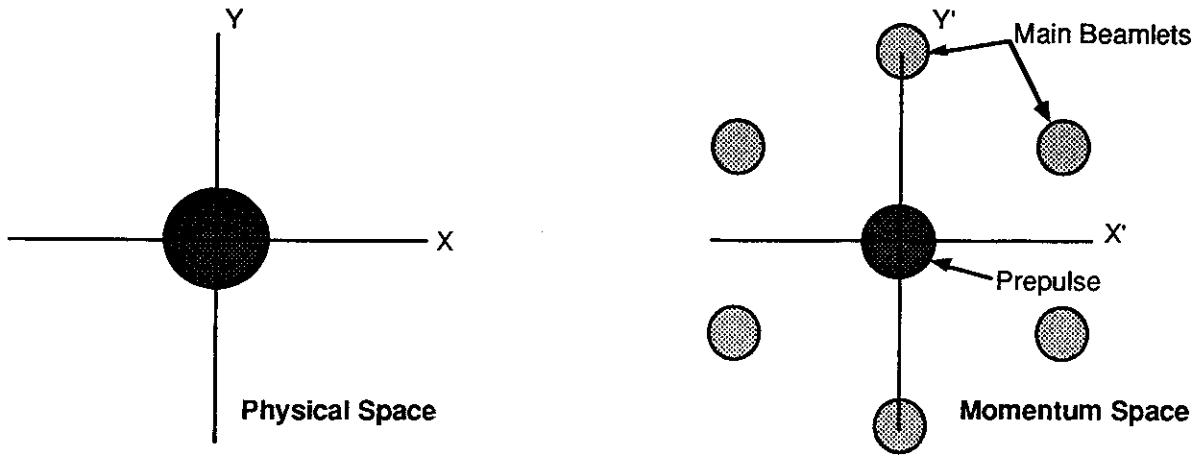

Figure 6.5.2-43. Typical Beamlet Envelopes at Channel Formation Point

The magnetic field associated with the main beam current is sufficient to overcome the initial divergence of the individual beamlets, assuming charge neutralization of the beam within the target chamber (almost certain) and no reverse plasma current (uncertain). This also happens with the precursor, and although the current is down by a large factor, the initial divergence is also much smaller. Figure 6.5.2-44 illustrates the current margin for self-pinching at two possible charge states.

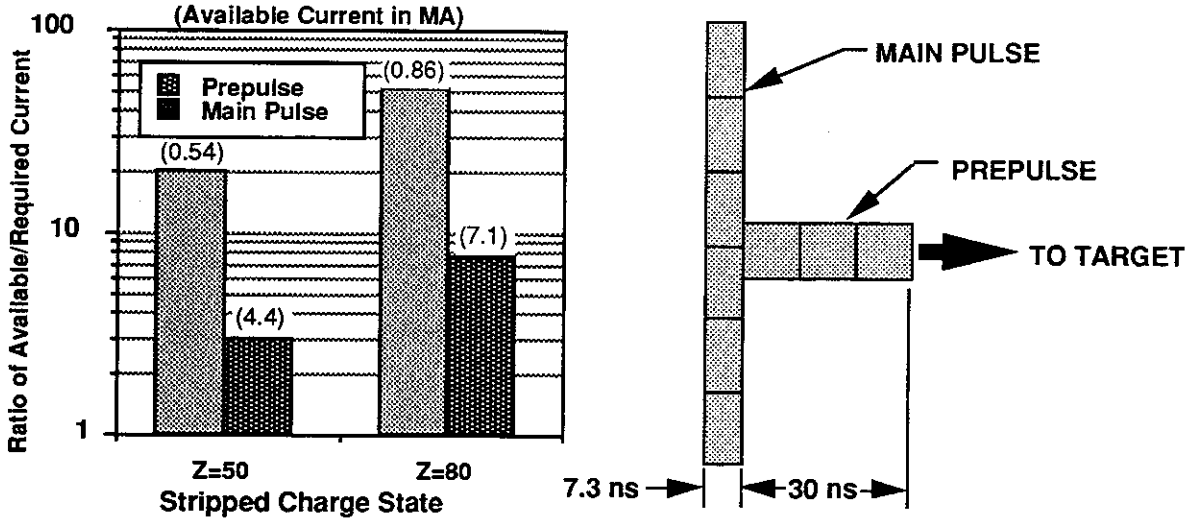

Figure 6.5.2-44. Current Margin for Beam Self-Pinching Indicates Channel Formation Is Feasible in Both Prepulse and Main Beamlets

Use or disclosure of data
subject to title page restriction

The equilibrium radius (the radius at which the beam would propagate at fixed size without radial oscillations) is determined by balancing emittance terms ($\sim r^{-2}$) and pinching force ($\sim r^{1}$). Because the initial beam size is much larger than this equilibrium radius, the beam envelope first contracts to a much smaller spot, and then oscillates with period λ_B as it propagates, its maximum radius equaling the injection radius as shown in Figure 6.5.2-45. The two pinched beams (one from each side of the target chamber) continue until they strike the energy converter regions of the indirect drive target.

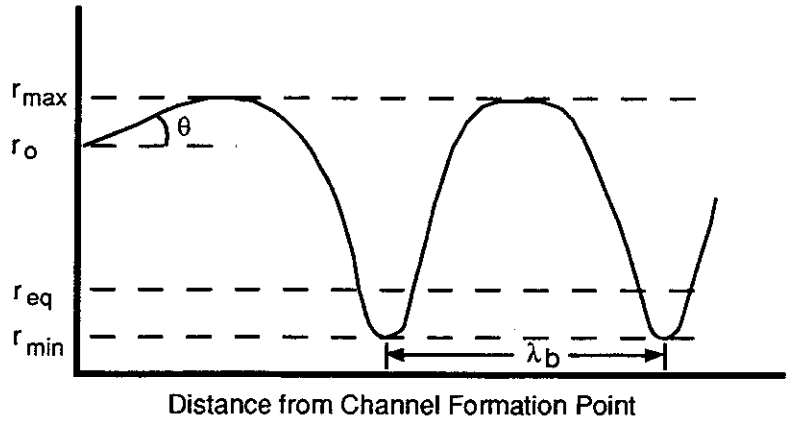

Figure 6.5.2-45. Beam Envelope Oscillation in Channel

Justification. This pinched mode transport is highly speculative, and researchers differ as to whether the plasma return current is sufficiently low that the net current is able to drive the pinch. However, the many engineering advantages of this mode of transport (few reactor blanket penetrations, small shielding penetrations, high chamber operating pressure) make one loathe to give it up without a fight. A definitive experiment would require an ion beam with parameters close to those of the HIF driver.

In the late 1970's, there was considerable interest in the process, but the work was halted due to program redirection. Simulations performed to date have yielded mixed results. Early simulations of the process indicated that the beam head would not be contained. The simulations assumed that the beam entered the gas-filled chamber in a low charge state and that it stripped to a higher charge state and ionized the gas as it went toward the target. As the gas ionized, the conductivity would increase and the magnetic flux would be frozen in, generating a plasma return current to nearly cancel the beam current. The beam head would expand rather than contract.

Recently, preliminary simulations have indicated that the situation can be quite different in a preionized channel with no initial current (as opposed to a pre-formed Z-pinch as suggested for light ion drivers). Such a pre-formed plasma channel can be formed by directing intense pulses of laser light along the chamber axes, ahead of the

Use or disclosure of data
subject to title page restriction

precursor beams, and ionizing the gas in the target chamber. In these simulations, the fully stripped ion beam draws electrons ahead of it into it. This sets up an axial current that reinforces the pinch current rather than canceling it, permitting transport to the target.

Other Issues. Assuming that the pinched mode of transport is given, some questions remain concerning the ability to hit the target. The beam must hit a target 5 m away with a high accuracy of the order of ±1 mm.

First note that the ion beam is so stiff that it is virtually impossible to steer the beam to track the target. Instead, the target delivery system must deliver the target to the right place. The "target" for the beams is actually the two conversion plugs in the indirect drive pellet, each of which must face one of the pinched beams.

The questions are whether imbalances between net beamlet current causes steering of the pinched beam on a shot-to-shot basis and whether variations within the beamlets during a pulse can cause steering. The answers depend on whether or not the precursor provides a focusing mechanism; if not, then limits on the allowable current variations in the beamlets can be set for the axisymmetric 6-beam system set on an 8.5-degree cone.

Reference for 6.5.2

1. B. Badger, et al., "HIBALL II: An Improved Heavy Ion Beam Driven Fusion Reactor Study," UWFDM-625, University of Wisconsin Fusion Technology Institute (1984); see also KfK-3480, Kernforschungszentrum Karlsruhe (1984) and FPA-84-4, Fusion Power Associates (1984).

2. Ho, et al., 1987 IEEE Particle Accelerator Conference, 87 CH2387-9, pg. 1994.

Use or disclosure of data
subject to title page restriction

This page intentionally left blank.

6.5.3 Common Driver Subsystems - For both types of drivers, several subsystems with common functions are required even though the specific implementation may vary. The following sections delineate those envisioned common systems.

6.5.3.1 Power Supplies - Due to our limited resources and past conceptual design work[1] on EDEL pulsed power systems by Spectra Technology, Inc. (formerly Math Sciences Northwest), the present study invested minimal effort on defining the details of the pulsed power system. The pulsed power requirements are summarized in Table 6.5.3-1. These are comparable to the earlier design developed by Spectra Technology, Inc.

Table 6.5.3-1 Pulsed Power Requirements for EDEL

Parameter	Discharge	E-Beam
Aperture, A (cm)	44 x 44	44 x 200
Length, L (cm)	200	
Voltage (kV)	200	500
Current Density* (A/cm^2)	60	3
Total Current (kA)	530	38
Impedance (Ω)	1	30
Pulse Duration (ns)	300	300
Energy (kJ)	32	5.7
Inductance** (nH)	60	

* Indicated e-beam current is in gas, 70% diode to gas transmission assumed to find total current.
** Inductance estimated at $\mu_o A/2L$.

The Spectra Technology, Inc. study[1] compared coaxial and triaxial (Blumlein) pulse forming line PFL configurations with mylar, water, and ceramic dielectrics. They selected a coaxial water dielectric PFL based on its self-healing characteristics and demonstrated capability to meet the design requirements. However, they noted that ceramic PFLs were also very attractive because their higher dielectric constants (~1500 as compared to ~80 for water) led to smaller sizes. In addition, ceramic PFLs can be slow charged which reduces the demands on the charging circuitry. Ceramic PFLs were, therefore, selected for the present design study. Development work is required to realize their full potential in the present application but their packaging advantages over water PFLs make them an attractive alternative, especially given the 2030 timescale of this study.

The resulting PFL design configuration is summarized in Table 6.5.3-2. There are 32 discharge PFLs and 2 e-beam PFLs for each beamline group of 16 EDELs. The overall system is, thus, packaged as indicated in Figures 6.3.1-7 and 6.3.1-8. Two discharge PFLs are arranged end-to-end along the side of each EDEL as indicated in

Use or disclosure of data subject to title page restriction

Figure 6.3.1-9. The discharge lasers are driven by two PFLs in parallel to minimize the connection inductance at the laser. The 1.2 m PFLs provide a relatively flat 250 ns pump pulse for the EDELs. A single e-beam PFL is located in the center vacuum chamber of the group driving all eight e-beam electrodes in parallel.

Costs for the laser pulsed power system are estimated based on $5/Joule of delivered energy. Pulsed power efficiencies are assumed to be comparable to those reported by Spectra Technology, Inc. They are summarized in Table 6.5.3-3.

The pulsed power system for the single-beam heavy ion driver is a key development area. Due to the fast recycle timescales (10-20 kHz), the SBL pulsers will likely require field effect transistor (FET) switching networks. FET technology has already been developed for some high voltage applications but not to the scale needed for the present application. LLNL has evaluated such networks in the context of a recirculating ring accelerator and concluded that they hold significant promise. FET modulators can operate at repetition rates approaching 100 kHz, can provide variable pulse widths, and are inherently long lifetime devices.

Table 6.5.3-2 EDEL Ceramic PFL Design Parameters

Parameter	Discharge	E-Beam
Total Energy (kJ)	32	5.7
Dielectric Constant	1500	1500
Breakdown Voltage (kV/cm)	300	300
Line Length (m)	1.2	1.2
Inner Electrode Diameter (cm)	4	4
Outer Electrode Diameter (cm)	18	53
Load Impedance* (Ω)	2	4
Number Per 16 EDEL Group	32	2

* Since e-beam load impedance is higher, two e-beam PFLs can drive the entire group of 16 EDELs for each beamline.

Table 6.5.3-3 Laser Pulsed Power System Efficiency Summary

Parameter	Discharge	E-Beam
HV-DC Power Conversion (%)	94	94
Intermediate Storage (%)	92	92
PFL (%)	90	90
Output Line and Switch (%)	–	92
Load Transfer (%)	–	92
Gas Transfer (Habachi/Foil (%)	–	70
Rise/Fall Time Losses (%)	83	83
Net Pulsed Power Efficiency (%)	65	38

Use or disclosure of data subject to title page restriction

The main issue relative to such switching networks is cost. The pulsed power system cost factor for the SBL is, therefore, increased by a factor of ten above the $10/Joule value used for the MBL. Even with this assumption, the total SBL pulsed power system cost is comparable to that for the MBL because the total energy it must deliver per cycle is reduced by the number of beamlets. Technology development will nevertheless be required to realize this cost goal; however, comparable cost reductions are not unprecedented for advanced semiconductor devices.

System efficiencies for the SBL pulsed power system are comparable to those for the laser system. Power conversion, energy storage, and utilization are budgeted at 71%. Pulse forming and shaping are budgeted at 85% which is slightly lower than the laser system because pulse shape is more critical in an induction linac context.

6.5.3.2 Vacuum Systems - The laser driver system does not require a major vacuum system. Some local vacuum requirements may exist for maintenance purposes. There is a vacuum pumping requirement at both sides of the laser neutron pinhole to prevent beam breakdown in each of the 60 beamlines within the reactor building. This is conceptually illustrated in Figure 6.5.3-1.

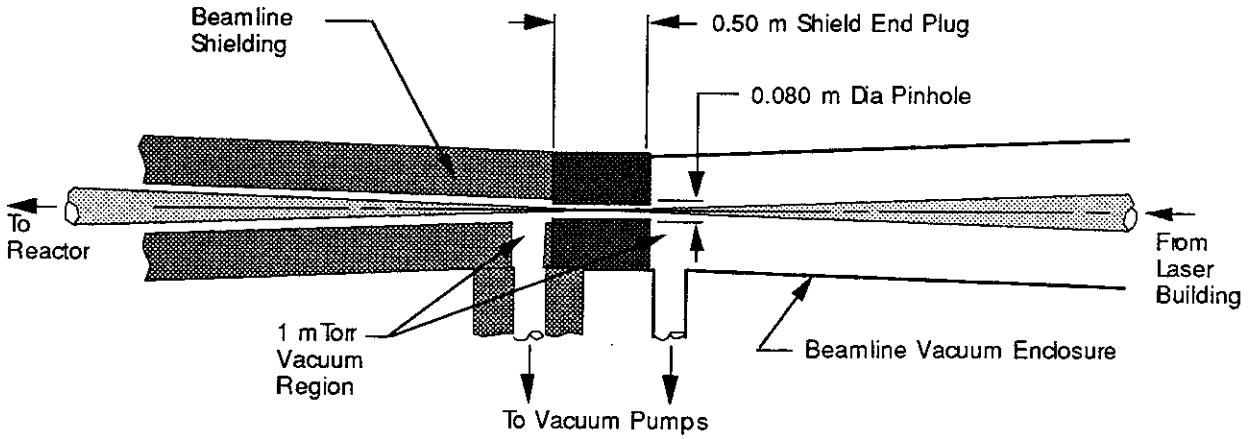

Figure 6.5.3-1. Conceptual Design of Neutron Pinhole to Limit Neutron Propagation into Driver Building (Typical 60 Places)

The heavy ion beam driver requires vacuum pumping in the region of the final ballistic focus of the beams. Figure 6.5.3-2 depicts the general arrangement. An enclosure provides a common vacuum plenum. The ion beam vacuum requirement in this region is 10^{-5} torr. Two cryogenic vacuum pumps are provided to achieve that level of vacuum. If additional pumps are needed for extra capacity or redundancy, they can easily be accommodated. The plenum region extends through the shield and vacuum enclosure to adjoin the back face of the blanket. This arrangement should provide minimal leakage into the plenum. The enclosure is modular which allows easy replacement and access to remove the blanket modules and associated plumbing.

Use or disclosure of data subject to title page restriction

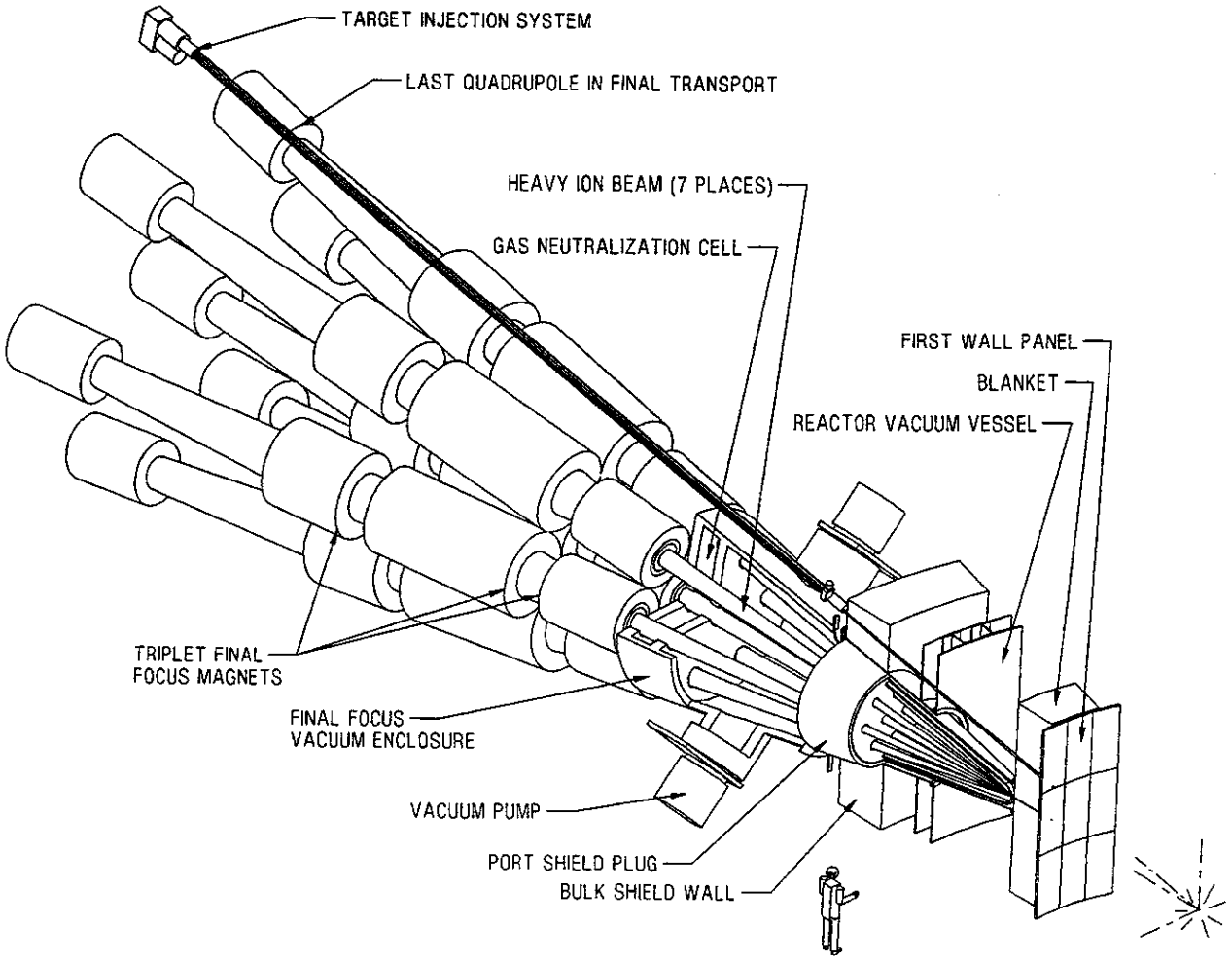

Figure 6.5.3-2. Common Enclosure of Heavy Ion Beams Provides Plenum for Attaining 10^{-5} torr Pressure Level

6.5.3.3 Instrumentation and Control - The general subject of instrumentation and control for systems as large and complicated as the Prometheus-L KrF laser driver and the Prometheus-H heavy ion driver requires an extensive research and development program itself in order to accomplish the enormous task of defining and specifying these important subsystems. For the current study, a brief overview of some of the control characteristics, problems, and issues will be provided. The major purpose of this brief discussion is to initiate an in-depth study of the problem, together with appropriate future development programs, to address the tasks in a timely manner.

Use or disclosure of data
subject to title page restriction

Adequate instrumentation and associated controls required for the two driver systems, Prometheus-L and Prometheus-H, must be based upon careful utilization of the following elements:

(1) Parallel processors
(2) Detailed integration of fast-response sensors with control circuits
(3) Emphasis on sensor and control redundancy
(4) Extensive use of artificial intelligence
(5) Development of expert systems to permit computer control over every aspect of Prometheus driver operation

Significant emphasis needs to be placed on fail-safe sensing and control methodology to insure that the basic safety features designed into the drivers are adequately exploited by the control system.

An example of this sensor and control methodology is the problem presented by the control systems monitoring the pulsed power to the electric-discharge excimer lasers (EDELs). The sensor set required to monitor the performance of each of the 1020 large EDELs would measure performance data. The control system data processing system would then normally record the current performance data and compare it with historical references.

Two general types of sensor and control operation have been identified:

(1) Deterioration and probable failure of an EDEL in normal operation
(2) Sudden failure occurring essentially without prior warning

For the first type of problem, the associated expert system would have pre-programmed the appropriate EDEL control system to recognize a potential failure mode in its early stages and schedule a shutdown for the EDEL prior to any catastrophic breakdown.

The second type of problem also requires implementation of expert system technology, but in this case there must be a pre-programmed shut-down mode to minimize further damage to the EDEL concerned and any other affected subsystem.

In the case of the Prometheus-H heavy ion driver, a comparable example of the operation of sensors and controls would be the placement of heavy ion beam sensors within the ramp and constant gradient sections of the linac for monitoring radiation levels and temperatures of cryogenic elements associated with the superconducting magnets. If significant numbers of ions from the beam were drifting into the cold

Use or disclosure of data
subject to title page restriction

magnet elements, prompt expert system analysis of the problem and a corrective action would have to be taken quickly to prevent possible magnet damage, loss of superconductivity, loss of beam current, and eventual shut down of the reactor.

Since human reflexes are at least six orders of magnitude too slow to deal with rapid developments within the Prometheus drivers, implementation of a state-of-the art instrumentation and control system is critical to permit these drivers to perform at their inherent design capabilities. Thus if a particular driver process can undergo a deterioration occurring on a microsecond time scale, an overall calculation of the length of time for the sensor to make the measurement, transmit the data, alert the control system, and still give the control system sufficient time to exercise a remedy will produce a series of specifications for the required speed of each of these operations.

The principal functions of the driver instrumentation include the following tasks:

(1) Monitor normal driver functions at data rates appropriate for the required response times for possible corrective action.
(2) Monitor abnormal driver functions (associated with catastrophic driver failures); these circuits must have priority over normal monitoring activities.
(3) Provide redundant inputs to detect, quickly sense, and/or control malfunction.

In many cases, the respective sensor must be orders of magnitude faster than the driver process being monitored, if abnormal operation is detected, in order to permit data to be collected, a corrective action taken, and the results analyzed.

The general controls category consists of five elements:

(1) Priority data way for abnormal driver function data.
(2) Normal operation data way for monitoring driver performance and needs for maintenance.
(3) Dedicated parallel processors for abnormal data evaluation, programming with expert system procedures to recommend a particular course of control action, together with high speed data links with the required driver elements involved in the expert system corrective action.
(4) Multilevel, multispeed, multipriority data ways with the central processing unit (CPU) responsible for overall driver control and performance evaluation.
(5) High speed apparatus for invoking control commands generated by CPU analyses.

A simple schematic of the instrumentation and control methodology is illustrated below in Figure 6.5.3-3.

Use or disclosure of data
subject to title page restriction

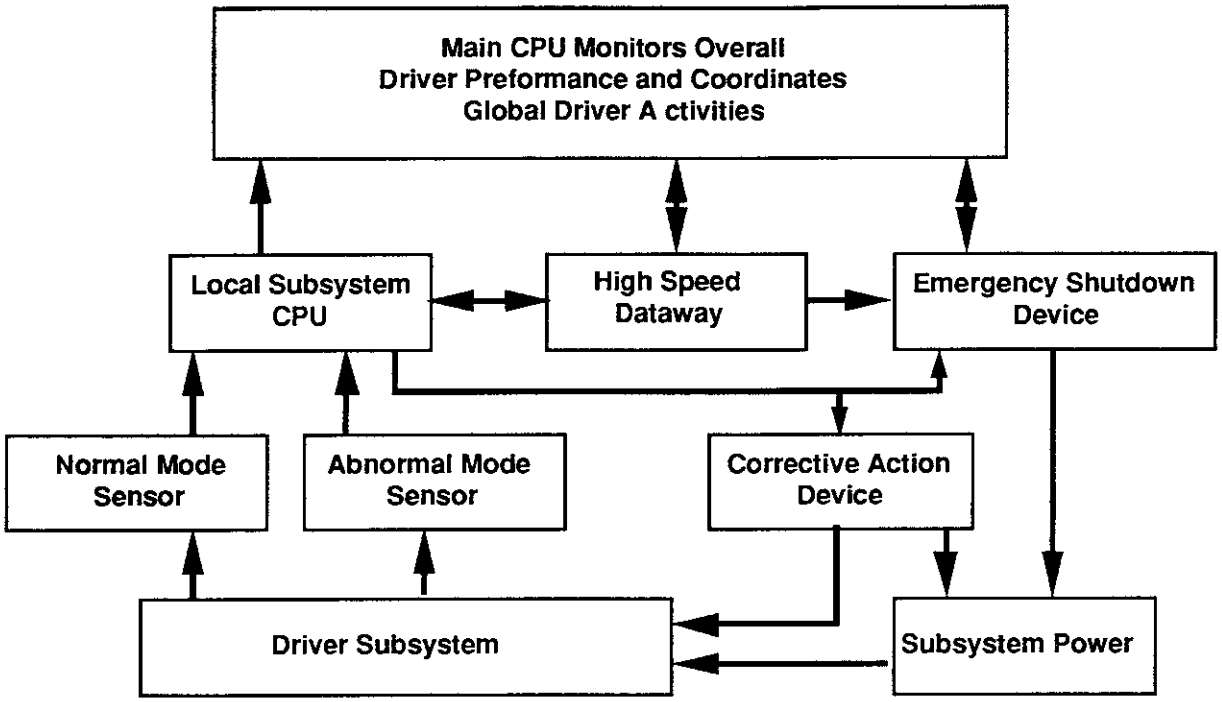

Figure 6.5.3-3 Prometheus Instrumentation and Control Methodology

In general, design, development, and engineering of instrumentation and control systems for large driver systems is a developing field which can draw upon the recent advances made in data processing, reduced instruction set computers, parallel processing, dedicated processors, etc., together with integration of the control methodology into the design of the monitoring sensors themselves. By fixing the technological cutoff for the year ~2030, the Prometheus driver designs have made assumptions regarding significant cost reductions for the instrumentation and control equipment, while giving this crucial subsystem the importance it deserves.

6.5.3.4 Driver Maintenance Equipment. - The maintenance of the components of the two driver systems within the Reactor Building is assumed to be a part of the Reactor Maintenance Equipment. This is partially because of the common location and also because of the commonality of the high radiation environment. However, maintenance of these systems will be briefly discussed. The final optics for the laser driver, the final focus mirrors and the GIMMs are long lived, perhaps the lifetime of the reactor. Nevertheless, these components must be replaceable with a short MTTR as replacement of one of these elements will bring the plant off-line. Dedicated maintenance equipment will service these optical elements.

Maintenance equipment within the Driver Building will also be dedicated equipment specific to handling precision optical elements, gas flow systems, and high power

Use or disclosure of data
subject to title page restriction

devices. These may be mounted off an overhead crane or a track mounted maintenance device. It is envisioned that the optical elements will have sensing devices which will self-diagnose their condition and make appropriate adjustments. Largely, maintenance will be only replacement of failing elements.

The heavy ion beam final focus coils are designed to be life-of-plant with very long MTBF requirements. This is required as a failure would cause the plant to be shutdown until the component is replaced. Again dedicated maintenance machines would replace the individual final focus coils. If the final focus vacuum plenum would need to be removed, some or all of the coil sets would be removed to gain access. For blanket removal, sufficient clearance would be provided to allow removal of the blanket and plenums.

The maintenance equipment within the heavy ion accelerator tunnel will be overhead crane-mounted equipment and rail-mounted manipulators to remove and replace linac components. Several sets of equipment will be required to enable parallel operations at different locations along the linac.

6.5.3.5 Driver Shielding - Care has been taken to provide adequate shielding to protect the personnel and equipment within the Driver Buildings and to provide personnel access to the Reactor Building within 24 hours of shutdown. The thicknesses of the laser and heavy ion beamlines were based upon the effectiveness of the composite bulk shield, the relative size of the beamline openings in the blanket and bulk shield, the distance from the neutron source, and (for the laser configuration) attenuation provided by beamline bends.

The general shielding provided by the laser beamlines is shown in Figure 6.5.3-4. Bulk shielding closely encloses the beamlines from the beam penetration through the bulk shielding wall to the GIMM, the final focusing mirror, and on to the neutron pinhole region. A neutron trap region is provided behind the GIMM to capture the high energy neutrons which penetrate the GIMM. The shielding material is the same B_4C, Pb, SiC, and water composite material which is used in the bulk shielding. The shielding thickness of the conical sections is 25 cm out to the final focus mirror, and thereafter the thickness is 20 cm. A shielding thickness of two meters is provided at both the end of the neutron trap and the end of the beamline at the final focus mirror. The thickness of the shield at the pinhole is 0.8 meters which is shown in Figure 6.5.3-1. Following the neutron pinhole, the beamline will be enclosed with a lightweight enclosure to the vacuum window at the beamline penetration at the reactor building wall.

Use or disclosure of data
subject to title page restriction

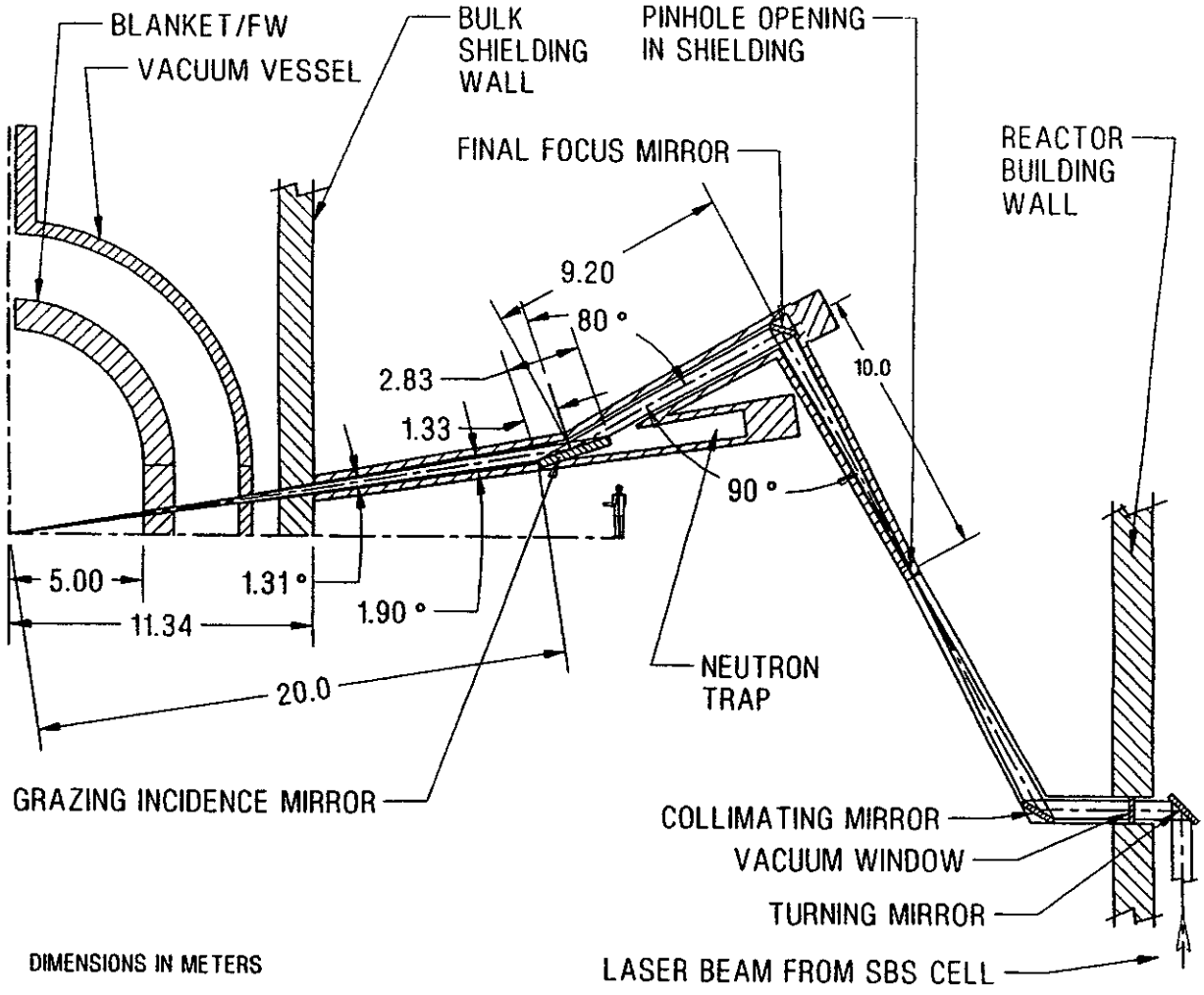

Figure 6.5.3-4. Shielding of Final Laser Optics Contains Radiation Within the Beamline

The beamlines of the heavy ion beams are afforded more protection by the blanket region. This is because the penetrations through the blanket are only 2 cm in diameter. Only the central beamline has direct line of sight through the shield and the blanket to the target as shown in Figure 6.5.3-5. All other beamlines have direct line of sight only to the back of the blanket. A port shield plug is sized to cover all areas except for the beams and the necessary radial clearances. The conical surfaces of the final focus vacuum enclosure is constructed of 15 cm of the composite shield materials. The vacuum pump extensions are 25 cm thick. The two disk-shaped shield elements just in front of the coils serve as shielding as well as a plenum region for the lead vapor neutralizing zone. Each of these disk elements is 25 cm thick to shield the ends of the superconducting coils. The only remaining parts to shield are the inner

Use or disclosure of data
subject to title page restriction

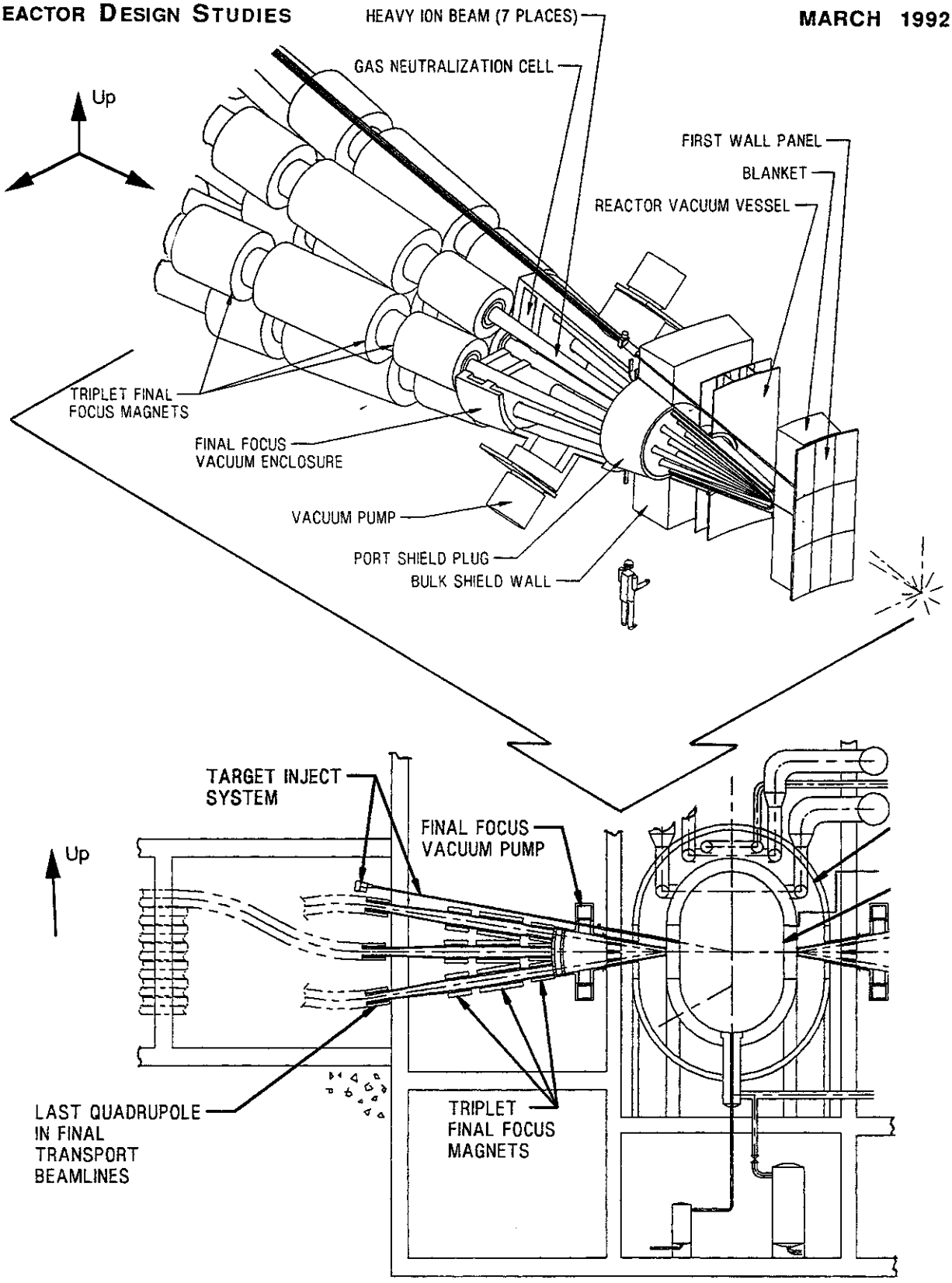

Figure 6.5.3-5. Details of Heavy Ion Beam Final Focus Shielding

Use or disclosure of data
subject to title page restriction

bores of the superconducting coils. The coils have been sized to enable a layer of shielding within the inner bores of the triplet magnets and dipoles. This shielding will extend down the beamline until the damage in the coils and insulators reaches acceptable levels. The lower half of Figure 6.5.3-5 indicates how the beams will be shifted out of plane before exiting the next building boundary.

Reference for 6.5.3

1. Mark Kushner, et al., "New Technologies for KrF Laser Fusion Systems," Interim Report for Los Alamos National Laboratory by Spectra Technology, Inc., Seattle, WA, 1989.

Use or disclosure of data
subject to title page restriction

This page intentionally left blank.

6.6 Vacuum System

Vacuum system requirements vary significantly between the two Prometheus reactor systems. Pressure requirements are significantly lower for the laser driven reactor which, when coupled with the higher mass flow, results in a significantly higher volumetric flow rate. The differences in the vacuum system requirements results in two different designs. These designs are presented separately in the following sections.

6.6.1 Laser Driven Reactor Vacuum System

6.6.1.1 General Description - The reactor requires both roughing and high vacuum systems. The high vacuum system maintains the reactor cavity pressure at the prescribed levels by pumping non-condensable gases, resulting from the fusion reaction, from unburned fuel and from target debris. The roughing vacuum system provides initial pumping from ambient pressure and serves as a backing system for the high vacuum pumps.

Many previous fusion reactor design studies have selected compound cryogenic pumps for the high vacuum system. Cryogenic pumps were also selected for this design. These pumps are a robust design which can provide adequate reliability in the power plant. Ten cryogenic pumps are located on each vacuum manifold. One vacuum manifold is attached to each of the three vacuum ports, providing a total of 30 cryogenic pumps for the high vacuum system. Each cryogenic pump has an isolation valve between it and the pump manifold to allow regeneration without affecting reactor operation.

The rough vacuum system consists of single stage roots blowers with single stage rotary vane backing pumps. A rough vacuum module is dedicated to each of the three ports. Each module consist of a roots blower backed by two rotary vane pumps. Inclusion of the roots blower in the rough vacuum system modules provides additional pumping speed and reductes oil migration at pressures near high vacuum cross-over. All rough vacuum system components are currently commercially available products with proven reliability.

Three vacuum system ports are used to evacuate the cavity and maintain high vacuum during reactor operation. Penetrations are provided in the lead shield wall for vacuum pumping and the ports are attached to the vessel walls behind these openings. The entrance to the vacuum ports are covered with high efficiency, H-type cold traps which preclude transmission of lead vapor into the pumping system during reactor operation.

Use or disclosure of data
subject to title page restriction

6.6.1.2 System Design - Reactor exhaust mass flow rates are stated in Table 6.6-1. Vacuum system volume flow rate at 800 K, the required reactor pressure, and vacuum system design parameters are also provided in Table 6.6-1.

Table 6.6-1
Laser Driven Reactor Vacuum System Design Requirements

Reactor Pressure Requirement:	3×10^{-3} torr
Mean Exhaust Gas Temperature:	800 Kelvin

REACTOR NON-CONDENSABLE GAS EXHAUST

	Mass Flow Rate	Volume Flow Rate
Hydrogen (total–all forms)	28.0 mg/sec	262,000 liters/sec
Tritium	12.24	67,800 liters/sec
Deuterium	8.16	67,800 liters/sec
Hydrogen	7.6	126,400 liters/sec
Helium	6.70 mg/sec	27,900 liters/sec
TOTAL	34.7 mg/sec	289,900 liter/sec

The lead vapor trap at the entrance to the vacuum system ports insures that exhaust gas temperatures do not exceed 800 K. The vacuum design does not take advantage of reduction in mean gas temperature between the lead vapor traps and the pumps. Temperature reduction will be required in the vacuum ducts to optimize cryogenic pump efficiency. Since thermal analyses were not performed for this portion of the study, a "conservative case" vacuum system design is presented. The perfect gas constant is utilized to convert from mass flow rate to volume flow, making the volume flow rate a direct function of the absolute temperature of the pumped gas. Conductance of the vacuum ducts is proportional to the square root of the absolute temperature of the pumped gas. Thus, the reader can appreciate the dependence of the vacuum system design on pumped gas temperature.

The arrangement of the vacuum system components and the design of the ducts provides two large volumes in each port. The first volume is located between the lead shield and the vacuum vessel wall. The second volume is the vacuum pump manifold. Both volumes were considered large enough to randomize the gas flow and were analyzed by the methods presented by D. J. Santeler.[1]

Several parametric studies were performed during the design process. These studies included pumping speed as a function of pump diameter, the number of vacuum ports

Use or disclosure of data subject to title page restriction

required as a function of port diameter, the number of pumps required as a function of number and size of ports, and pump hydrogen capacity as a function of diameter. Several iterations of the parametric studies were performed during the course of the vacuum system design. Multiple iterations insured that, as the design progressed, all previous decisions were included in the analyses. The last iteration of each parametric study is presented in this report. The parametric analyses presented in the following paragraphs were used to design the vacuum system.

Currently available cryogenic pump vendor data for hydrogen pumping speed was used to determine the effect of pump size on pumping speed. A plot of this data with a least squares curve fit is presented in Figure 6.6-1. The data, although not smooth due to step changes in pump design, was deemed adequate to conclude the relationship between pump size and pumping speed. The data curve demonstrates that significant increases in pumping speed may be obtained by increases in pump diameter. The least squares fit was considered acceptable to extend hydrogen pumping speed data to pumps of two meters diameter. Two-meter cryogenic pumps were selected for the high vacuum system. The curve fit projects a hydrogen pumping speed of 158,500 liters per second for two-meter diameter cryogenic pumps. A hydrogen pumping speed of 150,000 liters per second was used for the analyses. Additional increases in hydrogen and helium pumping speed may be obtained by optimizing the design for these gas species but this was not included in this study.

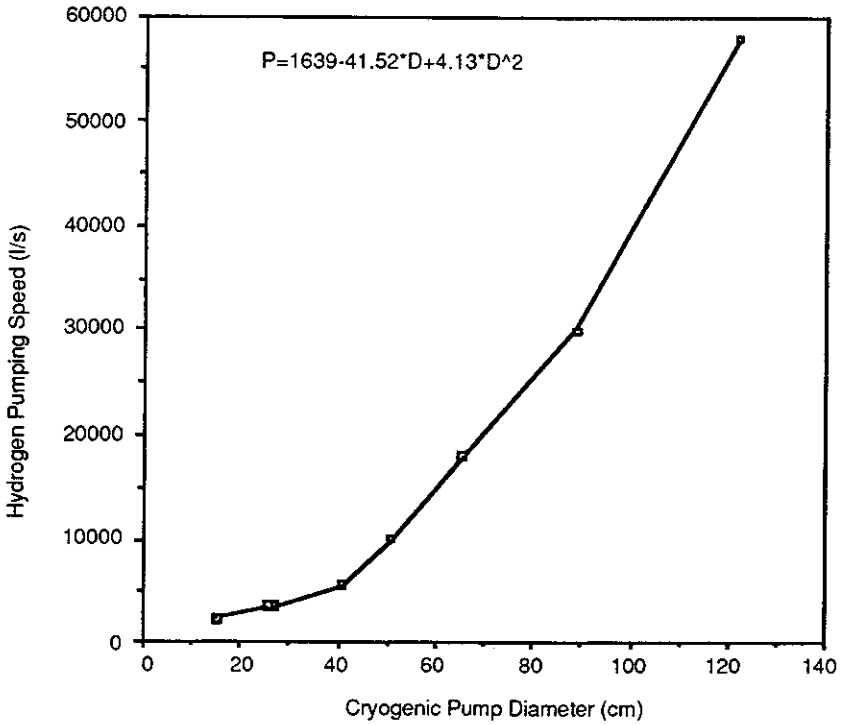

Figure 6.6-1. Hydrogen Pumping Speed Vs. Pump Diameter

Use or disclosure of data
subject to title page restriction

The minimum number of ports required to provide adequate conductance for the specified reactor exhaust gas flow is a function of port diameter. This is shown by the equations utilized to calculate conductance as well as by the curve presented in Figure 6.6-2. Previous reactor design studies have utilized small ports or have coupled the vacuum system to the laser beam ports. The parametric analysis performed for this study indicated that maximizing port diameter will decrease the number of vacuum ports required. Port sizes larger than two meters in diameter were deemed impractical due to spatial constraints. Three 2-meter diameter vacuum ports were selected for the design.

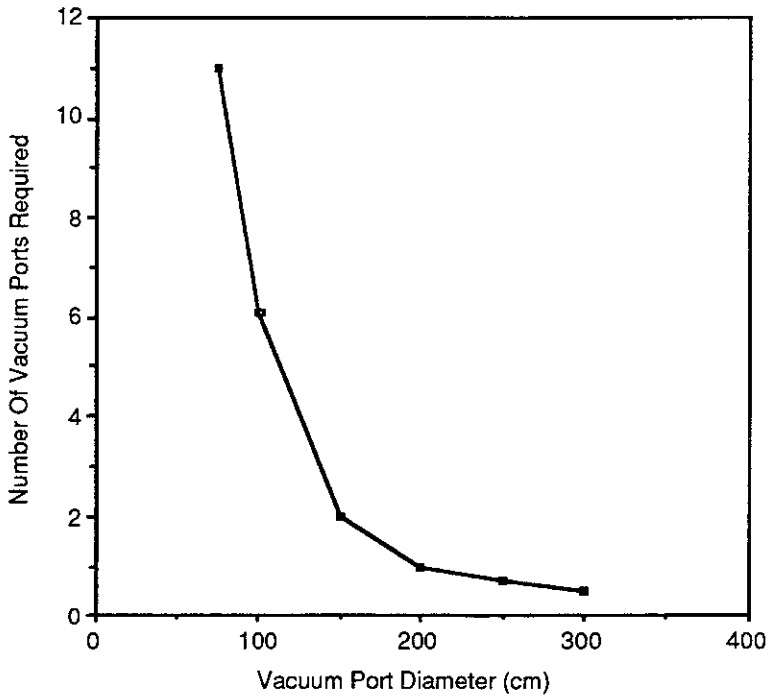

Figure 6.6-2. Vacuum Ports Required

The number of active cryogenic pumps required to obtain sufficient pumping speed for the specified reactor pressure, gas temperature, and gas flow rate is a function of the number and size of the high vacuum ports. Several previous studies have utilized one pump per vacuum port. The parametric study performed for this design indicated that manifolding several pumps on a large diameter pump port results in a reduction of the number of pumps required for the system. The results are shown in Figure 6.6-3. The shape of the curves produced in this parametric study confirmed the decision to choose three 2-meter diameter vacuum ports. The calculations and curves also

Use or disclosure of data
subject to title page restriction

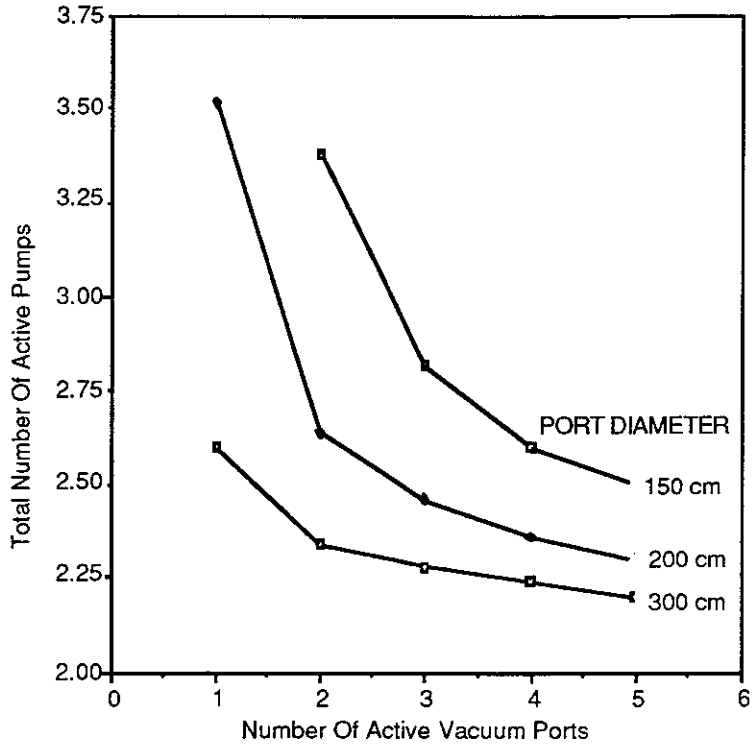

Figure 6.6-3. Total Active Cryogenic Pump Required Vs. Number of Vacuum Ports

demonstrate the requirement for a minimum of three active pumps during reactor operation. Hydrogen pumping speed and hydrogen pump capacity are the driving requirements. The total number of cryogenic pumps is, however, based on the hydrogen capacity of the cryogenic pumps.

Hydrogen, in various isotopes, is the primary gas species pumped during the reactor operation. A parametric study of cryogenic pump hydrogen capacity was performed. Vendor hydrogen capacity for commercially available cryogenic pumps was used to determine the effect of pump size on hydrogen capacity. A plot of this data with a least squares curve fit is presented in Figure 6.6-4. Extending the curve to pumps which are two meters in diameter indicates a hydrogen pump capacity of approximately 285 standard liters (24 grams). The following linear equation was utilized to determine the number of active cryogenic pumps and the time period before pump regeneration is required:

$T = C * N / m$ where: T = time period between regenerations
m = hydrogen mass flow rate (total)
N = number of active cryogenic pumps

Use or disclosure of data subject to title page restriction

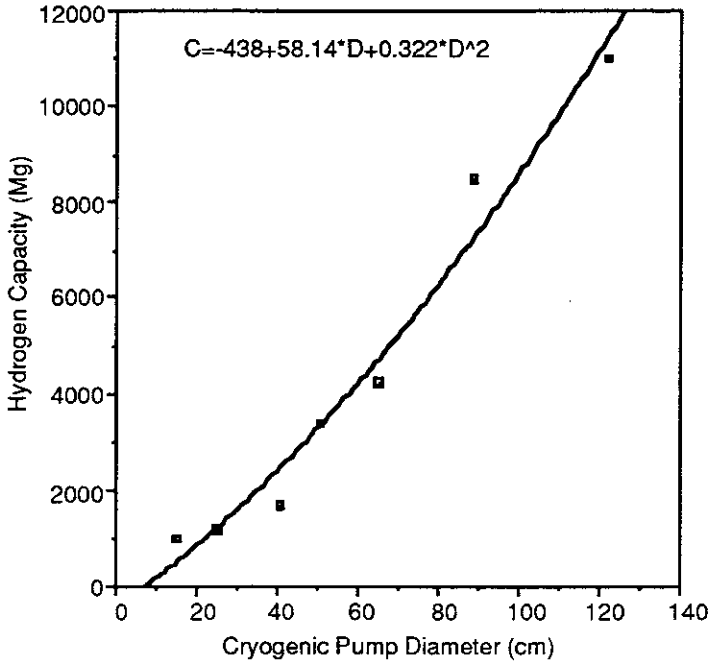

Figure 6.6-4. Cryopump Hydrogen Capacity Vs. Pump Diameter

This equation and the information presented in Table 6.6-1 was utilized to determine that a total of 12 active cryogenic pumps should be utilized. This will provide an active pumping time of approximately three hours and result in a total of approximately 132 grams of tritium and 88 grams of deuterium in the pumps at the beginning of regeneration. A total of 30 cryogenic pumps are specified for this design. This number will allow one active set, one set in regeneration, and an additional six pumps which may be valved into the system to compensate for the reduction in pumping speed of the active pumps as they approach capacity. The additional pumps also provide some margin for pump failures. The laser-driven reactor vacuum manifold arrangement is shown in Figure 6.6-5.

Significant increases in hydrogen pump capacity are probable for the tenth-in-kind reactor. Increases in hydrogen capacity could be achieved by optimizing the design for pumping of hydrogen at the expense of other species. This would extend active pumping periods for the pumps and result in pump regenerations on a once-per-eight-hour basis. This may be advantageous for the vacuum system operation but has consequences for the fuel processing system and tritium/deuterium inventory.

Use or disclosure of data
subject to title page restriction

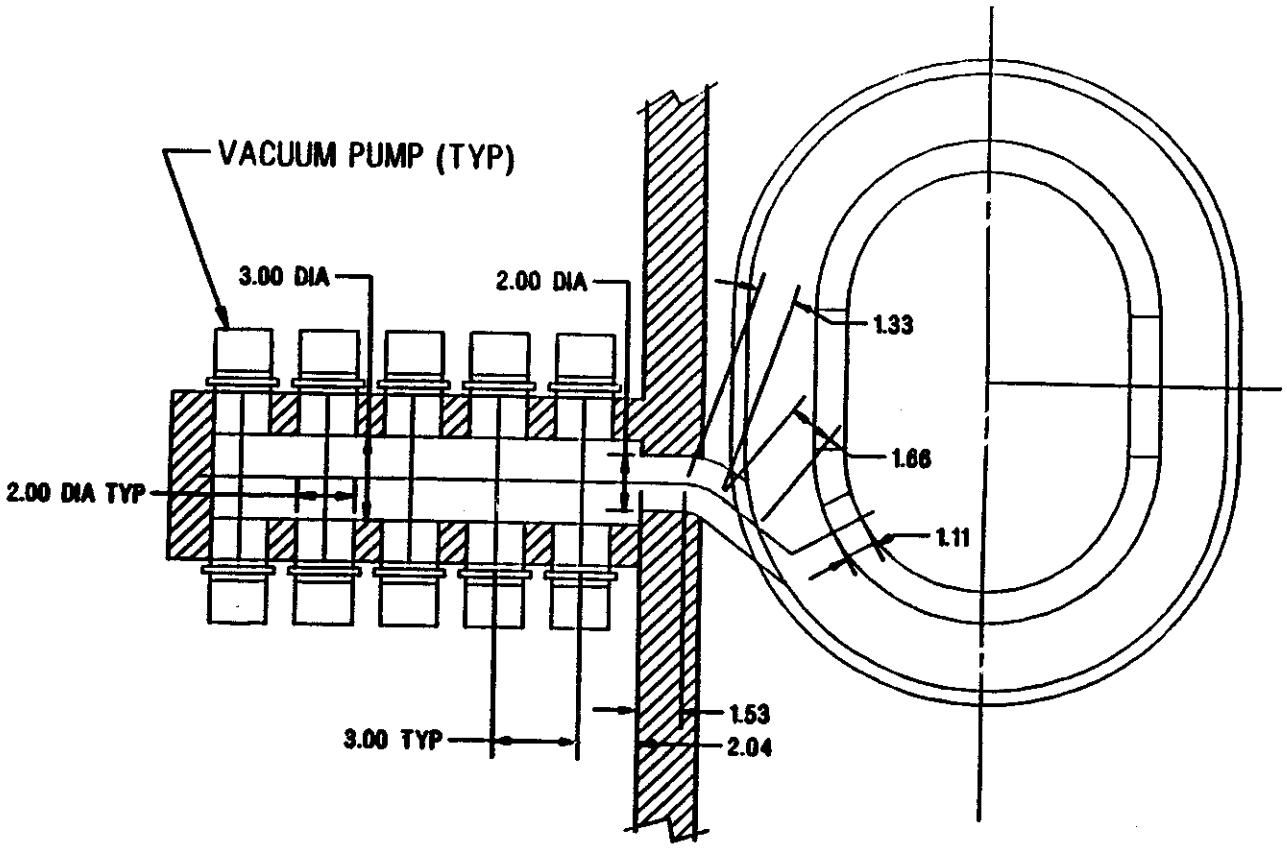

Figure 6.6-5. Laser-Driven Reactor Vacuum Manifold System Arrangement

6.6.2 Heavy Ion-Driven Reactor Vacuum System

6.6.2.1 General Description - This reactor requires a vacuum system capable of maintaining the reactor cavity pressure at the prescribed levels by pumping non-condensable gases, resulting from the fusion reaction, from unburned fuel and from target debris. The vacuum system consists of a set of single stage roots blowers with single stage rotary vane backing pumps. Three vacuum modules is dedicated to each of the four ports. Each module consists of a roots blower backed by two rotary vane pumps. The roots blower provides additional pumping speed and reductions in oil migration during the roughing operation. In addition, the roots blower is capable of maintaining the vacuum required during reactor operation. All vacuum system components are currently commercially available products with proven reliability.

Three vacuum system ports will be used to evacuate the cavity and maintain high vacuum during reactor operation. Penetrations are provided in the lead shield wall for

Use or disclosure of data
subject to title page restriction

vacuum pumping and the ports are attached to the vessel walls behind these openings. The entrance to the vacuum ports are covered with high efficiency, H-type cold traps which preclude transmission of lead vapor into the pumping system during reactor operation.

6.6.2.2 System Design - Reactor exhaust mass flow rates are stated in Table 6.6-2. Vacuum system volume flow rate at 800 K, the required reactor pressure, and vacuum system design parameters are also provided in Table 6.6-2. The increased hydrogen exhaust flow is due to the mass of the indirect drive target radiation case and energy convertor plugs.

The lead vapor trap at the entrance to the vacuum system ports insures that exhaust gas temperatures do not exceed 800 K. Like the Laser-Driven Vacuum System design, this design does not take advantage of reduction in mean gas temperature between the lead vapor traps and the pumps. Temperature reduction will be required in the vacuum ducts to preclude over temperature conditions in the roots pumps. However, since thermal analyses were not performed for this study, a "conservative case" vacuum system design is presented. The perfect gas constant is utilized to convert from mass flow rate to volume flow, making the volume flow rate a direct function of the absolute temperature of the pumped gas. Conductance of the vacuum ducts is proportional to the square root of the absolute temperature of the pumped gas.

Table 6.6-2
Heavy Ion Driven Reactor Vacuum System Requirements

Reactor Pressure Requirement: 1×10^{-1} torr
Mean Exhaust Gas Temperature: 800 Kelvin

REACTOR NON-CONDENSABLE GAS EXHAUST

	Mass Flow Rate	Volume Flow Rate
Hydrogen (total–all forms)	104.6 mg/sec	47,308 liters/sec
Helium	6.0 mg/sec	748 liters/sec
TOTAL	110.6 mg/sec	48,056 liter/sec

The arrangement of the vacuum system components and the design of the system ducting provides two large volumes in each port, similar to the Laser-Fired Reactor Vacuum System. Again, the first volume is located between the lead shield and the vacuum vessel wall while the second volume is the vacuum pump manifold. The methods presented by D. J. Santeler[1] were again utilized for the analyses.

Use or disclosure of data
subject to title page restriction

Parametric studies, similar to those performed for the Laser-Fired Reactor Vacuum System, were performed during the design process. The studies were more limited in scope due to the higher reactor chamber pressure and only included the number of vacuum ports required as a function of port diameter and the number of pumps required as a function of number and size of ports. Iterations in the studies were minimized by the limited effect of these parameters due to the higher reactor pressure. The final design is a result of the parametrics; however, the parametric curves are not presented.

Vendor data for currently available roots pumps were used for the basis of system design. System roots pumps with three times the currently available roots pump speed were deemed an achievable advance for support of the reactor. Advances in pump size were required only in response to a desire for space savings and for probable maintenance advantages. The system could be reconfigured for currently available roots pumps with minimal alterations to the design presented herein.

Analyses were performed to determine an optimum number and size for the vacuum ports required to provide adequate conductance for the specified reactor exhaust gas flow rates. The higher operating pressure for this reactor design allows a significant reduction in the size of the vacuum ducts. Port sizes larger than one meter in diameter are not warranted since increases in effective pumping speed are marginal for significant increases in the port diameter. Four 1-meter diameter vacuum ports were selected for the design. The general manifold arrangements for the heavy ion-driven reactor is shown in Figure 6.6-6.

The number of roots pumps required to obtain sufficient pumping speed for the specified reactor pressure, gas temperature, and gas flow rate is a function of the number and size of the vacuum ports. The parametric study performed for this design confirmed the conclusion of the Laser-Fired Reactor Vacuum System and indicated that manifolding several pumps on a large diameter pump port results in a reduction of the number of pumps required for the system. The calculations showed that a minimum of eight active roots pumps are required during reactor operation. Hydrogen is the main component of the reactor exhaust and effective hydrogen pumping speed is the driving requirement. A total of twelve 9,500 liter/sec roots pumps, three per reactor vacuum port, are specified for the design.

Use or disclosure of data
subject to title page restriction

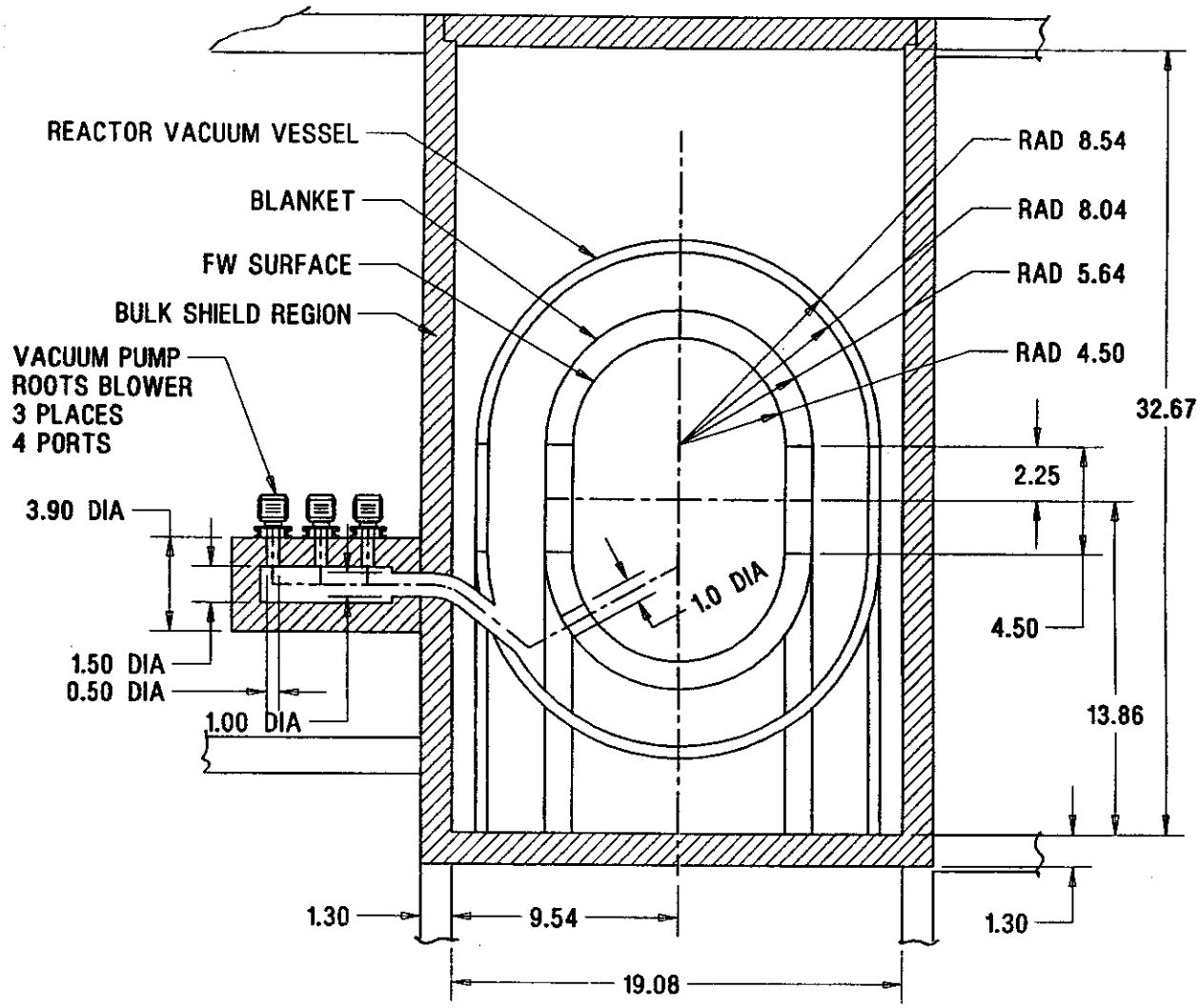

Figure 6.6-6. Heavy Ion Reactor Vacuum Manifold Systems Arrangement

Reference 6.6

1. D. J. Santeler, Journal of Vacuum Science and Technology, Vol. 4, No. 3, May/June 1986

Use or disclosure of data
subject to title page restriction

6.7 Fuel Processing Systems (FPS)

6.7.1 Basic Requirements and Functions - The basic function of the Fuel Processing Systems (FPS) is to manage and process the tritium in various fuel-related systems to enable recovery and recycling of tritium as a fuel component in a safe and reliable manner. The FPS arrangement is shown in Figure 6.7.1-1. Flows and compositions of various streams in the FPS are defined in Table 6.7.1-1 for the laser or L-alternative. A similar table could be constructed for the Heavy Ion Beam or H-alternative. The main functions of the systems are also defined in Table 6.7.1-2.

6.7.2 Technology Options - Fuel processing technology has been developing rapidly over the past years with the result that new and better process options have become available at least every five years. It is anticipated that by the time an IFE type machine is built, Fuel Processing options will have improved through several generations. The present technologies proposed for this study have already reached very low tritium inventories and consequently no major improvement in inventory may be expected regardless of the eventual process selected. Table 6.7.1-2 indicates the services provided by the FPS and the proposed options considered to be optimal for each of the diverse tasks.

6.7.3 Selection of Reference Process Options - Development Trends

Isotope Separation - Although many technologies such as Thermal Diffusion[1] and Gas Chromatography are being developed for Isotope Separation, Cryogenic Distillation (CD) has been successfully demonstrated at a larger and more complex scale than that required for Prometheus. With the burn fraction in the 30% region and with the elimination of the need for producing purified deuterium streams, the overall tritium inventory has been lowered to the 48 g and 68 g range for the L and H alternatives respectively. Recent CD technology developed at Ontario Hydro has resulted in a five fold decrease in the tritium inventory for the small final product columns where most of the tritium inventory resides. Although intensive development for extending these results to large IFE applications is still not complete, it is highly probable that this will be successful. In such a case, the last column inventory of 17 and 28 g for the L and H option could be reduced to 5 and 8 g, respectively. The overall ISS inventory could then be in the 36 and 47 g for the L or H option, respectively.

Chamber Exhaust Purification (EP) - A number of options are being developed for this purpose.[2,3,4,5] Cryogenic adsorption on molecular sieve beds is the most viable competitor to the proposed permeator-based purification system. Permeation is a continuous process as compared to adsorption, which must be operated batch-wise. Thus, permeation-based technologies are considered less complex, more reliable, and have lower tritium inventory. Depending on the desired tritium recovery, permeation systems could require relatively large vacuum pumps. Present designs

Use or disclosure of data
subject to title page restriction

For specification of streams, see Table 6.7.1-1 for L option.

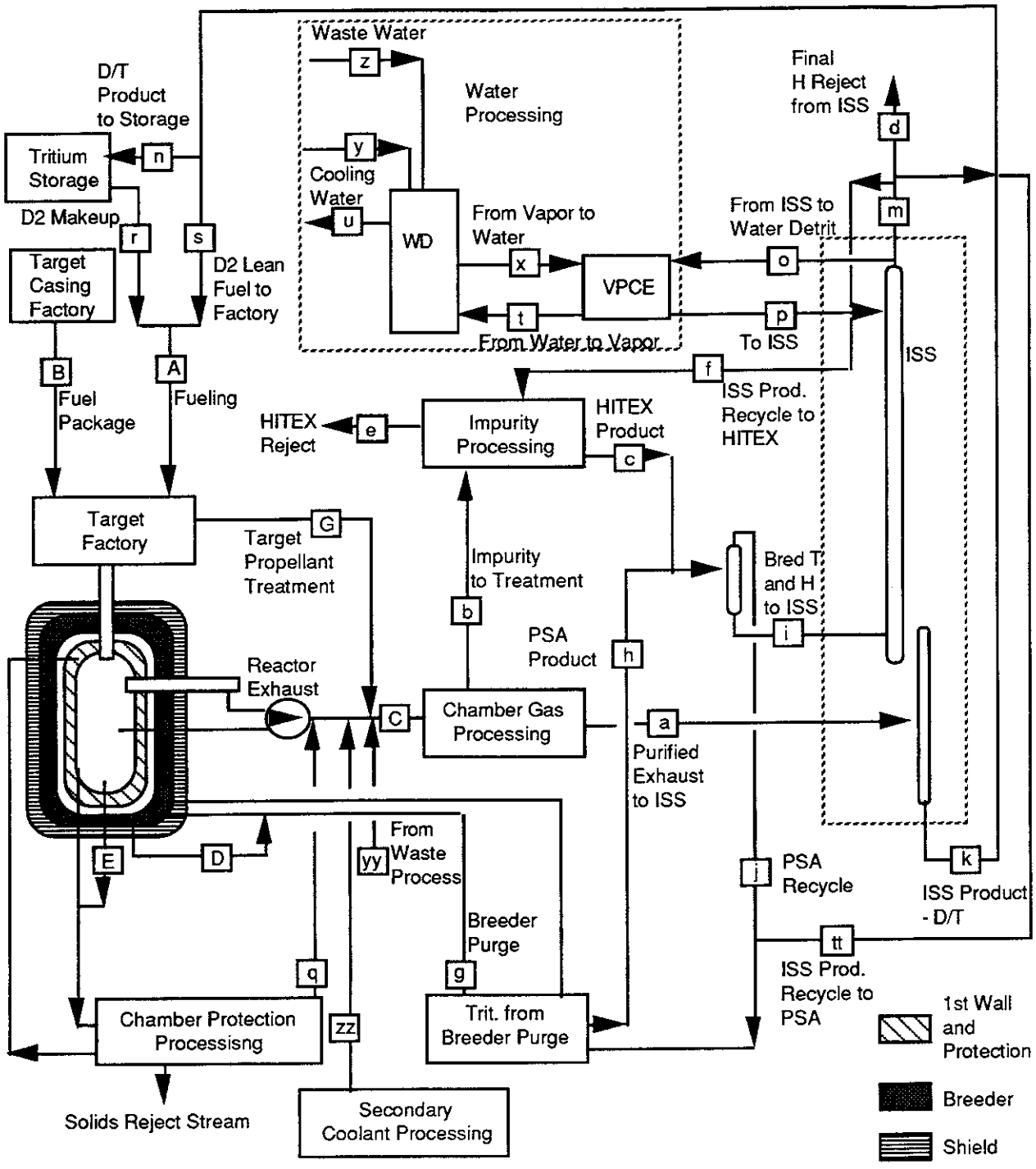

Figure 6.7.1-1. Fuel Processing Systems Arrangement

Use or disclosure of data
subject to title page restriction

Table 6.7.1-1 FPS Design Data - L - Laser Option - Stream Identification Is Consistent with Figure 6.7.1-1

		Units			Units
Fusion Power	2807.00	[MWf]	Fuel Propellant	0.00	[mol/mol]
Max. T in Coolant	1.00	[Ci/kg]	PSA H addition	5.00	[H2/HT]
T rel. -chronic	10.00	[Ci/day]	PSA H extraction	0.52	fraction
Breeding Ratio	1.20	fraction	HiTEX H addition	80.00	[H2/b]
Burn-up Fraction	0.29	fraction	Pd Perm. Sep. fact	3.00	[out/inp]
H2 in Target Fuel	0.66	[mol/mol]	Propellant	0.00	[mol/mol]
H2 in Target Case	0.00	[mol/mol]	H2 in breeder purge	0.20	[%]
			H/T in Br. purge	20.00	ratio

Stream	Name	[mol/h]	H	D	T	He	CH4	NH3	CO2,Q2O
A	Fueling	20.54	2.00e-03	4.99e-01	4.99e-01				CO,N,O,Ar
I	H from Casing	0.00	1.00e+00						
B	H Total Added	13.56	1.00e+00						
G	Propellant	0.00	0.00	1.00e+00					
C	Chamber Exhaust	34.10	3.99e-01	2.13e-01	2.13e-01	1.75e-01	1.12e-02	8.00e-04	4.00e-03
D	Breeder T prod.	3.57			1.00e+00				
a	Purified Exhaust	28.15	4.83e-01	2.58e-01	2.58e-01				
b	Impurity to HITEX	1.64							
c	HITEX Product	130.93	9.93e-01	3.59e-03	3.59e-03				
c+h	CD3 feed	506.21	9.91e-01	9.30e-04	7.99e-03				
e	HITEX Reject	0.55							
f	HITEX Recycle	129.84	1.00e+00						
g	He Blanket Purge	68731.55	1.04e-03	0.00	5.20e-05	9.99e-01	1.00e-06	1.00e-06	8.67e-06
h	PSA prod. to ISS	375.27	9.90e-01	0.00	9.52e-03				
j	PSA Recycle	371.70	1.00e+00						
i	HIT.+PSA to ISS	134.50	9.68e-01	3.59e-03	2.91e-02				
d	ISS Product - H2	144.49	1.00e+00						
l	ISS Product - D2	0.00		1.00e+00					
k	ISS Product - DT	18.16	2.00e-03	4.02e-01	5.98e-01				
n	DT to Storage	1.00		4.02e-01	5.98e-01				
s	DT to Factory	17.16		4.02e-01	5.98e-01				
r	D2 Make-up	3.38	1.00e+00						
o	ISS to Q2O detrit.	90.00							
p	Q2O detrit.to ISS	90.00							
x	from Q2O to VPCE	30.00							
t	from VPCE to Q2O	30.00							
z	Waste Water	1517.80	1.00e+00	1.50e-04	1.55e-07				

Use or disclosure of data
subject to title page restriction

Table 6.7.1-2. Fuel Processing Services and Proposed Technologies for Prometheus IFE

	Fuel Processing Task	Technology Proposed	Tritium Inventory [g] IFE-L	(-H)
1	Isotope Separation	Cryogenic Distillation (CD)	48	(68)
2	Impurities from Fuel	Permeation	4	(8)
3	Tritium from Impurities	High Temp. Isotopic Exchange (HITEX)	0.5	(0.8)
4	Tritium from Breeders	Pressure Swing Adsorption (PSA)	2.8	(2.4)
5	Tritium from Water	Water Distillation + Vapor Phase Catalytic Exchange (VPCE)	0.3	
6	Tritium from Atmospheres	Recombiner + Dryer	25	
7	Fuel Storage	Uranium Getters	700	
8	Tritium from Na Coolant	Yttrium Gettering	0.5	
9	Solid Waste Detritiation	Plasma Discharge Cleaning	0.5	
		Total	781.6	(805.5)

rely on palladium-silver metallic membranes but a number of alternative permeation membranes are under development. For this reason, the permeation technology is selected as the reference process.

Tritium Extraction from Impurity Reject Streams - Fuel purification, as well as purification of other streams, will result in a tritiated impurity stream being produced containing hydrocarbons, ammonia, and other compound molecules. The reference process, High Temperature Isotopic Exchange or HITEX,[4] relies on isotopic exchange at high temperature in the presence of a catalyst, followed by permeation of the tritium enriched hydrogen. The apparent disadvantage of this process is that it dilutes the product with hydrogen. In the optimized design, however, a small distillation column is added to economically correct this deficiency. Alternative technologies such as catalytic cracking are being developed,[4] some designated to be integrated with the permeator.

Tritium Extraction from Solid Ceramic Breeder Blankets - This service requires the extraction of hydrogen, which acts as a tritium dilutent, from a large flow of helium purge gas. Early getter-based designs were superseded by a Thermal Swing Adsorption (TSA) process proposed for ITER.[6] Recently, a Pressure Swing Adsorption (PSA) process[7] has been developed. This promises low tritium inventories and is proposed for this application. Future development is most likely going to focus on membrane-based processes or high velocity adsorption processes. Unfortunately all the sorption-based processes are inherently discontinuous, and their size and tritium inventory is proportional to the length of the sorption/desorption cycle. For example, in one year of development, the cycle duration was reduced from 3-4 hours for the TSA to 10 minutes for the PSA process. The Thermally Coupled Pressure Swing Adsorption (TCPSA) process (see Section 6.7.3.1) is targeted for 20-200 pressure-sorption cycles per minute.

Use or disclosure of data subject to title page restriction

Tritium Recovery from Aqueous Streams - Recent studies[2] compared 16 combinations of processes suitable for extracting tritium from water. A subsequent study[8] made a detailed analysis of the best two alternatives and the Water Distillation coupled to the ISS through a Vapor Phase Catalytic Exchange was chosen as optimal. In the longer term for example, developing a laser-based tritium removal system (see Section 6.7.3.2) could replace the simple, but large and costly water distillation process.

Tritium Recovery from Atmospheres - Present systems are based on a combination of catalytic recombiners and molecular sieve dryers. For detritiation of inert atmospheres, getter-based alternatives have been developed and are in commercial use. For air, the most likely new processes may be based on permeation membranes.[9,10] These will offer continuous operation instead of the inherent batch operating mode associated with sorption processes. Getters which are tolerant to oxygen may also be developed, but will also share the disadvantage of batch operation compared to membrane processes. This would enable optimum hybrid combinations where, for example, the emergency high detritiation rates could be performed by a permeation membrane-based process and the low flow, high purity detritiation could be obtained through a conventional polishing recombiner/dryer.

Fuel Management and Storage - The getter-based hydrogen storage technology could rely on a number of metals namely uranium, zirconium-cobalt and others. Zr-Co getters have been evaluated as alternatives to the supposedly pyrophoric uranium. However, recent air exposure tests for uranium are encouraging and may result in uranium maintaining its status as the process of choice for tritium with best properties for frequent use at high capacity.

Tritium Removal from Na coolant - The use of a double-tube heat transfer system with sodium in the interspace is unique and innovative. Sodium provides a high thermal conductivity bridge between the two concentric heat transfer tubes, resulting in a relatively uninterrupted heat transfer pathway. However, high solubility of hydrogen in sodium can result in unacceptable permeation rates of tritium. A barrier must be provided for interrupting the tritium permeation flux by maintaining the partial pressure of tritium in sodium at sufficiently low level in order to lower the permeation rate to steam to acceptable levels. The low partial pressure is achieved by yttrium gettering. Future development in this area may result in advanced materials, such as silicon carbide or permeation barriers, which are compatible with the heat transfer fluid and which will eliminate the need for tritium extraction from the double-tube interspace.

Solid Waste Detritiation - Solid waste detritiation is well developed due to fission reactor needs and therefore very little development is occurring at present. One notable development is in the area of Plasma Discharge Cleaning which is consistent with the technologies used for vacuum vessels for MFE machines.

Use or disclosure of data subject to title page restriction

6.7.3.1 Thermally Coupled Pressure Swing Adsorption

Breeder Tritium Extraction - The breeder generates tritium which is carried in the breeder purge stream. The portion of the breeder purge gas to be treated (Figure 6.7.3-1) is first cooled countercurrently against the already treated return gas, then dried and cooled. TCPSA separator #1 extracts hydrogen from the breeder purge gas at 90% recovery. This, in comparison with the reference PSA process described in Section 6.7.5 and in comparison with data in Table 6.7.1-1, lowers the purge gas flow to be treated by approximately 40%.

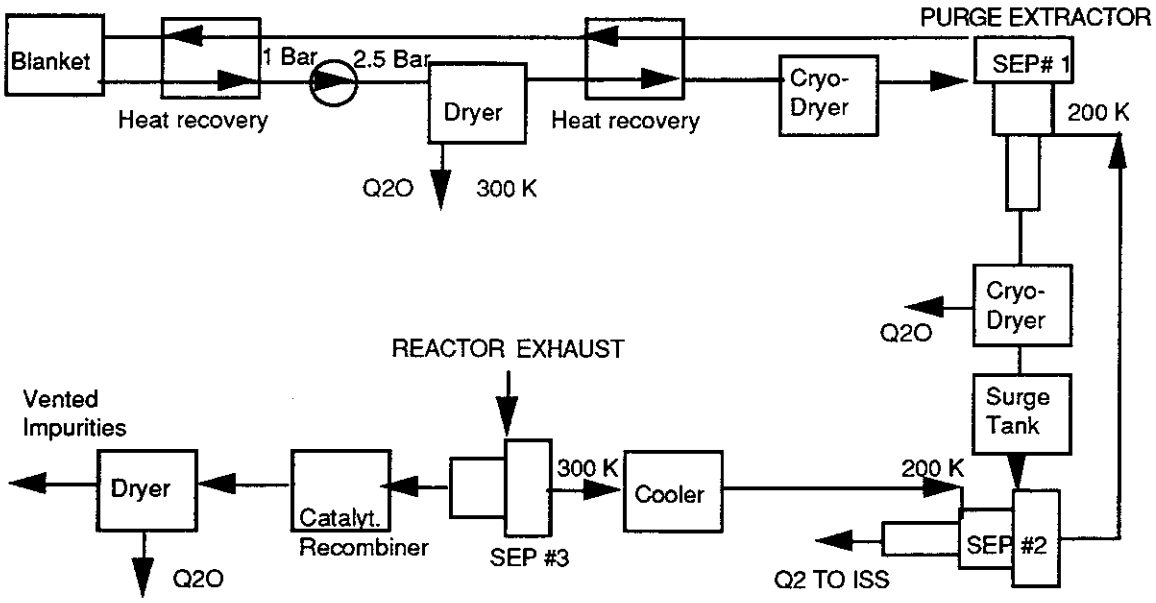

Figure 6.7.3-1. Thermally Coupled Pressure Swing Adsorption (TCPSA) for Fuel Treatment

TCPSA separator #1, by purifying the helium purge recycle flow to the breeder, concentrates the hydrogen isotope mixture to about 50% H,T in helium. Impurities such as nitrogen are concentrated with the hydrogen. TCPSA separator #1 also accepts a recycle stream of dilute hydrogen in helium from downstream processing in separator #2. The purge hydrogen extractor will normally operate at ~200 K for optimal selectivity and working capacity of the adsorbent. The adsorbent may be a hydrophobic zeolite such as silicalite. Hydrophobicity of the adsorbent is expected to be advantageous to minimize the need for periodic shutdown for adsorbent deactivation due to cumulative water uptake, to minimize reactivation due to cumulative water uptake, and also to minimize static tritium inventory with water of hydration. The adsorbent will be supported in a composite laminated structure (channel width ~50 microns) for effective mass transfer and attrition resistance at cycle frequency of 100 RPM.

Use or disclosure of data
subject to title page restriction

Physical parameters of the hermetically-enclosed TCPSA purge hydrogen extractor (separator #1) include internal displacement of 0.7 m^3 and active zeolite adsorbent inventory of 84 kg. Estimated tritium inventory is estimated 0.4 g.

The schematic for TCPSA separator #1 represents multiple, smaller TCPSA machines in parallel. Mechanical elements are electromagnetically excited through the hermetic enclosures of the TCPSA apparatus.

During start-up procedures, the breeder purge hydrogen extractor may be operated with the helium purge at ambient temperature in order to extract air, carbon oxides, and water vapor from the breeder loop.

TCPSA separator #1 is an alternative to a vacuum regenerated PSA system operating at 77 K. The TCPSA system is more energy efficient, mainly due to reduced refrigeration load.

Hydrogen Isotope Purification - TCPSA separator #2 is provided to purify hydrogen isotope streams from separator #1, containing up to 50% helium, before admission to the Isotope Separation System. This unit will achieve final removal of helium from the hydrogen product. The unit can also accept otherwise purified hydrogen isotope streams with helium impurity at different concentrations. As shown in Figure 6.7.3-1, TCPSA separator #2 may be used to remove helium from the reactor exhaust from separator #3, after prior removal of all heavy impurities. Impurities include tritiated water, ammonia and methane, and carbon oxides and nitrogen.

With a similar adsorbent laminate and 100 RPM operating frequency as TCPSA separator #1, TCPSA separator #2 will have a working displacement of 0.05 m^3 and contain up to 15 kg of active zeolite adsorbent. Estimated tritium content is 0.9 g.

The feed gas to TCPSA separators #1 and #2 will have been dried at 200 K for removal of carbon dioxide and water vapor. Any permanent gas impurities such as nitrogen may be accepted in minor amounts by these separators and will be concentrated into the hydrogen product. Larger amounts of permanent gas impurities could be removed by another TCPSA separator (not shown in the figure) operating at about 300 K in cascade with TCPSA separator #2. Residual amounts of permanent gas impurities in the hydrogen product of TCPSA separator #2 may be removed by a palladium diffuser, whose reject may be processed by TCPSA separator #3 to recover tritium bearing hydrogen from the total impurity stream.

Reactor Exhaust Purification - The reactor exhaust contains heavy impurities (more strongly adsorbed than hydrogen) and the light impurity of helium isotopes. TCPSA separator #3 removes the heavy impurities including tritiated compounds and delivers a rich stream of hydrogen isotopes and helium to the hydrogen purification module of

Use or disclosure of data
subject to title page restriction

TCPSA separator #2. The impurity stream containing tritiated compounds must be processed further, either by catalytic oxidation to recover all tritium as water, or by catalytic isotope exchange to concentrate tritium into the reduced phase.

TCPSA separator #3 also uses zeolite adsorbent laminate beds operated at 100 cycles per minute and has a displacement volume of 0.012 m^3 and active zeolite inventory of 2 kg. Estimated tritium inventory is 0.18 g.

6.7.3.2 Laser-Based Hydrogen Isotope Separation - The laser-based detritiation system is based on the isotopically selective multiphoton dissociation of trifluoromethane, CF_3H. At wavelengths around 9 micrometers in the infrared, tritiated trifluoromethane, CF_3T, is a strong absorber of infrared radiation, while the non-tritiated component, CF_3H, is almost transparent. By irradiating mixtures of CF_3H and CF_3T with intense pulses of laser radiation in this wavelength region, it is possible to excite the absorbing CF_3T molecules so that they dissociate as follows:

$$2CF_3T \rightarrow 2TF + C_2F_4$$

Under the right conditions, the above process is 10,000 times more likely than the equivalent dissociation process for CF_3H. Consequently, by this process one can transform a dilute mixture of CF_3T in CF_3H to a concentrated photoproduct (TF/HF) which has a T concentration 10,000 times higher than the original feedstock.

In the conceptual design of a complete water detritiation system based on the laser idea, the separation would be performed in a cyclic three stage process.

The first stage of the process is an exchange unit where the tritiated water feed exchanges hydrogen with the process gas, trifluoromethane. In this step of the process, tritium would pass from the water feed to the trifluoromethane.

The second step of the process is the laser dissociation cell where isotopically selective dissociation of the tritiated component of the trifluoromethane occurs. After passing through this cell, the majority of the tritiated trifluoromethane would be converted to TF and C_2F_4 as described above.

The final step of the process is a chemical separation unit where the TF/HF photoproduct is removed from the trifluoromethane. Following removal of the TF/HF, the detritiated trifluoromethane is then returned to the exchange unit to begin the cycle again.

Over the last few years, a complete conceptual design for a water detritiation system has been developed based on the above cycle, and all the essential process elements have been tested at lab scale.

Use or disclosure of data subject to title page restriction

A schematic diagram of the process is shown in Figure 6.7.3-2. The exchange step of the process is carried out in the exchange liquid regenerator and exchange tower shown on the left hand side of the schematic diagram. In the exchange liquid regenerator, the feed water would be vaporized and contacted with an exchange liquid consisting of water, DMSO, and sodium hydroxide. The exchange liquid would then pass to the exchange tower proper, where it would be contacted with trifluoromethane. This unusual two-step approach to transferring tritium from water to trifluoromethane has been shown to be superior to one step processes.

After leaving the exchange tower, the trifluoromethane is dried and then decompressed and cooled so that it enters the dissociation cell at a temperature of around -70°C and a pressure of around 100 torr. These conditions of temperature and pressure are known to lead to efficient and highly selective dissociation of the tritiated component of the gas.

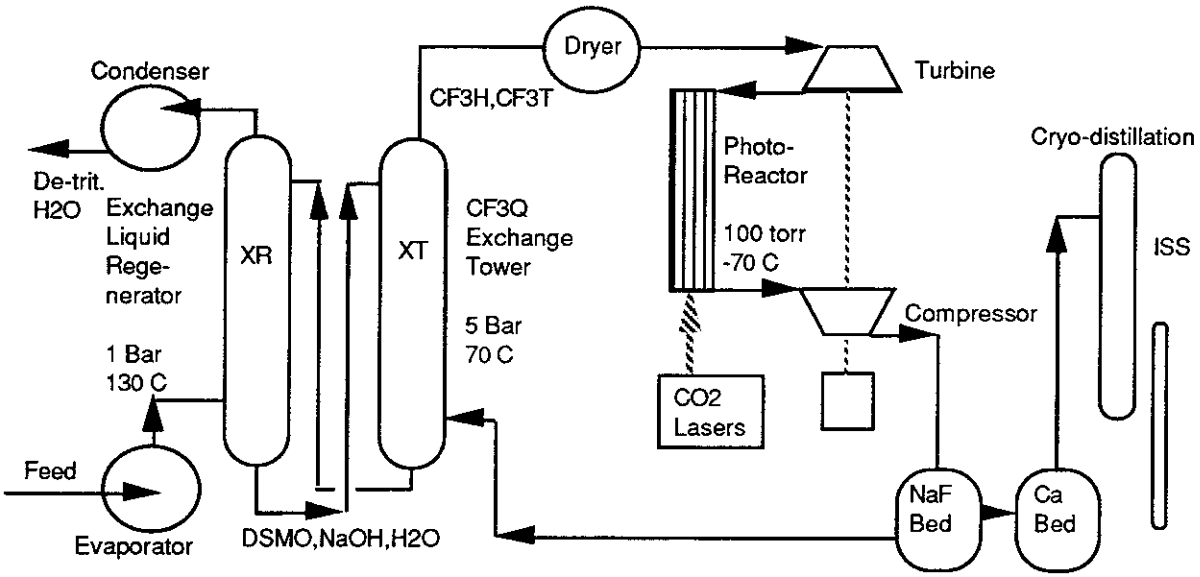

Figure 6.7.3-2. Laser-Based Isotope Separation System

The essential design problem in the dissociation cell is that fluences (laser energies per unit area) in excess of acceptable limits for long life of optical components are required to trigger the dissociation process. Consequently, one must devise a scheme where large volumes of gas can be exposed to high fluences without exposing optical components to unacceptable levels of fluence. A number of solutions to this problem have been proposed, and a selection process to determine the best solution is currently underway. All the proposed solutions rely on waveguiding of the laser radiation to create a large, high fluence region.

The final stage of the process, the separation of the HF/TF photoproduct, is the simplest step of the whole process. It is well known that, when cooled, NaF is a very

Use or disclosure of data
subject to title page restriction

selective absorber of HF/TF, and that this HF/TF can be recovered later by heating the NaF. In a continuous process then, one would have two beds—one cooled and connected in the process loop to absorb the HF/TF from the trifluoromethane stream and one heated and connected to a separate post-processing system. In this post-processing system, the HF/TF evolving from the heated NaF bed would first be converted to an $H_2/HT/T_2$ mixture by passing over a bed of Ca, before entering a small conventional cryogenic distillation column where the final stage of isotopic enrichment would be performed.

6.7.4 Chamber Exhaust Purification (EP) and Impurity Treatment - The use of permeation as the main tool for separating hydrogen from impurities is motivated by the following considerations:

- It is a simple and continuous process
- Has been used on an industrial scale
- Can deliver high purity hydrogen for direct feed into the ISS
- Has very low tritium inventory
- May promote cracking of ammonia[3]
- Produces no waste other than the membrane
- Can be made insensitive to poisoning.

The process has a disadvantage—the membrane can fail suddenly; but research into alternative materials and frequent replacement of the relatively inexpensive membranes will make this the most desirable alternative.

6.7.4.1 Process Description and Control - The process is suitable for a wide range of flows. The nominal mass throughput is determined by the chamber exhaust flow which is 34 and 150 mole/h for the L and H options, respectively. In addition to the 5-6 mol/h of helium, the chamber exhaust gas flow also contains impurities estimated to be in the range of 1-2%. The main constituents are expected to be hydrocarbons, ammonia, CO_2, water vapor, CO, N, O and traces of Ar. A schematic of the proposed process is in Figure 6.7.4-1. It can be seen that the permeator produces a tritiated impurity stream from which tritium must be removed before it is discharged. The process proposed for this application is based on high temperature isotope equilibration in the presence of a catalyst. First, helium may be removed from the chamber exhaust stream. This can be conveniently done to reduce volumetric throughput, but is not absolutely necessary for the process.

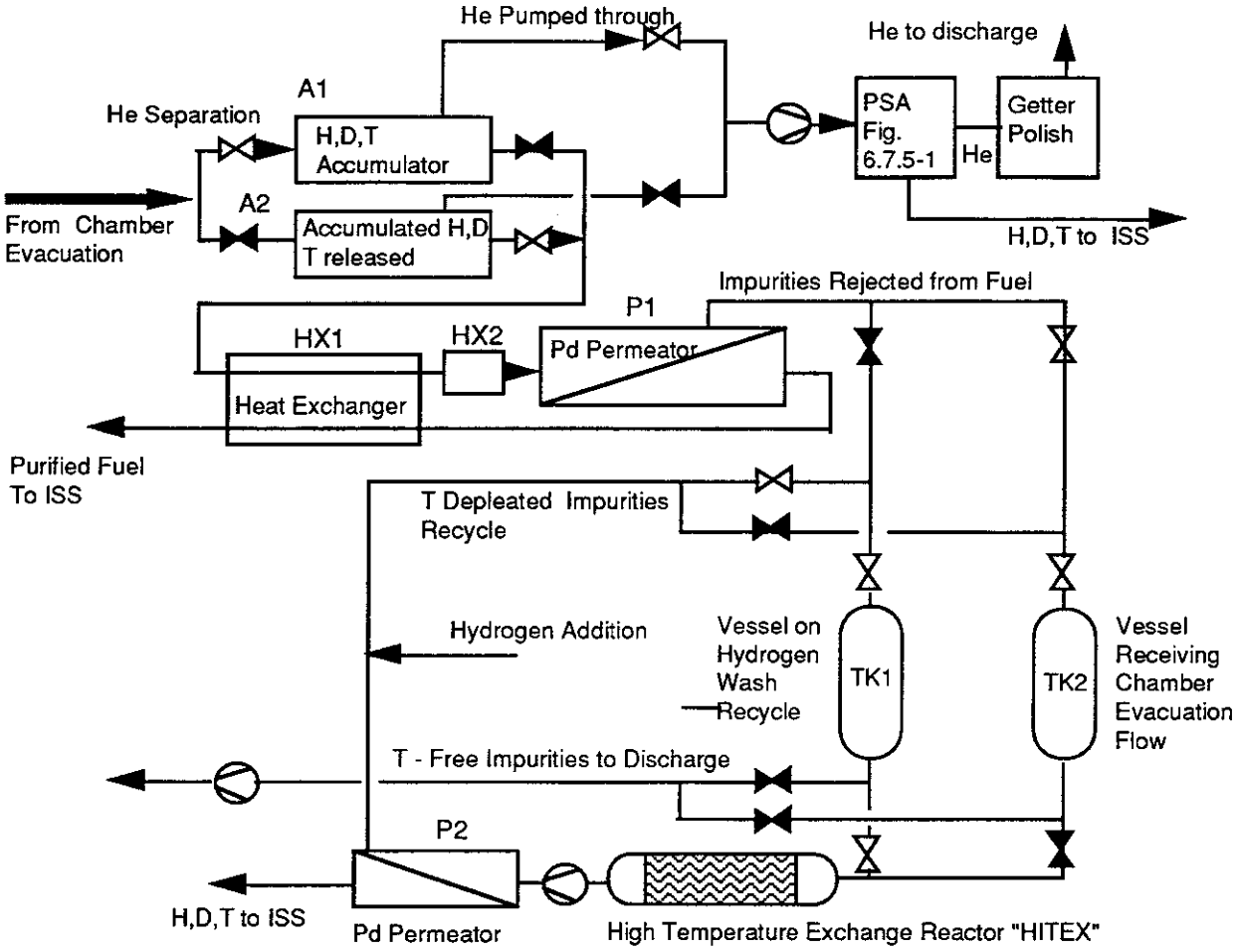

Figure 6.7.4-1. Chamber Exhaust Purification and Impurity Treatment System

The chamber exhaust is pumped through a heat recovery exchanger, HX1, and trim heater, HX2, into the permeator from which the permeate is sent directly into the ISS after heat recovery in HX1. The impurity stream is collected in TK2. In the meantime, the previously filled TK1 operates in a purification mode as follows. Impurities are mixed with hydrogen and pumped through the HITEX reactor where the hydrogens are equilibrated. Tritium in compound molecules is replaced with hydrogen, and free hydrogen (now contaminated with tritium) is separated in the permeator P2 and sent to the ISS. The remaining impurity stream is recirculated through TK1 and new hydrogen is added as required until the tritium level is reduced to below releasable levels. Then the TK1 is pumped out and its function is reversed with TK2.

Use or disclosure of data
subject to title page restriction

The following equipment design data are proposed:

Parameter		Dimension L-Option	Value H-Option
P1 Surface	[m^2]	1	2.5
Hydrogen Pressure P1	[kPa]	100	100
P1 Operating Temperature	[C]	400	400
P2 Surface	[m^2]	2	6
Hydrogen Pressure P2	[kPa]	300	300
P1 Operating Temperature	[C]	400	400
TK1,TK2 Size	[m^3]	10	10
HITEX Volume	[m^3]	0.25	0.5

6.7.5 Tritium Extraction from Breeder Blanket (PSA) - Pressure Swing Adsorption (PSA) is a well established industrial process for separating and purifying industrial gases. For the tritium extraction from breeder blankets, however, the hydrogen dilution (0.2% of H and 0.01% T in He) requires extreme design parameters for the proposed system.

The PSA process has an inherent advantage over a recently proposed Temperature Swing Adsorption (TSA) design because it allows much faster cycling (10 versus 480 minutes) and therefore has correspondingly lower tritium inventory. For this application, the PSA process has reached proof of principle[7] with molecular sieve 5A at 77 K, with pressure cycling from 1-2 MPa during the adsorption cycle, to a rough vacuum during regeneration. Research with potentially better performing adsorbents still continues. A dynamic simulation model has been developed to facilitate system design and optimization. Simulation results indicate that a single-pass hydrogen isotope recovery of 50-80% is achievable but 52% was used for the optimized design. Hydrogen purity of more than 99% is possible to obtain in the stream regenerated from the beds.

6.7.5.1 PSA - Functional and Performance Requirements - In a recirculating system, there is no need for complete hydrogen isotope removal from the He purge stream on each pass through the PSA column. Secondly, the pressure ratio required for enriching the 0.2% hydrogen isotope concentration in the feed to greater than 99% in the product is unusually high (>10^3). Finally, H_2 is added to the column at the beginning of the evacuation cycle in order to displace adsorbed HT, and thus increase the HT partial pressure during column pump-out.

The dynamic simulation of the PSA process for H_2 and He separation was broken down into four distinct steps:

Use or disclosure of data
subject to title page restriction

(1) Initial pressurization of the PSA column from vacuum to the adsorption pressure
(2) Flow of the hydrogen/helium gas mixture through the PSA column
(3) Depressurization and initial pump-out of He
(4) Hydrogen addition and evacuation of the PSA column to recover the HT and H_2 species.

The gas mixture withdrawn from the column during evacuation is greatly enriched in hydrogen isotopes as compared to the feed. The results of the simulation are in Figures 6.7.5-1 and 6.7.5-2.

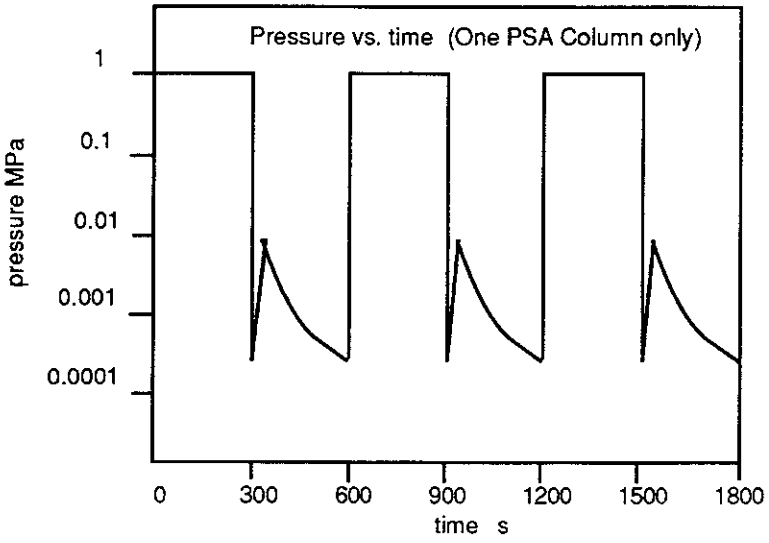

Figure 6.7.5-1. PSA Column Pressure Variation with Time

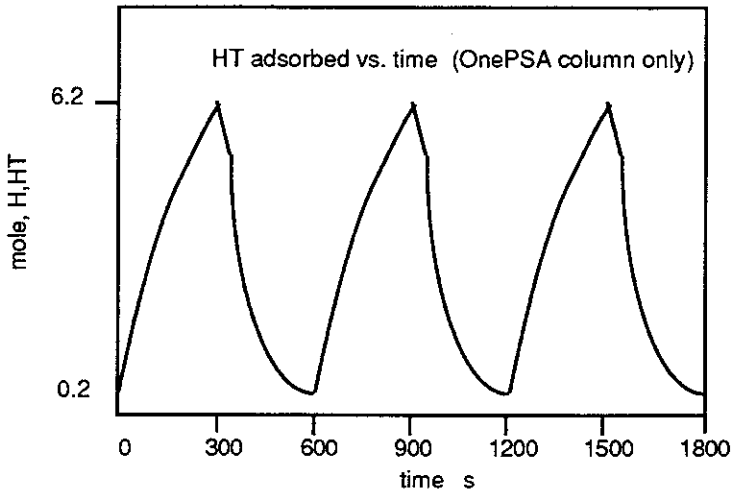

Figure 6.7.5-2. PSA HT Adsorbed as Function of Time

Use or disclosure of data
subject to title page restriction

Figure 6.7.5-1 shows the PSA column pressure variation for the 1 MPa feed pressure. At the start of each evacuation cycle, the initial rapid drop in pressure corresponds to He being removed from the column. The following sharp rise in pressure is due to H_2 addition, and the subsequent slower drop in pressure is due to hydrogen isotope product pump-out. The purpose of H_2 addition at the beginning of the evacuation cycle is to promote the desorption of HT. Without H_2 addition, only a small fraction of the hydrogen isotope desorption occurs at a hydrogen isotope partial pressure above approximately 0.6 kPa. Experimental results suggest that further desorption by vacuum pumping is impractical.

Figure 6.7.5-2 shows Q_2, the quantity HT (mole), adsorbed within the PSA column as a function of time. The rise in Q_2 corresponds to the adsorption phase of the PSA cycle, and the fall corresponds to desorption. The maximum tritium inventory for a 10 minute PSA cycle is less than 0.5 g.

The Prometheus PSA design is greatly simplified by operating it to complete breakthrough. The formation and movement of concentration profiles down the column is of little concern. It is only necessary to ensure that sufficient feed is passed through the column to achieve near saturation of the adsorbent.

6.7.5.2 PSA - Process Description and Control - During PSA column pressurization and feed flow, the feed rate to the column is kept constant (see Figure 6.7.5-3). The purge gas pressure in the breeder is kept under 10 Bar. This is suitable for the PSA sorption process, and consequently a gas circulator is needed only for recirculating the purge flow through the sorption beds. Column pump-out proceeds in three stages:

(1) He Removal – He is much less strongly adsorbed than hydrogen and most of it can be removed before significant desorption of hydrogen isotopes occurs. Therefore, for a short initial evacuation time, the exhaust from the vacuum pump P1 is recycled to the blanket through V2 (with V1 closed). After helium removal, valve V2 is closed and the column is ready for hydrogen isotope pump-out.

(2) H_2 Addition – Pure H_2 is introduced into the column through valve V3 to reach a partial pressure of about 20 kPa. The effect of this is to displace adsorbed HT and increase HT partial pressure during pumpout. The only penalty associated with this procedure is further dilution of the T in H, thus increasing the ISS feed. In the optimized design, this increase is compensated by adding a small pre-enrichment column which reduces the ISS feed from this stream by a factor of 4-5. This CD column would have only 0.57 g of T_2 and reduces the ISS inventory by approximately 5 g.

Use or disclosure of data
subject to title page restriction

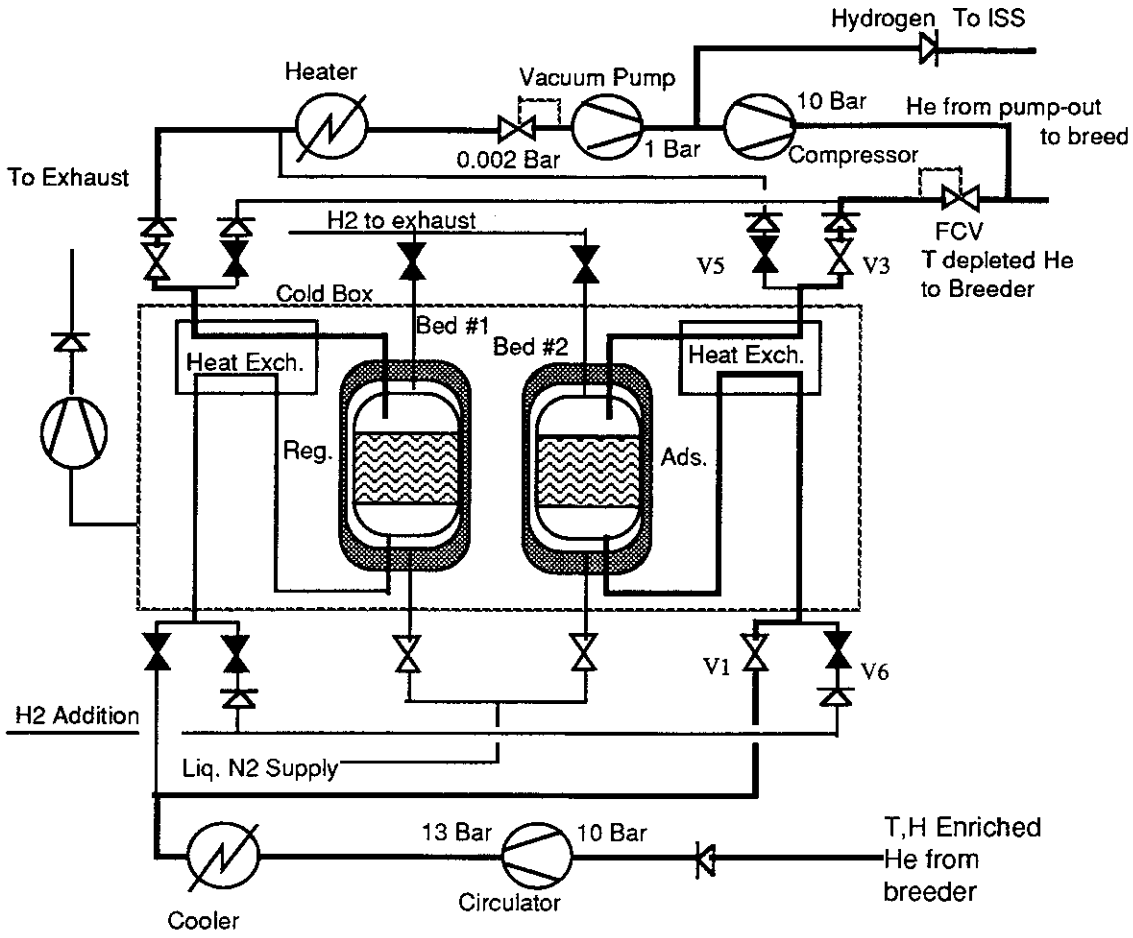

Figure 6.7.5-3. PSA for Tritium Extraction from Breeder

(3) H_2, HT Product Pump-out – Valve V1 is opened and the H_2 and HT contents of the PSA column are pumped out in order to withdraw product and to prepare the column for the next cycle.

The PSA column pump-out time is the same as the pressurization and feed time. For this design, in order to provide continuous processing of feed, two PSA columns are operated simultaneously. The feed flow is to one column while the other column is being evacuated. The flow in the columns is in the same direction during feed and evacuation.

The vacuum pumping requirements can be met by commercially available tritium compatible pumps. For example, two Model 600 Normetex pumps operated in parallel would give the pumping speed required for this application.

6.7.6 Air Detritiation Systems (ADS) - In principle, the fuel systems are designed to prevent chronic leaks from equipment, and therefore, rooms are normally intended to be ventilated without continuous tritium recovery. However, ADS systems

Use or disclosure of data
subject to title page restriction

are provided to service a room where tritium escape has been detected. The rooms are also isolated from each other in order to minimize cross contamination and facilitate clean-up operations. However, there may be exceptions where equipment is under inert atmosphere with no access during operation. The tritium processing equipment is, from the containment point of view, divided into the following categories:

- Concentrated tritium gas under pressure – In double containment such as the cryogenic distillation unit and fuel storage system.
- Concentrated tritium gas at sub- or atmospheric pressure– In single containment.
- Hydrogen with less than 1% tritium at less than 20 bar – In single containment.
- Tritiated water at atmospheric pressure – In single containment.

The design approach will assume that during normal operation there are no chronic releases from the system. This is complemented by operating the rooms at a sub-atmospheric pressure of just a few millimeters of water column with the ADS on stand-by. All rooms are independently monitored for tritium and, in the event of tritium excursion, the ADS is activated and valved into the affected room. The following kind of systems will be used:

- Conventional Ventilation System (VS).
- Exhaust Atmosphere Detritiation System (EADS) - Such a system will be connected in series with RADS and will detritiate the air to be discharged into the atmosphere. This will keep the room(s) affected by a tritium release at mild under-pressure for tritium spread containment purposes.
- Recirculating Air Detritiation System (RADS) - These systems will be in normal operation on stand-by and will be activated only during emergencies such as during tritium release into a room. In some areas where chronic tritium release occurs, part of the RADS may operate continuously.

In addition, there will be a need to remove tritium from a process and its purge gas. Where possible, this will be carried out by the process itself, but final polishing will be done in a Gaseous Waste Processing System which is similar to the system described in Section 6.7.4.

Figure 6.7.6-1 indicates the functional arrangement of these systems. Normally the flow-through ventilation will keep the rooms well ventilated through a flow pattern directed from the clean zone, kept at atmospheric pressure, to the potentially contaminated zones maintained at progressively increasing negative pressure. The ventilation system will also be able to immediately isolate the system from a room in which any trace of activity is detected. In such event the normally stand-by RADS will be activated and valved-in to the affected zone. The function of the EADS is to maintain negative pressure in the potentially contaminated zones by processing a small amount of the building air and discharging it into the environment through the

Use or disclosure of data
subject to title page restriction

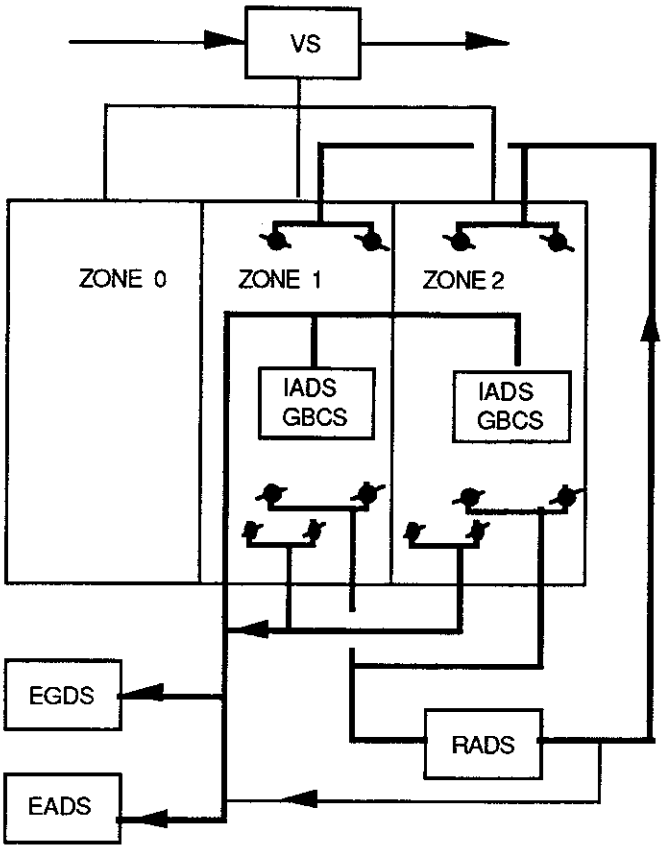

Figure 6.7.6-1. Functional Arrangement of ADS

stack. With the exception of attention to leak tightness and the room isolation feature, the VS is conventional and, in this design, is considered to be part of the HVAC system included in the balance-of-plant systems design.

6.7.6.1 ADS - Functional and Performance Requirements - The ADS requirements for the facility are summarized in Table 6.7.6-1.

The following general equation applies for the tritium clean-up time:

$$C = C_{max} * e^{-Q*t*f/V}$$

where:

- C - Tritium concentration in building air (Ci/m^3) at time t
- C_{max} - Initial release tritium concentration in building air (Ci/m^3)
- Q - Flow of air to the extraction facility (m^3/h)
- t - Time into the clean-up cycle (h)
- f - Fraction of tritium removed from the clean-up flow, at decontamination factor 900, f = (1-1/900) = 0.99888
- V - Size of the room to be cleaned (m^3)

Use or disclosure of data
subject to title page restriction

Table 6.7.6-1 ADS Design Parameters

Room/Space Name	Volume (m^3)	Tritium Inventory (kCi)	Single Failure Release (kCi)	Release Conc. (Ci/m^3)	Clean-up Time to 1 MPCa (h)	RADS Flow for 3 Days to 100 MPCa (m^3/h)	EADS Flow (m^3/h) 1% Max.
Reaction Chamber							
L-Option	7050	n/a (1)	3 (2)	0.43	5.5	600	70
H-Option	7050	1000	10 (3)	1.42	3.1	900	70
Driver Building							
L-Option	180000	1000	10	0.56	6.7	10000	1800
H-Option	2x16000	1000	3	0.19	3.7	1800	300
Vacuum Pump Room	8000	1000	1000	8	4.5	1000	80
Coolant Recirculation Room	120000	0	0	0	0	0	0
Contaminated Pb	2500	10	10	4	4.6	300	25
Contaminated Na	2500	192	192	76.8	4	400	25
Pb Coolant Room	10000	10	10	1	4.4	950	100
Breeder Purge Processing	6200	40	40	6.45	4.4	800	60
Fuel Factory	20000	$7x10^4$	3500	174	5	3300	200
Fuel Processing Water Dist.	4000	0.128	0.128	0.032	7	200	40
Tritium Storage	2000	$2x10^4$	1500	750	3.8	400	20
ISS							
L-Option	2500	480	480	192	4	450	25
H-Option	2500	700	700	280	6	300	25
FCU							
L-Option	1500	80	40	27	3.7	250	15
H-Option	1500	160	80	53	3.9	250	15
Turbine Building	130000	0	0	0	0	0	
Auxiliary Building	130000	0	0	0	0	0	

(1) Total tritium content in the chamber is not evaluate
(2) Gas content of chamber only
(3) Fuel injector failure, no chamber failure

Use or disclosure of data
subject to title page restriction

The exhaust detritiation flow is designed to be in the range of 1% of room volume per hour. This is primarily to cope with air infiltration. The proposed sizes of RADS are defined in Table 6.7.6-1.

From Table 6.7.6-1, it is evident that the total amount of RADS capacity in the reactor building is 10,000 m^3/h. This is required if the fuel injector fails and releases 10 kCi of tritium into the large mirror building for the L-option. The largest RADS requirement for the Fuel Factory is up to 3300 m^3/h of air but up to 330 g of tritium could be released into the room. It needs to be reiterated that the large tritium releases could occur only in missile type of events since there are several layers of containment, and consequently, there will be no tritium release into accessible areas from a single component failure.

6.7.6.2 ADS - Process Description and Control - The ADS requirements shown above are met by modular design. This allows operation of different numbers of modules depending on the room volumes to be serviced. The arrangement of these modules could be flexible and reliability could be achieved by providing redundancy in the inherently less reliable components such as rotating equipment-blowers or entire units. Typical Recombiner-Dryer module schematics is shown in Figure 6.7.6-2 and a membrane-based module is in Figure 6.7.6-3. Such modules will have a capacity in the range of 7,000 to 10,000 m^3/hr. The deployment strategy is based on the following assumptions:

- It is not credible that a large spill will occur simultaneously in all rooms with risk potential.
- The capacities required by some of the rooms may be too small to warrant a dedicated system.
- Common units allow for high reliability of the system and economically increased redundancy.

All ADS units will be skid-mounted for easy factory assembly, pre-testing, commissioning, and replacement/maintenance.

Recombiner-Dryer Based System - The Recombiner-Dryer based air detritiation is shown in Figure 6.7.6-2. The major components are designated with the following acronyms:

FR1	Inlet filter
B1	Blower(s)
FR2	Activated charcoal filter
HTR1	Preheater(s)
RB1	Recombiner
CD1,2	Condensers
TK1	Condensate collection tank
HX1	Air/air heat exchanger
DY1,2	Dryer beds with molecular sieves, regeneration loop, diagnostics (temperatures, flows, humidity, tritium)

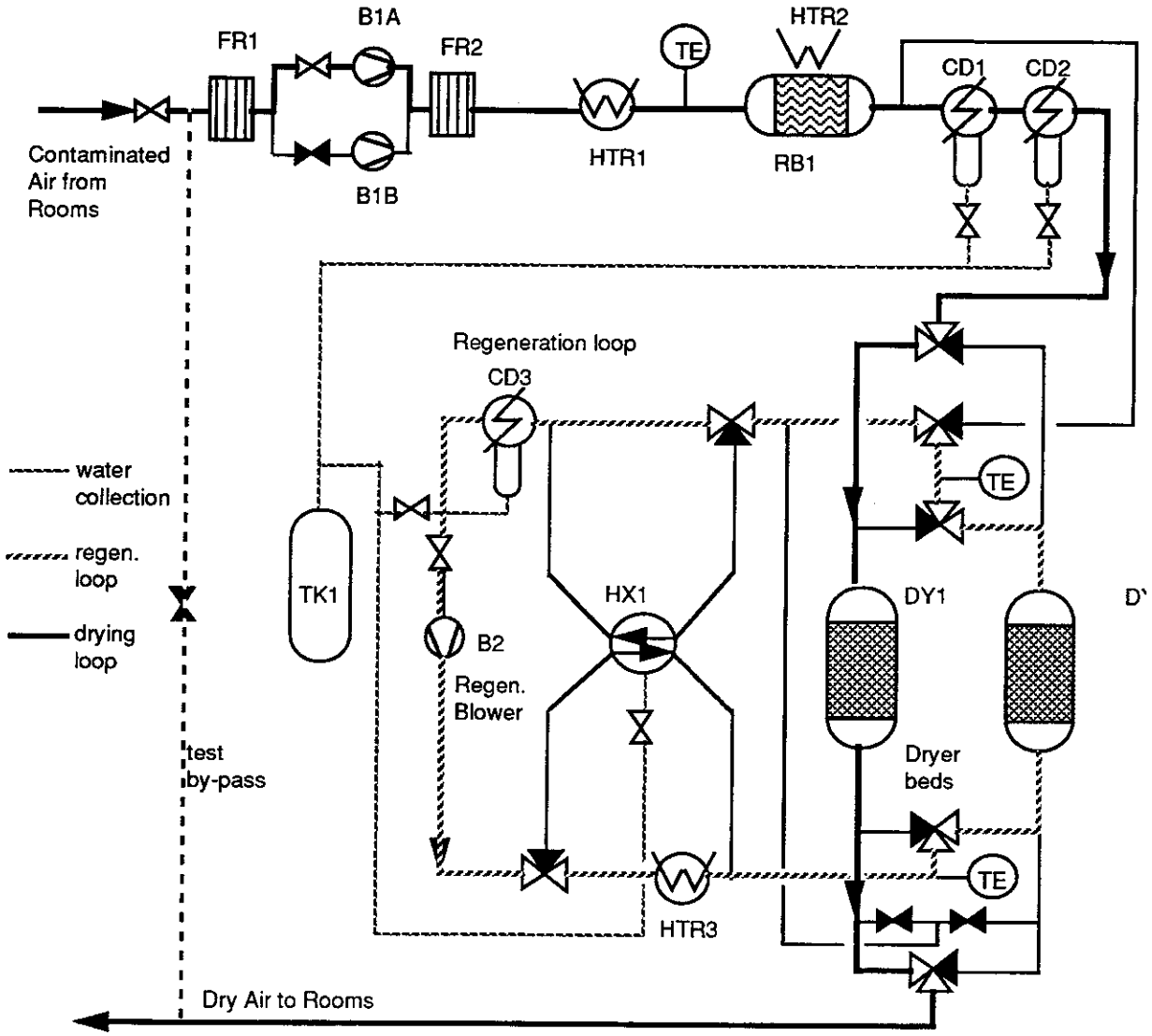

Figure 6.7.6-2. Recombiner-Dryer Based Air Detritiation System

Use or disclosure of data
subject to title page restriction

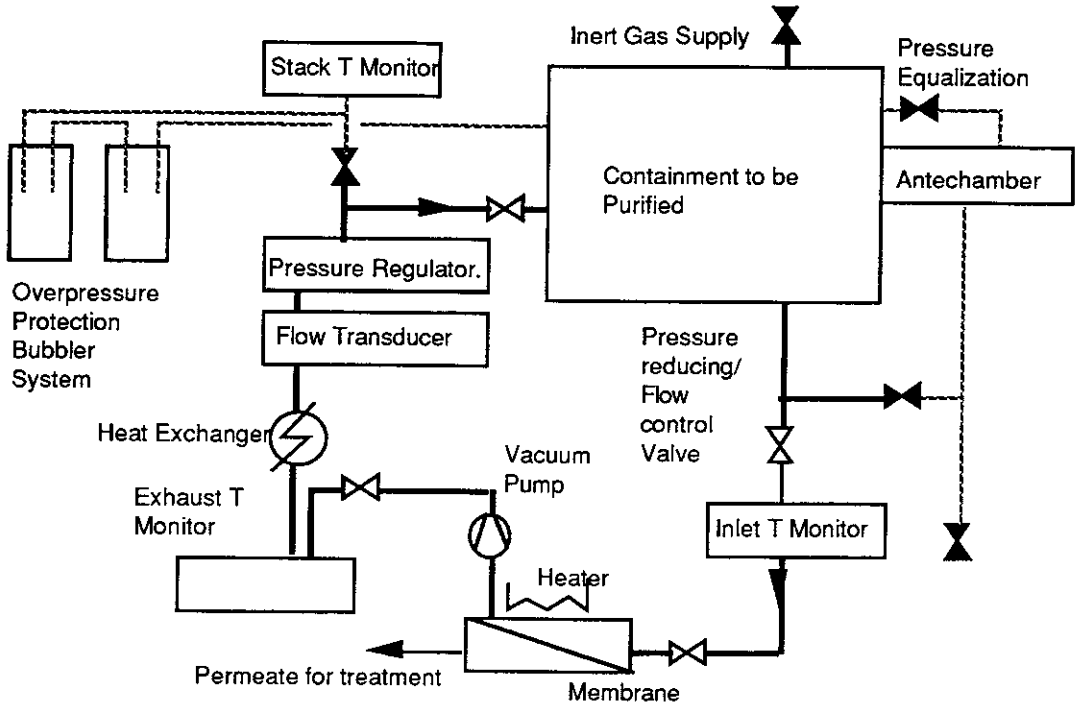

Figure 6.7.6-3. Membrane Based Air Detritiation System

The detritiation cycle is initiated by high tritium readings in an affected space. First, the affected area is isolated from the ventilation system. The contaminated air is then directed to a RADS unit. The air entering RADS is heated partially by the heat of compression and trim heated to approximately 150°C. At this temperature, the catalytic recombiner converts H, D, and T into water vapor which can be adsorbed in the molecular sieve beds. Prior to entering the beds, free moisture is separated in the upstream condensers cooled and chilled to 5°C. The return air from the dryers is up to 99.998% moisture free with a discharge dewpoint as low as -65°C. The on-line capacity of a single adsorption bed is 12 hours before requiring regeneration. A small amount of dry air from RADS is further processed in the EADS and discharged into the environment. This flow is used for controlling the negative pressure in the affected area of the facility.

During regeneration the air is heated to 300°C in HTR3 and recirculated through the bed where it heats up the bed and provides heat of desorption. Humidified regeneration air flows through the heat recovery exchanger HX1 and subsequently deposits the moisture in the condenser CD3. When the bed outlet temperature reaches approximately 280°C, the heating process is considered complete. The bed is flushed with dry air from the dryer discharge. The fraction of the regeneration flow is 1/7 of the overall dryer throughput. This side stream is recirculated into the drying loop upstream of the condensers CD1 and CD2 and returned upstream of the drying bed until the regenerating bed outlet dew point of -85°C is reached. The entire regeneration process will take approximately eight hours. The subsequent cooling of

Use or disclosure of data subject to title page restriction

the bed takes place by recirculating air in a closed loop through the CD3 which removes the residual heat until the final temperature of 28°C is reached.

Membrane-Based ADS - Figure 6.7.6-3 indicates a typical arrangement of such as system.

These types of processes are in the initial stage of experimentation with tritium, but commercial dryers based on permeation membranes already exist.[10] The system is designed as a typical permeation membrane process consisting of a gas circulator, permeation module, reject stream treatment loop, and appropriate diagnostic equipment.

The two most valuable features of the process are that:

- Permeation of hydrogen in gaseous and oxide form occur and no recombiner is needed.
- It is a continuous process.

The following characteristic process design parameters were published:[9]

Feed pressure	400–500 torr
Permeated side pressure	1.1 torr
Temperature of membrane	80–100°C
Recovery 80% T	At 0.1 of feed stream at $4x10^{-2}$ to 10^{-1} micro-Ci/cc and humidity 2,000-12,000 ppm
Recovery 70% T	At $2x10^{-1}$ micro-Ci/cc and humidity 440 ppm.

This process may feature instantaneous start-up, insignificant sensitivity to residual contamination, and continuous operation. Consequently, it will be particularly suitable for RADS operation. For the EADS service, the added security of the recombiner-dryer process may be required.

6.7.7 Inert Atmosphere Detritiation System (IADS) - A number of inert atmosphere detritiation concepts were described in References 11, 12, 13, and 14. The process of choice is the getter-based atmosphere purification system (Figure 6.7.7-1). The application of IADS will be on a modular basis where each room or secondary containment is serviced by its own dedicated system. For very large applications, the systems described for the air detritiation systems of the recombiner-dryer type shown in Figure 6.7.7-2 may offer the optimum solution.

Use or disclosure of data subject to title page restriction

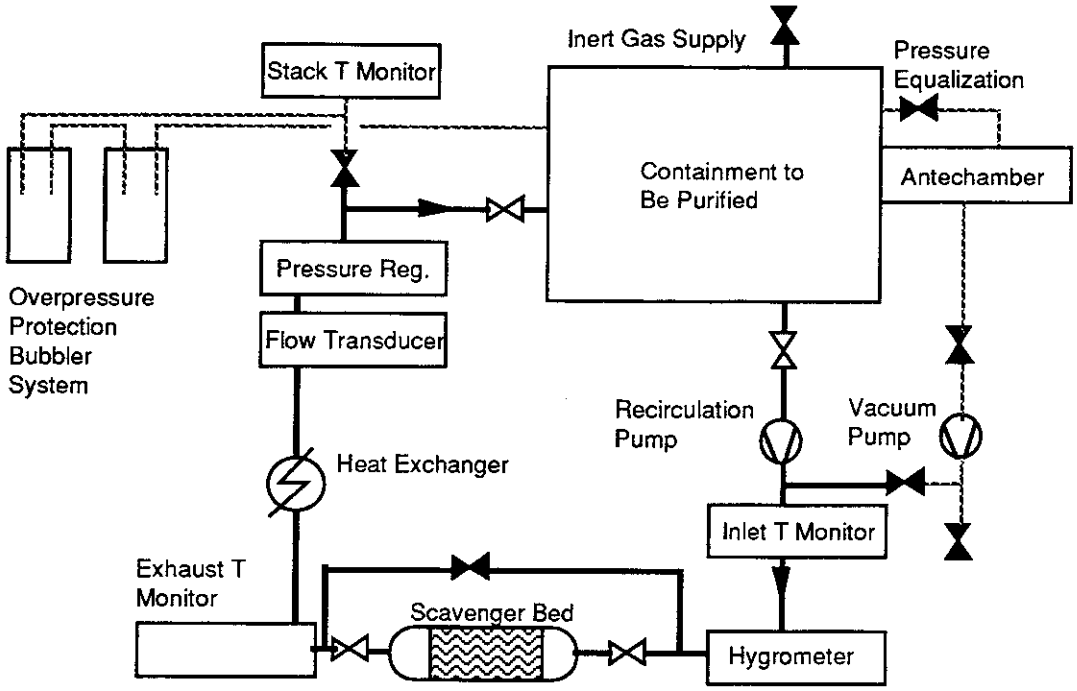

Figure 6.7.7-1. Getter-Based Inert Gas Detritiation System

Recombiner-Dryer Based IADS - The IADS will have the following components (as shown in Figure 6.7.7-2):

FR1	Inlet filter
B1	Blower(s)
FR2	Activated charcoal filter
HTR1	Preheater(s)
RB1	Recombiner
CD1,2	Condensers
TK1	Condensate collection tank
DY1,2	Dryer beds with molecular sieves
OXY1,2	Oxygen removal beds
HTR3,4	Oxygen removal bed heaters
HX1	Gas/gas heat exchanger, regeneration loop, diagnostics (temperatures, flows, humidity, tritium)

Use or disclosure of data subject to title page restriction

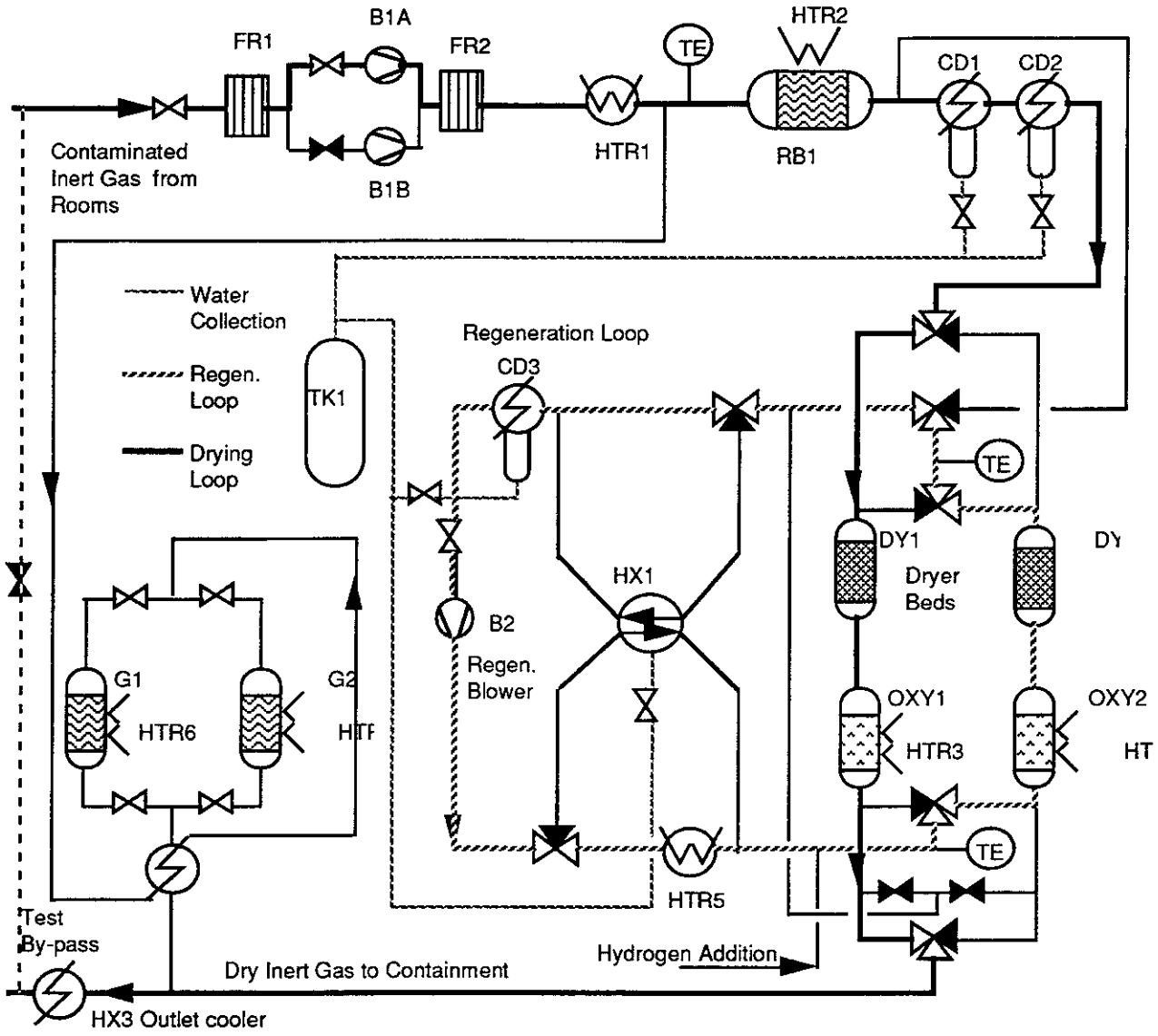

Figure 6.7.7-2. Recombiner/Dryer Based Inert Gas Detritiation System

The detritiation cycle is initiated by high tritium readings in an affected space. First, the affected area is isolated. Recombiner-dryers operate in the same manner as described in Section 6.7.6.2. In addition, downstream oxygen removal beds operate at 175°C to remove excess oxygen from the purified inert gas. The returning gas is finally cooled in HX3 to the ambient temperature.

Regeneration of the beds is similar to the process described in Section 6.7.6.2.

6.7.8 Fuel Storage and Management System (FSMS) - Fuel in the tritium concentration range (between 50–70% tritium) is required to be stored and assayed in a safe manner. This will be done in the Fuel Storage and Management System (FSMS).

Use or disclosure of data
subject to title page restriction

6.7.8.1 FSS - Functional and Performance Requirements - In order to obtain uninterrupted production of fuel, the free tritium inventory in all the systems will be in the order of 7 kg. Table 6.7.8-1 indicates the in-process inventories of systems containing tritium. During shutdown, all the free tritium inventory will have to be stored in metal hydride storage beds. A single storage bed size is proposed to contain no more than 200 g of tritium. On the basis of 50% DT fuel, there will have to be approximately 7000/200 = 35 storage beds available for fuel storage alone. The nominal 200 g tritium per bed target for the 50% fuel overall storage capacity will be 200/6 * 2 = 67 mol of hydrogen. For the L-option, a bed could be theoretically filled with fresh fuel enriched from the ISS (59.8% T) to 67 * 0.598 * 6 = 240 g of tritium. If the 200 g limit is required, the beds for ISS-L could be deliberately undersized for 200/(6*0.598) = 55.7 mol of hydrogen. One of the largest rundown sources will be the ISS which contains approximately 860 g of hydrogen isotopes of which only 68 g is tritium (H-case). The purpose of the system is to provide:

- Storage for all free hydrogen gas contained in process for shutdown purposes.
- In-process surge capacity in the form of tanks where required.
- Storage for fuel make-up.
- Assay capability.

In addition, the tritium storage and management system will rely on a number of storage tanks for temporary shutdown storage. The following tanks are foreseen to be used and are defined in Table 6.7.8-2.

Table 6.7.8-1 Tritiated Hydrogen Storage Requirements

System	T_2%	[g] Gas	[moles]	Number of Beds
Factory Fuel, DT	50	7000(T)	2333	35
D_2 Make-Up	0	5000	1250	–
H_2 Propellant		1000	500	8
Chamber Pumping L-Option	39	28	70	1
Chamber Pumping H-Option	4	12	300	5
Isotope Separation	3	70	300	5
Impurity Extr. from Fuel L	26	4	7.26	
Impurity Extr. from Fuel H	4	8	33.3	1
Tritium Extr. from Impurity*				
Tritium from Solid Breeders	5	2.6	8.7*	
Tritium Removal from Na	4	15	60	1
Tritium from Water	–	–	5*104	**
Tritium from Atmospheres	–	–	–	–
Fuel Management and Storage	50	700	233	4
Solid Waste Detritiation	–	–	60	1
Total Number of Beds with 23% Excess Capacity				75

* Included in impurity extraction from fuel
** This amount is actually water vapor which, during shutdown, condenses. No storage is required.

Use or disclosure of data subject to title page restriction

Table 6.7.8-2 Tritium Storage Tank Requirements

System	Pressure (Bar)	Tank Volume (m^3)	Quantity to be Stored (mole)	Location of Tank
Fuel Factory Fuel	n/a			
D_2 Make-up	10	3	1250	Fuel Factory
H_2 Propellant	10	2	500	Fuel Factory
Chamber Pumping L-Option	n/a			
Chamber Pumping H-Option	n/a			
Isotope Separation	10	2	300	ISS
Impurity Extraction	n/a			
Tritium Recovery from Breeders	n/a			
Tritium Removal from Na	1	1.5	60	Tritium Removal Room
Tritium Recovery from Water	n/a			
Tritium from Atmospheres	n/a			
Fuel Management and Storage	1			
Solid Waste Detritiation	1	1.5	60	Fuel Storage

6.7.8.2 FSMS - Process Description and Control - The FSMS flow diagram is shown in Figure 6.7.8-1. The diagram is simplified to show only two of the overall number of beds required.

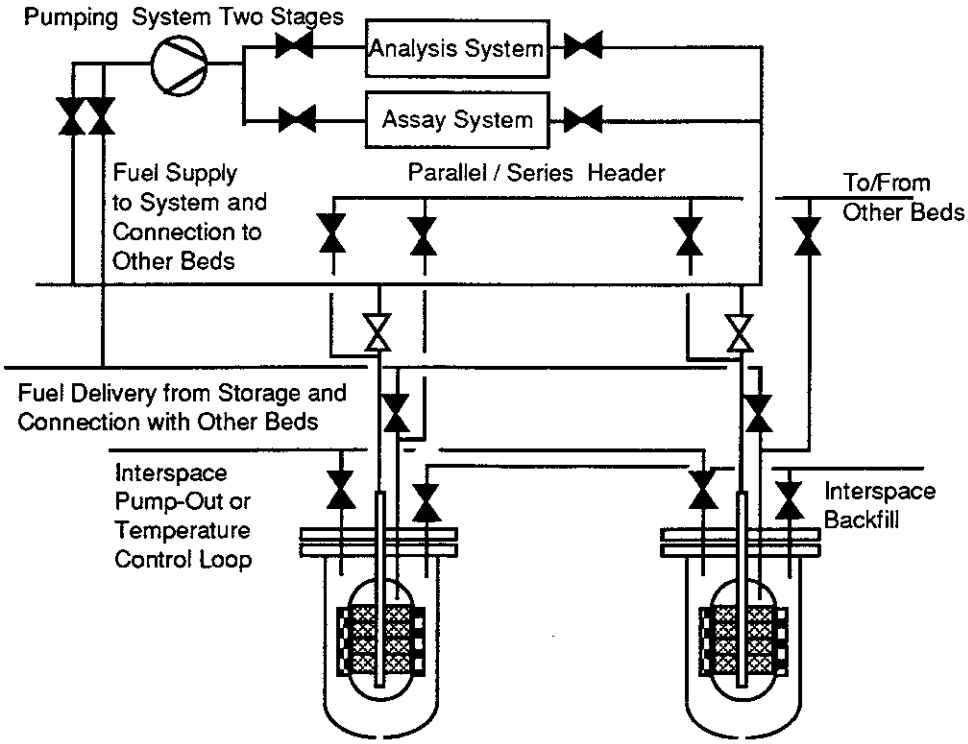

Figure 6.7.8-1. Fuel Storage and Management System Diagram

Use or disclosure of data subject to title page restriction

The storage medium is uranium or zirconium-cobalt.[15] The storing material is contained in the primary container which is provided with heater, temperature, and pressure control devices. Process heating is by way of built-in replaceable electric heaters. The primary envelope is enclosed in a secondary vessel designed and tested for pressure and vacuum operation. This secondary vessel provides vacuum insulation, prevents tritium release in the event of primary envelope failure, and provides opportunity for active temperature control and for tritium permeation capture and recovery. The getter assembly is located in a glove box or solid steel vessel type tertiary containment with inert atmosphere which is continuously monitored for tritium and serviced by an inert gas purification system. The entire storage capacity will have 23% redundancy for excess hydrogen and partially for compensating for lost or degraded storage capacity. In addition, each bed will be designed for 50% loading. The overloading avoidance control will rely on control by procedural means. In situ tritium assay will take place by way of calorimetric measurement of decay heat.

The conventional pressure-volume-temperature measurement can also be used. Temperature control will take place by electrical heating as described above. Heat removal from the bed will be facilitated through filling the interspace between the primary and secondary containment with inert gas. This will facilitate heat convection from the primary and radiation from the secondary. More aggressive cooling could occur if the tertiary containment gas is circulated through a cooler, or more directly if the interspace gas is circulated through a cooler.

The short term, in-process storage capacity by tanks will rely on double walled tanks with interspace leak control.

Accidental bed failure could occur only as a dual failure, namely a combination of heater run-away and failure of diagnostics to recognize this. For this purpose, rupture disc-type relief devices could be used. However, since such devices require inherently high maintenance and since any maintenance on the primary envelope is undesirable, relief devices are avoided.

Each storage bed contains the gettering material in four to five layers separated through sintered grids. Each layer locates the material in copper blocks shaped for optimum heat transfer to achieve uniform operating temperatures. At the inlet and outlet, main filters are located. The main objective of the filters is to prevent the powdered getter material from escaping from the bed. All beds will be installed to permit flow through operation.

6.7.9 Isotope Separation System (ISS) and Water De-tritiated System (WD) - A number of waste water detritiation front-end options were considered but the water distillation is proposed. The final tritium enrichment is accomplished by

Use or disclosure of data
subject to title page restriction

cryogenic distillation (CD). The entire ISS, including all the interlinked water distillation columns, VPCE, equilibrators, and CD units has been simulated using Ontario Hydro's FLOSHEET steady-state process simulator.[16]

6.7.9.1 Functional and Performance Requirements - The requirements for hydrogen isotope separation arise from chamber exhaust gas processing, breeding blanket tritium recovery, air cleanup, and other safety and waste processing systems. The functional relationship between the ISS and the fuel processing systems is shown in Figure 6.7.1-1, and the corresponding flows and compositions of the ISS feeds are specified in Table 6.7.1-1 for the L option, respectively. The CD system configuration represented in Figure 6.7.9-1 has undergone several refinements in order to simplify the design, to improve robustness, and to minimize tritium inventory. The specific feed and product flows and compositions are defined in Figure 6.7.9-1. The following processing streams apply for the isotope separation system:

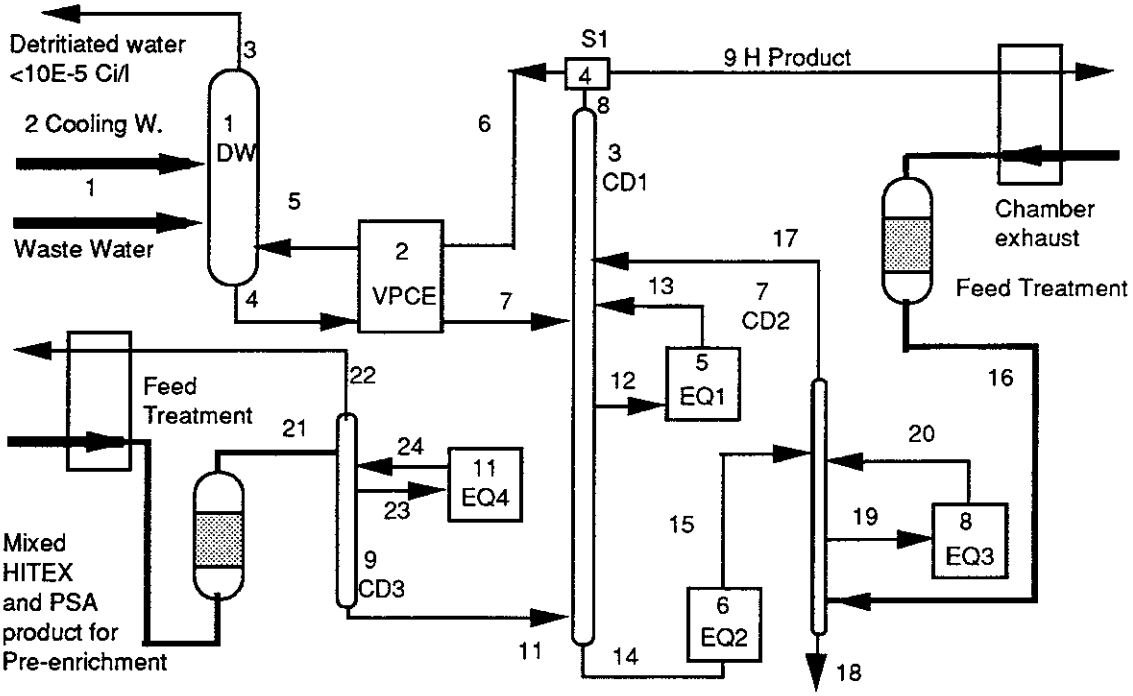

Figure 6.7.9-1. ISS and Water Detritiation - Flow Diagram

Feeds to the ISS - The elemental hydrogen streams which are external feeds to the cryogenic distillation system are assumed to be isotopically equilibrated at a temperature of 300 K.

- Tritiated Waste Water - Stream z (in Figure 6.7.1-1) or 1 (in Figure 6.7.9-1), shown as z/1.
- Solid Breeder Tritium Extraction - Stream h/21. Tritium must be extracted from the solid breeder through a He/hydrogen purge gas stream. The composition is 0.2% H and 0.01% T.

Use or disclosure of data
subject to title page restriction

- Chamber Exhaust Gas - Stream a/16. The H/D/T mixture from plasma exhaust gas processing must be isotopically separated. This is different between the laser and heavy ion options mainly due to the significantly different hydrogen component where the heavy ion option target contains approximately ten times more hydrogen than the laser option.
- Target Injector Propellant Cleanup - This applies only to the heavy ion option. Most of the propellant gas is trapped and recovered in a chamber just before the entry shutter to the chamber. Only a small portion of the gas enters the chamber and is mixed with the chamber exhaust gas. Deuterium and protium were considered as alternative propellants. It was established that as long as the propellant component is in excess of the deuterium makeup which in this case is threefold, the excess deuterium propellant must be separated to a reasonable purity. This makes the ISS design complicated to the extent that two additional columns are required and the tritium inventory is substantially increased. Consequently, protium was selected as propellant.
- Product from the HITEX Process - Stream c/na is mixed with stream h.

ISS Products

- Detritiated Waste Water - Stream u/3. This stream must contain less than 10 micro-Ci/kg of tritium. Therefore, the mole fraction of HTO in the product must be less than 6.2×10^{-12}.
- Protium Product - Stream d/9. The tritium atom fraction in the detritiated protium stream (H_2 with Trace HD) must be less than 1.0×10^{-9}.
- DT Product - Stream k/18. Although there is no tritium enrichment required, the DT composition is still T enriched due to the addition of the T from the breeder product.

6.7.9.2 Waste Water Detritiation Options - Two waste water detritiation processes were considered for this application:

- Distillation for HTO concentration and Vapor Phase Catalytic Exchange (VPCE) process for transporting T from HTO to HT for processing in the ISS.
- Combined Electrolysis and Catalytic Exchange (CECE) process which transfers tritium from water to hydrogen in direct contact in the presence of a hydrophobic catalyst.

Final selection of the waste water detritiation process was made on the basis of factors such as cost, flexibility, and safety. The reference case for this application is the DW + VPCE option. The characteristic features of the process are:

- Tritiated water is fed near the bottom of the column (the optimum feed point is determined by feed composition), detritiated water is withdrawn from the top of

the column, and a small stream of concentrated tritiated water is fed from the bottom of the column to the VPCE.

- In the single stage VPCE, tritium is transferred to hydrogen gas, which returns to the CD system for detritiation.
- The tritium-depleted water stream returns from the VPCE to the water distillation column.

The attractive features of the process are:

- Safety: Water distillation is inherently a safe process, since it involves very moderate process conditions (temperature: 50-60°C; pressure 10-30 kPa), it has no associated explosion hazard (such as electrolysis), and it has an excellent operating history with large-scale industrial units processing tritiated water.
- Reliability: Reliability of water distillation is proven by more than 20 years of large scale industrial use.
- Availability: Large scale units are available, with no extrapolations of existing technology.
- VPCE Catalyst Lifetime: Since the VPCE catalyst is operated at 200°C under conditions which are favorable for catalyst lifetime, the expected lifetime is in excess of 20 years.

The disadvantages of the DW + VPCE process are primarily that the equipment is physically large (3 columns, 25-m high, 0.6-m diameter) and the process may require up to 1600 kg/h of low grade steam. (This can be reduced if a heat pump is used.)

The following source terms for waste water were estimated:

Source	Flow [mole/h]	Tritium Concentration [mole fraction]
Chronic Drain	232	$3.1 * 10^{-8}$
Chronic ADS Collection	463	$3.1 * 10^{-8}$
Inert Atmosphere Detrit.	93	$3.1 * 10^{-10}$
Decontamination Water	463	$3.1 * 10^{-8}$
Chamber Maintenance	3.4	$3.1 * 10^{-8}$
Post Accident Drain	85	$7.8 * 10^{-7}$
Post Accident ADS	170	$7.8 * 10^{-7}$
Post Accident Clean-Up	8.4	$3.0 * 10^{-9}$

The overall flow is 1517 mole/h with blended concentration of $1.55 * 10^{-7}$ mole fraction.

Use or disclosure of data subject to title page restriction

6.7.9.3 ISS - Process Description

Water Distillation - Although the water detritiation equipment is large, it contains very little tritium, mainly due to the low concentration of tritium in the waste water and limited tritium enrichment in DW1. The design parameters of the distillation columns is given in Table 6.7.9-1.

Table 6.7.9-1. Water Distillation Column Parameters

		L-Option and H-Option
No. Theoretical Stages		450
Pressure (kPa)	Top	11
	Bottom	25
Temperature (K)	Top	320.9
	Bottom	338.2
Diameter (m)		0.59
Packing Height (m)		54
Reflux Ratio		27
Holdup (mole/stage) Column		110.6
	Reboiler	884.7
Total Holdup (mole)	H_2O	5x104
	D_2O	58.2
	T_2O	0.05
Steam Consumption (kg/h)		740
Feed Location, Stage	Stream 1	300
	Stream 2	350
	Stream 5	425
Drawoff Loc. Stage	Stream 3	1
	Stream 4	450

VPCE - The vapor phase catalytic exchange is carried out over a Pt on alumina catalyst at 200°C. A liquid stream is withdrawn from the reboiler of DW1, evaporated, mixed with a detritiated hydrogen stream from CD1, superheated to a temperature of 200°C, passed through the catalyst bed, and finally passed to a condenser for hydrogen/water separation. Detritiated water is returned to DW1 and tritiated hydrogen is returned to CD1.

Cryogenic Distillation - The cryogenic distillation system is comprised of three cryogenic distillation columns (CD1, CD2 and CD3), four equilibrators (EQ1, EQ2, EQ3, and EQ4), and one stream splitter (S1). The purpose of the first cryogenic distillation column, CD1, is to remove tritium from streams containing mostly hydrogen with trace tritium and to produce a highly detritiated hydrogen stream (Stream 8) as the overhead product and a D_2/DT stream as the bottom product for further processing in the final column CD2. CD1 also receives a recycle stream from the downstream columns CD2. In addition, a small column CD3 was added to reduce the H_2 content of diluted streams h and c from the PSA and HITEX processes. This reduces the CD1 size and tritium inventory by approximately 5 g.

Use or disclosure of data subject to title page restriction

Since the hydrogen from CD1 may be discharged to the environment, it is essential that the design of CD1 be conservative to ensure that tritium emissions will be acceptably low. The reflux ratio for CD1 is, therefore, conservatively set at 3.7—more than twice the minimum reflux ratio. This conservatism results in a somewhat larger diameter and power consumption for CD1 than the minimum possible.

In the lower portion of CD1, a side stream is taken off and passed through equilibrator EQ1 and then returned to CD1. The purpose of the equilibrator is to promote the reactions: $HT + HD = H_2 + DT$ and $HT + D_2 = HD + DT$. Immediately downstream of CD1 is equilibrator EQ2, which serves to promote the reaction $HT + D_2 = DT + HD$, in order to convert traces of tritium in the form of HT into DT.

The bottom product of CD2 is the final DT stream. A side stream is taken from CD2 and passed through equilibrator EQ3 in order to promote the reaction: $2\ DT = D_2 + T_2$.

The CD1, CD2, and CD3 cryogenic distillation column parameters are summarized in Table 6.7.9-2. Process simulations results are shown in Tables 6.7.9-3, 6.7.9-4, 6.7.9-5, and 6.7.9-6 for the gas, liquid streams, and the L and H options, respectively.

6.7.9.4 Water and Hydrogen Distillation - Control Description - Control systems for the distillation units is well proven in a number of heavy water upgraders, and the same control philosophy is proposed to be adopted for this application. The operating pressure of water distillation column DW1 is controlled by automatic adjustment of cooling water flow to the column condenser. The flow of steam to the reboiler is at a constant rate and is normally set only at column startup. Withdrawal of overhead product is controlled by reboiler level. Feed forward to the downstream VPCE and associated feedback are kept constant. Since a single stage VPCE unit is used for transferring tritium to the gas phase, its control is simple. Low pressure steam to the evaporator is on evaporator level control, and the flow of high pressure steam to the superheater is controlled by the superheater exit temperature.

The CD system is the heart of the ISS and is also the most complex part of the system. The pressure in the CD cascade is designed to progressively decrease from column CD3 to CD1 and CD2. The purpose is to provide enough inter-column differential pressure to control the forward flows in the cascade. This control strategy deliberately avoids the use of pumps to transfer these enriched streams. On the contrary, return streams in the cascade which are depleted in tritium are pumped against the pressure gradient. The boil-up in each column is set by controlling the power input to the electrically heated column reboilers. Once the boil-up in a column is defined, the appropriate fraction of vapor flowing up the column must be condensed and returned within the column as reflux. Thus, the helium refrigerant flow to each column condenser is modulated to condense the correct amount of vapor and maintain the column pressure at the desired value.

Use or disclosure of data
subject to title page restriction

Table 6.7.9-2. Cryogenic Distillation Column Parameters

		L-Option			H-(where different)		
Parameter		**CD1**	**CD2**	**CD3**	**CD1**	**CD2**	**CD3**
Number of Theoretical Stages		120	30	20			
Pressure (Pa)	Top	120	100	150			
	Bottom	125	101	152			
Temperature (K)	Top	20.98	24.74	21.79	9.2	5.2	13
	Bottom	24.74	24.54	21.91			
Column Diameter (cm)	Top	9.00	3.85	13.14			
	Bottom	–	–	–			
Packing Height (m)		6.6	1.65	1.11			
Reflux Ratio		3.7	6.5	3.5			
Intermediate Reboiler	Stage	–	–	–			
	Power (W)	–	–	–			
Holdup Profile (mol/stage)	Top	1.45	0.27	2.93	1.5	0.47	2.7
	Bottom	1.45	0.27	2.93	1.5	0.47	2.7
	Int. Reboiler	–	–	–			
	Reboiler	4.34	0.81	8.79	4.5	1.4	8
Total Holdups (mole)	H_2	95	0.6	64.21	111	1.9	58
	D_2	118	5.23	0.018	66	5.8	0.015
	T_2	4.87	2.78	0.25	6.3	4.8	0.23
	T_2 (g)	29.27	16.69	1.5	37.7	28.7	1.4
Condenser Duty (W)							
Feed Locations, Stage	Stream 7	20					
	Stream 11	70					
	Stream 13	90					
	Stream 17	80					
	Stream 25				85		
	Stream 15		10				
	Stream 16		24				
	Stream 20		15				
	Stream 21			7			
	Stream 24			15			
Drawoff Locations, Stage	Stream 8	1					
	Stream 12	93					
	Stream 14	120					
	Stream 17		1				
	Stream 18		30				
	Stream 19		17				
	Stream 9			20			
	Stream 22			1			
	Stream 23			17			

Use or disclosure of data
subject to title page restriction

Table 6.7.9-3 ISS Liquid Flows, L-Option

Flow No.	Composition Liquid Mole Fraction mole/h	H_2O	HDO	HTO	D_20	DTO	T_2O
1	1517	9.9985e-01			1.4998e-04		1.5398e-07
3	1518	1.0000e+00	2.7992e-06	1.1091e-10	2.0619e-12	1.5926e-16	3.2371e-21
4	30	9.4344e-01	5.5664e-02	2.8529e-05	8.6426e-04	8.6346e-07	2.2702e-10
5	30	9.5776e-01	4.2100e-02	1.3723e-05	1.2837e-04	8.1729e-08	4.9902e-11

Table 6.7.9-4 ISS Gas Flows, L-Option.

Flow No.	Composition Gas Mole Fraction mole/h	H_2	HD	HT	D_2	DT	T_2
6	90	9.8347e-01	1.6553e-02	5.8884e-09	1.1849e-09	1.4414e-14	3.5287e-20
7	90	9.7858e-01	2.1284e-02	5.1348e-06	1.3116e-04	6.6813e-08	8.7293e-12
8	234.5	9.9993e-01	7.0116e-05	2.6781e-10	1.1958e-10	1.4212e-15	3.2683e-21
9	144.5	9.8347e-01	1.6553e-02	5.8884e-09	1.1849e-09	1.4414e-14	3.5287e-20
11	134.5	9.3645e-01	6.1311e-03	5.7011e-02	7.3078e-06	1.2661e-04	5.7278e-04
13	400	4.1816e-02	2.7728e-01	2.1606e-02	5.5963e-01	9.5420e-02	4.2503e-03
14	20	2.0047e-12	8.4888e-06	2.4313e-04	3.8808e-01	5.6965e-01	4.2023e-02
15	20	2.0225e-08	1.7362e-04	7.6331e-05	4.5365e-01	4.3642e-01	1.0968e-01
16	28.2	2.5227e-08	2.3839e-01	2.2403e-01	6.8565e-02	1.4100e-01	7.5745e-02
17	30	1.7276e-01	4.0969e-01	1.3610e-01	2.4262e-01	3.7804e-02	1.0335e-03
18	18.2	2.1246e-04	5.0948e-03	2.1720e-02	9.6937e-02	5.4140e-01	3.3464e-01

Table 6.7.9-5 ISS Liquid Flows, H-option.

Flow No.	Composition Liquid Mole Fraction mole/h	H_2O	HDO	HTO	D_20	DTO	T_2O
1	1517	9.9985e-01			1.4998e-04		1.5398e-07
2	1	9.9985e-01			1.4998e-04		3.0995e-07
3	1518	1.0000e-00	4.3791e-06	1.1110e-10	5.0464e-12	2.4958e-16	3.2483e-21
4	30	8.4174e-01	1.5109e-01	2.6038e-05	7.1372e-03	2.3976e-06	2.1196e-10
5	30	8.5143e-01	1.4671e-01	1.2548e-05	1.8535e-03	3.0116e-07	4.6928e-11

Table 6.7.9-6 ISS Gas Flows, H-option.

Flow No.	Composition Gas Mole Fraction mole/h	H_2	HD	HT	D_2	DT	T_2
6	90	9.2056e-01	7.9439e-02	1.5895e-08	4.0323e-08	1.1603e-13	7.2425e-20
7	90	9.1757e-01	8.0429e-02	4.9519e-06	1.9975e-03	2.5968e-07	8.6585e-12
8	597	9.2056e-01	7.9439e-02	1.5895e-08	4.0323e-08	1.1603e-13	7.2425e-20
9	507	9.2056e-01	7.9439e-02	1.5895e-08	4.0323e-08	1.1603e-13	7.2425e-20
11	377	9.9883e-01	5.6002e-04	6.1022e-04	5.6516e-08	1.3611e-07	1.5325e-08
12	600	3.2983e-03	2.5315e-01	2.7941e-02	6.8033e-01	3.4830e-02	4.5453e-04
13	600	2.3933e-02	2.3156e-01	8.2627e-03	6.8191e-01	5.3245e-02	1.0861e-03
14	20	3.2864e-13	4.5734e-06	9.2436e-05	4.1303e-01	5.6776e-01	1.9114e-02
15	20	3.0304e-09	6.9679e-05	2.7324e-05	4.8765e-01	4.1845e-01	9.3803e-02
16	145	5.8848e-01	2.6336e-01	8.3067e-02	3.5871e-02	2.4758e-02	4.4641e-03
17	150	5.2008e-01	3.5310e-01	7.7214e-02	4.7537e-02	2.0404e-03	2.2101e-05
18	15	3.4561e-04	4.1748e-03	7.2594e-03	1.1175e-01	6.1039e-01	2.6608e-01

Use or disclosure of data
subject to title page restriction

The overhead vapor product from a column is withdrawn through a control valve which controls the reboiler level in that column at the desired value and thus ensures that mass balance is maintained within the column. This control strategy ensures a mass balance for each column, provides for pressure and reboiler-level control for each column, ensures the correct column internal flows, and allows transfer of tritium-rich streams without the use of circulating pumps.

6.7.9.5 Safety Analysis - The ISS contains most of the free or releasable tritium in the fuel processing systems. For this reason, this system was selected for sample safety analysis. Safe design and operation of the ISS requires that the process fluids contained within the ISS equipment not be released or leaked to the surrounding environment under any postulated event. In considering the safety of the Isotope Separation System, the effect of possible failures on equipment groups has been analyzed to show that the system design is safe. The following generic failure modes have been considered and have been applied where applicable:

- Utility failure as a common mode failure: loss of power, loss of chilled water, loss of liquid nitrogen or gaseous cold or hot nitrogen, and loss of vacuum in coldboxes.
- Closed valve at equipment outlet.
- Controller failure: level control, flow control, temperature control, pressure control.
- Catalyst poisoning (loss of efficiency).
- Failure of composition analysis.
- Failure of interlocks.

The evaluation of the above failures is summarized in Table 6.7.9-7.

6.7.10 Heat Transfer Media Detritiation - The major heat transfer media from the reactor to the steam generators are helium and lead. The helium coolant handles the largest portion of the reactor power with a minimal transfer of tritium to the steam cycle. However, the higher solubility of tritium in the lead poses a problem which must be addressed. Approximately one third of the heat produced in the reactor (750 MW) will be removed by liquid lead and transferred into the ultimate heat transfer medium, steam, which will convert this into electrical energy in a steam turbine or generator. The permeation rate from the Pb side of the heat exchanger was analyzed and the data is summarized in Table 6.7.9-8. The lead steam generators are equipped with double-walled heat transfer tubes with the interspace filled with sodium. The tritium permeation control will be facilitated by maintaining the partial pressure of tritium in the sodium channels below a value that would prevent the permeation rate to increase above the 10 Ci/day limit. The parameters shown in Table 6.7.9-8 apply.

The tritium solubility in Pb was obtained from Reference 17 which quoted a temperature independent value of 1.2×10^{-2} (appm H in Pb/torr$^{1/2}$).

Use or disclosure of data
subject to title page restriction

Table 6.7.9-7 Failure Modes and Effects Analysis (FMEA) for the ISS

Equipment	Purpose	Failure Mode	Effect	Detection	Mitigation
CD1, CD2, CD3, CD4	Distill. columns	Lost power	Warm Up	High pressure	Expansion tanks limit pressure
		Loss of cold-box vacuum	"	"	"
		Loss of refrigeration	"	"	"
		Closed outlet valve	Higher pressure	High pressure	Design pressure adequate, shut heat to reboil.
DW	Condenser	High water level, LC failure	Water in product line	High level alarm	Lower setpoint
VPCE	Cooler	No chilled water	High temperature	Temperature alarm	Restore water flow
	Cryogenic adsorbers	LN_2 failure	High bed temperature	High T alarm	System shutdown
		Hot N_2 failure	Long regeneration time	Low T persists	Switch beds
		Closed outlet during regeneration	High pressure	High P alarm	Relief valve to expansion tank
VPCE, EQ1, EQ2, EQ3, EQ4,		Low catalyst efficiency	Off-specification product	Analyses	No hazard
Pumps, Compressors		Closed outlet	High pressure	High pressure alarm	Relief valve to suction

Table 6.7.9-8 Heat Transfer Media Must Be Processed to Keep Tritium Permeation Within Acceptable Limits

Parameter	L-option [g/h]	H-option [g/h]
Amount of tritium dissolved in Pb and transported from chamber into steam generator	0.321	0.797
Permeated from Pb through the first tube or amount to be removed from interspace to prevent permeation to steam	0.11	0.28
Tritium returned from steam generator in cooled Pb coolant	0.211 torr	0.51 torr
Required partial pressure of tritium in Na loop to keep permeation below 10 Ci/day	3.6×10^{-11}	3.6×10^{-11}

Use or disclosure of data subject to title page restriction

6.7.10.1 Tritium Extraction from Sodium-Filled Heat Transfer Tube Interspace - In general, the following options for maintaining low partial pressure of tritium in Na below 3.6×10^{-11} torr are available: cold trapping, solvent (Salt/Electrolysis) extraction, distillation, adsorption, purging and isotopic dilution, and gettering. From these options, only the last one is proposed to be used for the reference design.

The final design does not rely on permeation barriers which, in the oxide form, could be applied only at the steam side. For a 1000 and 100 fold improvement due to the permeation barriers, according to Bell,[18] the partial pressure will be 3.6×10^{-5} torr and 4×10^{-4} torr, respectively. Considerable work was done in yttrium gettering from lithium. The yttrium gettering capability is best expressed in Reference 19 from which Figure 6.7.10-1 was reproduced. It is evident that tritium levels in the 1 ppm range need to be maintained if the permeation rate is to be kept below the 10 Ci/day limit. This can be achieved through the following design parameters:

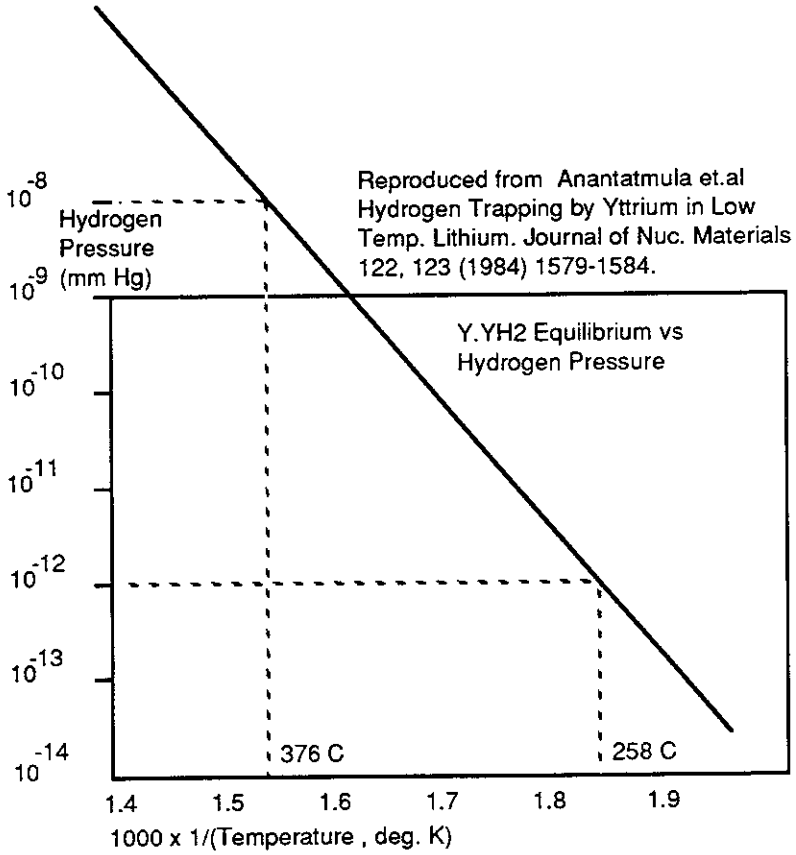

Figure 6.7.10-1. Y.YH2 Formation vs. Equilibrium Hydrogen Pressure

Use or disclosure of data
subject to title page restriction

- No permeation barriers, partial pressure 10^{-11} torr is needed which requires getter temperature of 546 K or 273°C.
- Permeation barrier with 100 fold improvement; this will need partial pressure 10^{-7} torr which is achievable with getter operating at 680 K or 407°C.
- Permeation barrier with 1000 fold improvement; this will need partial pressure 10^{-5} torr, achievable with getter at 730 K or 430°C.

The proposed system parameters for the L-option (and H-option) are:

- For removing 0.3 (0.8) g, T_2 per hour.
- 2 wppm equilibrium concentration in the Na-filled interspace.
- 1 wppm concentration of returning purified stream.
- Required Na processing rate is 300 (800) [kg/h].
- Yttrium getter needed is in the order of 0.4 (0.7) kg.
- Cycle length is approximately 24 hours.
- Vessel size is approximately 0.25 (0.5) m^3.
- Getter temperature is 270°C; no reliance on permeation barriers.

The system is indicated in Figure 6.7.10-2.

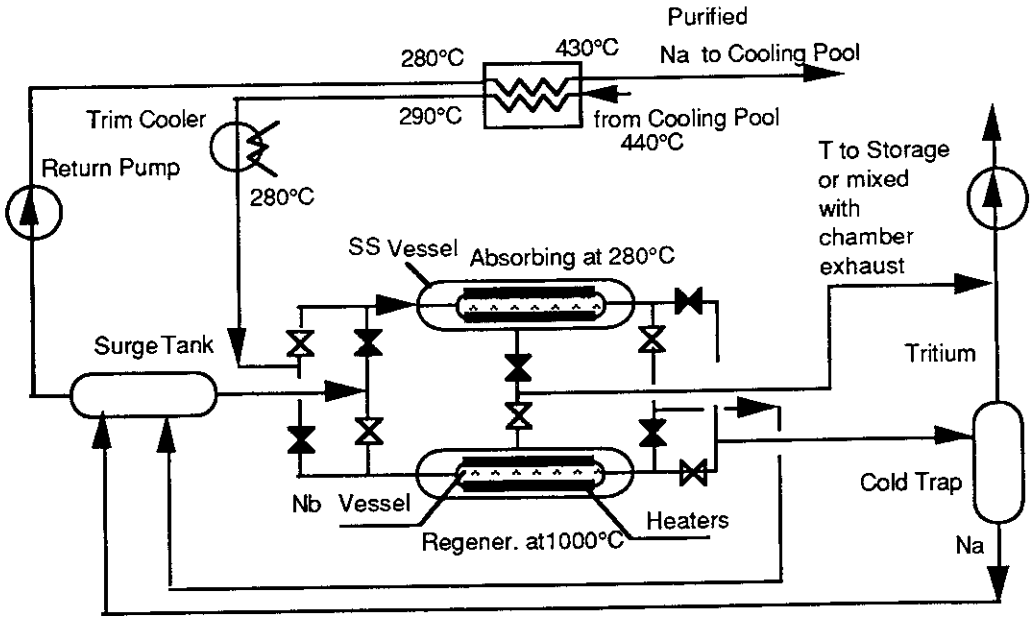

Figure 6.7.10-2. Recovery of Tritium from Na by Yttrium Gettering

6.7.10.2 Permeation Through SiC - From Breeder Purge Gas to He Coolant - Permeation from the breeder purge gas (at atmospheric pressure) to the coolant would take place through the silicon-carbide heat transfer area. The

Use or disclosure of data subject to title page restriction

conditions on the breeder side are determined by the breeder purge gas-helium which is at 10 Bar. The permeation investigation was done with the following parameters:

- Partial pressure of tritium is estimated to be in the range of 1-10 Pa; namely, there is 0.1% hydrogen in the purge gas and the tritium dilution is 1:20.
- Breeder temperature is 725 K.
- Size of the heat transfer area is assumed $4x10^5$ (m^2).
- Wall thickness is 3 mm.

The permeation was found to be in the range of 40 milli-Ci/day. This is substantially less than the 10 Ci/day release limit and consequently no tritium recovery from the helium coolant will be required.

6.7.11 Solids Removal from First Wall Protection - It is assumed that the lead used for first wall cooling will be purified to the degree required prior to use in the reaction chamber. The in-process generation of impurities can be recognized in the following categories:

- Gaseous Impurities – These are assumed to be not soluble in Pb to the extent that such removal is required. It was analyzed that the only substance of concern, tritium, will not be possible to remove from Pb to the extent that tritium permeation through the first layer of coolant wall can be avoided. For this reason, no gas removal of dissolved gases is foreseen to be required.
- Solids – The most consistent solid material to be deposited in the Pb is carbon originated from fuel target material, with a laser direct-drive target deposition rate of 160 g/h. The heavy ion, indirect-drive option would have nearly an order of magnitude higher deposition rate. In addition, there could be fractions of structural material corroded, ablated, or otherwise mobilized from the surfaces with which the first wall coolant is in contact. All this material is expected not to form an alloy and will be experienced as free material floating on the surface (C, SiC) or depositing in areas of low turbulence (metals). The light impurities will easily be separated by a static skimmer or alternatively in cyclone type separator. The bottom Pb drain in the reaction chamber will have to be designed to avoid accumulation of C by securing sufficient turbulence to carry the light and insoluble carbon from the chamber. Alternatively, where the Pb flow can be slowed down below the level of turbulence when carbon can separate, in situ separation can be applied.
- Impurities Forming an Alloy – One such impurity is potentially identified as bismuth. The normal concentration of bismuth in commercially purified lead is approximately 100 ppm. In addition, the production rate of bismuth during operation is approximately 10 ppm/MW-yr/m^2. The goal of the initial and on-line separation system is to maintain bismuth concentration at the 1 ppm level, mainly to improve on the hazard potential. The bismuth separation will not be a simple task since its occurrence is as an alloy with Pb.

Use or disclosure of data subject to title page restriction

6.7.12 Tritiated Waste Processing - Tritiated solid waste processing will rely on conventional fission processes. Large tritiated components such as breeder blanket modules will be removed only after in-situ surface and internal decontamination occurs to the optimum degree. Decontamination of the first wall will consist of removing the Pb coolant and, subsequently, plasma discharge cleaning, with inert gas purge to follow. The tritium-carrying inert gases would be purified in processes described in Sections 6.7.6 and 6.7.7. Internal decontamination will take place through continuing recirculation of the purge gas and its subsequent purification in the PSA process described in Section 6.7.5.

When the in-situ decontamination is completed, the module is removed and placed into a hot cell for dismantling or packaging for reprocessing The hot cell atmosphere, depending on its composition, will be treated in ADS-type equipment. Breeder material could be de-tritiated by combination of heat, purging, and evacuation. Metal components may be helium glow discharge decontaminated as indicated in Figure 6.7.12-1. [20] The main components of such a system are a furnace, purge gas recirculation loop, tritium extraction system which could be similar to the breeder purge gas separation described in Section 6.7.5, and tritium monitoring devices.

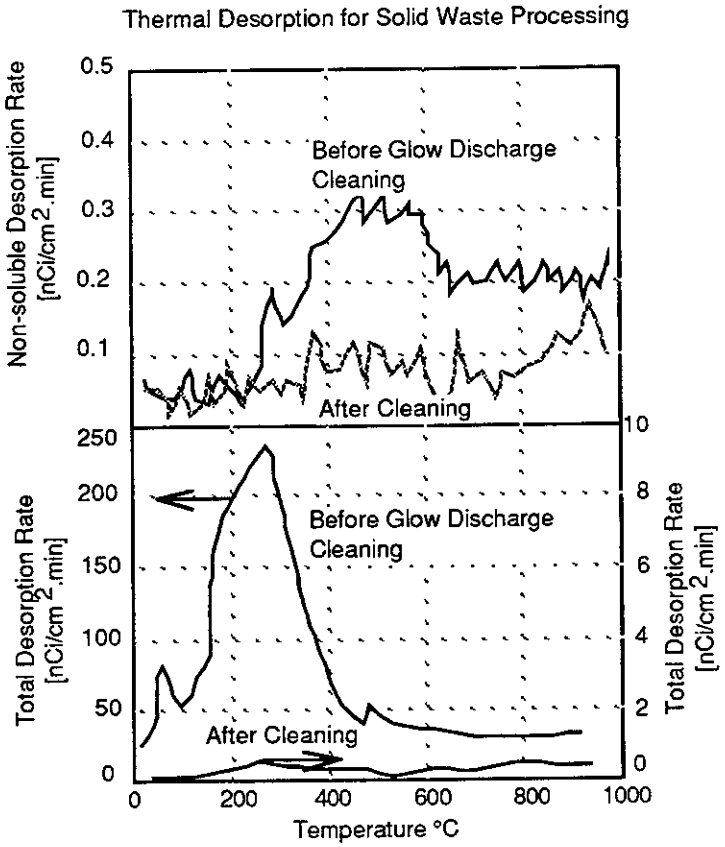

Figure 6.7.12-1. Effects of Glow Discharge Cleaning on the Total Thermal Desorption Spectra

Use or disclosure of data subject to title page restriction

References for 6.7

1. J. Mitsui, Y. Okada, F. Sakai, T. Ide, I. Yamamoto, A. Kanagawa, K. Hirata, T. Yamanishi, K. Okuno, and Y. Naruse, "Separation of Hydrogen Isotopes by an Advanced Thermal Diffusion Column Using Cryogenic Walls," Fusion Technology Vol. 19, May 1991.

2. S. K. Sood, O.K. Kveton, et al., "Tritium Systems Concepts for the Next European Torus (NET)," CFFTP 86-020, October 1986.

3. M. Glugla, R. Penzhorn, "Tritium Experiments with Catalytic Fuel Cleanup Loop," Fourth Topical Meeting on Tritium Technology in Fission, Fusion, and Isotopic Applications, Albuquerque NM, 29 September-4 October 1991.

4. R. S. Wilms, A. Busigin, S. K. Sood, K. M. Kalyanam, B. Dean, "ITER Fuel Cleanup System," Conceptual Design Description, 20 June 1990.

5. J. W. Barnes, et al., "Experience with International (Japanese American) Fusion Fuel Processing Hardware Project," Fourth Topical Meeting on Tritium Technology in Fission, Fusion, and Isotopic Applications, 29 September-4 October 1991, Albuquerque NM.

6. D. K. Sze, R. Clemmer, P. Finn, L. Greenwood, M. Billone, Y. Gohar (Argonne National Laboratory), "Blanket Fuel Processing - Solid Breeders," Presented at the ITER Fuel Cycle Workshop, 1-11 August 1989.

7. S. K. Sood, C. Fong, K. M. Kalyanam, A. Busigin (Nitek Corp.), O. K. Kveton, D. M. Ruthven, "A New Pressure Swing Adsorption (PSA) Process for Recovery of Tritium from the ITER Solid Ceramic Breeder Helium Purge Gas"

8. A. Busigin, S. K. Sood -OH, O. K. Kveton (CFFTP), R. H. Sherman, J. L. Anderson (TSTA/LANL), "ITER Isotope Separation System," Conceptual Design Description Revision 2.0, ITER-IL-FC-9.2-0-18, 5 June 1990.

9. H. Ito, T. Suzuki, T. Takanaga, Y. Matsuda, S. Konishi, Y. Naruse (JAERI) and S. Hirata (Kawasaki Heavy Industries, Ltd), "Separation of Tritium Using Polyimide Membrane."

10. R. W. Spillman, M. B. Sherwin, "Grace Membrane Systems: Gas Separation Membranes: The First Decade," Chemtech, 378-384, June 1990.

11. W. T. Shmayda, N. P. Kherani (OHRD), B. Wallace (CFFTP), F. Mazza (SAES), "Inert Gas Secondary Enclosure Clean-up System."

Use or disclosure of data subject to title page restriction

12. W. T. Shmayda, N. P. Kherani (OHRD), F. M. Ghezzi, G. Bonizzoni (SAES), "St 737 For Tritium Service: An Experimental Evaluation."

13. N. P. Kherani, W. T. Shmayda, R. A. Jalbert, "Tritium Removal from Inert Gases Using ST 198 Alloy," CFFTP 88-039, October 1988.

14. T. Yamanishi, M. Kinoshita, K. Okuno, and H. Yoshida, "A Brief Review of Tritium Recovery from Inert Gases by Uranium Getter Beds," Report JAERI-M85-174, Japan Atomic Energy Research Institute, 1985.

15. G. R. Longhurst, A. G. Heics, R. L. Rossmassler, W. T. Shmayda, "Experimental Assessment of the Consequences of Air-Ingress Accidents in Uranium Beds," 4th Topical Meeting on Tritium, Fission, Fusion, and Isotopic Applications, 29 September-4 October 1991.

16. A. Busigin and S. K. Sood (Ontario Hydro), "Process Simulation with Microcomputers: A Generalized Simulation Code for Application to Fission and Fusion Systems," CNS Bulletin, Vol. 9, No. 3, May/June 1988.

17. E. M. Larsen, M. S. Ortman, K. E. Plute (University of Wisconsin), "Comments on the Hydrogen Solubility Data for Liquid Lead, Lithium, and Lithium-Lead Alloys and Review of a Tritium-Solubility Model for Lithium-Lead Alloys," UWFDM-415 (1981).

18. J. T. Bell, J. D. Redman (Chemistry Division, Oak Ridge National Laboratory), "Tritium Permeation Through Steam Generator Materials," American Chemical Society, 8412-0513- 2/79/0779-331, 1979.

19. R. P. Anantatmula, H. Katsuta, "Hydrogen Trapping by Yttrium in Low Temperature Lithium; Westinghouse Hanford Company, P.O. Box 1970, Richland, Washington 99352," Journal of Nuclear Materials 122 & 123, 1579-1584 (1984).

20. A. B. Antoniazzi, W. T. Shmayda (OHRD), R. A. Surette (AECL), "Decontamination of Tritiated Stainless Steel," CFFTP G-9114, Fourth Topical Meeting on Tritium Technology in Fission, Fusion, and Isotopic Applications, Albuquerque NM, 29 September-4 October 1991.

Use or disclosure of data subject to title page restriction

6.8 Cavity Design and Analysis

The cavity consists of components directly surrounding the exploding targets, including the first wall, blanket, coolant manifolding, vacuum vessel, and shield. These components contain the energy of the blast, absorb the neutrons produced, convert energy into usable heat, breed tritium to sustain the DT fuel cycle, and shield components and personnel from the high radiation environment. Thus, it has a central role in determining the major attributes of the reactor, such as cost, safety and environmental features, engineering attractiveness, and technical feasibility.

Several fundamental principles were established at the beginning of the cavity design process and guided the major study design decisions. The final design results from a large number of trade-offs which incorporated these design goals.

A top priority was the desire for inherent safety and minimum activation. This desire influenced material choices for the first wall, blanket, and shield. The first wall employes low-activation SiC composite. Both long-term and short-term activation is small, thus minimizing waste disposal problems and providing negligible decay heat. Li and LiPb were rejected for safety reasons in favor of a Pb wall protectant. Pb has toxicity and radioactivity concerns, but these were carefully estimated and minimized in the design. The blanket also uses SiC structure and reflector, with low-activation Li_2O breeder and He coolant. The tritium inventory in the breeder was minimized . Use of He at relatively low pressure, together with multiple containment barriers, maked blanket failures unlikely and the consequences benign. The shield material also was chosen to reduce activation. Instead of concrete, Prometheus uses an innovative, highly-effective shield consisting of Al structure, water coolant, and B_4C, Pb, and SiC absorbers.

Another major guiding principle was the incorporation of a sound engineering basis. While not all of the design choices use proven technologies, an attempt was made to minimize required R&D and technical risk by adopting near-term technologies that can be extrapolated from existing data. SiC composites are commercially available today, although some development will be required for use in a neutron radiation environment. Pb has been used as a coolant in the past and technologies for using liquid metal as a coolant are well-developed. Similarly, in the blanket, He cooling is an established technology. The data base for Li_2O is being rapidly developed for the MFE fusion program. While not a driving force in the design, the relevance of Prometheus technology to MFE allows an effective R&D program to be developed with minimum cost and time to completion. The R&D needs are bounded and predictable, since the extrapolation from existing technologies is minimized. Cost penalties can be expected as compared with design concepts which are novel, or even radical; however, this was judged to be a reasonable strategy given the time schedule for fusion development.

Use or disclosure of data
subject to title page restriction

The Prometheus design concept and configuration were chosen following a careful review of existing designs in both the IFE and MFE literature. The design options considered are described in more detail in Chapter 4. Following this survey, a wetted-wall design was adopted with separate first wall and blanket. Wetted walls have many potential engineering advantages, including good beamline accommodation, relaxed repetition rate limitations (as compared with thick films), flexible engineering features, and low inventory and flow rate of the liquid film.

Figures 6.8-1 and 6.8-2 show perspective views of the cavity with and without laser beams. The overall configuration of Prometheus is a low aspect ratio cylinder with hemispherical end caps. This configuration was selected for several reasons:

(1) Maintenance of a cylinder is easier than a sphere. Maintenance paths are all straight vertical lines and the configuration allows independent removal of FW panels and blanket modules.
(2) A cylinder provides better control of film flow. Problems protecting the upper hemisphere can be reduced with higher aspect ratio, in which the distance from the blast to the upper end cap can be maximized.
(3) A cylindrical configuration is more consistent with conventional plant layouts.

The main disadvantage of this concept is nonuniform power distribution and higher peak loads. The higher peak-to-average loading leads to larger size and higher cost for a given total reactor power. To minimize these disadvantages, the aspect ratio is kept relatively low—of the order of 1-2; however, this also limits the advantage of upper end cap protection.

The wall protection scheme chosen for Prometheus uses a thin liquid Pb film supplied from Pb coolant tubes through a porous structure of SiC composite material. The first wall coolant must have acceptable neutronic properties (either breed, multiply neutrons, or be transparent), such that the choices are limited to Li-bearing materials and neutron multipliers. Pb was selected for a number of reasons. Pb has a safety advantage over Li, good neutron multiplication, and chemical compatability with SiC. Its thermophysical properties provide good operating temperature ranges. Its relatively high saturation temperature leads to good conduction heat transfer into the coolant, its boiling point is not too high for materials temperature limits and compatibility, and the relatively high bulk coolant temperature gives good thermal conversion efficiency. Bi and BiPb were considered as alternate multipliers, but they have much higher radioactivity. Some of the outstanding disadvantages of Pb include high density and activation.

Use or disclosure of data
subject to title page restriction

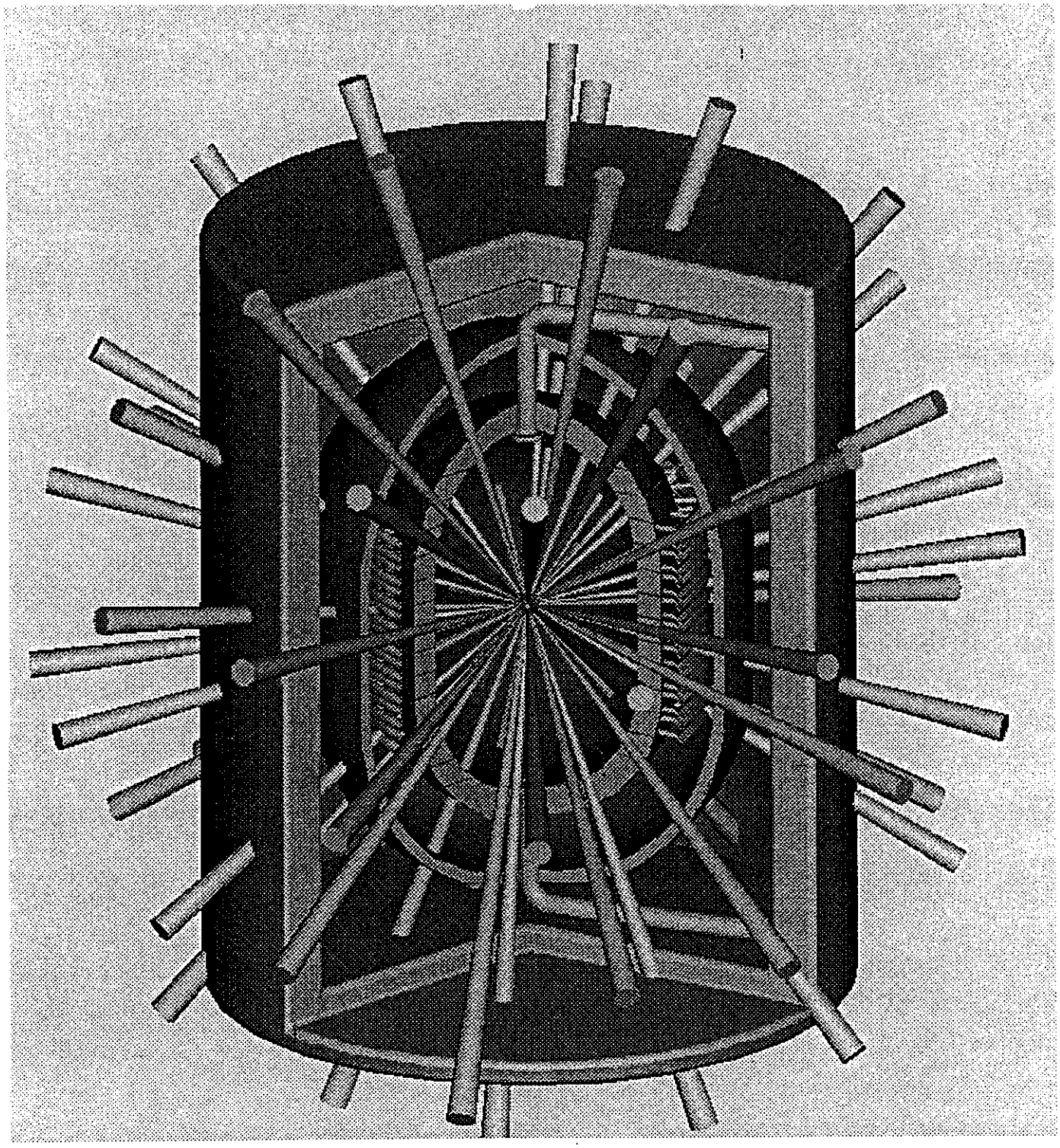

Figure 6.8-1. Perspective View of the Cavity with Laser Beams

Use or disclosure of data
subject to title page restriction

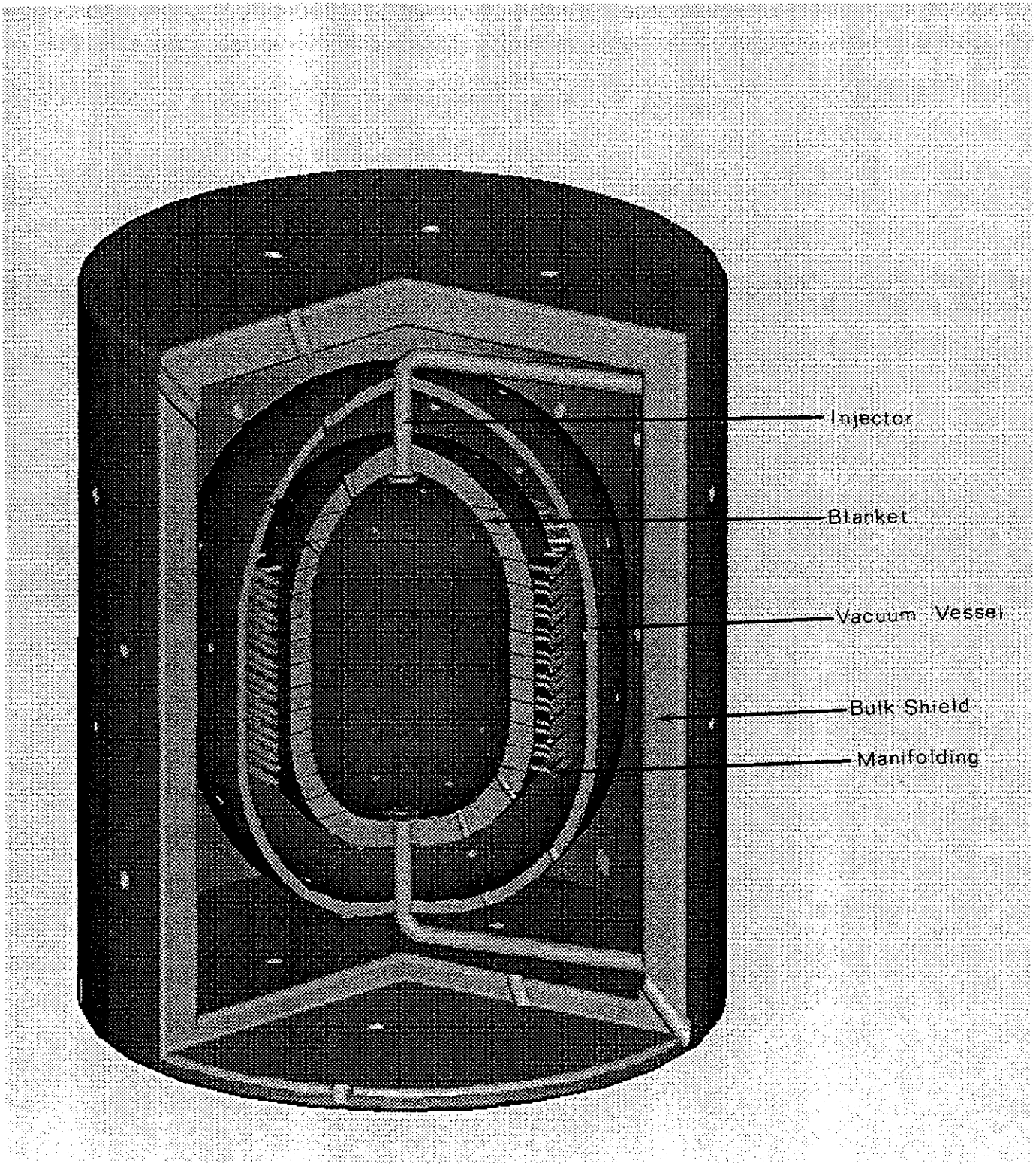

Figure 6.8-2. Perspective View of the Cavity without Laser Beams

McDonnell Douglas Aerospace

Use or disclosure of data
subject to title page restriction

The SiC structure must be flexible enough to withstand cyclic loading from the blast, but strong enough to support itself and the internal pressure of the film. A supply region behind the porous structure serves to slowly feed the liquid and also to remove the heat from the first wall (40% of the total fusion power). Blast energy is removed from the cavity initially by evaporation. During the recondensation phase of each pulse, heat is conducted through the relatively thin film and into the first wall coolant.

Design of the Prometheus wetted wall concept considers several important first wall issues, including: (1) cavity vapor hydrodynamics; (2) limits on cavity clearing time due to the requirment to conduct heat out radially; (3) film flow uniformity, wetting, and drainage; and (4) mechanical response of the first wall system. A detailed description of the first wall system and analysis of the major issues are found in Section 6.8.2.

The first wall system and blanket are physically separated. The environmental conditions and functions performed by these two components are very different; separation allows for better optimization of performance, more flexibility, and good maintenance features. The blanket is protected from the blast and is designed to optimize breeding, energy conversion, reliability, and maintainability. The major penalty is the need for an attachment and locking mechanism and more complicated maintenance scheme.

The first wall system consists of individual plates which are locked into a support system attached to the blanket. The ability to provide removable panels which lock into the blanket is essential to allow more frequent maintenance of the first wall panels and still mitigate the mechanical effects of the blast by absorbing the loads into the blanket and support system.

The blanket consists of several rings through the cylindrical and hemispherical sections. Blanket modules are pre-assembled into the rings, which stack vertically on top of one another. At laser penetration holes, the corresponding module length is shortened to allow for penetration space. The blanket modules are made of SiC and contains a number of U-bend woven SiC tube sheets inside which the pressurized He coolant flows. The Li_2O is placed in packed bed form between the tube sheets and is purged by He flowing along the axis of the module. Use of Li_2O in conjunction with the first wall Pb coolant provide the potential for adequate tritium breeding without the need for Be as a multiplier. A more detailed description of the blanket is found in Section 6.8.3. Neutronics, thermal hydraulics, thermomechanics, and tritium analyses are presented.

Use or disclosure of data
subject to title page restriction

The first wall and blanket are maintained by removing the upper end cap. The first wall panels can then be removed separately, or the entire blanket rings can be lifted. Preliminary analysis suggests that the first wall service life is of the order of five years, whereas the blanket might last ten years with the heavy ion option slightly less due to the higher power density.

Figure 6.8-3 shows the radial build from the first wall through the shield which is typical for both the -L and -H option. The cavity radius is nominally 4.5 m for the Prometheus-H cavity. Relatively large manifolding is needed behind the blanket to keep the He coolant pressure drop low. The manifolding is made from SiC composite up to the vacuum vessel and shield, where a transition is made to more conventional ferritic/martensitic steel. The vacuum vessel is also made of steel.

The radiation shield for Prometheus has been designed to protect components and personnel. It consists of (1) a bulk shield circumscribing the blanket, (2) penetration shielding around the driver beam lines and vacuum ducts, and (3) a biological shield, which also serves as the reactor building wall. The system was designed to achieve several goals: (a) the biological dose rate outside the reactor building during operation is below 2.5 mrem/hr, (b) neutron-induced activation in all components outside the blanket but inside the reactor building (e.g., heat transport system and steam generators) is minimized, and (c) the biological dose rate in the reactor building outside the blanket decays to <2.5 mrem/hr within 48 hours after shutdown in order to permit personnel access, if needed, although the reactor system is designed for fully-remote maintenance operations. More detail can be found in Section 6.8.4.

Safety and environmental issues are treated separately in Section 6.8.5. Safety and environmental concerns weighed heavily in the design choices made in Prometheus, and contribute to the overall attractiveness of the concept.

Use or disclosure of data
subject to title page restriction

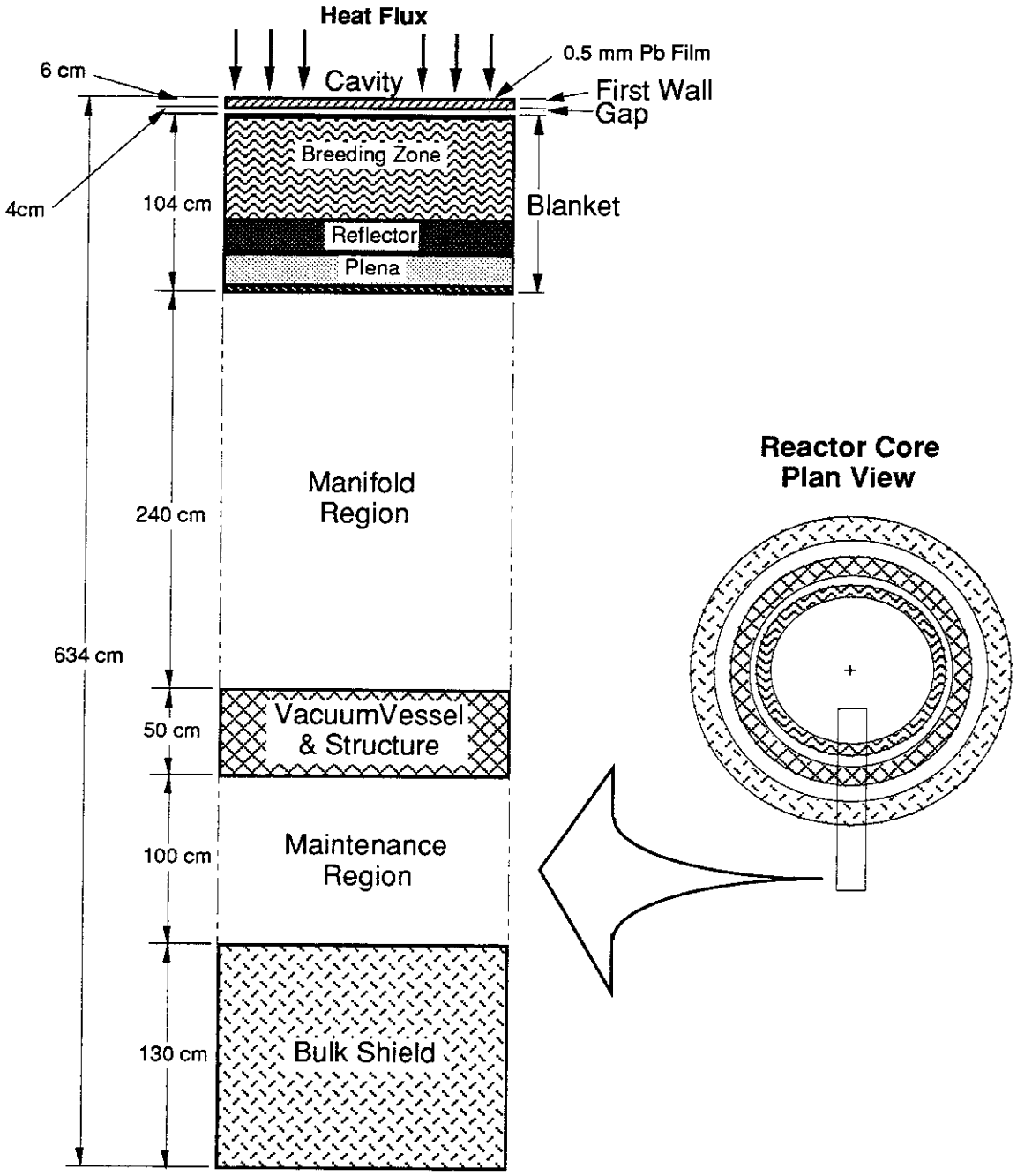

Figure 6.8-3 Radial Build of the Cavity

Use or disclosure of data
subject to title page restriction

This page intentionally left blank.

Use or disclosure of data
subject to title page restriction

6.8.1 Neutronics Analysis

6.8.1.1 Introduction – The energy and angular distributions of neutrons incident on the first wall of IFE reactors differ appreciably from those found in MFE reactors. Neutrons (and gamma-rays) generated from the microexplosion at the center of the cavity are incident perpendicular to the first wall, particularly if the chamber is close to spherical in shape, whereas in MFE reactors they impinge on the first wall with various incident angles. Thus, to produce the same wall load or fluence at the first wall (expressed either in MW/m^2 or $MW\text{-}y/m^2$), more neutrons are required in the case of MFE reactors as compared to ICF reactors. Furthermore, the incident neutrons in IFE reactors are degraded in energy (~12 MeV) due to their slowing down process in the target after the microexplosion, whereas in MFE their energies are rather well defined around 14.1 MeV. Therefore, more neutrons with degraded incident energies are required to produce a given wall load as compared to the MFE case. These angular and spectral differences impact the neutronics characteristics of the first wall and blanket systems, particularly the damage parameters in the first wall.

In the present study, target neutronics calculations were not performed. Instead, the incident neutron spectrum of the SIRIUS-M[1] reactor design was used. About 78% of the target neutrons are 14.1 MeV neutrons, 21% are in the energy range 3.5-14.1 MeV and ~1% are in the energy range 1.5 MeV-3.5 MeV. Thus, the average neutron energy incident on the first wall/blanket systems is ~12.87 MeV. No gamma-rays were considered from the target. In addition, time-dependent calculations were not performed. This neglects effects due to instantaneous heating or damage rates which are time-dependent due to differences in the arrival time of neutrons to the first wall.

Time-averaged values are reported below for the key parameters, including blanket power multiplication (M) and tritium breeding ratio (TBR).

6.8.1.2 Base Case Configuration – The cavity consists of four distinct systems: the first wall system, blanket/reflector/plena system, vacuum vessel, and bulk shield system. Figure 6.8.1-1 shows the compositions and radial build through the center of the cavity.

The first wall system carries away the energy deposited by the x-rays and debris, as well as the nuclear heating resulting from neutron and gamma-ray transport in the first wall system. Energy also is deposited in the lead film that covers the inner surface of the cavity. Lead is a good neutron multiplier and has been proposed for that purpose in several conceptual blanket designs.

Use or disclosure of data
subject to title page restriction

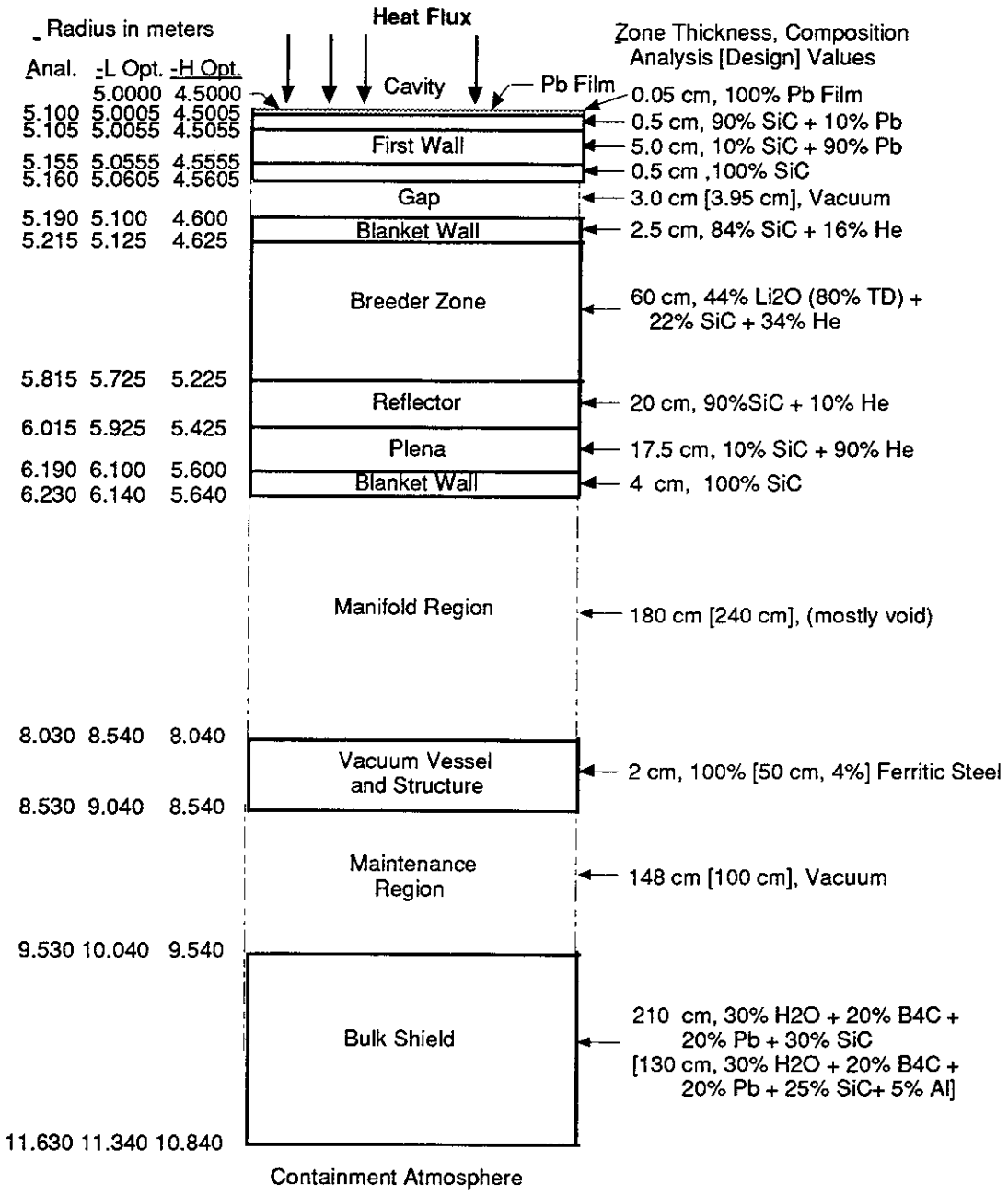

Figure 6.8.1-1 Material Composition in the 1-D Cavity Model

Use or disclosure of data
subject to title page restriction

Beryllium was considered for use in the blanket to enhance the power multiplication and tritium production rate. Its neutron multiplication characteristics are superior to lead. Neutron multiplication basically occurs through (n,2n) reactions whose threshold energy is lower for beryllium (~2.8 MeV) than for lead (~7.5 MeV), although at ~12 MeV, the (n,2n) cross-section is larger in lead than in beryllium (~2 barns for lead, 0.5 barns for beryllium). With 5 cm of Pb in the first wall region, Be is not required in the blanket and so the baseline design has no Be.

Lead flows through near-rectangular channels in a zone of width 5 cm and has been optimized to have a large volume ratio of 9:1 compared with the structural material (SiC) in order to enhance tritium breeding ratio and power multiplication. A porous SiC first wall is used with ~10% by volume Pb seeping out to the inner surface of the cavity. The back wall of the first wall system is a 100% SiC of a thickness 0.5 cm.

The blanket/reflector/plena (BRP) system utilizes SiC everywhere as the structural material. Neutronically, SiC has lower absorption cross-section for neutrons as compared to iron-based structure, leading to a higher chance for neutrons to be absorbed in lithium. On the other hand, energy multiplication in steels is normally larger than in SiC due to the larger exothermic (n,γ) reactions in steels. However, the high activation level in steels is a concern which was one of the motivations behind selecting SiC as the structural material in Prometheus design. Additionally, SiC was selected as the reflector material behind the breeding zone due to the high neutrons reflectivity characteristics of carbon. The thickness of the breeding zone was selected to be 60 cm based on parametric analysis which is discussed in Section 6.8.3.3. It consists of 43.6% by volume Li_2O with theoretical density (T.D.) of 80%, 22% SiC, and helium as the coolant (34.4%). The blanket first wall is 2.5-cm thick and is cooled with helium (84%SiC, 16%He). The reflector and plena zones are 20-cm and 17.5-cm thick, respectively, with a 4-cm 100% SiC back wall.

The manifold region is assumed to be 180-cm thick and is mostly void. The vacuum vessel is 2-cm thick made of 100% ferritic steel, followed by a maintenance zone of 148 cm. The final design resulted in a manifold region 240-cm thick, a vacuum vessel 50-cm thick (4% steel), and a maintenance region 100-cm thick. The design of the bulk shield in Prometheus calls for allowing personnel access 48 hours after shutdown. The analysis used an effective shielding material made of 20%Pb, 20%B_4C, 30%SiC, and 30% water. The final design shield used 20% Pb, 20% B_4C, 25% SiC, 30% water, and 5% aluminum structure. The flux attenuation characteristics of this shielding material is approximately an order of magnitude reduction in neutron flux level every 20 cm (see Section 6.8.4). Based on adopting a flux level of 1×10^6 n/cm^2•sec at the back of the shield during operation such that personnel access is permitted 24 hours after shutdown (for a more conservative estimate, see

Use or disclosure of data subject to title page restriction

Section 6.8.4), the bulk shield thickness was estimated to be 130 cm. Reinforced concrete (87% concrete, 8% carbon-steel, and 5% water) was also examined as an option for the bulk shield material. The neutron flux attenuation characteristics for this material was calculated to be an order of magnitude reduction in the neutron flux level for every 25 cm. Thus, a thicker shield is required in this case as compared to the Pb/B_4C composite shield when personnel access to the inside of the reactor building is permitted one day after shutdown. By adopting this design criterion, the required bulk shield thickness in the concrete case is estimated to be 165 cm.

6.8.1.3 Results – The neutronics parameters of the base design were calculated by performing one-dimensional calculations in spherical geometry using the ANISN 1-D discrete ordinates transport code[2] along with the the MATXS5 (30-g neutrons, 21-g) library[3] based on ENDF/B-V nuclear data. The radial build is shown in Figures 6.8-1 and 6.8.1-1. Figure 6.8.1-1 also shows the material volume fractions used in the calculations. This final baseline design evolved from parametric studies presented in Section 6.8.3.3. Note that a bulk shield thickness of 210 cm was considered in the calculations, while a thinner shield was adopted in the final design as discussed above. It was shown that tritium breeding ratio and blanket power multiplication are insensitive to an increase in the bulk shield thickness beyond ~1 m.

The results reported here are based on an incident neutron power of 2027 MW in the laser reactor design (1,818 MW in the heavy ion design). For an average neutron energy of 12.87 MeV, the incident neutron source is estimated to be 9.83×10^{20} n/sec (8.82×10^{20} n/sec in the heavy reactor design). Also, while the first wall in the model shown in Figure 6.8.1-1 is placed at a radial distance of 510 cm from the cavity center, the cavity radius in the final laser reactor design is 500 cm. Thus, a correction factor of $(510/500)^2 \sim 1.04$ should be applied to the absolute local profiles reported here. Likewise, the cavity radius in the heavy ion reactor design is 450 cm, and the factor to be applied to local values in this case is $(510/450)^2 \cdot (8.82/9.83) \sim 1.15$.

Table 6.8.1-1 summarizes the key neutronics parameters for the baseline design of Prometheus-L and -H. The heating rates, power multiplication, damage rates in Si, and tritium production rates are described in more detail below.

Cavity Power Multiplication (M) and Nuclear Heating Rate Profiles – Figure 6.8.1-2 shows the nuclear heating rate in the baseline design as a function of the radial distance from the cavity center. Figures 6.8.1-3, 6.8.1-4, and 6.8.1-5 show these heating profiles in the first wall system, the blanket/reflector/plena system, and the bulk shield system (concrete case), respectively.

Use or disclosure of data
subject to title page restriction

Table 6.8.1-1 Key Neutronics Parameters for Prometheus-L and Prometheus-H

	-L	-H
^{6}Li Enrichment	25%	25%
TBR	1.2	1.2
Li Annual Burnup	0.5%	0.6%
Peak-to-Average Burnup	3	3
Net Power Multiplication	1.14	1.14
Peak Power Densities (MW/m^3)		
Pb Film	32	37
Pb Coolant	28	32
First Wall	24	28
Breeder	20	23

In the first wall system, the largest power density takes place in the lead film covering the inner surface of the cavity since this film is the first material zone to intercept the highly energetic neutrons resulting from the blast. The power density in this film is ~32 MW/m^3 and is due mainly to heat deposited by gamma rays produced by neutron interactions with lead, particularly inelastic scattering reactions. The energy deposited by these gamma rays is ~25 MW/m^3 while the energy deposited by neutrons is only ~8 MW/m^3. Gamma-ray heating also dominates the total heating rate in the lead channel zone (by ~80%) where the average total heating rate is ~25 MW/m^3. The total heating rate in the first wall (90%SiC, 10%Pb) is 24 MW/m^3 and is dominated by neutron heating (~75%) as can be seen from Figure 6.8.1-3.

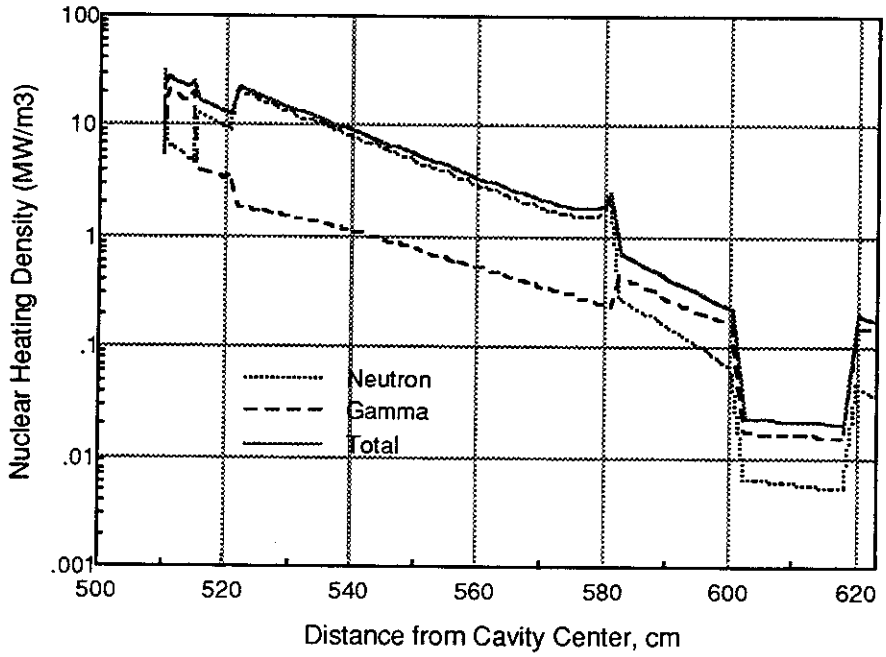

Figure 6.8.1-2. Nuclear Heating Rate Profile in the Baseline Design

Use or disclosure of data
subject to title page restriction

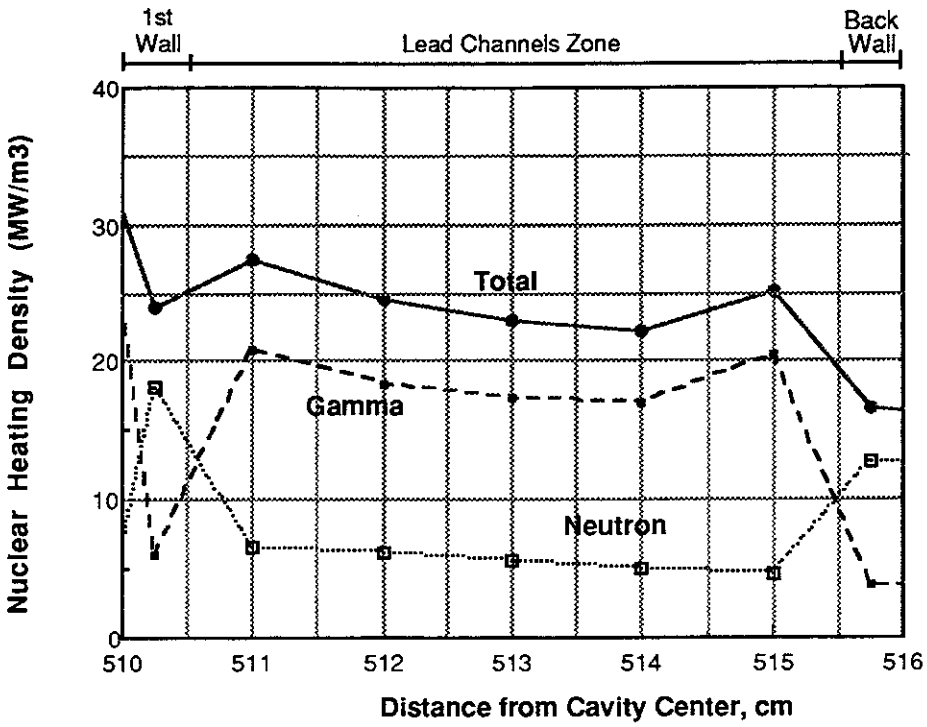

Figure 6.8.1-3 Nuclear Heating Rate Profile in the First Wall System

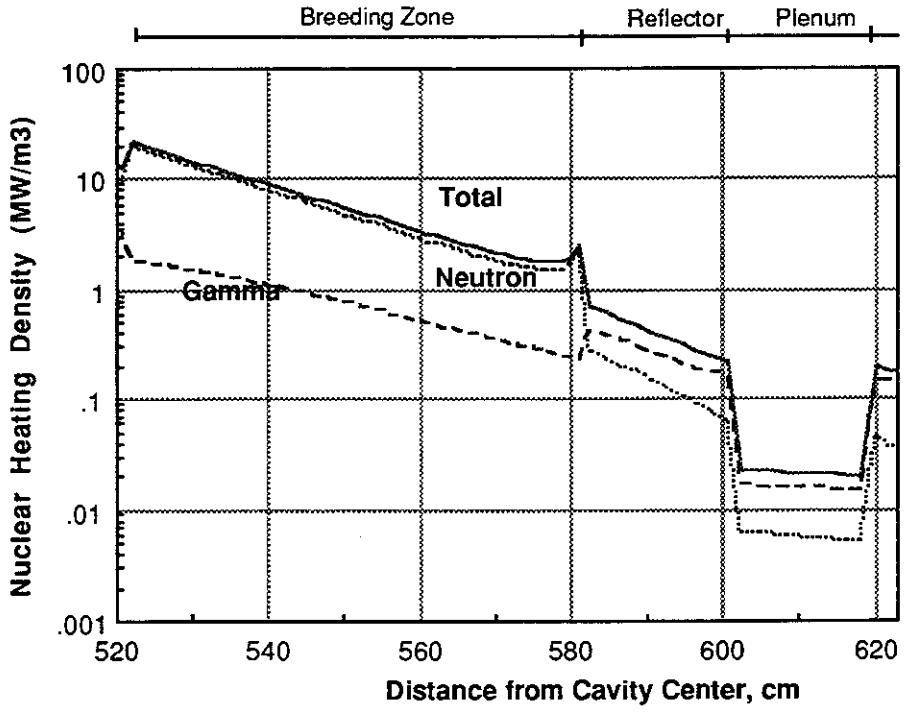

Figure 6.8.1-4 Nuclear Heating Rate Profile in the Blanket/Reflector/Plena System

Use or disclosure of data
subject to title page restriction

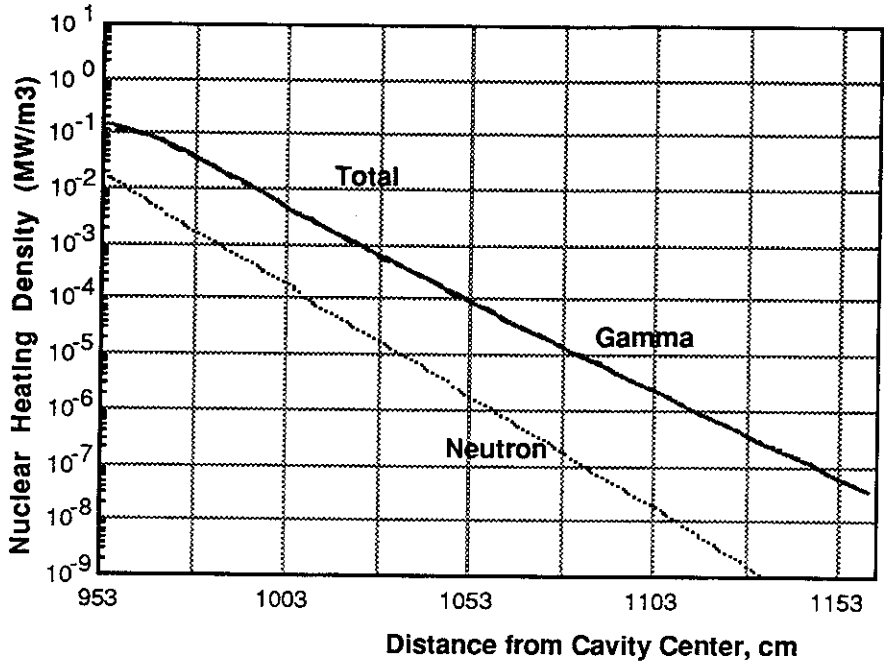

Figure 6.8.1-5 Nuclear Heating Rate Profile in the Concrete Bulk Shield Case

The largest nuclear heating rate in the breeding zone is ~20 MW/m^3 just behind the first wall of the blanket/reflector/plena system (see Figure 6.8.1-4). In the breeding zone, nuclear heating is mainly due to neutron absorption events in ^{6}Li through the tritium producing reactions, (n,α), for an enrichment of 25% in ^{6}Li. This enrichment level was shown to be the optimal value for larger TBR (see Section 6.8.3.3). The power density in the first wall of the blanket (cooled with helium) is ~12 MW/m^3. The average heating rates in the reflector and the plena regions are ~0.5 MW/m^3 and ~0.02 MW/m^3, respectively. The attainable heating rate level in the vacuum vessel is ~0.5 MW/m^3.

Total heating rate in the bulk shield is generally low. In the concrete shield case, the maximum heating rate at the front edge of the shield is ~0.15 MW/m^3 and the local values drop noticeably by distance (see Figure 6.8.1-5). After 1 m depth, the local heating rate drops ~3 orders of magnitude; that is, an order of magnitude reduction in local heating takes place for every ~33 cm. The nuclear heating in this type of shielding material is mainly due to gamma-ray heating. The gamma flux level in this concrete shield is about 1-2.5 orders of magnitude larger than the neutron flux level, with a larger difference (a factor of 2.5) occurring at a depth of ~165 cm (see Section 6.8.4).

Use or disclosure of data
subject to title page restriction

As is shown in Section 6.8.4, the gamma flux in the concrete shield attenuates slower than the neutron flux during operation. The nuclear heating profile in the concrete shield (dominated by gamma-ray heating) has the same attenuation characteristics as the gamma flux and biological dose (in mremlhr) which is an order of magnitude reduction in their values occurs for about every 33 cm. At a distance of 165 cm, the heating rate is as low as ~10^{-6} MW/m^3.

Table 6.8.1-2 summarizes the fraction of power deposited in the various zones of the cavity. In the table, the integrated power is expressed in Joules per incident source neutron and, thus, the entries are independent of the total fusion power, neutron yield, etc. To convert the entries given in Table 6.8.1-2 to absolute values (in MW), the following formula could be used:

(power deposited, J/n) • (incident neutron power, MW) • 4.85 x 10^{11}

or alternatively,

(% of power deposited, by zone) • (incident neutron power, MW) • 1.14,

where the cavity power multiplication factor, M, is ~1.14. The total nuclear power in the cavity is the product of the incident neutron power and the cavity power multiplication, M.

In the case of the laser reactor (neutron power ~2027 MW), the cavity nuclear power is 2311 MW. It is ~2073 MW in the heavy ion reactor design. As shown in Table 6.8.1-2, ~21% of this power is deposited in the first wall system while ~77% is deposited in the blanket/reflector/plena system. The fraction of the cavity nuclear power deposited in the bulk shield is low (1.4%).

Table 6.8.1-3 summarizes the cavity energy balance, assuming a yield of 497 MJ and repetition rate of 5.6 Hz for the laser reactor while these values are 719 MW and 3.5 Hz in the heavy ion reactor, respectively. The fraction of the fusion power (2807 MW) in the laser reactor carried away by neutrons, debris, and x-rays are 72.23%, 21.53%, and 6.24%, respectively. These fractions are slightly different in the heavy ion reactor whose fusion power is ~2543 MW. The power load in the first wall system includes both surface heating (from the x-rays and debris) and the nuclear heating resulting from neutrons and gamma-ray interactions with the first wall system materials. By accounting to the power loads in the various components of the cavity, the total thermal power is 3092 MW in the laser reactor case and 2797 MW in the heavy ion reactor case.

Use or disclosure of data
subject to title page restriction

Table 6.8.1-2 Nuclear Heating in Prometheus First Wall/Blanket/Shield Systems (Per Incident Neutron)*

System	Zone Number	Zone Name	Material Composition	Thickness (cm)	Power Deposited J/neutron	% (by zone)	% (by system)
First Wall Protection System		Lead film	100% Pb	0.05	5.345-15	0.288	
	1	Front SiC Layer	90% SiC, 10% Pb	0.5	4.084-14	1.743	
	2	Lead tubes	10% SiC, 90% Pb	5	4.188-13	17.869	
	3	Back SiC Layer	100% SiC	0.5	2.896-14	1.236	(21.076)
Gap	4	Vacuum	—	3	—	—	(0)
Blanket/Reflector System	5	Blanket First Wall	84% SiC, 16% He	2.5	1.142-13	4.873	
	6	Breeding Zone	43.6% Li2O, (0.8 TD), 22% SiC, 34.4% He	60	1.649-12	70.359	
	7	Reflector	90% SiC, 10% He	20	3.795-14	1.619	
	8	Plenum	10% SiC, 90% He	17.5	1.834-15	0.078	
	9	Back SiC Wall	100% SiC	4	3.758-15	0.160	(77.089)
Manifolds	10	Vacuum	—	180	—	—	(0)
Vacuum Vessel and Structure	11	Vacuum Vessel	100% Ferritic Steel in the first 2 cm, rest is vacuum	50	9.101-15	0.388	(0.388)
Maintenance Gap	12	Vacuum	—	100	—	—	(0)
Bulk Shield	13	Reinforced concrete cooled with water	87% Concrete 8% Ferritic Steel 5% Water	210	3.386-14	1.445	(1.445)
Total					2.347-12	100	100
Power Multiplication (M)					(1.14)+		

* Entries given are per incident source neutron.

\+ Evaluted as energy deposited in the entire system (MeV) divided by the average energy per incident source neutron (of SIRIUS-M type) of ~12.87 MeV

(1) Read as 5.345×10^{-15}

Damage Rate Profile – Figure 6.8.1-6 shows the displacement per atom (dpa) per full power year (FPY) in silicon as a function of distance from the cavity center. In the 0.5-cm thick first wall (90% SiC, 10%Pb), the maximum dpa rate in silicon is ~127 dpa per full power year based on 9.83×10^{20} n/sec incident neutron source of an average energy of 12.87 MeV in the laser reactor. This value is ~146 dpa/FPY in the heavy ion reactor. The average wall loads in the laser reactor is 6.5 MW/m^2 and 7.3 MW/m^2 in the heavy ion reactor. The dpa rate in the first wall of the blanket (2.5-cm thick, 84%SiC, 16%He) is ~85 dpa/FPY in the laser reactor and is ~98 dpa/FPY in the heavy ion reactor design.

Use or disclosure of data subject to title page restriction

Table 6.8.1-3 Cavity Energy Balance

	Laser	Heavy Ion	Units
Total Yield	497	719	MJ
Repetition Rate	5.65	3.54	Hz
Fusion Power	2807	2543	MW
Yield Distribution			
X-ray	6.24	6.40	%
Debris	21.53	22.11	%
Neutrons	72.23	71.49	%
Yields			
X-rays	31	46	MJ
Debris	107	159	MJ
Neutrons	359	514	MJ
Power			
Surface Heating	780	725	MW
Neutrons	2027	1818	MW
Neutron Source Strength*	9.83×10^{20}	8.82×10^{20}	n/sec
FW/Blanket/Shield Characteristics			
TBR	1.2	1.2	
Power Multiplication	1.14	1.14	
Nuclear Power	2311	2073	MW
Nuclear Power Distribution			
First Wall System	21.1	21.1	%
Blanket/Reflector/Plenum	77.1	77.1	%
Vacuum Vessel	0.4	0.4	%
Shield	1.4	1.4	%
Power Loads			
First Wall System	1268	1162	MW
Blanket/Reflector/Plenum	1782	1598	MW
Vacuum Vessel	9.2	8.3	MW
Shield	32.4	29	MW
Total Thermal Power	3092	2797	MW

* Average incident neutron energy ~12.87 MeV

Use or disclosure of data
subject to title page restriction

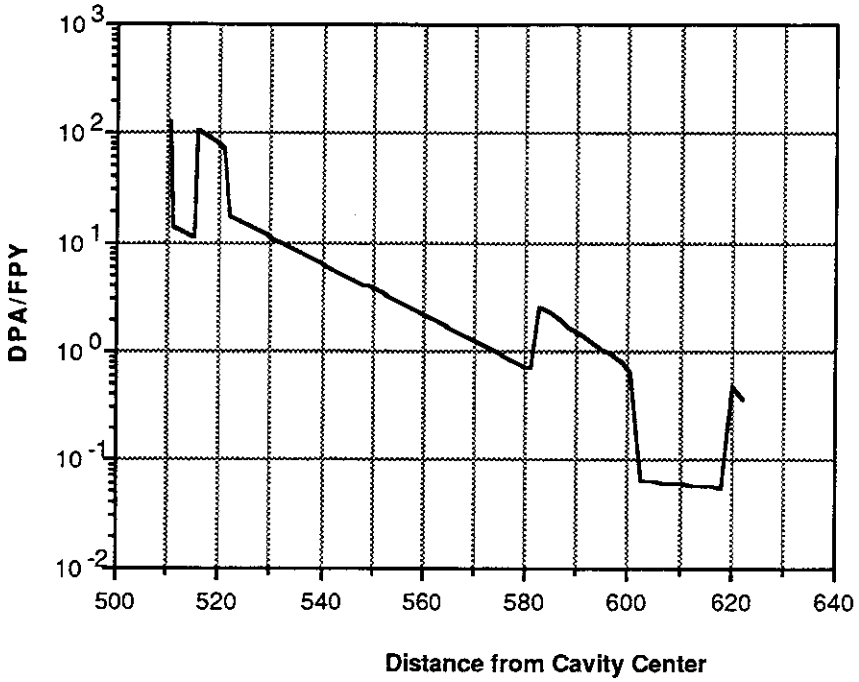

Figure 6.8.1-6 Displacement Per Atom Per Full Power Year (dpa/FPY) in Silicon

Tritium Breeding Ratio (TBR) and Tritium Production Profiles – Based on the parametric studies reported in Section 6.8.3.3 on the variation of the TBR as a function of the ^{6}Li enrichment, lead zone thickness in the first wall system, and the breeding zone thickness, the optimal value attainable in the base design is TBR ~1.2. The profiles for tritium production rate (TPR) from ^{6}Li (T-6) and from ^{7}Li (T-7) are shown in Figure 6.8.1-7. The TPR from ^{6}Li is more than an order of magnitude larger than the TPR from ^{7}Li just behind the first wall of the blanket/reflector/plena system and this difference narrows towards the back locations in the breeding zone. The T-7 profile is more or less steady throughout the blanket while T-6 profile is steep, particularly at the front locations in the breeding zone.

Neutron Spectrum - The neutron flux in the first wall of the FWS and in the first wall of the blanket/reflector/plena system is shown in Figure 6.8.1-8 for each of the energy groups (30-group) used in the 1-D transport calculations for the baseline configuration. The results shown are expressed in terms of flux per incident source neutron ($n/cm^2 \cdot sec \cdot n$). Figure 6.8.1-9 shows the absolute values of the flux ($n/cm^2 \cdot sec$) for incident neutron source of 9.83×10^{20} n/sec which corresponds to neutron power of 2027 MW in the laser reactor design. In the heavy ion reactor, the absolute values of the flux can be obtained from Figure 6.8.1-9 (and Figure 6.8.1-11 below) by applying a factor of 1.15. The total neutron flux is the summation of each group flux shown in Figures 6.8.1-8 and 6.8.1-9.

Use or disclosure of data
subject to title page restriction

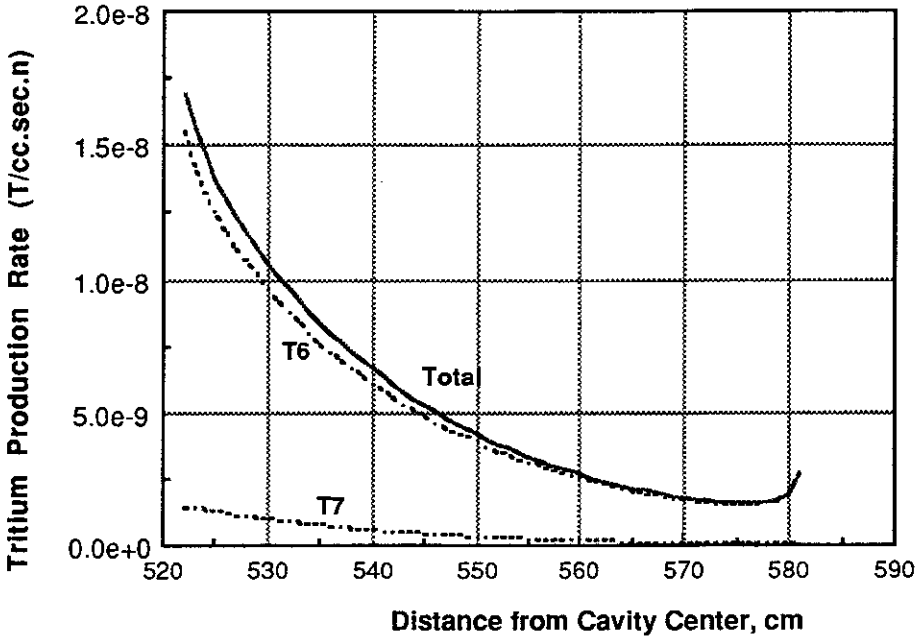

Figure 6.8.1-7 Tritium Production Rate (TPR) Profile in the Breeding Zone Per Incident Neutron

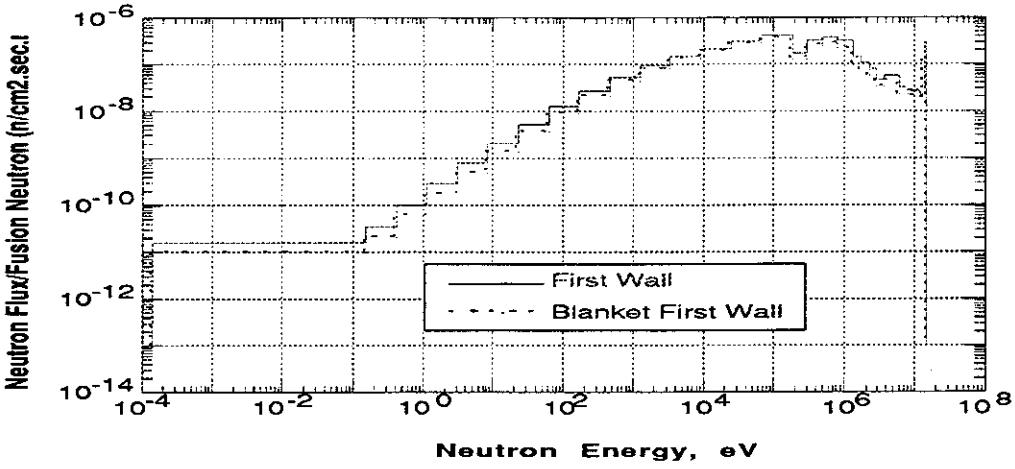

Figure 6.8.1-8. Neutron Flux (by Group) in the First Wall of the FWS and in the First Wall of the Blanket/Reflector/Plena System per Incident Neutron

Use or disclosure of data
subject to title page restriction

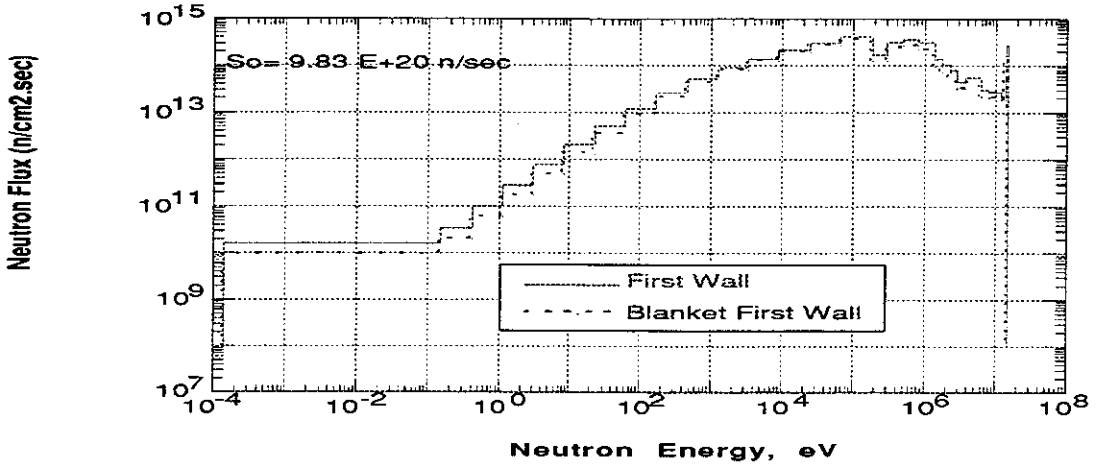

Figure 6.8.1-9. Neutron Flux (by Group) in the FW of the FWS and the FW of the Blanket/Reflector/Plena System (n/cm2•sec)

The fraction of the uncollided neutrons (14.1 MeV) that are confined in the first energy group (13.5 MeV-15.0 MeV) of the total flux (3.22×10^{15} n/cm^2•sec) in the FW of the FWS is ~8.6%. This is to be compared to the percentage of the 14.1 MeV neutrons in the incident neutron source which is ~78%. This indicates that an appreciable softer neutron component exists in the total flux in the FW due to neutrons colliding with the FWS materials (and blanket) and reflected back to the first wall. The total neutron flux above 0.2 MeV in the FW of the FWS is ~1.97×10^{15} n/ cm^2•sec and is ~1.37×10^{15} n/cm^2•sec in the FW of the B/R/P system. These neutrons represent ~61% and ~55% of the total neutron flux at these locations, respectively. (The total neutron flux in the FW of the B/R/P system is ~2.47×10^{15} n/cm^2•sec.) Most of these neutrons are in the energy range 0.2 MeV-2.2 MeV (~46% and ~43% of the total flux, respectively).

Figure 6.8.1-10 and 6.8.1-11 show the neutron flux above 0.2 MeV per source neutron and for incident neutron source of 9.83×10^{20}n/sec. The total fluxes above 0.2 MeV are 1.97×10^{15} n/cm^2•sec and 1.37×10^{15} n/cm^2•sec in the FW and in the FW of the B/R/P systems, respectively. The corresponding fluxes in the heavy ion reactor are 2.27×10^{15} n/cm^2•sec and 1.58×10^{15} n/cm^2•sec. These fluxes were used to estimate the lifetime of the FWS and the blanket.

Use or disclosure of data
subject to title page restriction

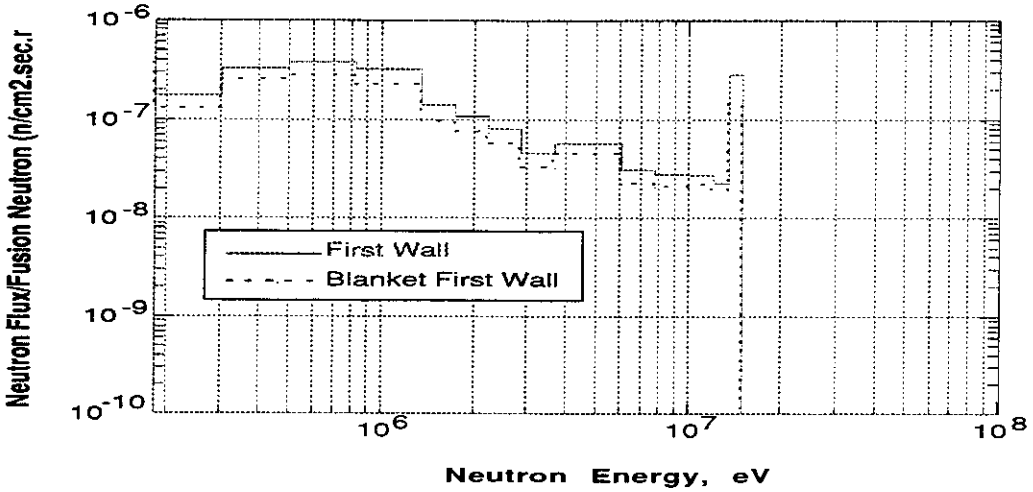

Figure 6.8.1-10: Neutron Flux Above 0.2 MeV in the FW of the FWS and in the FW of the Blanket/Reflector/Plena System per Incident Neutron (n/cm2•sec•n)

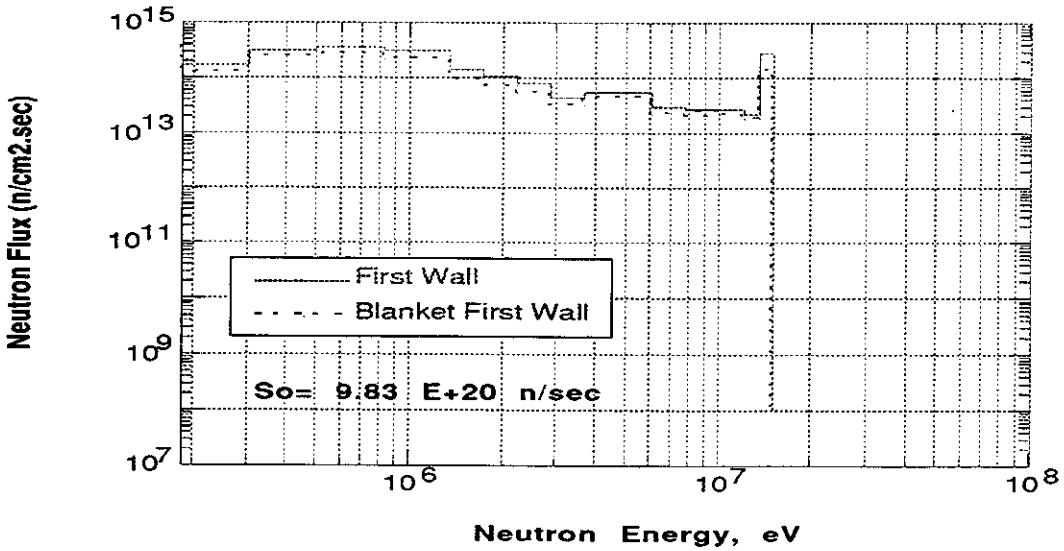

Figure 6.8.1-11: Neutron Flux (by Group) in the FW of the FWS and in the FW of the Blanket/Reflector/Plena System (n/cm2•sec)

Use or disclosure of data
subject to title page restriction

References for 6.8.1

1. B. Badger, et al.,"SIRIUS-M: A Symmetric Illumination, Internally Confined Direct Drive Material Test Facility," UWFDM-711, Fusion Technology Institute, University of Wisconsin, October 1986.

2. W. W. Engle, Jr., "A User's Manual for ANISN," K-1693 (1967).

3. R. E. MacFarlane, " TRANSX-CTR: A Code for Interfacing MATXS Cross-Section Libraries to Nuclear Transport Codes for Fusion Systems Analysis," LA-9863-MS, Los Alamos National Laboratory, February 1984.

Use or disclosure of data
subject to title page restriction

This page intentionally left blank.

Use or disclosure of data
subject to title page restriction

6.8.2 First Wall Protection System

6.8.2.1 Introduction and Overall Configuration – The first wall system surrounds the entire cavity chamber. It uses a SiC/SiC composite structural material and Pb coolant and film protectant. The cavity has a central cylindrical section and upper and lower end caps. The baseline design has a cylinder height equal to the radius. Longer cylinders were also considered, but rejected primarily due to their lower average power density.

As shown earlier in Figure 6.8-1, the Prometheus-L cavity is encircled and penetrated by 60 beamlines. Accommodation of these beams is a very challenging engineering problem, but the choice of a wetted wall makes the problem more tractable than with a thick liquid curtain.

The first wall system consists of a series of panels 2-m wide which are lowered into the cavity vertically. Figure 6.8.2-2 shows a cross sectional view of a first wall panel. The cooling channels are 5-cm thick to provide neutron multiplication needed for tritium breeding. The first wall is kept thin (5 mm) to provide good heat conduction into the coolant. The film thickness is also minimized for good heat transfer as well as to reduce the problem of liquid entering the cavity.

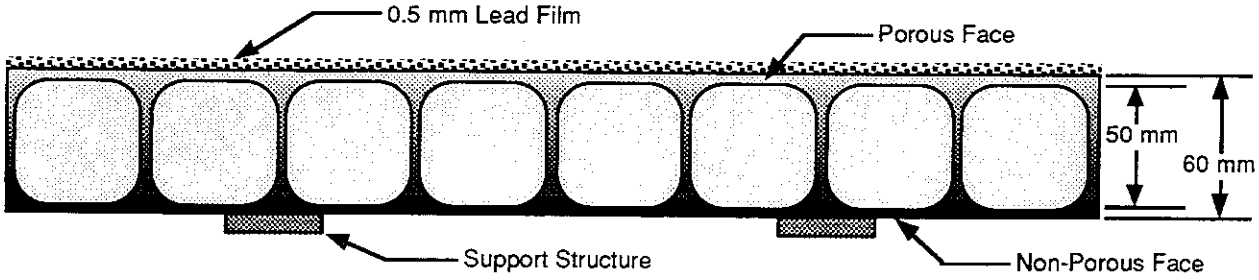

Figure 6.8.2-1 First Wall Panel; Cross Sectional View

The cooling system is separate from the blanket. The total amount of heat deposited in the first wall system is large (~1200 MW), requiring substantial flow of the Pb coolant. The large first wall system heating rate (as compared with MFE designs) is due in part to the conversion of neutron energy to x-ray and debris energy in the pellet and also the large amount of neutron power deposited in the thick Pb coolant. A more detailed description of the cooling system thermal hydraulics is found in Section 6.8.2.2.

Pb also acts as the first wall protectant. A film nominally 0.5 mm in thickness is allowed to form on the surface facing the pellet explosions. The porosity of the bulk

Use or disclosure of data
subject to title page restriction

SiC is tailored to allow Pb from the cooling channels to slowly seep onto the surface. This surface film evaporates in response to the intense heat flux from the target explosions and then recondenses prior to the next shot. The energy deposition characteristics are central to several key responses in the cavity, including vapor dynamics, cavity clearing, and mechanical loading on the first wall system. Section 6.8.2.3 gives a detailed account of the x-ray and debris energy deposition. Nuclear heating is described in more detail in Section 6.8.1.

The behavior of the cavity vapor is very important in determining the loadings on the wall and the recondensation which is required for a high repetition rate. The actual behavior of the cavity vapor following an explosion is very complex, involving time-dependent non-linear processes. Two simplified analyses were performed to help provide insight into this complex behavior. Section 6.8.2.4 examines the vapor response using a 1-D time-dependent hydrodynamic model. These calculations provide the pressure and temperature histories at the wall and throughout the vapor.

In the Prometheus design, cavity clearing requires good conduction heat transfer into the cooling channels. Prometheus-L requires the cavity vapor to drop below 1 mtorr before the laser beams are fired, whereas Prometheus-H has a window of 10-100 mtorr. The lower limit is needed to establish proper channel transport conditions, and the upper limit is based on target injection constraints. Section 6.8.2.5 examines vapor clearing using a simplified (lumped parameter) model of vapor condensation, but more sophisticated modeling of the thermal responses. Adequate clearing times are predicted for both reactors.

Protection of the first structural wall is accomplished using a thin film which wets the surface. Wetting of SiC by Pb is assisted by coating the SiC with a metal as part of the CVD process. Protection of the upper end cap is a particularly difficult problem. In order to maintain a fully-wetted surface without Pb falling off into the cavity, we inject a thin Pb jet at the top of the upper end cap. The jet injector structure (SiC) is exposed to the blast effects and is made easily accessible for repair or replacement, as required. The fluid leaves the injector and flows along the surface. Figure 6.8.2-1 shows the overall configuration of the film flow system. Section 6.8.2.6 provides analysis of the film flow characteristics, including flow through porous structures and film flow along the wall.

The first wall system structural material is SiC/SiC composite. The material is woven from SiC fabric and then impregnated with SiC using a chemical vapor deposition (CVD) process. These panels are inserted and removed from the reactor vertically. They are structurally attached to the blanket through a locking mechanism described

Use or disclosure of data
subject to title page restriction

in Section 6.11. The ability of these panels to withstand the cyclic loading from the blast is analyzed in Section 6.8.2.7.

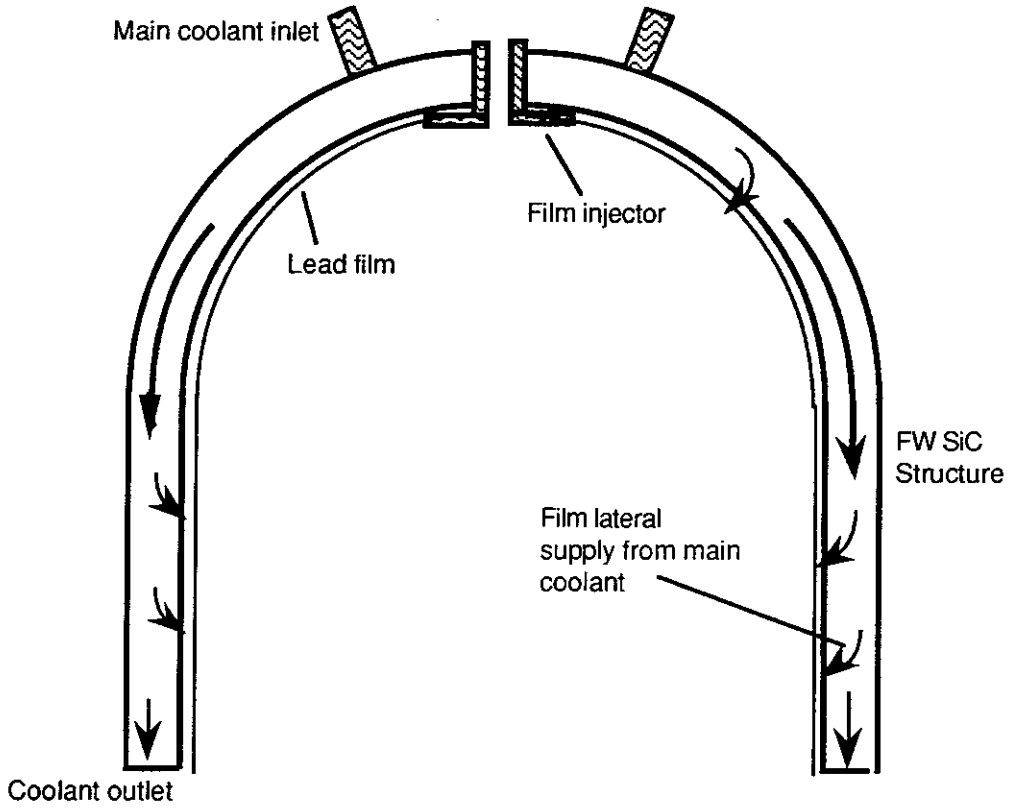

Figure 6.8.2-2 Schematic View of Film Supply Systems

The expected lifetime of the first wall panels has been estimated as five years. This is primarily due to radiation damage in the SiC and to surface damage and fatigue caused by pulsing.

Tables 6.8.2-1 and 6.8.1-2 summarize the major parameters of the first wall system. In the analysis that follows, some discrepancies may appear in the values used for the major system parameters. The final design point was determined after most of these more detailed analyses were completed.

Use or disclosure of data
subject to title page restriction

Table 6.8.2-1 First Wall System Major Parameters

	Laser	HI	
First Wall Radius	5.0	4.5	m
Cylinder Height	5.0	4.5	m
Total Height	15	13.5	m
Surface Area	471	382	m^2
Volume	916	668	m^3
Film Thickness		0.4-0.6	mm
Cooling Channel Wall Thickness		5	mm
Cooling Channel Diameter		5	cm
Mean Fiber Pore Diameter		50	μm
Porosity		10	%
Permeability		1.76×10^{-14}	m^2
Pb Inlet/Outlet Temperature		375/525	°C
Inlet/Outlet Pressure		2.0/1.5	MPa
Pumping Power (In Reactor)		3-4	MW
Maximum SiC Temperature		775	°C

Table 6.8.2-2 First Wall Power Balance

	Laser	HI	
Total Yield	497	719	MJ
Neutron Yield	359	514	MJ
X-ray Yield	31	46	MJ
Debris Yield	107	159	MJ
Repetition Rate	5.6	3.5	Hz
Surface Power	780	725	MW
Nuclear Heating	488	437	MW
Total First Wall System Power	1268	1162	MW

Use or disclosure of data
subject to title page restriction

6.8.2.2 Cooling System Thermal-Hydraulics - The cooling system is designed to provide the necessary flow conditions to maintain all components within allowable temperature and pressure limits. A summary of values of the thermal hydraulic parameters and heat transfer properties used in this study is given in Table 6.8.2-3. More details on the film thermal hydraulics can be found in Sections 6.8.2.5 and 6.8.2.6.

The Pb bulk temperature rise in the main coolant is maximized in order to reduce the flow rate. The Pb must be kept well above the melting point (327°C) but low enough to avoid compatibility limits with steel in the heat transport loop. This led to inlet and outlet temperatures of 375° and 525°C.

The first wall power comes from both surface heating (from x-rays and debris) and nuclear heating. The lead flow rate needed to remove the first wall thermal power is estimated using:

$$\dot{m}\, C_p\, \Delta T = \dot{Q}_{fw} \qquad (6.8.2\text{-}1)$$

Where $\dot{m}$ is the mass flow rate and $\dot{Q}_{fw}$ is the power to the first wall. The lead velocity in the vertical side of the chamber is determined from the total flow area:

$$A \cdot V = \dot{m} \qquad (6.8.2\text{-}2)$$

The frictional pressure drop is calculated as:

$$\Delta P = f \frac{\rho V^2 L}{2 D_h} \qquad (6.8.2\text{-}3)$$

where f is the friction factor obtained from the Moody diagram using a relative roughness of 0.001. L is the coolant flow path length and D_h is the equivalent diameter. The pumping power for the cavity chamber is the product of the pressure loss in the chamber times the volumetric flow rate:

$$P\rho = \frac{m\, \Delta P}{\rho \eta} \qquad (6.8.2\text{-}4)$$

Use or disclosure of data
subject to title page restriction

Table 6.8.2-3 First Wall System Thermal Hydraulic Parameters

	Prometheus-L	Prometheus-H	Units
Fusion Thermal Power	3092	2797	MW
Total FW Thermal Power	1268	1162	MW
Coolant	Pb	Pb	
Impurities	Bi, Sb, W	Bi, Sb, W	
Film Thickness	0.4 – 0.6	0.4 – 0.6	mm
Cooling Channel Diameter	5	5	cm
Inlet Bulk Temperature	375	375	℃
Outlet Bulk Temperature	525	525	℃
ΔT_{bulk}	150	150	℃
Mass Flow Rate	58,770	54,422	kg/s
Volume Flow Rate	5.65	5.21	m^3/s
Coolant Flow Area (vertical side of chamber)	1.1775	1.1775	m^2
Average Velocity	4.8	4.42	m/s
Reynolds Number	$1.2x10^6$	$1.12x10^6$	
Frictional Factor	0.02	0.02	
Coolant Path	12.85	12.34	m
Frictional Pressure Drop	0.615	0.5	MPa
Inlet Pressure (top)	1.0	1.0	MPa
Outlet Pressure (bottom)	1.385	1.5	MPa
Pumping Power (85% efficiency)	4.1	3.0	MW
Properties			
c_p (Pb)	154		J/kg-K
ρ (Pb)	10400		kg/m^3
μ (Pb)	$2.059x10^{-3}$		$N-s/m^2$
k (Pb)	34		W/m-K
T_{mp} (Pb)	327		℃
hfg	862,500		J/kg

6.8.2.3 X-ray and Debris Spectra and Energy Deposition – Energy deposition from the blast is estimated by calculating the attenuation of x-rays and debris in the cavity vapor and deposition profiles in the film. The x-rays reach the wall in ~20 ns—prior to the debris ions—and cause substantial evaporation of the Pb protective film. Debris energy then deposits primarily in the cavity vapor. Depending on the yield, spectra, and attenuation coefficients in the liquid film, some amount of liquid is raised beyond the boiling point and is immediately vaporized. Additional liquid is vaporized by intense thermal radiation from the hot cavity gas. (We call this latter process "secondary evaporation".) In this subsection, calculations are described for:

(1) X-ray energy deposition in the cavity vapor
(2) X-ray deposition profile of the lead film and vaporization depth
(3) Debris energy deposition in the cavity vapor
(4) Reactive impulse due to the vaporized gas.

Secondary evaporation is covered in more detail in Section 6.8.2.5.

For this analysis, the x-ray spectra of SIRIUS[1] and LIBRA[2,3] were used for the KrF and heavy ion designs, respectively (see Figure 6.8.2-3). Other base case chamber parameters used for these calculations are shown in Table 6.8.2-4.

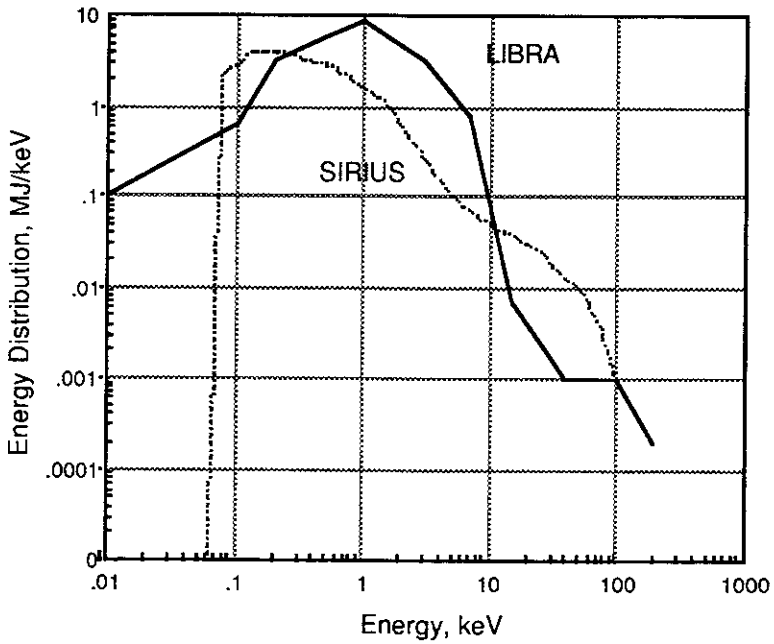

Figure 6.8.2-3 Target X-ray Spectra Used for Prometheus-L (SIRIUS) and -H (LIBRA)

Use or disclosure of data subject to title page restriction

Table 6.8.2-4 Chamber Parameters (Base Cases)

	Laser	HI	Units
Pressure Limit @ 0°C	0.001	0.1	torr
Background Gas Density	3.5×10^{13}	3.5×10^{15}	cm^{-3}
Total Yield	497	719	MJ
Neutron Yield	359	514	MJ
X-ray Yield	31	46	MJ
Debris Ion Yield	107	159	MJ
Cavity Radius	5.0	4.5	m
Cavity Height	15	13.5	m
First Wall Area	471.2	381.7	m^2
Cavity Volume	916.2	668.0	m^3

X-Ray Absorption in the Cavity Vapor – As the x-rays travel toward the wall, some are absorbed by the background gas. The attenuation of x-rays is exponential. At low energies, this process is dominated by the photoelectric interaction. In this process, electrons are ejected from the Pb atoms. (We assume for this calculation that the cavity gas contains only Pb.) When the vacancies are refilled, additional x-rays may be emitted; however, their energy will be substantially lower where the absorption cross section is very high. Most of the energy is ultimately transformed into kinetic energy of the gas. The attenuation cross section in lead is shown in Figure 6.8.2-4. [4] Note how strongly dependent it is on energy.

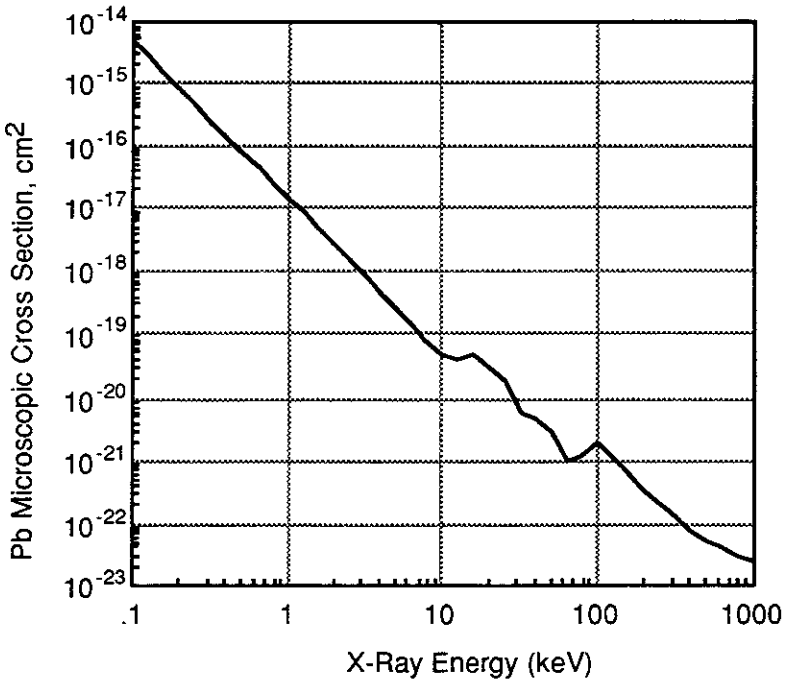

Figure 6.8.2-4 Cross-Section in Pb as a Function of X-Ray Energy

Use or disclosure of data
subject to title page restriction

The equations used to calculate the x-ray energy attenuation in the cavity vapor are:

$$E_{dep} = 4\pi \int_0^r r^2 \sum_{i=1}^{n} q_i \, d\,r \qquad [J] \qquad (6.8.2\text{-}5)$$

$$q_i = \mu_{iv} \frac{E_i}{4\pi r^2} e^{-\mu_{iv} r} \qquad [J/m^3] \qquad (6.8.2\text{-}6)$$

where E_{dep} is the energy deposited within a depth r, q_i is the volumetric energy deposition at r for the i^{th} x-ray energy group, E_i is the total energy in group i (in Joules), and μ_{iv} is the macroscopic absorption cross section in the vapor (at a given pressure) for energy group i. These equations were solved and then normalized to the initial x-ray yield.

The fraction of x-rays absorbed as a function of radius for the laser and heavy ion reactors is shown in Figure 6.8.2-5. The heavy ion cavity absorbs a much larger amount of energy due to its higher base pressure (100 mtorr vs. 1 mtorr). The remainder of the energy is absorbed in the film.

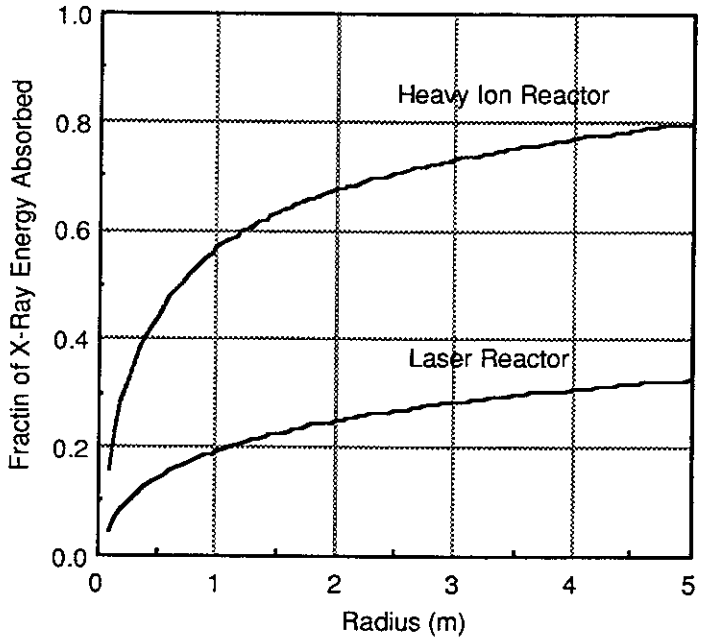

Figure 6.8.2-5 Fraction of X-ray Energy Absorbed by the Lead Vapor.

Use or disclosure of data
subject to title page restriction

Energy Deposition and Evaporation of the Film – Similar equations can be used in the film region to find the approximate depth of evaporation that is caused by the x-rays. The geometry in this case is linear, rather than cylindrical, leading to the following equations:

$$E_{dep} = 4\pi R^2 \int_0^x \sum_{i=1}^{n} q_i \, dx \qquad [J] \qquad (6.8.2\text{-}7)$$

$$q_i = \mu_{if} F_i e^{-\mu_{if} x} \qquad [J/m^3] \qquad (6.8.2\text{-}8)$$

$$F_i = \frac{E_i}{4\pi R^2} e^{-\mu_{iv} R} \qquad [J/m^2] \qquad (6.8.2\text{-}9)$$

where F_i is the x-ray energy flux incident on the wall, R is the radius of the wall, x is the depth into the film, and μ_{if} is the macroscopic absorption cross section of the film. Figure 6.8.2-6 shows the resulting energy deposition profiles for both the laser and heavy ion cases.

The energy per unit volume required to raise the lead to its boiling point is given by:

$$E_{bp} = C_p (T_{sat} - T_{surface}) \qquad (6.8.2\text{-}10)$$

and the energy required to evaporate is given by:

$$E_{vap} = h_v + C_p (T_{sat} - T_{surface}) \qquad (6.8.2\text{-}11)$$

where

h_v	= 862,500 J/kg	heat of evaporation per unit volume
C_p	= 154 J/kg-°K	heat capacity
T_{sat}	= ~1500 °K	(saturation temperature following the blast)
$T_{surface}$	= 950-1150 °K	(surface temperature preceding the blast)
E_{bp}	~ 54-85 x 10^3 J/kg	
E_{vap}	~ 10^6 J/kg	

The depth corresponding to E_{bp} is called X_{bp} and the depth corresponding to E_{vap} is called X_{vap}. In the region between these two depths, the lead will be in a two-phase state. This is modeled by assuming some additional vaporization. The additional thickness (X_{tot}–X_{vap}) of the vaporized layer beyond X_{vap} is computed by integrating the energy deposited in the two-phase region and determining the amount of mass this energy would evaporate:

Use or disclosure of data
subject to title page restriction

$$X_{tot} - X_{vap} = \frac{\int_{X_{vap}}^{X_{bp}} (q - C_p \Delta T)\, dX}{h_{fg}} \qquad (6.8.2\text{-}12)$$

Figure 6.8.2-7 is a plot of the integral of the deposition profile – $\int q\, dX$. This is used in Eq. 6.8.2-12 to obtain the net depth of evaporation. The mass of vaporized lead then can be calculated simply as:

$$M = \rho\, 4\pi R^2\, X_{tot} \qquad (6.8.2\text{-}13)$$

Table 6.8.2-5 summarizes the results. Note, the total mass evaporated during a pulse is much larger than shown in the table because thermal radiation was not considered here. These results represent only the initial evaporation from x-rays. Section 6.8.2.5 provides more information on the effects of thermal radiation.

Table 6.8.2-5 Mass and Thickness of Layer Vaporized by X-Rays

	Laser	HI	
X-ray Energy Absorbed in Vapor	9.9	28.9	MJ
X-ray Energy Deposited in Film	21.1	8.1	MJ
X_{vap}	0.6	0.5	μm
X_{bp}	5.5	5.9	μm
Vaporized Film Thickness, X_{tot}	1.3	1.6	μm
Surface Area	471	382	m2
Vaporized Mass	5.9	6.4	kg

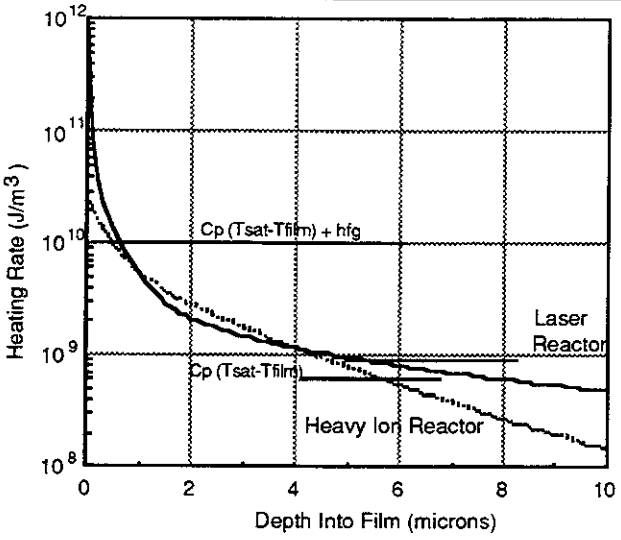

Figure 6.8.2-6 Energy Deposition Profile in Pb Film

Use or disclosure of data
subject to title page restriction

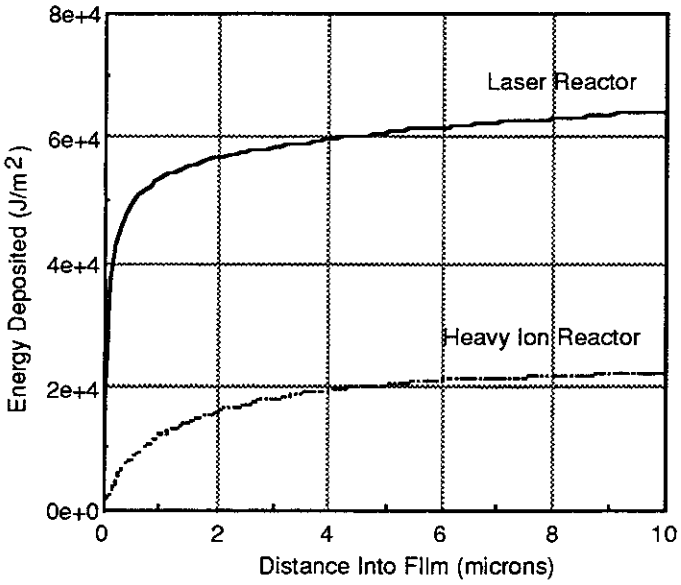

Figure 6.8.2-7 Integrated Energy Deposition Profile in Pb Film

Debris Energy Deposition – Debris energy deposition into the cavity gas was calculated using the methods in References 5 and 6. The debris spectra were estimated by assuming the ions are all ejected at the same velocity.[1] If all ions have the same velocity, then the debris yield (E) is given by:

$$E = \frac{1}{2} M v^2 \qquad (6.8.2\text{-}14)$$

$$M = (M_D + M_T + M_{He} + M_C + M_H + M_{Pb}) \qquad (6.8.2\text{-}15)$$

where M_i represents the total mass of debris species i. If m_i is the mass of a single ion and e is the energy per ion, then:

$$e = \frac{1}{2} m_i v^2 = \frac{E m_i}{M} \qquad (6.8.2\text{-}16)$$

Table 6.8.2-6 lists the debris types, their masses, and energies. The mass of He is computed assuming a burn fraction of 30%.

Use or disclosure of data
subject to title page restriction

Using these values, the fraction of debris energy absorbed in the cavity was calculated and is shown in Figure 6.8.2-8. For the heavy ion reactor conditions (assuming 100 mtorr), essentially all of the debris is stopped by the cavity vapor. For the laser

Table 6.8.2-6 Target Debris Ion Spectra and Masses

Laser				HI		
Ion	e (keV)	Mass (mg)	No. of Ions	e (keV)	Mass (mg)	No. of Ions
D	30.57	1.33	4.01×10^{20}			
T	45.85	2.0	4.01×10^{20}	Similar data can be generated for		
He	41.45	1.14	1.72×10^{20}	the Heavy Ion Option Target Debris		
C	183.59	16.27	8.16×10^{20}			
H	15.3	1.36	8.16×10^{20}			
Pb	0	0	0			

case (1 mtorr), 20% of the debris energy reaches the wall. However, since the debris travels much slower than the x-rays, by the time the ions approach the film, the density of the evaporated lead vapor is so high that it can be assumed that the debris will lose all its energy before reaching the liquid layer.

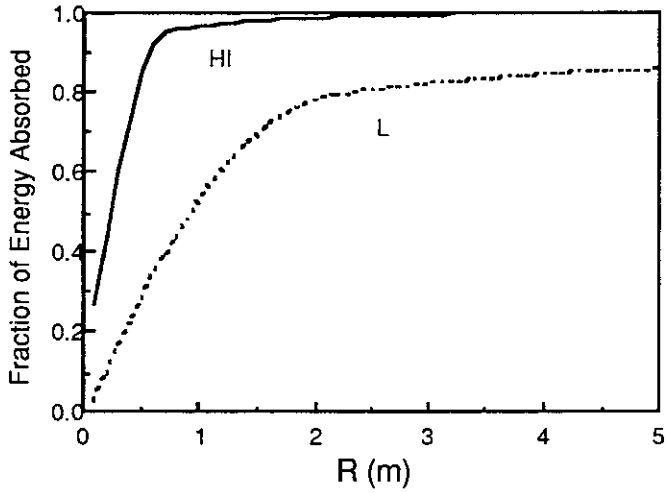

Figure 6.8.2-8 Debris Ion Deposition Profiles in Cavity Vapor

Impulse Due to Vaporized Gas – The reactive impulse of vaporized gas is estimated as $M_{gas}V$, where V is the average gas velocity. The average gas velocity can be estimated using the bulk kinetic energy of the vaporized fluid, which is equal to the deposited x-ray energy less the energies of ionization, vaporization, and dissipation in the film.

$$E_{kinetic} = f_{wall} E_{yield} - E_{vaporization} - E_{ionization} - E_{dissipation\ in\ film} \qquad (6.8.2\text{-}17)$$

Use or disclosure of data
subject to title page restriction

$$= \frac{M_{gas} V^2}{2} \qquad (6.8.2\text{-}18)$$

$$\Delta I_{x\text{-}ray} = M_{gas} V \qquad (6.8.2\text{-}19)$$

To estimate the energy of ionization, we need to know the amount of gas ionized. The fraction of the gas ionized can be determined by the Saha equation, which is written as:

$$f = \frac{N_i}{N_o} = \left(2.4 \times 10^{15} \frac{T^{3/2}}{N_o} e^{(-U_i/kT)} \right)^{0.5} \qquad (6.8.2\text{-}20)$$

The fraction of the gas ionized at a gas temperature of 7 eV (81,200 K) is about 18% and decreases to 0.21% at a gas temperature of 1 eV. For Prometheus-L, the vaporized gas temperature is about 5000 K, as estimated from the equation of state. Then the amount of ionized gas is small and can be neglected. For this case, the reactive impulse due to x-ray vaporized gas is 10,400 N-s. This is relatively small, indicating that the mechanical responses in the structures should be manageable. The reactive impulse due to x-ray vaporized gas for the Prometheus-H is negligible due to the gas having a small amount of kinetic energy.

References for 6.8.2.3

1. B. Badger, et al., "SIRIUS-T: A Study of a Symmetrically-Illuminated Inertial Confinement Fusion Tritium Production Facility Final Report" UWFDM-850, December 1990.

2. M. E. Sawan, et al., "Chamber Design for the LIBRA Light Ion Beam Fusion Reactor," Fusion Technology, Vol.15, No. 2, Part 2A, p. 766, March 1989.

3. G. A. Moses, et al., "Overview of LIBRA Light Ion Beam Fusion Conceptual Design", Fusion Technology, Vol. 15, No. 2, Part 2A, 756 (1989).

4. F. H. Attix and W. C. Roesch, "Radiation Dosimetry; Volume I Fundamentals," Academic Press, New York, p. 119, 1968.

5. H. H. Anderson and J. F. Ziegler, Hydrogen Stopping Powers and Ranges in All Elements", Pergammon Press (1977).

6. J. F. Ziegler, Helium Stopping Powers and Ranges in All Elements, Pergammon Press (1977).

Use or disclosure of data subject to title page restriction

6.8.2.4 Cavity Hydrodynamics – It has been shown in the previous section that energy deposition of x-rays and ion debris in the lead film leads to evaporation, subsequent energy absorption in the evaporated lead, and energy re-radiation. A complete and accurate description of the hydrodynamics of these processes is essential in two respects:

(1) The re-condensation rate of Pb vapor is sensitively dependent on the exact temperature and pressure conditions at recondensation surfaces. Hence, the frequency of microexplosions is highly dependent on detailed hydrodynamical calculations.
(2) The mechanical response of the SiC structure is dictated by the magnitude and duration of the Pb vapor pressure at the surface. It is also depedent on the reactive impulse due to vaporized Pb.

Hydrodynamical modeling of the Pb vapor, including space-time energy deposition in the Pb vapor, gas ionization, and coupled radiation transport is obviously complicated and requires extensive resources. However, the fundamental hydrodynamical behavior of the system can be studied if a number of approximations are made. These are:

(1) The fluid equations are solved in one-dimensional cylindrical geometry (i.e., ignoring effects of end caps).
(2) Coupled particle and photon transport is approximated by a lumped model, where the total energy deposited in the vapor by x-rays and ion debris is delivered to the lead film as Q"(t).

These simplifying assumptions render the hydrodynamical model greater simplicity, as described in the next sections. We will first state the problem and follow this by a description of the governing fluid equations. The numerical scheme developed for the solution of the fluid equations is then presented. Results are finally given in the last section.

Problem Statement – The evaporation and condensation processes are analyzed using a one-dimensional (1-D) hydrodynamic model of the vapor flow in the cavity as shown in Figure 6.8.2-9.

Use or disclosure of data
subject to title page restriction

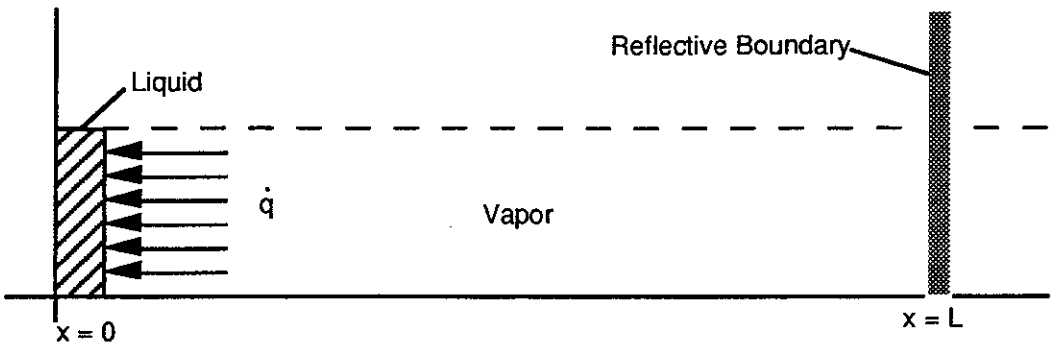

Figure 6.8.2-9 Mathematical Model of the Vapor Flow in the Cavity

Governing Equations – The governing equations are the time-dependent continuity, momentum, and energy equations of compressible fluid flow. An equation of state relates the pressure to the temperature and density. These equations in normalized, one-dimensional (1-D) form are:

$$\frac{\partial \rho}{\partial T} + \frac{\partial \rho u}{\partial x} = 0, \tag{6.8.2-21}$$

$$\frac{\partial \rho T}{\partial \tau} + \frac{\partial \rho u u}{\partial x} = \frac{\partial p}{\partial x} + \frac{\partial}{\partial x}\left(\frac{1}{Re}\frac{\partial u}{\partial x}\right) \tag{6.8.2-22}$$

$$\frac{\partial \rho T}{\partial t} + \frac{\partial \rho u T}{\partial x} = \frac{\partial}{\partial x}\left(\frac{1}{RePr}\frac{\partial T}{\partial x}\right) \tag{6.8.2-23}$$

$$p = \rho T \tag{6.8.2-24}$$

and are solved on the domain $(x, t) \in (0, L) \times (0, t_f)$. In these equations, ρ is density, u is velocity, T is temperature, and p is pressure in nondimensional form. The nondimensional parameters are Reynolds number, Re, and Prandtl number, Pr, defined as:

$$Re = \frac{\rho u_o D}{\mu}$$

$$Pr = \frac{\mu C_p}{k} \tag{6.8.2-25}$$

where ρu_o is the inlet mass flux at x=0, t=0; μ is dynamic viscosity; k is thermal conductivity; C_p is specific heat; and D is the cavity diameter.

Use or disclosure of data
subject to title page restriction

Initial and Boundary Conditions - The pressure in the cavity is assumed initially to be very low, p_o (1 mTorr for the KrF laser systems and 100 m Torr for the HI system). Furthermore, there is no input heat and the stagnant vapor is in thermodynamic equilibrium with the wall-protecting liquid. The initial conditions are, therefore, formulated as:

$$\rho(x,0) = 1$$

$$\rho u(x,0) = 1 \qquad (6.8.2\text{-}26)$$

$$T(x,0) = T_{sat}(p_o)$$

The mass flux at the liquid-vapor interface is determined by equating the energy flux absorbed in the liquid layer (or the heat flux conducted out in the condensation process) to the evaporation (or condensation) rate times the latent heat of evaporation. The vapor temperature and density at the interface are assumed to have the saturation value according to the interface pressure. The boundary conditions are, therefore, formulated as:

$$\rho(0,t) = \rho_{sat}(p)$$

$$\rho u(0,t) = \frac{\dot{q}}{h_{fg}(T)} \qquad (6.8.2\text{-}27)$$

$$T(0,t) = T_{sat}(p)$$

where $\dot{q}$ has different values in the evaporation or condensation process. In the evaporation process,

$$\dot{q} = \frac{Q}{A\,\Delta t}$$

where Q is the total heat absorbed by the Pb in the cavity, A is the surface area, and Δt is a characteristic absorption time. In the condensation process,

$$\dot{q} = \frac{-k_{eff}}{\delta_{eff}}(T - T_w)$$

where k_{eff} and δ_{eff} are the effective conductivity and thickness of the wall and the protecting liquid. T_w is the outside temperature of the wall.

At the centerline of the cavity, the symmetry conditions are applied; that is,

$$\frac{\partial \rho\,(L,t)}{\partial x} = 0$$

$$\rho u(L,t) = 0 \qquad (6.8.2\text{-}28)$$

$$\frac{\partial T\,(L,t)}{\partial x} = 0$$

Here the subscript "sat" denotes properties of the vapor under saturation conditions.

Numerical Solution – The governing Eqs. 6.8.2-21 through 6.8.2-23 are solved for ρ, ρu, and T, respectively, with p recovered from the equation of state Eq. 6.8.2-24. For the sake of analysis, the nonlinear partial differential equations are cast in the general form:

$$\frac{\partial \Phi}{\partial t} + \frac{\partial}{\partial x}\left(u\Phi - \Gamma \frac{\partial \Phi/\rho}{\partial x}\right) = S \qquad (6.8.2\text{-}29)$$

This equation is discretized on the staggered grid shown in Figure 6.8.2-10. The temperature, density, and pressure are calculated at points indexed by i and the mass flux, ρu, is calculated at points indexed by ij where j = i +1/2.

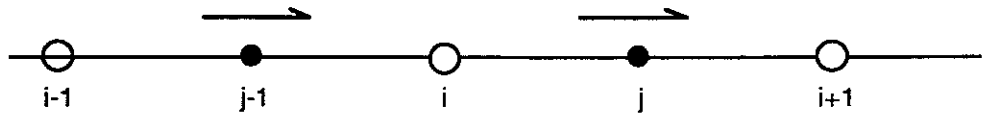

Figure 6.8.2-10. The Staggered Grid and Nodes

Using the backward Euler algorithm for time differencing and centered differences in space, Eq. 6.8.2-29 is approximated by:

$$-a_{1,i}\,\Phi_{i-1} + a_{2,i}\,\Phi_i - a_{3,i}\,\Phi_{i+1} = b_i \qquad (6.8.2\text{-}30)$$

where

$$a_{1,i} = D_{j-1}\,(1 + 1/2\ Pe_{j-1}), \qquad (6.8.2\text{-}31a)$$

$$a_{3,i} = D_j\,(1 - 1/2\ Pe_{j-1}), \qquad (6.8.2\text{-}31b)$$

$$a_{2,i} = a_{1,i} + a_{3,i} + (u_j - u_{j-1}) + \Delta x/\Delta t, \qquad (6.8.2\text{-}31c)$$

Use or disclosure of data
subject to title page restriction

$$b_i = \Delta x\, S_i + \left(\frac{\Delta x}{\Delta t}\right)\Phi_i^n, \qquad (6.8.2\text{-}31d)$$

with

$$D_{j-1} = \frac{\Gamma_{j-1}}{\rho_{i-1}\,\Delta x},\quad D_1 = \frac{\Gamma_j}{\rho_{i+1}\,\Delta x},\quad Pe_1 = \frac{u_j\,\Delta x}{D_j}.$$

For stability and a unique solution, the coefficients of Eq. 6.8.2-30 should be positive. If the grid Peclet number, Pe_i is greater than two in magnitude, some of the coefficients defined by Eqs. 6.8.2-31 are not positive.

The governing equations generalized in Eq. 6.8.2-29 are nonlinear and coupled. Therefore, the coefficients of the difference equation, Eq. 6.8.2-30 are not constant. Block Gauss-Seidel method was used to solve Eqs. 6.8.2-21 through 6.8.2-23 for ρ, ρu, and T, successively. The coefficients were then evaluated using the data of the most recent iteration. The resulting linear systems were then solved by standard linear algebra methods. Iteration on the equations was stopped after convergence of all variables.

Standard Schemes - The coefficients of Eq. 6.8.2-30 are written in a general form as:

$$a_{1,i} = D_{j-1}\,A(Pe_{j-1}) + \max(0,u_{j-1}), \qquad (6.8.2\text{-}32a)$$

$$a_{3,i} = D_j\,A(Pe_j) + \max(0,-u_j), \qquad (6.8.2\text{-}32b)$$

$$a_{2,i} = a_{1,i} + a_{3,i} + (u_j - u_{j-1}) + \Delta x/\Delta t, \qquad (6.8.2\text{-}32c)$$

Expressions for A(Pe) for different schemes are listed in Table 6.8.2-7. Derivation of A(Pe) for first-order upwinding and power-law schemes can be found in Patankar[1] and for the CONDIF scheme in Runchal.[2] The parameter R appearing in Table 6.8.2-7 for the CONDIF scheme is defined as:

$$R = \frac{\Phi_{i-1} - \Phi_i}{\Phi_i - \Phi_{i-1}} \qquad (6.8.2\text{-}33)$$

It is clear, as discussed in Reference 2, that this provides a means of locating local extrema in the grid function Φ_i. If there is a sharp variation in Φ, then R may be quite large and, conversely, if there is only a small variation in Φ, R will be small. Therefore, a limit is imposed on R so that:

$$1/R_{max} \le R \le R_{max} \qquad (6.8.2\text{-}34)$$

Use or disclosure of data
subject to title page restriction

Table 6.8.2-7 The Function A(Pe) for Different Schemes

Scheme	A(Pe)
CDS	$1.05\|Pe\|$
Upwinding	1
Power law	$\max[0,(1-0.1\|Pe\|)^5]$
CONDIF	$A(Pe_{j-1}) = 1 - \max(0,Pe_{j-1}/2) + R\max(0, Pe_j/2)$
	$A(Pe_j) = 1 - \max(0,Pe_j/2) + \frac{1}{R}\max(0, Pe_{j-1}/2)$

It can be seen, using the appropriate formulas from Table 6.8.2-7, that R_{max} controls the amount of numerical diffusion in the scheme. In particular, large values of R result in significant numerical diffusion while small values cause little diffusion. As noted in Reference 2, typical values are in the range $4 \leq R_{max} \leq 10$.

Filtering - Engquist, et al.[3] introduced nonlinear filters for shock computation. These filters are used as post-processors in conjunction with standard finite difference schemes. The difference equations are solved at the current time level, then the solutions are processed with the filter to eliminate oscillations before proceeding to the next time level. The filters control the total variation (i.e., they possess the TVD property), produce sharp shocks (they are second order away from shocks), and they are simple to use.

For the calculations reported herein, we use CDS and a nonlinear filter, as described below (for details, see Reference 3). The principles of the filtering technique are illustrated below using Fig. 6.8.2-11. Figure 6.8.2-11(a) shows the solution Φ^n at time t^n. Using Central Differential Scheme (CDS), the typical solution at time t^{n+1}, φ^{n+1}, is shown in Figure 6.8.2-11(b). This solution exhibits an overshoot, as would be expected. Results of filtering are displayed in Figure 6.8.2-11(c) where it can be seen that the overshoot has been completely removed. The basic principles of the filtering process are the following:

(1) $\varphi_{i_o}^{n+1}$ is detected as an overshoot via the test $\left(\Delta_-\varphi_{i_o}^{n+1}\right)\bullet\left(\Delta_+\varphi_{i_o}^{n+1}\right) < 0$.

(2) $\varphi_{i_o}^{n+1}$ is decreased in such a way that the new value of $\varphi_{i_o}^{n+1}$ is not less than $\varphi_{i_o-1}^{n+1}$

(3) $\varphi_{i_o+1}^{n+1}$ is increased by the same amount as $\varphi_{i_o}^{n+1}$ is decreased in order to maintain conservation properties and, thus, to obtain the right shock speed.

Use or disclosure of data
subject to title page restriction

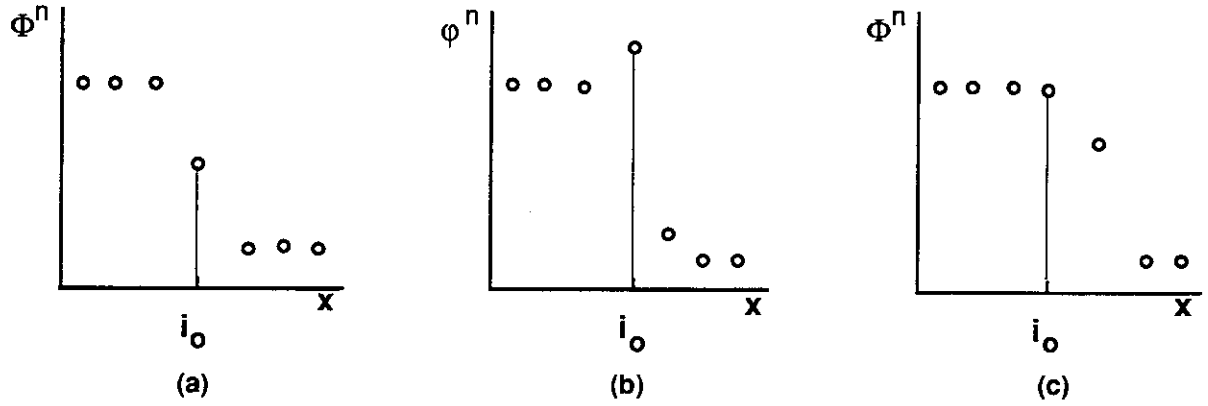

Figure 6.8.2-11 Filtering Process Applied to the CDS Result

The symbols Δ_- and Δ_+ denote the backward and forward differences, respectively, and are defined as $\Delta_\pm \Phi_i = \pm (\Phi_{i\pm1} - \Phi_i)$. It is of interest to note that the test used to detect overshoots is quite similar to that employed in CONDIF (Eq. 6.8.2-33), but subsequent steps of the algorithm are very different.

The algorithm for this filtering and also for more complicated ones, can be found in Reference 3, in which the nonlinearity and TVD properties of the filtering technique have been shown. We should emphasize that the above basic three-step process is not TVD, but the modifications needed (discussed in detail in Reference 3) are straightforward.

Input Heat - The calculations are carried out for two different working liquids: lithium and lead. The thermal properties of these liquids are listed in Table 6.8.2-8 which were obtained from Reference 4.

The total heat, Q, released in the case with lithium as working fluid is 100 MJ. The heat was assumed to be absorbed in the liquid layer in 10^{-6} seconds. Therefore, the input heat flux $\dot{Q} = 10^{14}$W, and the input heat flux per unit area $\dot{q} = 6.37 \times 10^{11}$W/m^2. The effective total area is $A_{eff} = 157$ m^2; that is,

$$q(t) = 6.37 \times 10^{11} \text{ W/m}^2 \qquad 0 < t \leq 10^{-6} \text{ s}$$

$$q(t) = 0 \qquad t > 10^{-6} \text{ s}$$

For the case with lead as working fluid, the released heat is in two parts: $Q_1 = 39.2$ MJ at time, $t = 10^{-8}$ s, and $Q_2 = 137.3$ MJ at time $t = 10^{-6}$. For the same effective area as

Use or disclosure of data
subject to title page restriction

Table 6.8.2-8 Properties of Liquids Used in Hydrodynamics Calculations

Lithium		
Thermal Conductivity	liquid	$k = 48.4$ W/m-K
	vapor	$k = 0.04$ W/m-K
	effective	$k_{eff} = 23.15$ W/m-K
Specific Heat		$c_p = 4.17$ kJ/kg-K
Viscosity	vapor	$\mu = 7.6 \times 10^{-6}$ N-s/m^2
Latent Heat of Vaporization		$h_{fg} = 19.6$ MJ/kg
Effective Liquid Thickness		$\delta_{eff} = 1.5$ cm
Saturation Temperature		$T(K) = 7877.9/(4.8831 - \log_{10} p)$
Lead		
Thermal Conductivity	vapor	$k = 6.884 \times 10^{-4}\ \Omega \sqrt{T}$ W/m.K
	effective	$k_{eff} = 20.0$ W/m.K
Specific Heat		$c_p = 139.0$ J/kg.K
Viscosity	vapor	$\mu = 4.575 \times 10^{-6}\ \Omega \sqrt{T}$ N.s/m^2
Latent Heat of Vaporization		$h_{fg} = 0.85$ MJ/kg
Effective Liquid Thickness		$\delta_{eff} = 5.0$ cm
Saturation Temperature		$T(K) = 11290.0/(11.34 - \log_{10} p)$

Where, Ω is a function of temperature and is tabulated below.

T(K)	255.3	340.4	425.5	510.6	595.7	680.8	765.9	851.0	1702.
Ω	0.359	0.401	0.443	0.484	0.524	0.562	0.597	0.630	0.851

used for lithium, the first heat release is assumed to be absorbed in the liquid layer in 10^{-8} seconds and the second heat release in 10^{-6} seconds. Therefore,

$$\dot{q}(t) = 2.50 \times 10^{13} \text{ W/m}^2 \qquad 0 < t \leq 10^{-8} \text{ s}$$

$$\dot{q}(t) = 8.745 \times 10^{11} \text{ W/m}^2 \qquad 10\text{-}8 < t \leq 10^{-6} \text{ s}$$

$$\dot{q}(t) = 0 \qquad t > 10^{-6} \text{ s}$$

Results and Discussion - In the design of an IFE reactor, the pressure of the cavity and the pressure exerted on the liquid layer during the time between two heat release pulses are important factors. Figure 6.8.2-12a shows the pressure field in the cavity at different times for the case with lithium as working fluid. The pressure field is shown at the early time of the process. A sudden heat release in the liquid layer causes an intensive evaporation and increase of pressure on the liquid layer. A shock wave is created at this point which moves toward the cavity center. Because of the spherical symmetry of the model, two shocks originated at the same time on opposite walls are reflected at the cavity center. Shock reflection in the cavity center cause an increase in the local pressure. When the reflected shock reaches the wall, another shock

Use or disclosure of data
subject to title page restriction

reflection occurs and the wall pressure increases. These multiple shock reflections continue until a steady-state condition is reached and the cavity pressure relaxes to the initial pressure. The transient time for the pressure waves to reach a steady condition is found to be about 50 ms when the working fluid is lithium. The information on the periodic variation of wall pressure is needed in calculations of the pressure loading on the wall, as will be discussed in Section 6.8.2.5.

The same process of shock reflections is also observed for lead as working fluid; the results are shown in Figure 6.8.2-12b. The slight difference of pressure wave behavior in this case is because of different input heats at different times. The transient time in this case is found to be about 150 ms. It is noted that the higher viscosity of lead results in faster damping of the shock waves as compared to the lithium case. The multiple shock reflections on the wall are shown in these figures to cause a periodic variation in the wall pressure.

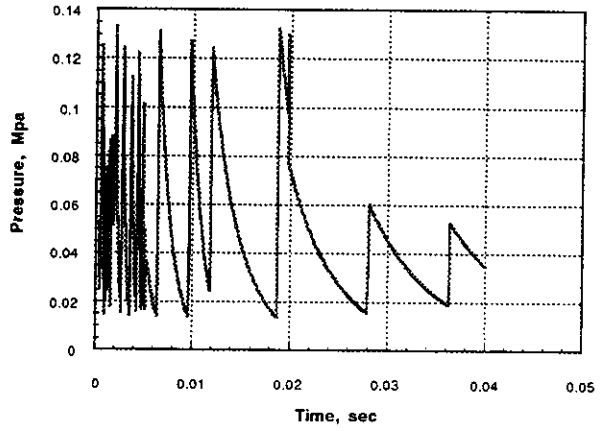

Figure 6.8.2-12a. Instantaneous Uniform Pressure on the Wall with Lithium Vapor

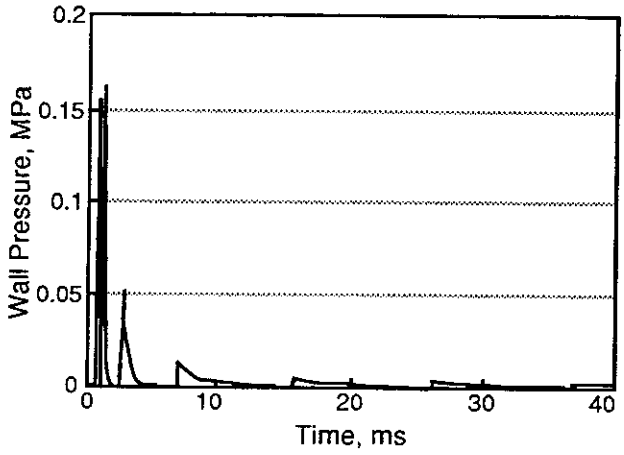

Figure 6.8.2-12b. Instantaneous Uniform Pressure on the Wall with Lead Vapor

References for 6.8.2.4

1. S. V. Patankar, Numerical Heat Transfer and Fluid Mechanics, Hemisphere Publishing Company, New York, 1980.

2. A. K. Runchal, Int. J. Numer. Methods Eng., 24, 1593 (1987).

3. B. Engquist, P. Lotstedt, and B. Sjogreen, Math. Comp., 52, 509 (1989).

4. J. O. Hirschfelder, C. F. Curtiss, and R. B. Bird, Molecular Theory of Gases and Liquids, John Wiley, New York, 1954.

6.8.2.5 Cavity Clearing – Energy released from target microexplosions results in evaporation of substantial mass from the liquid Pb wall protection scheme (of the order of 50-100 kg). This mass must recondense or be evacuated in order to provide a sufficiently low pressure in the cavity gas to allow propagation of the laser or ion beams and the targets. The requirement given for beam and target propagation in Prometheus is 1 mTorr @0°C for the direct-drive target KrF driver and 100 mTorr@0°C for indirect drive target heavy-ion driver. The limit for the laser reactor is determined by electrical breakdown of the cavity vapor and overheating of the unshielded direct drive targets. The channel transport mechanism used for the heavy ion reactor, together with the more robust indirect-drive target, allows a higher cavity base pressure (see Sections 6.5.1.7.4 and 6.5.2.6 on beam and target propagation). The main issue for cavity clearing is whether we can ensure that these low pressures indeed will be obtained.

In addition to the Pb vapor, a small amount (roughly 1 gram) of noncondensible gas remains in the cavity from the plastic case, He reaction product, and unburned D and T. This mass must be evacuated through the vacuum pumping system. The issue of vacuum pumping is treated in Section 6.8.6.

To help understand the nominal cavity gas behavior and transfer of blast energy into the first wall coolant following the explosions, a heat and mass transfer computer model "RECON" was developed. RECON computes the blast energy deposition and solves the time-dependent heat and mass transfer rates in the cavity and film. The initial conditions in the cavity and wall are not known a priori, so RECON solves successive pulses until a quasi-equilibrium condition is obtained. In the following sections, the various parts of the model are described, including mass evaporation and condensation rates, thermal radiation, and conduction into the coolant. (Analysis of energy deposition following a microexplosion is described in Section 6.8.2.2.3.) Results for the base case and parametric studies are then presented for both laser and heavy ion reactors.

Figure 6.8.2-13 shows the geometry of the wall region and the energy transport mechanisms included in the model. The model homogenizes the cavity vapor, assigning a single temperature, pressure, and mass to the cavity volume. The wall region is discretized in the radial direction away from the film surface. All of the energy from the blast ultimately is transferred to the cooling channel.

The crude treatment of the vapor leads to some inaccuracy, particularly in the early part of the pulse; however, the simplicity of the code allows parametric studies to be performed quite easily. For this design concept, the time required for recondensation is limited to a large extent by conduction through the film and into the cooling

Use or disclosure of data
subject to title page restriction

channels. Attaining a film surface temperature near the saturation temperature at the required pressure is critical; the RECON model has highly accurate modeling in this region.

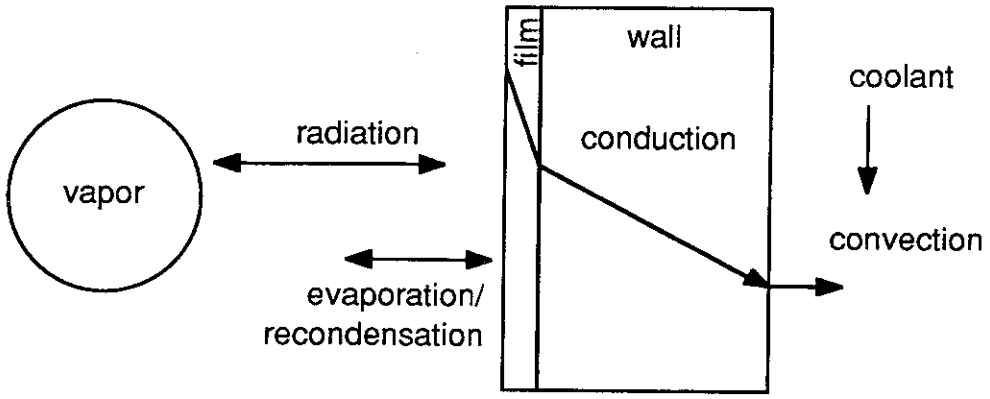

Figure 6.8.2-13 Energy Transport Pathways and Overall Geometry

Mass Evaporation and Recondensation – During the early stages of the cavity response, the cavity vapor is much hotter than the film surface and evaporation occurs. The rate of evaporation, $\dot{m}_e$, is determined from an energy balance between the thermal radiation absorbed at the surface and conduction into the film.

$$h_{fg}\,\dot{m}_e = (q_{rad} - q_k)\,A \qquad (6.8.2\text{-}35)$$

The conduction rate is easily computed from the film temperature gradient at the surface:

$$q_k = k\,\frac{dT}{dx} \text{ at the surface} \qquad (6.8.2\text{-}36)$$

As the cavity vapor cools and q_{rad} drops, recondensation begins. The expression for condensation mass flux used in RECON is based on the work of Pong,[1] which derives a mass diffusion coefficient by the theory of Labuntsov and Kryulov.[2] The mass flux is given by:

$$j = \frac{1.67}{\sqrt{2\pi RT}}\left(P_v - 0.579\,P_{gas}\,\frac{M_{gas}}{M_v}\,P_l\right)\left(1 + 0.515\,\ln\left(\frac{P_v}{P_l}\left(\frac{T_l}{T_v}\right)^{1/2}\right)\right)$$

$$x\left(1 + 4.3\left(\frac{P_{gas}}{P_l}\right)^{0.52}\left(\frac{M_{gas}}{M_v}\right)^{0.74}\left(\frac{T_l}{T_v}\right)^{4.712}\right)^{-1} \qquad (6.8.2\text{-}37)$$

Use or disclosure of data
subject to title page restriction

It includes the effect of noncondensible background gas, which in this case would represent He and unburned D and T. Since the molecular weight of these species is so much smaller than that of Pb, a substantial amount of background gas can be tolerated without interfering in the recondensation process. When the heat flux into the surface is greater than the conduction rate, evaporation takes place. Evaporation is assumed to be instantaneous and quantitatively equal to the difference in heat fluxes divided by the latent heat of evaporation.

Thermal Radiation – Thermal radiation in high temperature gases is a complex subject. For this work, we used two simplified models. Radiation heat transfer at lower temperature ranges is based on a classical Stefan-Boltzmann law (T^4 scaling) with an optical thickness parameter (τ) controlled by the user:

$$q_{rad} = \frac{\sigma (T_v^4 - T_l^4)}{1 + \frac{3}{4}\tau} \qquad (6.8.2\text{-}38)$$

The sensitivity of the results to changes in the radiation heat flux was tested by varying τ and observing the effect.

At very high temperatures (above ~100 eV), radiation cooling rates can be obtained from Post.[3]

Prometheus conditions immediately following the blast are at intermediate temperatures of a few eV. In this regime, the vapor is partially ionized. To properly treat the the radiative heat transfer from the gas in this regime, Zel'dovich[4] suggested the following model which is valid for temperatures of a few electron volts and higher.

The cooling rate is expressed as a modified Boltzmann relation:

$$q''' = \frac{4 \sigma T_{vap}^4}{l_1} \qquad (6.8.2\text{-}39)$$

Where T_{vap} is the temperature of the vapor, σ is the Stefan–Boltzmann constant, and l_1 is the frequency averaged photon mean free path. This equation is valid for mean free paths that are less than the characteristic lengths of the cavity. An approximate expression for l_1 is given as:

$$l_1 = \frac{1.1 \times 10^{23} T_{vap}^{7/2}}{N^2 \bar{m} (\bar{m} + 1)^2 \bar{x}_1} \times 10^{-2} \text{ [m]} \qquad (6.8.2\text{-}40)$$

Use or disclosure of data
subject to title page restriction

Where N is the gas density in #/cm^3, T_{vap} is the vapor temperature in Kelvin, $\overline{m}$ is the average charge state of the gas, and $\overline{x_1}$ is defined as the ratio of the average ionization potential to the temperature of the vapor:

$$\overline{x_1} = \frac{\bar{I}}{kT_{vap}} \qquad (6.8.2\text{-}41)$$

$\bar{I}$ can be defined in terms of $\overline{m}$ by:

$$\bar{I}\ (\overline{m} + 1/2) = kT \ln\left(\frac{6 \times 10^{21}\ T(eV)^{3/2}}{\overline{m}\ N}\right) \qquad (6.8.2\text{-}42)$$

$\overline{m}$ is obtained from the LIBRA report[5] with an assumption that, at the temperatures of interest, 1 ~ 4 eV (1 eV ~ 11,600 K), the average charge state has a fairly weak dependence on the gas density so it can be assumed that the charge state is independent. LIBRA used $Li_{17}Pb_{83}$ as the liquid metal. Since it is a eutectic, there will be some error incurred from using the charge states presented in LIBRA. However, since lithium lead is 83% lead, the error is believed to be small. The data points for $\overline{m}$ are interpolated between the distinct charge states (i.e., $\overline{m}$ equals 1, 2, 3, etc.) to obtain a continuous function. At these temperatures, the average charge state is approximately constant with the gas density.

The specific energy per unit volume of the lead vapor (ε) can be calculated from:

$$\varepsilon = \frac{3}{2} N (1 + \overline{m}) KT + N Q_{\overline{m}}$$

where Q_m is the summation of the ionization potential from 1 to the charge state m:

$$Q_{\overline{m}} = \sum_{j=1}^{\overline{m}} I_j$$

The discrete function Q_m is turned into a continuous function by interpolating between the discrete values of Q_m. The equation for the specific energy can be inverted to get the temperature of the gas for a given amount of energy being contained in the gas.

Figure 6.8.2-14 gives the internal energy of a gas vs. gas temperature. Note that the continuously changing slope of the curve indicates different levels of ionization. There are no discontinuities shown on the graph as is expected for a single atom; this is because we are dealing with a large number of atoms and these atoms will contain a distribution of energies and different ionization levels.

Use or disclosure of data
subject to title page restriction

This model is applied to the transient conditions experienced in a local dry spot, where the high heat flux during the first few fractions of a millisecond cause the sublimation of the SiC first wall structure. This problem is discussed in Section 6.8.5.3.

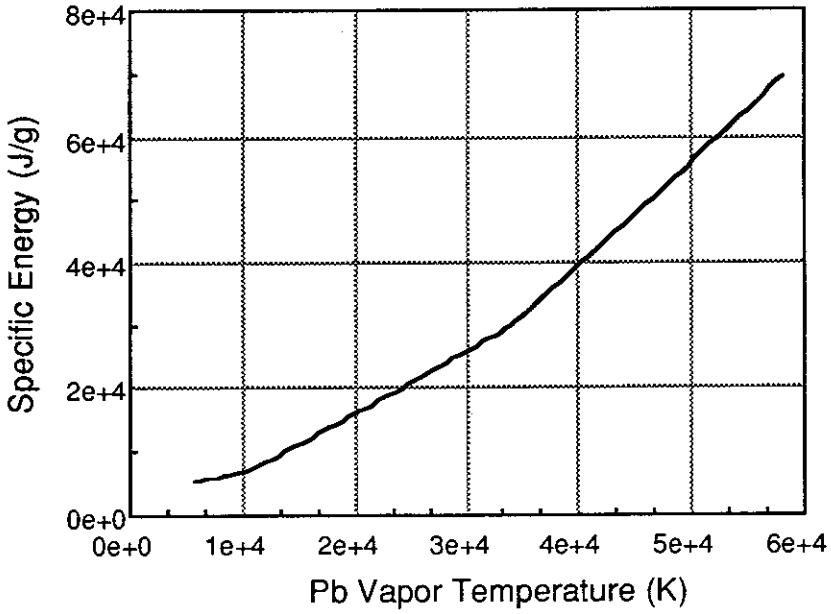

Figure 6.8.2-14 Specific Energy of Pb Vapor vs. Temperature

Conduction in the Film and Wall – The energy equation is finite differenced in the wall:

$$\alpha \frac{\partial^2 T}{\partial x^2} = \frac{\partial T}{\partial t} \qquad (6.8.2\text{-}43)$$

and boundary conditions are applied at the film surface and cooling surface as follows:

$$\frac{k}{\Delta x}(T_1 - T_2) = q_{in} = q_{ec} + q_{rad} \qquad (6.8.2\text{-}44)$$

$$h\,(T_n - T_b) = \frac{k}{\Delta x}(T_{n-1} - T_n) \qquad (6.8.2\text{-}45)$$

Transient conduction at the film surface is an important heat transfer mechanism. The grid is tailored with many grid points near the surface and a stability condition is imposed on the overall time step:

$$\Delta T < 0.5 \frac{(\Delta x)^2}{\alpha} \qquad (6.8.2\text{-}46)$$

Use or disclosure of data
subject to title page restriction

Results – This section is divided into two main parts: (1) presentation of base case clearing results for the laser and heavy ion reactors, and (2) parametric studies. First, a few simple observations are given to provide a better understanding of recondensation in the cavity. The behavior following a microexplosion can be divided into roughly four phases.

(1) At or near t=0, x-ray energy is deposited in the cavity gas and in the first few microns of the protective film. Only ~5 kg of Pb is evaporated and the cavity gas temperature reaches several eV.
(2) In the first millisecond, thermal radiation from the cavity gas is very intense and causes "secondary evaporation" from the surface. The mass of Pb in the cavity grows to ~100 kg. Thermal radiation is so rapid that the cavity gas pressure decreases even though the mass increases. Figures 6.8.2-15 and 16 show example cavity pressure and mass histories following the blast.
(3) After conduction near the surface exceeds the rate of thermal radiation, the recondensation phase begins. At early times, conduction is very efficient because the temperature gradient near the surface is high as a result of the energy deposition from the blast. Recondensation is driven by the pressure difference between the cavity gas and the saturation pressure at the surface, so the rate steadily decreases.
(4) No clear boundary exists between the third and fourth stages. However, as the cavity pressure approaches the saturation pressure at the surface, the condensation rate can slow significantly. In this stage, the ultimate cavity pressure is determined primarily by conduction through the bulk of the film and wall and by the bulk coolant temperature.

In the wetted wall cavity, the recondensation process is limited by heat conduction through the wall and into the first wall cooling system. In order to obtain the best performance, the structures between the chamber and the first cooling channel must have high thermal conductivity and be kept as thin as possible. It is important not to overload the system with too high a power density. A simple heat removal formula was included in the Prometheus system codes:

$$\frac{\dot{Q}_w}{A} < \frac{k_{eff}\,(T_{sat} - T_c)}{\delta} \qquad (6.8.2\text{-}47)$$

This formula was then tested against several RECON runs and correction factors applied to make it consistent with the more detailed simulations.

Use or disclosure of data
subject to title page restriction

The saturation pressure vs. temperature is given by:

$$T_{sat}(Pb) \sim \frac{11290}{11.34 - \log_{10}(p)} \qquad (6.8.2\text{-}48)$$

This is plotted in Figure 6.8.2-17. Since cavity pressure limits are traditionally expressed at 0°C, the curve is also shown in temperature-corrected form. Note, operation at 1 mTorr requires that the surface temperature be cooled below ~950 K; operation at 100 mTorr requires a surface temperature below ~1150 K.

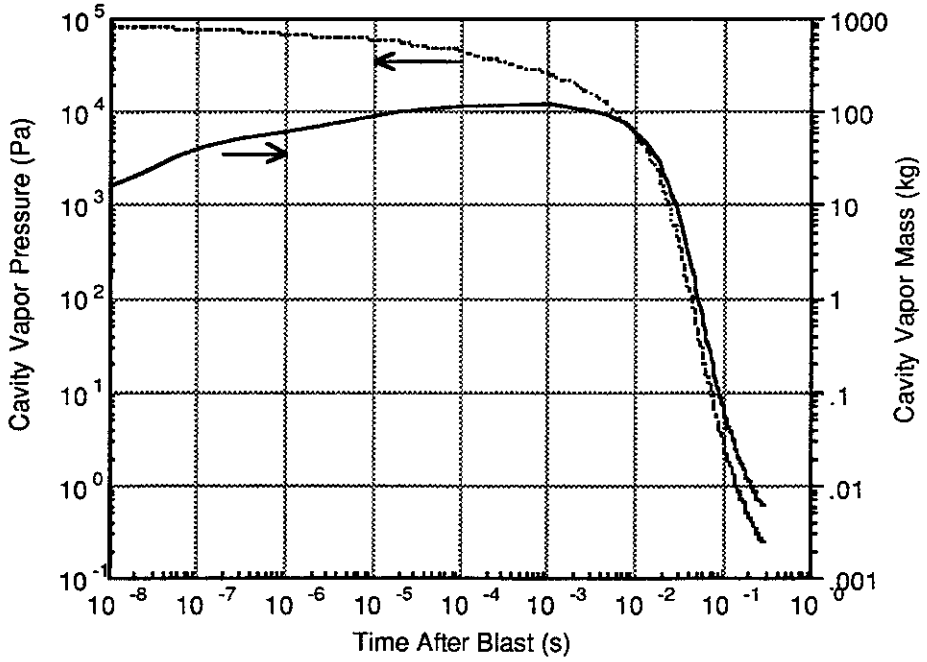

Figure 6.8.2-15 Cavity Vapor Pressure and Mass Histories for Prometheus-L

Use or disclosure of data
subject to title page restriction

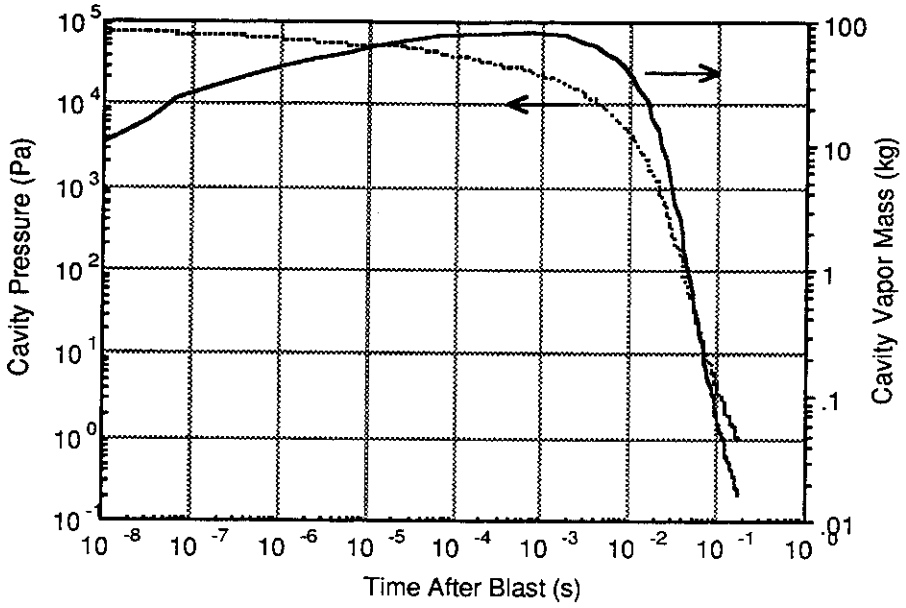

Figure 6.8.2-16 Cavity Vapor Pressure and Mass Histories for Prometheus-H

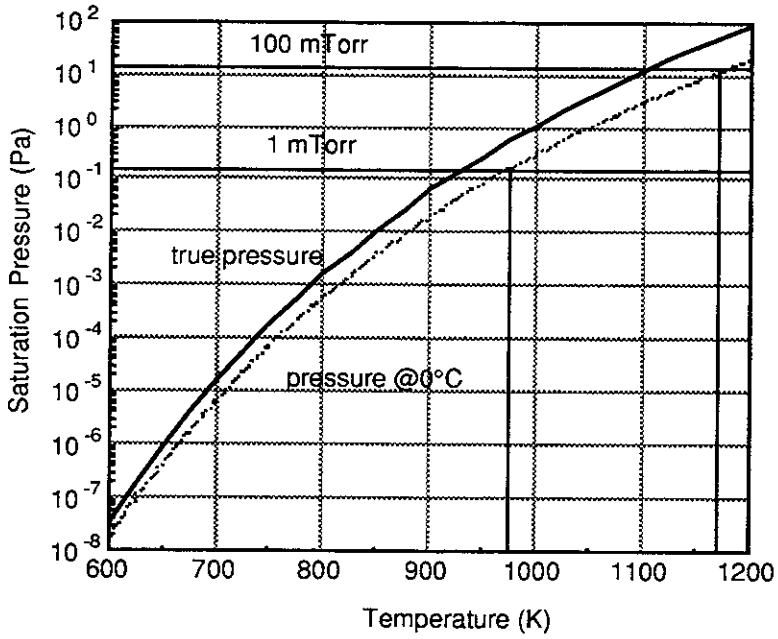

Figure 6.8.2-17. Saturation Pressure of Pb (Solid Line) and Saturation Pressure Corrected to 0°C (Dotted Line)

Base Case Results – Results are shown below for Prometheus-L and -H. Figures 6.8.2-18 and 19 show the cavity vapor temperature and pressure histories as calculated by RECON using the input parameters shown in Table 6.8.2-9. Based on

Use or disclosure of data
subject to title page restriction

this analysis, the laser cavity pressure drops below 1 mTorr (@0°C) before the next shot (at 0.25 s) if the cavity cylindrical section height is 10 m. With a height of 5 m, the base pressure is ~3 mTorr, which is judged to be acceptable (the uncertainties in the pressure limit as well as the recondensation calculation are high enough that strict adherence to the 1 mTorr limit is not considered mandatory). The final pressure for the HI case is ~10 mTorr (@0°C).

Table 6.8.2-9 Base Case Parameters

	Laser	HI	Units
Bulk Coolant Temperature	648	648	K
Pb Film Thickness	0.5	0.5	mm
SiC Wall Thickness	5	5	mm
Cavity Radius	5.0	4.5	m
Cavity Cylinder Height	5.0	4.5	m
Surface Area	471	382	m^2
Volume	916	668	m^3
X-ray Yield	31	46	MJ
Debris Yield	107	159	MJ
Rep Rate	5.6	3.5	Hz
Emissivity	1	1	
Noncondensible Gas Pressure	3	100	mTorr @ 800 K

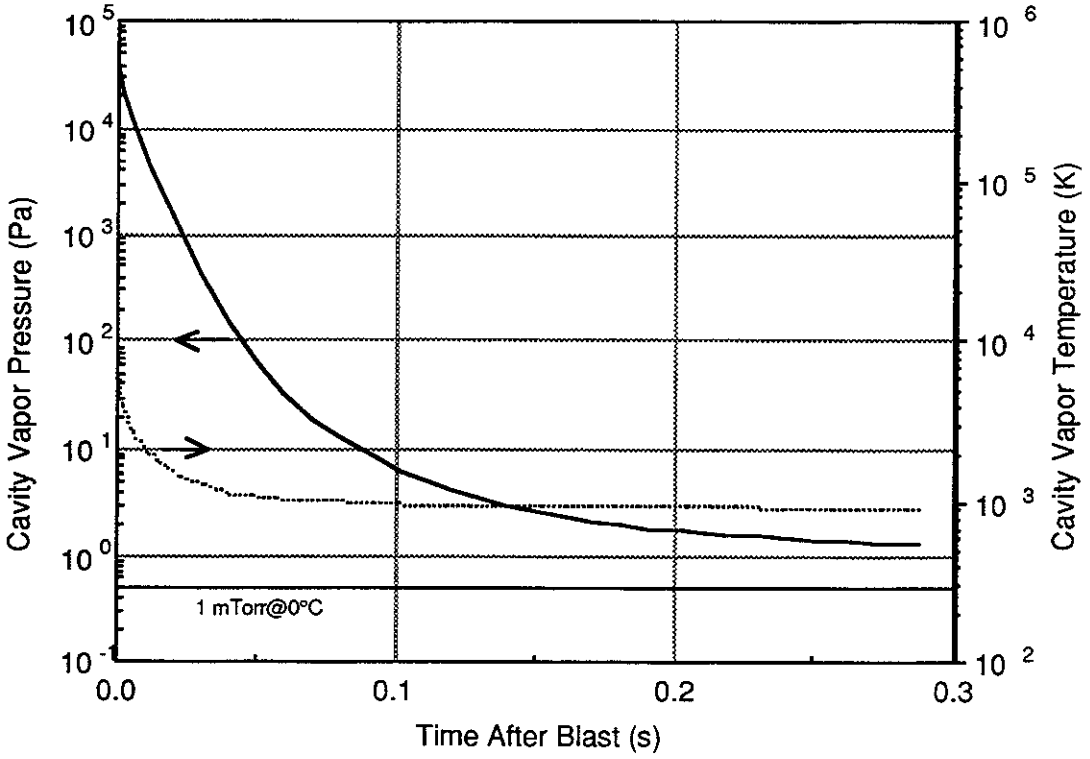

Figure 6.8.2-18 Base Case Cavity Vapor Temperature and Pressure Histories for Prometheus-L

Use or disclosure of data
subject to title page restriction

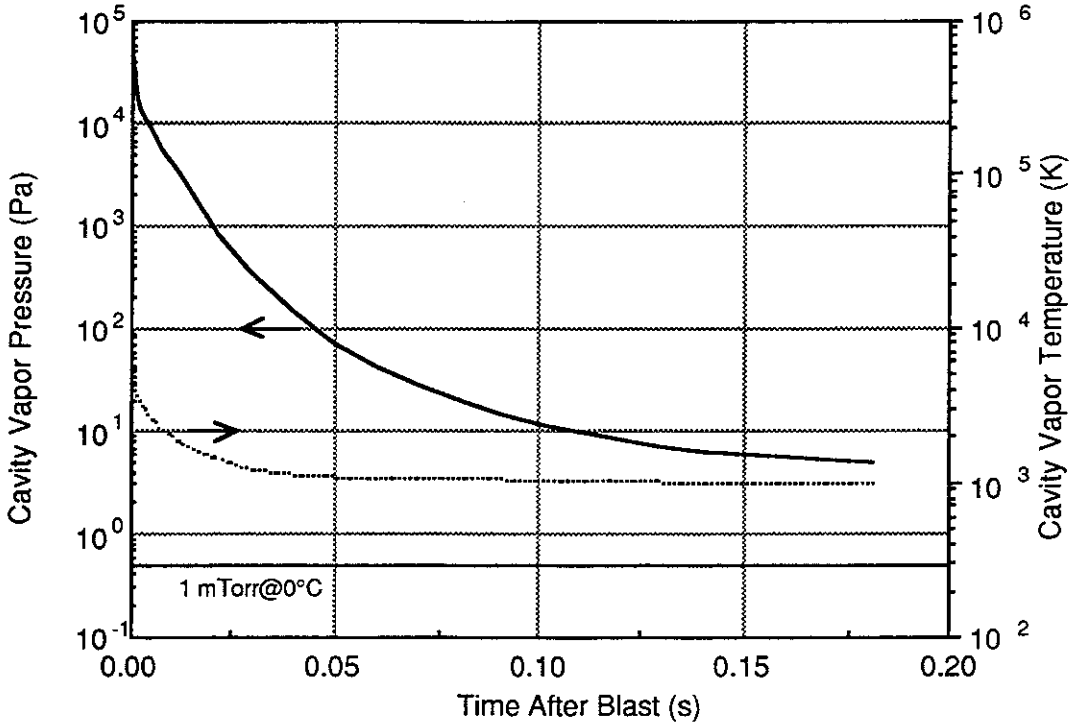

Figure 6.8.2-19 Base Case Cavity Vapor Temperature and Pressure Histories for Prometheus-H

Most of the initial blast energy is absorbed in the cavity gas. Approximately 5 kg of Pb are evaporated by direct energy deposition. The initial (averaged) cavity vapor pressure and temperature are estimated as 49 kPa and 550,000 K respectively. A much larger amount of Pb is evaporated due to rapid radiation cooling of the cavity vapor. Before the recondensation phase begins, about 80 kg of Pb (10 μm) are evaporated.

Figure 6.8.2-20 shows the temperature at the surface of the film and at the interface between the film and SiC structure. The SiC temperature is always well below the compatibility limit with Pb (~1000°C). The surface temperature drops very quickly immediately following the blast and asymptotically falls towards the bulk coolant temperature. The ultimate cavity vapor pressure is very sensitive to this slow conduction-dominated phase of the process because the vapor pressure is strongly temperature-dependent. By maintaining a thin first wall and low coolant temperature, adequate recondensation can always be assured (within the scope of this simplified model).

Use or disclosure of data
subject to title page restriction

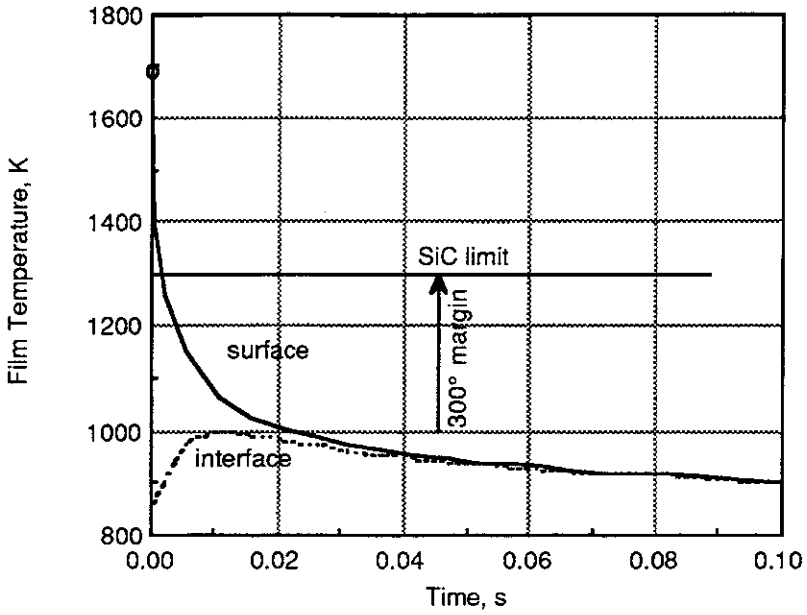

Figure 6.8.2-20. Base Case Temperatures at the Film Surface and Interface Between the Film and SiC Wall for Prometheus-L

Parametric Studies – To aid in the design of the cavity and to provide a better understanding of the behavior following the blast, a series of parametric studies were performed using RECON. A base case was defined using the laser reactor parameters listed in Table 6.8.2-9 except that, for these cases, the background (non-condensible) gas pressure was 1 mTorr.. Variations were made in the repetition rate, background pressure of non-condensible gases, and the cavity geometric parameters (radius, area and volume).

(1) Effect of Repetition Rate Under Constant Power - For this study, the total surface power was held fixed at 718 MW. The repetition rate was varied from 3 to 8 Hz while adjusting the yield to maintain constant power. Figure 6.8.2-21 shows the resulting cavity pressure at the end of a pulse. As the repetition rate increases, the cavity base pressure also increases, even though the yield is decreasing proportionately.

Use or disclosure of data
subject to title page restriction

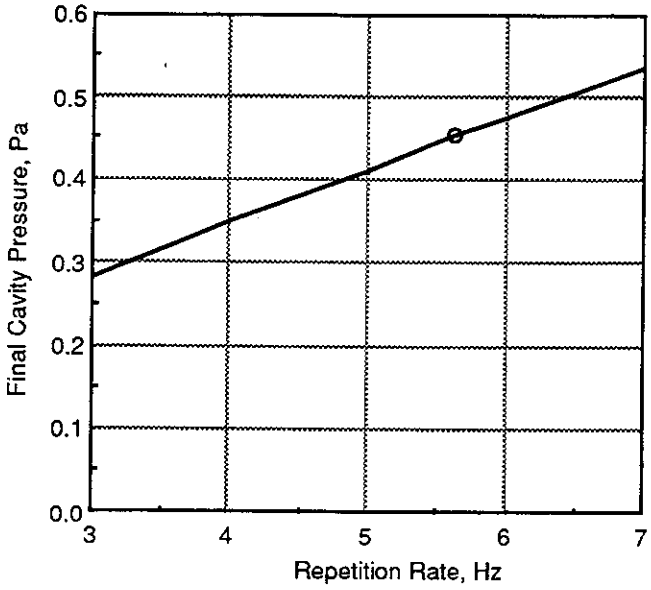

Figure 6.8.2-21 Effect of Rep. Rate on the Cavity Pressure Following a Blast

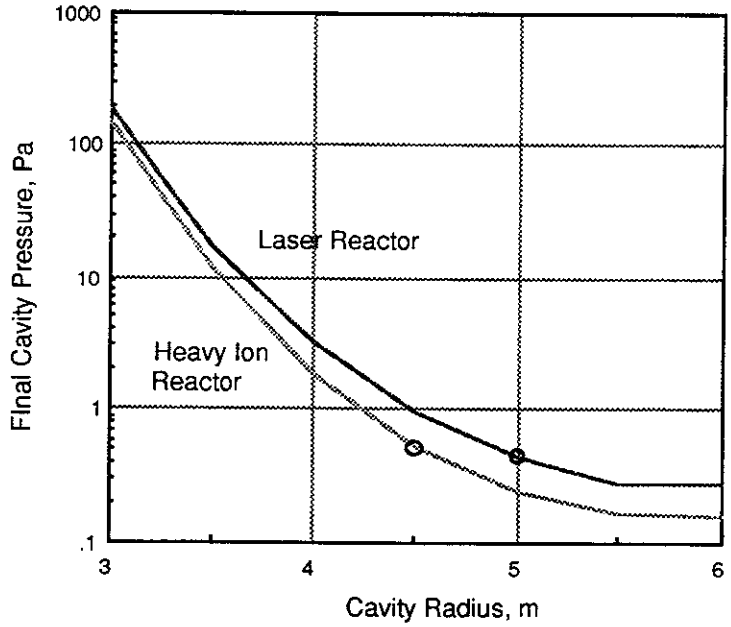

Figure 6.8.2-22. Effect of Increasing the Cavity Size on the Cavity Pressure Following a Blast

Use or disclosure of data
subject to title page restriction

(2) Effect of Geometric Parameters - Figure 6.8.2-22 shows the effect of varying the radius for both the laser and heavy ion reactor cavities. The area and volume were also changed to maintain constant aspect ratios. The values used were:

Radius (m)	Area (m^2)	Volume (m^3)
3	170	198
3.5	231	314
4	302	469
4.5	382	668
5	471	916
5.5	570	1220
6	679	1583

Above ~5 m radius, little additional reduction in pressure is made. Below ~4 m, the pressure rises rapidly.

Parametric studies were also performed by varying the surface area and volume independently. Of course, in a real system, the dimensions would all change in a self-consistent manner. For the purpose of this study, we varied only one at a time in order to determine the true effect of each separate parameter. Figures 6.8.2-23 and 24 show the results. The effect of changing the wall surface area is very pronounced below ~400 m^2. It is impossible to achieve pressures below ~0.05 Pa which corresponds to the vapor pressure at the coolant outlet temperature.

Figure 6.8.2-24 shows the effect of changing the cavity volume with the surface area held constant. The pressure decreases as the volume decreases, subject to the same limitation as above (due to the vapor pressure at the coolant outlet temperature). This trend seems counter-intuitive; one might expect the clearing time to improve with larger chambers. It is important to recall that the surface area effect is not present here, as the area is fixed.

Figure 6.8.2-25 shows the pressure history for two cases with different volumes. The volume could be increased without changing the area by making the cavity more spherical. The curves show an interesting result. Initially, a larger cavity has a lower pressure, because both cases have roughly the same mass evaporated (evaporated mass depends primarily on the yield). However, the time to recondense is longer for larger volumes. This is because the recondensation mass flux is driven by the pressure in the cavity. At a given pressure, the mass flux will be the same in both cases, but the amount of mass to be removed is greater with the greater volume.

Use or disclosure of data
subject to title page restriction

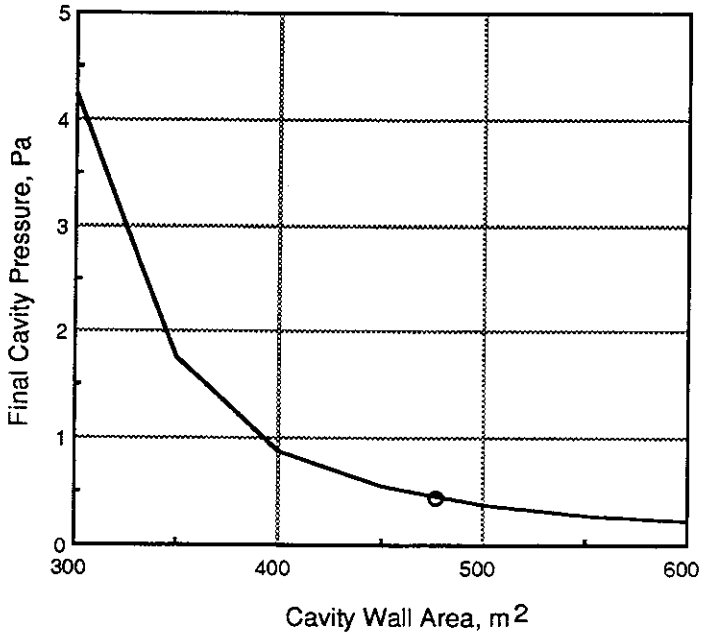

Figure 6.8.2-23 Effect of Changing the Cavity Area with the Volume Fixed

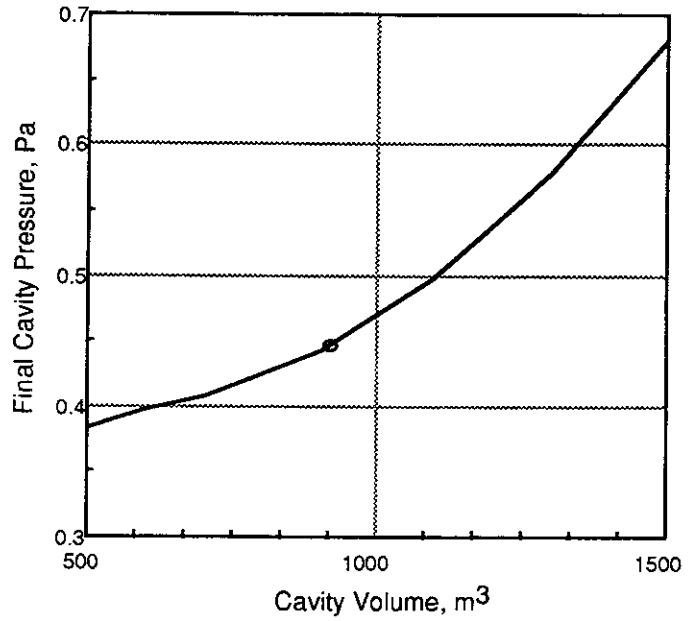

Figure 6.8.2-24 Effect of Changing the Cavity Volume with the Area Fixed

Use or disclosure of data
subject to title page restriction

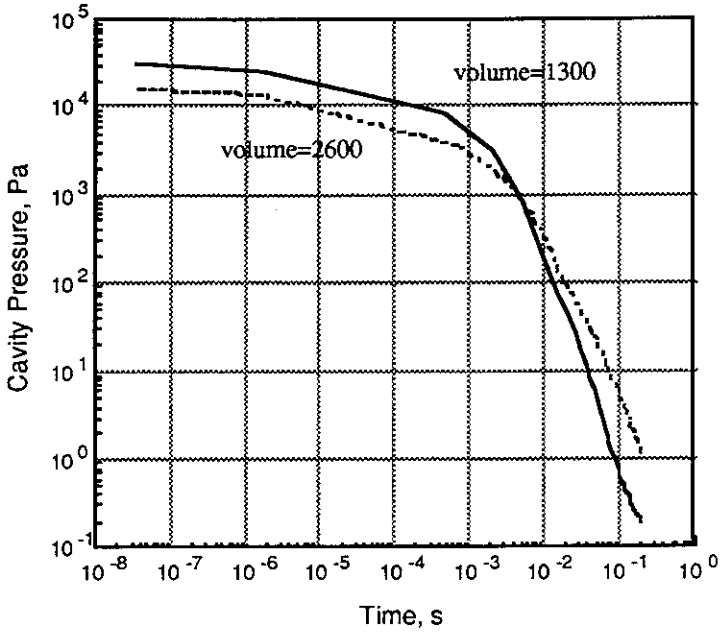

Figure 6.8.2-25 Effect of Increasing the Cavity Volume on the Pressure History

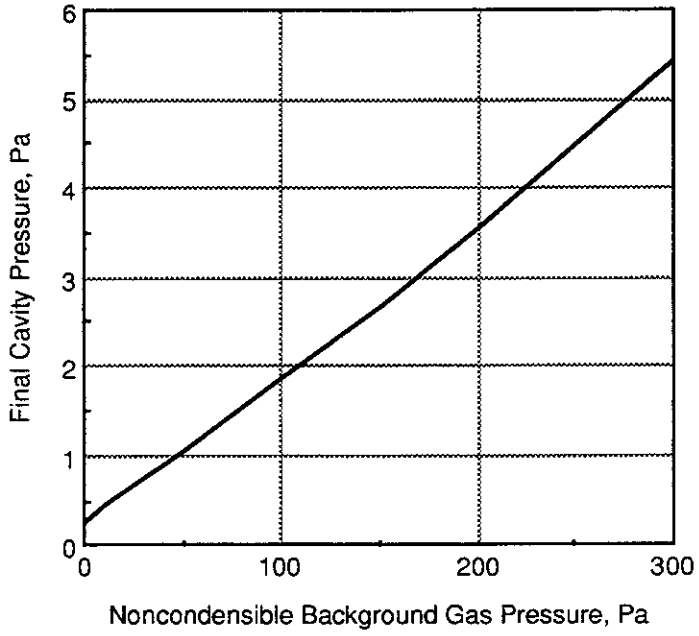

Figure 6.8.2-26 Effect of Non-condensible Gas Pressure on the Final Cavity Pressure

Use or disclosure of data
subject to title page restriction

The results show that larger volume results in higher pressure at the end of the pulse (or longer time to recondense to a given pressure). A larger cavity volume results in lower initial pressure, because the initial mass of Pb evaporated depends primarily on the total yield. However, the rate at which mass is evacuated is smaller for larger volumes. Recondensation is driven by the pressure in the cavity. At a given pressure, the mass flux will be the same in both cases, but the amount of mass to be removed is greater with the greater volume.

(3) Effect of Non-condensible Gas - The pressure of non-condensible gas was increased to determine how much vacuum pumping is needed. For this calculation, the average Z was set to 2. Figure 6.8.2-26 shows the results.

References for 6.8.2.5

1. L. Pong, et al.,"Liquid Metal Condensation in the Cavity of the HIBALL Heavy Ion Fusion Reactor," Nuc. Eng. and Design/Fusion 3, 47-57 (1985).

2. D. A. Labuntsov and A. P. Kryukov, "Analysis of Intensive Evaporation and Condensation," Int. J. Heat Mass Transfer, Vol. 22, 989 (1979).

3. E. Post, et al., "Steady State Radiative Cooling Rate for Low Density High Temperature Plasmas," Atomic and Nuclear Data Tables (20), p 397, 1977.

4. Ya. B. Zel'dovich and Yu. P. Raizer, "Physics of Shock Waves and High-Temperature Phenomena," Academic Press, New York and London, 1966.

5. B. Badger, et al., "LIBRA – A Light Ion Beam Fusion Conceptual Reactor Design," Univ. of Wisconsin, UWFDM-800, July 1989.

Use or disclosure of data subject to title page restriction

6.8.2.6 Film Flow

Introduction – In this section, the major characteristics of the first wall protective film are described and several special problem areas are analyzed.

There are several possible methods to inject the wall protectant and control its thickness. In the Prometheus baseline design, the liquid lead film is supplied partly by seepage through the porous first wall coolant channels and partly from an injector at the top of the upper hemisphere (see Figure 6.8.2-1). The seepage flow rate must be sufficient to maintain good coverage, but not so high as to detach or destabilize the film. As Pb reaches the surface of the first wall, it forms a continuous film which flows to the bottom of the cavity by gravity. This drainage is desired to maintain a clean surface. The film flow removes condensible impurities generated from target debris and, to some extent, by wastage of the first wall panels.

Additional Pb is injected into the upper hemisphere to ensure coverage of the upper end cap without dripping into the cavity. The inertia of the jet is adequate to provide attachment onto the entire surface. This jet is allowed to flow down the vertical section of the first wall and ultimately into the drain. Protection of inverted surfaces is a special problem for this type of wetted wall chamber and several solutions have been proposed and analyzed.

Design of the film system was undertaken with several key objectives in mind. The thickness of the film is a key parameter, since Prometheus uses primarily conduction through the film to remove the surface heating power. Calculations are described here for the evolution of the film thickness and velocity, subject to several constraints imposed on the flow. For example, a minimum film thickness is required to ensure adequate protection against the blast but, if the film becomes too thick, it loses its ability to conduct the surface heating power to the cooling channels. A minimum jet velocity is required to ensure attachment onto the upper hemisphere; however, higher velocities entail thicker films. The calculations described below were performed in order to define the allowable range of operating conditions and to optimize the film flow system.

There are several design options which were also considered:

(1) If the film thickness is too large, then conduction alone may be insufficient to remove the surface heating power. The possibility for convective heat removal was explored.
(2) Protection of the upper end cap presents unique problems. The requirements for jet injection at the upper end cap provide a less attractive film on the remainder of the cavity wall if this jet is allowed to fall to the bottom of the cavity.

Use or disclosure of data
subject to title page restriction

Extraction of this jet at the upper hemisphere and optimization of the film thickness along the vertical section was considered.

(3) Finally, control of the film thickness could be made considerably easier with the use of guiding magnetic fields. Modest field strengths could maintain a much thinner film than that available from an inertial jet. Enhanced stability of the film would be an additional benefit.

Flow Characteristics – In order to maintain the film on the upper hemisphere, a jet is injected at the top. The relatively high speed required to keep the jet attached to the wall leads to turbulence in the film. A number of previous studies have explored the wave structure of a vertical turbulent falling film.[1,2] These studies indicate that the wave structure is complex—there appear to be several classes of waves and each class has certain random features. Waves formed at the film interface appear to be a combination of large waves with small ripples superimposed on the large waves. Film waviness is complicated further by variations in both film thickness with film travel. An illustration of turbulent film wave structure given in Chu and Dukler 's study is shown in Figure 6.8.2-27 which indicates that various film thicknesses can be observed in this

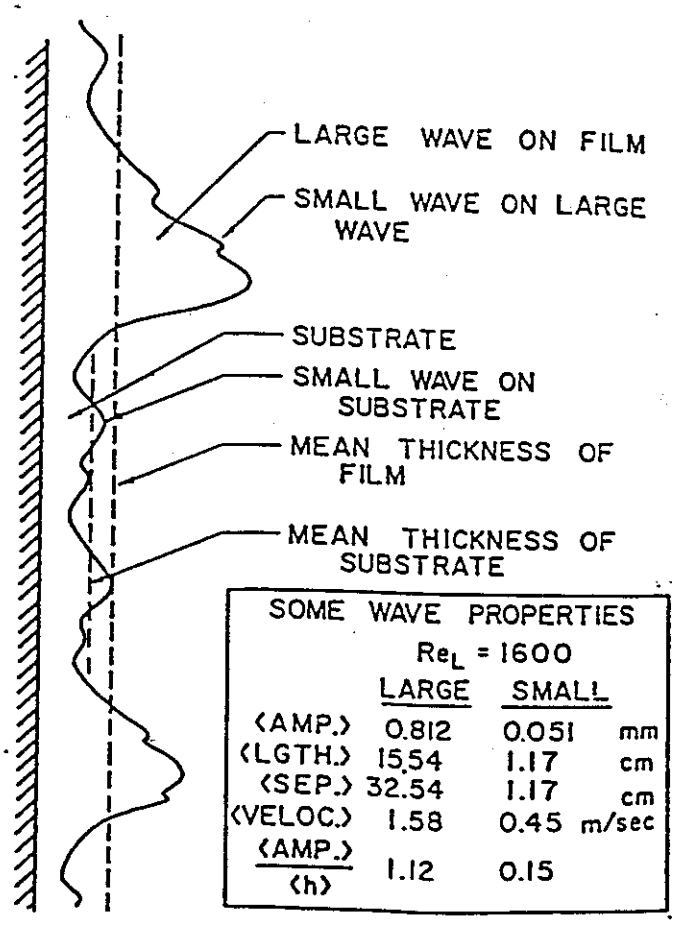

Figure 6.8.2-27. Identification of Wave Classes[1]

Use or disclosure of data subject to title page restriction

type of film. While using this turbulent liquid film for the first wall protection, the concern is whether a minimum film thickness can be greater than the required film thickness for x-ray and debris protection (such as 100 mm). The experimental study of Takahama[2] shows that the minimum film thickness decreases toward the entrance region, however, almost constantly independent of Reynolds number and the longitudinal distance. The minimum film thickness identified in their study was about 300 mm. Figure 6.8.2-28 illustrates their results of film thickness variations along the longitudinal direction.

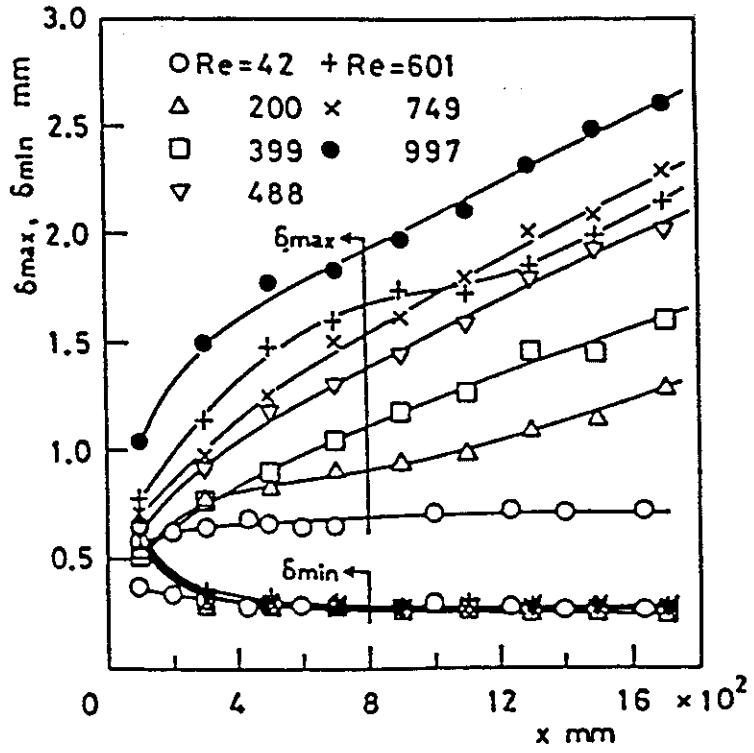

Figure 6.8.2-28. Longitudinal Distribution of Maximum and Minimum Film Thickness[2]

Flow through the Porous Wall – The porous first wall structure allows coolant to seep from the cooling channels onto the wall surface. The supply rate must be high enough to provide good coverage, but not so high as to impart momentum into the film and cause detachment. Ideally, the permeability would be tailored to provide optimum flow control but, in this work, we assume a constant permeability.

The seepage rate depends on the cooling channel pressure and the permeability of the wall, and is estimated using Darcy's formulation:[3]

$$-\nabla P - \frac{\mu}{\kappa} v \delta_{wall} = 0 \qquad (6.8.2\text{-}49)$$

Use or disclosure of data
subject to title page restriction

where v is the average seepage velocity, P is the pressure, μ is the dynamic viscosity of the fluid, and κ is the permeability of the wall. The permeability is calculated as:

$$\kappa = \frac{d^2}{175}\frac{\varepsilon^3}{(1-\varepsilon)^2} \qquad (6.8.2\text{-}50)$$

where d is the fiber diameter, ε is the porosity, and the seepage rate q^* is defined by:

$$q^* = v\,A_l \qquad (6.8.2\text{-}51)$$

where A_l is the lateral flow area.

Figure 6.8.2-29 shows the baseline pressure distribution along the coolant channel and the resulting seepage rate.

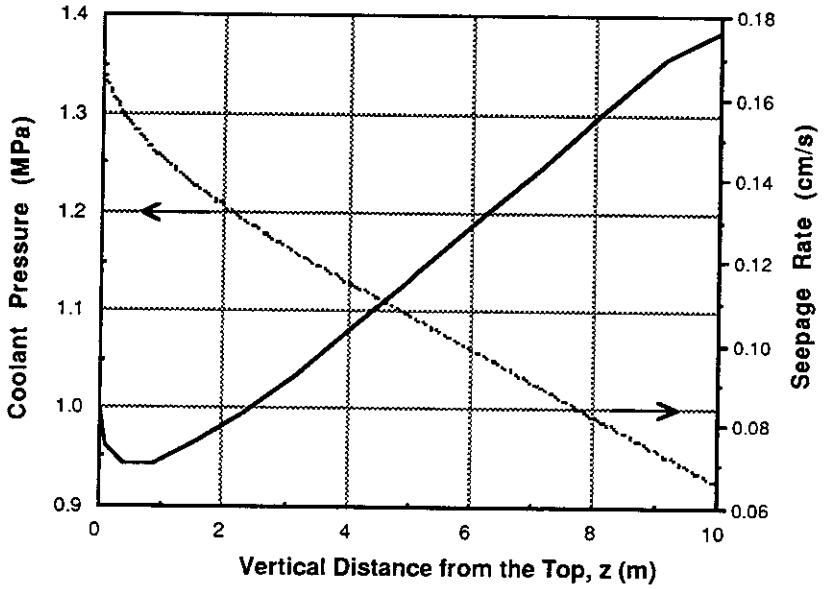

Figure 6.8.2-29. Baseline Pressure Distribution and Seepage Rate Along the First Wall

Basic Film Flow Equations – The film flow is driven mainly by gravity, which is then balanced by the drag along the wall and the flow accelerational force. The force balances in the normal and tangential directions for a fluid element are shown schematically in Figure 6.8.2-30 and are written as:

$$\rho\frac{u^2}{r_v}\delta = \frac{2\sigma\cos(\theta)}{R} + \frac{2\sigma}{r_v} + \rho g_c \delta \sin(\theta) \qquad (6.8.2\text{-}52)$$

$$\rho u \delta \frac{\partial u}{\partial l} = \rho\, g_c\, \delta \cos(\theta) - \tau_D \qquad (6.8.2\text{-}53)$$

where ρ is the fluid density, u is the liquid film velocity in the tangential (flow) direction, δ is the film thickness, r_v is the radius of curvature, σ is the surface tension, g_c is the

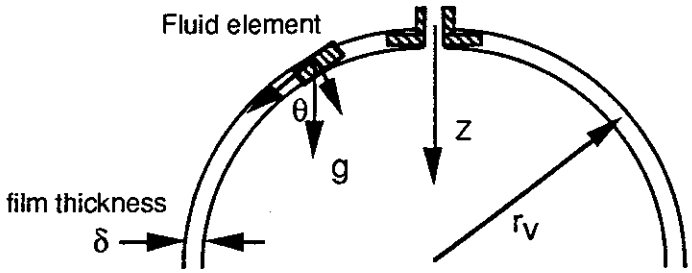

Figure 6.8.2-30. Illustration of Force Elements Acting on the Upper Wall Film

acceleration due to gravity, τ_D is the wall friction force exerted on the fluid along the flow direction, θ is the angle that the tangent to the fluid element forms with the z axis, and l is the distance measured along the flow direction.

The mass conservation equation is also needed:

$$\frac{\partial(uA)}{\partial l} = q^* \qquad (6.8.2\text{-}54)$$

where A is the film cross-sectional flow area, u is the mean velocity of flow in the longitudinal direction, and q^* is the seepage inflow rate per unit length.

To solve these equations, an expression is needed for the wall friction force in Eq. 6.8.2-53. In general, the turbulent wall friction force is expressed in terms of the friction factor as:

$$\tau_D = \frac{f}{4\delta}\frac{u^2}{2g_c} \qquad (6.8.2\text{-}55)$$

where f is the friction factor.

There are several possible methods to evaluate the friction factor for turbulent film flow. For Reynolds numbers less than 100,000, the frictional factor given by the Blasius formula[4] provides the closest estimate of the turbulent film thickness when compared to the empirical correlation of turbulent falling film thickness (δ_t) presented by Gimbutis.[5] The Blasius formula for friction factor is given by:

$$f = \frac{0.316}{Re^{0.25}} \qquad (6.8.2\text{-}56)$$

where the Reynolds number is defined as:

$$Re = \frac{4\psi}{\rho\nu_f} \qquad (6.8.2\text{-}57)$$

and ψ is the flow rate:

$$\psi = u\,\delta_t\,\rho \qquad (6.8.2\text{-}58)$$

Use or disclosure of data
subject to title page restriction

The Gimbutis's turbulent film thickness (δ_t) is expressed as:

$$\delta_t = 0.136\left(\frac{\nu_f}{g}\right)^{1/3} Re^{0.583} \qquad (6.8.2\text{-}59)$$

Before solving for film velocities and thicknesses, two important constraints must be considered: (1) the minimum required thickness to ensure protection of the substrate, and (2) the minimum velocity required to maintain attachment on the upper end cap.

Minimum Film Thickness – The minimum required film thickness is determined from the evaporation caused by target explosions. This depends on the target energy spectrum, yields, absorption characteristics of the film material, and vapor radiation processes. Energy deposition is covered in detail in Section 6.8.2.3. The depth of evaporation was estimated there to be only about 10 μm per shot. This amount of Pb will be condensed back into the film before the next shot. While under ideal conditions only ~10 μm is required, additional thickness is allowed for nonuniformities and extra margin. For this study, we assume a minimum film thickness of 100 μm.

Requirement for Attachment on the Upper End Cap – The film velocity in the upper end cap must be sufficiently high such that the film remains attached to the surface. Since the film velocity and thickness are related (by Eq. 6.8.2-59), higher velocities entail thicker films. To minimize the film thickness, it is desirable to operate near the attachment limit.

The solution of Eq. 6.8.2-52 provides the minimum velocity required to prevent the fluid from separating from the wall. At different locations on the curved surface, there is a different minimum velocity. Figure 6.8.2-31 shows these minimum required velocities as a function of distance away from the upper end cap (radius = 5 m). The minimum velocity decreases as the flow proceeds downstream; the highest minimum velocity is 7 m/sec. With this minimum velocity and the minimum film thickness for x-ray and debris absorption (~100 μm), the fluid is always turbulent, with Reynolds number larger than the critical film Reynolds number (Re_c~1600).

For each location on the upper end cap, the turbulent film thickness (based on Gimbutis's formula) and the mass flow rate are estimated using the minimum velocities from Figure 6.8.2-31. The results are shown in Figure 6.8.2-32. They indicate that, in order to maintain the flow attached to the surface, the film thickness must be greater than 6.4 mm. The minimum volumetric flow rate increases first, reaches a peak value, and decreases as the flow proceeds to downstream locations.

Once the film travels to the straight portion of the cavity wall, there is no minimum film velocity required. In fact, after the peak required flow rate is achieved (just beyond 1 m from the top), a thinner film can be maintained and control of the film becomes easier.

Use or disclosure of data
subject to title page restriction

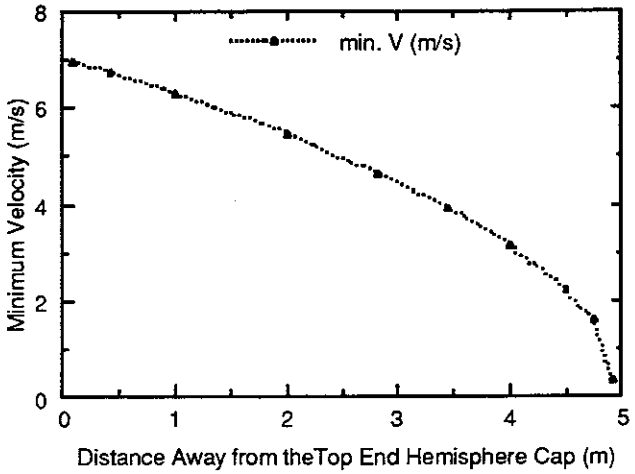

Figure 6.8.2-31. Minimum Required Film Velocity for Attachment on the Upper Hemisphere Wall

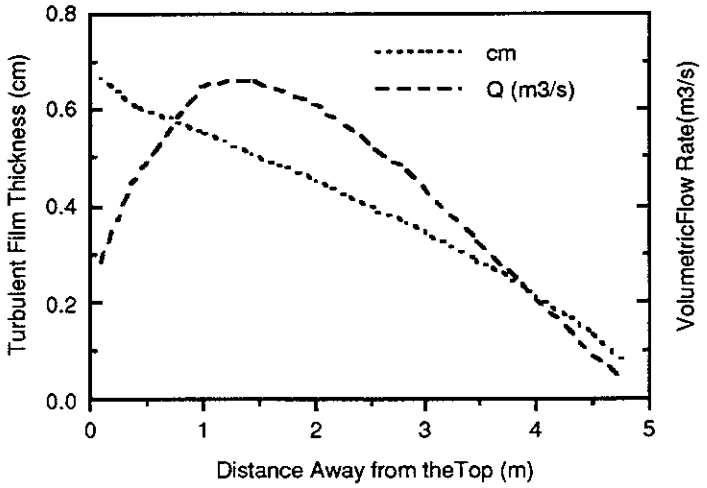

Figure 6.8.2-32. Turbulent Film Thickness and Minimum Volumetric Flow Rate for Attachment

One of the major design options for film control is to remove the jet at this point and use an injection scheme primarily supplied by seepage from the coolant channels.

Results – Eqs. 6.8.2-53 and 6.8.2-54 were solved for the film thickness and velocity along the flow direction for different initial flow rates and wall characteristics. Example results are shown in Figure 6.8.2-33 for film thickness and Figure 6.8.2-34 for velocity.

There are several parameters which affect the film characteristics. These are injection angle, film injection velocity and initial film thickness, wall permeability, and lateral supply rate. Two cases were analyzed: Case 1 has a relatively modest injection velocity of 15 m/s and Case 2 increases this to 40 m/s. For both cases, the film flow is initiated by injection at an angle of 82° (defined as the angle between the flow and the direction of gravity) with a wall permeability of 1.764×10^{-14} m^2. Table 6.8.2-10 summarizes the parameters.

Use or disclosure of data
subject to title page restriction

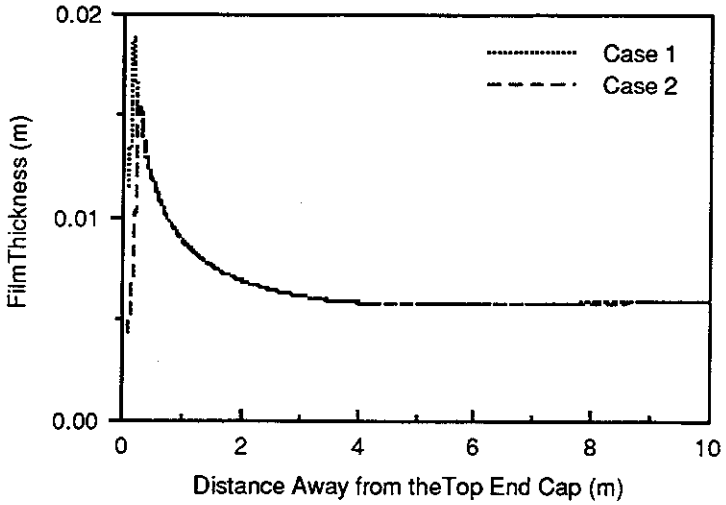

Figure 6.8.2-33. Film Thickness as a Function of Distance Away from the Top End Cap

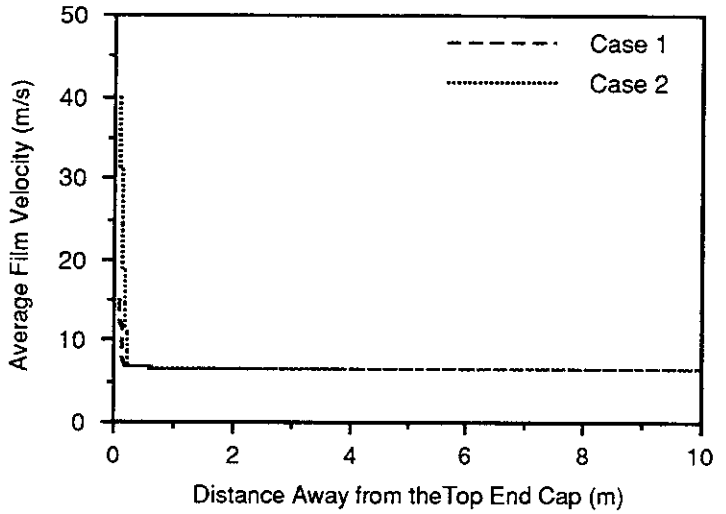

Figure 6.8.2-34. Average Film Velocity as a Function of Distance from the Top End Cap

Table 6.8.2-10 Summary of Cases Analyzed

Parameter	Case 1	Case 2
Injection Velocity	15 m/s	40 m/s
Initial Thickness	1.15 cm	0.43 cm
Maximum Thickness	1.9 cm	1.6 cm
Ultimate Thickness	0.6 cm	0.6 cm

Beyond the injector region, there is little difference between the two cases. In each case, the velocity decreases immediately due to the wall drag. The film thickness increases first due to the reduction of film velocity and later decreases because of the expansion of the flow area. The maximum film thickness decreases from 1.9 to 1.6 cm as the injection velocity increases from 15 to 40 m/s. For both cases, the ultimate film thicknesses are about 0.6 cm.

These film thicknesses are much larger than that required for x-ray and debris absorption and may be too large for removing heat by conduction. To reduce the film thickness on the curved hemispheric wall, the lateral supply from the main stream can be reduced by decreasing the wall permeability once the flow reaches the peak point.

Convective Heat Transfer in the Film – The analysis of film flow on the upper hemisphere indicates that maintaining a film smaller than a few mm is not possible. As the film thickness grows, heat removal by conduction is reduced. In order to prevent high surface temperatures (which prevent high repetition rates), good convection heat transfer may be required.

Thermal analyses were performed for two different cases. In both cases, the film is supplied by both injection at the top and laterally from the cooling channels. Parameters were chosen in order to provide as uniform a film thickness as possible. In Case 1, the flow injection rate at the top end cap is maximized and the porosity of the wall is 15%. In Case 2, the lateral supply rate is maximized and the porosity of the first wall is 30%.

The total amounts of flow from the lateral supply for Cases 1 and 2 are 4% and 35% of the ultimate flow rate, respectively. Under these conditions, the lateral momentum flux is only a few percent of the longitudinal momentum flux, so that 1-D analysis should be adequate.

Results are shown in Figures 6.8.2-35 and 36. The film flow is initiated by injecting the flow at an angle of 82° (about 10 cm away from the top). Initial velocities of 35 and 40 m/s and initial film thicknesses of 4 and 2.5 cm are assumed for Cases 1 and 2, respectively. The results show that in each case the velocity decreases very rapidly initially due to wall drag. The film thickness first increases due to the reduction of the film velocity, and then decreases later because of the increase in flow area.

For Case 1, the peak film thickness is 5.4 cm and the ultimate thickness is 1.54 cm. For Case 2, the peak, mean film thickness is about 3.9 cm and the ultimate, mean film thickness is about 1.6 cm. If the initial velocity can be further increased, a more uniform mean film thickness can be obtained.

Use or disclosure of data
subject to title page restriction

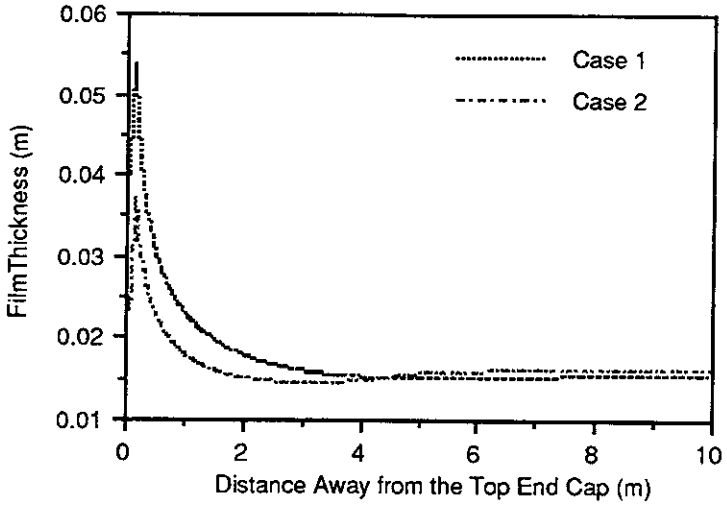

Figure 6.8.2-35. Film Thicknesses as a Function of Distance Away from the Top End Cap

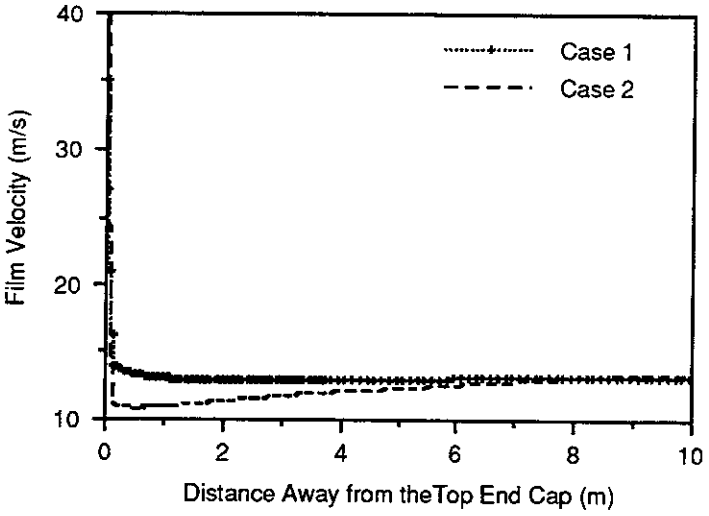

Figure 6.8.2-36. Film Velocities as a Function of Distance Away from the Top End Cap

The concerns of using a couple of cm thick film are whether the temperature on the first wall is beyond the design limit and whether the temperature on the film surface is too high for the condensation to take place. At pressure of $1x10^{-3}$ torr, the saturation temperature is about 627°C; the saturation temperature increases to 838°C as the pressure increases to $1x10^{-2}$ torr. In order to have a significant amount of condensation on the film surface, the film surface temperature should be less than 627°C for laser driven IFE and 838°C for heavy ion driven IFE. The film heat transfer coefficient given by Lee[6] is examined for this purpose. The turbulent film heat transfer coefficient for liquid metal is of the same order as the laminar heat transfer coefficient. The non-dimensional laminar heat transfer coefficient for condensation was expressed in terms of Reynolds number and written as:

Use or disclosure of data
subject to title page restriction

$$\left(\frac{\nu^2}{g_c}\right)^{1/3}\frac{h_{av}}{k} = 1.47\,Re^{-1/3} \qquad (6.8.2\text{-}60)$$

At Reynolds number of 8.5×10^5, which corresponds to the Reynolds number at the vertical section of the reactor chamber, the heat transfer coefficient is estimated as 1.51×10^4. For heat flux of 2.7×10^6 W/m^2, the film temperature drop is about 200°C; this gives the maximum film surface temperature of 725°C.

The first wall surface temperature can be estimated by the turbulent heat transfer coefficient at the wall from the Colbrun correlation,[7] which is stated as:

$$\frac{h}{\kappa}\left[\frac{\mu^2}{\rho^2 g}\right]^{1/3} = 0.056\,Re^{0.2}\left(\frac{C_p\mu}{\kappa}\right)^{1/3} \qquad 6.8.2\text{-}61$$

The estimation of film temperature gradient based on the turbulent heat transfer coefficient predicted from the aforementioned equation and heat flux of 2.7×10^6 W/m^2 is about 10°C.

Although these preliminary calculations indicate that the film surface is cold enough for condensation to take place in a heavy ion driven IFE cavity and the first wall surface temperature is low, further analysis on the cavity clearing and liquid metal turbulent film heat transfer coefficient for condensation are needed to demonstrate that this concept is feasible.

Effect of Time-Dependent Cavity Pressure – Once an explosion occurs, some of the Pb film is vaporized and increases the cavity pressure. Under these circumstances, Pb may be pushed back into the cooling channels and the film will thin, slow down, and possibly become dry at the wall. In addition, the reactive impulse due to vaporized liquid and cavity shock waves may cause the same phenomenon, as well as disrupting the film surface. Here, the transient behavior of the film velocity and thickness are examined due to cavity pressure buildup. The effect of impulsive loading is beyond the scope of this work.

It is assumed that the pressure difference between the main coolant and the cavity can be expressed as:

$$\Delta P = P_{inlet} - 0.5\times10^6 \times (1 - e^{-t/3\tau}) \qquad (6.8.2\text{-}62)$$

where τ (~0.25 s) is the time interval between the explosions. This is a conservative estimate, since cavity clearing calculations estimate <0.1 MPa peak overpressure (see Section 6.8.2.5).

Figure 6.8.2-37 shows the assumed cavity pressure and pressure difference histories at the uppermost point of the cavity. The above equation does not attempt to simulate the real cavity pressure. (The cavity pressure at time of 0.25 seconds following the microexplosion falls below 1 mtorr.)

Use or disclosure of data subject to title page restriction

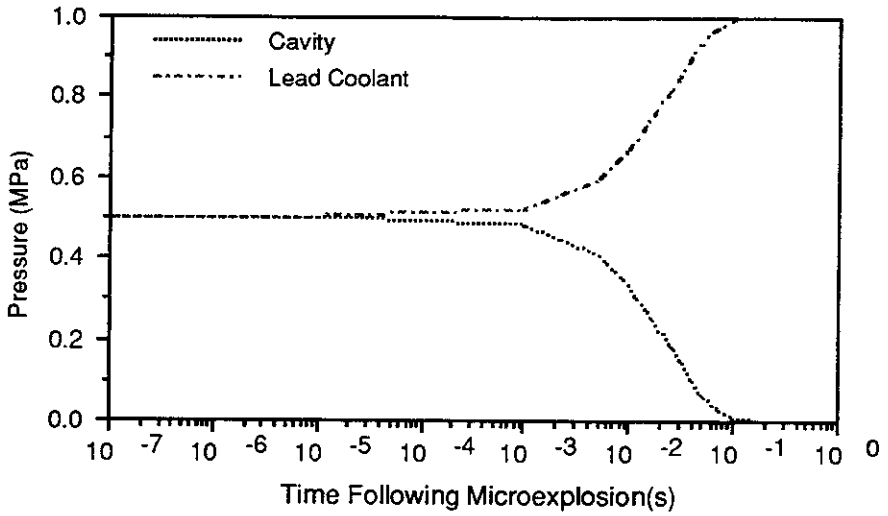

Figure 6.8.2-37. Cavity and Differential Pressure Histories at the Uppermost Point of the Cavity

The fluid equations include the transient Darcy's equation:

$$\rho\frac{\partial v}{\partial t} = -\frac{\partial P}{\partial y} + \frac{\mu}{\kappa}v \qquad (6.8.2\text{-}63)$$

and the transient film momentum equation:

$$\frac{\partial V}{\partial t} = -V\frac{\partial V}{\partial l} = g_c\cos(\theta) - \tau_D \qquad (6.8.2\text{-}64)$$

Example results of the ultimate film thickness and velocity histories following the cavity pressure build-up is shown in Figure 6.8.2-38. The case shown is for an initial jet velocity and film thickness of 20 m/s and 0.9 cm, respectively. The calculations indicate that the film velocity tends to decrease. If the initial jet velocity is not high enough, the film could even recede to the level where a dry wall occurs. For the case shown, the film approaches asymptotic (steady state) behavior at about 0.2 seconds following the cavity pressure build-up.

Flow Guiding Using Magnetic Forces – The analysis above indicates that a very thin film (<1 mm) is not obtainable on the inverted surface. (There is no limitation on the minimum film thickness on the vertical surface.) A possible mechanism to reduce the flow rate and film thickness while maintaining attachment is the use of guiding magnetic fields. Simple scaling analysis for achieving a thin film using a magnetic field was performed by Chao and Tillack.[8]

Summary – Although thin film flow provides attractive features for first wall protection, there are several technical issues remaining to be investigated to assess the feasibility of this concept. These include: (1) wetting characteristics of the lead on the SiC material, (2) flow on inverted surfaces, (3) problems in providing uniform coverage over large engineering structures, (4) flow past obstacles, such as beam penetrations,

Use or disclosure of data
subject to title page restriction

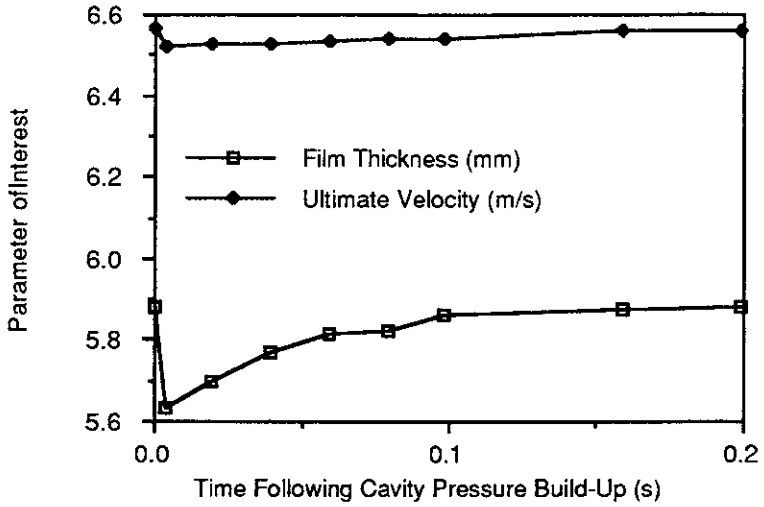

Figure 6.8.2-38. Ultimate Film Thickness and Film Velocity Histories Following the Cavity Pressure Build-Up

(5) stability of the film subjected to pressure impulses, (6) integrity of porous composite SiC material which is immersed in lead metal and subjected to a high radiation environment, and (7) consequences of dry spots.

References for 6.8.2.6

1. K. J. Chu and A. E. Duker, Statistical Characteristics of Thin, Wavy Films: Part II. Studies of the Substrate and its Wave Structure, A.I.Ch.E. Journal, Vol. 20, No. 4, 695 (1974).

2. Heishichiro Takahama and Seizo Kato, Longitudinal Flow Characteristics of Vertically Falling Liquid Films Without Concurrent Gas Flow, Int. J. Multiphase Flow, Vol. 6, pp. 203-215 (1980).

3. S. Ergun, Fluid Flow Through Packed Columns, Chemical Engineering Prog., 48, 89 (1952).

4. Richard H. French, Open-Channel Hydraulics, McGraw-Hill, New York, 1985.

5. G. Gimbutis, Heat Transfer for a Turbulent Falling Film, Proc. 5th Int. Heat Transfer Conf., Tokyo, Japan, Vol. 2, pp. 85-89 (1974).

6. Jon Lee, "Turbulent Film Condensation," A.I.Ch.E. Journal, p. 540, July 1964.

7. J. G. Collier, Convective Boiling and Condensation, Second edition, McGraw-Hill, New York, pp. 330-332, 1972.

8. T. C. H. Chao and M. Tillack, Evaluation of Alternatives to Avoid Dripping of Liquid Lead at the Upper End Cap in an IFE Reactor Cavity, UCLA-IFNT-8, October 1991.

Use or disclosure of data subject to title page restriction

6.8.2.7 Mechanical Response and Component Lifetime – Fatigue lifetime is a crucial issue in designing the first wall (FW) and blanket components of an IFE reactor. In order to assess the fatigue characteristics, a detailed structural response of the FW/B is required. Other factors such as the operating temperature, corrosive actions, etc., must also be investigated. A powerful method of analysis (e.g. Finite Element Method) should be used to extract the important fatigue data. However, some fatigue parameters, such as maximum stress level and frequency, can be reasonably estimated using analytical or finite difference methods. These methods can also be used to compare different design concepts, e.g., continuous FW versus segmented (modular) FW. In this part of the report, the rationale behind the structural material choice will be introduced. The mechanisms of mechanical loading of the wall will be identified. A discussion of specific results which enable the choice of the FW final configuration will be presented. Finally, an assessment of fatigue and lifetime of FW/B is discussed.

A SiC-SiC composite[1] manufactured by Societe Europeenne de Propulsion (SEP) is proposed as a reference structural material. This material reveals desired mechanical properties and oxidation resistance up to 1300°C. The basic mechanical properties of SEP 2D SiC-SiC composite are shown in Table 6.8.2-11 up to 1400°C. Preliminary tensile-tensile fatigue results at 100°C show that the material can survive 10^5 cycles at $\Delta\sigma \simeq 150$ MPa, with a residual ultimate tensile strength of ~90% of pre-test value. Toughness test results have also shown that SEP 2D SiC-SiC is ~50 times tougher than monolithic sintered SiC (in terms of energy absorbed at fracture).

Table 6.8.2-11 Properties of SEP-2D SiC-SiC*

Property	Units	Temperature		
		23°C	1000°C	1400°C
Density	g/cm^3	2.5	2.5	2.5
Porosity (Unirradiated)	%	10	10	10
Young's Modules (Tensile)	GPa	230	200	170
Poisson's Ratio				
ν_{12}		0.15	NA	NA
ν_{13}		0.4	NA	NA
Flexural Strength	MPa	300	400	280
Compressive Strength				
In Plane	MPa	580	480	300
Through the Thickness	MPa	420	380	250

* Adopted from Ref. 1.

Use or disclosure of data
subject to title page restriction

The mechanical loading on the FW includes two basic mechanisms: (1) surface ablation momentum as a result of the early deposition of x-rays, and (2) time dependent pressure loading caused by evaporation from the protecting liquid lead film. Detailed description of the nature of the second mechanism is given in Section 6.8.2.4. The initial ablation momentum is introduced into the mechanical model as an initial velocity of the structure (using the principle of conservation of momentum). For a total impulse, I, uniformly distributed over the surface, the initial velocity, v_o, is given by:

$$v_o = \frac{1}{\rho h}\left(\frac{dI}{dA}\right) = \frac{1}{\rho A h} \qquad (6.8.2\text{-}65)$$

where A, ρ, and h are the total surface area, effective density, and thickness of the FW. Typical ablation momentum is found to be 3.17×10^3 N·s for the pellet parameters used in this study. A typical time variation of the local pressure (load) at FW is shown as a result of detailed hydrodynamics calculations, in Figure 6.8.2-39 for a base case of 5-m radius cavity.

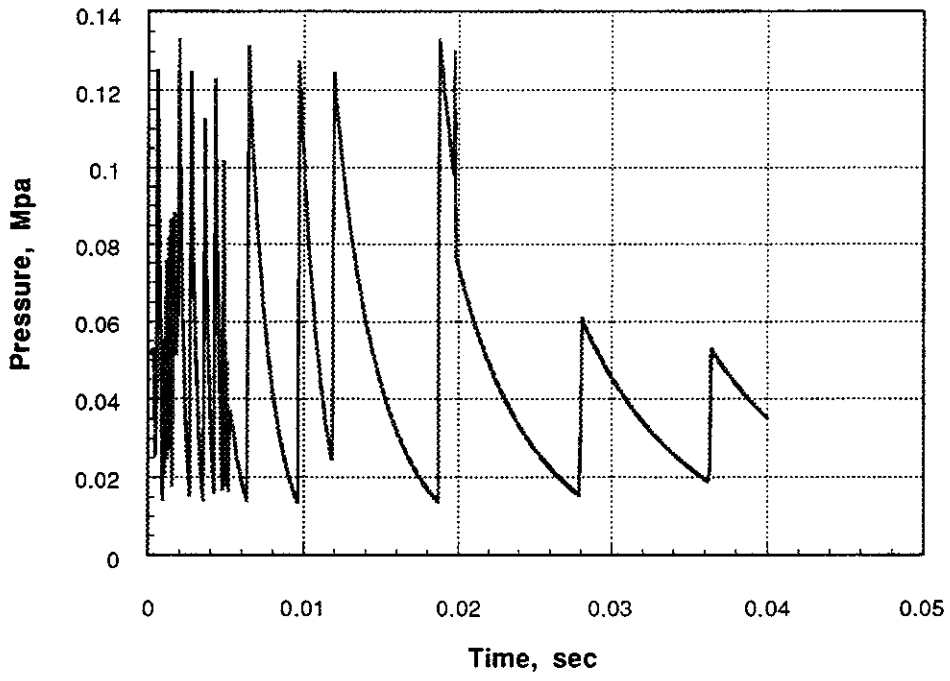

Figure 6.8.2-39. The History of the Pressure Loading on the First Wall Following the Microexplosion.

Use or disclosure of data
subject to title page restriction

Spherical Shell Model – For a preliminary estimate of fatigue parameters of the cavity, a spherical shell model is considered (R = 5 m and h = 1 cm). The equation of motion is written as:[2]

$$\ddot{u} + \omega^2 u = \frac{P(t)}{\rho h} \qquad (6.8.2\text{-}66)$$

where u is the radial displacement, $\omega = \sqrt{\frac{2E}{\rho R^2}} = \frac{2\pi}{T}$ is the radial frequency of vibration, and P(t) is the time dependent pressure. For E = 200 GPa, the natural period, T, is ~2.5×10^{-3} sec. The hoop stress, σ, in the spherical shell is given by

$$\sigma(t) = E\frac{u(t)}{R}. \qquad (6.8.2\text{-}67)$$

The displacement and the radial velocity of the vibrating shell are shown in Figure 6.8.2-40. The hoop stress is shown in Figure 6.8.2-41. Notice that $u_{max} - u_{min}$ ~ 3.5 mm and $\Delta\sigma$ ~ 100–140 MPa at steady state. These values are not acceptable from the design point of view. Figure 6.8.2-42 shows the time dependent kinetic energy of the vibrating wall. Conclusions to be emphasized at this level of analysis are:

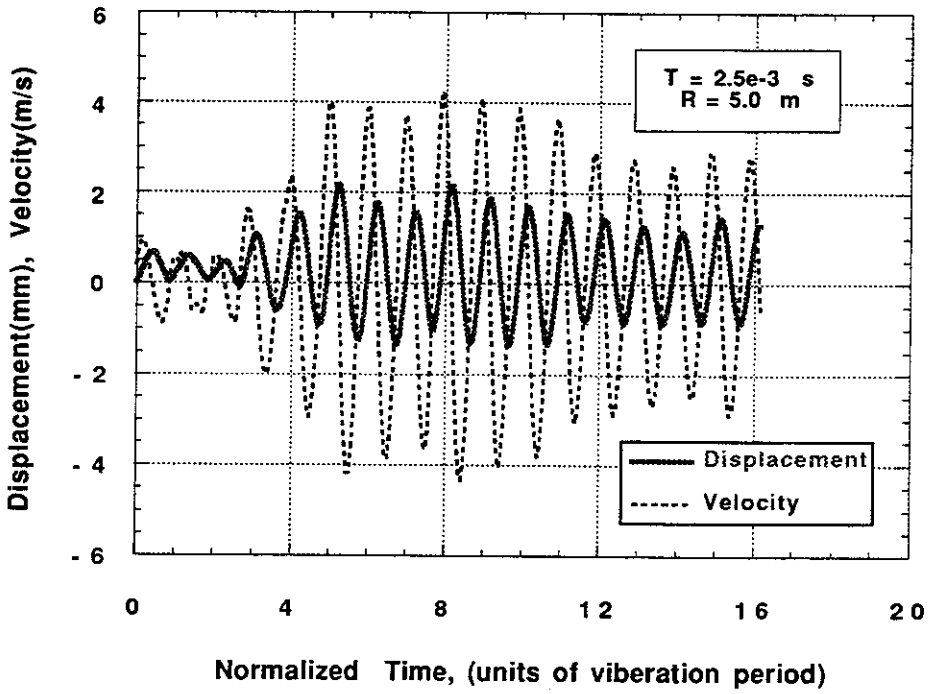

Figure 6.8.2-40. Instantaneous Velocity and Radial Displacement of the Continuous (Spherical Shell) First Wall.

Use or disclosure of data subject to title page restriction

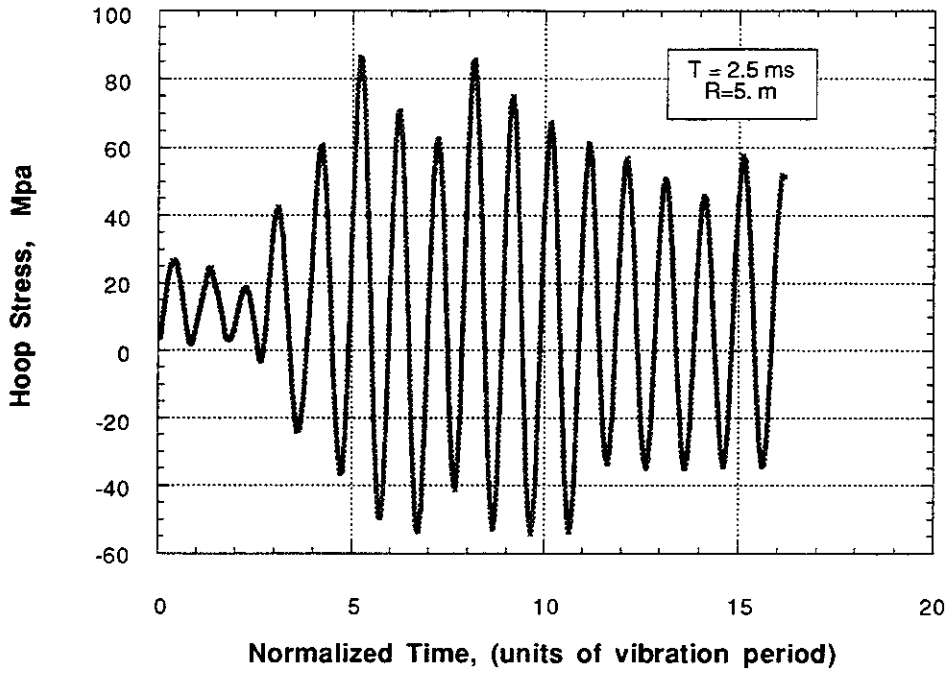

Figure 6.8.2-41. Hoop Stress History in the Continuous First Wall.

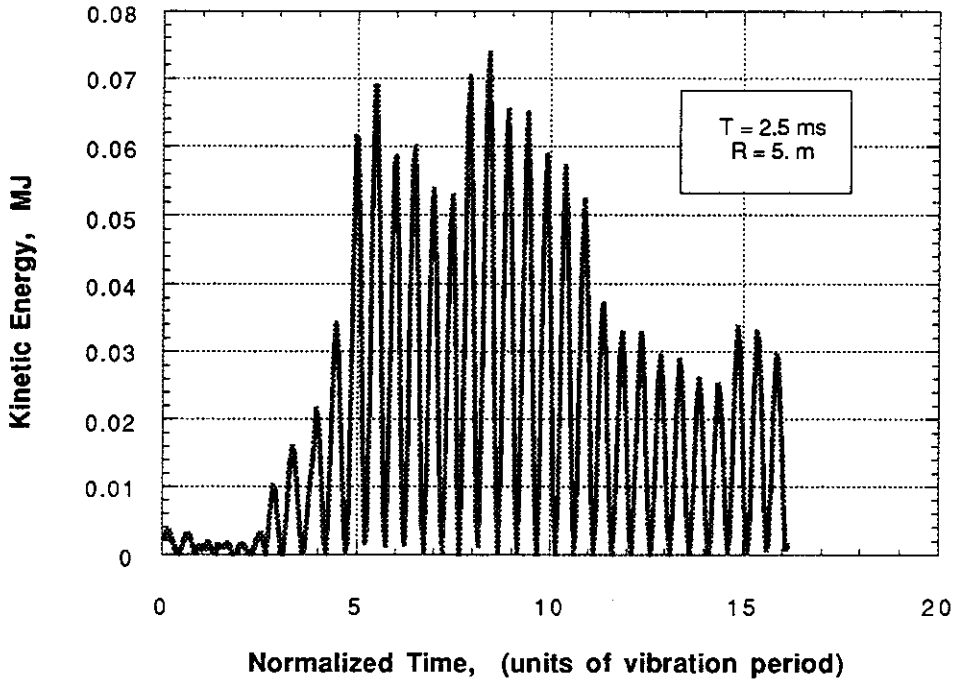

Figure 6.8.2-42. Kinetic Energy of the Vibrating Continuous First Wall.

Use or disclosure of data
subject to title page restriction

(1) To avoid high stresses, segmentation of the FW is preferable. Integration of the FW with the blanket is also a reasonable design approach since it will constrain the vibration of the first wall.

(2) Because of the high velocity of vibration of the FW, the stability of the protecting film is an important issue.

(3) The maximum kinetic energy of the vibrating wall is ~0.07 MJ compared to pellet yield of ~655 MJ. This suggests that no damping mechanism is required.

First Wall Plate Model – According to the proposed configuration of the Prometheus-L reactor cavity, the FW is basically planar panels with an overall thickness of 6 cm. The panel can be viewed as a double-plate with both sides mechanically attached by perpendicular ribs, which separate the FW coolant channels. The panel size and method of support are determined by two factors: (1) the requirement that the maximum stress must be below its design limit, and (2) the maintenance scheme. Considering the mechanical support scheme for the FW, a planar panel can be modeled as a clamped plate subjected to ablation and pressure loading as a result of the pellet microexplosion. The effective plate thickness could be less than 6 cm due to the presence of coolant channels. Moreover, the presence of liquid lead provides very large inertial effects to the FW. Hence, the results underestimate the magnitude of the stress throughout the plate. The governing equation for the out-of-plane displacement u(x,y,t) is given by:[3]

$$P(t) = D_1 \frac{\partial^4 u}{\partial x^4} + 2D_3 \frac{\partial^4 u}{\partial x^2 \partial y^2} + D_2 \frac{\partial^4 u}{\partial y^4} + (\rho h) \frac{\partial^2 u}{\partial t^2} \qquad (6.8.2\text{-}68)$$

where $D_{1,2,3}$ are the orthotropic bending rigidity coefficients, (ρh) is the effective mass per unit area of the FW panels. Eq. 6.8.2-68 assumes that mid-plane symmetry exists. It also assumes zero transverse shear across the plate thickness. The orthotropic bending rigidity coefficients are given by:[3]

$$D_1 = \frac{E_1 h^3}{12(1 - \nu_{12}\nu_{21})}, \qquad D_2 = \frac{E_2 h^3}{12(1 - \nu_{12}\nu_{21})}$$

$$D_3 = D_{12} + 2D_{66}, \qquad D_{12} = \nu_{21} D_1,$$

$$D_{66} = \frac{G_{12} h^3}{12} \qquad (6.8.2\text{-}69)$$

where G_{12} is the shear modules in the plane of the panel, $E_{1,2}$ are the Young's moduli, and ν_{12}, ν_{21} are the Poisson's ratios.

Use or disclosure of data
subject to title page restriction

The in-plane stresses can be recovered from the out-of-plane displacement as follows:

$$\sigma_x = (Q_{11}k_x + Q_{12}k_y)z ,$$

$$\sigma_y = (Q_{12}k_x + Q_{22}k_y)z ,$$

$$\sigma_{xy} = 2Q_{66}k_{xy}\, z \qquad (6.8.2\text{-}70)$$

where Q_{ij} = stiffness coefficients of the composite material, z is the distance measured from the mid-plane (as shown in Figure 6.8.2-43) and k_x, k_y, and k_{xy} are given by:

$$k_x = - \partial^2 u/\partial x^2 , \qquad k_y = - \partial^2 u/\partial y^2 ,$$

$$k_{xy} = - \partial^2 u/\partial x \partial y \qquad (6.8.2\text{-}71)$$

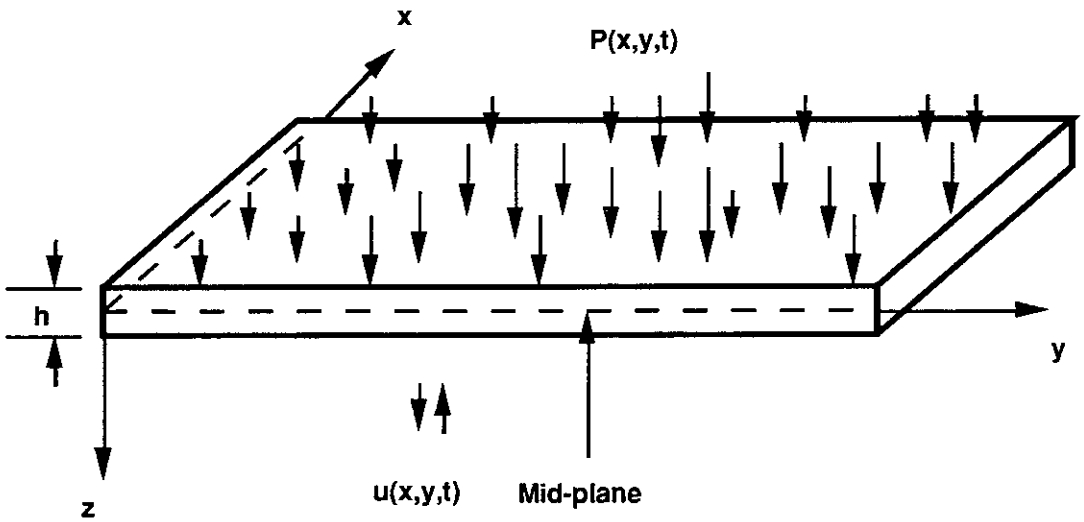

Figure 6.8.2-43 Schematic of Mechanical Loading of the FW Panels.

The equation of motion is solved using the finite difference technique.[4] The solution is formulated for different mesh size along x and y axis. The resulting matrix equation is written as :

$$A\, u = b \qquad (6.8.2\text{-}72)$$

where A is constant coefficient matrix, u is the nodal displacement vector, and b is the time dependent load vector. At each time step, the load vector is evaluated in terms of the instantaneous local pressure and the last time step values of the displacement vector. The matrix A is NxN where N is the total number of nodal points. At each node, the initial displacement is zero and, by using Eq. 6.8.2-65, the initial velocity is determined to be 0.03 m/s all over the plate. At clamped edges, the displacement and its first spatial derivative are set equal to zero at all times. Upon enforcing these boundary conditions, a Guassian Elimination Technique[5] is used to solve the matrix Eq. 6.8.2-72 at each time step. The stresses are recovered from the solution for the displacement using Eqs. 6.8.2-70 and 6.8.2-71.

Use or disclosure of data
subject to title page restriction

The results for a clamped plate 1m x 1.5m are shown in Figures 6.8.2-44 through 6.8.2-46. The fundamental frequency of vibration was found to be ~800 Hz. It is observed that the resonance between the mechanical response of the FW panels and the pressure loading is of small probability since the frequency with which the pressure changes (Figure 6.8.2-39) is variable over the time between two microexplosions. Maximum displacement of about 0.1 mm is determined, which can be allowable. The maximum stresses always occur at the clamped edge (Figure 6.8.2-46). The implications on the fatigue and failure of the structure will be explained through the following discussion.

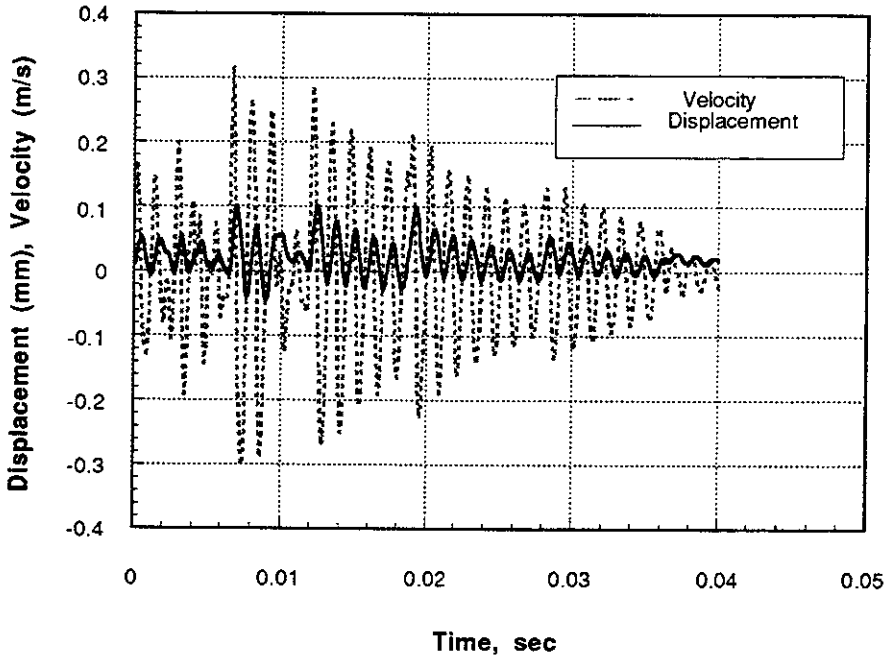

Figure 6.8.2-44. Instantaneous Velocity and Displacement at Center of First Wall Plate (1m x 1.5m)

Use or disclosure of data
subject to title page restriction

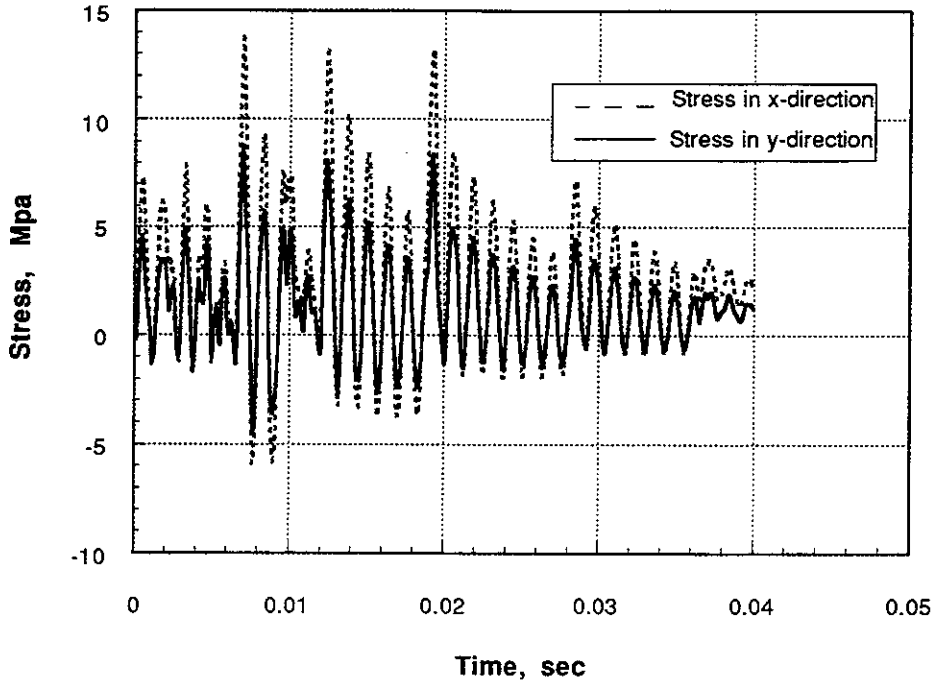

Figure 6.8.2-45. The History of Stresses at Center of FW Plate (1m x 1.5m)

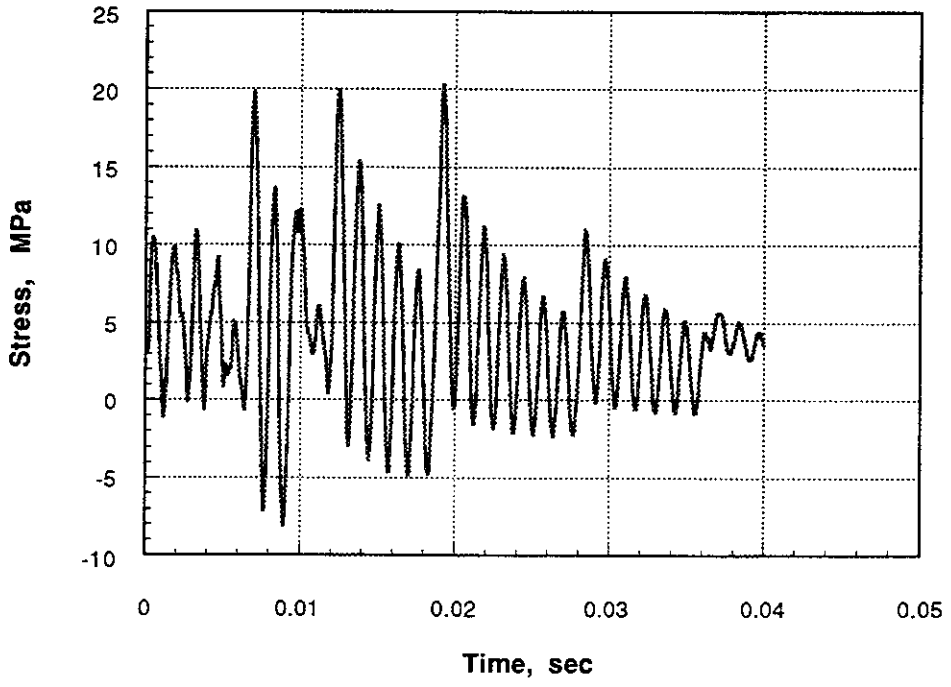

Figure 6.8.2-46. The History of Stresses at Clamped Edge of FW Plate (1m x 1.5m)

Use or disclosure of data
subject to title page restriction

First Wall Fatigue Damage – The process of fatigue damage and failure in composites is highly complicated. As a result, standard methods have not been established to define design criteria for fatigue design with composite materials. However, some designers assume the classical method, S-N diagrams, to apply.[6] Others[7] have presented a systematic conceptual scheme for evaluation of fatigue performance of composites based on certain damage mechanism maps, called fatigue-life diagrams. In the later approach, failure is based on a strain criterion; that is, for a composite material, the fatigue limit is defined as the strain corresponding to the boundary between the non-propagating matrix cracks and the propagating matrix cracks at 10^6 cycles. However, the fatigue-life diagrams have been established only for a limited number of materials.

Figure 6.8.2-47 shows the stress-strain diagram for SEP 2D SiC/SiC composite material[1] in which the fatigue tested material is compared to the pre-test material. For 10^6 cycles at 100 MPa, the fatigue tested material shows a very promising behavior. It can be noted that the rupture characteristics were maintained. Only the modules at the origin dropped slightly by ~18%. The maximum stress (Figure 6.8.2-46) in the present

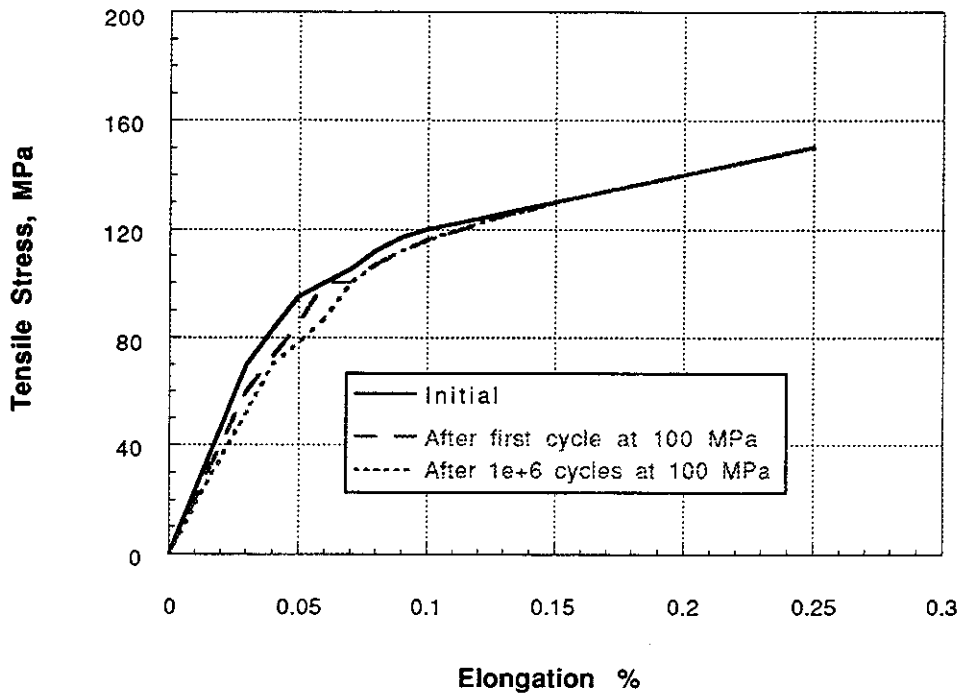

Figure 6.8.2-47. The Stress-Strain Diagram for SEP 2D SiC/SiC Composite (Fatigue Tested vs. Virgin Material). Data from Reference 1.

Use or disclosure of data subject to title page restriction

design is observed to be ~20 MPa which is far below 100 MPa. This means that, as a first approximation, the FW structure can survive at least 10^6 cycles at the given stress conditions. It is concluded here that the lifetime of the FW structure is not controlled by fatigue damage, but rather by radiation effects on the structural properties of the SiC-SiC composite material.

References for 6.8.2.7

1. A. Lacombe and C. Bannet, "Ceramic Matrix Composites, Key Materials for Future Space Plane Technologies." AIAA Second International Aerospace Planes Conference, 29-31 October 1990, Orlando, FL, USA.

2. L. A. Gleen and D. A. Young, "Dynamic Loading of the Structural Wall in a Lithium-Fall Fusion Reactor.", Nucl. Eng. Design 54, 1-16 (1979).

3. J. R. Vinson and R. L. Sierakowski, "The Behavior of Structures Composed of Composite Materials.", Kluwer Academic Publishers, 1987.

4. S. P. Timoshinko and J. N. Goodier, "Theory of Elasticity.", 3rd Ed., McGraw-Hill Book Co., 1987.

5. C.F. Gerald and Patrick O. Wheatley, "Applied Numerical Analysis.", 3rd Ed., Adison-Wesley Pub. Co., 1984.

6. International Encyclopedia of Composites, Vol. 2. Editor: Stuart M. Lee. 1990.

7. Ramesh Talreja, "Fatigue of Composite Materials.", Technomic Pub. Co., 1987.

Use or disclosure of data
subject to title page restriction

6.8.2.8 Component Lifetime Assessment - Determination of the lifetimes for various structural components is highly dependent on uncertainties in structural modeling and in the materials data base. However, a first-order assessment of first wall and blanket (FW/B) lifetimes is possible if a number of assumptions are made. For the purposes of this analysis of FW/B component lifetimes, the effects of the following factors were analyzed.

(1) Mechanical loading fatigue damage.
(2) Compatibility with Pb and He coolants.
(3) Radiation effects.

Fatigue Damage - As outlined in the previous section, fatigue damage of the FW should be carefully considered. A complicated spectrum of cyclic stresses results from the impact of the rapid pressure and impulse loading on the first wall. The edge of the FW plates are identified as critical because of the constraint conditions imposed. It is seen from Figure 6.8.2-46 that the maximum in-plane stress is on the order of 20 MPa and that its frequency is approximately 3-4 times per shot. Many other smaller amplitude stress cycles can also be seen, but their effects are neglected at the present time. The large amplitude stress cycles are not fully reversed, but they range approximately between +20 MPa to -5 MPa. Prometheus-L approximate parameters were used for the spectral effects of cycling.

Stress Cycle	=	+20 MPa to -5 MPa
Frequency	=	5.6 x 4 = 22.4 Hz
No. of Cycles/Year	=	7×10^8

The approximate stress characteristics diagram is shown in Figure 6.8.2-48.

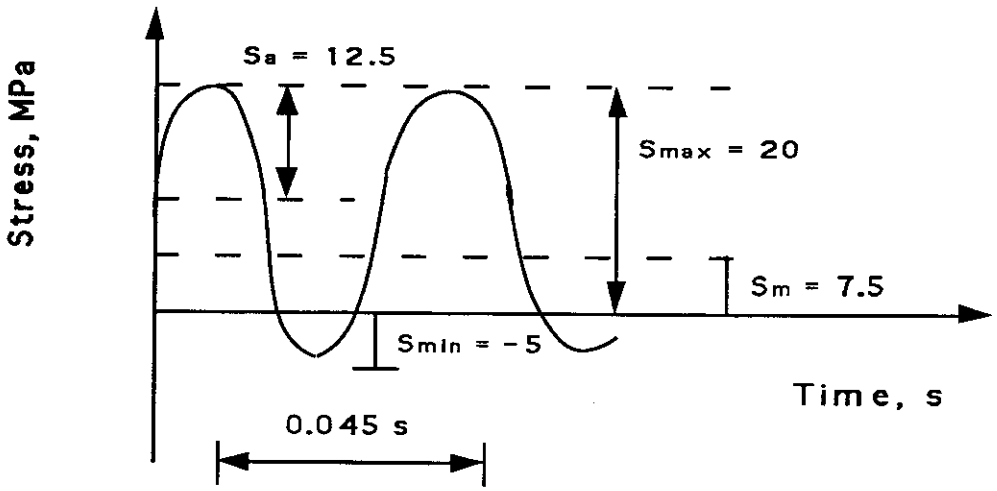

Figure 6.8.2-48. First Wall Stress Characteristics Diagram

Use or disclosure of data subject to title page restriction

Tensile data on SEP 2D SiC/SiC composites indicate that the effective ultimate strength is on the order of 160 MPa. However, significant deviations from linear stress-strain behavior are deserved at about 80-100 MPa. Such behavior is indicative of matrix micro-cracking. For lack of extensive fatigue experience with ceramic matrix composites, we follow a conservative approach was used such as in low ductility metallic structures (i.e., high strength steels). A fatigue ratio in the range of 0.35 to 0.5 is obtained for all high strength, low-ductility materials(1).

The S-N diagram will be constructed on the basis of the most conservative of the following for the fatigue endurance limit, S_f,

Modified Goodman, $$\frac{S_a}{S_f} + \frac{S_m}{S_u} = 1$$

Gerber, $$\frac{S_a}{S_f} + \left(\frac{S_m}{S_u}\right)^2 = 1$$

Morrow, $$\frac{S_a}{S_f} + \frac{S_m}{\sigma_u} = 1$$

In these equations, S_a is the alternating stress, S_f the endurance limit, S_m is the mean stress, σ_f is a fracture stress, and σ_u is the ultimate stress. We will not use the Soderberg line because it is more appropriate for ductile metals with a definite yield point. The approximate S-t diagram gives the following:

$Sm = 7.5$ MPa

and the SEP data shows that:

$S_u \simeq \sigma_f \simeq 100$ MPa

Following the Morrow (or Goodman) analysis, we get

$$\frac{S_a}{40} + \frac{7.5}{100} = 1 \qquad \therefore S_a = 37 \text{ MPa}$$

Since the allowed S_a is larger than 12.5 MPa, the structure is safe as far as fatigue life is concerned. A safety factor of 3 indicates a high degree of structural reliability. It accounts for fatigue data uncertainties, as well as any stress concentrations around notches and stress raisers. The S-N diagram is shown in Figure 6.8.2-49.

We conclude from our analysis that the fatigue endurance limit of the SiC/SiC composite will not be exceeded. The lifetime will, therefore, be determined by other issues, such as coolant compatibility and radiation effects.

Use or disclosure of data
subject to title page restriction

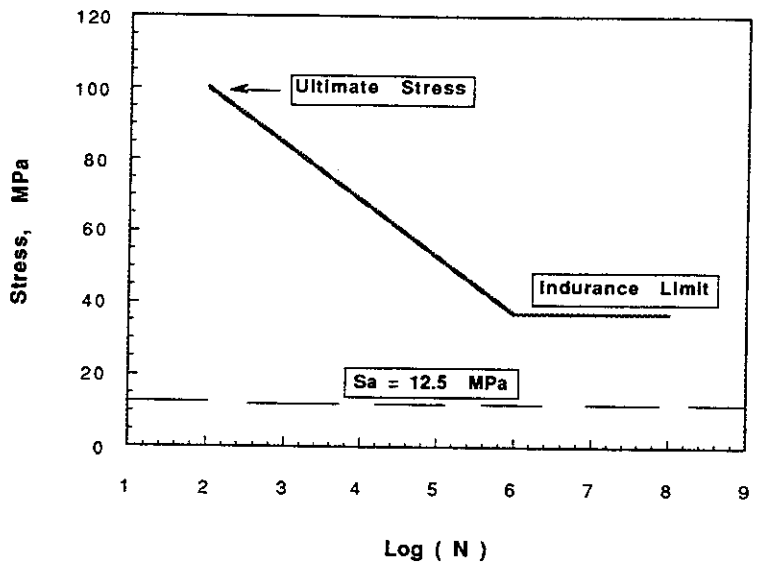

Figure 6.8.2-49. S-N Fatigue Design Curve for the SiC First Wall

Coolant Compatibility - Two main coolants are used in the FW/B systems of Prometheus. Thermodynamic data on the compatibility of Pb with SiC is very scarce, and the indications point to a thermodynamically compatible system. However, even though helium is an inert gas, it will contain low level impurities of O_2 and H_2O. Since the fiber-matrix interface will be C, BC_4 or BN at the present time, we must also investigate the effects of oxygen impurities on the chemical stability of the interface.

When SiC is exposed to a highly oxidizing atmosphere, such as air, a dense SiO_2 layer forms on the surface and further oxidation is retarded. Because of this passivation, SiC exhibits excellent oxidation resistance at high temperatures. However, when the supply of oxygen is not sufficient (in reducing or inert atmospheres), the protective SiO_2 layer cannot form and weight loss occurs by decomposition or active oxidation of the SiC. Such corrosion can significantly affect the strength of the SiC by introducing flaws to the surface or reducing the load-bearing cross section.

Under fusion conditions, the average temperature is generally in the range 773 and 1273 K, and the impurities in the helium coolant average between 100 and 1000 ppm. For these conditions, we have a typical hot corrosion process. The growth of an oxide can be compared with current flow around a circuit containing an electrolytic cell. It will include both electronic and ionic parts. The ionic current produces two effects:

(a) The ionization of metal atoms, Me = M(Z+) + z electrons
(b) The ionization of oxygen atoms, O + 2 electrons = O(2-)

Use or disclosure of data
subject to title page restriction

The computer code CET (Chemical Equilibrium Thermodynamic) Code developed by NASA was used in the present study to calculate the equilibrium compositions of the system. This procedure is based on minimization of the total free energy of the system, which was originally developed by Gorden and McBride and revised by Zeleznik.[2]

The total Gibbs free energy of a system is given by the equation:

$$G=\sum_{i=1}^{n} n_i g_i=\sum_{i=1}^{n} n_i\left(g_i^0 + RT \ln a_i\right) \qquad (1)$$

(6.8.2-73)

where G is the total Gibbs free energy of a system, R is the ideal gas constant, T is the thermodynamic temperature, n_i is the moles of chemical species "i", and a_1 is the activity of species "i".

Calculations with the CET program were performed for a wide range of conditions which are relevant to the study. The stability of SiC and possible interfaces such as BN, B_4C, and C was also investigated in the temperature range 773 - 1273 K. The conditions are summarized in Table 6.8.2-12.

Table 6.8.2-12 Conditions for Chemical Compatibility of SiC/SiC Composites with Helium

Materials	SiC, BN, C
Impurity Levels	100-1000 ppm
Impurity Type	H_2O, O_2
Temperature Range	773-1273 K

Hydrogen, oxygen and water moisture are expected to be contained in the main coolant, helium.

Silicon carbide will chemically react with O_2, H_2O, and H_2, according to the following reactions:

$SiC(s) + O_2(g) = SiO(g) + CO(g)$
$2SiC(s) + 3O_2(g) = SiO(g) + CO_2(g)$
$2SiC(s) + O_2(g) = SiO(g) + C$
$SiC(s) + O_2(g) = Si + CO_2(g)$
$2SiC(s) + O_2(g) = Si + CO(g)$
$SiC(s) + 2H_2O(v) = SiC(g) + CO(g) + 2H_2(g)$
$SiO_2(s)(\text{Protective layer}) + H_2(g) = SiO(g) + H_2O(v)$

Use or disclosure of data subject to title page restriction

Relevant reactions for forming a protective layer are given below:

$$SiC(s) + 2O_2(g) = SiO_2(s) + CO_2(g)$$
$$2SiC(s) + 3O_2(g) = SiO_2(s) + CO(g)$$
$$SiC(s) + O_2(g) = SiO_2(s) + C(s)$$

For the C and BN fibers we have the next relevant reactions:

$$C(s) + O_2(g) = CO_2(g)$$
$$2C(s) + O_2(g) = 2CO(g)$$
$$2BN(s) + 2O_2(g) = 2BO_2(g) + N_2$$
$$2BN(s) + 3H_2O(v) = B_2O_3(g) + 2NH_3$$

The kinetics of these reactions can be affected by the formation of a protective layer of SiO_2 at high partial-pressure of O_2 such that SiC is stable in many corrosive environments.

The molar fractions of gases in equilibrium with SiC in contact with the helium coolant containing 100 ppm O_2 to 1000 ppm O_2 are shown in Figures 6.8.2-50 through 6.8.2-53. In these cases, the primary gaseous products were found to be CO and CO_2 and small amounts of SiO and SiO_2 in equilibrium with the condensed phase of SiO_2 protective layer. Figures 6.8.2-50 and 6.8.2-51 show the molar fraction of the dominant gaseous species, while Figures 6.8.2-52 and 6.8.2-53 give the molar fraction of the condensed species SiO_2 and graphite as function of temperature. The dominance of CO and CO_2 gaseous oxides indicate that the surface of SiC tubes and structures in the blanket will be quickly enriched with Si and, hence, will form a protective SiO_2 coating.

The effects of water moisture on the formation of gaseous oxides are illustrated in Figures 6.8.2-54 through 6.8.2-57. In this case, additional hydro-carbons (CH_3 and CH_4) form. However, the same behavior is exhibited where the protective SiO_2 layer forms.

The following conclusions can be made from the studies:

(1) The dominant gaseous species which form in equilibrium with SiC are CO, CO_2, SiO, and SiO_2 where the helium coolant contains O_2 impurities.
(2) When water moisture is trapped in the helium coolant, additional hydro-carbons (CH_3 and CH_4) will form.
(3) In all cases considered, graphite and SiO_2 will exist in the solid phase. Thus, further hot corrosion of the SiC surface will halt.

Use or disclosure of data subject to title page restriction

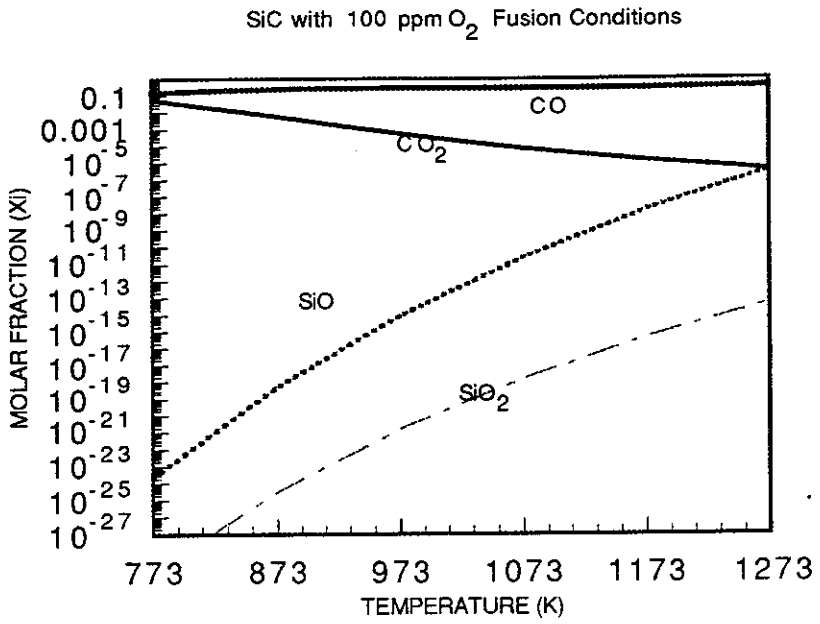

Figure 6.8.2-50. Molar Fractions of Main Chemical Species in SiC with 100 ppm O_2 Impurity Level

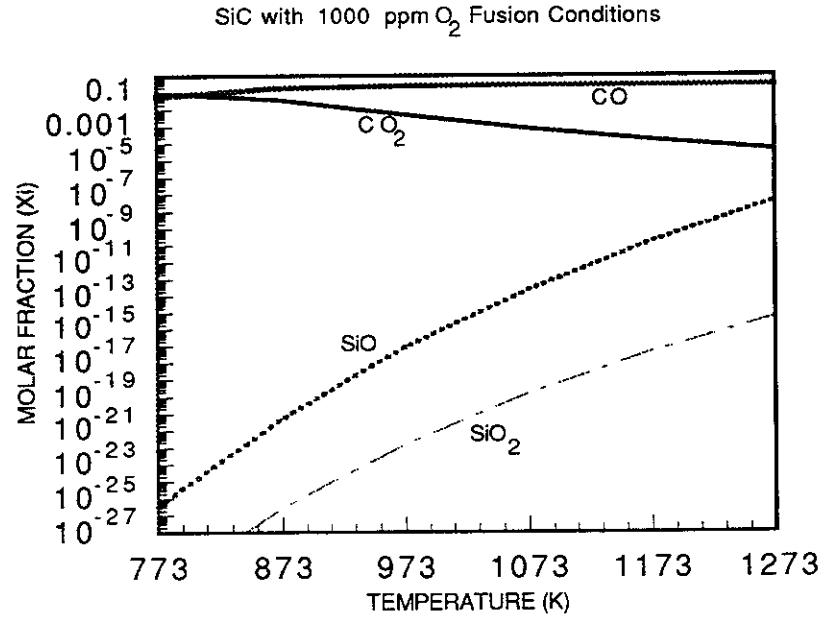

Figure 6.8.2-51. Molar Fractions of Main Chemical Species in SiC with 1000 ppm O_2 Impurity Level

Use or disclosure of data
subject to title page restriction

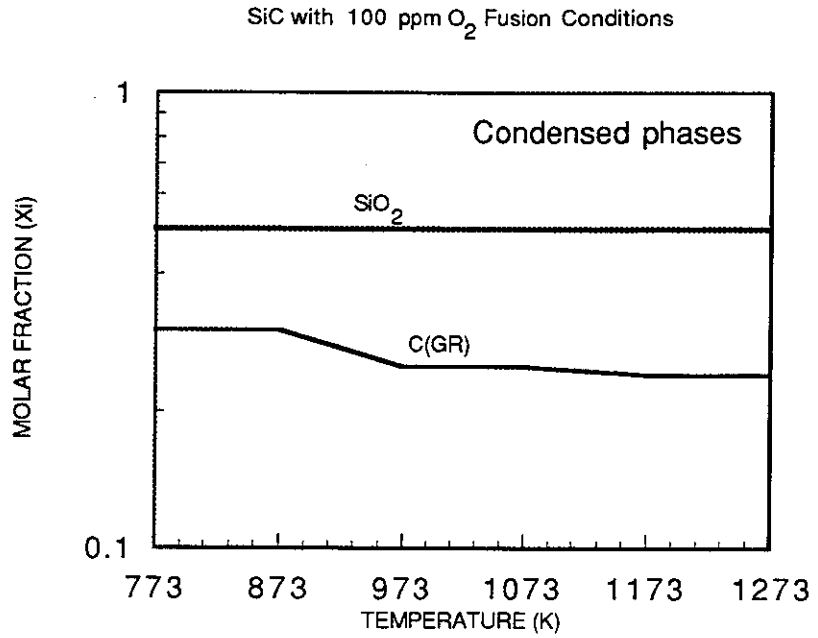

Figure 6.8.2-52. Molar Fractions of Solid (Condensed) Phases in SiC with 100 ppm O_2 Impurity Level

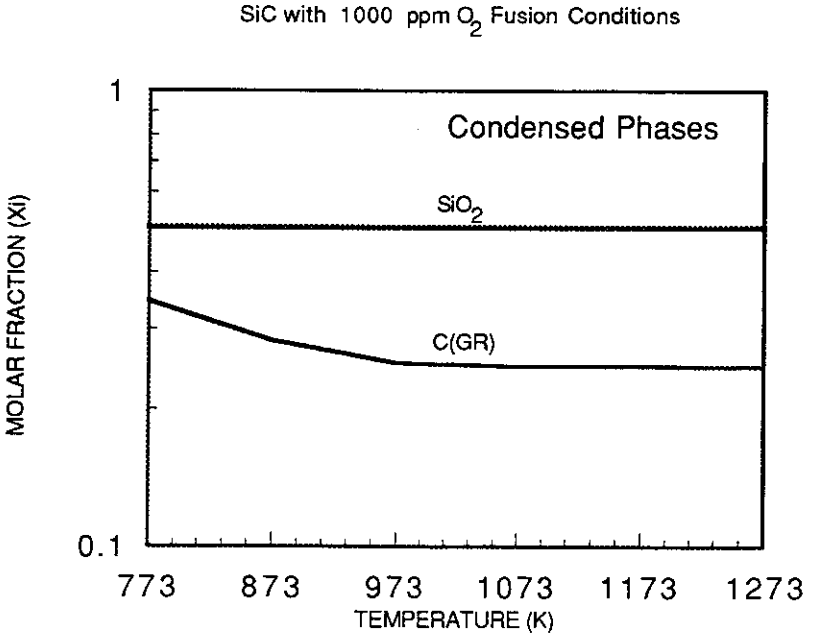

Figure 6.8.2-53. Molar Fractions of Solid (Condensed) Phases in SiC with 1000 ppm O_2 Impurity Level

Use or disclosure of data
subject to title page restriction

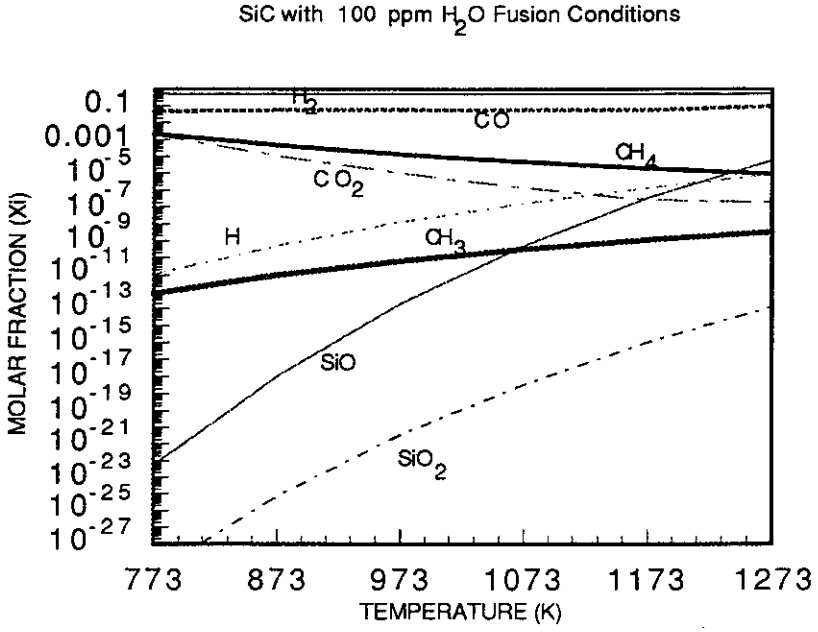

Figure 6.8.2-54. Molar Fractions of Main Chemical Species in SiC with 100 ppm H_2O Impurity Level

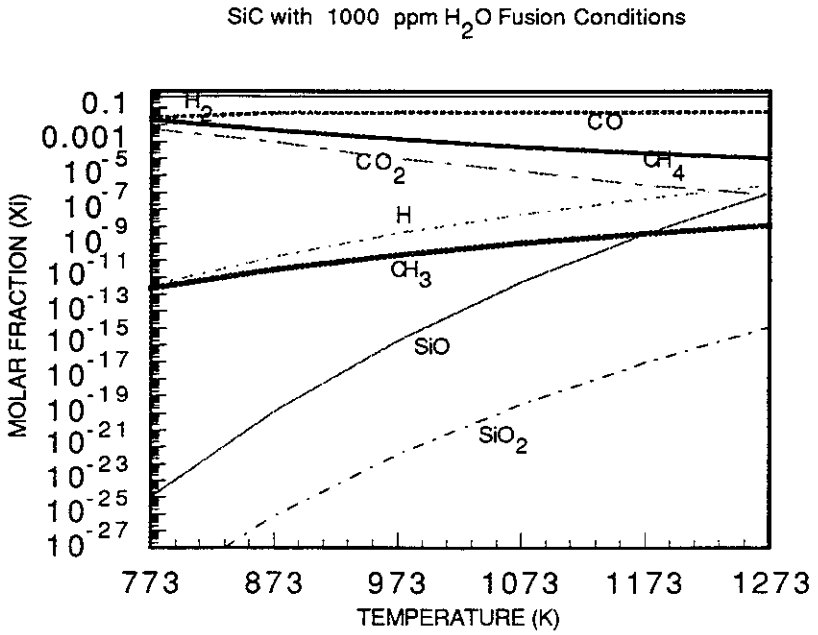

Figure 6.8.2-55. Molar Fractions of Main Chemical Species in SiC with 1000 ppm H_2O Impurity Level

Use or disclosure of data
subject to title page restriction

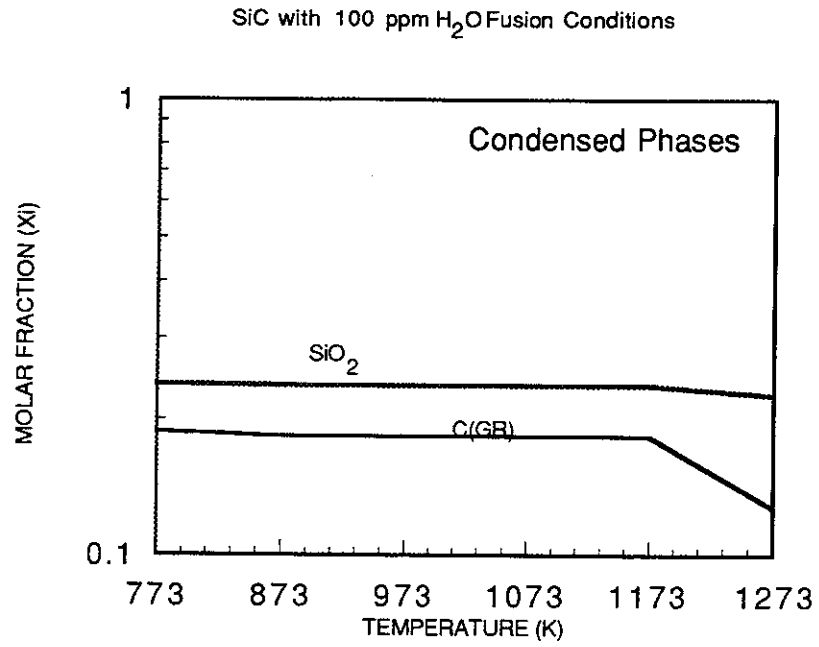

Figure 6.8.2-56. Molar Fractions of Condensed (Solid) Phases in SiC with 100 ppm H_2O Impurity Level

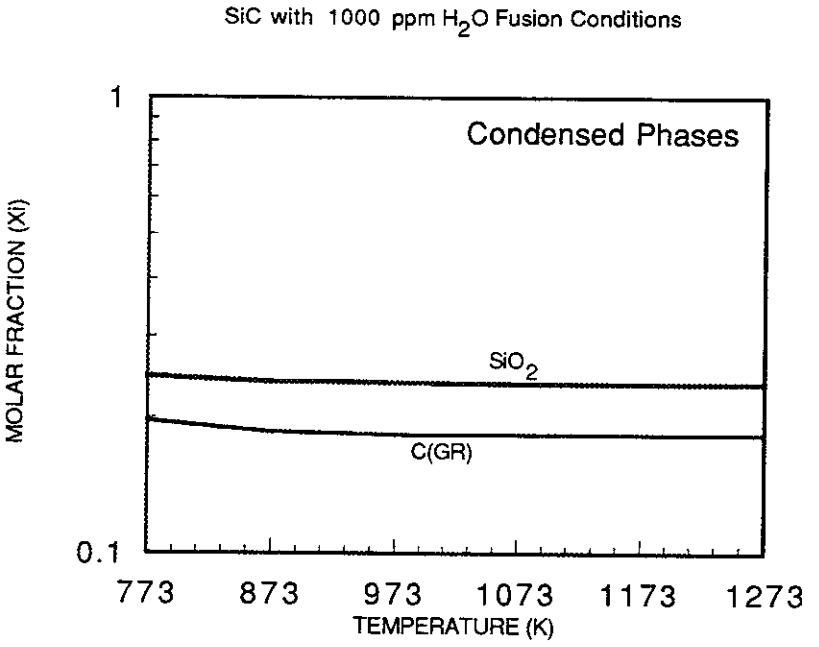

Figure 6.8.2-57. Molar Fractions of Condensed (Solid) Phases in SiC with 1000 ppm H_2O Impurity Level

Use or disclosure of data
subject to title page restriction

Oxidation of the interface between the fibers and the matrix can be a serious issue because it may lead to strength degradation. Our detailed studies of the chemical stability of C and BN interfaces indicate that these two types of interfaces will not be stable under the conditions outlined in Table 6.8.2-12. A search for an appropriate low-activation and chemically stable fiber/matrix interface is, therefore, identified as an important area which needs further development.

The main conclusion we draw from this work is that SiC will be chemically stable in the coolant environment of the blanket. Care, however, must be taken to determine the stability of the fiber/matrix interface.

Radiation Effects - The strong directional bonding and the mass difference between Si and C atoms render the crystalline form of β-SiC exceptional radiation resistance characteristics. Recent Molecular Dynamics (MD) studies[3] show that Replacement Collision Sequences (RCS's) are improbable and that the displacement of C atoms is much easier than Si. MD computer simulations[3] show the average threshold displacement cascade differs substantially from that of the matrix. It is also observed that energetic Si PKA's displace multiple C atoms which end up on <111> planes. Experimental observations at temperatures below 1000°C corroborate this conclusion.[15] Vacancies and He atoms exhibit considerable mobility above 1000°C. These fundamental considerations may explain some of the observed features of SiC dimensional changes as function of temperature and fluence.[4-7]

Price[4] observed Frank-type loops on {111} planes which may be C-rich. Below 1000°C, point defects tend to form loops on {111} planes and swelling is, therefore, expected to saturate. For example, Harrison and Correli[8] observed large loops (10-200 nm) in β-SiC after neutron irradiation to fluence of 1.8×10^{23} cm^{-2}. At temperatures above 1000°C, cavities form and swelling does not saturate. The presence of helium results in further increases in the swelling rate by the known gas-driven swelling mechanism. Swelling of β-SiC in temperature range 625-1500°C and at neutron fluence (E>0.18 MeV) of 1.2×10^{22} cm^{-2} [Ref4] is represented by two separate polynomials with two different sets of coefficients below and above 1000°C, respectively. The coefficients and the general swelling behavior as a function of temperature is shown in Figure 6.8.2-58. Additional helium will drive swelling to higher values, particularly at temperatures above 1200°C.[20] The limited accumulated evidence from radiation effects data indicate that the upper temperature limit for use of SiC in structure design is in the range of 900-1000°C.

Use or disclosure of data
subject to title page restriction

Figure 6.8.1-9 shows the neutron spectrum for Prometheus-L for a neutron source, $S_0 = 9.83 \times 10^{20}$ n/s. Since the swelling data is correlated to the fast neutron flux (E>0.18 MeV), an estimate of the swelling rates in the blanket and first wall can be made by finding the flux for $E \geq 0.2$ MeV. The high energy neutron spectrum is also shown in Figure 6.8.1-11. Table 6.8.2-13 shows the relevant neutron flux for design purposes.

Table 6.8.2-13 Total Neutron Flux $\Phi x 10^{-15}$ ($n/cm^2/s$) ($E \geq 0.2$ MeV)

	Prometheus-L	Prometheus-HI
FW	1.97	2.27
B	1.37	1.58

SiC/SiC composites manufactured by the CVI process will contain porosity, ranging from 10-30%. On the basis of the limited swelling data shown in Figure 6.8.2-58, the volumetric swelling of the first wall and blanket are shown in Figures 6.8.2-59 and 6.8.2-60. The design limit will be set here on the basis of a maximum volumetric deformation of 5-6% (i.e., accumulated inelastic linear strains of ~2%). It can be concluded here that the lifetime of first wall structure is estimated at 2.5 to 7.7 years for Prometheus-L and 2.1 to 6.7 years for Prometheus-H. The blanket lifetime is likewise estimated at 3.5 to 11 years for Prometheus-L and at 3 to 9.6 years for Prometheus-H.

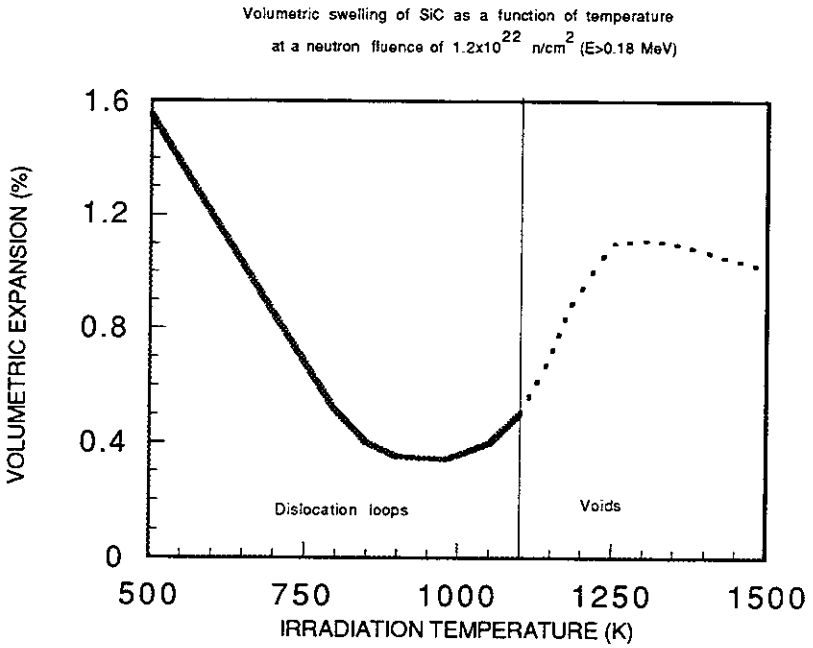

Figure 6.8.2-58. Volumetric Swelling of SiC as a Function of Temperature at a Neutron Fluence of 1.2×10^{22} ncm^{-2} ($E > 0.14$ MeV)

Use or disclosure of data
subject to title page restriction

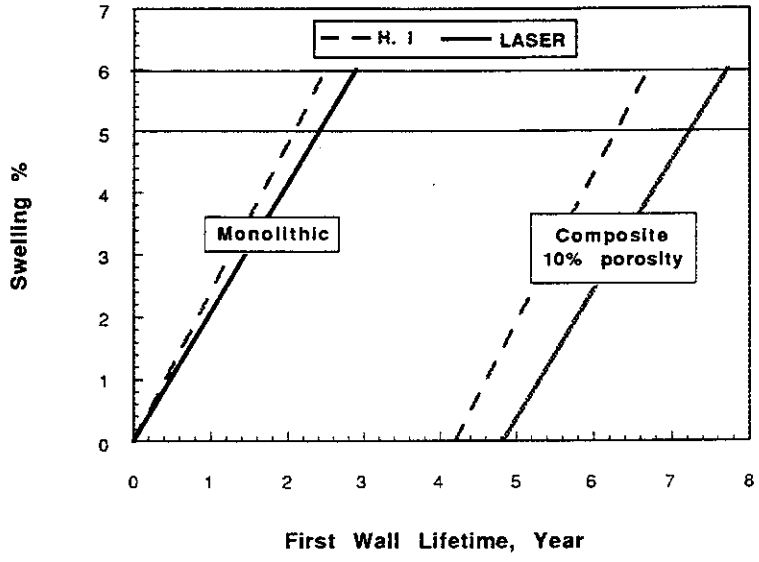

Figure 6.8.2-59. Estimated Total Volumetric Swelling for the First Wall Structure

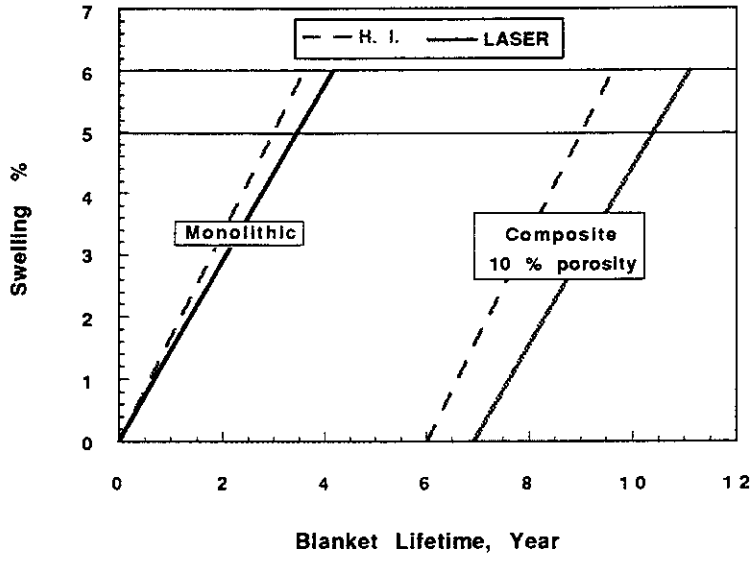

Figure 6.8.2-60. Estimated Total Swelling for the SiC Blanket Structure

Use or disclosure of data
subject to title page restriction

References for 6.8.2.8

1. H. O. Fuchs & A. I. Stephens, Metal Fatigue in Engineering, John Wiley & Sons, N. Y., 1980

2. S. Gorden & B. J. McBride, "Computer Program for Calculation of Complex Chemical Equilibrium Compositions, Rocket gas and Reflect Shock", NASA Lewis Research Scientific and Technical Information Office, Report # NASA-SP-273, March 1973

3. A. Elazab and N. M. Ghoniem, Proc. of Fifth Int. Conf. on Fusion Reactor Materials, Clearwater, FL, November 1991

4. R. J. Price, J. Nuclear. Materials, 46, p. 268, (1973).

5. R. Blackstone and E. H. Voice, J. Nuclear. Materials, 39, p. 319 (1971).

6. A.M. Carey, F. J. Pineau, C. W. Lee, and J. C. Corelli, J. Nuclear. Materials, 103 & 104, p. 789 (1981).

7. K. Hojou and K. Izui, J. Nuclear. Materials, 160, p. 334, (1988).

8. S. D. Harrison and J. C. Corelli, J. Nuclear. Materials, 122 & 123, p. 833, (1984)

This page intentionally left blank.

6.8.3 Blanket - The approach for developing the Prometheus blanket design was strongly based on considerations of safety, reliability, simplicity, and flexibility. Safety considerations led to the choice of a helium-cooled, solid-breeder blanket with low activation materials—SiC structure and neutron reflector and Li_2O breeder. Use of Li_2O in conjunction with the first wall Pb coolant provided the potential for adequate tritium breeding without the need for Be as a multiplier. Considerations of simplicity and design flexibility led to a well-studied, multi-layered, modular configuration similar to that used in the ARIES study,[1] which uses assumptions consistent with those of the present study. This design approach was adapted with minor modifications to both the laser and heavy ion reactor concepts.

6.8.3.1 Configuration - The blanket configuration consists of modular rings stacked around the cavity chamber. Each ring contains a number of modules placed circumferentially next to each other. At each beam penetration hole, the corresponding module length is shortened or the module side wall is curved to allow for penetration space. This is the major difference between the laser and heavy ion concepts, the former requiring allowances for 60 beam penetrations whereas the latter requires allowances for only 2 small beam penetrations, thereby resulting in simpler module design and assembly. Vacuum penetrations are required on both designs. A blanket module schematic is shown in Figure 6.8.3-1. It consists of a simple layered configuration of SiC. The module contains a number of U-bend woven SiC tube sheets which contain the pressurized flowing He coolant. The Li_2O is in a packed bed formed between the tube sheets and is purged by He flowing through the U-bend Li_2O regions.

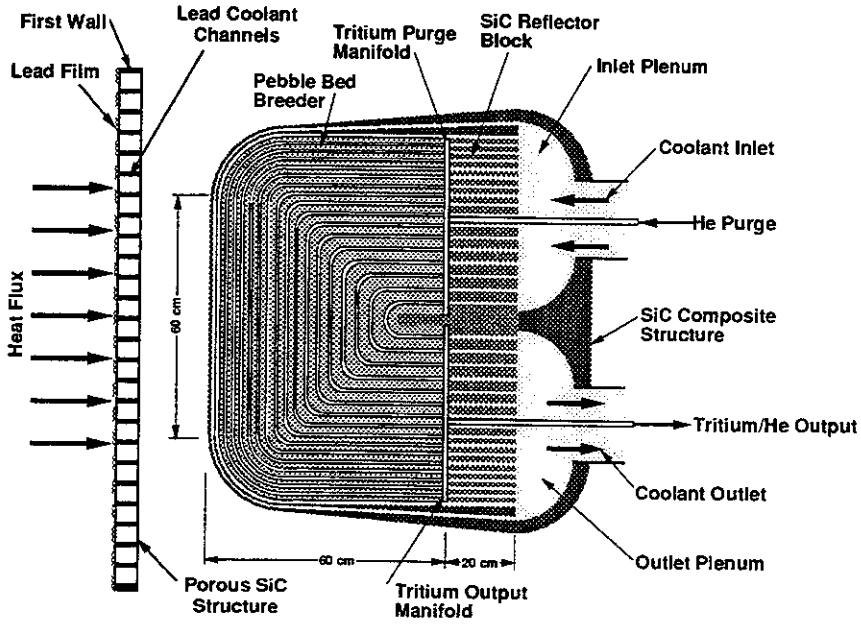

Figure 6.8.3-1. Schematic of a Blanket Module

Use or disclosure of data subject to title page restriction

Figure 6.8.3-2 shows an enlarged cutaway of the breeder region indicated in Figure 6.8.3-1. The SiC tube sheets on each side of the breeder region are 1-cm thick. The breeder region thickness increases with the distance from the plasma based on the local heat generation and minimum and maximum Li_2O operating temperature limits. These limits were conservatively set at 400°C and 800°C based on considerations of LiOT precipitation and sintering, respectively. For comparison, the corresponding temperature limits assumed in the ITER design study were 320°C and 1000°C, respectively.[2]

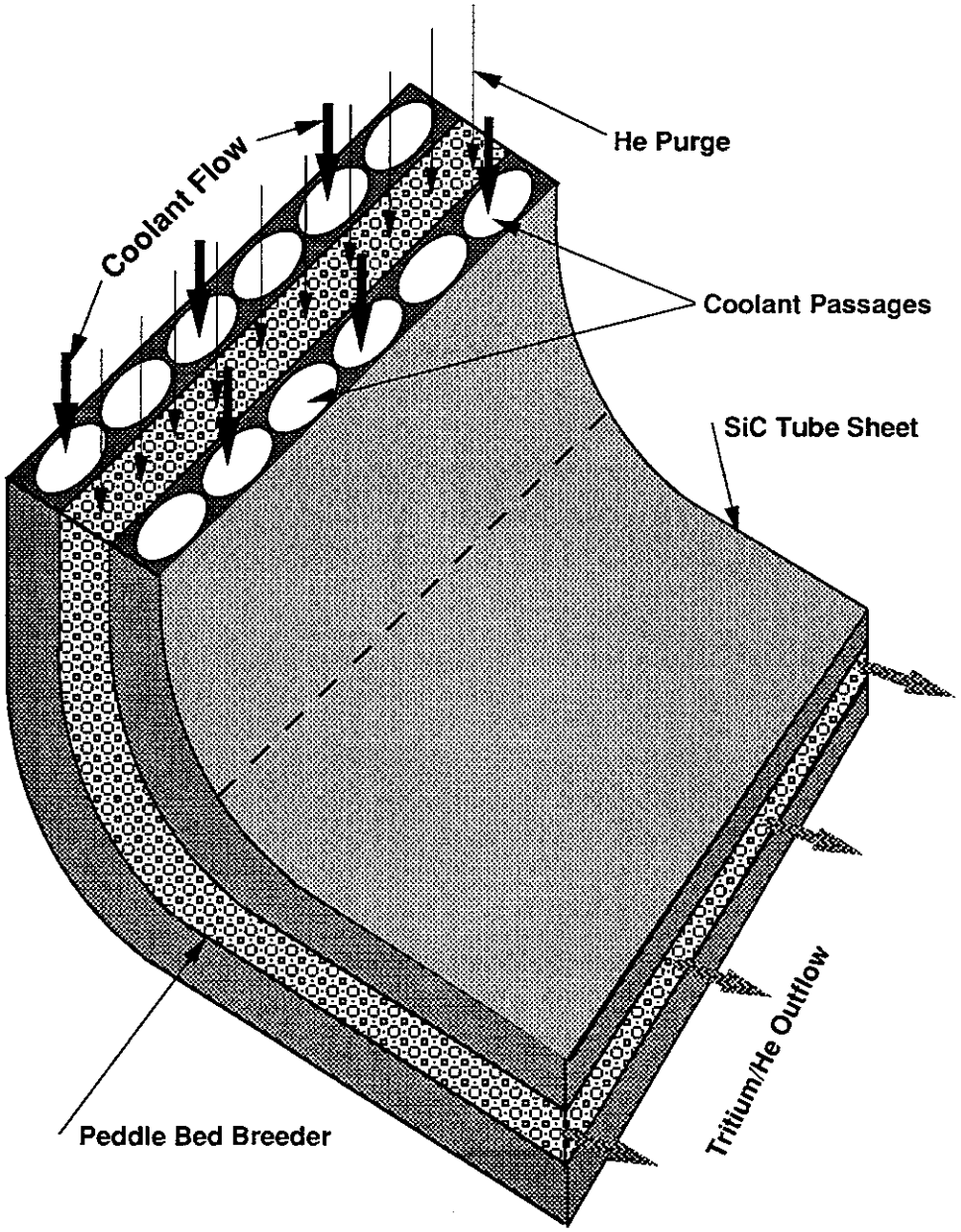

Figure 6.8.3-2. Enlarged Breeder Region Cutaway

Use or disclosure of data
subject to title page restriction

Figure 6.8.3-3 shows the internal structure of a blanket module, including the coolant and purge manifolds. Reinforcing ribs are placed about every 25 cm along the module axis in order for the module to withstand the coolant pressure in case of failure of the coolant tubes. This effectively provides double containment of the coolant, thereby increasing the safety and reliability of the design.

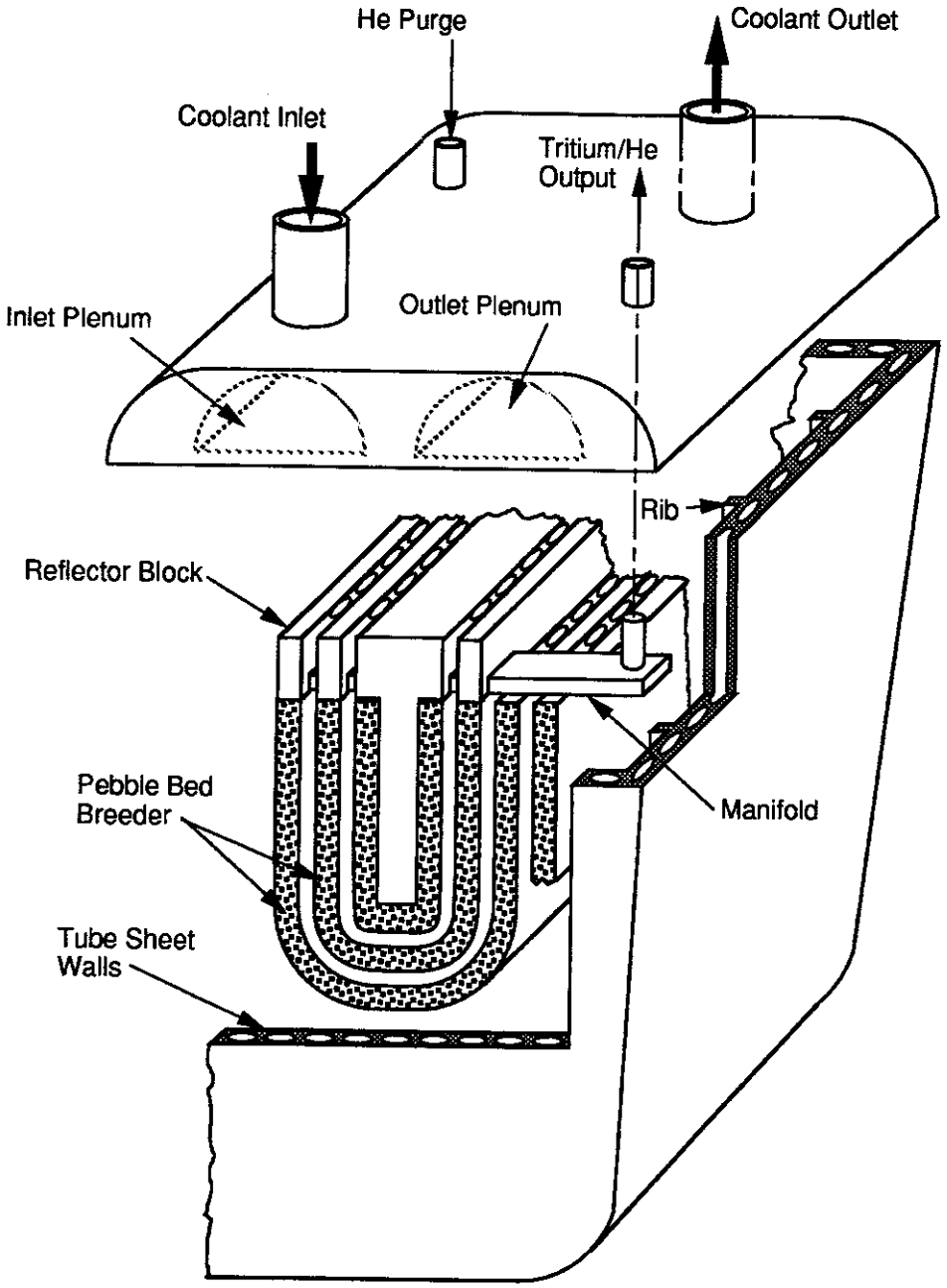

Figure 6.8.3-3. Blanket Module Internal Structure Showing Coolant and Purge Manifolds and Reinforcing Ribs

Use or disclosure of data
subject to title page restriction

The final blanket performance parameters are summarized in Table 6.8.3-1 for both the laser and heavy ion reactor concepts. The main difference between the two concepts is small differences in the fusion and blanket power capacities. The design calculations and analyses in the key areas of neutronics, thermal-hydraulic, thermomechanics, tritium inventory, and tritium permeation are described in Sections 6.8.3.2 to 6.8.3.5.

Table 6.8.3-1 Final Blanket Performance Parameters

	Laser	Heavy Ion
Blanket Loop Power	1782 MW	1597 MW
Helium Inlet Temperature	400°C	400°C
Helium Outlet Temperature	650°C	650°C
Helium Inlet Pressure	1.5 MPa	1.5 MPa
Helium Velocity	46 m/s	42 m/s
Pressure Drop	24 kPa	19 kPa
Li_2O Min. Temperature	425°C	422°C
Li_2O Max. Temperature	800°C	765°C
Breeder Volume	92 m^3	75 m^3
Avg. Annual Li Burnup	0.5%	0.6%
Peak-to-Avg. Burnup	3	3
Tritium Breeding Ratio	1.2	1.2
Tritium Inventory	100 g	100 g
Purge Composition	He+0.2%H_2	He+0.2%H_2
Purge Pressure	1 MPa	1 MPa
SiC Min. Temperature	400°C	400°C
SiC Max. Temperature	800°C	765°C

6.8.3.2 Blanket Neutronics - Several neutronics calculations have been performed to arrive at the baseline design for the first wall/blanket/shield configuration. The objectives have been to maximize both the cavity power multiplication factor, M, and tritium breeding ratio, TBR. The incident neutron spectrum of the SIRIUS-M [3] reactor design was used as the representative neutron source resulting from the blast. About 78% of the target neutrons are 14.1 MeV neutrons, 21% are in the energy range 3.5-14.1 MeV, and ~1% are in the energy range 1.5–3.5 MeV. Thus, the average energy of the incident neutrons is ~12.87 MeV. No gamma-rays were considered. In addition, no time-dependent calculations were performed to calculate the instantaneous heating or damage rates in the first wall/blanket system due to

The module assembly is constructed by positioning the SiC woven U-tubes in the module box. The breeder regions between the coolant tubes are then packed with the Li_2O particles, starting with the larger size. The purge manifolds are then positioned, followed by the solid SiC block reflector region. Finally, the module top cover is assembled.

Use or disclosure of data
subject to title page restriction

differences in the arrival time of neutrons to the first wall. Thus, the results reported here are the time-averaged values for the key parameters such as blanket power multiplication and tritium breeding ratio.

As discussed in Section 6.8.1, the incident neutron power in the laser reactor design is ~2027 MW and ~1818 MW in the heavy ion reactor (see Table 6.8.1-3). For an average neutron energy of 12.87 MeV, the incident neutron source is estimated to be ~9.83 x 10^{20} n/sec and 8.82 x 10^{20} n/sec in the two reactors, respectively.

One-dimensional and spherical model calculations were performed by using the ANISN 1-D discrete ordinate transport code[4] along with the the MATXS5 (30-g neutrons, 21-g) library[5] based on ENDF/B-V nuclear data. The 1-D model used is shown in Figure 6.8.3-4 for the final baseline design which was evolved from the parametric study given below. The material volume fractions used in the calculations are shown in Figure 6.8.3-5. The model considered a manifold zone of thickness ~1.8 m and a 1.48-m thick maintenance gap behind the vacuum vessel (2-cm thick). SiC has been selected as the structural material in the first wall and blanket/reflector/plena systems. It was also chosen as the reflecting material in the reflector/plena regions (40-cm thick) due to the high neutron reflectivity property of carbon. SiC has lower absorption cross-section for neutrons when compared to stainless steels. This choice is advantageous as far as tritium breeding is concerned because a lower absorption rate in the structural material leads to a higher absorption rate in the breeding material. However, power multiplication in steels are normally larger than in the SiC structure due to the larger energy release from the (n,γ) reactions in steels.

In the parametric study performed, a stainless steel-reinforced concrete (87% concrete, 8% carbon-steel, and 5% water) was considered for the bulk shield behind the vacuum vessel, although a composite shielding material consisting of 20% Pb, 20% B_4C, 25% SiC, 30% water, and 5% aluminum was adopted in the baseline design. Note that the bulk shield thickness in the calculational model shown in Figure 6.8.3-4 is 210 cm thick. In the final design, a thinner shield was adopted (165-cm thick in the concrete bulk shield case, 130-cm thick in the composite bulk shield case). The criterion used in estimating the required bulk shield thickness behind the vacuum vessel is discussed in Section 6.8.1 and in Section 6.8.4. It was shown that the tritium breeding ratio and cavity power multiplication are less sensitive to an increase in the bulk shield thickness beyond 1 m.

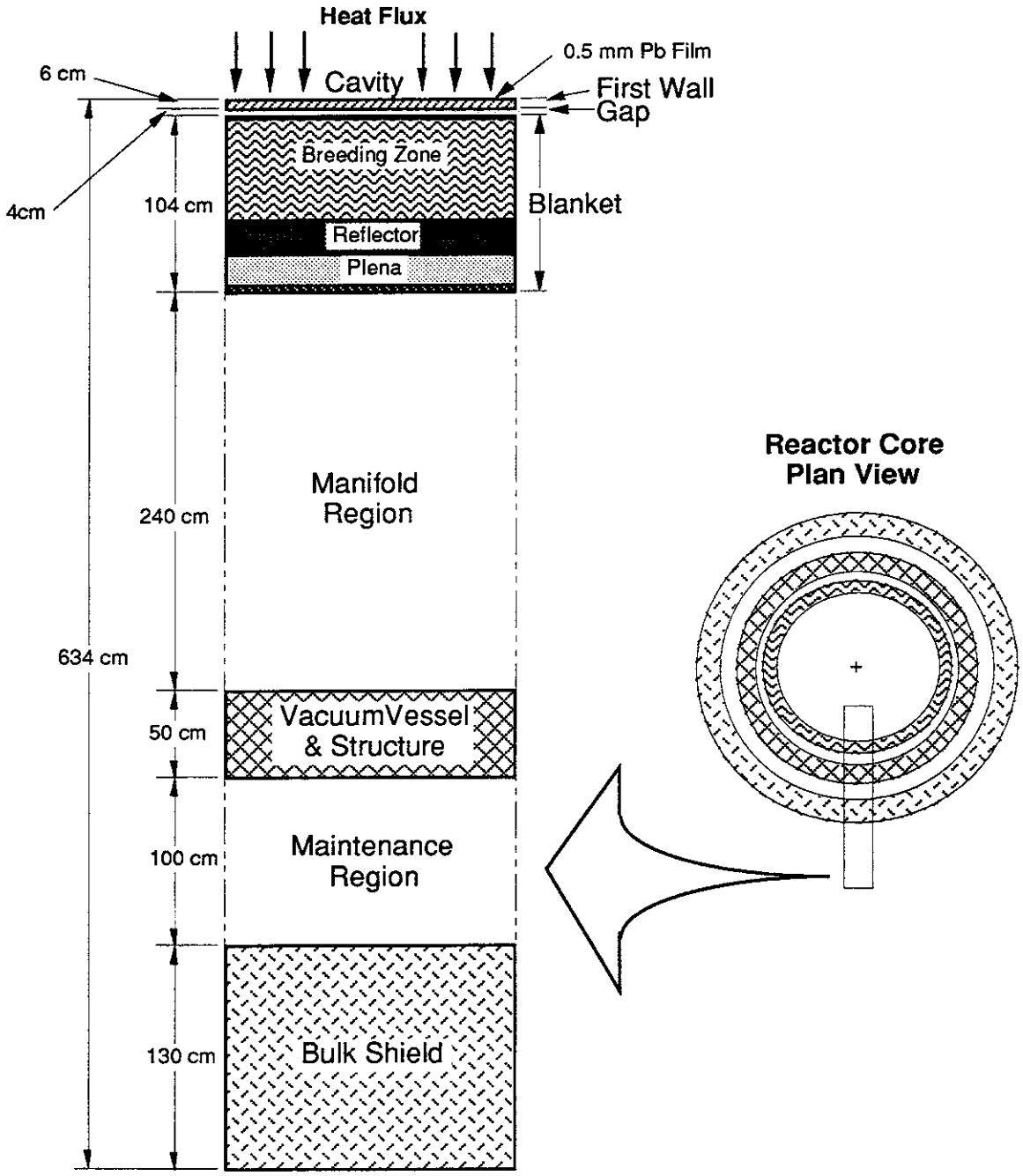

Figure 6.8.3-4. The Radial-Build of the Prometheus Cavity

Use or disclosure of data
subject to title page restriction

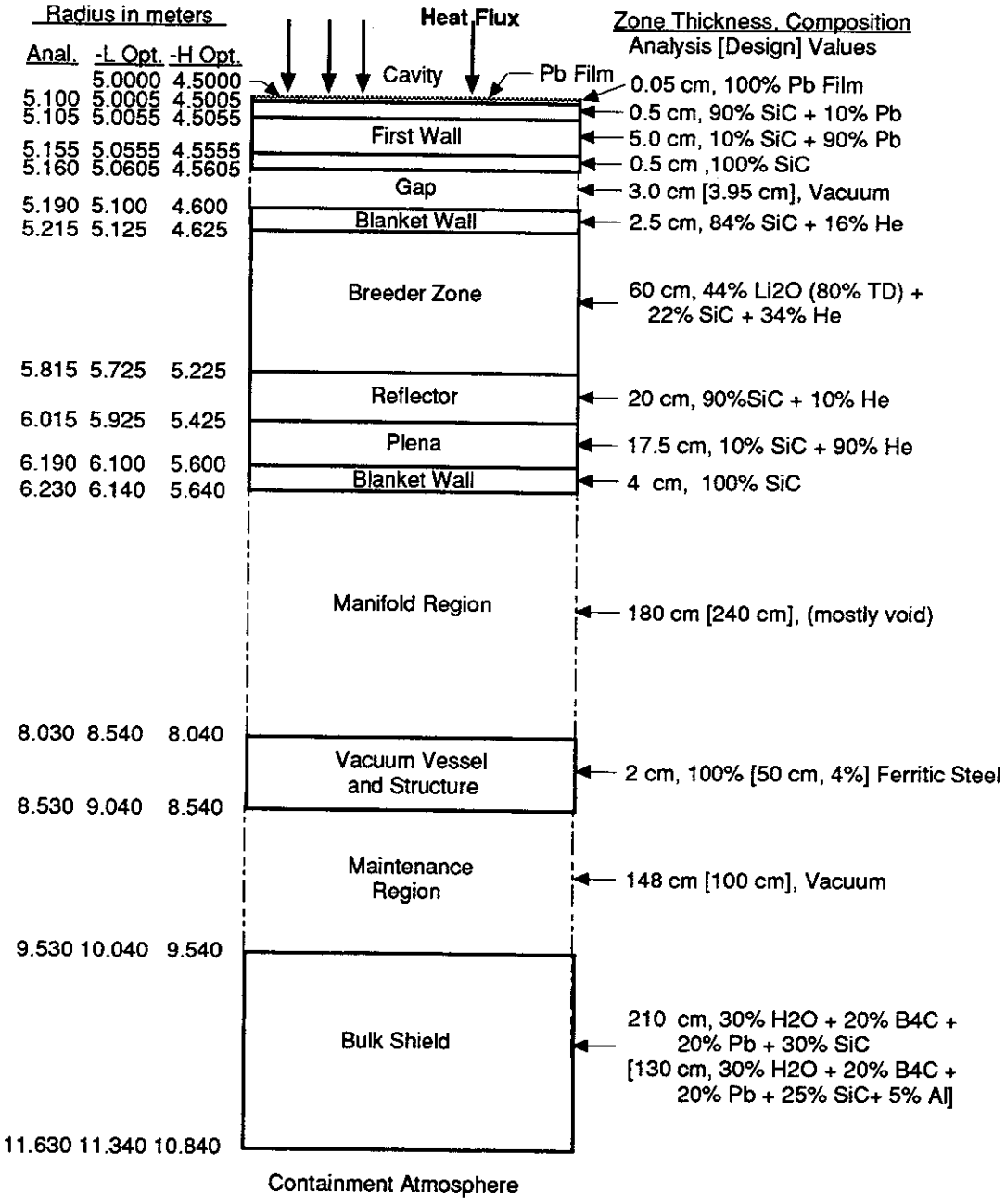

Figure 6.8.3-5. Material Composition in the 1-D Cavity Model

Use or disclosure of data
subject to title page restriction

Geometry Normalization - The first wall in the analytical model shown in Figure 6.8.3-4 and Figure 6.8.3-5 is placed at a radial distance of 510 cm from the cavity center. The cavity radius in the final laser reactor design is 500 cm and, thus, a normalization factor of $(510/500)^2 \sim 1.04$ should be applied to local absolute values such as the local heating rate profiles. The cavity radius in the heavy ion reactor design is 450 cm. Considering the slight difference in the neutron source strength between the two reactors, the normalization factor to be applied to local absolute values in this case is $(510/450)^2 \cdot (8.82/9.83) \sim 1.15$.

Effect of Design Variation on Tritium Breeding Ratio and Cavity Power Multiplication - Factors varied in the parametric analysis performed were the ^{6}Li-enrichment, the diameter of the lead cooling channels in the first wall system (FWS), and the thickness of the breeding zone (X_B) in the blanket/reflector/plena system (B/R/P) (see Figure 6.8.3-4). In the first wall system, lead flows through near-rectangular channels in the zone between the first wall (0.5 cm-thick, 90% SiC, 10% Pb) and the back wall of the first wall system (0.5 cm-thick, 100% SiC). The volume fraction of the SiC and lead was kept to 9:1 in this zone whose thickness, denoted Xp, was varied in the present study.

For a total thickness of 104 cm for the B/R/P system, while keeping the thicknesses of other zones shown in Figure 6.8.3-5 the same, the power multiplication factor M has increased from 1.096 to 1.152 (~5% increase) for increasing X_p from 1 cm to 7 cm (see Figure 6.8.3-6). For the same change, the TBR [dominated by tritium production from ^{6}Li (T-6), 25% ^{6}Li-enrichment] has increased from 0.98 to 1.28; i.e., ~30% increase (see Figure 6.8.3-7). The fraction of nuclear power deposited in the first wall system is appreciable due to the interaction of neutrons and gamma rays with lead. This fraction increased from ~0.1 to ~0.25 for increasing X_p from 1 cm to 7 cm. The balance of the nuclear power is deposited mainly in the B/R/P system. This can be seen in Figures 6.8.3-8 and 6.8.3-9 which give the fraction of power deposited in the various components of the cavity. Note, in particular, the small fraction of power deposited in the vacuum vessel and shield systems .

The profiles for the nuclear power density (heating rate) as a function of the lead zone thickness, Xp, are shown in Figures 6.8.3-10 and 6.8.3-11 in units of J/cc.sec.n and in MW/m^3, respectively. For an Xp value of 1 cm, the power density in the lead and the back wall of the FWS is as high as 45 MW/m^3, while it is ~28 MW/m^3 in the first wall (see Figure 6.8.3-11). The power density in the lead film (0.05 cm-thick) covering the inner surface of the cavity is ~42 MW/m^3 in this case. As Xp increases, the power density in the first wall system decreases rapidly, while the power deposited in the blanket/reflector/plena system increases. For the baseline design (Xp = 5 cm), the power density in the lead film is ~32 MW/m^3 and mainly due to gamma rays produced

Use or disclosure of data
subject to title page restriction

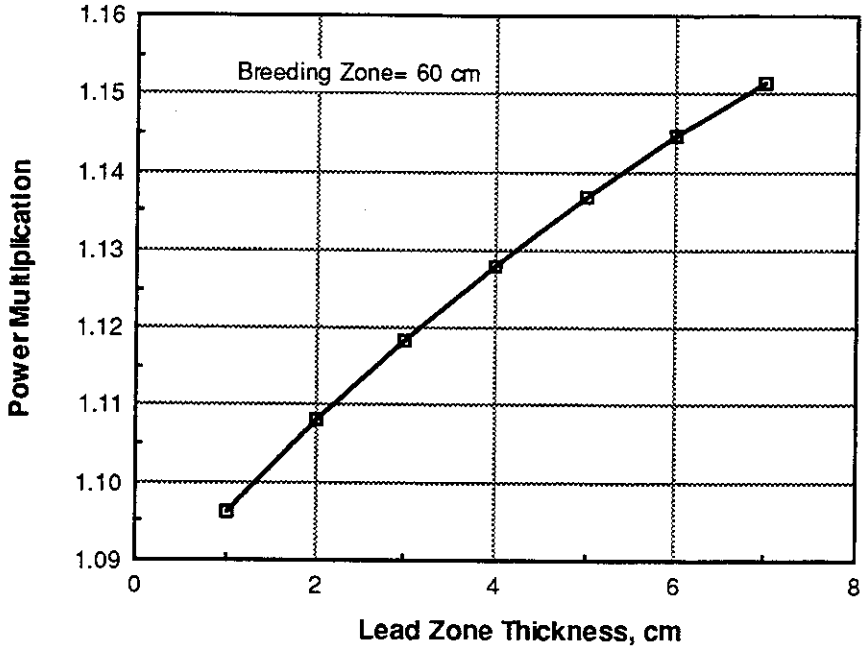

Figure 6.8.3-6. Nuclear Power Multiplication as a Function of Lead Zone Thickness

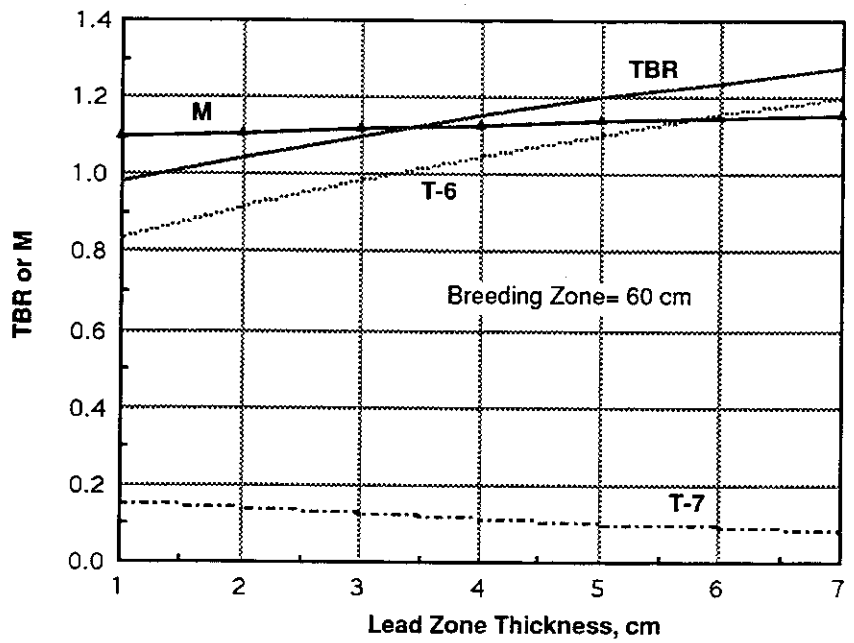

Figure 6.8.3-7. Tritium Breeding Ratio and Nuclear Power Multiplication as a Function of Lead Zone Thickness

Use or disclosure of data
subject to title page restriction

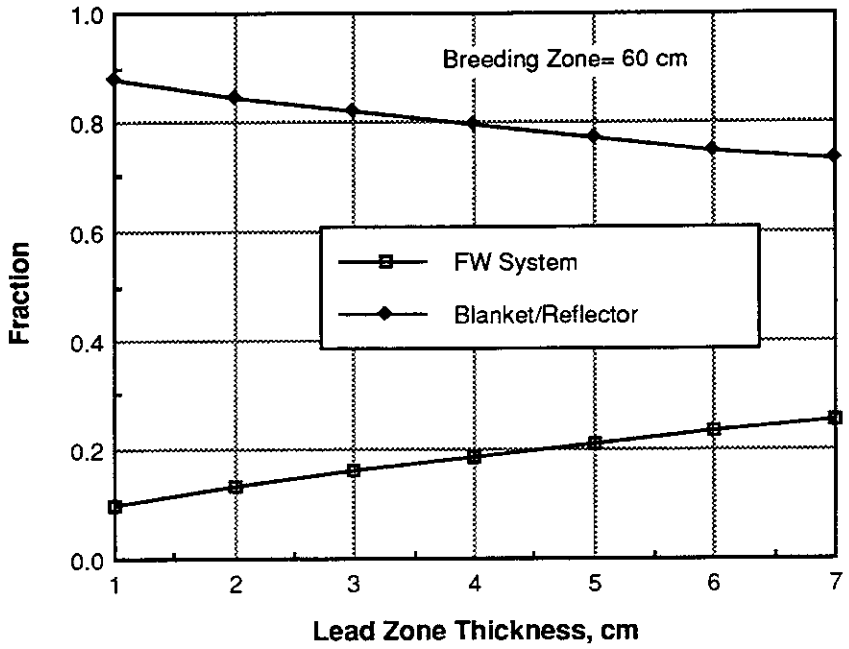

Figure 6.8.3-8. Fraction of Nuclear Power Deposited in the First Wall and Blanket/Reflector Systems as a Function of Lead Zone Thickness

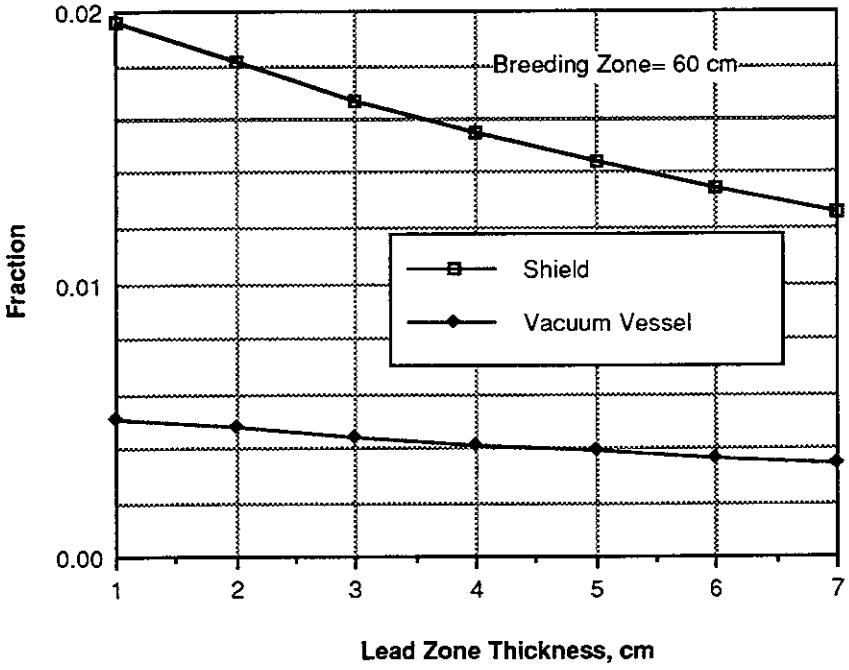

Figure 6.8.3-9. Fraction of Nuclear Power Deposited in the Vacuum Vessel and Shield Systems as a Function of Lead Zone Thickness

Use or disclosure of data
subject to title page restriction

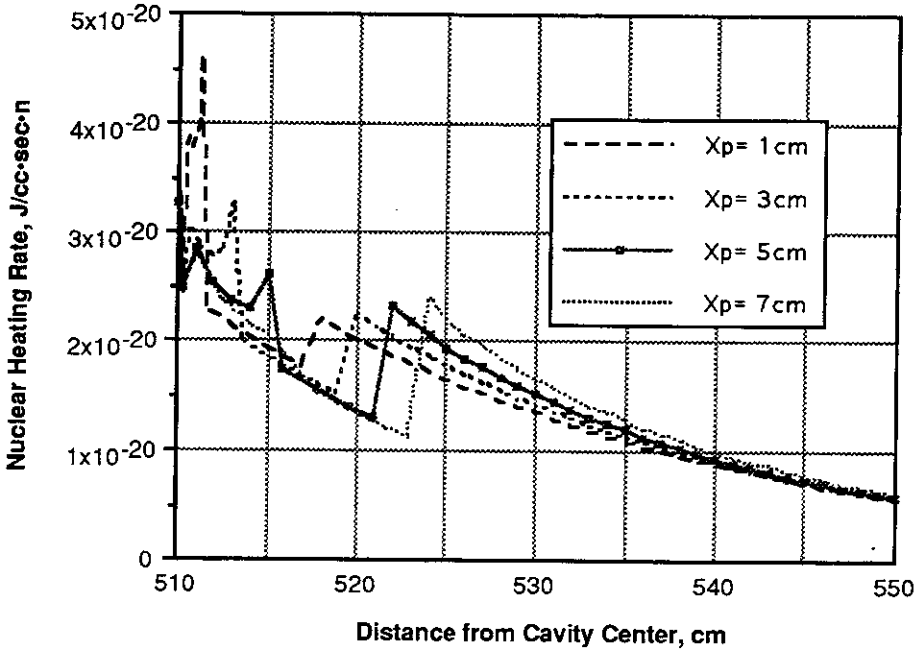

Figure 6.8.3-10. Nuclear Power Density as a Function of the Lead Zone Thickness

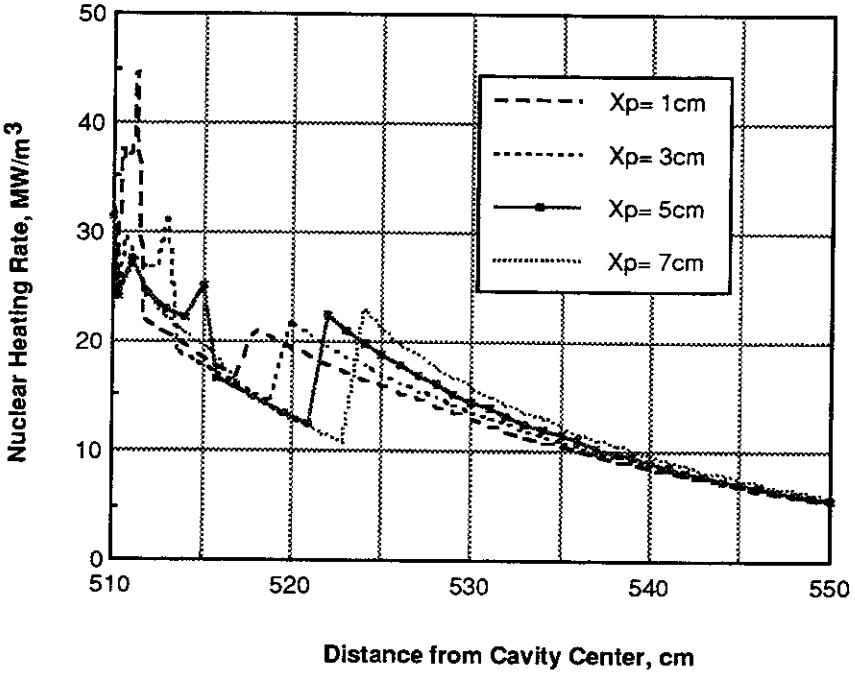

Figure 6.8.3-11. Nuclear Power Density as a Function of the Lead Zone Thickness

Use or disclosure of data subject to title page restriction

by neutron interactions with lead, particularly the inelastic scattering reactions (see Figure 6.8.1-3 in Section 6.8.1). The total nuclear heating rate in the first wall is ~24 MW/m^3 and is dominated by neutron heating (~75%). The average power density in the lead channel zone is ~25 MW/m^3, mainly from gamma ray heating (~80%). For the baseline case, the maximum heating rate in the breeding zone is ~20 MW/m^3 which occurs just behind the blanket first wall (2.5-cm thick, 84% SiC, 16% He). Nuclear heating in the breeding zone is attributed mainly to neutron interactions, particularly Li-6(n,α)T reactions.

The profiles for the tritium production rate (TPR) from Li-6 (T-6) are shown in Figure 6.8.3-12 as a function of Xp. By increasing the lead zone thickness, both neutron multiplication and inelastic collisions in lead increase, leading to larger TPR from Li-6 (and consequently a larger TBR) in approximately the first 30 cm in the breeding zone . This increase is more apparent just behind the first wall of the B/R/P system. For an increase in Xp from 1 cm to 7 cm, the local T-6 production rate is increased from 8.5x10^{-9} T atoms/cm^3•sec•n to 1.8x10^{-8} T atoms/cm^3•sec•n (a factor of 2.3 increase) at the front edge of the breeding zone. In the baseline case, this maximum local value is 1.5x10^{-8} T atoms/cm^3•sec•n.

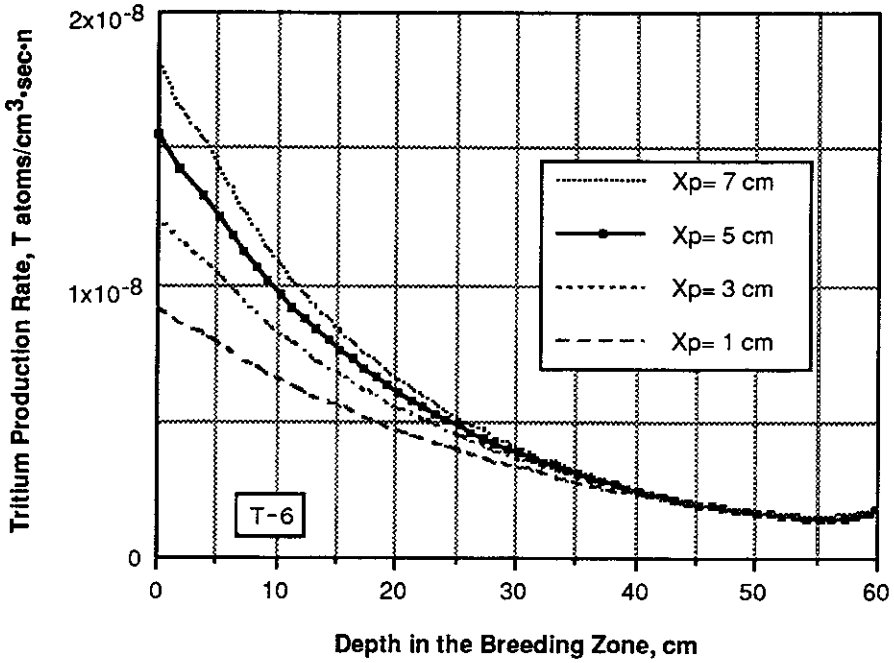

Figure 6.8.3-12. Tritium Production Rate From Li-6 (T-6) as a Function of Lead Zone Thickness

Use or disclosure of data subject to title page restriction

Figure 6.8.3-13 shows the corresponding profiles for the tritium production rate from Li-7 (T-7). By increasing lead in the FWS, the increase in the high-energy reactions in lead [e.g., (n,2n), inelastic] tends to decrease the tritium producing reactions in lithium-7, Li-7(n,n'α)T, whose threshold energy is ~2.8 MeV. However, the TPR from Li-7 is about an order of magnitude less than that from Li-6 behind the first wall of the blanket and, thus, increasing Xp leads to a net increase in the total TPR (and TBR). Note from Figures 6.8.3-12 and 6.8.3-13 that the profiles for T-7 are less steep than those for T-6 near the blanket first wall. The effect of increasing the lead zone thickness is less at the back locations in the breeding zone. In the baseline design (Xp = 5 cm), the TPRs from Li-6 and Li-7 are ~1.5×10^{-8} T/cm^3•sec•n and ~1.5×10^{-9} T/cm^3•sec•n, respectively, just behind the blanket first wall.

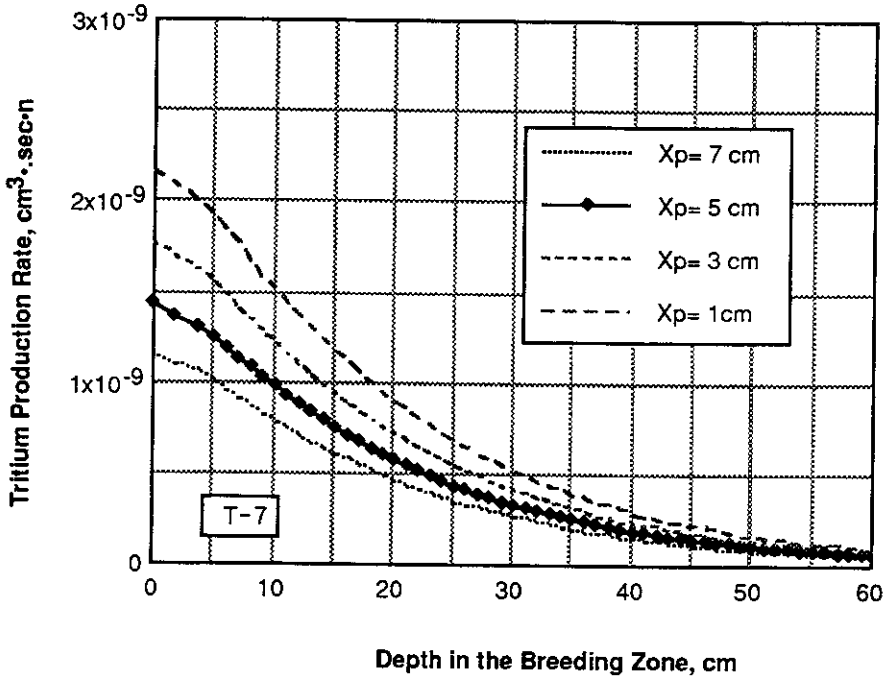

Figure 6.8.3-13. Tritium Production Rate from Li-7 (T-7) as a Function of Lead Zone Thickness

The impact of increasing the breeding zone thickness, X_B, on both M and TBR are shown in Figures 6.8.3-14 and 6.8.3-15, respectively. For Xp = 5 cm, the multiplication factor M slightly decreased upon increasing X_B while the TBR decreased. By increasing XB from 40 cm to 100 cm, M decreased from 1.146 to 1.131 (~2% decrease) while the TBR increased from 1.13 to 1.23 (~9% increase). The fraction of nuclear power deposited in the first wall system (~21%) is insensitive to this design change whereas the power deposited in the B/R/P system slightly increased from 0.74 to 0.79 (~7% increase). The fractions of power deposited in the various components are shown in Figures 6.8.3-16 and 6.8.3-17.

Use or disclosure of data
subject to title page restriction

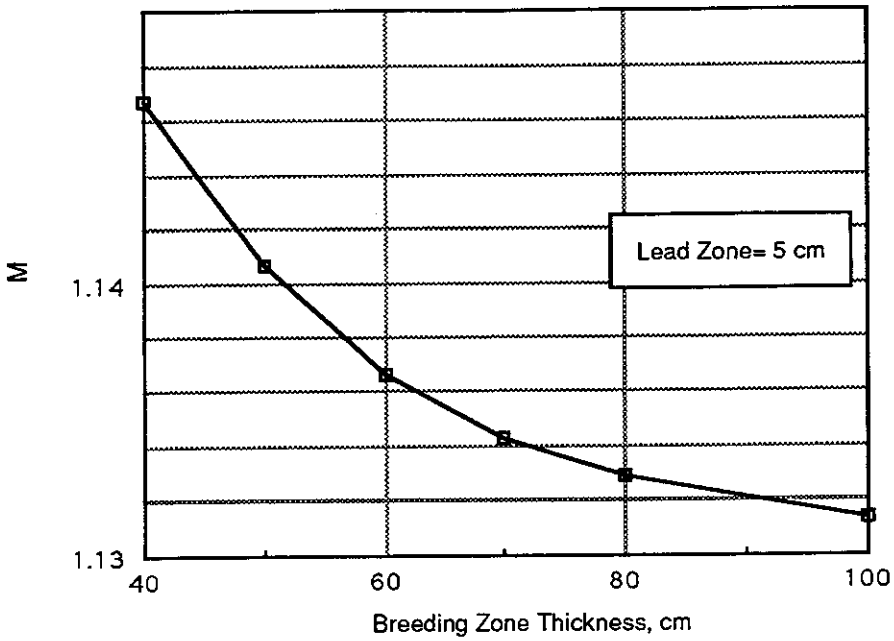

Figure 6.8.3-14. Nuclear Power Multiplication as a Function of the Breeding Zone Thickness

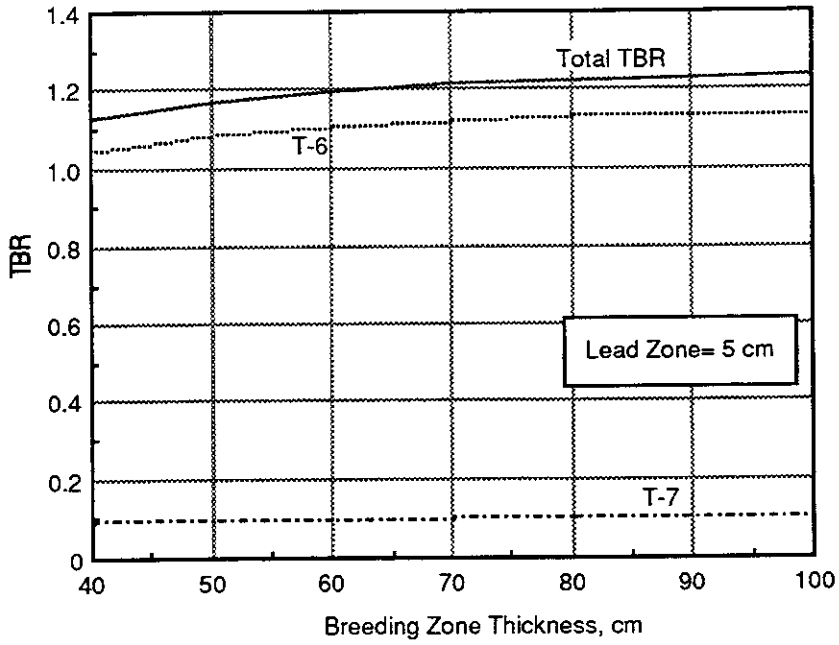

Figure 6.8.3-15. Tritium Breeding Ratio as a Function of the Breeding Zone Thickness

Use or disclosure of data
subject to title page restriction

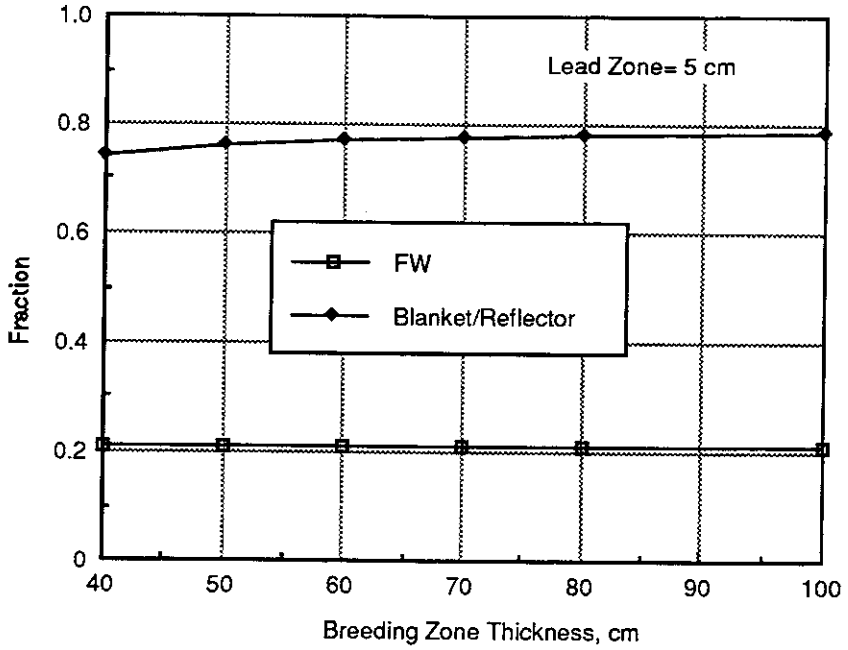

Figure 6.8.3-16. Fraction of Nuclear Power Deposited in the First Wall and Blanket/Reflector Systems

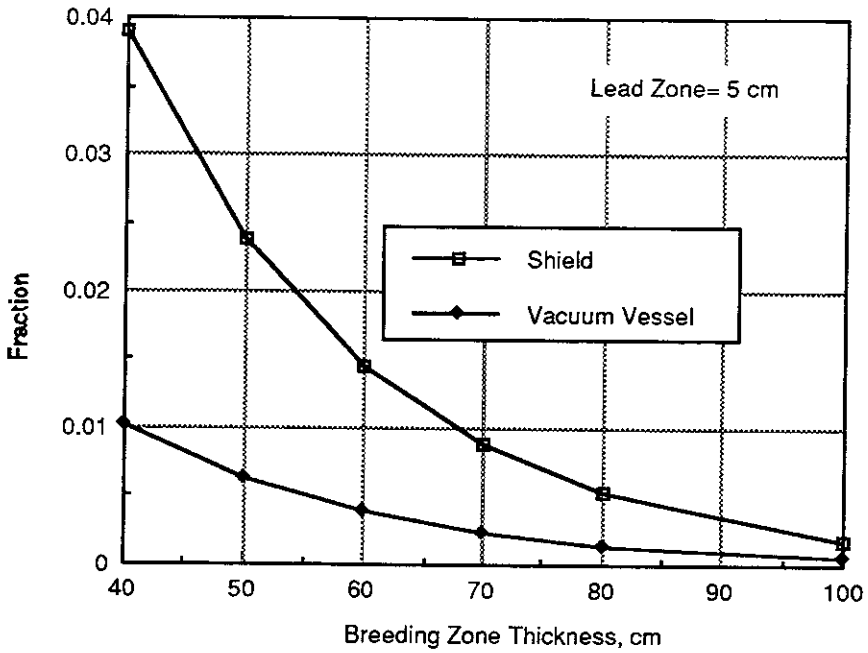

Figure 6.8.3-17. Fraction of Power Deposited in the Vacuum Vessel and Shield Systems

Nuclear Performance of the Baseline Design - From the above results, it was concluded that the nuclear power multiplication in our design is less sensitive to design variations than the TBR, which is most sensitive to the thickness of the Pb zone. The ^{6}Li-enrichment used in the parametric analyses was 25% which was determined to be optimal value in our design. In the baseline design, the Pb zone thickness and the breeding zone thickness are X_p = 5 cm and X_B = 60 cm, respectively. In this case, M ~ 1.14 and TBR ~ 1.2. The fractions of power deposited in the FWS, B/R/P, vacuum vessel, and the shield are 0.21, 0.77, 0.004, and 0.014, respectively. Table 6.8.1-2 in Section 6.8.1 lists these fractions (in %) by material zone as well as by system. The integrated power in each zone is expressed in terms of joules per incident source neutron and, thus, the entries do not depend on the fusion power, neutron yield, etc. To convert the entries given in Table 6.8.1-2 to absolute values (in MW), the following formula could be used:

(power deposited, J/n) • (incident neutron power, MW) • 4.85×10^{11}

or alternatively,

(% of power deposited, by zone) • (incident neutron power, MW) • 1.14

In the laser reactor design, the incident neutron power is 2027 MW while it is 1818 MW in the heavy ion reactor case. When the cavity power multiplication factor M=1.14 is applied, the nuclear power in the two reactors are 2311 MW and 2073 MW, respectively. Table 6.8.1-3 in Section 6.8.1 gives the cavity energy balance in the two reactors.

Effect of Including a Beryllium Zone on Blanket Characteristics – The nuclear characteristics of the reference blanket could noticeably be improved upon by incorporating beryllium in the blanket system. Several neutron transport calculations were performed in which the Li_2O in the first few centimeters of the breeding zone was replaced by beryllium (80% theoretical density). Figures 6.8.3-18 to 6.8.3-21 show the effect of this design change on the nuclear power multiplication, M, the tritium breeding ratio, TBR, and the power distribution in the FWS, B/R/P, vacuum vessel, and shield systems. With a beryllium zone thickness of 8 cm (i.e., replacing Li_2O in the first 8 cm in the 60-cm thick breeding zone with beryllium), the TBR increased from 1.198 to 1.279 (~7% increase) while M increased from 1.137 to 1.188 (~5% increase). This design variation could improve the COE and tritium fuel cycle.

Use or disclosure of data
subject to title page restriction

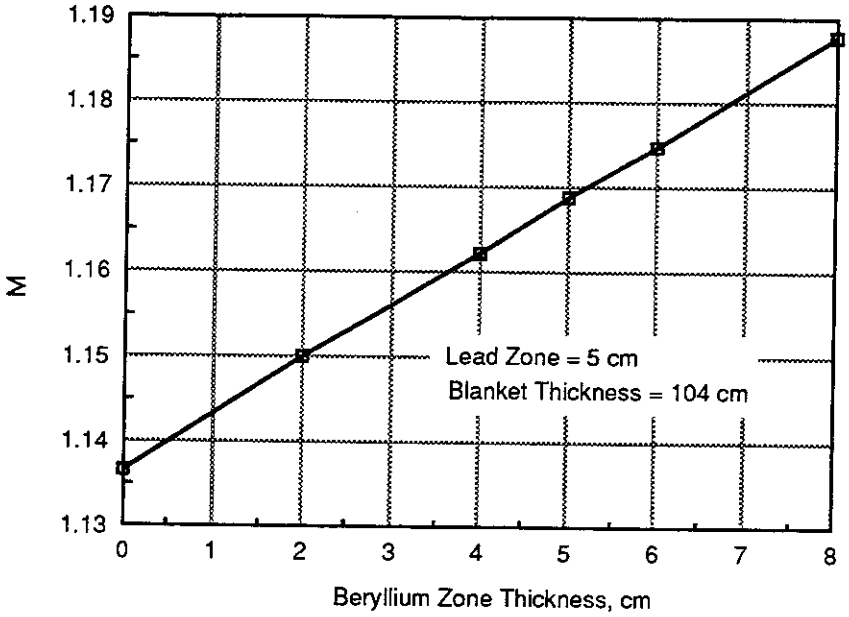

Figure 6.8.3-18. Nuclear Power Multiplication as a Function of the Beryllium Zone Thickness

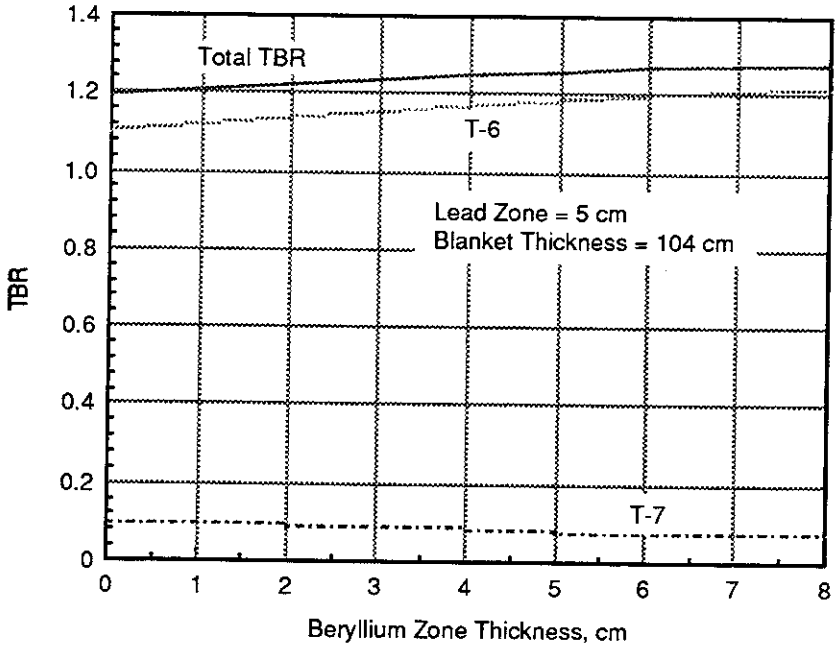

Figure 6.8.3-19. Tritium Breeding Ratio as a Function of Beryllium Zone Thickness

Use or disclosure of data
subject to title page restriction

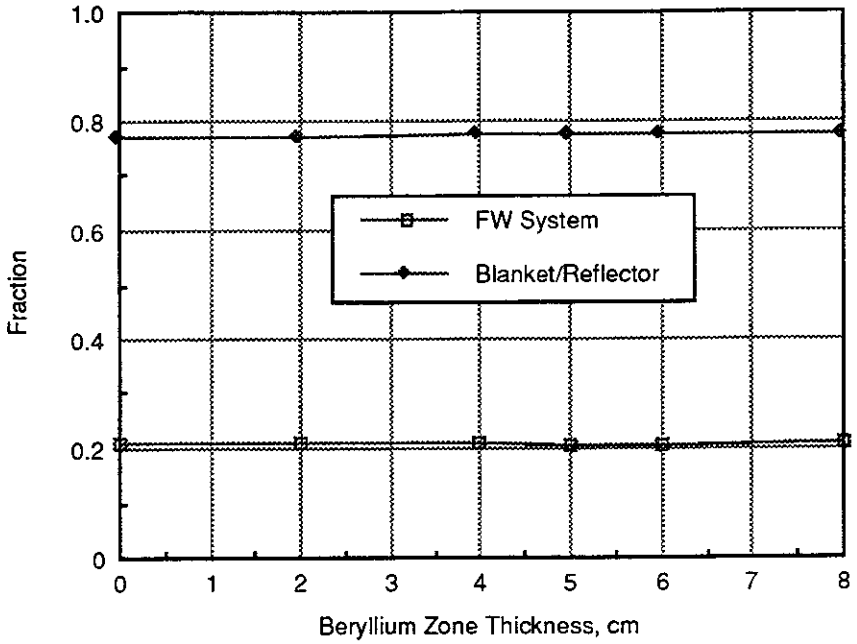

Figure 6.8.3-20. Fraction of Nuclear Power Deposited in the First Wall and Blanket/Reflector Systems as a Function of Beryllium Zone Thickness

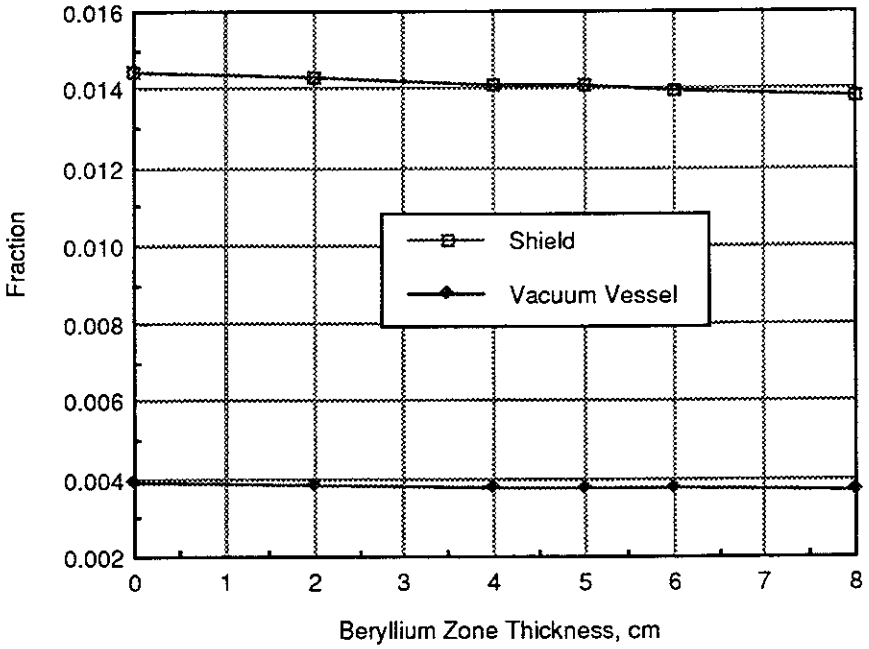

Figure 6.8.3-21. Fraction of Nuclear Power Deposited in the Vacuum Vessel and Shield Systems as a Function of Beryllium Zone Thickness

Use or disclosure of data
subject to title page restriction

6.8.3.3 Thermal Hydraulics

Helium Coolant – The first wall protection system absorbs virtually all the energy from the x-rays and debris from the micro-explosion as well as a significant fraction of the neutron energy. This results in less than 60% of the total thermal power being deposited in the blanket, which opens the possibility of flowing the He at moderate pressure while keeping the pressure drop and velocity at reasonable levels.

A parametric study explored this possibility. The helium inlet temperature was set at 400°C to ensure that the solid breeder temperature would be higher. The outlet temperature was set at 650°C based on a tradeoff between maximizing the power conversion efficiency and the design simplicity. A high outlet temperature would result in higher power conversion efficiency whereas a lower outlet temperature would result in thicker breeder regions for the same breeder maximum temperature limit, and, thus, in fewer breeder layers per module and in a simpler design and assembly. Figure 6.8.3-22 shows the helium velocity as a function of the inlet pressure for different fractional flow areas for a temperature rise of 250°C and blanket power and total area of 1782 MW and 470 m^2, respectively.

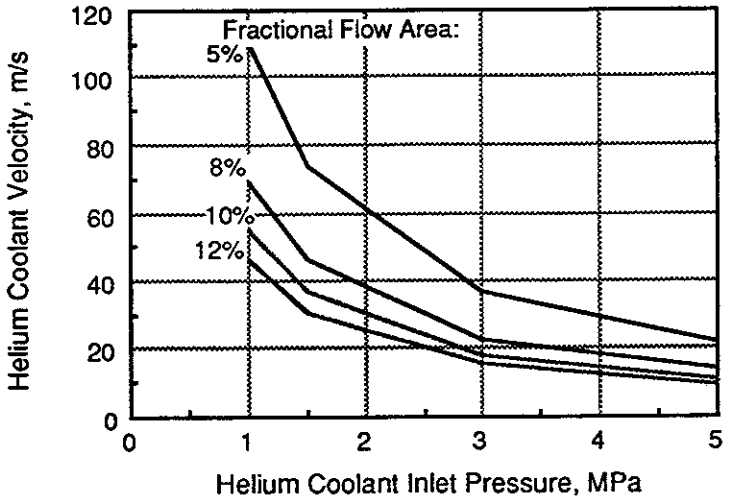

Figure 6.8.3-22. He Coolant Velocity in the Blanket as a Function of the Inlet Pressure for Different Fractional Flow Areas

The total He pressure drop in the blanket, ΔP_{tot}, was calculated as the sum of the pressure drops due to friction, ΔP_f, losses, ΔP_l, and acceleration, ΔP_a. The friction pressure drop component was calculated as follows:

Use or disclosure of data
subject to title page restriction

$$\Delta P_f = \frac{fL}{d_H}\frac{\rho u^2}{2} \qquad (6.8.3\text{-}1)$$

where ρ is the density, u the velocity, L the flow length (~2 m), d_H the hydraulic diameter (~ 6 mm), and f the friction factor. For turbulent flow in smooth pipes, the friction factor can be estimated from the Reynolds number, Re, based on the Blasius equation:

$$f = 0.316\,Re^{-0.25} \qquad (6.8.3\text{-}2)$$

In addition, in the absence of specific data on the roughness of the SiC channels, a roughness factor of 2 was conservatively assumed in the calculation of the friction factor.

A value for ΔP_l was estimated from a loss coefficient, K, whose value was set at 3 based on assumed pressure losses through one expansion, one U-bend, and one constriction.

$$\Delta P_l = K\frac{\rho u^2}{2} \qquad (6.8.3\text{-}3)$$

Finally, ΔP_a was estimated based on the helium densities at the inlet and outlet.

$$\Delta P_a = \rho u^2\left(\frac{1}{\rho_{out}} - \frac{1}{\rho_{in}}\right) \qquad (6.8.3\text{-}4)$$

Figure 6.8.3-23 shows the total pressure drop in the blanket as a function of the fractional flow area for different inlet pressures and fixed inlet and outlet temperatures of 400°C and 650°C, respectively. For a fractional flow area of 8% (which corresponds to 16% of the total blanket area since space has to be provided for both inlet and outlet flows), the blanket pressure drop is only 24 kPa for an inlet pressure of 1.5 MPa. This is reasonable; however, the pressure drop in the cooling system outside the blanket could be quite high, leading to a lower overall cycle efficiency than would have been the case for a higher inlet pressure. This has to be evaluated against the improved reliability and safety associated with a moderate coolant pressure. In particular, a 1.5 MPa pressure provides the possibility of double containment of the coolant in the blanket. The possibility of using a moderate coolant pressure (1.5 MPa) is seen as being a distinctive feature for this blanket since previous designs made use of He at high pressure (5 MPa or more) and is chosen for the reference case. If operation at high pressure is shown to provide an acceptable level of reliability and safety, the blanket operating parameters can be changed accordingly for higher overall plant

Use or disclosure of data
subject to title page restriction

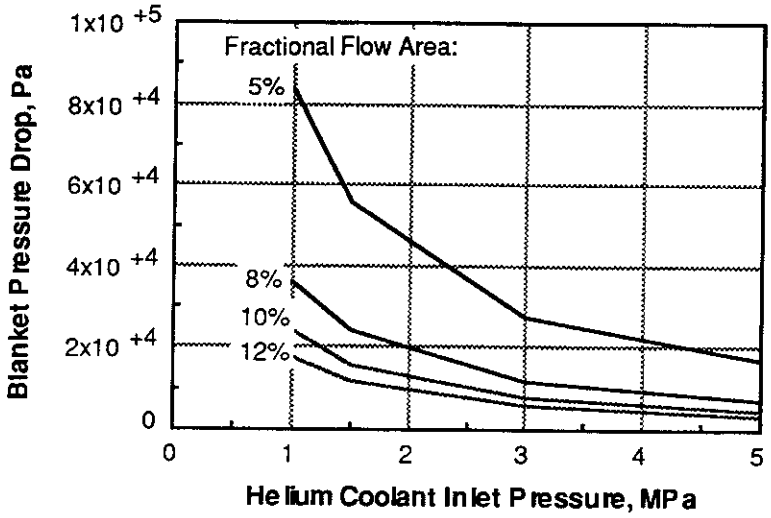

Figure 6.8.3-23. He Coolant Pressure Drop in the Blanket as a Function of the Inlet Pressure for Different Fractional Flow Areas. The Helium Temperature Rise is Fixed at 250°C

efficiency. From Figure 6.8.3-22, the corresponding velocity for an inlet pressure of 1.5 MPa is 46 m/s, resulting in a Re of about 6100.

Helium Purge - As shown in Figures 6.8.3-1 and 6.8.3-3, the purge flows in through an inlet manifold to the breeder regions. At the top of each breeder region at the inlet and outlet, a spacer acts like a plenum distributing the purge uniformly over the region at the inlet and guiding the purge to the manifold at the outlet. Orifices are placed in the inlet manifold so that, for the same pressure drop, the purge flow rate through each breeder region results in the same tritium partial pressure based on the tritium generation rate in the given region.

The packed bed form is selected for the breeder material instead of the sintered block form based mostly on perceived advantages in the accommodation of thermal expansion and swelling and in thermomechanical performance. In order to maximize the breeder volume fraction over the blanket region and, hence, the tritium breeding ratio, a binary Li_2O packed bed is chosen. The pebble sizes are 1.2 mm and 0.2 mm based on maintaining at least a ratio of 10 between the larger pebble size and the breeder region thickness (for better thermal performance predictability) and at least a ratio of 6 between the larger pebble size and the smaller pebble size (for better packing). The total Li_2O volume fraction in the breeder region is assumed to be 64%, which includes both the breeder theoretical density fraction (0.8) and the pebble bed packing fraction (0.8).

Use or disclosure of data
subject to title page restriction

The purge pressure drop, ΔP_p, across the blanket region was estimated as a function of the pebble bed packing porosity, ε, and of the purge inlet pressure, $P_{p(in)}$ based on the Blake-Kozeny correlation for laminar flow (which is the regime of interest).

$$\frac{\Delta P_p}{L_b} = 150 \frac{(1-\varepsilon)^2 \mu V_0}{\varepsilon^3 d_{peff}} \qquad (6.8.3\text{-}5)$$

where L_b is the length of the breeder region over which the purge flows, μ is the fluid viscosity, V_0 the superficial velocity based on the total cross-section of the bed, and d_{peff} the effective particle diameter. V_0 can be estimated from the total mass flow rate of the helium purge, the helium density based on the inlet pressure and the total breeder region cross-section area. This area was estimated from a total blanket flow area of 235 m^2 and a breeder region area fraction of 0.55. The partial pressure of HT in the purge was set at 10 Pa based on tritium inventory considerations. For a tritium generation rate of 516 g/day (based on a fusion power of 2807 MW and a TBR of 1.2), the total purge mass flow rate is 1.61 kg/s. The value of d_{peff} is estimated by equating its reciprocal value to the summation of the ratio of weight fraction to diameter of each particle size. For a packed bed with 66% of particles of diameter 1.2 mm and 33% of particles with diameter 0.2 mm, d_{peff} is 0.45 mm.

Figure 6.8.3-24 shows the purge pressure drop per unit length in the blanket as a function of the bed packing fraction, (1-ε), for different purge inlet pressure and for an

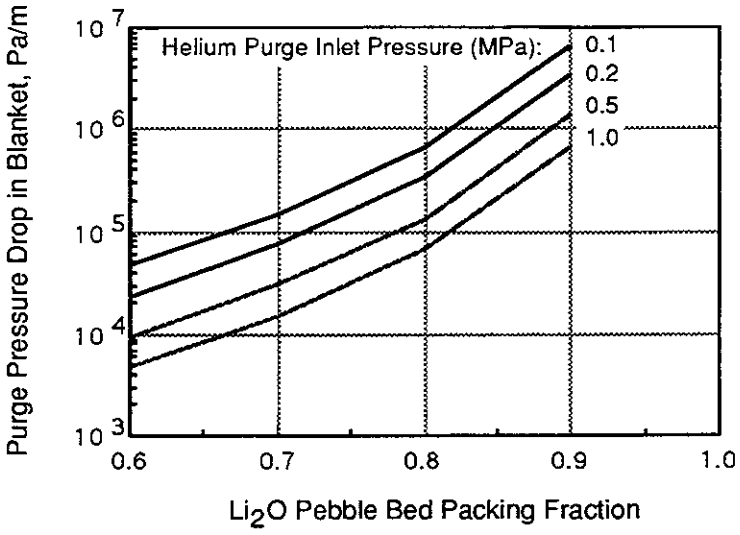

Figure 6.8.3-24. He Purge Pressure Drop in the Blanket as a Function of the Li_2O Bed Packing Fraction for Different Purge Inlet Pressures. The Flow Length Was Set at 2 m and the Effective Particle Size at 0.45 mm

Use or disclosure of data
subject to title page restriction

average temperature of 700°C. The pressure drop is quite high and imposes a constraint on the choice of the purge inlet pressure. For example, for a packing fraction of about 0.8, a flow length of about 1.5 m and, assuming an arbitrarily set limit of 10% on the pressure drop to inlet pressure ratio, the required inlet pressure is about 1 MPa. This pressure is acceptable since it is lower than the coolant pressure (1.5 MPa), thereby preventing tritium contamination of the coolant in the case of a leak between the coolant and purge. Note that the pressure drop outside the blanket is relatively small and the total purge pressure drop will be set basically by the blanket pressure drop. The corresponding pumping power required for the purge is about 0.18 MW based on an assumed pump efficiency of 0.9.

6.8.3.4 Thermo-Mechanics – The moderate coolant pressure provides the possibility for each module to independently withstand the 1.5 MPa pressure in the unlikely event of a SiC tube sheet leaking or rupturing. This would be an added safety advantage, effectively resulting in double coolant pressure boundaries. To assess this possibility and to determine the required module dimensions, a simple stress analysis was carried out. The side wall thickness increases towards the back of the module to the same thickness of the back wall (see Figure 6.8.3-1) and stresses there can be more easily accommodated, in particularly since the thermal stresses are low. The stresses in the side walls toward the front of the module and the front walls are higher and more limiting and, thus, were the focus of the analysis.

Figure 6.8.3-25 shows a typical cross-section of the front wall. The total wall thickness is t_w, while the thickness of the SiC region on each side of the cooling tube region is t_h.

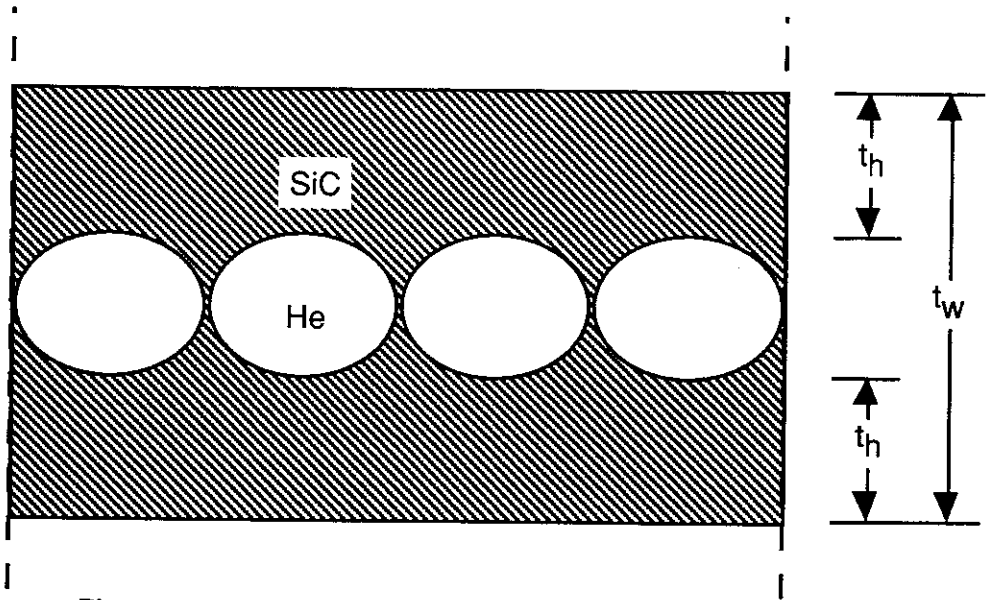

Figure 6.8.3-25. Cross-Section of the Module Front Wall Showing the He Cooling Channels

Use or disclosure of data subject to title page restriction

The thermal stress, σ_{th}, was first estimated based on the following expression:

$$\sigma_{th} = \frac{E\,\alpha\,\delta T}{2(1-\nu)} \qquad (6.8.3\text{-}6)$$

where E is Young's modulus of elasticity for SiC composite, α the coefficient of thermal expansion, and ν Poisson's ratio. δT is the temperature drop between the edge of the wall and the coolant channel which can be estimated from the distance, t_h, between the coolant channel and the wall edge, the heat generation per unit volume, q''', and the thermal conductivity of the SiC composite, k.

$$\delta T = \frac{q''' t_h^2}{2k} \qquad (6.8.3\text{-}7)$$

Figure 6.8.3-26 shows the thermal stress as a function of t_h for a q''' of 10 MW/m^3, typical of the front wall, and for the SiC composite properties listed in Table 6.8.3-2 based on those used in Reference 1.

Table 6.8.3-2. Properties of SiC Composite Used in the Stress Calculations

Young's Modulus of Elasticity, E	200 GPa
Coefficient of Thermal Expansion, α	4.5×10^{-6} K^{-1}
Thermal Conductivity, k	15 W/m-K
Poisson's Ratio, ν	0.18
Tensile Strength, S_T	200 MPa
Allowable Stress (assumed 2/3 S_T)	134 MPa

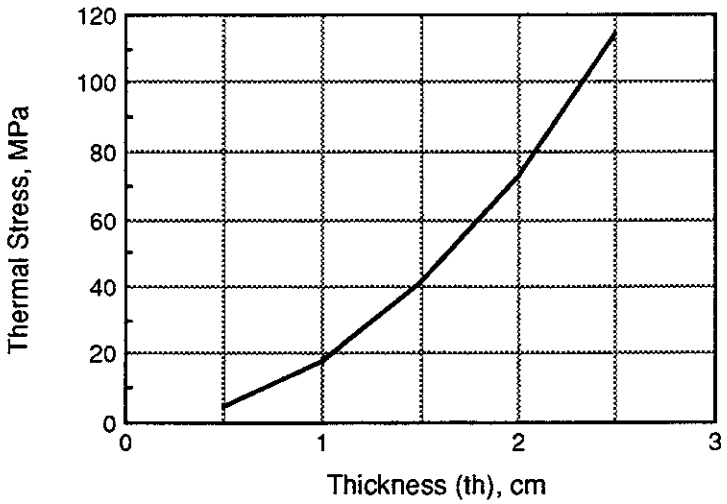

Figure 6.8.3-26. Thermal Stress in the Module Wall as a Function of the Distance Between the Coolant Channel and the Wall Edge

Use or disclosure of data
subject to title page restriction

The bending stress was estimated by considering the module side walls and front wall (see Figures 6.8.3-1 and 6.8.3-3) as a series of plates with built-in edges of length 60 cm and width, w_r, set by the pitch between successive reinforcing ribs. The rounded corners linking the front wall to the side walls were considered separately and the stresses there were estimated using the simple hoop stress equation for a thin wall vessel.

From Reference 6, the maximum bending stress, σ_M, in a plate with built-in edges is given in terms of the maximum bending moment, M, and of the plate thickness, t_p.

$$\sigma_M = 6\frac{M}{t_p^2} \qquad (6.8.3\text{-}8)$$

For a plate with a length-to-width ratio greater than 2, the following expression is given in Reference 3 for M as a function of the pressure, P, and plate width, w_r (assuming a Poisson's ratio of 0.3):

$$M = 0.0833\, P\, w_r^2 \qquad (6.8.3\text{-}9)$$

Figure 6.8.3-27 summarizes the results. It shows the maximum bending stress in the plate as a function of the plate width for different plate thicknesses. From the results for a plate width of 0.25 m and thickness of 2 cm, the stress is 116 MPa. The plate thickness, t_p, here is assumed equivalent to 2 t_h from Figure 6.8.3-25. From Figure 6.8.3-26, the corresponding thermal stress is 18 MPA, resulting in a total stress of 134 MPa, which is acceptable. Thus, the wall thicknesses proposed for the reference case are t_w = 2.5 cm and t_h = 1 cm, and the proposed distance, w_r, between successive U-shape strengthening ribs along the length of the module is 25 cm. From the analysis, this set of dimensions would result in the module withstanding the 1.5 MPa coolant pressure in case of leak or failure. Development of SiC composite with higher tensile strength would provide more flexibility in setting these module wall dimensions.

The hoop stress in the rounded corners was estimated as being low, 15 MPa for t_p = 2 cm and for a pressure and radius of curvature of 1.5 MPa and 20 cm, respectively.

The results from the analysis are encouraging. However, in order to fully understand the stress behavior of the modules, an integrated 3-D analysis for the whole module is required which would take into account the effect of the ribs, the tapering wall thickness, and of the wall curvature in locations where space must be provided for beam penetration.

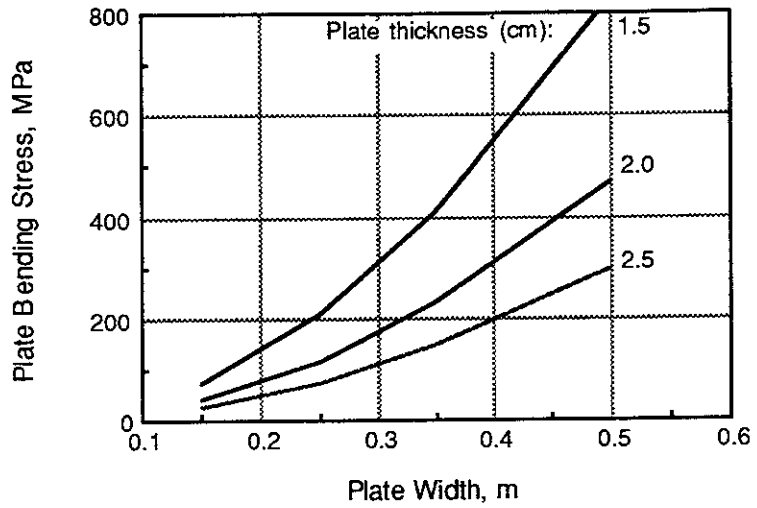

Figure 6.8.3-27. Maximum Bending Stress in a Plate with Built-In Edges as a Function of the Plate Width for Different Plate Thicknesses

6.8.3.5 Tritium Analysis - Accurate calculation of the tritium inventory in the Prometheus Li_2O blanket requires the knowledge of different properties, parameters, and conditions associated with the blanket. Unfortunately, many properties are not known for lithium ceramics. Therefore, an estimation can be made of the tritium inventory based on parametric studies and estimations of those missing data.

Calculations were made using the MISTRAL code.[7] This code includes the effects of the following transport processes:

(1) Diffusion of atomic tritium within the grain to the grain boundary.
(2) Diffusion of tritium along the grain boundary paths between adjacent grains to the solid/gas interface.
(3) Dissociative adsorption of gas species present in the pore onto the surface, "adsorption" of atomic tritium from the solid, surface recombination reactions, and associative desorption of tritium-bearing species to the pore.
(4) Diffusion of tritium-bearing species through the network of interconnected pores to the purge carrier.

In addition, a dissolution flux accounting for the return of some tritium atoms from the surface back to the bulk was also included in the code.

Assuming all other data is known and given, the tritium inventory will be mainly determined by the activation energy of solution and the heat of adsorption.[8] The activation energy of solution, E_s, is known for Li_2O. This energy was estimated by

Use or disclosure of data subject to title page restriction

Katsuta[9] as 16 kJ/mol for H_2 in Li_2O and 19 kJ/mol for D_2. For an HT mixture, Kudo and O'hira[10, 11] found E_s to be 24 - 25 kJ/mol.

The heat of adsorption, Q, is defined as

$$Q = E_{des} - E_{ads} \qquad (6.8.3\text{-}10)$$

where E_{des} is the activation energy of desorption and E_{ads} is the activation energy of adsorption.

The heat of adsorption is not known. However, although the adsorption energy is not known for most lithium ceramics, it is usually small for metals[12] and is between 3-15 kJ/mol for $LiAlO_2$, between 200 and 500°C.[13] Therefore, it can be safely assumed to be less than 25 kJ/mol. The activation energy of desorption was reported by several authors. For example, Bertone found E_{des} equal to 119 kJ/mol;[14] Miller, et al.[15] obtained a value between 125 and 140 kJ/mol from the CRITIC-I experiment; while Tanifuji [16] found E_{des} to be 148 ± 18 kJ/mol. Therefore, it is reasonable to assume the heat of adsorption in the range of 90-170 kJ/mol.

In estimating the tritium inventory, the effect of both the activation energy of solution and the heat of adsorption was examined. The effect of only these two energies was considered because the other energies are either known (such as the bulk diffusion activation energy) or do not have a significant effect on the inventory. Table 6.8.3-3 shows the input that was used in the code based on initial reactor and blanket parameters.

Table 6.8.3-3 Input Used in MISTRAL to Calculate the Blanket Tritium Inventory Results (See Figures 6.8.3-28 and 6.8.3-29)

Li_2O Theoretical Density Fraction	0.8
Li_2O Density (kg/m^3)	2.01×10^3
Helium Pressure (Pa)	2×10^5
Tritium Generation Rate (g/day)	362
Internal Surface Area of Porous Solid (m^2/kg)	50
Grain Radius (μm)	10
Maximum Temperature (°C)	800
Minimum Temperature (°C)	425
Amount of Protium in Purge (%)	0.2
Volume of Breeder Material (m^3)	92
Grain Diffusion Coefficient:	
Pre-exponential Factor (m^2/s)	6.81×10^{-7}
Activation Energy (kJ/mol)	84.8

Figure 6.8.3-28 shows the effect of the activation energy of solution on the tritium inventory at constant heat of adsorption (115 kJ/mol). The inventory decreases exponentially with increasing E_S in the range of concern (15-30 kJ/mol). This is consistent with Sievert's law which shows the solubility inventory to be proportional to $(\exp(-E_S/RT))$, where R is the universal gas constant and T is the temperature. For a given E_S, the solubility inventory would then increase exponentially with temperature, which has to be taken into account when setting the solid breeder operating temperature. Figure 6.8.3-29 shows the effect of the heat of adsorption on the tritium inventory at constant activation energy of solution (20 kJ/mol). The tritium inventory in this case has two distinct regimes. In the first region, the inventory is constant with Q. This is due to the fact that most of the inventory in this case is in the bulk, whereas Q affects mainly the surface inventory. In the second region, the surface inventory becomes dominant and, thus, the total tritium inventory increases exponentially with increasing the heat of adsorption.

From these two figures, a reasonable upper limit for the tritium inventory is 30 g, which corresponds to an activation energy of the solution of 15 kJ/mol and a heat of adsorption of 170 kJ/mol.

To reflect the latest reactor parameters, the tritium generation rate was increased to 516 g/day and the purge pressure to 1MPa and the resulting tritium inventory was still about 30 g. It should be noted, however, that these estimates do not include the effect of irradiation on the tritium transport which is not yet well characterized and still being studied. There is also a measure of uncertainty regarding the pre-exponential constants for the different surface fluxes, as reflected by the range of values obtained experimentally for the pre-exponential constant in the solubility expression for H_2 in Li_2O.

To account for unknowns, such as the irradiation effect, the proposed blanket inventory value is 100 g. This value corresponds to 0.5 wppm, which is of the same order as the results of EXOTIC 2 experiment ($\approx$ 0.1 and 1.5 wppm), CRITIC-I experiment ($\approx$0.6 wppm), and VOM 15H experiment ($\approx$0.7 wppm), which provide the only available measured inventory in irradiated Li_2O samples.[17] Note that these experiments were performed using materials with different microstructures and temperature levels, and that the Li_2O microstructure and the purge chemistry can be tailored for better tritium release.

A concern that needs to be addressed and better characterized is the effect of hydrogen in the purge on the SiC at high temperature. Reduction of the protective SiO_2 layer by hydrogen can result in formation of hydrocarbons and in loss of structural integrity of the SiC walls.

Use or disclosure of data
subject to title page restriction

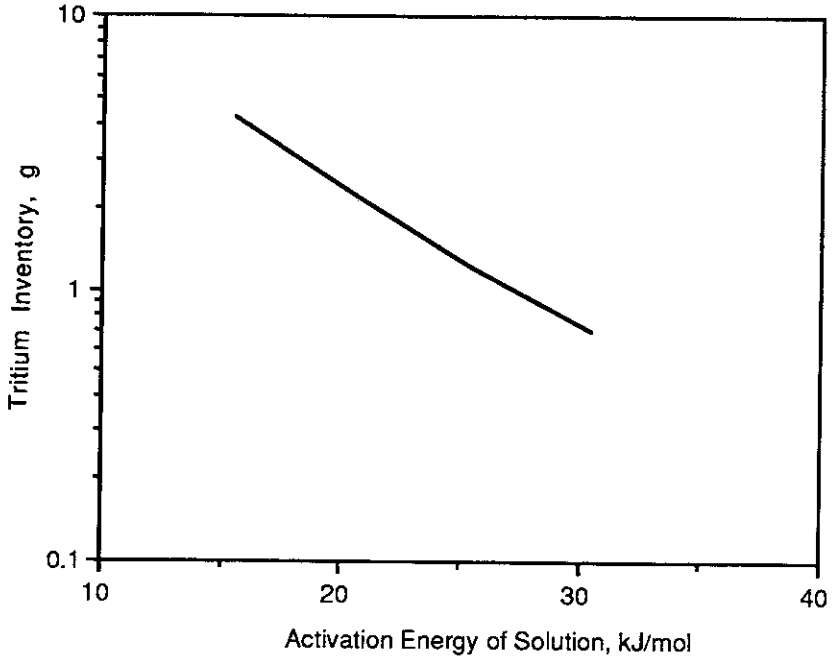

Figure 6.8.3-28. Tritium Inventory as a Function of the Activation Energy of Solution for Constant Heat of Adsorption (= 115 kJ/mol).

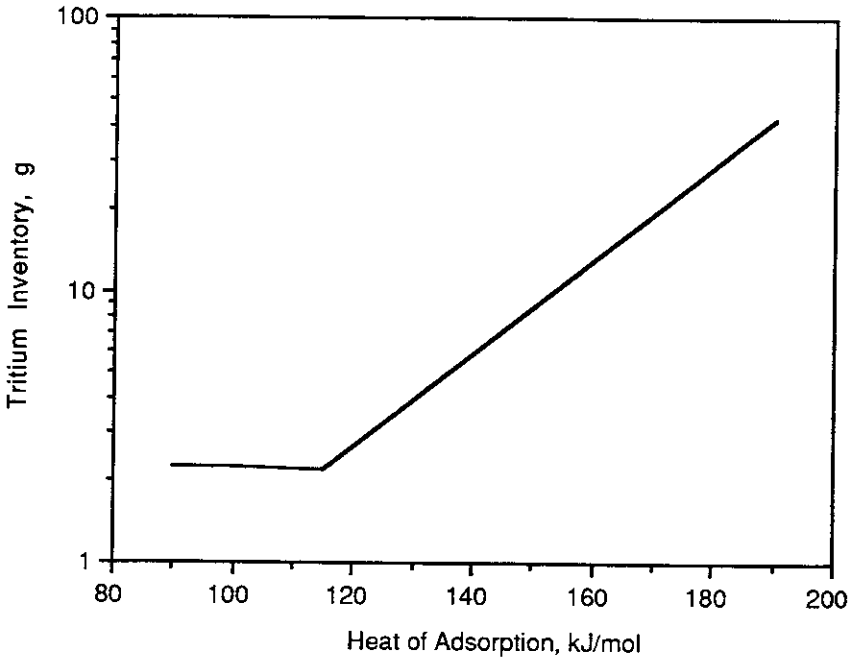

Figure 6.8.3-29 Tritium Inventory as a Function of the Heat of Adsorption for Constant Activation Energy of Solution (= 20 kJ/mol).

Use or disclosure of data
subject to title page restriction

The tritium permeation through the SiC tube sheet wall from the purge to the coolant was also estimated based on a diffusion coefficient of 3×10^{-19} m^2/s at 600°C for β-SiC.[18] The tritium permeation flux was found to be negligible.

References for 6.8.3

1. F. Najmabadi, R. W. Conn, and the ARIES Team, "The ARIES-1 Tokamak Reactor Study," 16th Symposium on Fusion Technology, London, UK, 3-7 September 1990.

2. Y. Gohar, et al., "U.S. Technical Report for the ITER Blanket/Shield - A. Blanket," ITER-TN-BL-5-0-3, Garching, Germany, Section 3, July-November 1990.

3. B. Badger, et al.,"SIRIUS-M: A Symmetric Illumination, Internally Confined Direct Drive Material Test Facility," UWFDM-711, Fusion Technology Institute, University of Wisconsin, October 1986.

4. W. W. Engle, Jr.," A User's manual for ANISN," K-1693 (1967).

5. R.E. MacFarlane, " TRANSX-CTR: A Code for Interfacing MATXS Cross-Section Libraries to Nuclear Transport Codes for Fusion Systems Analysis," LA-9863-MS, Los Alamos National Laboratory, February 1984.

6. S. Timoshenko and S. Woinowsky-Krieger, "Theory of Plates and Shells," Second Edition, McGraw-Hill, New York, p197, 1959.

7. G. Federici, A. R. Raffray, and M. A. Abdou, "MISTRAL: A Comprehensive Model for Tritium Transport in Lithium-Base Ceramics – Part I and II," Journal of Nuclear Materials, 173, p. 184–228 (1990).

8. A Badawi and A.R. Raffray, "Analysis of Surface Fluxes of Hydrogen Species in Lithium Ceramics, "UCLA-FNT-50, December 1991.

9. H. Katsuta, S. Konishi and H. Yoshida, "Solubility and Diffusivity of Hydrogen in Li_2O, "Journal of Nuclear Materials, 116, p. 244-248 (1983).

10. S. O'hira, T. Hayashi, K. Okuno and H. Kudo, "Tritium Dissolution in and Release from Li_2O, " Fusion Eng. Design, 8, p. 335-338 (1989).

Use or disclosure of data
subject to title page restriction

11. H. Kudo, K. Okuno and S. O'hira, "Tritium Release Behavior of Ceramic Breeder Candidates for Fusion Reactors," Journal of Nuclear Materials, 155-157, p. 524-528 (1988).

12. M.A. Pick and K. Sonnenberg, "A Model for Atomic Hydrogen-Metal Interactions - Application to Recycling, Recombination and Permeation," Journal of Nuclear Materials, 131, p. 208-220 (1985).

13. A.K. Fischer and C.E. Johnson, "Adsorption, Dissolution and Desorption Characteristics of $LiAlO_2$-H_2O(g) System," Semiannual Progress Report, DOE/ER-0313, p. 419-421, May 1989.

14. P.C. Bertone, "The Kinetics that govern the Release of Tritium from Neutron-Irradiated Lithium Oxide," Journal of Nuclear Materials, 151, p. 281-292 (1988).

15. J. M. Miller, R.A. Verrall, D.S. MacDonald and S.R. Bokwa, "The CRITIC-I Irradiation of Li2O - Tritium Release and Measurement," Fusion Technol., 14, p. 649-656 (1988).

16. T. Tanifuji, K. Noda, S. Nasu and K. Uchida, "Tritium Release from Neutron-Irradiated Li2O; Constant Rate Heating Measurements," Journal of Nuclear Materials, 95, p. 108-118 (1980).

17. M. C. Billone, "Modeling of Tritium Recovery from Lithium Ceramics," presented at the Second Workshop on Ceramic Breeder Interactions, Clearwater, Florida, 22-23 November 1991.

18. "Hydrogen Diffusion and Solubility in Silicon Carbide," Journal of American. Ceramic Society, p. 223, May-June 1978.

Use or disclosure of data subject to title page restriction

This page intentionally left blank.

Use or disclosure of data
subject to title page restriction

6.8.4 Primary Shield

6.8.4.1 Introduction – Two types of shielding materials have been considered for the bulk shield and the shielding of the beamlines of the Prometheus-L and -H reactor designs. The first type is a concrete-based shield consisting of 87% concrete, 8% carbon-steel, and 5% water. The other type is a composite material shield made of 20% Pb, 20% B_4C, 25% SiC, 30% water, and 5% aluminum. The motivation behind considering the second shielding type is the low-activation level attainable in this composite material after reactor shutdown as compared to the concrete-based type. Additionally, long-term activation with this composite shield is 2-3 orders of magnitude lower than with the concrete-based shield. (see Section 6.8.5.2 for more details).

To address the shielding requirements in the Prometheus design, the nuclear field attenuation characteristics of these two types of shielding materials were examined and are discussed below. Based on results from this 1-D comparative analysis, the required shield thicknesses for the bulk shield, the beamlines shield, and the reactor building wall were estimated. Some of these estimates were compared to the 3-D calculation results performed for the shielding design of the SIRIUS-M reactor.[1]

Shielding design depends largely on the criteria for personnel access to components inside and outside the reactor building. Thhree alternative design criteria wwould determine the required shield around the cavity and outside the reactor building. These are:

(a) Shield design allows for personnel access during operation. In this case, the design requirements call for reducing the biological dose rate outside the cavity and around beamlines during operation to values below 2.5 mrem/hr. This limit ensures that the reactor personnel will receive no more that 1.25 rem per quarter in restricted areas around beamline and cavity. The purpose of the reactor building in this case is merely to encompass the cavity chamber and other equipment (e.g. cranes, etc.).

(b) Shield design allows for hands-on maintenance of the cavity chamber and beamlines one day after shutdown where the dose rate should not exceed 2.5 mrem/hr.

(c) Shield design does not allow for personnel access to the interior of the reactor building.

Attenuation characteristics for the two types of shielding materials (concrete and composite) are given in Section 6.8.4.2. In the final Prometheus reactor design, the

composite shield was adopted for the bulk and beamline shielding as well as for other penetration ducts. Concrete-based material was chosen for the reactor building in both laser and heavy ion reactor designs. The personnel access criterion adopted in the design allows for hands-on maintenance 48 hours after shutdown, although the more conservative estimates given below are for the case of permitting personnel access inside the reactor building one day following shutdown. The final configuration of the integrated system, including the cavity, bulk shield, beamlines, and their associated shield for the laser reactor, can be found in Section 6.3.1. Configuration of the shielding for the beamlines and other penetrations in the heavy ion reactor design is also shown in that section and general discussions on the design are cited in Sections 2.4 and 2.5. The final thicknesses for the required shield in both designs were decided based on the analysis given here and on expert judgement.[2]

6.8.4.2 Nuclear Field Attenuation Characteristics of the Shielding Materials Considered – The 1-D calculations using the ANISN transport code were performed using a spherical model for the first wall system, blanket/reflector/plena system, vacuum vessel, and bulk shield system shown in Figures 6.8.3-4 and 6.8.3-5. The 1-D calculations for the shield assumed a preliminary shield composition of 20% B_4C, 20% Pb, 30% SiC, and 30% H_20. The final shield composition was determined to be 20% B_4C, 20% Pb, 25% SiC, 5% Al, and 30% H_2O, but the calculations were not iterated for this composition. In the two cases (concrete and composite), the bulk shield is located at a distance of 9.53 m from the cavity center and has a tentative thickness of 2.1 m. The objective of analyzing this thick shield is to examine the attenuation of the neutrons and gamma rays fluxes, the nuclear heating rates, and the biological dose rate during operation as a function of depth inside the bulk shield. Based on these attenuation profiles, the required shield thickness to meet the adopted personnel access criterion is determined for both types of shielding materials.

Figure 6.8.4-1 shows the neutron and gamma ray fluxes in the concrete shield as a function of location inside the bulk shield. The neutron and gamma fluxes at the beginning of the bulk shield is ~2.8×10^{13} n/cm^2•sec and 7×10^{12} γ/cm^2•sec, respectively, based on incident neutron source strength of 9.83×10^{20} n/sec (average neutron energy is ~12.87 MeV) corresponding to neutron power of 2027 MW (see Section 6.8.1). The first wall of the model, shown in Figures 6.8.3-4 and 6.8.3-5, is located at a distance of 510 cm from the cavity center. In the final laser reactor design, the cavity radius is 500 cm and thus a normalization factor of $(510/500)^2 \sim 1.04$ would be applied to the local values shown in Figures 6.8.4-1 and 6.8.4-2. In the heavy ion reactor design, the cavity radius is 450 cm, the neutron source strength is 8.82×10^{20} n/sec (corresponding to a neutron power of 1818 MW), and the normalization factor in this case is $(510/450)^2$ (8.82/9.83) ~ 1.15.

Use or disclosure of data
subject to title page restriction

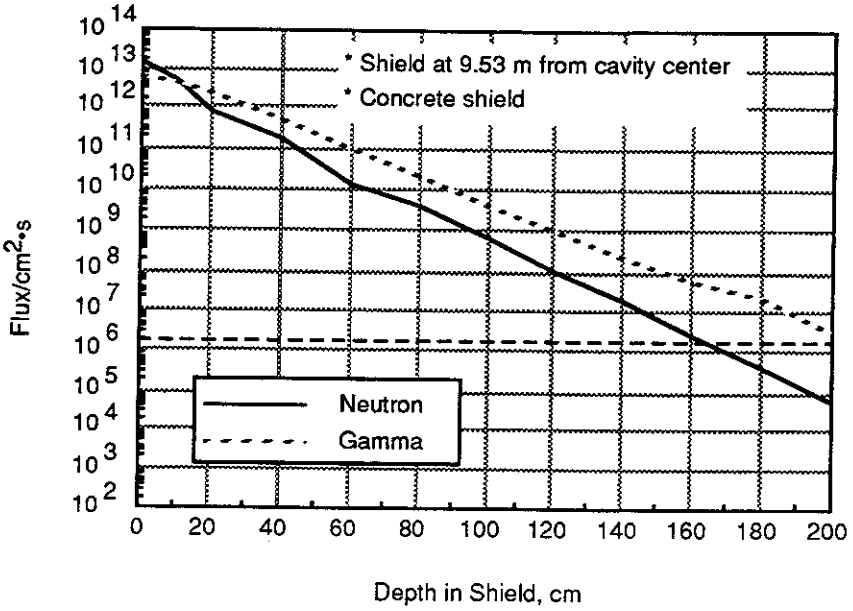

Figure 6.8.4-1 Neutrons and Gamma Ray Fluxes in the Concrete Bulk Shield as a Function of Depth Inside the Bulk Shield

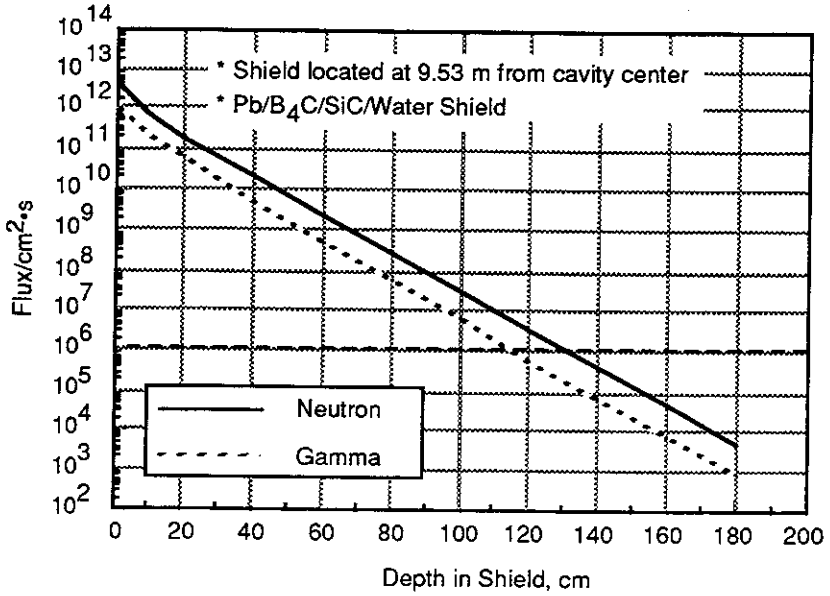

Figure 6.8.4-2. Neutron and Gamma Ray Fluxes in the Composite Bulk Shield as a Function of Depth Inside the Shield

At a shield thickness of 200 cm, the neutron and gamma fluxes drop to $3x10^4$n/cm^2•sec and $3.3x10^6$ γ/cm^2•sec, respectively. Therefore, the flux attenuation coefficient $\lambda_{con,f}$ is ~10.9 cm; i.e., an order of magnitude reduction in the neutron flux level occurs every ~25 cm. As for gamma rays, the flux attenuation factor $\lambda_{con,f}$ is ~13.7 cm, i.e., an order of magnitude reduction in the flux takes place for every 31.5 cm. It was reported in Reference 1 that the biological dose during operation in this type of shield is dominated by the gamma ray dose, and that the dose level drops by an order of magnitude for every 32 cm. Also, it was shown in Section 6.8.1 that the nuclear heating during operation in the concrete shield is attributed mainly to gamma ray heating whose profile decreases by an order of magnitude for every 33 cm (see Figure 6.8.1-5). For gamma ray-related parameters, the attenuation coefficient is ~13.7-13.9.

The criterion adopted in the case of allowing personnel access inside the reactor building one day after shutdown is to attain a neutron flux level of $2x10^6$ n/cm^2•sec at the back of the (concrete) shield. In magnetic fusion reactors, it was shown[3] that by attaining this neutron flux level during operation, the biological dose one day after shutdown from activation of the shield and outlying components is ~2.5 mrem/hr. This will allow hands-on maintenance inside the reactor building. By examining Figure 6.8.4-1, a neutron flux level of $2x10^6$ n/cm^2•sec occurs at a depth of ~1.65 m, which is an estimate for the required thickness of the bulk concrete shield. Note that the actual neutron flux at the back of a 1.65-m thick bulk shield could be less than the limit of $2x10^6$ n/cm^2•sec (means thinner shield) since the flux shown in Figure 6.8.4-1 at a depth of 1.65 m has a reflected neutron component (~20%) from the rest of the shield beyond 1.65 m. Thus,

X(bulk) = 1.65 m (concrete shield).

Figure 6.8.4-2 shows the corresponding neutron and gamma ray fluxes in the case of the composite bulk shield. The neutron and gamma fluxes at the front edge of the bulk shield are $5x10^{12}$ n/cm^2•sec and $1x10^{12}$ γ/cm^2•sec, respectively. At a depth of a 100 cm, they are ~ $5x10^7$ n/cm^2•sec and $6x10^6$ γ/cm^2•sec. The neutron flux attenuation factor $\lambda_{comp,f}$ is ~ 8.69 cm; i.e., an order of magnitude reduction in flux level occurs for every 20 cm. The gamma ray attenuation factor is ~ 8.3 cm and an order of magnitude decline in gamma flux level is achieved for every ~19 cm. This shows that the attenuation characteristics of the composite shield is better than those of concrete. Note in this case that neutron flux is always larger than gamma ray flux throughout the bulk shield, a trend that is reversed to the one found for the concrete shield . Since the gamma flux in this composite shield is about an order of magnitude less than neutron flux, the dose during operation is dominated by the contribution from the neutrons whose flux declines by an order of magnitude for every 20 cm. Thus, the dose

Use or disclosure of data
subject to title page restriction

attenuation coefficient for this type of shield was considered to be the same as the flux attenuation coefficient; i.e., $\lambda_{comp,d}$ ~ 8.69 cm.

Similar to the concrete bulk shield case, an assumption is made that by attaining a neutron flux level of $1x10^6$ n/cm^2•sec at the back of the shield during operation, the biological dose one day after shutdown would be ~2.5 mrem/hr. This assumption needs validation for these composite shield materials. The results of activation level post shutdown (see Section 6.8.5.2) indicate that this could be a valid assumption since, at shutdown, the radioactivity level in the composite shield case is an order of magnitude less than that for concrete. By adopting this design criterion and by considering the results shown in Figure 6.8.4-2, the required bulk shield thickness is ~130 cm. Thus,

X(bulk) = 1.30 m (composite shield).

References for 6.8.4

1. B. Badger, et al., "SIRIUS-M: A Symmetric Illumination, Inertially Confined Direct Drive Material Test Facility," UWFDM-711, Fusion Technology Institute, University of Wisconsin, October 1986.

2. M. Abdou, private communication, February, 1992.

3. B. Logan, et al., "MARS: Mirror Advanced Reactor Study Final Report," UCRL-53480, Lawrence Livermore National Laboratory, (1984).

This page intentionally left blank.

Use or disclosure of data
subject to title page restriction

6.8.5 Cavity Safety and Environmental Impact

6.8.5.1 Introduction – The primary goal associated with cavity safety is to design a cavity which is inherently safe. The adopted design elementsinclude: (1) selection of materials which are inherently low activation, (2) minimization of corrosion and chemical interactions, (3) promotion of tritium release, and (4) minimization and control of tritium permeation. Safety concerns include source term characterization (or activation products) and accident tolerance in the cavity. Table 6.8.5-1 lists the possible failure modes which might occur in the cavity and their associated consequences. The safety hazards posed by activation products are the potential off-site dose if those isotopes are released to the environment and the decay heat available to damage structures if cooling is inadequate.

Radioactive materials existing in the cavity are: (1) tritium; (2) activated debris from burned pellets; (3) activated structural and shielding material in the first wall, blanket, reflector, and radiation shield; and (4) activated coolant.

Tritium inventory within the blanket is estimated at less than 100 grams. Permeation of tritium from the coolant into the steam cycle is a safety concern. Helium and lead are two major heat transfer media in the reactor designs. A major portion of the thermal energy is transferred with the helium coolant which has a low solubility for tritium. Low pressure breeder gas permeation through the SiC blanket structure is very small (~40 mCi/day). Helium coolant does not significantly contribute to tritium leakage from the plant. See Section 6.7.10.2 for further details. The higher solubility of tritium in the lead coolant requires additional safeguards and permeation barriers. The lead steam generators are a double-walled heat transfer tube design with the interspace filled with sodium. Tritium will continually be extracted from the sodium to maintain a low tritium partial pressure in order to meet the plant tritium loss requirements. Section 6.7.10 discusses the heat transfer media de-tritiation analyses and design approaches.

No analysis was performed for target debris activation; however, with the exception of lead, the constituents of the target are expected to have low activation. Since Pb is already present in the coolant, the same type of radionuclides are produced.

The quantities of the different radioactive first wall, blanket, and shield materials were computed using the DKRICF code for a period of 2 and 30 years of full power operation. (Note: The design life of the first wall is anticipated to be five years and the blanket ten years.) The results of these calculations are discussed in Section 6.8.5.2. Lead presents the largest activation concern and results in a considerable inventory compared to the blanket system. Considerable emphasis was given to bismuth impurity control and removal and the safe storage of ^{210}Po from the lead coolant. All radioactive materials are present either in liquid or solid form. Their release to the

Use or disclosure of data
subject to title page restriction

environment under normal operation can be excluded. The Pb radionuclides are classified as elements somewhat volatile in accidents (ESECOM Class III).

Various first wall failure modes with possible consequences are identified and tabulated in Table 6.8.5-1. Within these failure modes, accident analyses were performed for component thermal responses following loss-of-cooling accidents, lead decay heat removal under accident conditions, and first wall behavior due to local dry spots. These analyses provide a guideline for the cavity safety design.

Table 6.8.5-1 Cavity Failure Modes and Consequences

	Failure Mode	Consequences
1.	Failure to drain Pb and to remove the decay heat	Local structure damage, replace FW segment
2.	Loss of coolant in FW with continuing pellet explosions	FW structure damage from blast, closure of interconnected porosity – replace FW segment
3.	Loss of cooling in blanket with continuing pellet explosions	Blanket module temperatures build up, leading to structural failure and/or breeder sintering (causes increased tritium inventory or necessitates blanket replacement)
4.	Loss of flow (pump failure) in FW with pellet explosions	FW overheating and mechanical damage
5.	FW panel local dry spot	Possible FW structure damage, closure of interconnected porosity
6.	FW fatigue due to blast effects	FW panel mechanical failure or damage
7.	Blanket cooling tube rupture (5 MPa design)	Module overpressure, module failure, cascade failures, purge system overpressure, purge system rupture, and tritium release to reactor building
8.	Purge line rupture	Tritium release to reactor building
9.	Pb coolant manifold or pipe rupture	Radioactive leak of Pb to reactor building
10.	He coolant manifold or pipe rupture	Reactor building overpressure, some tritium release

6.8.5.2 Radioactivity in the Cavity – Activation analysis has been performed for the Prometheus IFE first wall, blanket, shield, and cover gas environment as defined in Figure 6.8.5-1. The main constituents of the first wall are the SiC structure and the lead coolant. The blanket uses Li_2O breeder, which has low activation characteristics, with SiC structure and helium coolant. Behind the blanket system, there is a vacuum vessel which is made of 100% ferritic steel and 210 cm of biological shield. (Final

Use or disclosure of data subject to title page restriction

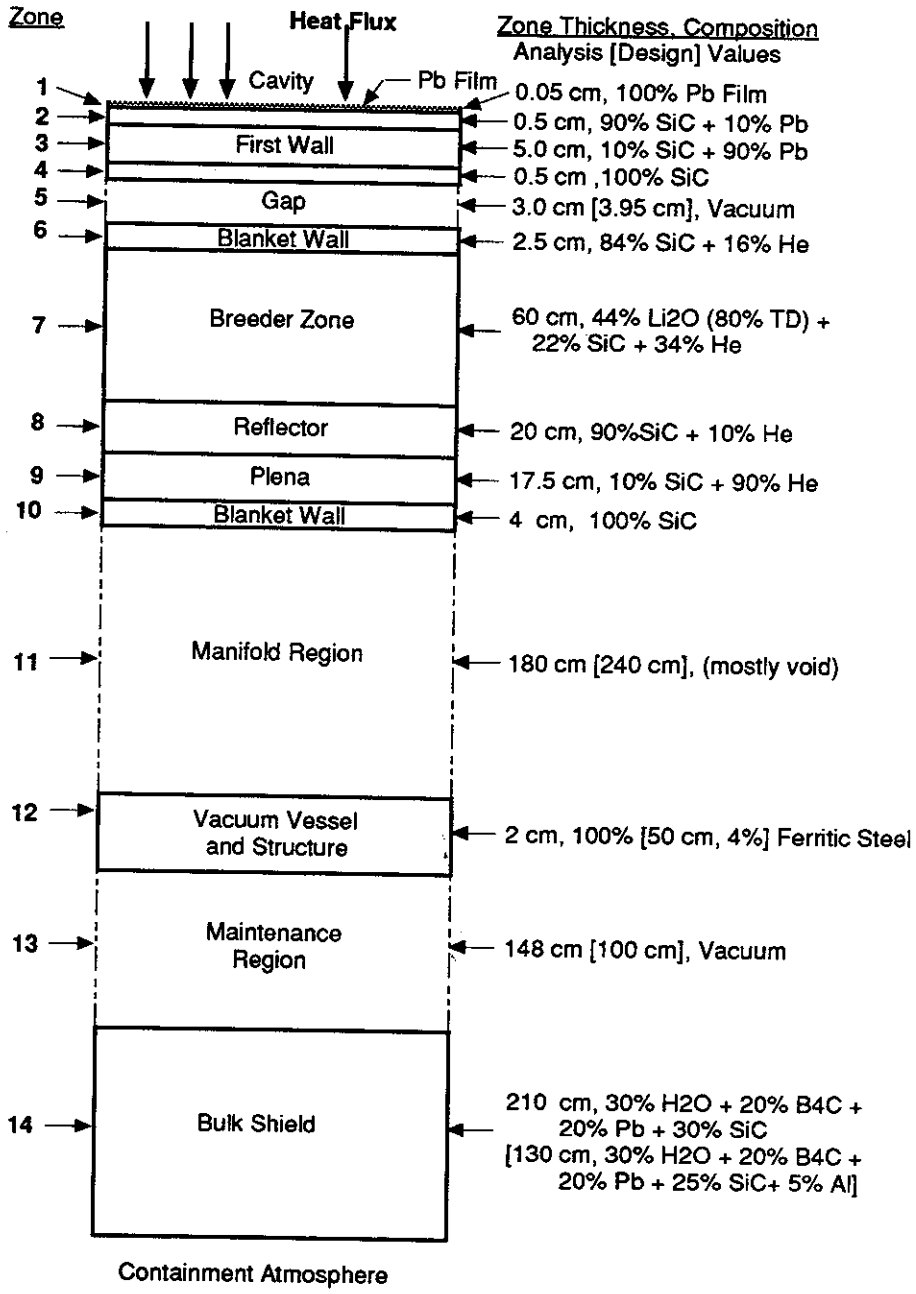

Figure 6.8.5-1 Cavity Cross-Section and Zone Designation

shield thickness is 130 cm.) The shield consists of Al structure, H_2O coolant, and B_4C, Pb, and SiC absorbers. Finally, ordinary air at STP is assumed to surround the cavity. Descriptions of the geometric configuration, dimensions and material volume fraction of the aforementioned components can be found in previous sections.

Calculational Procedure – Figure 6.8.5-2 shows the calculational procedures as well as the codes and libraries used to calculate the radioactivity. A neutron transport calculation was carried out first using ANISN[1] to determine the neutron flux and energy spectrum at various locations in the cavity. During ANISN calculations, a P_3S_8 approximation and the neutron/photon cross section data derived from ENDF/B-V[2] have been employed. The problem has been modeled in spherical geometry with materials and dimensions consistent with a cut through the midplane of the cavity. A point source was used at the center of the 510-cm radius cavity. The SIRIUS-M[3] target neutron spectrum was used to represent the source spectrum. The source neutron strength has been obtained as 9.636×10^{20} n/sec by considering the average neutron energy (12.87 MeV) of the SIRIUS-M source spectrum and the neutron power (1987 MW) of the Prometheus design.

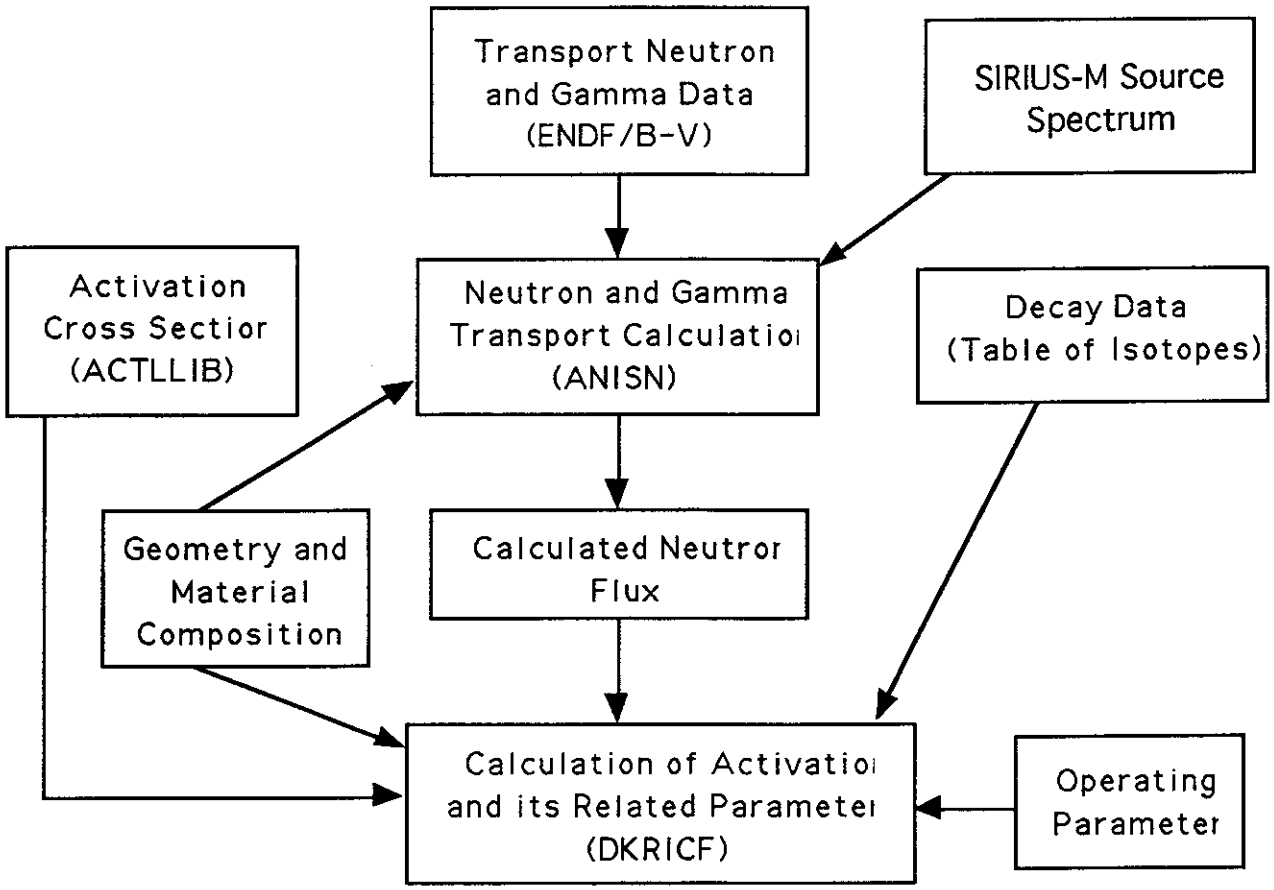

Figure 6.8.5-2 Radioactivity Calculational Procedure

The neutron flux obtained from the neutron transport calculation was used as input to the activation calculation, which used the DKRICF[4] code. For the results reported here, the machine was assumed to operate for 40 years with 75% availability, which corresponds to approximately 30 years of continuous operation at full power. The

Use or disclosure of data subject to title page restriction

blanket and shield were assumed to operate through the entire 30 full-power years (FPY); the first wall system is assumed to be replaced after 2 FPY. Note that a first wall lifetime of 5 FPY and a blanket lifetime of 10 FPY were chosen for the final design point.

The exact time-dependent operation scheme is not considered in this study. It has been reported[5] that even though the employment of continuous operation scheme underestimates the short-term radioactivity production when compared to the actual pulse-shaped operation scheme, the former scheme produces the same amount of long-term (less than one week after shutdown) radioactivity as the latter scheme does. Therefore, the use of continuous operation should not affect the long-term radioactivity calculations in this study.

Results and Discussion

a. Radioactivity - Table 6.8.5-2 summarizes the calculated results as a function of time after shutdown. Table 6.8.5-3 shows the important reaction products and their originating reactions. Figures 6.8.5-3 through 6.8.5-5 are the graphical form of the results presented in Table 6.8.5-2. In the following, specific quantities given for "activation level" refer to specific radioactivity, i.e., radioactivity per unit volume.

In Zone 1, which is 100% Pb film, the activation level at short times after shutdown (0 ~ 1 week) is dominantly governed by the Pb^{203} (2.17d, $Pb^{204}(n,2n)$) and Pb^{209} (3.25h, $Pb^{208}(n,\gamma)$). After that, Tl^{204} (3.78y, $Pb^{204}(n,p)$) takes over the leading role until about 10 years after shutdown. Then, Pb^{205}(1.9×10^{7}y, $Pb^{204}(n,\gamma)$ or $Pb^{206}(n,2n)$) has the responsibility for the very long-term radioactivity level in this zone. The same behavior of the activation level is found in Zone 3, which consists of 10% SiC and 90% Pb, except Al^{28} (2.24 min., $Si^{28}(n,p)$) is one of the major contributors at very short times after shutdown. In Zones 4, 6, 8, 9, and 10 where only SiC is the main material, the activation level in the time span of 0 to ~5 minutes after shutdown is mainly due to Al^{28}.

After most of the Al^{28} decays away, Si^{31} (2.62h, $Si^{30}(n,\gamma)$) becomes the leading contributor between 1 hour ~ 1 day after shutdown. Then, beyond one week after shutdown, Be^{10} (1.6×10^{6}y, $C^{13}(n,\alpha)$) and C^{14} (5.73×10^{3}y, $C^{13}(n,\gamma)$)

Table 6.8.5-2 Zonal Specific Radioactivity (Ci/cm^3) as a Function of Post Shutdown Times After 30 Years Full Operation. Also shown are the Dominating Isotopes and Their Contributions at Each Time. (Except First Wall System Which Is Assumed to Operate for Two Years)

Note: Final Design Determined a Wall Life of 5 Years and a Blanket Life of 10 Years

Post shutdown times	Zone number 1(*)	2(*)	3(*)	4(*)	6	7(+)
0	1.281+1(**) Pb203:59% Pb209:40%	1.093+2 Al28:91%	1.940+1 Al28:37% Pb203:27% Pb209:23%	7.450+1 Al28:93%	5.383+1 Al28:93%	4.791 Al28:77% N16:12%
1 min	1.278+1 Pb203:59% Pb209:40%	7.967+1 Al28:92%	1.676+1 Al28:39% Pb203:31% Pb209:26%	5.429+1 Al28:93%	3.923+1 Al28:93%	2.905 Al28:93%
1 hour	1.165+1 Pb203:64% Pb209:36%	1.305 Pb203:56% Pb209:32%	8.842 Pb203:59% Pb209:41%	1.442-1 Si31:91%	1.014-1 Si31:91%	8.881-3 Si31:93%
1 day	5.560 Pb203: 99%	5.458-1 Pb203:99%	3.884 Pb203:99%	3.001-4 Si31:100%	2.139-4 Si31:99%	3.706-5 Si31:51% C14:49%(@)
1 week	8.383-1 Pb203:96%	8.225-2 Pb203:96%	5.846-1 Pb203:96%	2.846-7 Be10:52% C14:48%	3.105-6 Be10:53% C14:47%	1.829-5 C14:99%(@)
1 month	2.398-2 Hg203:81% Tl204:17%	2.348-3 Hg203:81% Tl204:17%	1.647-2 Hg203:81% Tl204:17%	2.846-7 Be10:52% C14:48%	3.105-6 Be10:53% C14:47%	1.829-5 C14:99%(@)
1 year	3.541-3 Tl204:96%	3.473-4 Tl204:96%	2.437-3 Tl204:96%	2.846-7 Be10:52% C14:48%	3.105-6 Be10:52% C14:48%	1.829-5 C14:99%(@)
5 years	1.642-3 Tl204:99%	1.614-4 Tl204:99%	1.132-3 Tl204:99%	2.846-7 Be10:52% C14:48%	3.105-6 Be10:53% C14:47%	1.829-5 C14:99%(@)
10 years	6.632-4 Tl204:98%	6.560-5 Tl204:97%	4.567-4 Tl204:98%	2.846-7 Be10:52% C14:48%	3.105-6 Be10:53% C14:47%	1.829-5 C14:99%(@)
100 years	1.320-5 Pb205:100%	1.653-6 Pb205:78% Be10:13% C14:9%	9.224-6 Pb205:99%	2.827-7 Be10:52% C14:42%	3.081-6 Be10:53% C14:47%	1.807-5 C14:99%(@)
1,000 years	1.320-5 Pb205:100%	1.640-6 Pb205:79% Be10:13% C14:8%	9.224-6 Pb205:99%	2.687-7 Be10:55% C14:45%	2.940-6 Be10:56% C14:44%	1.620-5 C14:99%(@)
10,000 years	1.320-5 Pb205:100%	1.543-6 Pb205:84% Be10:13%	9.224-6 Pb205:99%	1.878-7 Be10:78% C14:22%	2.070-6 Be10:79% C14:21%	5.531-6 C14:98%(@)

(*) Two years of operation assumed for first wall system

(**) Read as 1.218 x 10^1

(+) Excluding tritium activation

(@) ^{14}C values in Zone 7 were obtained using the DKRICF cross-section library. Due to an error found in this library, the actual values are expected to be much lower (see text).

Table 6.8.5-2 Zonal Specific Radioactivity (Ci/cm^3) as a Function of Post Shutdown Times After 30 Years Full Operation. (Continued)

Post shutdown times	Zone number 8	9	10	12	14	15
0	9.187-1 Al28:92%	3.376-2 Al28:90%	2.479-1 Al28:90%	8.308-1 W187:44% Cr51:8% Fe55:27%	1.186-3 Al28:62% T:15% Li8:8%	8.270-17 Cl38:27% S37:25% S35:24% C14:17%
1 min	6.766-1 Al28:92%	2.504-2 Al28:89%	1.885-1 Al28:89%	8.283-1 W187:44% Cr51:8% Fe55:27%	8.323-4 Al28:65% T:21%	7.962-17 Cl38:27% S37:23% S35:25% C14:17%
1 hour	1.244-2 Si31:99%	9.344-4 Si31:99%	6.852-3 Si31:99%	7.840-1 W187:45% Cr51:8% Fe55:29%	2.453-4 T:72% Pb209:17%	4.664-17 S35:42% C14:29% Cl38:16%
1 day	2.821-5 Si31:99%	2.131-6 Si31:99%	1.562-5 Si31:99%	5.628-1 W187:32% Cr51:11% Fe55:40%	1.938-4 T:91%	3.812-17 S35:52% C14:36%
1 week	1.321-7 C14:76% Be10:24%	8.933-9 C14:87% Be10:13%	6.527-8 C14:87% Be10:13%	3.354-1 Fe55:65% Cr51:16%	1.791-4 T:99%	3.697-17 S35:51% C14:37%
1 month	1.321-7 C14:76% Be10:24%	8.933-9 C14:87% Be10:13%	6.527-8 C14:87% Be10:13%	3.003-1 Fe55:77% Cr51:10% Mn54:9%	1.760-4 T:99%	3.316-17 S35:47% C14:41%
1 year	1.319-7 C14:77% Be10:23%	8.933-9 C14:87% Be10:13%	6.527-8 C14:87% Be10:13%	1.883-1 Fe55:92%	1.670-4 T:99%	1.741-17 C14:79% Ar39:15%
5 years	1.319-7 C14:77% Be10:23%	8.926-9 C14:88% Be10:12%	6.502-8 C14:87% Be10:13%	6.277-2 Fe55:99%	1.333-4 T:99%	1.627-17 C14:84% Ar39:15%
10 years	1.319-7 C14:77% Be10:23%	8.926-9 C14:87% Be10:13%	6.502-8 C14:87% Be10:13%	1.729-2 Fe55:99%	1.005-4 T:99%	1.622-17 C14:85% Ar39:15%
100 years	1.308-7 C14:76% Be10:24%	8.840-9 C14:87% Be10:13%	6.450-8 C14:87% Be10:13%	3.243-4 Nb93m:70% Mo93:24%	6.343-7 T:99%	1.557-17 C14:87% Ar39:13%
1,000 years	1.205-7 C14:74% Be10:26%	8.046-9 C14:86% Be10:14%	5.882-8 C14:86% Be10:14%	2.745-4 Nb93m:70% Mo93:23%	3.711-9 C14:60% Be10:23% Pb205:17%	1.238-17 C14:99%
10,000 years	6.118-8 Be10:51% C14:49%	3.443-9 C14:68% Be10:32%	2.518-8 C14:68% Be10:32%	5.809-5 Nb93:55% Mo93:23% Nb94:19%	2.227-9 Be10:39% C14:33% Pb205:28%	4.103-18 C14:100%

Table 6.8.5-3 Reaction Products Resulting from the Neutron Irradiation of Reactor Materials

Product	Half-Life	Originating Reaction
T	12.3 y	$B^{10}(n,2\alpha)$
Be^{10}	1.6×10^{6} y	$C^{13}(n,\alpha)$
C^{14}	5.73×10^{3} y	$C^{13}(n,\gamma)$ $N^{14}(n,p)$, $O^{17}(n,\alpha)$
N^{16}	7.13 sec	$O^{16}(n,p)$
Al^{28}	2.24 min	$Al^{27}(n,\gamma)$ $Si^{28}(n,p)$, $Si^{29}(n,np/d)$
Si^{31}	2.62 h	$Si^{30}(n,\gamma)$
S^{35}	87.5 d	$Ar^{38}(n,\alpha)$
S^{37}	5.1 min	$Ar^{40}(n,\alpha)$
Cl^{38}	55.6 m	$Ar^{38}(n,p)$
Ar^{39}	269 y	$Ar^{38}(n,\gamma)$, $Ar^{40}(n,2n)$
Mn^{54}	312.2 d	$Fe^{54}(n,p)$, $Fe^{56}(n,t)$
Fe^{55}	2.73 y	$Fe^{54}(n,\gamma)$, $Fe^{56}(n,2n)$
Nb^{93m}	13.6 y	$Nb^{93}(n,\gamma)^{*}$ $Mo^{92}(n,\gamma)Mo^{93}\rightarrow Nb^{93m}$ $Mo^{94}(n,2n)Mo^{93}\rightarrow Nb^{93m}$ $Mo^{94}(n,2n)^{*}Mo^{93m}\rightarrow Mo^{93}\rightarrow Nb^{93m}$ $Mo^{95}(n,3n)Mo^{93}\rightarrow Nb^{93m}$
Nb^{94}	2.0×10^{4} y	$Nb^{93}(n,\gamma)$ $Nb^{93}(n,\gamma)^{*}Nb^{94m}\rightarrow Nb^{94}$ $Mo^{94}(n,p)$, $Mo^{95}(n,np/d)$, $Mo^{96}(n,t)$
Mo^{93}	3.5×10^{3} y	$Mo^{92}(n,\gamma)$, $Mo^{94}(n,2n)$ $Mo^{94}(n,2n)Mo^{93m}\rightarrow Mo^{93}$
W^{187}	23.9 h	$W^{186}(n,\gamma)$
Hg^{203}	46.6 d	$Pb^{206}(n,\alpha)$, $Pb^{207}(n,n\alpha)$
Tl^{204}	3.78 y	$Pb^{204}(n,p)$, $Pb^{206}(n,t)$
Pb^{203}	2.17 d	$Pb^{204}(n,2n)$
Pb^{205}	1.9×10^{7} y	$Pb^{204}(n,\gamma)$, $Pb^{206}(n,2n)$
Pb^{209}	3.25 h	$Pb^{208}(n,\gamma)$, $Bi^{209}(n,p)$

Use or disclosure of data subject to title page restriction

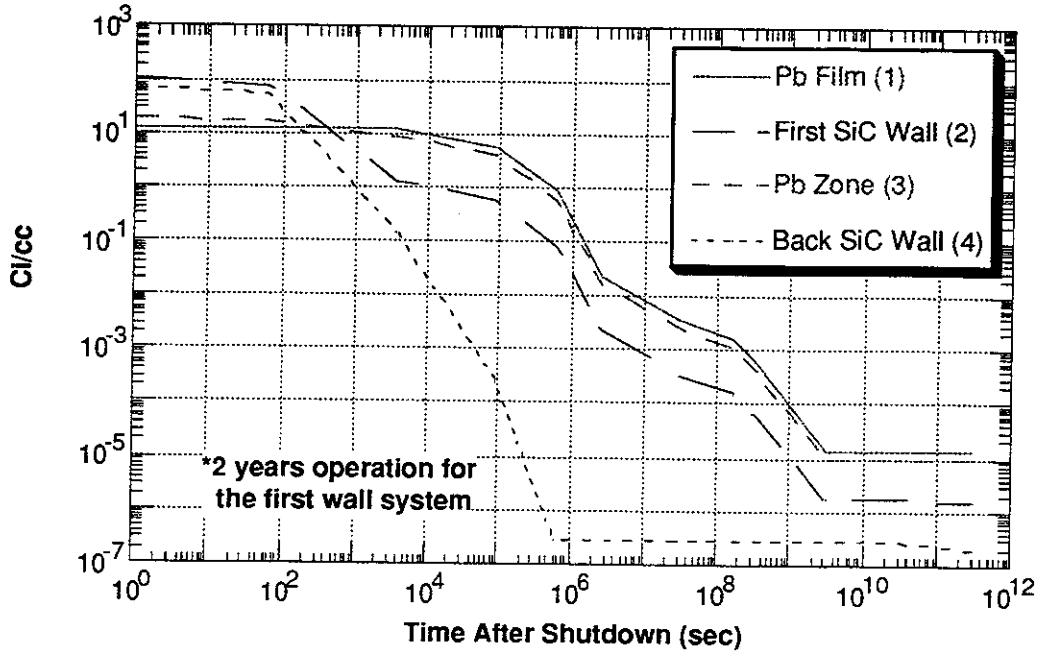

Figure 6.8.5-3 Specific Radioactivity in the First Wall System

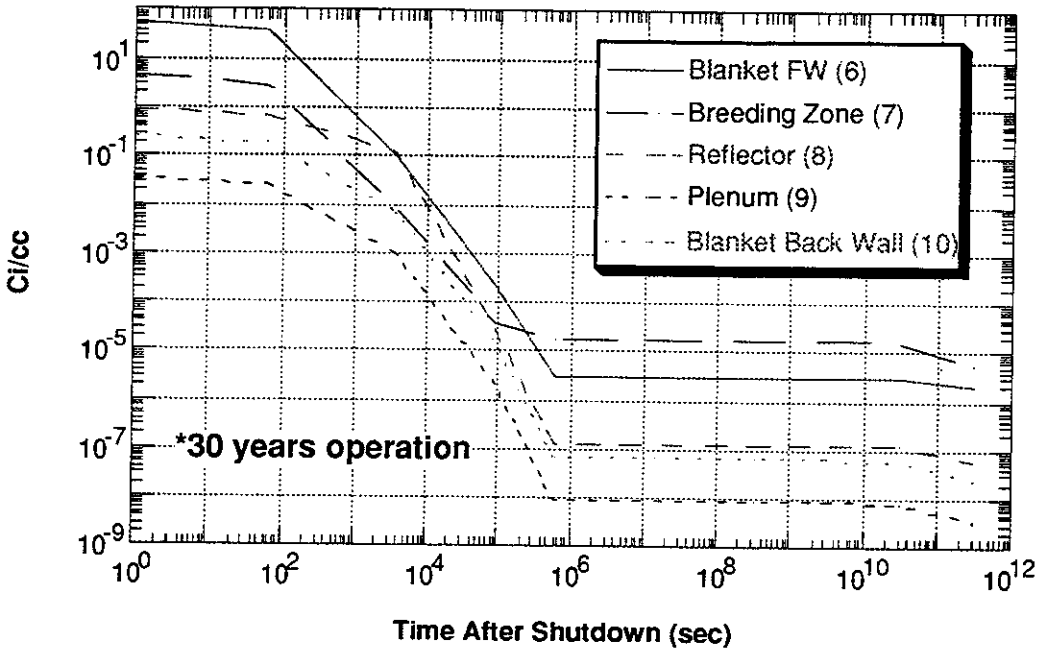

Figure 6.8.5-4 Specific Radioactivity in the Blanket and Reflector

Use or disclosure of data
subject to title page restriction

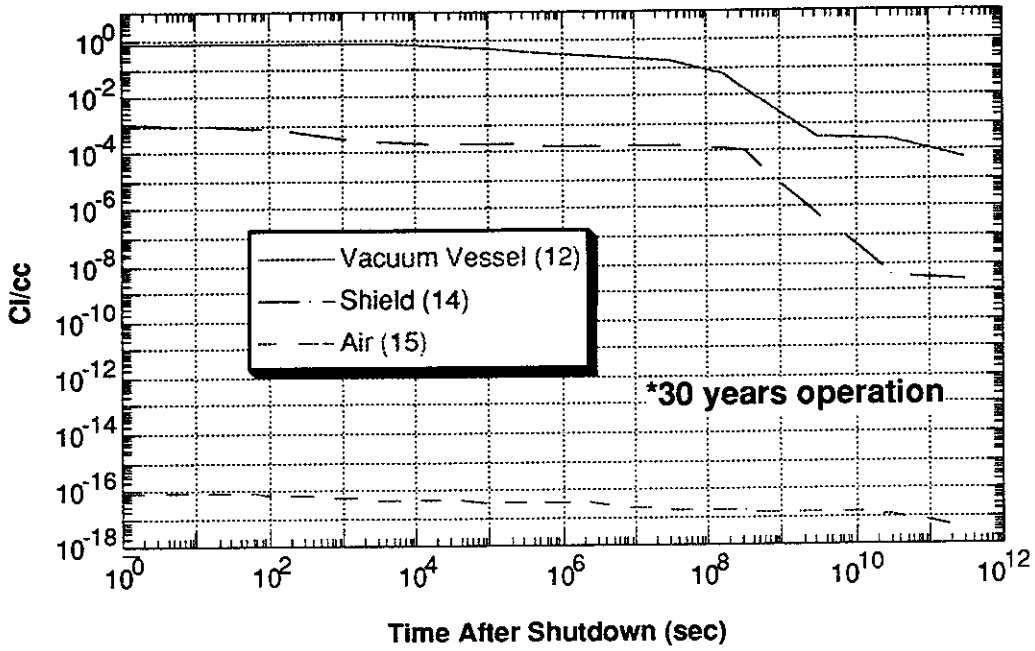

Figure 6.8.5-5 Specific Radioactivity in the Vacuum Vessel, Shield, and Surrounding Air

are responsible for the activation levels in these zones. Zone 2 (90% SiC and 10% Pb) has characteristics between the pure lead and pure SiC zones. Refer to Table 6.8.5-2 for the specific information on this zone.

Activation levels in Zone 7, which is the breeding zone, come mostly from the SiC structure and are governed primary by Al^{28} for the short-term and C^{14} for the long- and very long-term after shutdown radioactivity. Tritium activation was not included in this zone since most of tritium will be extracted and processed separately for future use. Note that C^{14} can be produced by two reaction channels in this zone — $C^{13}(n,\gamma)$ and $O^{17}(n,\alpha)$.

In the process of performing these calculations, it was discovered that the cross section library of DKRICF contains data for the $^{17}O(n,x)$ cross section which is highly suspect. The calculation was performed using the more plausible data from THIDA-2,[6] and the resulting zone-averaged ^{14}C radioactivity level in the breeding zone (Zone 7) is shown in Table 6.8.5-4. The long-term radioactivity is reduced by two orders of magnitude as compared with Table 6.8.5-2, easily meeting Class C waste disposal limits.

The activation characteristic of the vacuum vessel zone, which is made of ferritic steel, is more complex than the other zones because there are larger

Use or disclosure of data subject to title page restriction

Table 6.8.5-4 Zone-Averaged ^{14}C Radioactivity Level in Breeding Zone (Zone 7) After 30 Years, Using the THIDA-2 Cross Section Library

Time (Ci/cc)	Radioactivity from SiC (Ci/cc)	Radioactivity from Li_2O (Ci/cc)	Total
0	5.90-9 (a)	1.04-7	1.09-7
1 m	"	"	"
1 h	"	"	"
1 d	"	"	"
1 w	"	"	"
1 mo	"	"	"
1 yr	5.00-9	1.04-7	1.09-7
5 yr	"	"	"
10 yr	"	"	"
100 yr	4.80-9	1.03-7	1.08-7
1,000 yr	4.36-9	9.23-8	9.67-8
10,000 yr	1.48-9	3.11-8	3.26-8

(a) Read as 5.90×10^{-9}

numbers of isotopes involved. Briefly, W^{187} (23.9h, $W^{186}(n,\gamma)$), Fe^{55} (2.73y, $Fe^{56}(n,2n)$), and Nb^{93m} (13.6y, $Nb^{93}(n,n')^*$) are the important contributors for the short-, long-, and very long-term after shutdown radioactivity, respectively.

In the shield zone (Zone 14), which is composed of $B_4C+H_2O+Pb+SiC$, tritium is the most dominating radionuclide during 1 hour to 100 years after shutdown. Tritium is produced via $B^{10}(n,2a)$ reaction in this zone. The air activation (Zone 15), which is assumed to surround the reactor cavity, is also estimated. At shutdown, the activation of air is lower than that of the shield by 14 orders of magnitude. However, the air activation does not decay as fast as the other zones do, since C^{14} ($T_{1/2}$ = 5730 years) is the major radionuclide. During 10,000 years after shutdown, the air activation decays to only 5% of the activation level at shutdown.

Figure 6.8.5-6 compares the integrated radioactivity (in Curies) in the first wall, blanket, vacuum vessel, and shield regions. The following observations are made on the results in Figure 6.8.5-6:

(1) The radioactivity inventory of the total cavity at shutdown is about 2.5×10^9 Curies, which can be translated into ~0.9 Ci/W of thermal power. This value is comparable to that in other IFE design studies such as HIBALL[7] or in typical MCF designs such as ITER.[8]

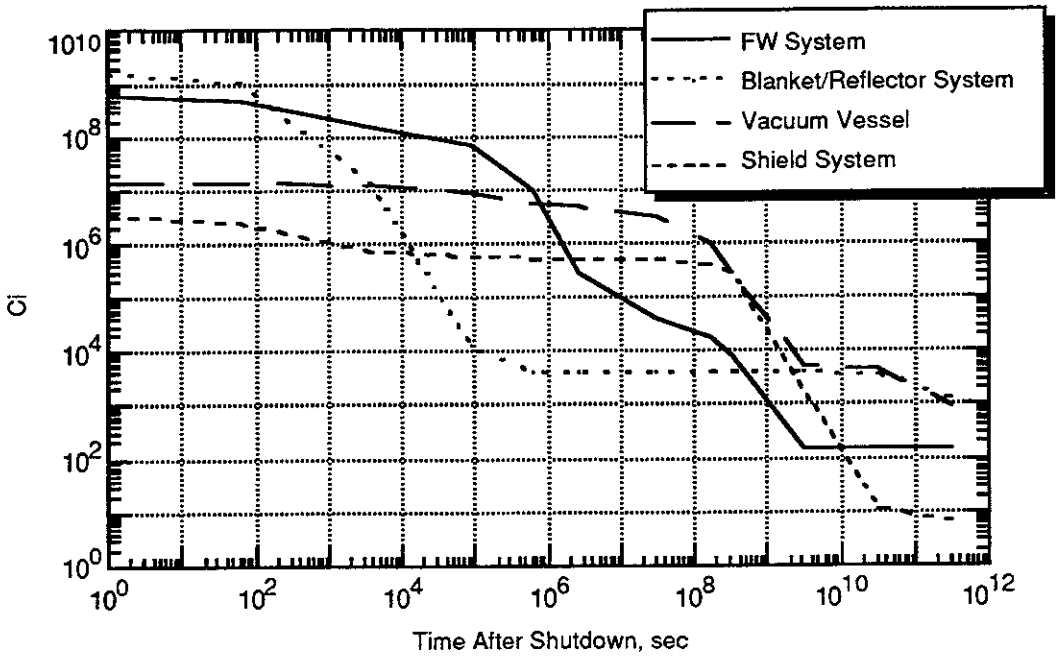

Figure 6.8.5-6. Integrated Radioactivity in Each Component as a Function of Time After Shutdown

(2) The blanket/reflector system has the highest radioactive inventory for both very short-term (less than a few minutes) and very long-term (greater than 100 years) after shutdown. The short term activity is mainly due to Al^{28} and the long-term is due to C^{14} and Be^{10}.

(3) The activation level in the first wall protection system does not decay as quickly as the blanket system does since it contains the Pb. In the first wall system, the long-term activities are mainly due to the reaction products from Pb.

(4) Even though it has the smallest volume of all systems, the vacuum vessel has the largest activation inventory because of the use of ferritic steel which results in much higher long-term radioactivity than that from the SiC/SiC composite used as the structural material in the other zones.

Also, the radioactivity inventory comparison study between our shield and a conventional concrete shield, which is made of 87% concrete + 8% ferritic steel + 5% H_2O, has been performed and the results are shown in Figure 6.8.5-7. As shown, the activation level of the Prometheus shield is always less than that of the concrete shield by one to three orders of magnitude. The use of ferritic steel could result in higher activation in the conventional concrete shield. The

Use or disclosure of data
subject to title page restriction

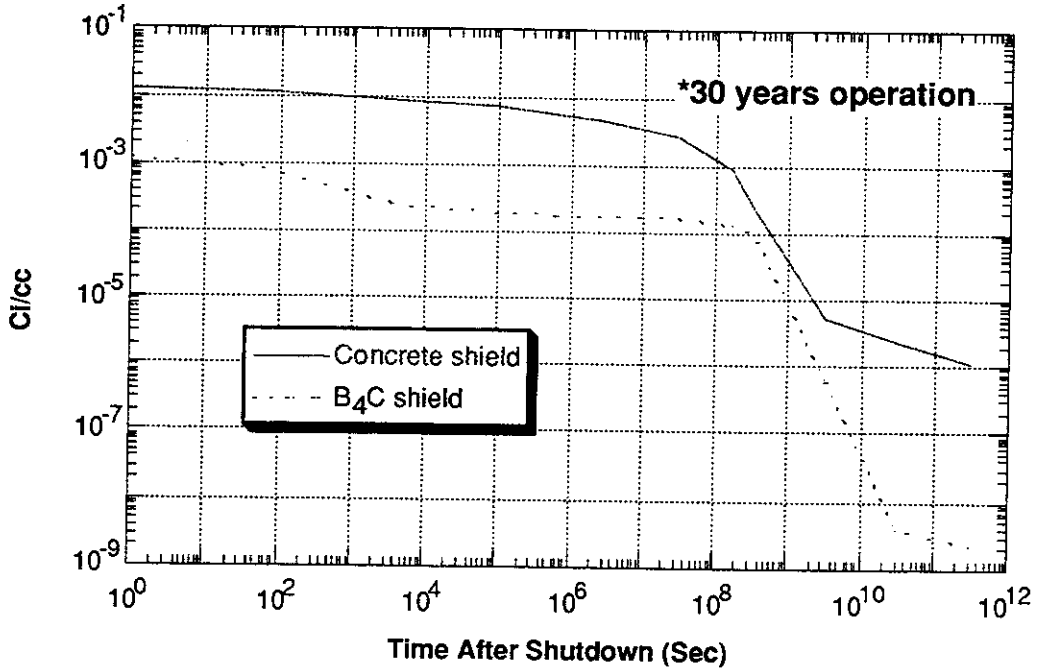

Figure 6.8.5-7. Comparison of Activation Levels Between Prometheus and Conventional Concrete Shield

use of B_4C gives lower activation in our shield design, since boron is a very strong neutron absorber so that the average population of low-energy neutrons in B_4C shield will be less than that in a concrete shield. The neutron and the photon fluxes during operation right behind the two different shields are displayed in Figures 6.8.5-8 and 6.8.5-9, respectively. It is apparent that the B_4C shield blocks or absorbs the large number of lower energy neutrons. The photon flux is also lower by about six orders of magnitude in the B_4C shield. Accordingly, the dose rate behind the B_4C shield will be much less than that behind the conventional concrete shield during reactor operation.

It has to be noted at this point that, by adopting the spherical geometry modeling, the results reported in this paper are conservative. In other words, if we consider the actual cylindrical modeling, the average activation level will be less than the results given here. This is because we have a point neutron source at the center of the cavity so that the neutron flux at position B (Figure 6.8.5-10) will be less than that at position A by roughly a factor of R_A^2/R_B^2. The average flux incident on the first wall can be obtained as:

[Text Continues on Page 6.8.5-15]

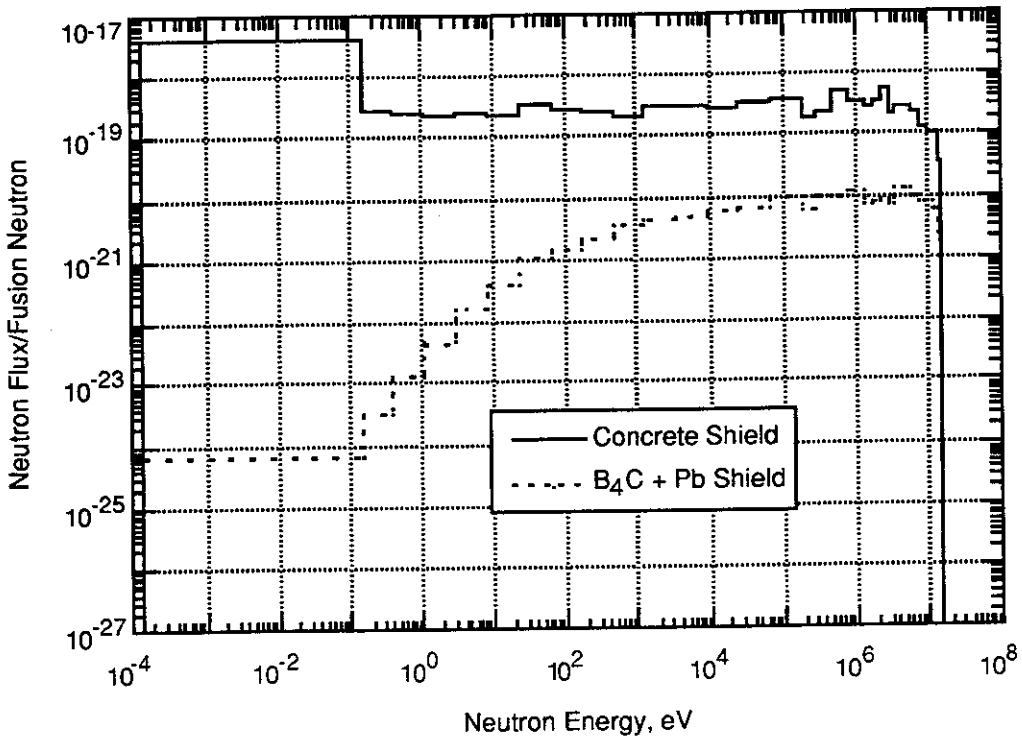

Figure 6.8.5-8. Neutron Flux Comparison Between Prometheus and Conventional Concrete Shield

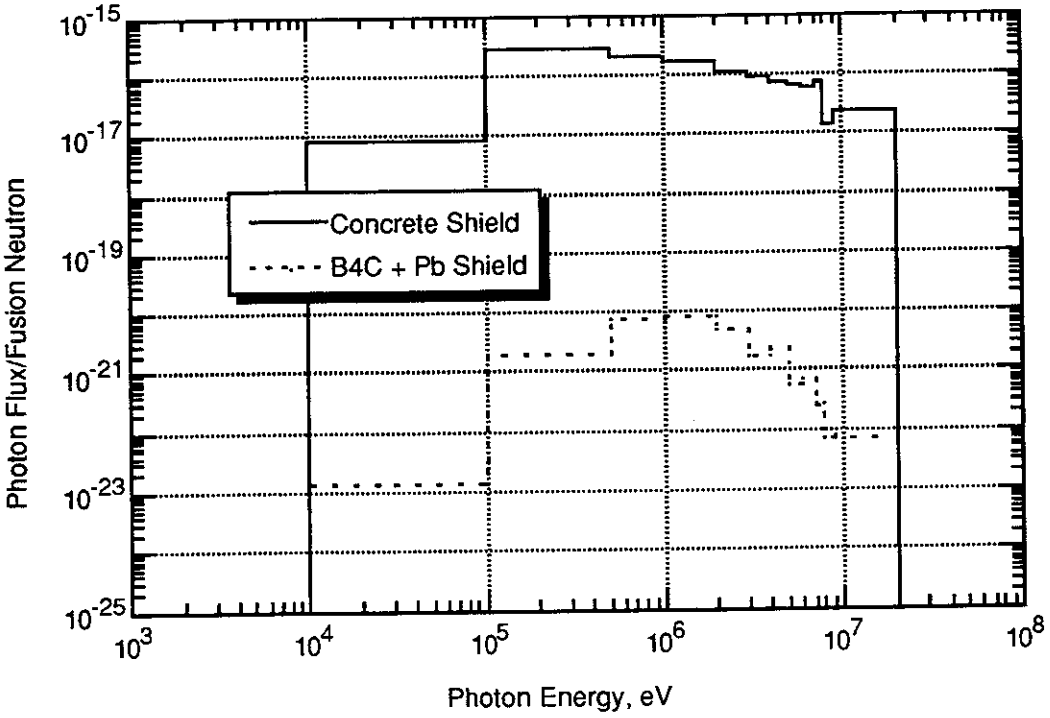

Figure 6.8.5-9. Photon Flux Comparison Between Prometheus and Conventional Concrete Shield

Use or disclosure of data subject to title page restriction

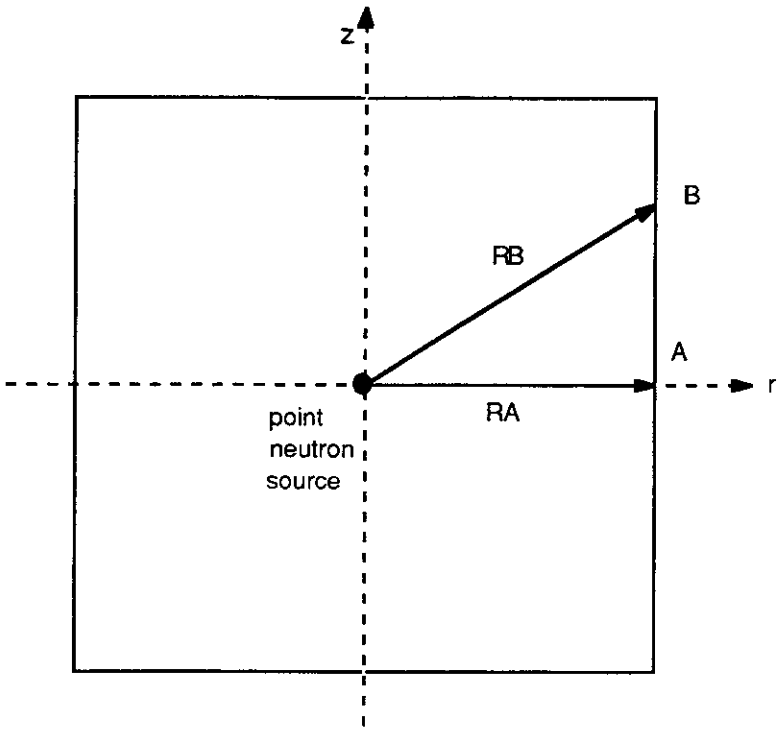

Figure 6.8.5-10. Cylindrical Modeling of the Cavity

[Text Continues from Page 6.8.5-13]

$$\phi_B = \frac{\phi_A}{\left[1+\left(\frac{z}{R}\right)^2\right]}$$

$$<\phi> = \phi_A \frac{\int_0^H \frac{dz}{1+(z/R)^2}}{\int_0^H dz}$$

$$= \phi_A \frac{R}{H}\tan^{-1}\left(\frac{H}{R}\right) \qquad (6.8.5.2\text{-}1)$$

In the above equation, ϕ_A is the flux at z=0 and H is the half-height of the cylinder. Therefore, if one is to be more accurate, one has to replace the flux term with the Eq. (6.8.5.2-1) in all the balance equations. As an example, let us consider the most common and simplest reaction/decay chain: A(n,x)B $\rightarrow$ C. Now we have a following set of equations.

$$\frac{dN_A}{dt} = -\sigma\phi N_A$$

Use or disclosure of data
subject to title page restriction

$$\frac{dN_B}{dt} = \sigma\phi N_A - \lambda N_B$$
$$\frac{dN_C}{dt} = \lambda N_B$$

Then, without the average flux consideration, we have:

$$N_B(t) = \frac{\sigma\phi_A N_{A0}}{1-\sigma\phi_A}\left(e^{-\sigma\phi_A t} - e^{-\lambda t}\right).$$

Now, with the average flux, we have:

$$\langle N_B(t)\rangle = \frac{\sigma\langle\phi\rangle N_{A0}}{1-\sigma\langle\phi\rangle}\left(e^{-\sigma\langle\phi\rangle t} - e^{-\lambda t}\right).$$

Therefore, we get:

$$\frac{\langle N_B(t)\rangle}{N_B(t)} = \frac{\langle\phi\rangle}{\phi_A}\,\frac{\lambda-\sigma\phi_A}{\lambda-\sigma\langle\phi\rangle}\,\frac{e^{-\sigma<\phi>t} - e^{-\lambda t}}{e^{-\sigma\phi_A t} - e^{-\lambda t}} \qquad (6.8.5.2\text{-}2)$$

Two extreme cases are interesting: (1) $\lambda >> \sigma\phi$ or $\sigma<\phi>$ and (2) $\lambda << \sigma\phi$ or $\sigma<\phi>$. In Case 1, Eq. (6.8.5.2-2) becomes

$$\frac{<N_B(t)>}{N_B(t)} \sim \frac{<\phi>}{\phi_A} e^{-\sigma\phi_A\left(\frac{<\sigma>}{\phi_A}+1\right)t}$$
$$= \frac{R}{H}\tan^{-1}\left(\frac{H}{R}\right) e^{-\sigma\phi_A\left[\frac{H}{R}\tan^{-1}\left(\frac{R}{H}\right)+1\right]t} \qquad (6.8.5.2\text{-}3)$$

For Case 2, Eq. (6.8.5.2-2) becomes

$$\frac{<N_B(t)>}{N_B(t)} \sim \frac{<\phi>}{\phi_A}\,\frac{\sigma\phi_A}{\sigma<\phi>}\,\frac{e^{-\lambda t}}{e^{-\lambda t}} = 1,$$

which means that accounting for the difference in the average flux is not necessary for the very long half-life radioactive products. With the typical values of $\phi_A \sim 10^{15}$ n/cm^{2}sec, $\sigma \sim 0.1$ barn, t ~ 1 year operation, and R=H=5m, $\frac{<N_B>}{N_B} \sim 0.78$ for Case 1. Therefore, the average activity in the Prometheus first wall protection system will be about 20% less than the values reported in Table 6.8.5-2, especially for the products whose half-lives satisfy the condition of $T_{1/2} << \sigma\phi_A$ or $\sigma<\phi>$.

b. Biological Hazard Potential (BHP) – In addition to the magnitude of radioactivity, the BHP values in each zone have been computed and the results are shown in Figures 6.8.5-11 through 6.8.5-13 as a function of time

Use or disclosure of data
subject to title page restriction

after shutdown. The BHP is a measure of the "Biological Hazard" of the radioactivity in various materials.

Figure 6.8.5-11 shows the BHP values in the first wall system. It shows that the lead containing zones (Zone #1 and #3) have the highest BHP values among the other zones all the time. The products such as Pb^{209} (3.25h, $Pb^{208}(n,\gamma)$) for short times after shutdown and Pb^{205}($1.9x10^7$y, $Pb^{204}(n,\gamma)$ or $Pb^{206}(n,2n)$) for long times after shutdown are responsible for the high BHP values in the Pb zone. In SiC zones (Zone #2 and #4), Al^{28} (2.24 min, $Si^{28}(n,p)$) is dominating

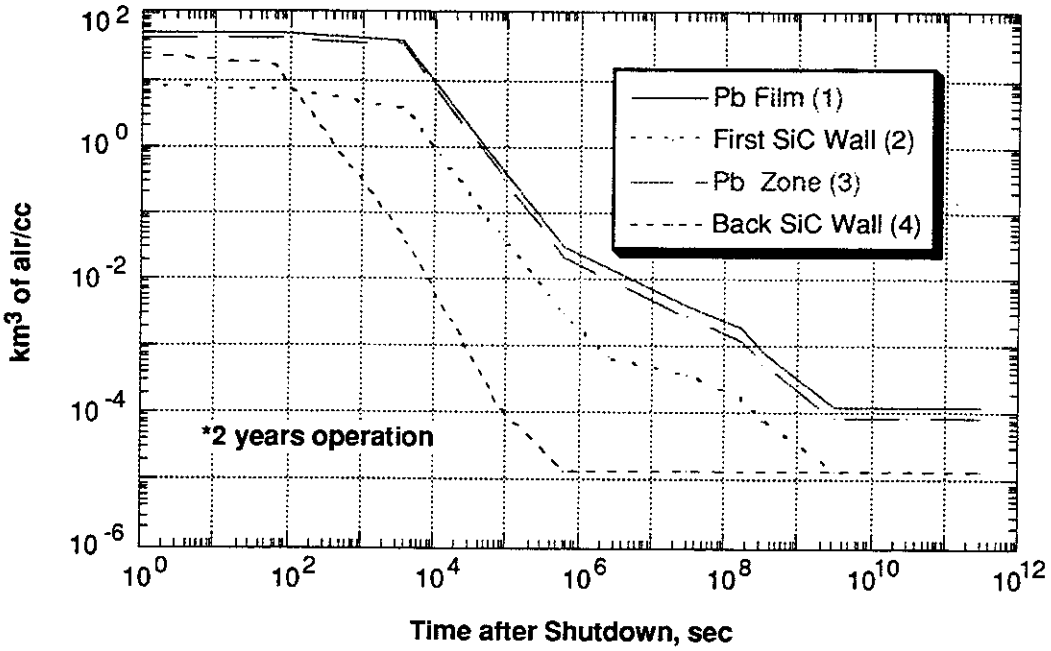

Figure 6.8.5-11. Specific BHP in the First Wall System

Use or disclosure of data
subject to title page restriction

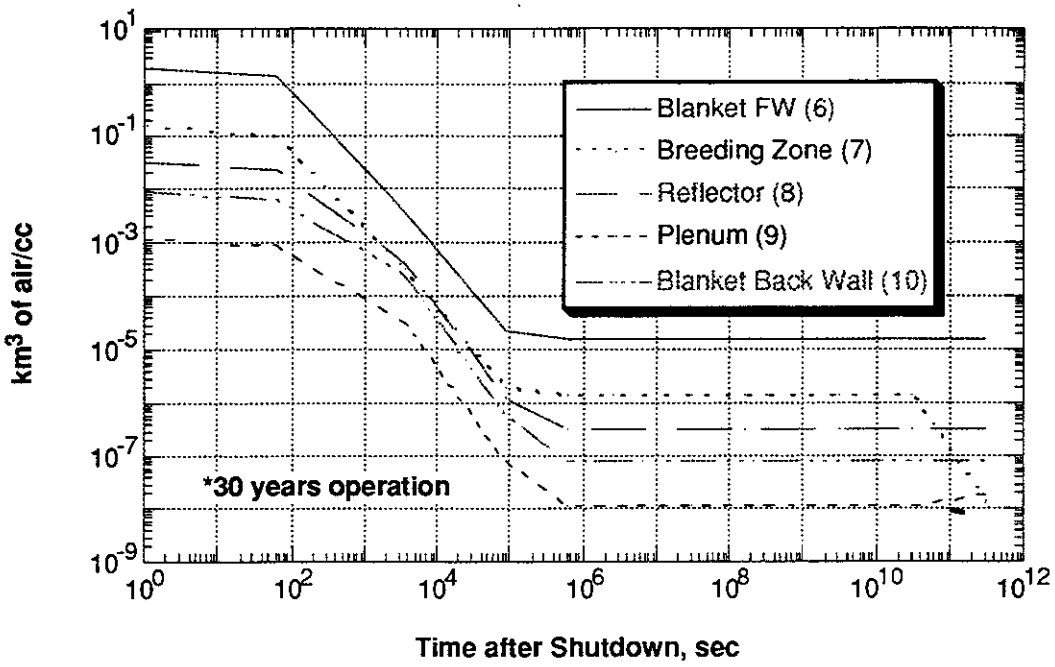

Figure 6.8.5-12. Specific BHP in the Blanket and Reflector

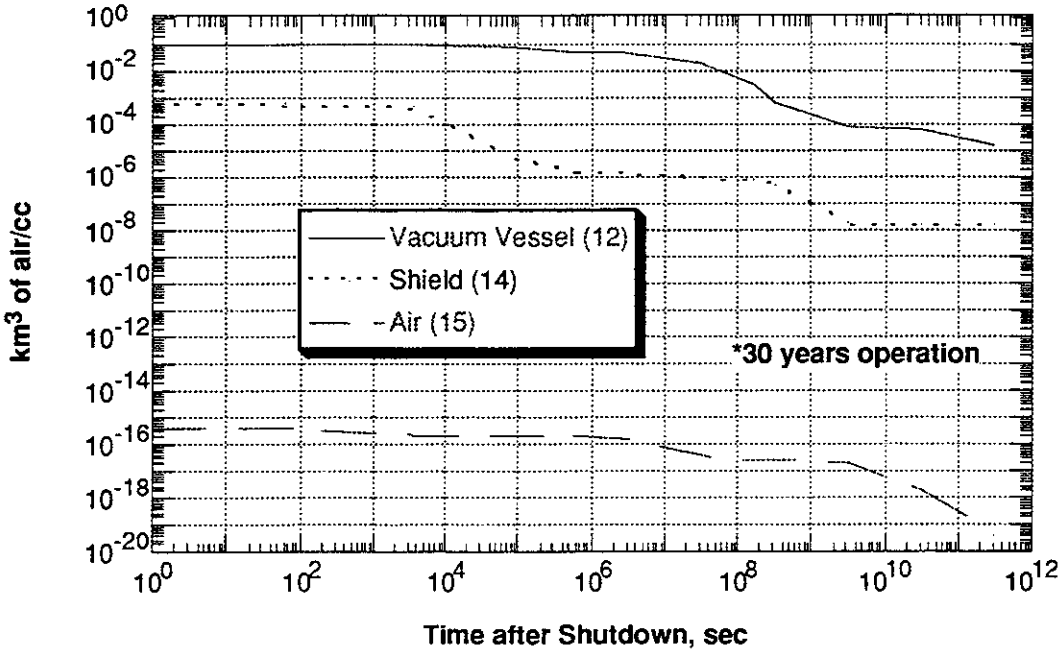

Figure 6.8.5-13. Specific BHP in the Vacuum Vessel, Shield, and Surrounding Air

Use or disclosure of data
subject to title page restriction

the BHP values for very short times after shutdown. After Al^{28} decays away, Be^{10} ($1.6x10^6$y, $C^{13}(n,\alpha)$) and C^{14} ($5.73x10^3$y, $C^{13}(n,\gamma)$) take over the leading role in the SiC zone. But, in general, the SiC zone has about 1~3 orders of magnitude lower BHP than the lead zone.

Figure 6.8.5-12 shows the specific BHP values in the blanket and reflector system. Since the SiC is the main material here, every zone in this system shows the same general trend. Furthermore, the deeper the zone is, the lower the BHP values are, because the average neutron flux is less in deeper zones. Figure 6.8.5-13 shows the specific BHP values in the vacuum vessel, shield, and the air around the cavity. Their general trend is found to be very similar to that of the magnitude of radioactivity discussed before for these zones. However, it has to be noted that Mn^{54} ($T_{1/2}$=312.2 day, $Fe^{54}(n,p)$) is the main contributor for the BHP in the vacuum vessel zone in the time span from shutdown to a few years after shutdown. Other important nuclides include W^{187} (23.9h, $W^{186}(n,\gamma)$), Fe^{55} (2.73y, $Fe^{56}(n,2n)$), and Nb^{93m} (13.6y, $Nb^{93}(n,n')^*$) in the vacuum vessel zone. The BHP in the shield zone is governed by Al^{28}, T, Be^{10}, and Pb^{205} for the very short-, long-, and very long-after shutdown times, respectively.

A particular concern in using lead in a high neutron field is the production of Po^{210}. Po^{210} is an α-emitter and volatile. Bismuth is a common impurity in natural lead. The neutron capture reaction with Bi^{209}, which is the only stable nuclide in bismuth, can result in the production of Po^{210}: $Bi^{209}(n,\gamma)Bi^{210} \rightarrow Po^{210}$. Other reaction/decay chains which can produce the Po^{210} are:

$Pb^{208}(n,\gamma)Pb^{209} \rightarrow Bi^{209}(n,\gamma)Bi^{210} \rightarrow Po^{210}$: chain #1
$Pb^{208}(n,\gamma)Pb^{209}(n,\gamma)Pb^{210} \rightarrow Bi^{210} \rightarrow Po^{210}$: chain #2

In general, there has been a deficiency in the literature of exact estimations of the Po^{210} production rate from the above two reaction/decay chains, even though it has important safety implications. In this work, a detailed estimation of the Po^{210} production from the first wall system in the Prometheus design has been made based on the available cross section and decay data. The necessary cross section data has been extracted from the activation cross section library in DKRICF and the decay data in the Table of Radioactive Isotopes[9] have been used. All three reaction/decay chains are considered. The bismuth impurity in the natural lead has been taken as 40 wppm throughout the calculation.

Use or disclosure of data
subject to title page restriction

First, the results of radioactivity calculations for Po^{210} in the lead film zone using DKRICF are presented in Tables 6.8.5-5 and 6.8.5-6 as a function of time after shutdown. Table 6.8.5-5 shows the radioactivity and Table 6.8.5-6 shows the BHP.

Table 6.8.5-5 Radioactivity (Ci/cm^3) of Po^{210} With Other Dominating Nuclides in the Pb Film

	Total	Most Dominant	Second Dominant	Third	Fourth	Po^{210}
At Shutdown	6.897	Pb^{203}: 3.977	Pb^{209}: 2.853	Hg^{205}: 4.362-2(a)	Hg^{203}: 1.611-2	1.054-4
1 min	6.879	Pb^{203}: 3.976	Pb^{209}: 2.309	Hg^{205}: 3.844-2	Hg^{203}: 1.641-2	1.054-4
1 hour	6.255	Pb^{203}: 3.924	Pb^{209}: 2.309	Hg^{203}: 1.610-2	Tl^{204}: 7.576-3	1.054-4
1 day	2.930	Pb^{203}: 2.889	Pb^{209}: 1.789-2	Hg^{203}: 1.588-2	Tl^{204}: 7.570-3	1.053-4
1 week	4.467-1	Pb^{203}: 4.243-1	Hg^{203}: 1.452-2	Tl^{204}: 7.546-3	Pb^{205}: 1.390-4	1.040-4
1 month	1.829-2	Hg^{203}: 1.032-2	Tl^{204}: 7.460-3	Pb^{203}: 2.719-4	Pb^{205}: 1.390-4	9.400-5
1 year	6.538-3	Tl^{204}: 6.304-3	Pb^{205}: 1.389-4	Hg^{203}: 1.099-4	—	1.756-5

(a) Read as 4.362×10^{-2}

Table 6.8.5-6 BHP (km^3 of Air/cm^3) of Po^{210} With Other Dominating Nuclides in the Pb Film

	Total	Most Dominant	Second Dominant	Third	Fourth	Po^{210}
At Shutdown	2.863+1	Pb^{209}: 2.85+1(a)	Pb^{203}: 6.634-2	—	—	1.756-2
1 min	2.853+1	Pb^{209}: 2.841+1	Pb^{203}: 6.628-2	—	—	1.756-2
1 hour	2.319+1	Pb^{209}: 2.310+1	Pb^{203}: 6.542-2	—	—	1.756-2
1 day	2.627-1	Pb^{209}: 1.789-1	Pb^{203}: 4.815-2	—	—	1.756-2
1 week	4.166-2	—	—	—	—	1.734-2
1 month	3.053-2	—	—	—	—	1.566-2
1 year	1.136-2	Tl^{204}: 7.007-3		—	—	2.922-3

(a) Read as 2.853×10^{1}

Use or disclosure of data subject to title page restriction

The results shown in these tables do not include the effect of build-up of Po^{210} from neutron interactions with natural lead (Chains #1 and #2). Even though the activity level of Po^{210} is small compared to the other dominant radionuclides, it has rather high BHP values because of the much lower maximum permissible concentration, especially during the period of time from one week to a few months after shutdown.

Figure 6.8.5-14 shows the Po^{210} build-up from each of the three reaction/decay chains described above as a function of irradiation time. It is apparent that the production of Po^{210} from the bismuth impurity is more important among the three chains up to about one year irradiation. After that, Chain #1 is mainly responsible for the Po^{210} production. Chain #2 is the least source of the Po^{210} until the irradiation time reaches about 10 years. Then the Po^{210} production from this chain exceeds that from the bismuth impurity. While the Po^{210} production from the Bismuth impurity in lead can be controlled since the Bismuth impurity in lead can be reduced with the extra purifying process, we do not have much control over the production of Po^{210} from Chains #1 and #2. However, replacing lead every year or so can reduce the production of Po^{210} from the lead reaction/decay chain. The isotopic tailoring method, which reduces the Pb^{208} content from the natural lead, can be one solution, but the extra cost is a major concern.

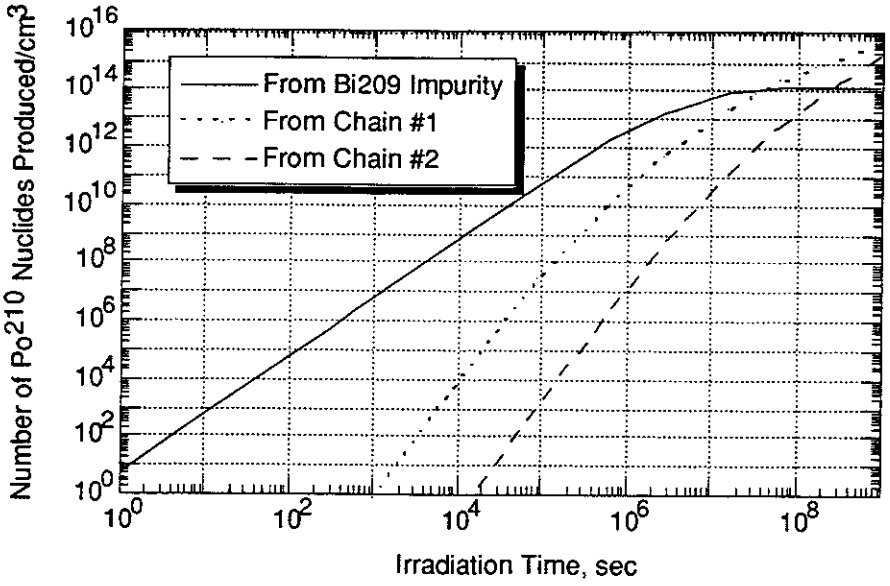

Figure 6.8.5-14 Po^{210} Buildup in the Prometheus First Wall System

Use or disclosure of data
subject to title page restriction

References for 6.8.5.2

1. W. W. Engle, Jr., "User's Manual for ANISN, A One-Dimensional Discrete Ordinates Transport Code with Anisotropic Scattering," K-1693, Oak Ridge Gaseous Diffusion Plant (1967).

2. R. R. Kinsey, Compiler, "Evaluated Neutron Data File, ENDF/B-V," ENDF Summary Documentation, ENDF-201, 3rd Edition, BNL (1979).

3. B. Badger, S. I. Abdel-Khalik, H. M. Attaya, et al., "SIRIUS-M: A Symmetric Illumination, Inertially Confined Direct Drive Materials Test Facility," UWFDM-711 (1986).

4. D. L. Handerson and Osman Yasar, "DKRICF: A Radioactivity and Dose Rate Calculation Code Package," UWFDM-714 (1986).

5. H. Y. Khater and M. E. Sawan, "Dose Rate Calculations for a Light Ion Beam Fusion Laboratory Microfusion Facility," UWFDM-809 (1989).

6. Y. Seki, et al., "THIDA-2: An Advanced Code System for Calculation of Transmutation, Activation, Decay Heat and Dose Rate," RSIC Computer Code Collection, CCC-410 (April 1987).

7. B. Badger, F. Arendt, K. Becker, et al., "HIBALL: A Conceptual Heavy Ion Beam Driven Fusion Reactor Study," UWFDM-450 (1981).

8. H. Attaya, Y. Gohar, and D. Smith, "US-ITER Activation Analysis," Fusion Technology, 19, 1837 (1991).

9. E. Browne and R. Firestone, "Table of Radioactive Isotopes," Jone Wiely and Sons (1986).

Use or disclosure of data
subject to title page restriction

6.8.5.3 Accident Analysis

First Wall and Blanket Thermal Response Under Loss-of-Cooling Accident – The temperature responses of the SiC first wall and blanket components under a loss of coolant accident are estimated in this section. It is assumed that the reactor can be shut down immediately after an accident occurs. The decay heat histories after reactor shutdown for various components are calculated assuming two full power years of operation. Results are shown in Figure 6.8.5-15. At the time of shutdown, the specific decay heat at the SiC first wall is about 0.6 W/cm^3 and drops to about 0.03 W/cm^3 at 10 minutes after shutdown. The specific decay heat of the lead coolant does not change significantly in the first 24 hours after shutdown.

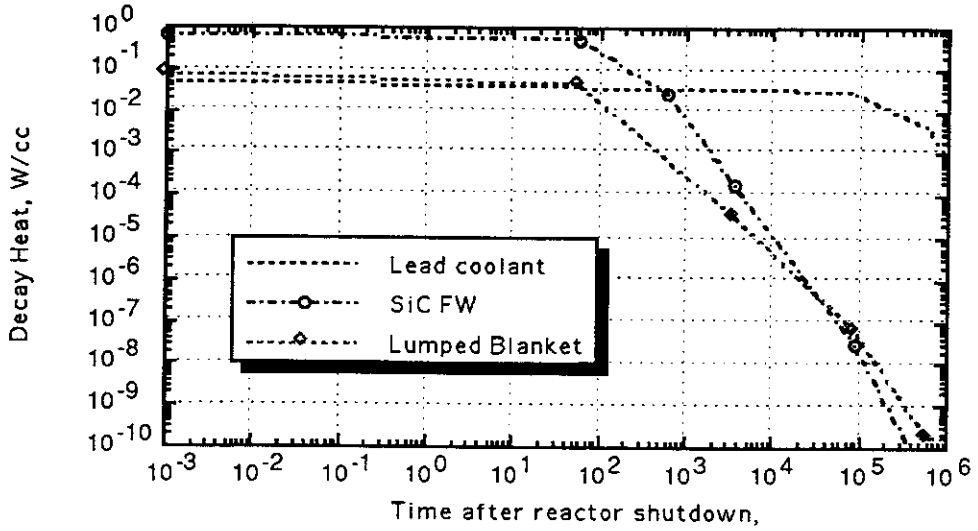

Figure 6.8.5-15. Specific Decay Heat Histories at Different Components

The component temperature history under adiabatic heatup with insulated boundaries can be estimated as:

$$\rho C_p \frac{\partial T}{\partial t} = q''' \qquad (6.8.5.3\text{-}1)$$

The assumption of adiabatic heatup with insulated boundaries is very conservative since in reality all the surrounding structures will also warm up. Figure 6.8.5-16 shows the temperature history of the SiC FW following a LOCA. The temperature of the SiC reaches about 445°C at 24 hours following reactor shutdown and stays quite flat for the following time.

Use or disclosure of data
subject to title page restriction

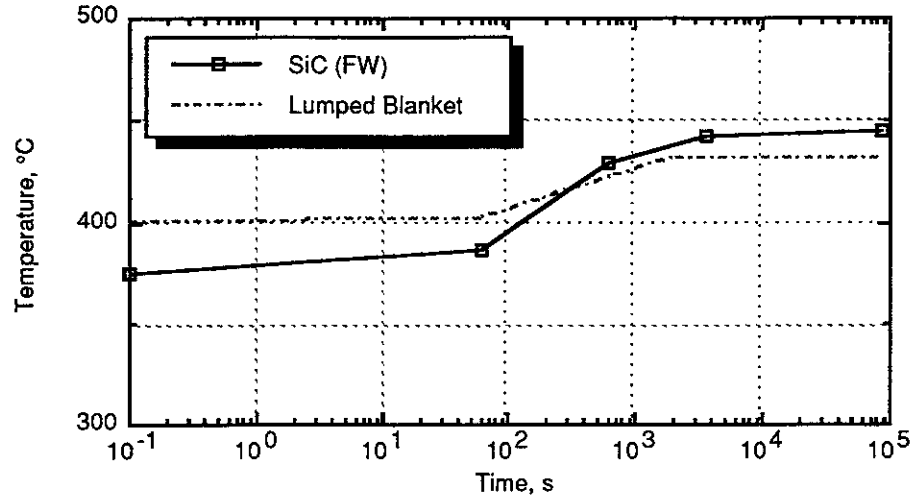

Figure 6.8.5-16. Temperature Histories at SiC FW and Blanket Components Following a Loss of Coolant Accident

As shown in Figure 6.8.5-15, the specific decay heat in the blanket is lower compared to that of the first wall structure. The lumped blanket temperature history under a LOCA with reactor shutdown is also shown in Figure 6.8.5-16. The results indicate that the temperature rise in the blanket module is about 35°C at one day following a loss of coolant accident.

Lead Decay Heat Removal Under Accident Conditions – Decay heat coming from radioactive lead poses a safety concern if it is not removed adequately following the reactor shutdown. Under normal plant shutdown, the decay heat can be removed by circulating the lead to the heat exchanger for about one week before it is transferred to the hot cell. However, under some off-normal conditions, additional heat removal mechanisms are required to remove the decay heat. Some of these scenarios include: (1) the lead spreads over the floor following a loss-of-coolant accident, (2) the lead becomes stagnant in the reactor due to failures of cooling pumps, or (3) a loss of heat sink (beyond the heat exchanger).

It is assumed that the plant design provides gravity-driven guided coolant drain paths. In this case, the lead can be collected in a pre-defined storage container and active cooling is suggested for the normal decay heat transport mechanism. In Prometheus, we go one step further to ensure that the decay heat can be removed passively, even in the event that all active cooling systems are lost.

There are four stages of heat removal which need to be considered: source term, transport pathways, intermediate heat storage, and ultimate heat sink. The source

Use or disclosure of data
subject to title page restriction

term has been obtained from radioactivity calculations and is shown in Figure 6.8.5-15. After one week, the decay heat drops rapidly and the need for further heat rejection is essentially eliminated.

Several intermediate and ultimate heat sinks are available, including: (1) the earth beneath the reactor building, (2) the air surrounding the reactor building, (3) existing components within the reactor building, and (4) engineered safety system for heat storage.

Four different passive heat removal mechanisms have been explored here. These include:

(1) Heat of vaporization.
(2) Heat of fusion.
(3) Heat storage in solids and conducting to the earth.
(4) Heat storage in solids and convecting to the air.

The advantages and disadvantages of each concept is summarized in Table 6.8.5-7 and described in more detail below. Heat of vaporization is the most effective heat removal mechanism. Heat removed by storing decay heat in solids and conducting to the earth is an attractive alternate method.

Table 6.8.5-7 Summary of Passive Lead Decay Heat Removal Systems

Concept	Advantage	Disadvantage
Heat of Vaporization	Simple in concept Simple operation High storage potential per mass	Large storage volume
Heat of Fusion	High energy storage potential per unit mass Least volume required	Heat stored inside the medium requires an additional heat removal mechanism; Material compatibility
Heat Stored in Solids	Simple in concept Simple operation	Large material volume; Additional heat removal mechanism (conduction or convection) required; Good thermal contact required between storage container and solid mass.

1. Heat of Vaporization - Water has a relatively high heat of vaporization (2.2569×10^6 J/kg @ 1 atm). Steam can be generated by conduction through the storage container and into a water enclosure. The non-radioactive steam generated is then diverted to the atmosphere, making this a very promising concept for lead decay heat removal. During the first day following the reactor shutdown, the amount of steam generated is about 0.5 kg/sec for a lead inventory of 30 m^3. The total amount of water vaporized during a one-week period is about 300 m^3. After one week following reactor shutdown, decay heat level drops about two orders of magnitude, at which time the amount of water vaporized becomes insignificant.

2. Heat of Fusion - This concept utilizes a molten salt with a melting point of approximately 627°C as the heat storage medium. The heat stored inside the molten salt can be conducted (and/or convected) out to the ultimate heat sink, such as earth or atmosphere, over a longer period of time without jeopardizing the structure material. The concept appears attractive because of the small volume of material needed to remove the lead decay heat. The heat of fusion of LiF-NaF eutectic is between 167 and 222 kcal/kg (about 8.4×10^5 J/kg). Calculations show that approximately 8×10^5 kg of this eutectic would be needed to transport the lead decay heat.

3. Storage in Solids and Conduction to the Earth Over a Longer Time Span - This concept involves a large iron liner beneath the reactor building and welded (or otherwise attached) to the lead storage container. Decay heat from the lead is transmitted to the liner and then dissipated by conduction to the earth. The material considered for heat storage and transmission is cast iron, which melts at 1810 K. The storage unit is to be located at the bottom level of the plant to minimize the possibility of radioactive lead migration. The volume required for a temperature rise of 300°C over a one-week period is about 600 m^3 for a lead inventory of 30 m^3. Further temperature rise of the iron storage unit is limited due to a significant drop of the decay heat level.

4. Storage in a Solid Mass and Transport to the Atmosphere Through Natural Convection of Air - This concept is similar to the previous one. However, in this case the storage unit must be located close to the reactor boundary for better heat removal by natural convection. In addition, since the convective heat transport rate increases with height, this concept requires much more vertical space (the example below assumes 30 m). The lead decay heat is transmitted to the heat storage unit (a solid mass such as cast iron) and convected to the air through natural convection. The average heat transfer coefficient for a flat vertical surface is given as:

Use or disclosure of data
subject to title page restriction

$$h = 0.555\,(GrPr)^{0.25}\left(\frac{k}{L}\right) \text{ for laminar flow}$$

$$= 0.021\,(GrPr)^{0.4}\left(\frac{k}{L}\right) \text{ for turbulent flow}$$

where the Grashof number (Gr) is calculated as:

$$Gr = \frac{\rho^2 g\beta\,(T_s - T_a)\,L^3}{\mu^2}$$

T_S and T_a are the surface and ambient temperatures, respectively, and L is the vertical height. The calculations show that, for an average surface temperature of 300°C and a height of 30 m, a surface area of 215 m^2 is needed. The volume of a storage unit using cast iron is about 600 m^3 for a temperature increase of 300°C.

Dry Spot Analysis – The SiC first wall behavior resulting from the formation of local dry spots has been analyzed using the radiation model discussed in Section 6.8.2.5. The formation of local dry spots has serious consequences on the performance and the expected lifetime of the reactor. A dry spot on the chamber wall will lead to erosion of the SiC structure, which could lead to an unscheduled shutdown of the reactor for maintenance. If the formation of these dry spots occurs frequently in a specific area, i.e. on the upper end cap, the maintenance costs of the design could increase drastically, thus decreasing the design's attractiveness.

The possible causes and effects of a dry spot are shown in Figure 6.8.5-17. Four different events that could lead to a local dry spot have been identified: blockage of the SiC, poor wetting of the first wall by the lead, hydrodynamic fluid instabilities, and uncovering of the wall by a loss of flow accident.

The porous SiC could become blocked by impurities in the liquid lead or by sintering of the structure at high operating temperatures. Since it is uncertain how corrosive liquid lead is at the temperatures of interest, solid particulates of the first wall system and the coolant pipes could flake off into the lead. These particulates could then clog the pores of the first wall. The high temperature environment of the reactor chamber could, after prolonged exposure to these temperatures, lead to sintering of the porous structure. If this happens, the lead will be blocked from reaching the surface of the blast chamber.

Use or disclosure of data
subject to title page restriction

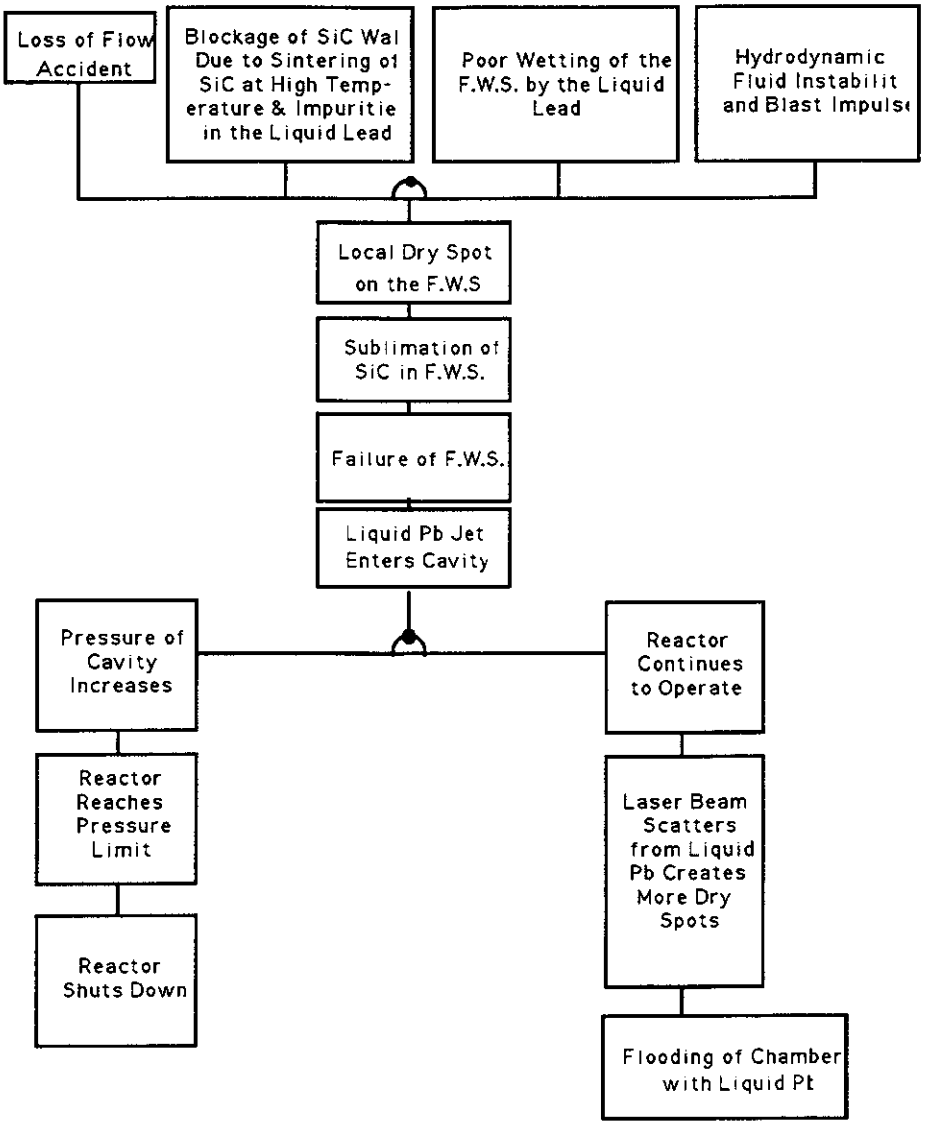

Figure 6.8.5-17 Scenarios of Dry Spot Formation Which Lead to a Reactor Shutdown.

Lead does not wet silicon carbide. Wetting agents are proposed to overcome this problem; however, the degree of wetting is still a concern. A heavy liquid film is very difficult to keep attached to an inverted surface even when the liquid wets the wall thoroughly. Along with the problem of wetting the inverted surface, the pressure waves created by a pellet explosion cause the wall to vibrate at frequencies of about 800 Hz. These vibrations can create instabilities in the liquid protectant causing the film to detach itself from the wall. The pressure wave can also cause the liquid lead to be pushed back far enough into the porous wall to prevent it from re-establishing itself on the surface in time for the next shot.

Use or disclosure of data
subject to title page restriction

If, for any of the above reasons, a dry spot is established, the high heat fluxes that are generated after a blast will cause the exposed SiC to sublimate. The amount and thickness of the material that is evaporated can be estimated on a per shot basis and, from this, an estimate can be made of the time before the first wall fails. The radiative and conductive heat fluxes are shown in Figure 6.8.5-18. For very short times, ~10^{-14} s, the temperature gradient is large enough to conduct the energy out, but between 10^{-14} and 10^{-4} s the radiative flux dominates and an excess amount of energy can sublimate the SiC. The amount of energy per second per unit area that goes into evaporating the first wall is then:

$$E_{sub} = q_{rad} - q_{cond}$$

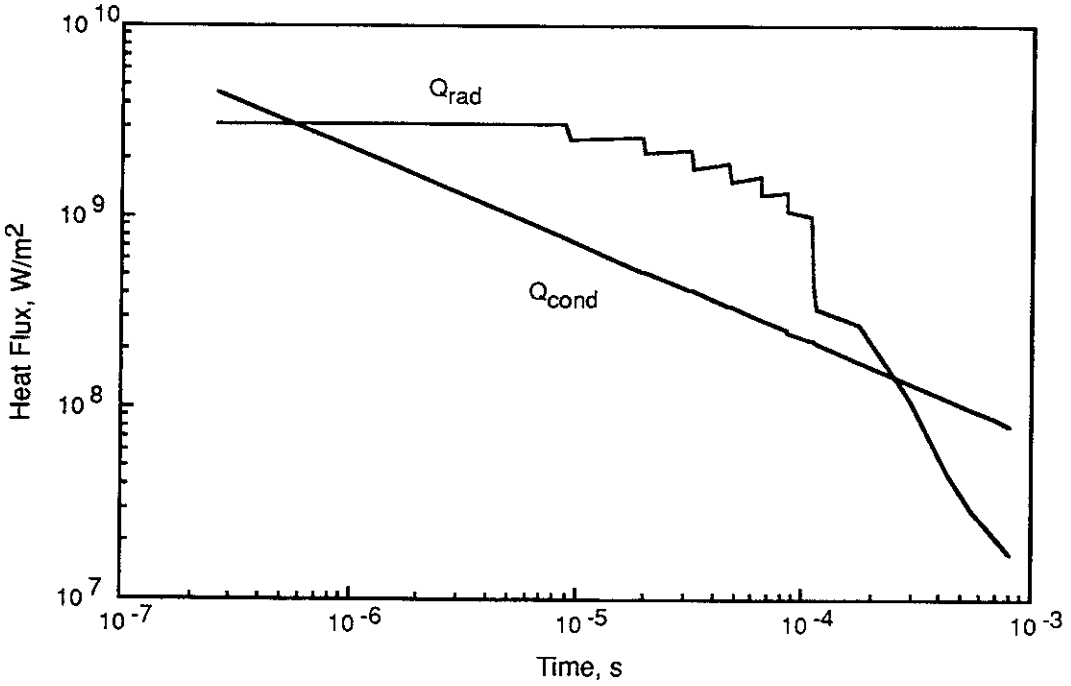

Figure 6.8.5-18. The Energy Available for Sublimation is the Difference Between the Radiative and Conductive Heat Fluxes.

The conductive heat flux is calculated by:

$$q_{cond} = k\frac{\Delta T}{\delta}$$

where δ is the thermal boundary layer thickness, which is defined as:

$$\delta = \sqrt{\pi \alpha t}$$

Use or disclosure of data
subject to title page restriction

To calculate the amount of mass evaporated from the wall during a shot, E_{sub} is equated to the energy of sublimation, $H_{sub} = m\ h_{sub}$. The heat of sublimation is obtained from the potential energy of the Si and C atoms in the SiC matrix.[1] It is calculated to be:

$$h_{sub} = 1.91 \times 10^7, \text{ J/kg}$$

From this the mass of evaporated liquid per unit area can be calculated from:

$$m = \int_{t_o}^{t_m} \frac{E_{sub}}{h_{sub}}\, dt$$

From which the sublimation thickness is defined:

$$\Delta X = \frac{m}{\rho}$$

For the laser base case, the evaporation thickness per shot is calculated to be $\delta = 0.79\ \mu m$. The mean time to failure can be estimated as the time to sublime 5 mm of SiC, which equates to approximately 19 minutes of full power operation.

This calculation shows that the damage caused by a local dry spot needs to be managed. There must not be any prolonged dry spots on the first wall, thus making the stability of liquid film and detection of dry spots important issues.

Reference for 6.8.5.3

1. E. Pearson, T. Tadayoshi, T. Halicioglu, and W. Tiller, "Computer Modeling of Si and SiC Surfaces and Surface Process Relevant to Crystal Growth From the Vapor," Journal of Crystal Growth, 70, pp. 33-40 (1984).

Use or disclosure of data
subject to title page restriction

6.8.5.4 Summary - The safety aspects of the Prometheus cavity have been addressed in this section. The analyses performed include radioactivity characterization and accident tolerances. The impacts of the resulted radioactive products and quantities from the cavity components on the environment are addressed in Section 6.13. Po^{210} is a safety concern when lead is chosen for the first wall coolant. The calculated Po^{210} inventory (due from bismuth impurity and bismuth generated from neutron interaction with lead) is one order of magnitude lower than the ESECOM Case 1 limiting case. It is concluded that the Prometheus design can be classified as LSA-1 with regards to Po^{210}.

To prevent lead coolant from spreading over the floor assuming a cooling tube rupture condition, the cavity is designed to allow the lead to be drained to a storage container through gravity-driven paths. In addition, several means of passive heat removal mechanisms have been explored. A passive safety feature with regards to lead decay heat removal under accident conditions can be met.

Formation of the dry spot on the first wall surface is considered unlikely. However, if the dry spot were sustained, the SiC structure could withstand 19 full-power minutes of operation before a failure of the FW would occur.

Based on all of the analysis performed, Prometheus is a very safe and environmentally attractive reactor concept.

Use or disclosure of data
subject to title page restriction

This page intentionally left blank.

Use or disclosure of data
subject to title page restriction

6.9 Heat Transport and Thermal Energy Conversion

Various heat transport and thermal energy conversion concepts were considered and evaluated during development of the Prometheus designs. This section addresses thermal energy sources, heat transport, and distribution systems.

High grade thermal energy sources available in the Prometheus reactor are: (a) first wall energy, (b) blanket energy, and (c) KrF laser waste heat. First wall heat is extracted by liquid lead, while helium coolants provide the transport for blanket energy and laser driver waste heat. These coolants transfer thermal energy to Rankine cycle steam generators, steam reheaters, and feedwater heaters.

6.9.1 Energy Sources - The Prometheus reactors develop energy from the fusion of deuterium-tritium fuel in the reactor cavity. Deuterium-tritium (DT) targets injected into the cavity are imploded using either laser or heavy ion beams, resulting in an energy gain of approximately 100. Each DT fusion reaction produces a 14.1 MeV neutron plus a 3.5 MeV alpha particle. Alpha particles are stopped by the first wall, while neutrons and secondary gammas are absorbed or thermalized in either wall or blanket components. Resultant heat is transferred, by lead or helium, to the energy conversion system.

Prometheus-L (laser) total energy is 3,264 MW which is derived from four sources as shown in Figure 6.9-1. Proceeding outward from the reactor chamber center, a flowing first wall protection film absorbs 22 MW of energy. This first wall protection consists of a liquid lead film to absorb a portion of the x-ray, neutron, and debris energy. Next, a first wall lead coolant loop extracts 1,267 MW of power deposited in this region. A helium-cooled loop is used to extract 1,782 MW from the blanket. Finally, the high temperature laser driver waste heat, 193 MW, is recovered via a helium transfer medium into the energy conversion process. Representative operating temperatures are: liquid lead = 977°F, blanket helium = 1,202°F and KrF laser waste heat = 900°F. Energy conversion is accomplished through six parallel steam generator circuits from the main reactor core. A representative Prometheus-L energy conversion system is shown schematically in Figure 6.9-2.

Prometheus-H (heavy ion) total energy is 2,780 MW which is derived from three sources as shown in Figure 6.9-1. Proceeding outward from the reactor chamber center, a flowing first wall protection film supplies 21 MW of energy. This first wall protection consists of a liquid lead film to absorb a portion of the x-ray, neutron, and debris energy. Next, a first wall lead coolant loop extracts 1,162 MW of power deposited in this region. Finally, a helium-coolant loop is used to extract 1,597 MW from the blanket. Power conversion, like the Prometheus-L, is accomplished through six parallel steam generator circuits from the main reactor core. A representative Prometheus-H energy conversion system

Use or disclosure of data
subject to title page restriction

Power Flow for Laser and Heavy Ion Systems

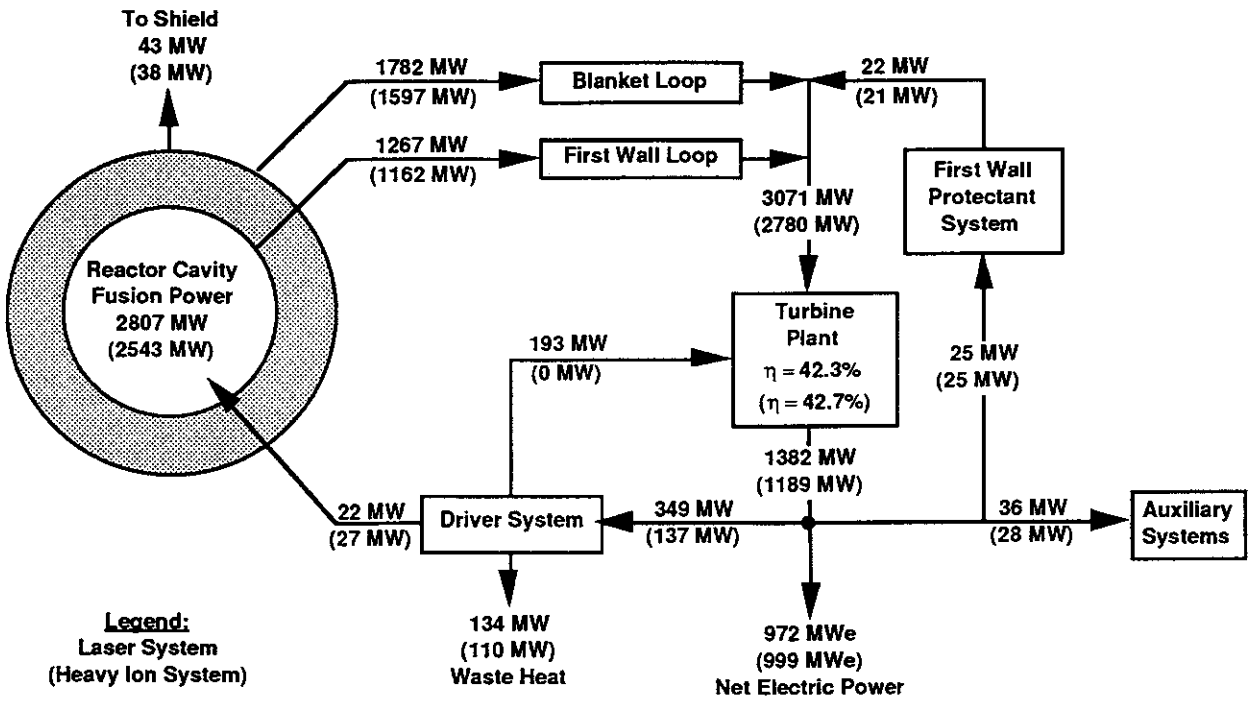

Thermal Source	-L	-H
Blanket Loop	1,782	1,597
First Wall Loop	1,267	1,162
First Wall Protection	22	21
Driver Loop	193	0
Total Energy	3,264	2,780

Figure 6.9-1. Prometheus Baseline Power Flow

is shown schematically in Figure 6.9-3. To achieve the same net electrical power, total Prometheus-H thermal power is 10% lower than Prometheus-L. This Prometheus-H advantage is due to higher driver efficiency.

6.9.2 Design Rationale – Study team members selected liquid lead and helium heat transfer coolants after examining safety aspects, heat transfer properties, and nuclear characteristics of alternate materials (see Reference 1 and Section 4.4). Liquid lead provides good heat transfer properties, first wall protection, and 40% energy absorption plus some neutron energy multiplication. In addition, liquid lead and water do not present a fire hazard. However, the maximum operating temperature of lead is limited (977°F) to minimize intergranular attack on the ferritic pipe and tubing materials.

Use or disclosure of data
subject to title page restriction

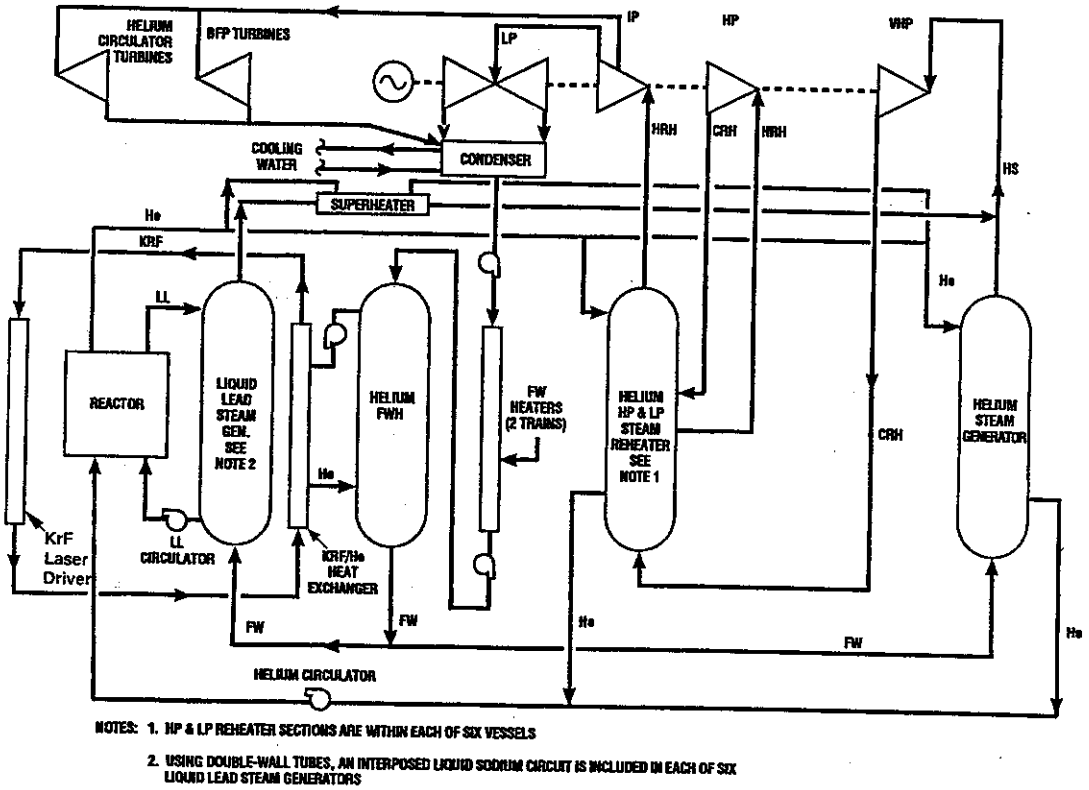

NOTES: 1. HP & LP REHEATER SECTIONS ARE WITHIN EACH OF SIX VESSELS

2. USING DOUBLE-WALL TUBES, AN INTERPOSED LIQUID SODIUM CIRCUIT IS INCLUDED IN EACH OF SIX LIQUID LEAD STEAM GENERATORS

Figure 6.9-2. Prometheus-L Energy Conversion System

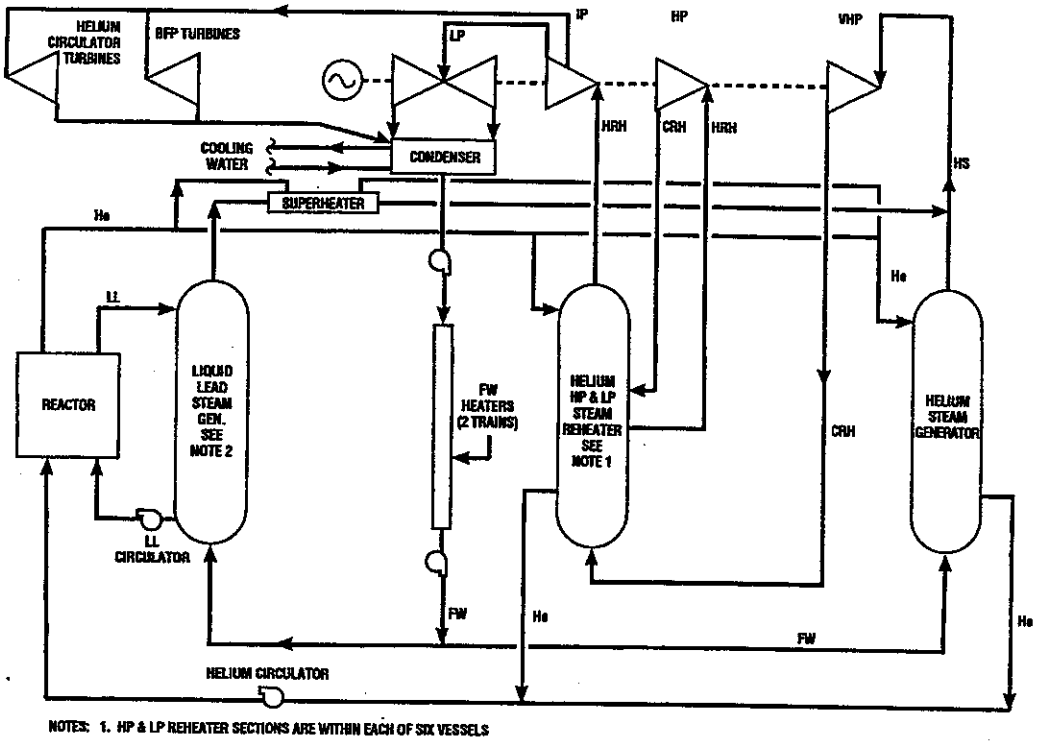

NOTES: 1. HP & LP REHEATER SECTIONS ARE WITHIN EACH OF SIX VESSELS

2. USING DOUBLE-WALL TUBES, AN INTERPOSED LIQUID SODIUM CIRCUIT IS INCLUDED IN EACH OF SIX LIQUID LEAD STEAM GENERATORS

Figure 6.9-3. Prometheus-H Energy Conversion System

Use or disclosure of data
subject to title page restriction

A helium-cooled blanket concept provides a high degree of safety, acceptable thermal properties chemically compatible with structural materials, and reduced radioactive material circulation. Prometheus-L laser system waste heat is transferred to the feedwater heating system through an intermediate helium coolant loop. An intermediate helium loop is incorporated to isolate a possible hot fluorine leak into the steam cycle.

6.9.3 Thermal Cycle - Two thermal cycles were considered for this nominal 1000 MW power station—a closed Brayton cycle and an advanced Rankine cycle. An advanced Rankine cycle (using supercritical steam and a double reheat turbine) was chosen. An advanced Rankine cycle features high thermal conversion efficiencies compatible at coolant temperatures and reasonable extrapolation of the existing database.

The selected advanced Rankine cycle uses a tandem compound double reheat turbine (see Figures 6.9-4 and 6.9-5). This turbine consists of a very high pressure (VHP) turbine, a high pressure (HP) turbine, and a double flow intermediate pressure (IP) turbine. The IP turbine exhaust steam then flows into three double flow low pressure (LP) turbine sections and to a surface condenser. Turbine input conditions are presented in Table 6.9-1.

Table 6.9-1. Turbine Input Conditions

Turbine Type	Parameter	Prometheus-L	Prometheus-H
VHP	Temperature (°F)	950	950
	Pressure, psia	3,715	1,184
HP	Temperature (°F)	950	950
	Pressure, psia	977	977
IP	Temperature (°F)	950	950
	Pressure, psia	334	334

Currently, large power stations use single reheat turbines, typically a 2,400 psia or 3,500 psia turbine with steam conditions of 1000°F/1000°F (throttle/reheat). Introducing a second reheat turbine raises cycle efficiency approximately 1.1% for 2400 psia throttle steam, 2.0% for 3500 psia steam, and 2.3% for 4500 psia steam. A double reheat turbine cycle, throttle/reheat1/reheat2 steam (1000°F/ 1000°F/1000°F), and raising throttle pressure from 2400 psia to 4500 psia increases thermal efficiency approximately 4%.[2] Therefore, in the interest of attaining a high thermal conversion efficiency, a double reheat turbine cycle was selected with steam conditions, ultimately limited by temperatures and flows of the reactor coolants, but finally set by the requirement for temperature differentials that permit reasonably sized steam generators and reheaters.

Use or disclosure of data
subject to title page restriction

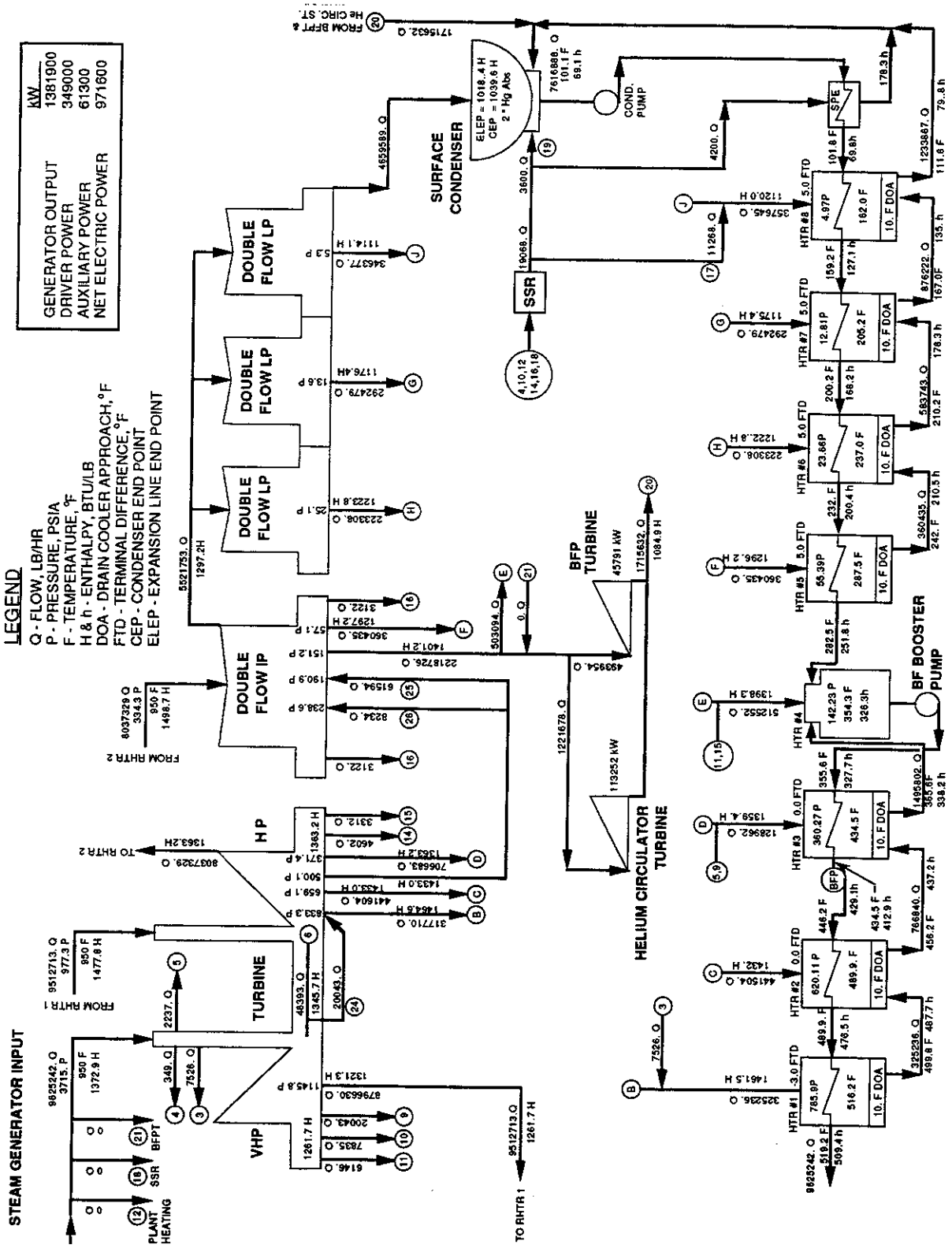

Figure 6.9-4. Prometheus-L Turbine Thermal Cycle

Use or disclosure of data
subject to title page restriction

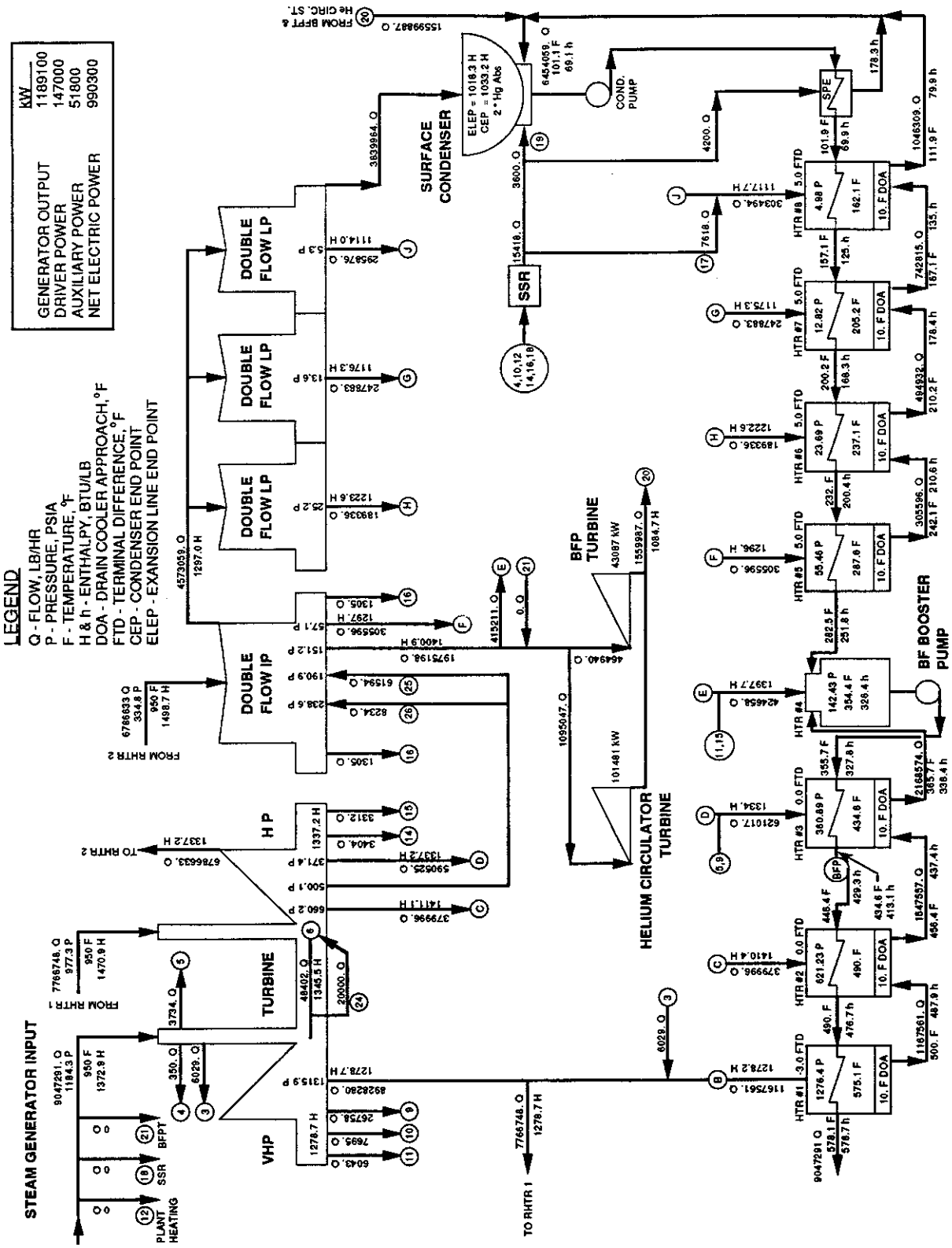

Figure 6.9-5. Prometheus-H Turbine Thermal Cycle

Use or disclosure of data
subject to title page restriction

The Prometheus-L generator gross output is 1382 MWe and a 1550 MVA rating at 0.9 power factor. The Prometheus-H generator has a gross output of 1189 MWe and a 1321 MVA rating. The tandem compound turbine-generator performance is predicated on the future availability of a single 3600 RPM generator of this size. Design and performance of the steam turbine-generator is based on information received from Brown Boveri Corporation.

Steam is generated in six identical helium-to-steam vessels and in six liquid lead-to-steam vessels. Steam exiting the generator is held at 800°F to maintain a reasonable terminal temperature difference between the lower temperature liquid lead and the steam. Steam is superheated to 955°F by helium, then joined with steam from the helium steam generator. (Refer to Section 6.9.5 for additional details.)

The Prometheus feedwater system consists of two parallel 50% capacity strings of eight regenerative feedwater heaters. The temperature of feedwater leaving each string is raised from 519°F to 578°F in its respective helium-to-water heat. Helium serving the last feedwater heater obtains its heat from the KrF-to-helium heat exchanger.

A recirculating water system transfers condenser heat to the atmosphere through a natural draft cooling tower. Alternative systems include "once through" condenser cooling that utilizes natural bodies of water and air cooled condensers where the site cannot make available the large water requirement to make up tower evaporation, drift, and blowdown losses (approximately 19 x 10^6 gallons/day). This "once through" system eliminates the circulating water pumps, piping, and surface condenser but requires more site area (50% to 100% greater) plus auxiliary power and installation costs.

6.9.4 Auxiliary Power - The steam turbine-generator supplies auxiliary power through transformers that step the 26 kV down to motor levels; i.e., 13200, 4150, and 480 volts. After auxiliary allocations, net power is transformed up to grid voltage of 345 or 500 kV.

Auxiliary power requirements of both Prometheus-L and H are summarized in Table 6.9-2. The total auxiliary power for Prometheus-L exceeds Prometheus-H by 10.5 MW. Prometheus-L requires 5.7 MW to circulate helium from the KrF heat exchanger to the feedwater heaters. The remaining 3.8 MW is derived from 10.5% greater heat input and corresponding larger, condensate, feedwater, cooling water, and liquid lead pumps.

Auxiliary power transformer losses amount to 0.4% plus driver power requirements, 1600 kW for Prometheus-L and 800 kW for Prometheus-H. Most of this auxiliary power increase is attributable to the large laser driver power requirement.

Use or disclosure of data
subject to title page restriction

Table 6.9-2 Auxiliary Power Requirements (kW)

		Prometheus-L	Prometheus-H
Condensate Pumps		2700	2300
Feedwater Booster Pumps		5600	5400
Circulating Water Pumps		8300	7000
Auxiliary Cooling Water Pumps		700	600
Steam Turbine Auxiliaries		3004	300
Water Treatment		300	300
HVAC		300	300
Lighting		200	200
Miscellaneous		600	600
Auxiliary Transformer Loss		1600	800
	Subtotal	20600	17800
Liquid Lead Pumps		25000	24000
Helium Circulator for KrF		5700	0
Reactor Auxiliaries		10000	10000
	Total	61300	51800

Diesel generators provide emergency auxiliary power for safe shutdown upon a trip of the steam turbine generator.

Diesel generators provide emergency power to these essential systems:

- Helium Circulator Drives
- Liquid Lead Pump
- Circulating Water Pump
- Auxiliary Cooling Water Pumps
- Liquid Lead Heat Tracing and Safety Air Conditioning
- Condenser Vacuum Pump
- Closed Cooling Water Pump
- Detritiation Systems
- Station Lighting, Controls, and Instrumentation

Helium and liquid lead circulation size determine the emergency diesel-generator system. Material design limits during an emergency shutdown and transient thermal analyses are the design drivers.

6.9.5 Plant Performance - Plant performance of both Prometheus-L and -H designs are summarized and compared in Table 6.9-3.

Table 6.9-3 Performance

	Prometheus-L	Prometheus-H
Heat Input, MWe	3091.0	2797.0
Gross Power Input, MWe	1381.9	1189.1
Driver Power, MWe	349.0	147.0
Auxiliary Power, MWe	61.3	51.8
Net Power Output, MWe	971.6	990.3
Gross Efficiency, %	44.7	42.5
Net Efficiency, %	31.4	35.4

Use or disclosure of data
subject to title page restriction

Efficiency is based on total heat input which is the sum of the thermal power in the blanket, wall protection, and shield power losses.

Net power output is to the primary side of the main transformers. Main transformers have an estimated loss of 3000 kW.

Gross efficiency at the generator terminals is 2.2% lower for a heavy ion-based plant. This is because the heavy ion plant supplies a smaller proportion of cycle heat (57.8% as compared to 58.4%) with helium (the hotter fluid) for the laser-based cycle. This lower efficiency heavy ion plant thermal conversion system is more than offset by the more efficient driver.

Disadvantages of this heavy ion, low gross cycle efficiency is offset by a 202 MW decrement in driver power requirement.

For the above reasons, as well as the auxiliary power differentials shown in Table 6.9-2, plant net efficiency for the heavy ion cycle is 35.4%, or four points above that for the laser cycle.

By extracting large quantities of steam from the IP turbine, the mechanical helium circulators reduce output at the generator terminals. Electric motors drive one or more helium circulators at startup and during shutdown. Future cycle optimization should consider higher pressure steam for the helium circulator drive turbines. Drive turbines would exhaust steam to either the HP reheater cold line or to the main condenser. Smaller steam turbines and lower cost could be weighed against a plant efficiency decrement.

6.9.6 Steam Generators, Reheaters, and Superheaters - Helium and liquid lead serve as reactor coolants, transferring reactor heat for steam generation, superheating, and reheating. Six parallel flow paths transfer thermal energy from the reactor to the turbine (see Figure 6.9-6). Both Prometheus-L and -H designs generate 75% of the total high pressure steam through a liquid lead-heated system loop. Remaining high pressure steam flow is produced in the helium system loop (see Figure 6.9-7). The helium loop also acts as a steam superheater for the liquid lead heater and for the high and low pressure steam returning from the turbine steam reheater.

(a) Helium Steam Generators - Six modules arranged in parallel helium flow paths make up the helium-heated steam generation system. Each module consists of three heat exchangers supplied with helium (1202°F) from the fusion reactor (Figure 6.9-7). Each heat exchanger has the same basic concept—horizontal tube banks suspended in a water-cooled, gas tight square enclosure. Water and steam flow through the inside of the tubing. Helium flows around the

Use or disclosure of data
subject to title page restriction

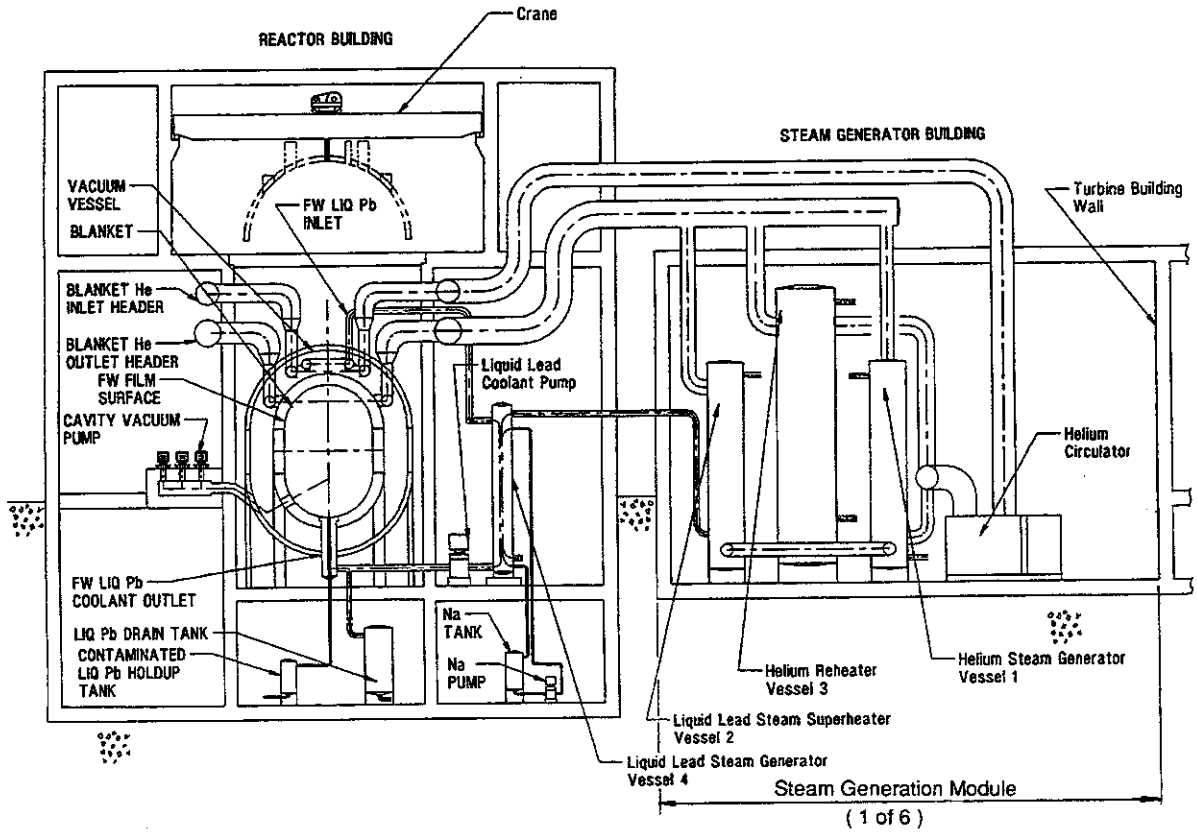

Figure 6.9-6. Coolant Distribution and Steam Generation

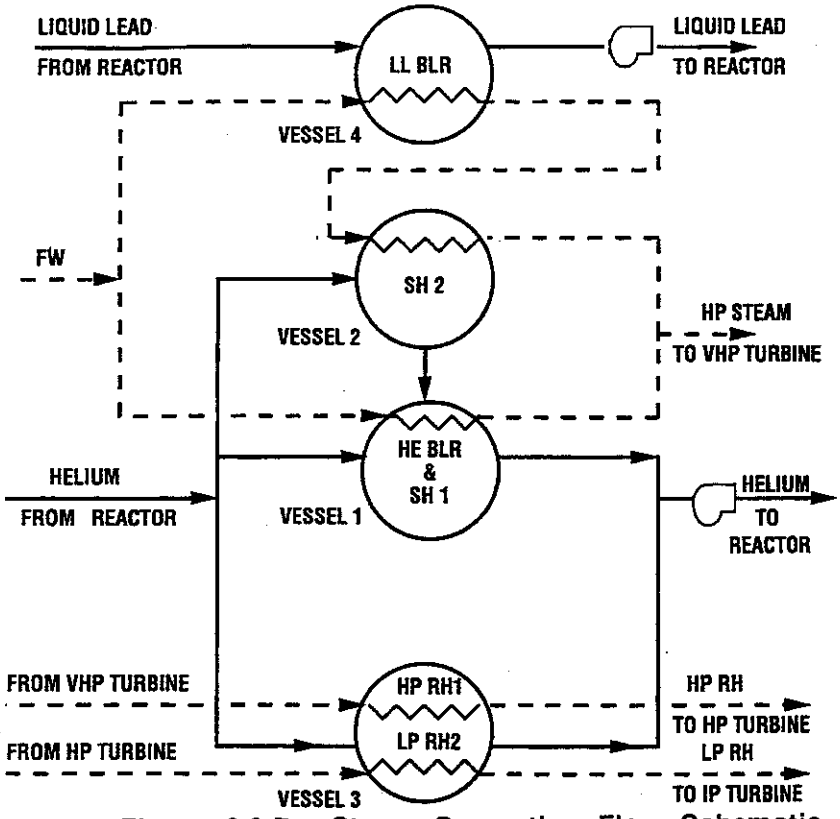

Figure 6.9-7. Steam Generation Flow Schematic

Use or disclosure of data subject to title page restriction

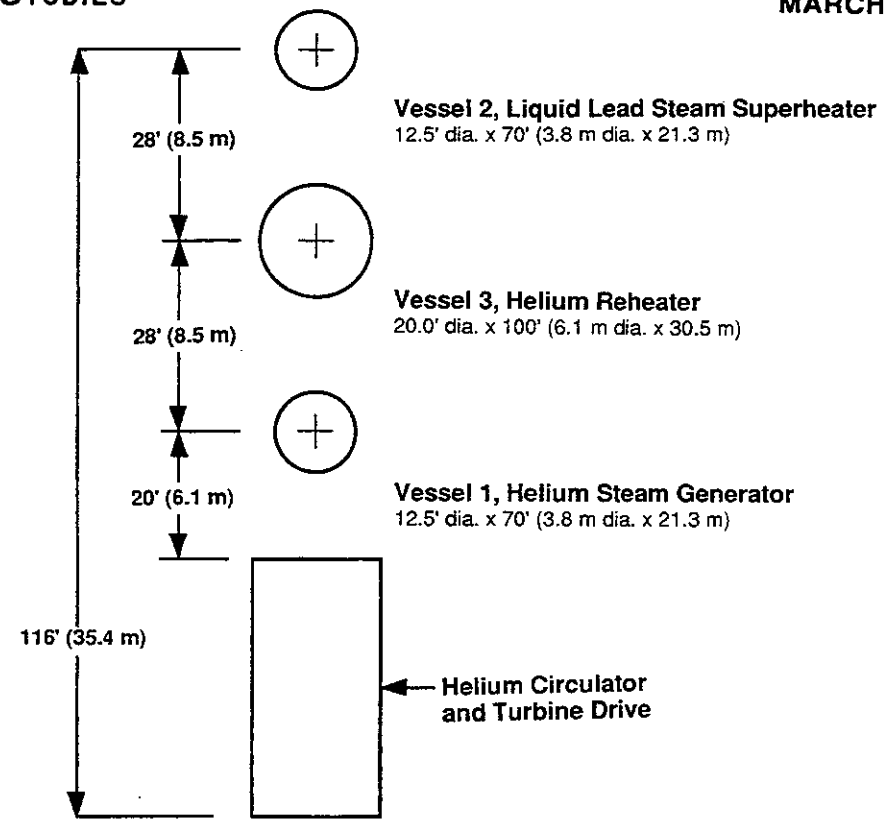

Figure 6.9-8. Helium Heat Exchanger Module

outside of the tube banks. Each tube bank and water-cooled enclosure is arranged vertically within a cylindrical pressure vessel. Hot helium circulates in such a way as to protect this pressure vessel from high temperature helium.

Only cooled helium contacts the pressure vessel after exposure to heat transfer surfaces. Hot helium enters the water-cooled enclosure through the inner pipe of a concentric gas inlet/outlet nozzle and passes over the tube banks. The cooled helium then flows through the annular space between the water-cooled tube bank enclosure and the pressure vessel wall and leaves the pressure vessel through the outer annulus of the gas inlet/outlet nozzle.

Vessel 1 (High Pressure Boiler/Superheater 1) - Vessel 1 contains a high pressure boiler and superheater (Figure 6.9-9). High temperature reactor helium enters the top of the pressure vessel and flows through the superheater. It then joins the liquid lead stream discharge (850°F), flowing downward through the high pressure boiler. Cooled helium leaves the boiler and flows upward along the pressure vessel walls. Helium exits through a side or top gas inlet/outlet nozzle for later circulation.

On the steam/water side, feedwater flows upward through the boiler and then the superheater. During startup conditions, Vessel 1 requires an external supply of saturated steam to the superheater to stabilize cooling flow.

Use or disclosure of data
subject to title page restriction

Vessel 1 Physical Data:

Pressure vessel	
Internal diameter	12.5 ft. (3.8 m)
Overall height	70 ft. (21.3 m)
Material	SA 299 (carbon steel)
Tubing	
Outside diameter	1.000 in.
Minimum wall thickness	0.165 in.
Materials	Ferritic steel
Heating surface, boiler (lower)	8264 sq.ft.
Heating surface, superheater (upper)	8264 sq.ft.

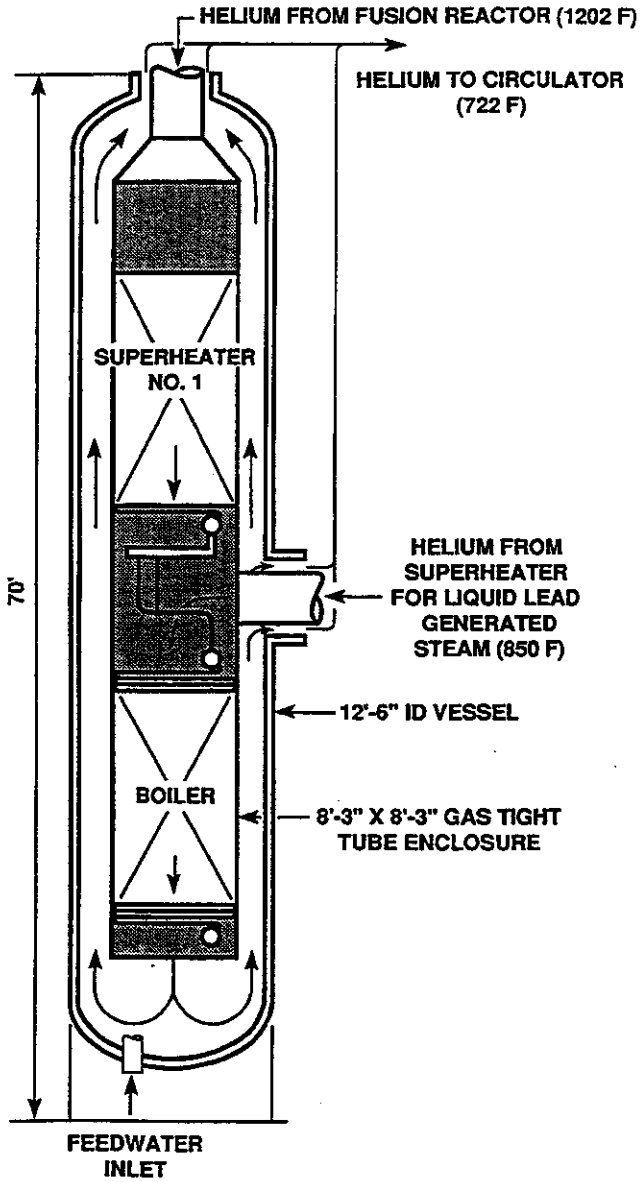

Figure 6.9-7. Vessel #1, Helium Steam Generator

Use or disclosure of data subject to title page restriction

Vessel 2 (Superheater 2) - Vessel 2 contains the heat exchanger transferring heat from the high temperature helium to the steam generated in the liquid lead heated steam generator to raise steam temperature to the final level. Reactor heater helium enters the pressure vessel through an inlet nozzle located at mid-height. Helium flow splits inside the superheater enclosure, flowing upward and downward through upper and lower superheater elements. Cooled helium, exiting each superheater, flows outward between pressure vessel walls and the superheater enclosure. The two cooled helium flows recombine before exiting the pressure vessel. On the steam side, the two superheater sections are arranged in parallel.

Steam enters the vessel from both the top and bottom and flows counter to local helium flow. Superheated steam is extracted from the middle of the pressure vessel.

Vessel 2 Physical Data:

Pressure vessel	
Internal diameter	12.5 ft. (3.8 m)
Overall height	70 ft. (21.3 m)
Material	SA 387 Grade 11
Tubing	
Outside diameter	1.250 in.
Minimum wall thickness	0.200 in.
Materials	Ferritic steel
Heating surface, boiler	21,785 sq.ft.

Vessel 3 (Reheater 1, Reheater 2) - Vessel 3 contains high pressure reheater RH-1 and low pressure reheater RH-2. High temperature reactor helium enters through side nozzles in the upper portion of the pressure vessel. Helium flow splits—half flows upward through RH-1 and half flows downward through RH-2. A second high temperature reactor helium flow, entering at the bottom of the pressure vessel, flows upward over RH-1. Helium cooled through the upper RH-2 reheater flows downward along the pressure vessel walls toward a bottom gas outlet. Helium flow streams of RH-1 and the bottom portion of RH-2 join at the top of RH-1 and flow from there downward along the pressure vessel wall to the gas outlet nozzle.

Vessel 3 Physical Data:

Pressure vessel	
Internal diameter	20.0 ft. (6.1 m)
Overall height	100 ft. (30.5 m)
Material	SA 299 (carbon steel)

Use or disclosure of data
subject to title page restriction

Tubing	
Outside diameter	2.000 in.
Minimum wall thickness	0.120 in.
Materials	Ferritic steel
Heating surface, RH-1	9,450 sq.ft.
Heating surface, RH-2	16,580 sq.ft.

Vessel 3 diameter requires on-site erection. A scheme utilizing two 12.5-ft. diameter RH-1/RH-2 vessels versus a single 20-ft. diameter vessel might offer a cost advantage.

Vessel 4 (Liquid Lead Steam Generators) - Vessel 4 liquid lead is a steam generator system consisting of six identical heat exchangers (Figure 6.9-10). Each heat exchanger utilizes vertical, concentric double wall tubes (Figures 6.9-11 and 6.9-12). High pressure water/steam flows upward through the inner tubes while liquid lead flows downward around the outer tubes. Liquid sodium slowly circulates through the annulus between inner and outer tubes to remove tritium and prevent contamination of the steam.

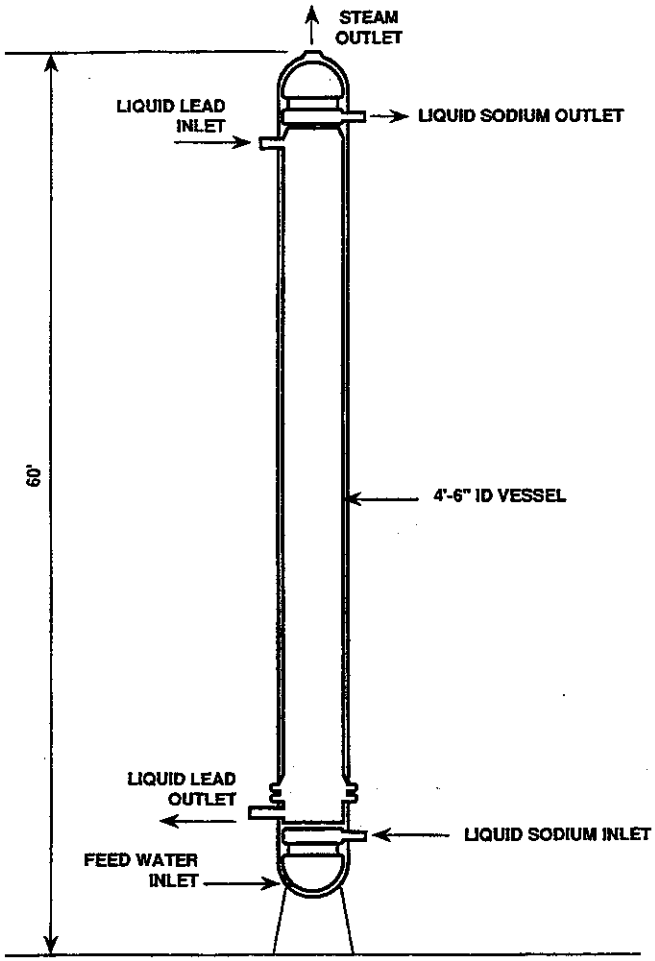

Figure 6.9-10. Vessel 4, Liquid Lead Steam Generator

Use or disclosure of data subject to title page restriction

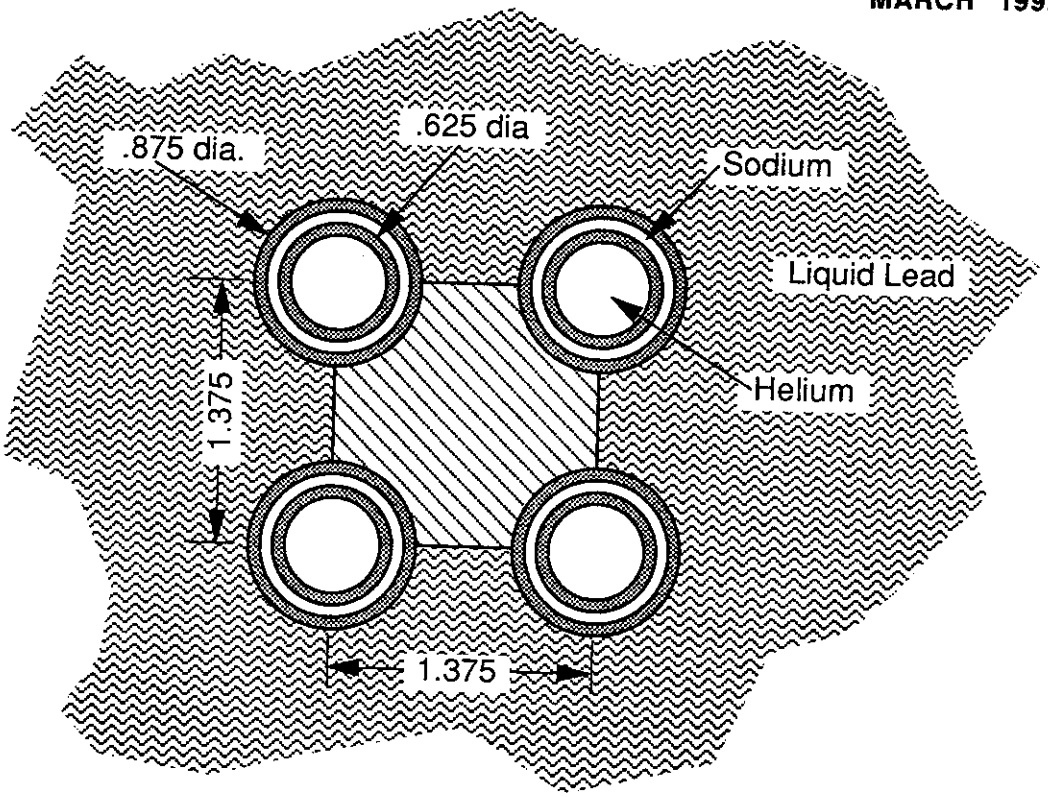

Figure 6.9-11. Liquid Lead Heat Exchanger – Cross Section

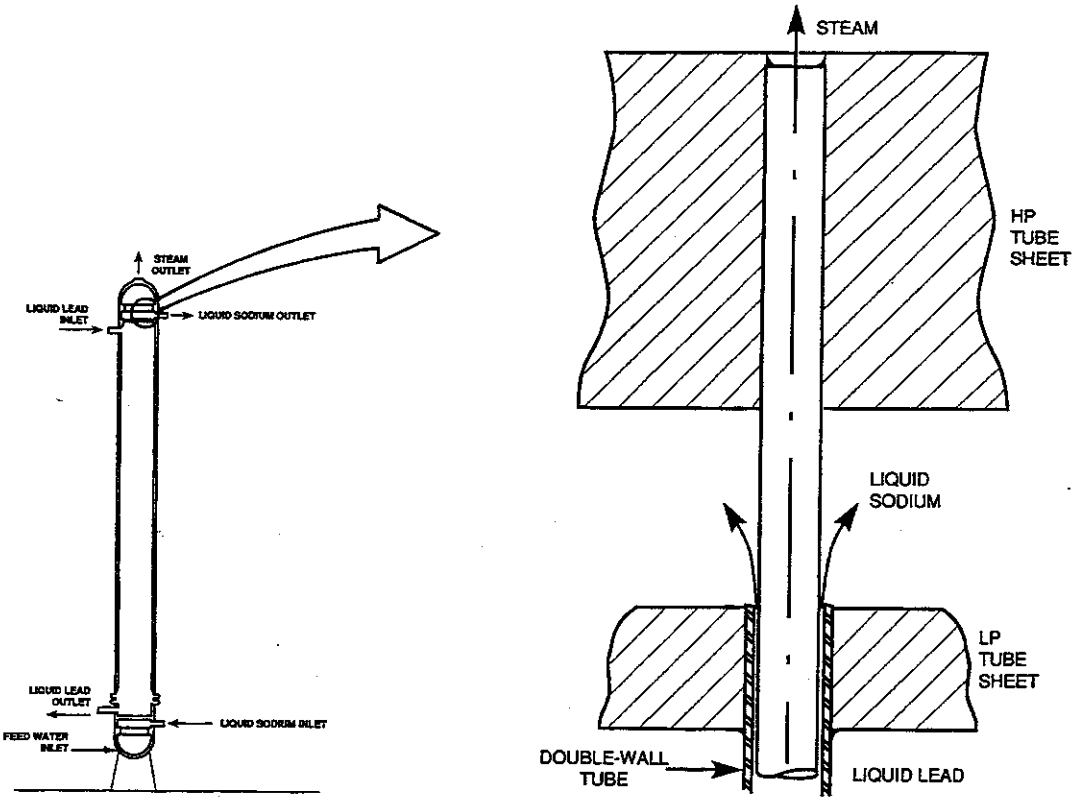

Figure 6.9-12. Liquid Lead Steam Generator – Top Tube Sheet Connections

High pressure feedwater enters the inner tubes, extending between the high pressure tube sheets, through the lower head of the pressure vessel. High pressure steam at 800°F leaves the upper vessel head and flows from there to the helium heated superheater. Liquid lead from the reactor, 977°F, enters the top of the pressure vessel, flows downward, and exits the lower portion of the heat exchanger.

Liquid sodium circulates between high and low pressure heat exchanger tubes. Flow is upward from the vessel bottom to an upper exit (Figure 6.9-12). Tritium is removed at a rate of about 1000 lb/hr and a temperature of 920°F. Detritiated sodium returns to the heat exchanger at a temperature of about 665°F.

A pressure vessel bellows-type expansion section accommodates differential expansion between tubing and shell.

Vessel 4 Physical Data	
Pressure vessel	
Internal diameter	4.5 ft. 1.4 m)
Overall height	60 ft. (18.3 m)
Material	SA 299 (carbon steel)
Inner Tubing	
Outside diameter	0.625 in.
Minimum wall thickness	0.105 in.
Outer Tubing	
Outside diameter	0.875 in.
Minimum wall thickness	0.050 in.
Heating surface	16,800 sq.ft.

(b) Design Options - A number of design options influence the relative size and cost of the steam generation system components. Design options considered were:

(1) Helium reheater vessel and steam generator supply routing in parallel versus in series.

When routed in parallel, the steam generator has approximately 34% less surface while the reheater has respectively 18% and 43% more surface for the high and low pressure sections. Because of the higher pressure requirements of the steam generator which influenced the 9% higher cost per unit heat transfer surface, parallel flow was selected.

Use or disclosure of data
subject to title page restriction

(2) Raise liquid lead heat exchanger stream temperature from 800°F to 900°F.

This reduces the liquid lead system load on the helium heater Superheater 2, releasing additional high temperature helium to the helium steam generator. The result is an increase of 50% in liquid lead steam generator surface and a decrease of 22.5% in helium steam generator surface. This option was rejected due to: (a) the 170% greater surface unit cost of the liquid lead steam generator which results from the double walled tubing, and (b) the difficulty of fitting larger liquid lead steam generators in the more congested area near the reactor vessel.

(3) Raise Turbine Inlet Steam Temperature

Increasing turbine inlet temperature and pressure will tend to improve cycle performance, but as the heat source temperatures are approached by the steam temperature, heat transfer equipment enlarges until crossovers between the hot and cold fluids occur. Holding the throttle pressure at 3715 psia and with parallel flow of helium, it was not possible to raise the throttle temperature to 1000°F without causing LP cold reheat steam temperature to rise above the temperature of helium leaving the reheater. Raising throttle pressure above 3715 psia aggravates this loss of temperature differential. It was, therefore, concluded that, for the available design flows and temperatures of the helium and liquid lead, inlet steam conditions of 3715 psia and 950°F would provide reasonable sizing criteria for the steam generators and reheaters. These reduced steam conditions also result in cost savings for the steam turbine, boiler feed pumps, and piping.

(4) Reduce the cold reheat pressure and temperature to eliminate crossovers of temperature of helium entering the reheater.

Although this permitted a 100°F rise in throttle temperature for the series connection of helium to the reheaters and steam generator, it re-established the low pressure turbine expansion line end point too close to the saturation line (2% moisture). At this new end point location, part load operation can cause the turbine last stage blades to pass higher temperature superheated steam with resulting loss in blade material strength properties and blade overstress. This option was, therefore, rejected.

6.9.7 Helium System Piping

(a) General - All helium piping and manifolds within the bulk shield are generally constructed of SiC. The transition joint from SiC to steel piping is planned to

Use or disclosure of data
subject to title page restriction

be in the region between the vacuum vessel and the shield or directly at the shield wall. Only the aspects of the external steel piping will be discussed in this section. Helium system pipes are pressurized to approximately 200 psig and operate at temperatures between 1202°F and 752°F. Helium entering the circulator and leaving the steam generators is 722°F due to pumping energy. Reactor helium flows through six branch pipes, each 9 ft. (2.7 m) diameter with 1.25 in. (32 mm) walls, at velocities of 170 ft/sec.

Current thick wall pressure vessel design experience in the chemical industry forms a serviceable basis for the helium piping.[3] However, special attention is required in the following areas and those sections of helium pipe at 1202°F.

- Pipe supports and connections need robustness to withstand seismic forces and thermal expansion. Pipe bearing and bending stresses can be controlled by a reduction in pipe support spans. However, pipe supports, anchors, and restraints are major structural assemblies that affect building space requirements. Special pipe connections are required to transmit the large reaction forces between anchors and restraints to the high temperature pipe.

- Vibration caused fatigue failure must be addressed. Flow induced vibrations are possible at fittings, internal bracing, and the helium circulator. Pipe reinforcement must be considered to stiffen local wall sections.

- Helium Pipe Isolation Valves - No industrial experience base addresses the combination of high temperature, large size (9' diameter) and leak-tight containment of 200 psig helium.

  Current technology industrial butterfly valves[4,5] can be adapted to meet the above criteria; e.g., for control of leakage from the system envelope, valve package can be modified by encasement of the valve stem in a bonnet that is pressurized with an external source of helium. For control of gas leakage past a closed isolation valve, metallic stressed seals have been used by one manufacture for temperatures to 650°F and to sizes of 216 in. (5.5 m) at a gas pressure of 18.8 psia. This arrangement consists of a thin annular metal band in the valve body which is inflated against the closed disk by a pressurized inert gas.[6]

  Upgrading the capability of such features to operate under the combined helium temperature and pressure conditions of a fusion power plant would require further engineering and testing.

(b) Pipe Sizing - The velocity and pressure loss rate criteria for sizing the helium piping was reviewed in terms of annualized capital costs for the helium

Use or disclosure of data
subject to title page restriction

circulators, value of energy use by the circulators, and the annualized cost of the helium piping system.

Pipe weight and installed cost are based on system wall thickness, hot and cold sections, plus a $21 per lb. unit cost. Piping materials assigned to the hot and cold sections were SA 407 Alloy 800H and SA 213T91, respectively. Seven supply pipe sizing velocities, from 100 ft/sec to 300 ft/sec, were investigated. Return pipe sizing velocities were reduced, 10 to 20 ft/sec, in order to maintain about the same pressure drop gradient.

Annual circulator energy cost was approximated using a plant capacity factor of 0.8 and energy cost of $.07/kWh. The steam turbine-driven axial helium compressors were assigned a polytropic efficiency of 88% and unit price of $400 per shaft kilowatt.

Indirect cost factors were 52% of Total Direct Cost (TDC), contingency 10% of TDC and Annual Fixed Charge Rate 10% of TDC.[8]

Minimum total annual cost occurs with supply pipe sizing velocities of 160 to 170 ft/sec. (reference Table 6.9-3 and Figure 6.9-13) when circulator power is 116 to 119 MW.

Pressure drops in Table 6.9-3 refer to external system piping which varies according to pipe size. However, total circulator duty is after addition of the following values:

	psi
Steam generator	3.50
Reactor headers	1.45
Reactor	3.63
Subtotal	8.58

Table 6.9-3 Helium Pipe Costs

Helium Velocity (Ft/Sec)		Piping Pressure Drop	Total Pressure Drop	Pipe Weight	Circulator Power	Annualized Cost (10^6 Dollars)			
Supply	Return	(Psi)	(Psi)	(1000 lb)	(MW)	Energy	Circ	Pipe	Total
300	280	6.96	15.54	3642	176.3	86.5	11.4	14.9	112.8
240	220	4.19	12.77	4585	144.4	70.8	9.4	18.7	98.9
200	180	2.81	11.39	5584	128.6	63.1	8.3	22.8	94.2
170	150	1.96	10.54	6571	118.8	58.3	7.7	26.8	92.8
160	140	1.71	10.29	6947	116.0	56.9	7.5	28.4	92.8
140	125	1.37	9.89	7897	111.4	54.6	7.2	32.2	94.1
100	90	0.67	9.25	10925	104.1	51.1	6.7	44.6	102.4

Use or disclosure of data subject to title page restriction

(c) Valving - Valves are positioned at key locations in the helium distribution system to support both operation and safety procedures. Valves permit maintenance and repair isolation of components while the system continues operation. Valves are essential to either startup or shutdown during normal or emergency conditions. Butterfly valves are assigned key locations in the Prometheus system (see Table 6.9-4).

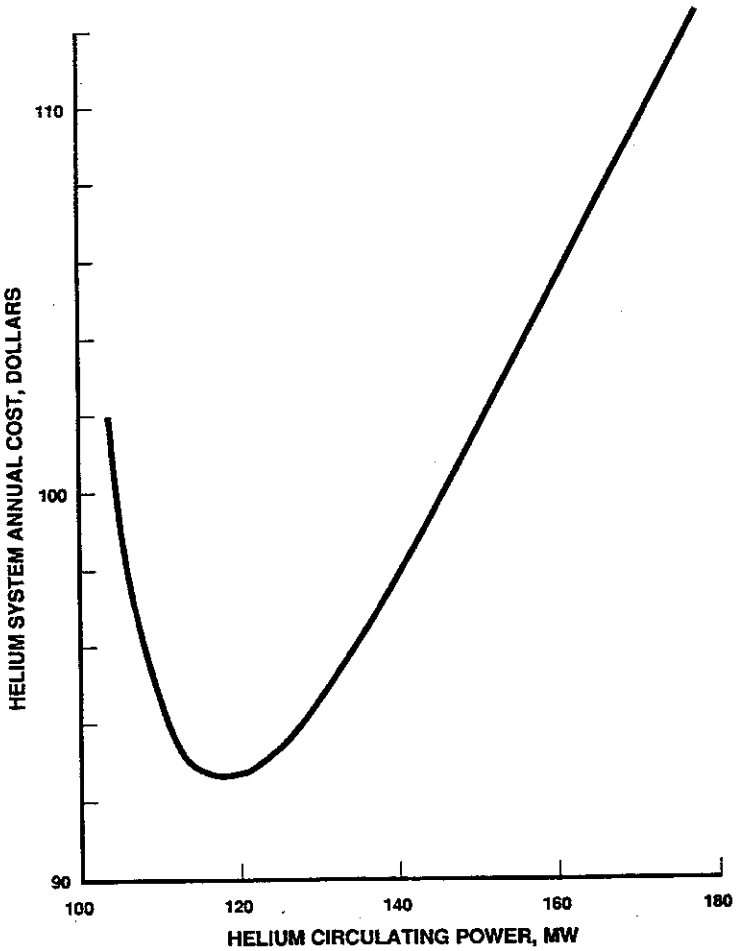

Figure 6.9-13. Helium System Cost vs. Circulating Power

Table 6.9-4. Key Helium System Valves

Location	Diameter (Inches)	Operating Temperature (°F)	Total Number Required
Supply Branches From Reactor	110	1202	6
Helium Steam Generators, In	78	1202	6
Helium Steam Generators, Out	68	722	6
Helium Reheaters, In	78	1202	6
Helium Reheater, Out	68	722	6
Helium Superheater 2-In	60	1202	6
Helium Feedwater Heaters, In	74	890	2
Helium Feedwater Heaters, Out	72	630	2
Helium Circulators, In	96	722	6
Helium Circulators, Out	96	752	6

Use or disclosure of data
subject to title page restriction

6.9.8 Liquid Lead System Piping - The lead piping and manifolds within the bulk shield are generally constructed of SiC. The transition joint from SiC to steel piping is planned to be in the region between the vacuum vessel and the shield or directly at the shield wall. Only the aspects of the external steel piping will be discussed in this section. The external liquid lead piping system uses martensitic alloy HT-9, 12 Cr-1 Mo steel and 0.48% nickel, with high resistance to liquid metal embrittlement.

Liquid lead operational limits (temperature) are predicated on corrosion rates of 5 micron/year. However, the corrosion rate varies by a factor of 10 from 3 ft/sec (low) to 23 ft/sec (high) flow velocities.[7]

A high liquid lead temperature, 977°F (525°C), is acceptable when considering liquid lead and ferritic or martensitic steel interactions. Further investigation will confirm and quantify these interactions as a function of temperature, flow velocity, and pipe metallurgy.

Prometheus liquid lead distribution piping was sized at 9.8 to 11 ft/sec. Individual 24-in. (61 cm) pipes supply each of six steam generators with pressure gradients of approximately 4 psi/100 ft. and a 180 psi friction loss.

References 6.9

1. M. S. Tillack, et al., "Initial Design of the Prometheus Wetted Wall IFE Reactor Cavity," UCLA-FNT-51, October 1991.

2. R. C. Spencer, "Design of Double Reheat Turbines for Supercritical Pressures," American Power Conference, April 1980.

3. Personal Communication, Nooter Corp.

4. Personal Communication, Henry Pratt Co.

5. Personal Communication, ITT Engineered Values, Inc.

6. J. C. McLane, Jr., "Large Butterfly Valves in the Propulsion Wind-Tunnel Facility at Arnold Center", Aviation Conference of American Society of Mechanical Engineers, March 1961.

7. N. M. Ghoniem, J. Blink, N. Hoffman", Selection of Alloy Steel Type for Fusion Power Applications in the 300°-500°C Temperature Range," Proceedings of Topical Conference on Ferritic Alloys for Use in Nuclear Energy, American Institute of Metallurgical Engineers, 1984.

Use or disclosure of data
subject to title page restriction

8. D. S. Zuckerman, D. E. Driemeyer, L. M. Waganer, D. J. Dudziak, "An Induction Linac Driven Heavy Ion Fusion Systems Model," p. 217, Fusion Technology, Vol. 13, February 1988.

9. C. F. McDonald and C. P. C. Wong "Closed Cycle Gas Turbine Applications for Fusion Reactors," GA-A16025, GA Technologies, Inc., August 1980.

10. M. H. Hasan, et. al, "Thermal Cycle Power Conversion for the Aries - I Tokamak Reactor," IEEE, 1989.

Use or disclosure of data
subject to title page restriction

6.10 Balance of Plant Systems

The Prometheus balance of plant (BOP) systems do not differ significantly from the BOP systems of a conventional fission nuclear power plant. The main purpose for including the BOP systems in the discussion is to ensure that all systems have been accounted for in the cost estimates.

The Prometheus BOP systems have been divided into four classes: Water Systems, HVAC Systems, Electrical Systems, and Auxiliary Systems. In addition to the BOP systems, there are numerous site preparation activates which are customarily performed by the BOP organization. These site preparation activities are briefly discussed following the descriptions of the BOP systems.

6.10.1 Water Systems

6.10.1.1 Circulating Water System - The Circulating Water System (CWS) provides the main condenser with a continuous supply of cooling water for removing the heat rejected by the main turbine, reactor feedwater pump, turbine, and main turbine bypass system over the full range of plant operating loads.

The CWS's function is to take cold water from the cooling tower basin, pump it through the condenser whereupon it is heated, and transport the heated water back to the cooling tower where it is cooled.

6.10.1.2 Closed Cooling Water System - The Closed Cooling Water System (CCWS) transfers heat rejected from reactor auxiliary equipment and components of the power conversion system to the Auxiliary Service Water System. The CCWS shall be designed to perform the following specific functions:

- Provide required cooling water to reactor, driver, auxiliary, and power conversion equipment during all modes of normal operation.
- Operate under a reduced load requirement in the event of loss of off-site power to maintain a continuous supply of cooling water to certain auxiliary equipment still requiring heat removal.
- Provide a closed cooling water loop between non-essential systems which potentially contain tritium and the auxiliary service water used for cooling, thus presenting an additional barrier between the potentially contaminated systems and the cooling water discharged to the environment.
- Provide sufficient redundancy and flexibility of components such that the system will be continuously able to perform its required cooling functions during all modes of normal plant operation.

Use or disclosure of data
subject to title page restriction

6.10.1.3 Auxiliary Service Water System - The Auxiliary Service Water System provides a continuous supply of cooling water for removing heat rejected by the Closed Cooling Water System (CCWS). The waste heat is transported by the Auxiliary Service Water System to the condenser cooling water outlet block, where the hot service water is combined with the hot cooling water. From there, the water flows to the cooling tower hot water distribution system where the rejected heat is transmitted to the air and the water is collected in the basin.

In the event of a CCWS heat exchanger tube failure, the auxiliary service cooling water operating pressure in the tube side will always be lower than that of the closed cooling water in the shell side, eliminating the possibility of leaking water into the demineralized water system.

6.10.1.4 Demineralized Water Makeup System - The objective of the Demineralized Water Makeup System is to take water from a natural source and produce water of a quality and quantity for pre-operation and normal operation of Prometheus. The Demineralized Water Makeup System provides water for the decontamination station, condensate makeup, laboratories, closed cooling water system makeup, and any other requirements where contamination is not acceptable.

6.10.1.5 Potable Water System - The Potable Water System provides the plant site with water suitable for human consumption. Depending on the source, water can sometimes be used without treatment or a complex variety of treatments may be required. In any case, the system must be designed to meet U.S. Public Health Drinking Water Standards as well as any local ordinances which may supersede the national requirements. The Potable Water System provides water of safe, sanitary quality and attractive for consumption by having the proper turbidity, color, taste, and odor.

6.10.1.6 Essential Services Cooling Water System - The Essential Services Cooling Water System (ESCWS) provide a reliable source (Ultimate Heat Sink - UHS) of cooling water for plant auxiliaries which are required for a safe reactor shutdown or to mitigate the consequences of an accident. These functions are performed during systems testing and abnormal plant operation only.

The ESCWS has been designed to:

(a) Circulate cooling water through heat exchangers which are required for safe shutdown conditions.
(b) Remove heat from plant equipment required for safe shutdown conditions.
(c) Condense reactor steam during hot standby when the main condenser is not available.

Use or disclosure of data
subject to title page restriction

(d) Provide an emergency backup source of makeup water to the spent fuel storage pool-system in the event the primary source of water is not available.
(e) Provide a means of flooding the drywell and containment, if required.
(f) Provide a means of preventing the leakage of radioactive contamination within the Reactor Heat Removal (RHR) system to the outside environment.

The Ultimate Heat Sink has been designed to:

(a) Provided a source of cooling water to dissipate reactor decay heat and essential cooling system heat loads after a normal reactor shutdown or a shutdown following an accident.
(b) Provide cooling water to permit safe shutdown and cooling down of the unit and maintain it in a safe shutdown condition.

6.10.1.7 Main Cooling Tower - A natural draft wet (hyperbolic) cooling tower of either cross-flow or counterflow design provides a cold water source for the Circulating Water System (CWS) and the Auxiliary Service Water System (ASWS).

The stack effect of the tall hyperbolic tower, approximately 525 ft. high, creates an air flow through which warm water from the condenser and the various heat exchangers of the Closed Cooling Water (CCW) system is passed. A small part of the water (approximately 2.8 percent) evaporates, cooling the remainder.

The cooling tower installation shall be designed for a wet bulb of 78°F and a relative humidity of 50 percent. Since the cooling tower shall serve both the CWS and the ASWS, the flows, duties, and temperature rises of both systems shall be considered in establishing the design data. The degrees approach is determined by economic evaluation of Condenser, Circulating Water, Auxiliary Service Water, and Cooling Water Systems. Design data and parameters for the Cooling Tower System are presented in Table 6.10-1.

6.10.1.8 Cooling Tower Water Treatment System - The object of the Cooling Tower Water Treatment System is to avoid loss in heat transfer and to prevent corrosion. The main functions of this system are:

(a) Control deposition of calcium salts thus preventing scale formation.
(b) Control delignification of tower wood.
(c) Prevent slime and algae growths to control biological fouling.
(d) Prevent tuberculation.
(e) Control corrosion due to acidic pH.

Use or disclosure of data
subject to title page restriction

Table 6.10-1. Cooling Tower System Design Parameters

Design Wet Bulb Temperature	78°F
Relative Humidity	50%
Maximum Cooling Duty	8,652 x 10^6 Btu/hr
Inlet Flow	603,100 gpm
Maximum Inlet Temperature	122.57°F
CWS Outlet Flow	555,600 gpm
CWS Maximum Outlet Temperature	94°F
CWS Temperature Range	28.6°F
CWS Approach	16°F
ASWS Outlet Flow	47,600 gpm
ASWS Maximum Outlet Temperature	90°F
ASWS Temperature Range	32.6°F
ASWS Approach	12°F
Maximum Evaporation	16,957 gpm
Blowdown and Drift Losses	8,469 gpm
Makeup to Power	25,425 gpm

Due to evaporation and drift losses, concentration of total solids and total alkalinity increases in the recirculation water. To prevent deposition of solids, recirculating water has to be blown down. The volume of blowdown depends on the number of cycles of concentration which depends on the quantity of calcium, magnesium, iron and silica present initially in the water.

Close control of pH is necessary to maintain the water at a balanced pH level which is sufficient to prevent excessive scaling but not so low that the water becomes corrosive due to excessive acidification. The optimum pH can be calculated by using the Langlier index. Normally sulfuric acid will be needed to adjust the pH. To meet the emergency of water becoming acidic, provision should be made in the system for the addition of caustic.

6.10.1.9 Condensate Storage System - The Condensate Storage System (CSS) functions as the storage and transfer medium for the reactor-turbine generator primary fluid. The functions of the CSS are:

(a) To ensure the operating level of condensate in the main condenser hotwell.
(b) To serve as a reservoir for excess condensate from the Condensate and Feedwater System during load changes and effluents from the FPCCS and Liquid Radwaste System.
(c) To provide water for the Condensate and Feedwater System fill, Auxiliary Steam System makeup, and Condensate Demineralizer Cleanup System regeneration.

Use or disclosure of data
subject to title page restriction

6.10.1.10 Chilled Water System - The Chilled Water System provides the cooling medium for the air cooling coils in systems where the closed cooling water and services water systems do not meet the requirements of temperature and availability. Two distinct systems are provided: Essential Services Chilled Water System and Normal Chilled Water System. The former serves safety related systems. The latter serves all other air cooling coils requiring chilled water.

The Chilled Water System has been designed to do the following:

(a) Shall supply chilled water to the air cooling coils in systems where the closed cooling water and service water systems do not meet the requirements of temperature and availability.
(b) Will meet function (a) assuming a single failure.

6.10.1.11 Chlorination System - The objective of the Chlorination System is to prevent fouling of condenser tubes, Component Cooling Water (CCW) heat exchanger surfaces, and associated piping by controlling biological growth in the Circulating and the Auxiliary Service Water Systems.

Chlorine is injected intermittently at a dosage which will ensure a 0.1 to 1 ppm chlorine residual downstream of the condenser and CCW heat exchanger surfaces.

The function of the Chlorination System is as follows:

(a) To control biological growth in the circulating and auxiliary service water system including condensers, component cooling water (CCW) heat exchanger surfaces, and associated piping.
(b) To maintain during chlorine treatment a specified residual chlorine level (in the range of 0.1 to 1 ppm, depending upon the chlorine demand of the circulating water and auxiliary service water) at the condenser and CCW heat exchanger outlet which ensures complete treatment of the circulating water.
(c) To be usable on a routine basis and not require specific testing to ensure operability.

6.10.1.12 Sanitary Waste System - The objective of the Sanitary Waste System is to treat all sanitary wastes from the plant site in a "packaged" extended aeration facility with subsequent chlorination. The effluent quality shall meet, as a minimum requirement, all discharge levels set by the local Environmental Protection Agency regarding sanitary plant discharges and as set forth in the plant's operating permit.

The Sanitary Waste System is designed to provide a facility to preclude the possibility of releasing any untreated plant sanitary wastes to the environment.

Use or disclosure of data
subject to title page restriction

The Sanitary Waste System is also designed to provide effluent quality as set forth in the Process Requirements section. It consists of secondary treatment and will include advanced treatment when there are local ordinances requiring further treatment.

In addition to any applicable local regulations regarding the effluent quality, the system reduces the organic waste load (as measured by the biochemical oxygen demand test by at least 85 percent based on a 5-consecutive day average of value), removes practically all of the suspended solids, is odor free, provide disinfection, provides for periodic removal of accumulated sludge, and reduces the quantities of oils, greases, acids, alkalis, toxic, taste and odor producing substances, color, and other substances.

6.10.1.13 Cooling Tower Makeup System - The objective of the Cooling Tower Makeup System (CTMS) is to provide makeup water to the cooling tower basin, accounting for evaporation, drift, and blowdown losses which occur during cooling tower operation over the full range of plant operating loads throughout the year. The Cooling Tower Makeup System also provides screened and strained water to the Screen Wash System.

The Cooling Tower Makeup System (CTMS) will take off-site water, screen it, strain it, and transport it to the cooling tower basin and, when required, to the Screen Wash System. The off-site source of water is an independent reliable water source, which shall supply makeup water to serve as circulating and auxiliary services water (for the purpose of cooling various equipment in the power plant) to compensate for evaporation, drift, and blowdown losses occurring during cooling tower operation.

The flow capability of the Cooling Tower Makeup System (CTMS) has been based on the requirement to maintain a cooling tower basin water inventory. The quantity of the makeup water was determined by totaling all the water losses due to cooling tower natural evaporation, drift, and basin blowdown during cooling tower operation. Only the amount of blowdown shall be altered by opening or closing the blowdown valve, thus changing the ratio of solids in the cooling tower basin to the solids in the makeup water, which shall also be called cycles of concentration.

Continuous blowdown from the cooling tower basin is required to maintain a controlled, dissolved solid ratio of 3 cycles of concentration, which shall be the design condition of the system.

6.10.1.14 Turbine Building Closed Cooling Water System - The Turbine Building Closed Cooling Water System (TBCCWS) consists of pumps, piping, and various heat exchange components. Forming a closed loop, utilizing demineralized water as the transfer medium, the system transports coolant to and from the heat

Use or disclosure of data
subject to title page restriction

exchange components of the Power Conversion System. The TBCCWS transfers the heat acquired in these various components to the Auxiliary Service Water System.

The function of the TBCCWS is to transport to the Auxiliary Service Water System the heat rejected from auxiliary plant equipment associated with the Power Conversion System over the range of normal operation.

The TBCCWS shall be operating as a low energy cooling water system and shall have the heat transfer capability needed to satisfy the requirements of all Power Conversion System components. The system's sole operating mode shall be that of normal plant operations which shall include normal startup and shutdown.

6.10.1.15 Steam Generator Blowdown System - The Steam Generator Blowdown System is part of the overall condensate water-quality control program. Overall secondary chemistry control is accomplished by (a) close control of feedwater to limit impurities that can be introduced (e.g. use of stainless steel in feedwater heaters, condensate demineralization, etc.); (b) chemical addition to establish and maintain proper environment to minimize corrosion; and (c) control in the steam generator blowdown. The Steam Generator Blowdown System removes part of the condensate side waste from each steam generator, cools and filters it after reducing both temperature and pressure, and delivers it to the Condensate System for purification in the Condensate Demineralizer System.

The steam generators tend to concentrate impurities in the secondary side in areas where there are restrictions, low velocities, and other effects which promote deposits and scale. The function of the Steam Generator Blowdown System is to remove particulate magnetite from the system, thus reducing the load on the Condensate Polishing System.

The Steam Generator Blowdown System is part of a continuous-operating closed loop and it continuously purifies these side streams before the water is reintroduced into the process.

It is not required for accident mitigation, offsite dose control, or safe shutdown. It is not a primary nuclear safety related system.

The process requirements of the Steam Generator Blowdown System shall be:

(a) By blowdown flow regulation, to maintain steam generator secondary chemistry parameters (e.g., pH, free hydroxide, cation conductivity, etc.) within control limits for normal operation and anticipated operational occurrences (such as a condenser tube leak).
(b) To process the blowdown through an electromagnetic filter to remove greater than 90% of particulate magnetite, and greater than 60% of the nonmagnetic oxides present in the blowdown.
(c) To operate at all modes of plant operation from no load to full power.
(d) To accommodate the requirements of steam generator wet layup (including N_2 purge) and Condensate and Feedwater System startup and cleanup recirculation.
(e) To provide a means of sampling a steam generator effluent for chemistry control.
(f) To meet the requirements of NRC Standard Review Plan 10.4.8 "Steam Generator Blowdown System" and Branch Technical Position - ETSB 11-1 "Design Guidance for Radioactive Waste Management Systems Installed in Light-Water Cooled Nuclear Power Reactor Plants."

6.10.1.16 Fresh Water Supply System - The Fresh Water Supply System maintains the required reserve of water for the Fire Protection System, while supplying fresh water to the Demineralized Water Makeup System and the Potable Water System. The Fresh Water Supply System takes its supply from the source of off-site water (river, lake, or well) and feeds two large fresh water-fire protection tanks, each with the capacity that includes the reserve volume recommended by the NRC Branch Technical Position APSCB 9.5-1 "Guidelines for Fire Protection for Nuclear Power Plants."

6.10.2 HVAC Systems - Heating, ventilation, and air conditioning (HVAC) systems are provided as required throughout all areas of Prometheus for personal comfort, personal safety, and protection of equipment. The HVAC systems are designed for the specific functional requirement of each building and/or room, including redundant Seismic Category I trains for essential systems.

Ventilation systems are division specific so that fire or smoke in an area containing a safety related division of equipment cannot migrate through the ventilation ducts to an area containing the redundant division of safety related equipment. Fire dampers are installed in fire-rated barriers and have the same fire resistance rating as the barrier.

6.10.2.1 Control Complex Air Conditioning System - The Control Complex Air Conditioning System is designed to maintain the environment in the Control

Use or disclosure of data subject to title page restriction

Complex envelope within acceptable limits for the operation of unit controls, for maintenance and testing of the controls required, and for uninterrupted safe occupancy of the Control Complex during post-accident shutdown. The Control Complex consists of the main control area, the technical support center, the computer room, the electric switchgear rooms, offices, and mechanical (including HVAC) support equipment areas. The Control Complex is shown on Figure 6.10-1.

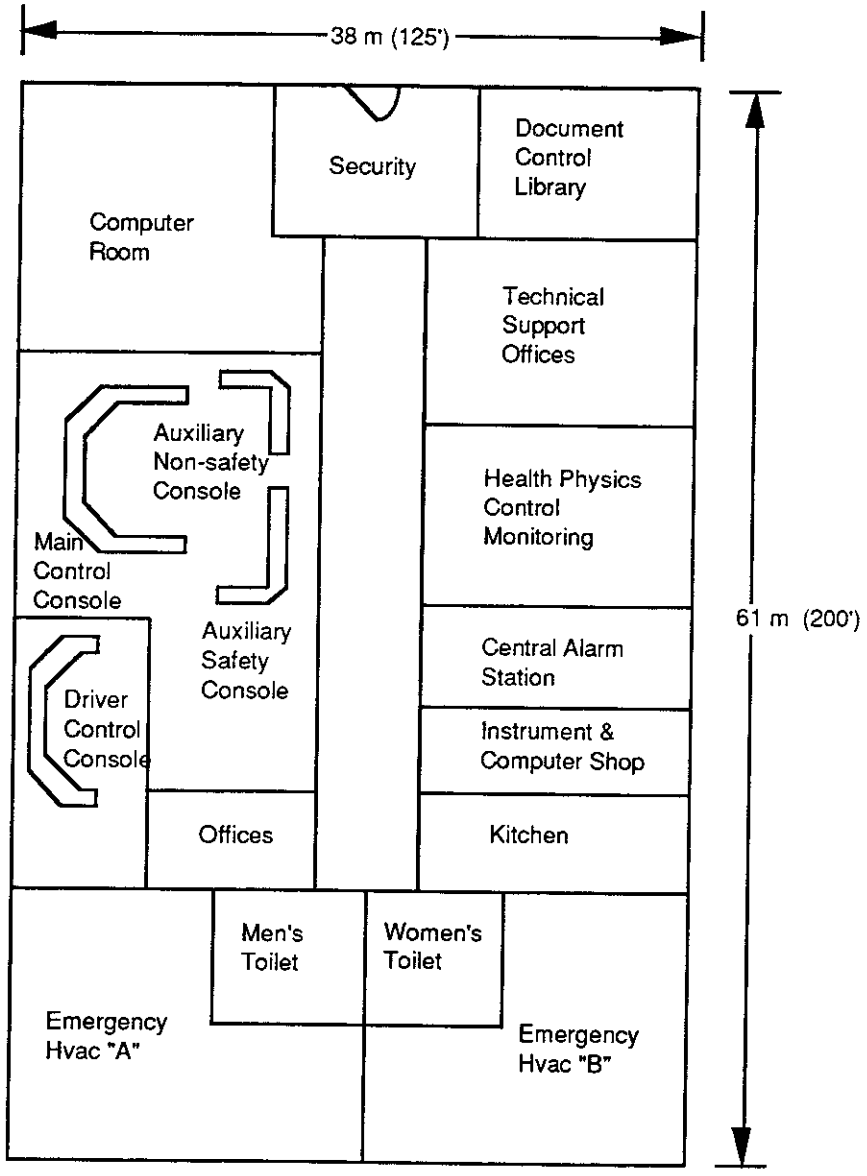

Figure 6.10-1 Prometheus Control Complex

The Control Complex Air Conditioning System consists of two physically separated essential portions, each of which is capable of maintaining habitable conditions in the Control Complex envelope. Each essential portion consists of an air conditioning unit and an atmospheric cleanup unit. The two portions are connected to common supply

Use or disclosure of data subject to title page restriction

and return ductwork, a normal operation outside air intake, normal exhaust fans, and two widely separated emergency outside air intakes which are normally closed. The system maintains the Control Complex at a positive pressure relative to the surrounding areas during normal operation. Following an atmospheric release of radioactivity or toxic gas, the normal operation outside air intake and exhaust openings are sealed automatically and recirculation through the atmospheric cleanup unit begins. Provisions are designed so that a small amount of outside air can be safely introduced into the Control Complex for respiration and pressurization.

A smoke purge fan is provided for the Control Complex to assist rescue and fire fighting efforts. The smoke venting is designed on the basis of manual execution by a well trained plant fire brigade. Infiltration of outside air through an open emergency exit door of the Control Complex envelope is used as a means to allow replacement of the vented air.

The Control Complex air conditioning system has been designed to:

- Maintain the Control Complex ambient temperature and humidity within comfort ranges.
- Maintain a safe chemical environment within the Control Complex envelope for respiration and comfort of the occupants.
- Maintain the Control Complex envelope under positive pressure relative to the surrounding areas at all times during normal operation.
- Provide a means to isolate the Control Complex from the surrounding atmosphere following an accident.
- Provide a means to maintain the Control Complex envelope under positive pressure relative to the surrounding atmosphere at the discretion of the operator following an accident.
- Limit infiltration of contaminated air into the Control Complex envelope and provide air cleanup such that the radiological and toxic gas exposures of personnel following an accident do not exceed allowable limits.

6.10.2.2 Containment Cooling System - The Containment Cooling System basic design objectives are to maintain proper containment thermal environment for personnel, the Steam Supply System, and structures during the normal plant operation, during shutdown periods, and following simultaneous losses of the normal plant onsite and offsite power sources.

The Cooling System is designed to remove heat from the containment atmosphere by the use of low temperature cooling water generated by the normal plant Chilled Water System during the normal plant operation and during shutdown periods. The Cooling System recirculates air in the upper containment through air-to-water heat exchangers

Use or disclosure of data
subject to title page restriction

and directs air from the upper containment to various heat producing enclosed spaces. Heat, which is carried out from the Containment by the chilled water, is transferred to the Auxiliary Service Water System for disposal at the plant main cooling tower. Following an emergency condition, the chilled water will be bypassed and the auxiliary service water will be used directly for the containment cooling.

The Cooling System consists of a number of recirculating-type fan coolers located above the containment operating floor and a number of localized fans to direct cool air from the upper containment to heat producing spaces.

The Cooling System is not used for the containment post-accident heat removal as this function is taken entirely by the Containment Spray System. The Containment Cooling System is designed and supported to withstand effects of the design basis earthquake and the post-accident pressure transient, thereby assuring that integrities of the reactor protection system and the post-accident heat removal system will not be impaired.

6.10.2.3 Containment Atmosphere Purification and Cleanup System - The Containment Atmosphere Purification and Cleanup System is designed to limit concentrations of airborne radioactive materials in the containment to levels below those required for personnel access during shutdown. The system does not provide for post-accident atmosphere cleanup.

If air were used in the reactor building in close proximity with the reactor cavity, it would become activated due to production of ^{14}C, ^{16}N, and ^{41}Ar. An analysis of this concern was conducted and reported in the STARFIRE report.[1] The inerting gases considered were helium, nitrogen, and carbon dioxide. Helium was eliminated due to cost and excessive leakage. Nitrogen and carbon dioxide were compared to air to determine the best choice. Both air and nitrogen remain highly radioactive due to the presence of ^{14}C for long periods of time (> five years). On the other hand, carbon dioxide is higher during operation but decays to acceptable levels immediately (< 10 minutes) after shutdown.

The Containment Atmosphere Purification and Cleanup System consists of an internal recirculation cleanup system, a low volume purge system, and a high volume purge system. During normal operation, the recirculation cleanup units recirculate the atmosphere through high efficiency particulate filters and a vapory recovery system to remove particulates and tritium from the atmosphere. Section 6.7.6 covers this topic in detail.

6.10.2.4 Auxiliary Building Ventilation System - The Auxiliary Building Ventilation System consists of a general supply and exhaust ventilation system that

Use or disclosure of data
subject to title page restriction

performs heat removal and air exchange functions. The ventilation system is supplemented by individual cooling units and ventilation system fans that serve essential mechanical equipment areas. The essential mechanical equipment room cooling systems are designed to maintain the space temperatures below 100°F at times when the served equipment must operate. At least one train of essential mechanical equipment rooms is maintained below 100°F, assuming a single failure of an active component concurrent with a loss of offsite power. Exhaust fans are powered from the diesel generators.

The essential mechanical equipment room cooling systems perform the required safety function following a safe shutdown earthquake and are able to withstand the effects of appropriate natural phenomena such as tornadoes, floods, and hurricanes.

The essential mechanical equipment room cooling systems are protected from the effects of internally generated missiles, pipe break effects, and water spray.

The Auxiliary Building Ventilation System is separated according to divisions with each 50% exhaust system containing a filter train complete with particulate filters and carbon adsorbers and two fans. The Auxiliary Building essential HVAC system is designed to limit the offsite and control room dose following an accident within the guidelines of 10CFR Part 100 and Standard Review Plan Section 6.4, respectively.

6.10.2.5 Driver Ventilation System

6.10.2.5.1 Laser Building Ventilation System - To enable the laser to operate properly, the laser building will be filled with argon to a nominal one atmosphere. If there is a problem with activation of the argon, carbon dioxide could be used if it is compatible with the laser operation. The use of an inert atmosphere will not be a problem during operation of the driver; however, during maintenance periods requiring human access, suited workers will be employed or the atmosphere will be exchanged with dry, clean air.

6.10.2.5.2 Accelerator Tunnel Ventilation System - The Accelerator Tunnel Ventilation System is designed to maintain the ambient conditions which are suitable for the accelerator and to heat the tunnel during a plant winter shutdown. The system exhausts air from the tunnel, causing an equal quantity of outside air to infiltrate into the tunnel to replace the amount that is exhausted. Exhausted air quantities are determined from the amount of outside air required to absorb heat dissipated by the accelerator equipment and give the desired temperature rises. During a plant winter shutdown, the system purges the tunnel with a minimum amount of outside air and provides heat to maintain the ambient temperature.

Use or disclosure of data
subject to title page restriction

The Accelerator Tunnel Ventilation System consists of power roof ventilators, roof mounted smoke vents, outside air intake louvers, localized fans to disperse air in congested areas, and electric unit heaters.

6.10.2.6 Turbine Building Ventilation System - The Turbine Building Ventilation System is designed to maintain the ambient conditions which are suitable for the steam electric power conversion process and to heat the building during a plant winter shutdown. The system exhausts air from the building, causing an equal quantity of outside air to infiltrate into the building to replace the amount that is exhausted. Exhausted air quantities are determined from the amount of outside air required to absorb heat dissipated by the turbine generator equipment and give the desired temperature rises. During a plant winter shutdown, the system purges the building with a minimum amount of outside air and provides heat to maintain the ambient temperature.

The Turbine Building Ventilation System consists of power roof ventilators, roof mounted smoke vents, outside air intake louvers on the building walls, localized fans to disperse air in congested areas, exhaust fans for the battery room and filtering equipment areas, and electric unit heaters.

6.10.3 Electrical Systems

6.10.3.1 DC Electrical Systems - The DC Electrical Systems provide uninterrupted stored power for control, instrumentation, and miscellaneous small loads throughout the plant during all normal and abnormal operating conditions. The functions of the various DC systems are as follows:

- Safety related 125 VDC systems will supply operating and control power to safety related switchgear, emergency diesel generator field flashing and control, and power to safety-related DC motor operated valves. They will also supply power to DC safety-related instrumentation and selected emergency lighting.

- Non-safety related 125 VDC systems will distribute operating and control power to turbine generator loads, non-safety related switchgear, and plant non-safety related loads and instrumentation.

The scope of the DC Electrical Systems includes the batteries, battery racks, battery chargers, switchgear, and distribution systems, complete with controls and instrumentation.

6.10.3.2 Standby Power Supply Systems - There are three separate on-site standby generating systems, each associated with one safety-related system. These

systems provide power for safety-related electrical loads required during loss of the preferred source of power. The scope of each system includes the diesel engine and its auxiliaries, the generator and excitation equipment, and the mainleads from the generator terminals, up to but not including the outgoing power circuit breaker.

Each standby generating system shall be designed to start automatically and to provide power to those safety-related electrical loads which are needed to achieve safe shutdown of the plant and to maintain it in the shutdown condition, and/or to mitigate the consequences of a loss of coolant accident in the event of a coincident loss of the preferred power supply. Such power availability assures that:

(a) Reactor coolant pressure boundary design conditions are not exceeded.
(b) The reactor core is cooled.
(c) Containment integrity is maintained.

The standby power generating system shall consist of diesel engine driven generators. Each diesel generator shall have a compressed air starting subsystem which is capable of starting its diesel engine within a specified time. The diesel generator shall then provide power for starting, accelerating, and supplying power to the safety-related electrical loads associated with its division. Power from each diesel generator shall be distributed through safety-related medium voltage (4.16 kV) switchgear.

6.10.3.3 120 VAC Systems - The 120 VAC systems provide power to instrumentation and control circuits and to miscellaneous small loads. These systems include the 120/208 VAC Normal Instrument Power System; the 120/240 VAC Uninterruptible Power System; the 120/208 VAC Instrument Power Systems, and the 120 VAC Reactor Protection Power System.

Use or disclosure of data
subject to title page restriction

The function of the various 120 VAC systems shall be as follows:

(a) The 208 /120 VAC Normal Instrument Power System shall distribute power for balance-of-plant control, instrumentation, and other nonsafety-related plant loads where an unregulated power supply will not affect their operation.
(b) The 120/240 V Uninterruptible AC Power System shall distribute regulated, uninterruptible power to nonsafety-related electrical loads such as plant communications, plant computers, and certain plant instrumentation which require a regulated and uninterrupted power source.
(c) The 120/208 VAC Engineered Safety Features Instrument Power Systems shall distribute power to Class IE control and instrumentation loads.
(d) The 120 VAC Reactor Protection System shall provide power to the logic systems for the Reactor Protection System.

6.10.3.4 Medium Voltage and Low Voltage Electrical Distribution Systems - The Medium Voltage (MV) and Low Voltage (LV) Electrical Distribution Systems (EDS) either directly or indirectly distribute startup, operating, and shutdown power to all electrically operated plant auxiliaries including motors, heaters, and lighting. The MV and LV Electrical Distribution Systems receive power input either from the generator via the unit auxiliary transformers or from the offsite power system via the startup transformers. In addition, those portions of the MV and LV Electrical Distribution System that are nuclear safety related can, during emergency circumstances, receive input power from the standby diesel generators.

The Medium Voltage and Low Voltage Electrical Distribution Systems functions are as follows:

(a) Distribute large quantities (approximately 100 MW) of power to plant auxiliaries
(b) Provide the means for automatic and manual control of plant electrical auxiliaries.

The entire Medium Voltage and Low Voltage Electrical Distribution Systems shall be designed to be operational during plant startup, normal operation, and normal shutdown. In addition, a portion of the MV and LV Distribution System designated as safety-related shall be designed to be operational during and following emergency shutdown or an accident situation, independent of the availability of normal onsite (turbine generator) power or offsite power.

6.10.3.5 Lightning Protection - A lighting protection system will be provided for Prometheus structures subject to damage by a lighting strike. Each structure to be protected has a separate lighting protection system, which is fully and permanently operational once the installation has been completed. Seismic and radiation

requirements are not applicable to the lighting protection system and only corrective maintenance is required.

The configuration of the system varies with the type of structure to be protected and is designed to prevent damage to structures and hazards to personnel, resulting from lightning discharges to earth, within the plant area.

Lightning protection systems for all types of structures have been designed to provide a low impedance path to or from the ground, for currents associated with lightning discharges, thus preventing damage to the structures as well as for equipment and persons within the structure.

Lightning protection systems are of a permanent nature and, once the installation has been completed, it is fully operational at all times.

6.10.3.6 Station Grounding System - The grounding system contributes to the safe operation of a power station by providing safety for the people and equipment from fault and lightning stroke currents. This safety is normally achieved by designing the grounding system (consisting of copper or Copperweld conductors and rods) in such a way as to:

(a) Limit the soil gradients (underground fault or lightning stroke conditions), inside and outside the power station area, to safe values.
(b) Achieve a low resistance to remote earth value for safe transfer potentials or otherwise provide the necessary measures to electrically isolate the plant grounding system from remote grounds.
(c) Provide adequate grounding for all station equipment.
(d) Provide adequate ground ties between the plant grounding grid and the switchyard grounding grid to minimize the potential difference between the two grids.

The grounding system, an integral part of the power station, functions as a system that:

(a) Protects the personnel and public from dangerous potentials such as transferred, step and touch potentials during normal operating and maximum ground fault conditions.
(b) Provides connection to ground for power equipment neutrals.
(c) Facilitates relaying in clearing ground faults.
(d) Dissipates static charges and/or induced current from carrying lines or parts thereof that need to be worked on.
(e) Dissipates lightning discharges.

6.10.3.7 240 kV System - The 240 kV system supplies startup power to the plant and connects Prometheus to the transmission network for power output from the main

generator. A four-bay 240 kV switchyard provides switching capability for the main generator, the two startup transformers, and the three outgoing transmission lines.

The 240 kV switchyard is connected to three transmission lines designated No. 1, No.2, and No. 3. Each line is connected to the breaker and bus section through a motor operated disconnected switch interlocked with a line-grounding switch. The ultimate switchyard arrangement will be a low, open-type radial system, double-bus three-breaker bay, with a breaker and a half scheme.

The 240 kV overhead line from the main transformer is connected to the east pull-off tower in Bay No. 1 and may be connected to any combination of the three transmission lines. Startup transformer 1A supplies power from the east bus in Bay No. 2 and startup transformer 1B supplies power from the west bus in Bay No. 4.

The main transformer bank receives power at 22 kV from the main generator and transforms it up to 240 kV for supply to the transmission system. The main transformer bank consists of two 3-phase transformers, 475 MVA each, forced oil and air (FOA) cooled, connected in parallel. Each transformer is equipped with separate cooling equipment. If one transformer needs to be taken out of service, the other can be uprated to 632 MVA by applying all the cooling equipment to the transformer in operation.

The two startup transformers each provide half capacity startup power and full capacity emergency auxiliary power from the 240 kV switchyard when required. The startup transformers are the preferred source of power for normal and emergency shutdown. The startup transformers have double secondary windings and supply power to auxiliary busses at 6.9 kV and 4.16 kV. Each transformer has its own forced oil and air cooling system.

6.10.4 Auxiliary Systems

6.10.4.1 Fire Protection System - The Fire Protection System (FPS) is designed and constructed to eliminate and/or mitigate fire and fire hazards throughout the plant by use of suitable equipment, instrumentation, operating procedures, and construction materials.

In the event of a fire occurring in any section of the plant, the FPS protects plant personnel from injury and equipment from damage.

The fire protection system shall be capable of extinguishing all types and classes of fires in various types of occupancy classifications within the plant.

Use or disclosure of data subject to title page restriction

Each area and type of fire hazard shall be considered and the fire fighting media most suitable for fire protection is selected for same.

Other design features such as assured means of egress, smoke evacuation, selections of suitable fire resistant materials, and temporary fire protection during construction will assure that any potential fire hazards will be either reduced or eliminated.
The functions of the Fire Protection System are:

(a) To provide automatic detection of hazardous smoke and fire conditions.
(b) To provide reliable automatic or manual fire extinguishment equipment or systems for fire fighting suitable for the materials of construction and equipment of the occupied space.
(c) To provide proper means of egress from all areas of the plant to assure personnel safety has been provided.
(d) To provide a reliable source of water for all automatic fixed extinguishment fire protection systems.
(e) To provide proper and reliable fire fighting media for special areas and hazards.
(f) To provide for proper smoke evacuation.
(g) To provide fire alarm systems to notify plant operating personnel of a fire condition so that proper countermeasures may be instituted.
(h) To provide manual fire fighting equipment of a class suitable for use by trained plant fire fighting brigade.
(i) To provide a reliable means of communication between control room and various other areas of the plant.
(j) To prevent damage to safety related equipment by inadvertent operation of the FPS.

The Fire Protection System has been engineered and constructed to protect the entire plant, its contents, and personnel from damage and injury caused by fire, excessive heat, and smoke. The methods used to protect the plant, contents, and personnel are, of necessity, varied to allow for different fire classifications and hazards in conjunction with insurance carrier and NRC requirements.

6.10.4.2 Compressed Air System - The Compressed Air System (CAS) provides and maintains compressed air at the required pressure, temperature, and quality for the operation and maintenance of all systems required for normal power generation and for maintenance and refueling operations performed during plant shutdown.

The system is not required for a safe shutdown or for limiting radiological releases. All safety system components using compressed air are designed to assume the positions required for nuclear safety if compressed air supply is lost.

Use or disclosure of data
subject to title page restriction

The CAS provides two qualities of compressed air:

(a) Filtered and dried compressed air, identified as instrument air, for pneumatic instruments and controls.
(b) Unfiltered and undried compressed air identified as station air, for servicing and pneumatic tools.

Instrument air is more essential for plant availability and is shown preference in the control of CAS operation.

The CAS includes all components used in the compression, filtration drying, and distribution of compressed air, up to and including each user isolation device.

The CAS shall be designed to ensure the availability of compressed air at the quality and pressure required for operation and maintenance of Prometheus including:

(a) The continuous supply of filtered, dried, oil-free air to plant instruments and controls.
(b) The availability of compressed air for maintenance, sparging, and general plant use.
(c) The capability to supply all compressed air requirements for maintenance and testing (except for containment leak rate testing) performed during plant shutdowns.

6.10.4.3 Process Sampling System - The Process Sampling System provides equipment for the taking of fluid and gaseous samples in order to provide a basis for control of the primary, secondary, radwaste, and CAS system chemistry and radiochemistry.

A primary sample system panel is supplied with liquid grab sample from the reactor coolant hotleg. A secondary sample system panel is supplied with liquid or steam grab samples from the feedwater, heater outlets, main steam, condenser hotwells condensate pump discharge, the condensate demineralizer cleanup system, and steam generator blowdown.

A radwaste sample system panel is supplied with liquid grab samples of drain sampling tank and other radwaste samples.

The functions of the system are as follows:

Use or disclosure of data
subject to title page restriction

(a) Provide representative liquid and gaseous samples for analysis in order to monitor and measure performance of the various systems and equipment.
(b) Provide a means to obtain and collect liquid samples containing entrained gases and suspended particles from various locations in the plant to be used for chemical radioactivity analyses.

6.10.4.4 Equipment and Floor Drainage Systems - The purpose of the Equipment and Floor Drainage Systems is to collect and remove liquid waste from floors, tanks, equipment, and all interior areas of the plant during normal operating or accident conditions and convey this effluent in pipes to disposal or treatment facilities without affecting the safety or operation of the plant.

The Equipment and Floor Drainage System has been designed to:

(a) Remove and convey liquid radioactive and potentially radioactive effluent from sources to the liquid radwaste treatment facilities.
(b) Remove and convey liquid nonradioactive effluent from sources to point of discharge into the industrial waste drainage system or to separate treatment of disposal facilities.
(c) Remove and convey radioactive/nonradioactive organic waste from source to local collection pits or treatment facilities.
(d) Remove and convey radioactive detergent and decontamination waste from sources to the detergent tanks.
(e) Protect plant personnel from radiation exposure and injury by draining accidental spillages from floors resulting from a failure or malfunction of piping and/or equipment.
(f) Remove, in time, any uncontrolled large quantity of liquid waste released as a result of failure or malfunction of piping and/or equipment or actuation of part of the fire protection system.

6.10.4.5 Communications Systems - The intraplant communication system shall be comprised of wireline and radio subsystems to furnish reliable facilities for establishing communication links within the plant and connecting to off-site communications networks for disseminating information and signals.

Safe and reliable plant operations shall be supported by the provision of a variety of telecommunications facilities working between the control room and important operating areas, and among the important operating/maintenance areas, thus furnishing the ability to locate and speak to mobile personnel throughout the plant. Further, telephone communication from or to the public telephone network shall be provided via the local telephone company central office. Dedicated facilities of several types shall be provided for plant ancillary operations which might not be served

Use or disclosure of data
subject to title page restriction

adequately by the main communication system or would occupy it for an inordinate amount of time.

6.10.4.6 Lighting Systems - Lighting systems shall provide illumination throughout the plant during normal and other than normal plant operation. To accomplish this, three lighting subsystems shall be utilized:

(a) Normal AC Lighting System
(b) Normal Emergency (N/E) AC Lighting System
(c) DC Emergency Lighting System

The lighting systems shall be designed to provide the appropriate illumination levels throughout the plant during all modes of plant operation.

(a) The Normal AC Lighting System shall provide lighting to non-safety related areas such as the Turbine Building; this system provides the bulk of the plant lighting load. The Normal Lighting System shall only be operable when the plant is in a normal operating mode. The normal operating mode includes the plant start-up mode with off-site power available, the plant running mode with the unit auxiliary transformers supplying auxiliary electrical power, and the plant hot or cold shutdown mode with offsite power available. Power for normal lighting shall be provided through the nonsafety-related electrical auxiliary system. The Normal Lighting System shall provide approximately 80 to 85 percent of the plant lighting load.

(b) The Normal Emergency AC Lighting System shall be capable of providing the necessary lighting during the safe and orderly shutdown of the plant following the loss of offsite power. The Normal Emergency Lighting System shall be energized whether the plant is in a normal operating mode or not. Power to the normal Emergency Lighting System shall be provided through the safety related electrical auxiliary system. When the plant is in a normal operating mode, power to the safety-related electrical auxiliary system shall be provided by either the Start-up Auxiliary transformer or the standby transformers. (These transformers provide two sources of offsite power to the Class IE buses.) When the plant is not in a normal operating mode, the standby diesel generators (onsite power source) shall supply power to the safety-related electrical auxiliary system which, in turn, shall supply the Normal Emergency Lighting System. The Normal Emergency Lighting System shall provide approximately 15 to 20 percent of the plant lighting load.

(c) The DC Emergency Lighting System shall provide illumination only during loss of the normal emergency lighting source. For the Control Room and the

Use or disclosure of data
subject to title page restriction

Remote Shutdown, the DC lighting system shall utilize the safety-related 125 V DC system batteries as the source of power. In other areas where safety-related functions may be performed, such as the safety related switchgear room, ECCS pump area, and access/egress routes to/from these areas, self contained storage battery lighting fixtures shall be utilized.

6.10.4.7 Auxiliary Steam System - The Auxiliary Steam System consists of an oil-fired auxiliary steam boiler which supplies auxiliary steam at low pressure to the Main Turbine Gland Sealing System, Liquid Radwaste System Solids Radwaste System, auxiliary boiler feedwater deaerator, condenser, and feedwater heaters.

The system is operated during plant startup, normal operation, and shutdown. The auxiliary boiler will be in operation during startup, shutdown, and plant low load periods. During normal operation, the source of steam is the Extraction Steam System or the Main Steam System.

The function of the Auxiliary Steam System is to supply dry saturated steam to the following systems:

(a) Main Turbine Gland Sealing System
(b) Radwaste System (floor drain evaporator, inorganic chemical waste evaporator, and solid reduction evaporator)
(c) Auxiliary boiler feedwater deaerator (heating steam)
(d) Condenser hotwell and feedwater heaters.

Auxiliary steam generated from the auxiliary boiler shall be fed to a common auxiliary steam header and then distributed to all equipment requiring auxiliary steam. A portion of the resulting equipment drains enters the feedwater cycle by draining to the auxiliary condensate collecting tank. This condensate shall be returned to the auxiliary boiler deaerator during plant startup and shutdown periods. A portion of the auxiliary steam is lost to the main cycle and removed from the auxiliary steam and condensate system. Accordingly, makeup water shall be required and shall be supplied from the condensate and emergency feedwater storage tank.

6.10.4.8 Freeze Protection (Electric Heating) System - A Freeze Protection System (FPS) prevents vessel or pipe contents (water) from freezing by utilizing heat generated by flow of electric current in an element of resistance or resistive component of an impedance. This heat is the equivalent of I^2R loss in the element (cable, ribbon, tape, pipe, strip or immersion heater, etc.).

Methods employed to bring these elements in contact with the surface of the equipment to be protected defines the particular FPS, e.g. in the method of providing

Use or disclosure of data subject to title page restriction

freeze protection by electric heat tracing, heater cables are run along and in contact with the surfaces of pipe lengths and equipment.

The FPS is ambient temperature actuated and controlled; i.e., cold ambient conditions are detected by temperature sensing devices which then initiate flow and provide heat which overcomes the heat loss (through pipe and vessel surfaces) due to cold conditions.

The scope of the Freeze Protection System covers selection and installation of heater cables, temperature sensing devices, and the various components of electrical power supply, e.g. transformer, distribution panels, starter, relays, etc.

6.10.4.9 Sanitary Drainage and Vent System - The purpose of the Sanitary Drainage and Vent System is to remove non-radioactive waterborne wastes from sanitary plumbing fixtures and other related equipment, and convey this effluent via a piped gravity system to sanitary treatment or disposal facilities.

The purpose of Sanitary Drainage and Vent System is:

(a) To provide sanitary plumbing fixtures for use of plant personnel
(b) To remove sanitary and other similar types of non-radioactive liquid borne wastes to treatment or disposal facilities.

6.10.4.10 Bulk Gas Storage System - The Bulk Gas Storage System provides safe storage and handling facilities for high pressure compressed hydrogen and nitrogen and low pressure liquid carbon dioxide which are necessary for plant operation. The compressed gas supply systems are provided to supply various gases for equipment and instrumentation cooling, purging, diluting, inerting, and welding. The major items of equipment are the high pressure gas cylinders and pressure regulators to control the pressure and distribution of the various gases used throughout the plant. These compressed gas supply systems are non-safety-related and any failure does not jeopardize the operation of any safety-related components or systems.

The Hydrogen Storage System consists of six seamless storage vessels, a compressor, piping valving, all necessary pressure reduction equipment, and instrumentation to ensure a safe storage system.

The Carbon Dioxide Storage System consists of two low pressure, low temperature storage vessels complete with refrigeration units, evaporators, and all piping, valving, pressure reduction equipment, and instrumentation necessary for a safe installation.

Use or disclosure of data subject to title page restriction

The Nitrogen Storage System consists of five seamless storage vessels, piping, valving, all necessary pressure reduction equipment, and instrumentation to ensure a safe storage system.

The control panels are complete with pushbuttons for all automatic valves, pressure, temperature and flow indicators, and alarms.

6.10.4.11 Decontamination Facilities - Decontamination facilities provide the means to perform various cleaning functions in order to reduce equipment surface radioactivity to acceptable levels prior to functional rehabilitation, operational reuse, or shipment off-site. Additional facilities provide for body washdown of contaminated personnel, as well as human deluge equipment in the event of an accident. The Prometheus decontamination facilities are:

- Central Equipment Decontamination Facility - The entire room will be lined with stainless steel plates with polished weld seams. Adequate shield walls will be provided to protect adjacent areas. Floors will be sloped to floor drains within the room and all entranceways will be provided with floor drains. All drains will be constructed of stainless steel with polished gates. Ventilation will be provided to reduce the spread of radioactive contaminants and to maintain room temperature at 75°F. The water supply for this facility will be from the Demineralized Water System.

- Local Decontamination Facilities - All components will be constructed from stainless steel plates with polished welded seams. Floor drains will be provided for local drainage. Ventilation for components will be from adjacent spaces, always going from areas of lesser potential radiological contamination to areas of higher potential.

- Health Physics Personnel Decontamination Facilities - Showers and lavatories for personnel decontamination will be provided, in designated areas, within the confines of the Health Physics area. Adequate shielded walls will provide protection for adjacent areas. Ventilation, heating, and cooling will be provided to remove airborne radioactivity and maintain a desirable atmosphere.

- Local Safety Eyewash and Showers - For personnel safety, emergency eyewash and shower stations will be located adjacent to hazardous areas of the plant. They will be supplied with cold water from the Potable Water Supply System. Floor drains will be provided in the immediate vicinity of these stations to accept the discharged water. Access to the emergency eyewash and shower stations will be clear and unobstructed by walls or curbs.

Use or disclosure of data
subject to title page restriction

6.10.5 Site Preparation - The activities that will be performed as part of the site preparation include: clearing, grubbing, grading, excavation, drainage, spoils disposal, borrow, and backfill. The site is assumed to be originally flat agricultural land requiring little clearing, regrading, or other site preparation. Soil removed by excavation for the main plant, the Circulating Water System, and the Accelerator Tunnel will be used to raise the elevation of areas occupied by temporary construction facilities. Spoils which are disposed of outside the construction area will be graded and seeded to prevent erosion.

Facilities that will be provided as part of site preparation include: construction offices, warehouses, access highway, parking lots, sanitary sewage, potable water, off-site electricity, and railroad spur and/or barge facilities. A concrete batch plant has not been included in the site preparation facilities.

Reference for 6.10

1. C. C. Baker, M. A. Abdou, et al., "STARFIRE - A Commercial Tokamak Fusion Power Plant Study," ANL/FPP-80-1, September 1980.

Use or disclosure of data subject to title page restriction

This page intentionally left blank.

Use or disclosure of data
subject to title page restriction

6.11 Remote Maintenance Systems

Remote maintenance systems required in the IFE reactor of the year 2030 will be many and varied. In view of the pace of technological advance in remote handling, it is impossible to predict the maintenance equipment that may exist in that time. However, by considering today's devices and looking at current research, it is possible to speculate on what may be employed. Automation technologies will play a key role in attaining the goal of total remote maintenance. This section reviews the various technology areas that are pertinent to the remote maintenance task and indicates the research directions that may be relevant in the future maintenance device concept development.

6.11.1 Manipulator Technology - A number of current fission and fusion development projects have extensive remote handling capabilities that are state of the art. Figure 6.11-1 shows the ITER In-Vessel Vehicular System.[1] Though the ITER reactor does not yet exist, a number of prototypes of this device are under construction. ITER has a deployable rail on which 1-ton payload telescopic manipulators perform maintenance tasks such as divertor replacement. Figure 6.11-2 shows various manipulators working in the lower vessel area of the ITER machine[2] on typical tasks. The small manipulators shown are the Mascot and RD 500; the large manipulators are the SPAR telescopic and 2500 devices. Figure 6.11-3 shows the Joint European Torus Telescoping Articulating Remote Manipulator (TARM) and Articulating Boom Manipulators,[3] examples of equipment currently being used. Figure 6.11-4 shows the SPAR 2500 manipulator and a Schilling manipulator in use at the DOE environmental cleanup technology demonstration project at Hanford.[4]

6.11.1.1 <u>Master/Slave Telemanipulators</u> - Master/slave manipulators (MSM) have evolved in the nuclear and undersea remote handling areas over several decades from basic mechanically-coupled systems to electronically-coupled systems using electrically or hydraulically-powered slaves. Figure 6.11-5 shows the Mascot, a typical current nuclear MSM.[5] The main feature of these systems is the highly intuitive mapping between human motion commands and manipulator responses. This results in advantages over other teleoperation devices: (1) highly dexterous manipulators can be realized because the issues normally associated with dual manipulator coordination, kinematic redundancy (i.e., more than six joints per arm), and kinematic singularities ("lock-up" of mechanical degrees of freedom) are automatically and naturally resolved by the operator; (2) relatively complicated tasks can be performed faster with less training; and (3) computational requirements are simplified (or potentially eliminated) by the elimination of inverse kinematic transformation algorithms.

Use or disclosure of data
subject to title page restriction

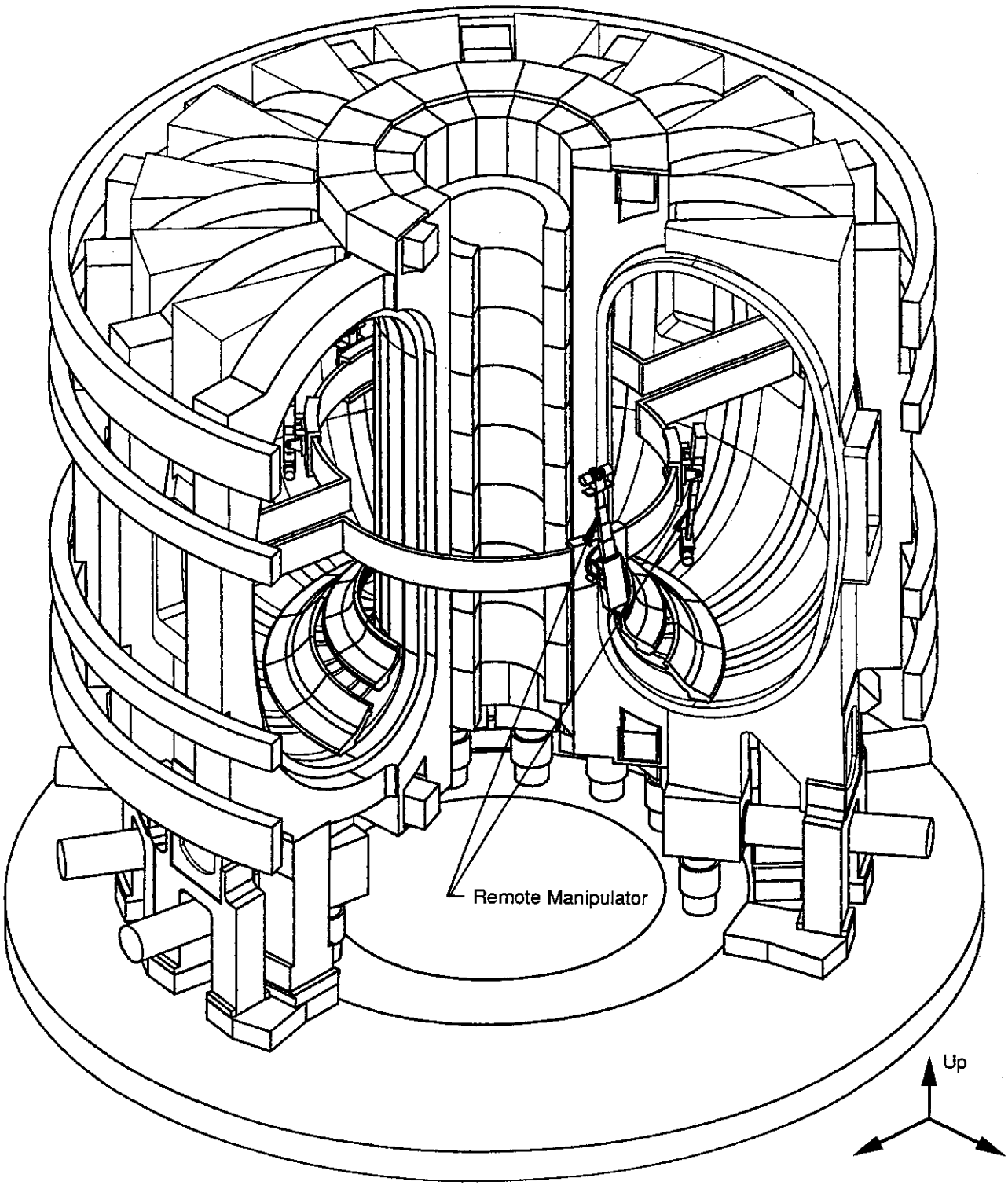

Figure 6.11-1. In-Vessel Vehicular System Represents Current State-of-the Art in Manipulator Technology

Use or disclosure of data
subject to title page restriction

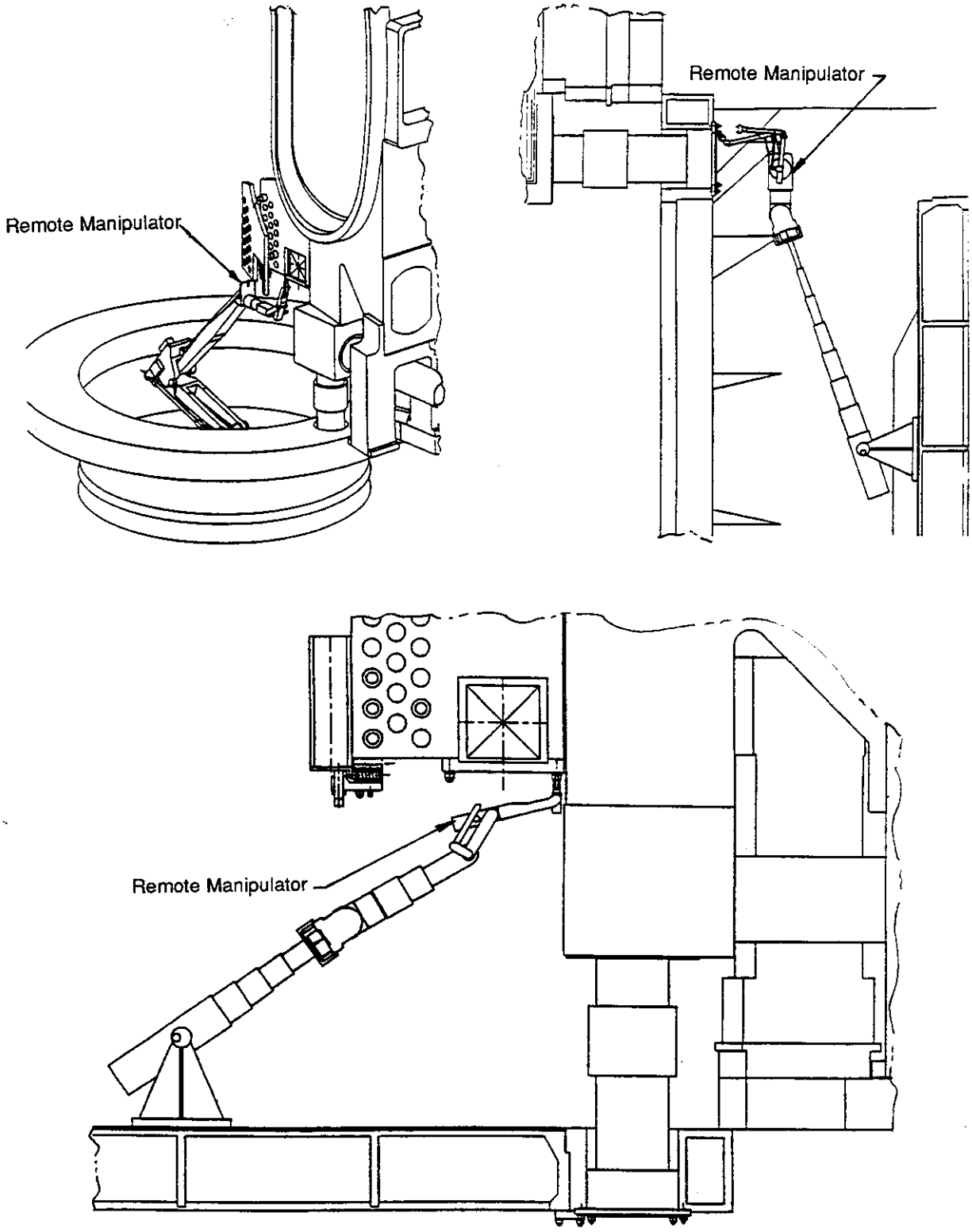

Figure 6.11-2. Remote Manipulators Performing Typical Maintenance Tasks on ITER

Use or disclosure of data
subject to title page restriction

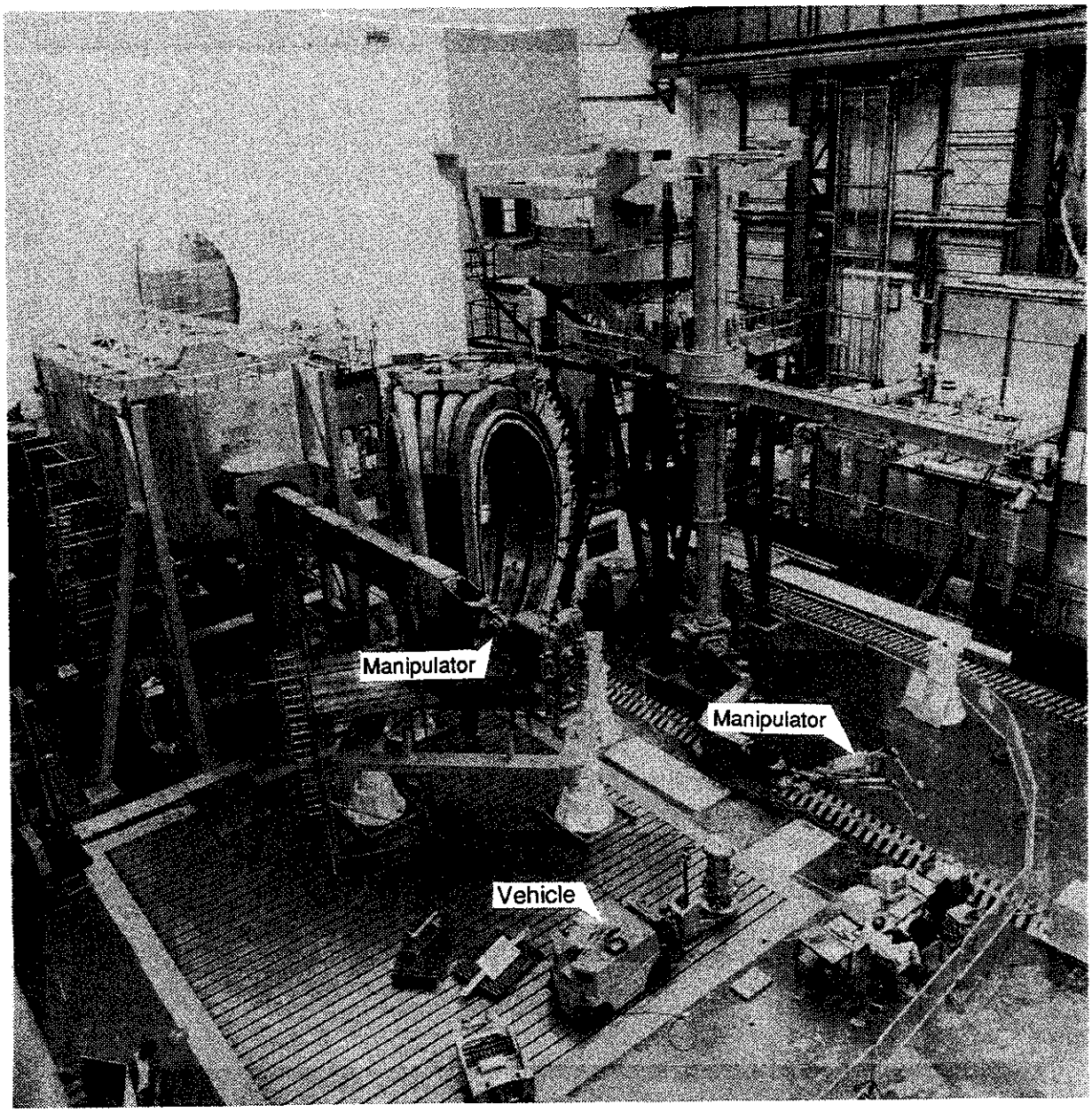

Figure 6.11-3. Maintenance Manipulators and Vehicle at the JET Facility

Use or disclosure of data
subject to title page restriction

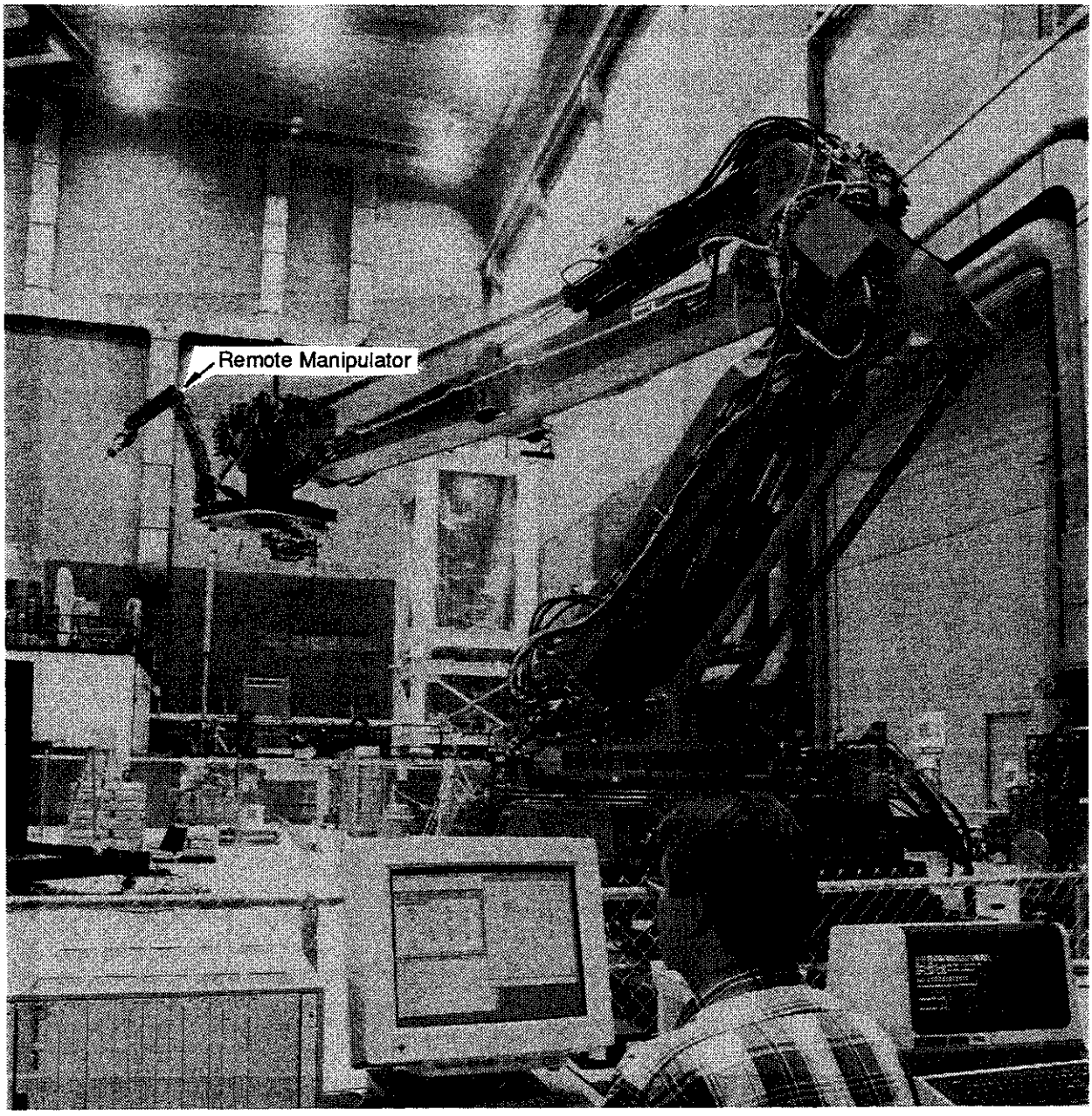

Figure 6.11-4. SPAR 2500 and Schilling Manipulator at the DOE Hanford Facility

Use or disclosure of data
subject to title page restriction

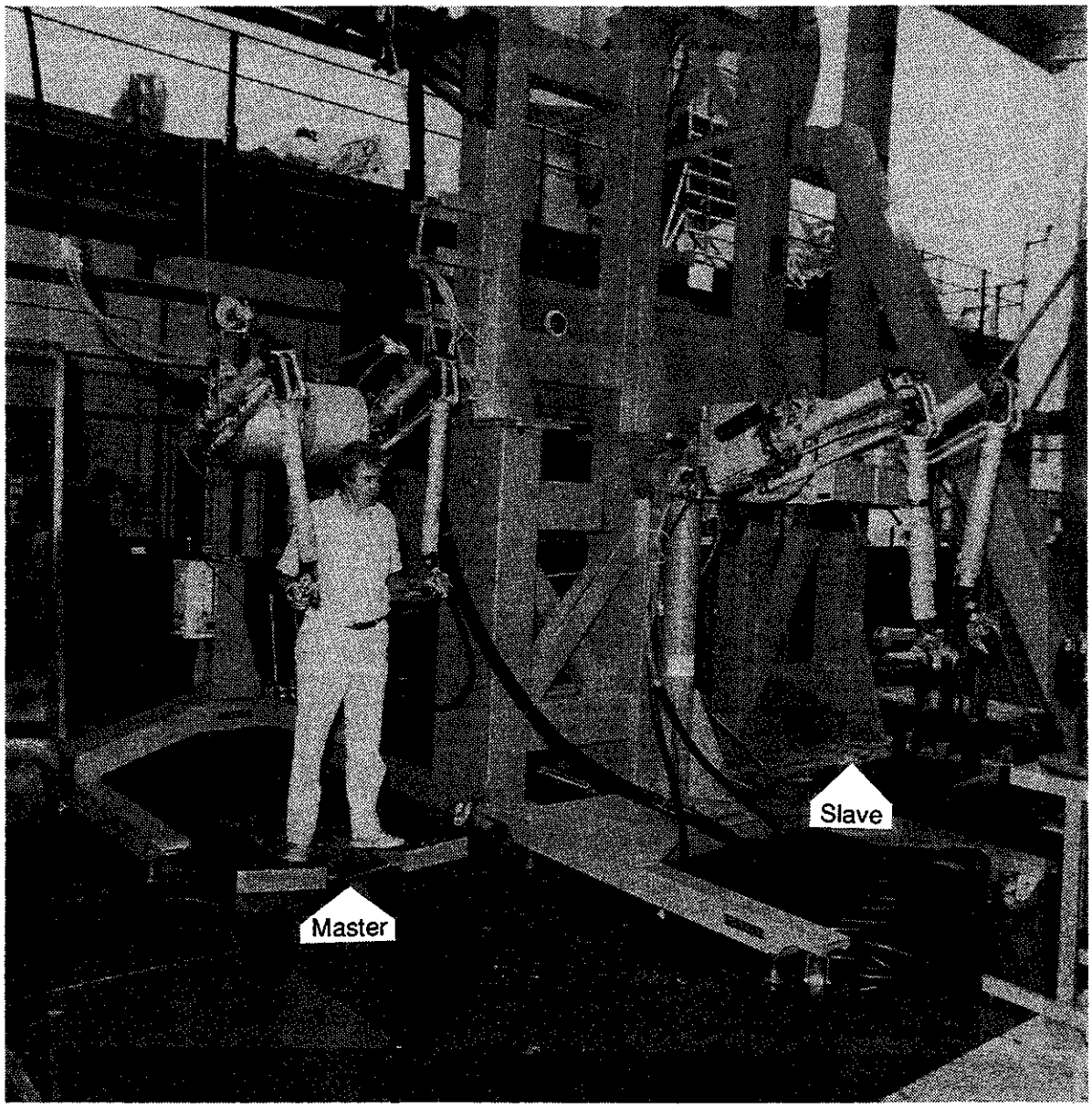

Figure 6.11-5. MASCOT, a Typical Small Nuclear Manipulator at the JET Fusion Facility

Use or disclosure of data
subject to title page restriction

Master/slave systems are limited because they generally do not "scale" well. Loads and motions should be in a "human range." If the time scales are too long or the manipulator is too large, one-to-one teleoperation becomes tedious or potentially dangerous. The tasks need to be of the type that humans would typically perform with their own limbs.

Present development directions in master/slave systems include:

- Miniature (hand-operated) as opposed to full-size (exoskeleton) masters
- Improved force-reflection fidelity
- Ability to relocate control reference frames
- Faster, stronger, lighter slaves (advanced actuators and materials)

Master/slave systems will continue to be used in remote handling situations where the environment and tasks are relatively unstructured and unforeseen. In these situations the master/slave systems offer the closest possible alternative to direct human presence.

6.11.1.2 Long-Reach Configurations - Situations often call for particularly long-reach capability but may also exclude standard manipulator configurations because of size constraints imposed by the environment, access to the work space, etc. Several approaches to achieve a highly cantilevered manipulator body have been developed for applications such as the tokamak in-vessel remote handling and hazardous waste storage tank inspection. These devices are generally used in a coarse/fine mode where a large manipulator positions a payload and a small manipulator accomplishes the detailed handling or maintenance actions. Types of large manipulators are described below.

Telescopic Booms - These are typically used as the "vertical-axis" in standard Cartesian (gantry) or polar manipulator systems. They have been generally avoided where side-loading is an issue.

Deployable Trusses - Many ingenious deployable truss designs exist from simple "scissors geometry" to more sophisticated forms. They exhibit high stiffness to mass. Their geometry can be designed to deploy in either a straight line or an arc. Current research in truss designs employs actively controlled, variable-length truss links to permit full six-degree-of-freedom motion capability. Figure 6.11-6 shows typical deployable trusses that are available and currently used.[6]

STEM Mechanisms - Storage Tubular Extendible Member (STEM) mechanisms are limited in stiffness and strength. However they offer an extremely high ratio of deployed length to stowed length and can deploy or retract quickly. They are suitable for tasks such as camera/lighting positioning. Figure 6.11-7 shows the method to deploy a STEM element. Figure 6.11-8 shows a typical STEM application with a camera.

Use or disclosure of data
subject to title page restriction

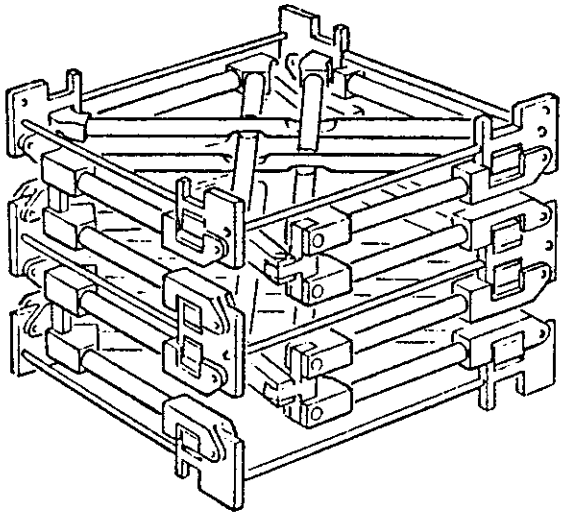

Stowed Configuration

Deployed Configuration

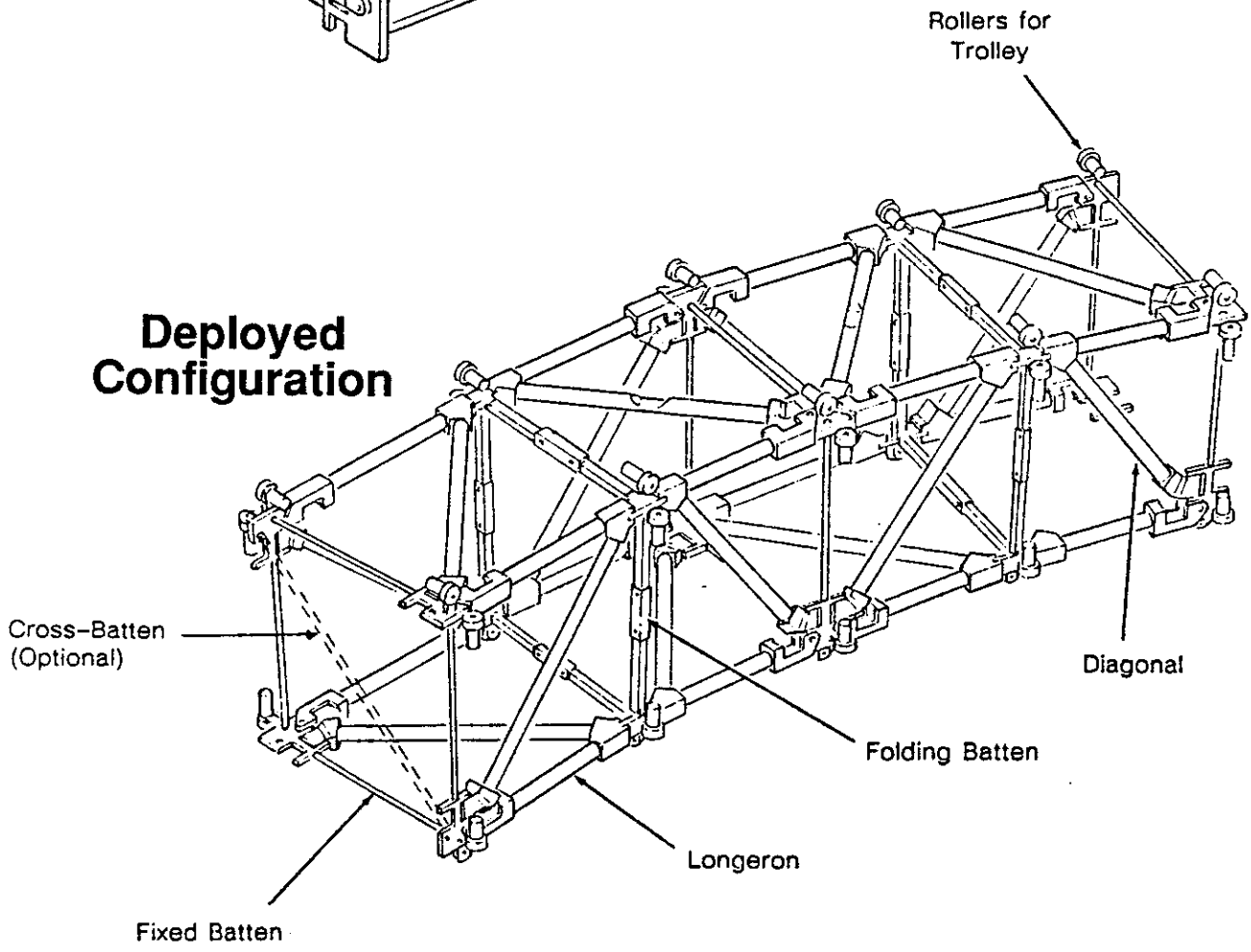

Figure 6.11-6. Curved Deployable X-Boom Truss

Use or disclosure of data
subject to title page restriction

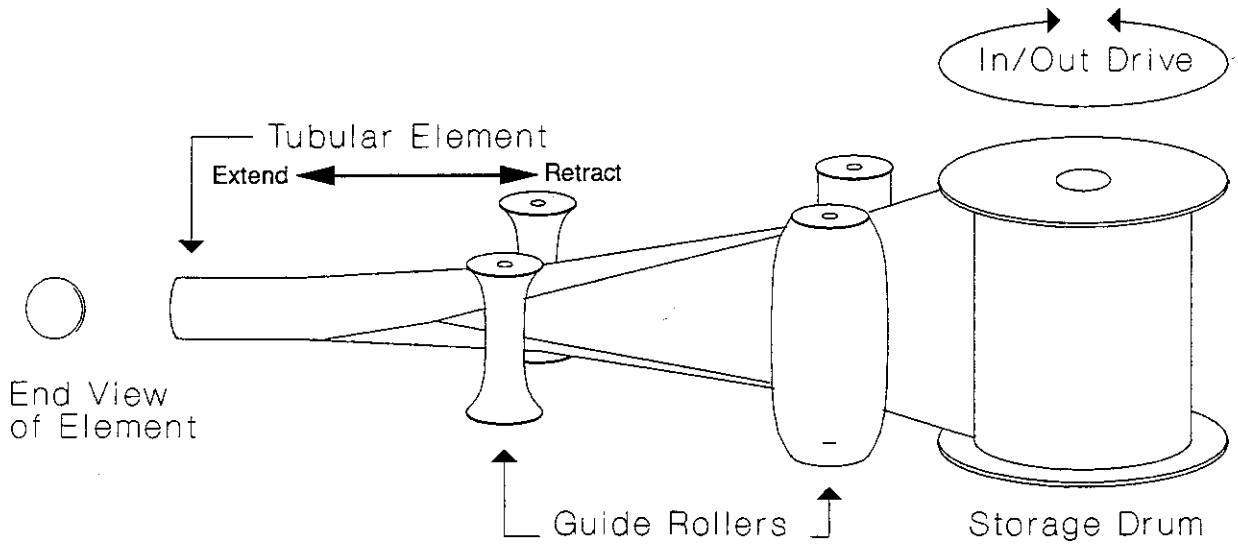

Figure 6.11-7. STEM Element Deployment

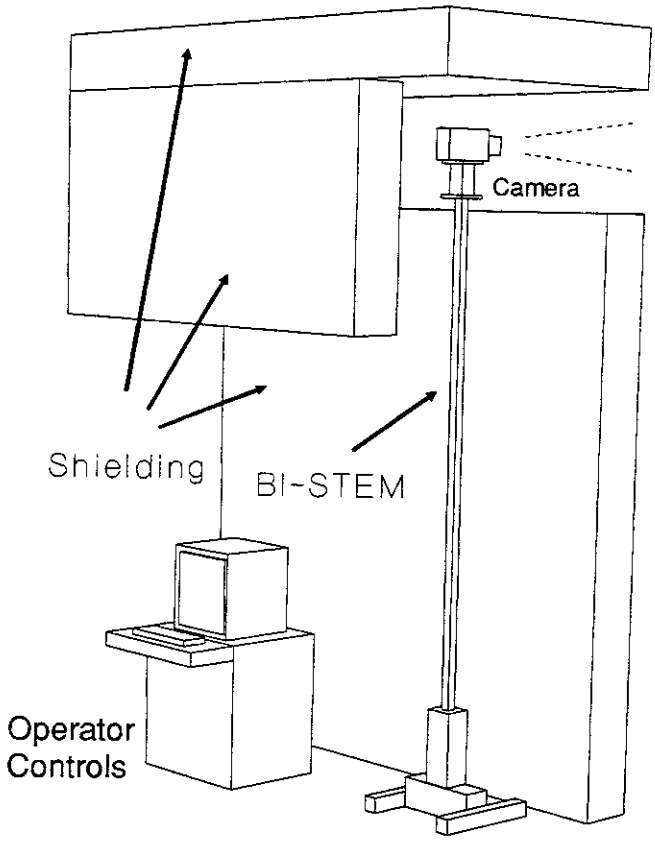

Figure 6.11-8. STEM Mounted Camera

Use or disclosure of data
subject to title page restriction

Articulated Boom Mechanisms - Articulated boom mechanisms were developed for servicing the interior volumes of tokamak reactors. They offer high cantilever stiffness and strength for their cross-section. They can be controlled to "bend" to avoid obstacles, go around corners, etc.

6.11.1.3 Large Payload Manipulators - When large, heavy payloads must be handled in a relatively dexterous manner (that is, where simultaneous control over several degrees of motion freedom is required), large serial link manipulators with hydraulic actuation are employed. With appropriate resolved motion control, such manipulators are capable of fairly precise trajectory following and positioning with resolutions to 1 cm.

Current large payload manipulator research is directed toward adding force-sensitive control and improved teleoperator interfaces.

6.11.2 Transport/Handling Technology

6.11.2.1 Mobile Platforms - Automatically guided mobile platforms are used to transport loads over relatively long distances and generally involve fixed paths if not restricted right-of-ways. There are examples of mobile platforms with load capacities as small as a few kilograms to as large as hundreds of tonnes. For payloads of up to a few tonnes, battery-powered electric propulsion is common but has the problem of frequent charging requirements and limited battery life. Propane-fueled combustion engines can ease, but not eliminate, the maintenance problem. A third alternative uses passive platforms with in-floor linear induction motor propulsion. Such systems have been proven in industrial handling applications, and while more costly, offer superior reliability, very low maintenance, higher payload capacity, and faster throughput. Belt and powered roller conveyer systems are generally too maintenance intensive to be considered for essentially human-free applications.

Current development directions in mobile platforms are to add more sophisticated self-navigation capability, including obstacle avoidance and real-time path planning. Automatic battery-charging/replacement systems, load-vehicle transfer systems, and supervisory control systems continue to be improved. Some development work has added manipulator capability to mobile platforms, but portable power capability remains a limiting issue for such systems.

6.11.2.2 Crawlers/Inspection Robots - Small mobile "robots" for traversing the interiors of pipes, ducts, and other severely confined areas have been developed. These generally have little or no manipulation capability but can carry cameras or other sensors for inspection purposes. In some situations, they could carry tools for

Use or disclosure of data
subject to title page restriction

welding, lubricant dispensing, etc. Examples of self-powered robots with telemetry control links exist, but trailing tethers are commonly used to provide power and data channels.

6.11.2.3 Tracked/Legged Robots - Tracked and legged approaches to robot locomotion have been developed to improve negotiation of obstacles, stairs, etc. The robots tend to be relatively slow and inefficient in terms of power use. If the plant infrastructure is designed with a total remote maintenance concept in place, the use of such robots will be minimized or eliminated.

6.11.2.4 Overhead Systems - Overhead gantry systems offer single or two-dimensional positioning of manipulators or the handling of large items over a large work space area. They can accommodate several ton loads. Current overhead handling systems offer POSI-CAST® control algorithms for much more stable and rapid hook positioning than is possible with purely manual operator control. Truss technology has been integrated to produce deployable cranes which allow either the complete crane or just its drives to be removed from an active environment when not in use. Figures 6.11-9, 6.11-10, and 6.11-11 show typical deployable cranes.

6.11.2.5 Elevator Systems - Scissors-lift and hydraulic elevator systems generally offer higher capacity and reliability than cable-driven systems. However they are generally limited in lift distance—typically less than 10 m.

6.11.3 Automatic Control Technology

6.11.3.1 Sensing and Control - The general trend in robotic technology has been toward increased autonomous capability. This has often involved the addition of more and better sensing and control loops. The pertinent areas are detailed below.

Robot Vision - Present capabilities in robot vision mostly relate to the recognition and spatial "acquisition" of known targets through closed-circuit television imaging for the purposes of referencing motion commands. An example of this would be the tracking of a moving target or planning the grasping of an object. Research directions include increasing use of laser-based imaging systems for creating true 3-D image maps.

Force Control - Whereas conventional robot control has been motion-based, there is an increasing trend toward force-sensitive and "active compliance" control strategies. These offer advantages in manipulation involving stiff contact and in situations where "accidental contact" could occur. Research is continuing in the areas of improved joint level sensing and higher bandwidth control.

Use or disclosure of data
subject to title page restriction

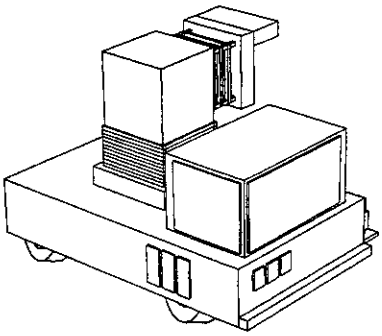

Folded for Transport

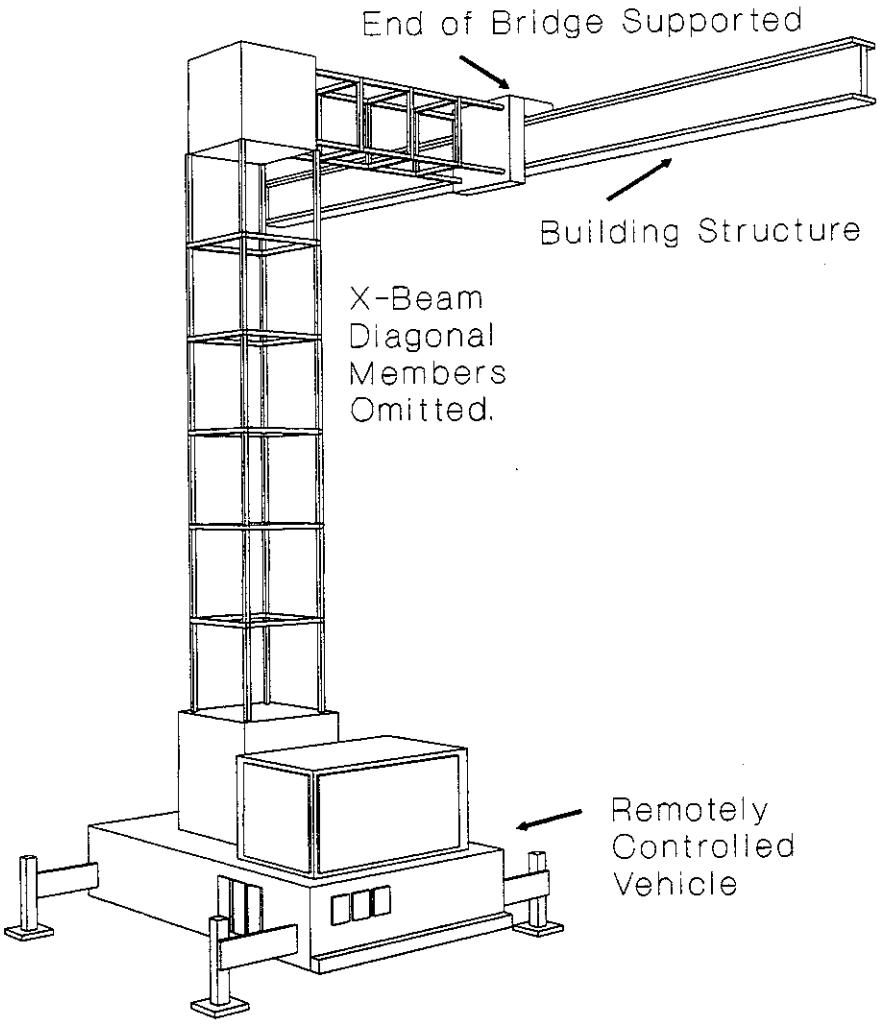

Deployed Configuration

Figure 6.11-9. Mobile Folding Crane

Use or disclosure of data
subject to title page restriction

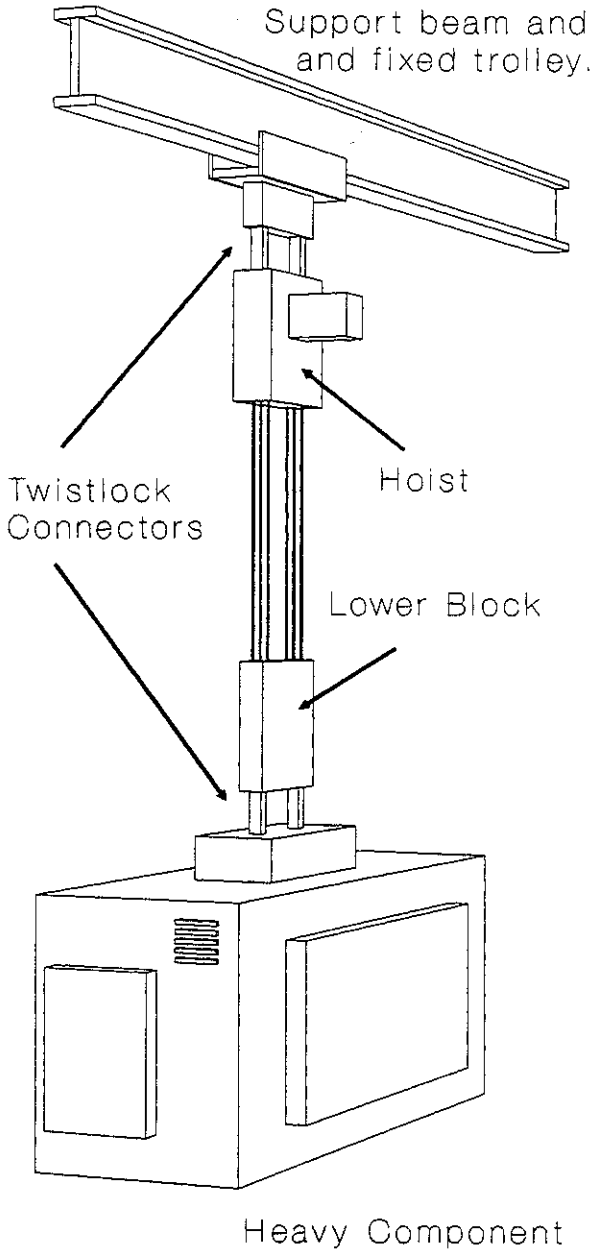

Figure 6.11-10. Deployable Crane Hoist

Use or disclosure of data
subject to title page restriction

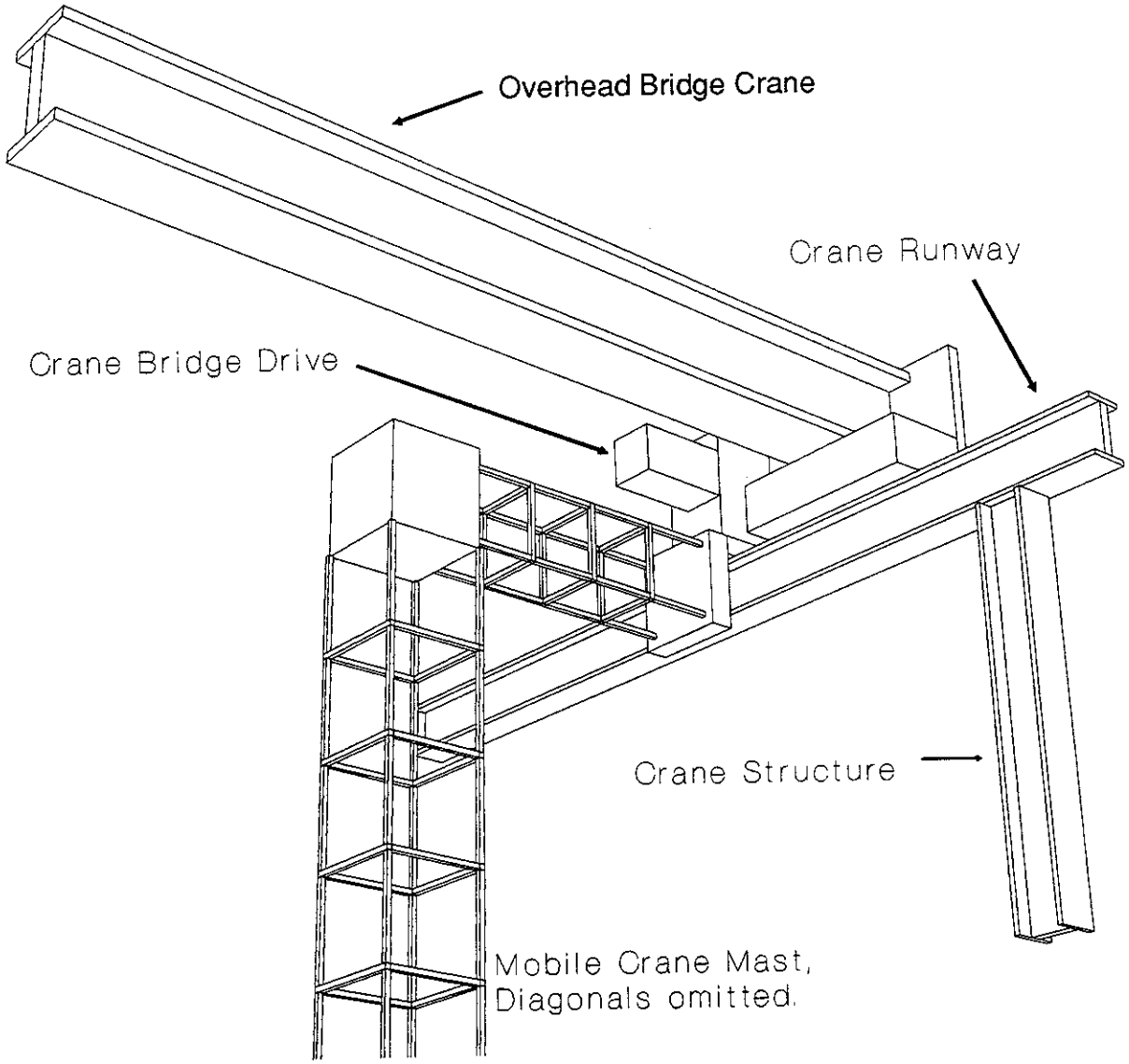

Figure 6.11-11. Heavy Crane with Removable Drives

Use or disclosure of data
subject to title page restriction

Tactile Feedback - Feedback via "tactile sensing arrays" allows sensing and control to acquire detailed surface information through "touch." Present examples of this technology are restricted to research labs. Such technology could be used in the reactor maintenance system through the use of a control algorithm designed for seam-tracking or edge-finding.

6.11.3.2 Robot "Intelligence" and Task Level Control - At one time it was assumed the limits of a robot's "cognitive" capabilities were due to hardware computational limits. It is now more widely recognized that the limitations are algorithmic. Research continues in the so-called AI domain, but in spite of names like "neural networks" and "heuristic reasoning," the expectations are now more modest. It is likely that robots will continue to improve but not become necessarily "smarter" over the next few decades. Traditional areas of higher level robot control such as real-time path planning and collision avoidance will continue to develop. Also, improvements in older programming methods such as "teach/trace" will continue as more kinds of sensory data and improved computer graphic simulation are integrated into the procedures.

6.11.3.3 Human-Machine Interface Technology - An area of particular significance for teleoperated remote systems is in the human-machine interface. Considerable research effort is being conducted in the areas of 3-D vision feedback, force, and tactile and auditory feedback, stimulated by rapid change of the applicable technologies. The relatively new concept of stereo television is being replaced by head-mounted wide-field displays. The head-mounted camera enables views that change in response to head and eye movement. These developments will ultimately enable master/slave teleoperation maintenance tasks to be quicker and more effective.

6.11.4 Tools - Tools are a key part of remote handling technology as evidenced by a large proportion of current development budgets being devoted to them. They are generally specific to applications. Figure 6.11-12 shows a JET cutter that is typical of a special application tool.

6.11.5 Principal Plant Manipulators

6.11.5.1 Overhead Bridge-Mounted Manipulator - The overhead bridge-mounted manipulator is located above the reactor. It has a working volume bounded by the projected area above the reactor and the inner wall of the biological shield. Figure 6.11-13 illustrates a typical overhead bridge crane with a manipulator.

Use or disclosure of data
subject to title page restriction

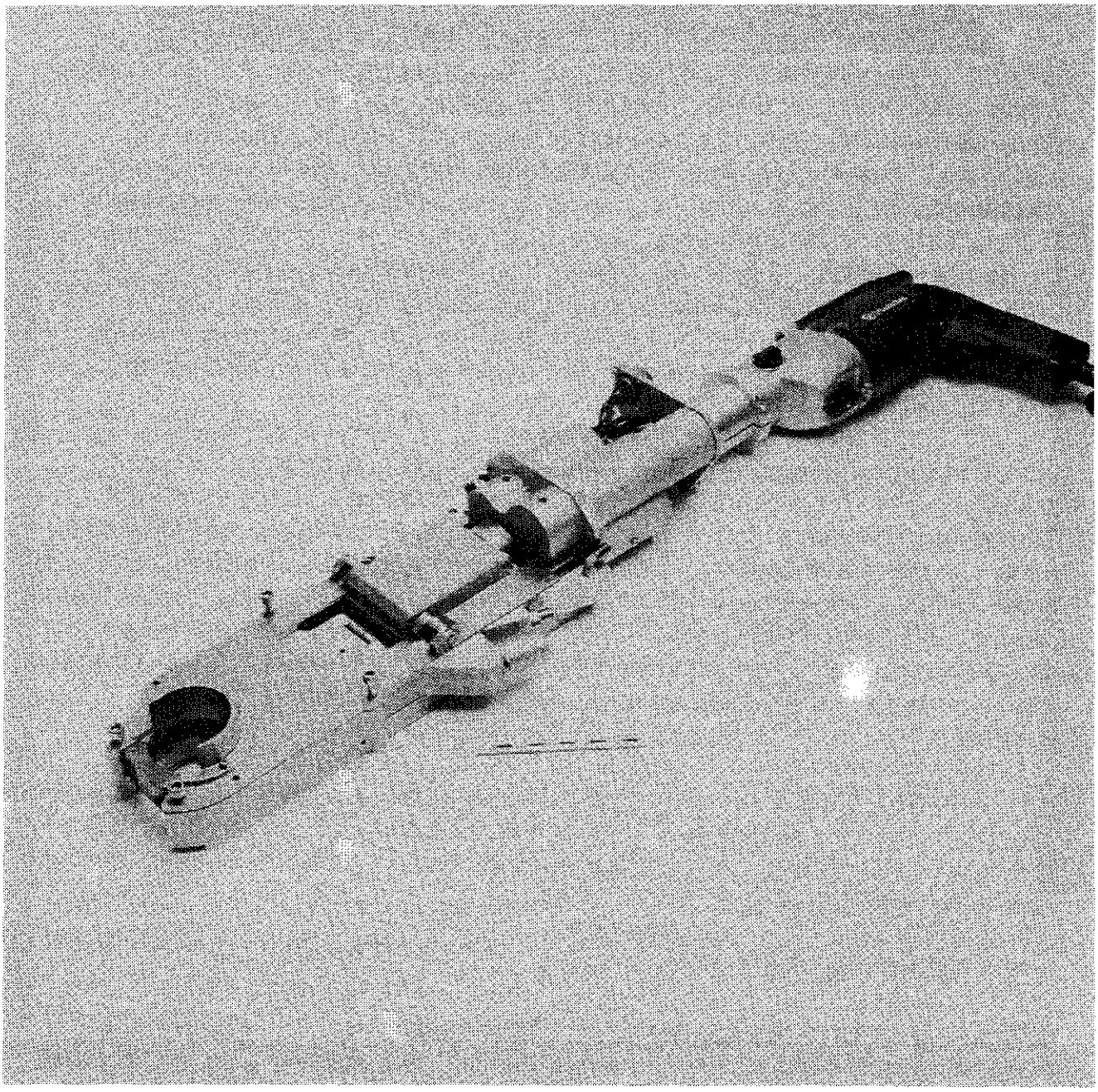

Figure 6.11-12. Typical Remote Handling Tool (JET Pipe Cutter)

Use or disclosure of data
subject to title page restriction

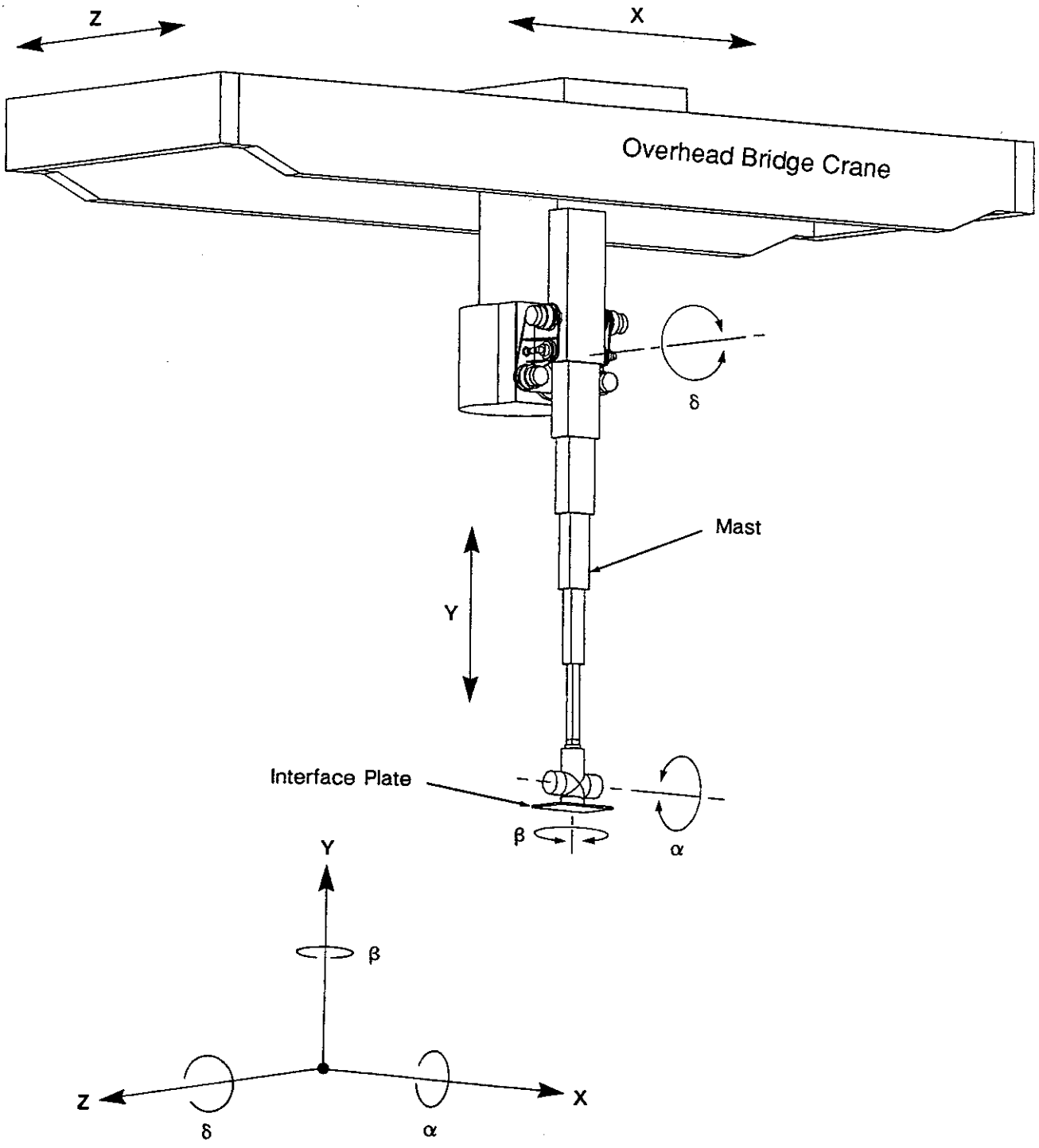

Figure 6.11-13. Upper Reactor Manipulator

Use or disclosure of data
subject to title page restriction

The manipulator is used to provide maintenance support when working on the external components of the reactor. It can also be used internal to the reactor when the upper hemisphere is removed.

The manipulator trolley is located on the bridge crane and supports the telescopic mast. The trolley has a turn-table drive that provides ±360° rotation. The mast is attached to the trolley via a rotational joint that provides a limited angular rotation.

The unit is a general purpose transporter that can supply dexterous manipulator capability and tools required when maintaining the upper section of the machine. It has an interface that can connect to the power and dexterous manipulators.

6.11.5.2 Deployable Heavy Lift Manipulator - The deployable heavy lift manipulator is shown in Figure 6.11-14. It has two major links attached to a rotary base. The base and link structure are detachable for easy transport to the work site. The base is transported to the work site and the stabilizers deployed to form a rigid base. The arm and lower pitch joint are transported separately and assembled on site.

The device is normally used for the maintenance of components that have access at ground level or below. It has power supplies and an interface plate that can mount a dexterous or power manipulator. The interface plate can also support heavy duty tools or dedicated maintenance machines for remote cutting and welding.

The links can be hydraulic or electrically actuated. If hydraulic fluid contamination is a problem, electrical screw jacks are provided. For heavy loads, hydraulic actuators provide a better load-to-weight ratio. The rotary yaw joint can be electrically or hydraulically driven. Three modes of control are provided:

- Preprogrammed automatic
- Teach and repeat
- Man-in-the-loop

6.11.5.3 Mobile Heavy Duty Manipulator - The mobile heavy duty manipulator is a self-driven device that is normally located away from the reactor and remotely deployed to the work site when required (see Figure 6.11-15). It has a lower lift capacity than the deployable manipulator. In position, stabilizers are deployed to form a steady base. The base houses the rotary drive and the transport system. It is used in areas where a clear access is provided for travel. It is normally used where access can be gained from below or from the side at ground level.

Use or disclosure of data
subject to title page restriction

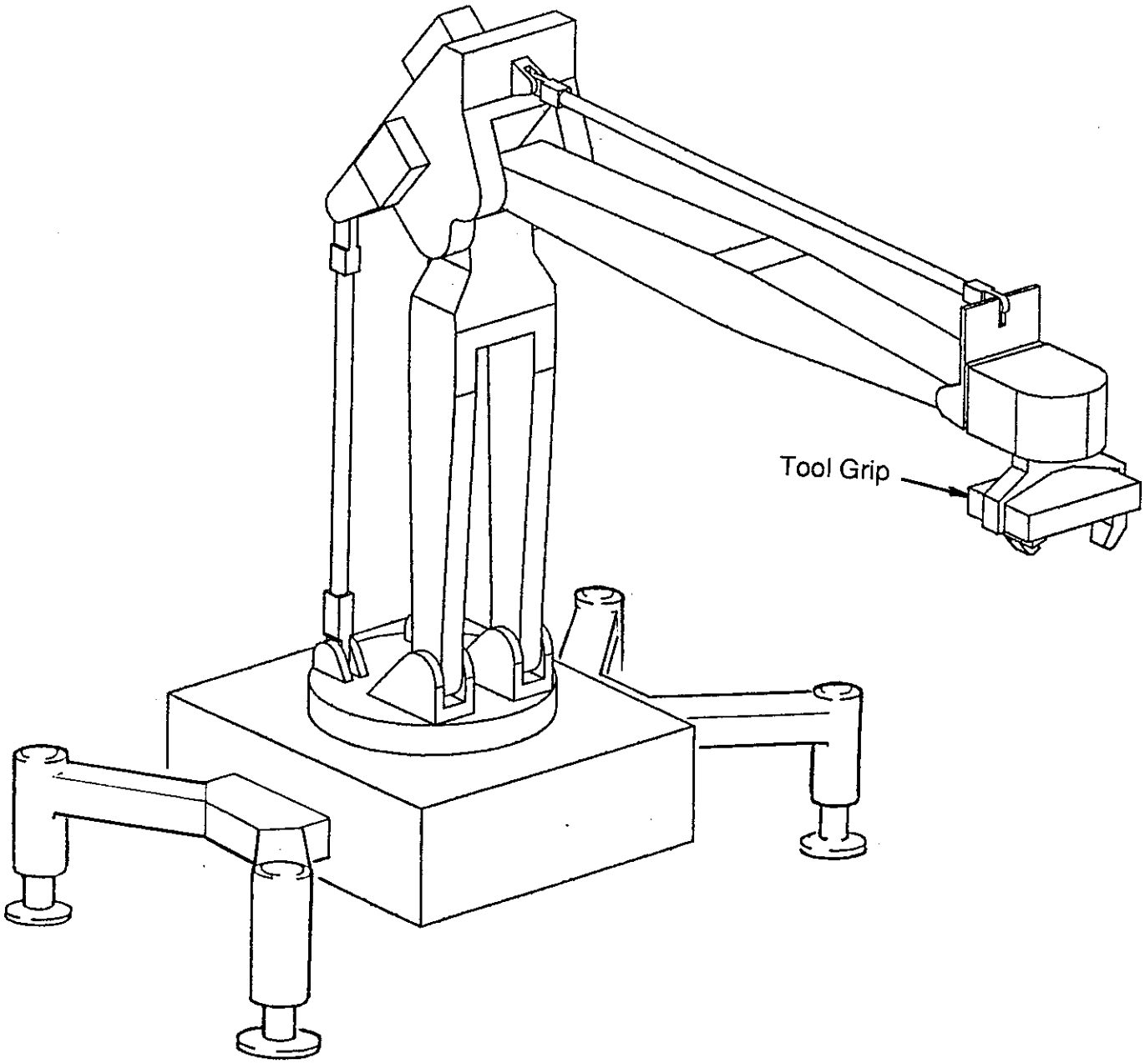

Figure 6.11-14. Deployable Heavy Duty Manipulator

Use or disclosure of data
subject to title page restriction

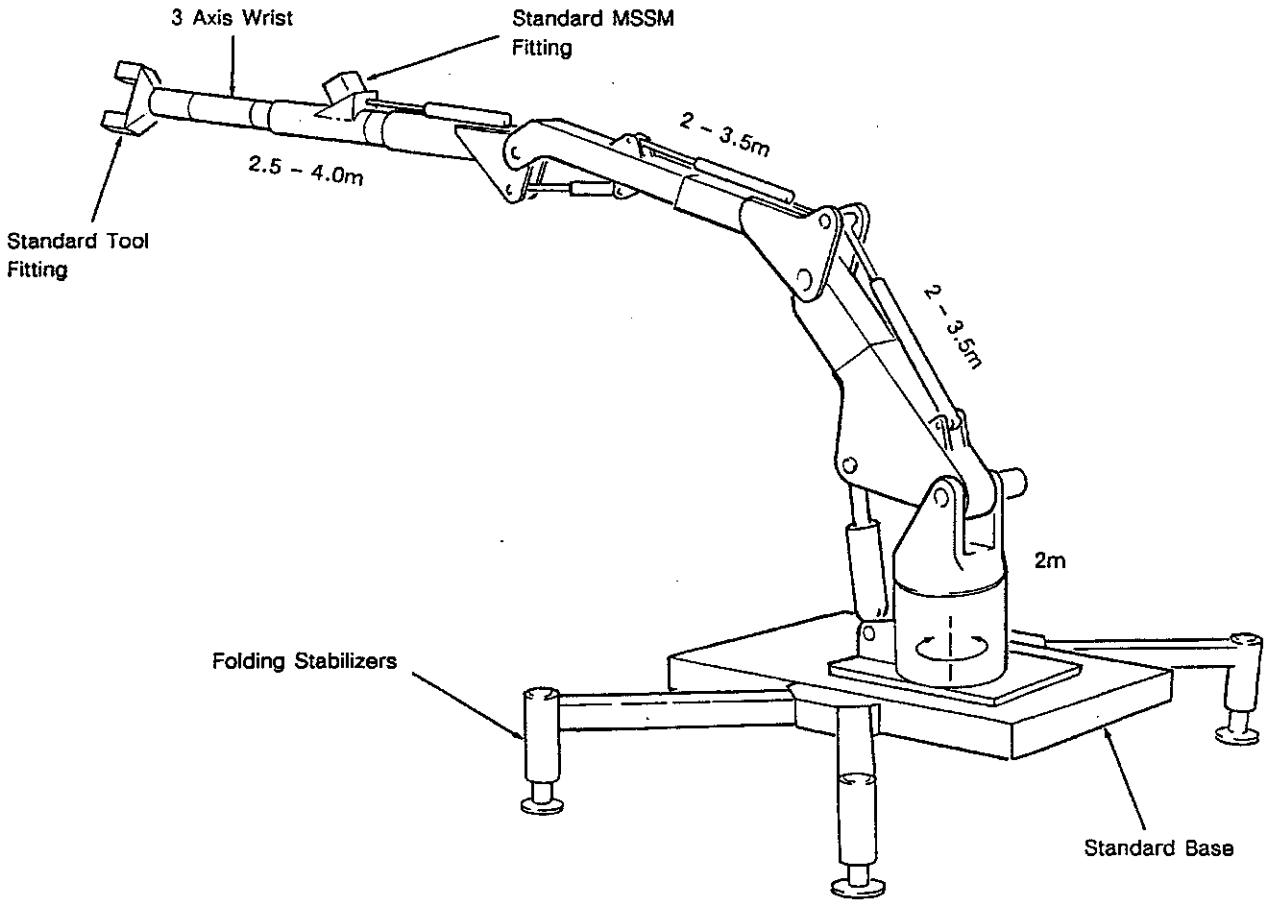

Figure 6.11-15. Mobile Heavy Duty Manipulator

Use or disclosure of data
subject to title page restriction

The manipulator and transporter are electrically driven. Three modes of control are planned similar to the deployable heavy lift manipulator. The manipulator has a powered interface that accommodates a dexterous or power manipulator.

6.11.5.4 Two-Armed Dexterous Manipulator - The Mascot[5] two-armed "master-slave" dexterous manipulator is shown in Figure 6.11-16. It has an "elbows up" configuration with enhanced force reflection capability. It has a highly sensitive "force reflection" capability and allows the operator to experience a sense of "feel" when exerting a force or manipulating an object. The manipulator may be divided into two separate halves that form two individual arms.

The manipulator is a general purpose tool where the slave is positioned at the workplace by one of the aforementioned transporters. The identical master is located at a remote work station. Operator movements of the master cause corresponding movements of the slave. Each arm is able to handle loads up to 20 kg in any direction for 15 minutes and 12 kg in any direction indefinitely.

Each arm has six degrees of freedom, plus jaw gripper movement and shoulder indexing. In addition to the normal "master-slave" control, the fully digital control system allows "teach and repeat" modes of operation. It has advanced control features which allow force scaling and pre-trajectory planning.

During use, the operator may arrange the relationship between the master and slave so that there is a comfortable working position; i.e., if working overhead, the master-slave relationship may be offset by 90°. Similarly, the force reflecting ratio may be scaled so that the weight experienced by the operator is less than the object being manipulated. When carrying out a difficult remote operation such as drilling or welding, the manipulator may be commanded to traverse a straight line.

6.11.5.5 Small Power Manipulator - Figure 6.11-17 shows the RD500.[7] It is a single-armed force-reflecting manipulator with a relatively high load capacity of 50 kg. It has been designed to be rugged and reliable. The primary control system is a "master-slave," but it can function in automatic mode as a robot.

The small power manipulator will be used as a general purpose manipulator where the slave is normally positioned at the work place by a larger transporter. The manipulator is normally used as an individual tool with a set of gripper jaws. Where necessary, the manipulator can hold a standard tool or it can position a special device, such as a welding tool, to carry out a particular task.

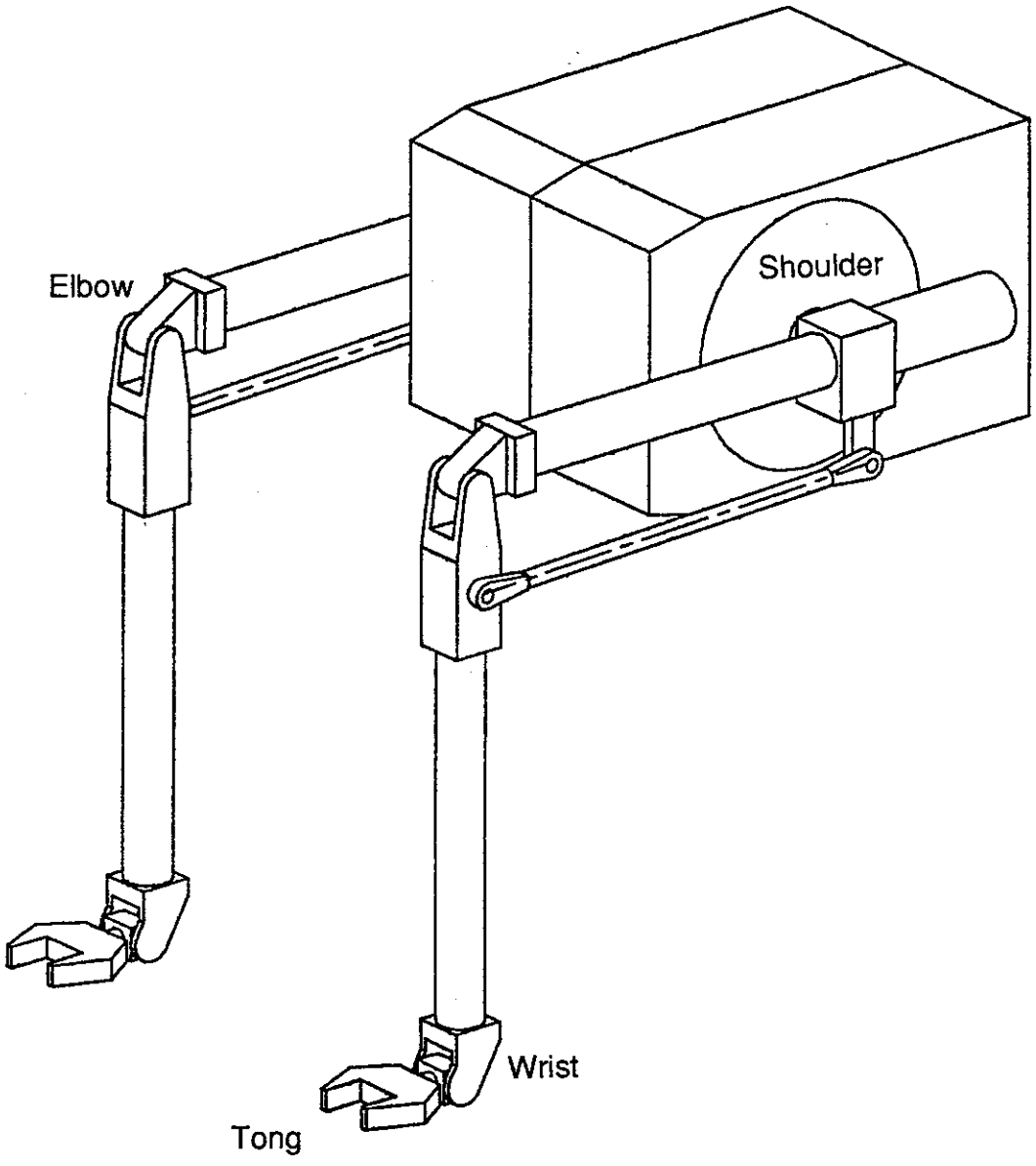

Figure 6.11-16. Two-Arm Dexterous Manipulator

Use or disclosure of data
subject to title page restriction

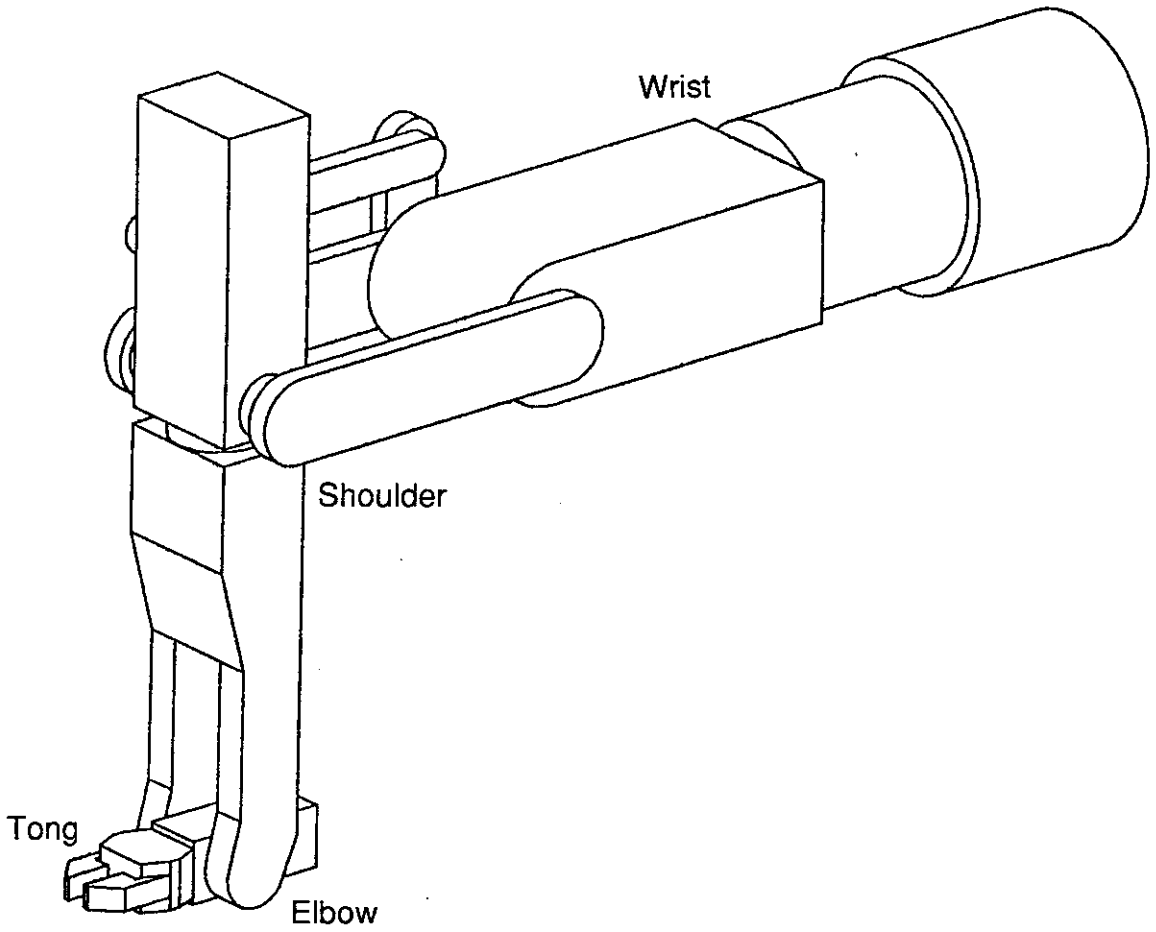

Figure 6.11-17. Small Power Manipulator

Use or disclosure of data
subject to title page restriction

The arm can support a nominal payload of 50 kg for limited periods and 33 kg continuously. The arm has 6 degrees of freedom and is powered by electric motors through harmonic-drive gear boxes.

During operation, the manipulator can select force scaling ratios of 1:10 or 1:4 as required by the operator. It has a geometric scaling ratio of 1:1.5; i.e., 150 mm movement of the master provides 100 mm movement of the arm. This allows the operator to tackle delicate positioning operations with increased dexterity.

6.11.5.6 Steam Generator Robot - Figure 6.11-18 shows the overall arrangement of the steam generator robot. This robot may be used to inspect and repair heat exchanger tubes. The robot has four axes in a plane at right angles to the tube sheet. All four joints are coordinated to provide X, Y, and Z positioning of a tool mounted on the end of the robot arm.

Each joint is a self-contained module, complete with drive motor, gearbox, and position sensor. Basic joint modules are bolted together with different length links to configure the robot to the different heat exchanger units; i.e., the liquid lead/steam generator or helium/steam generator. To enhance radiation resistance, the joints contain no electronics with all feedback provided by resolvers. Maintenance and decontamination are enhanced by providing the joint modules with a means of disassembly.

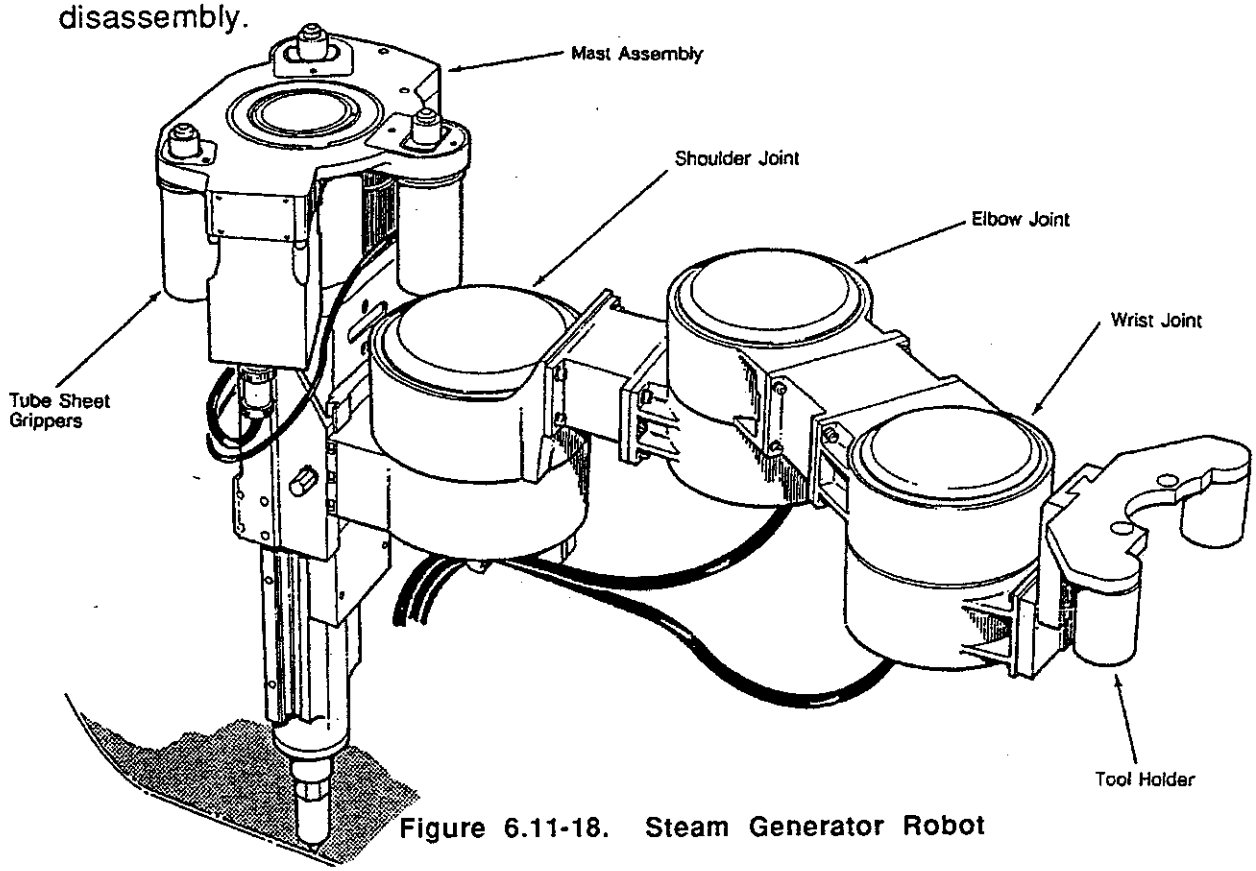

Figure 6.11-18. Steam Generator Robot

Use or disclosure of data subject to title page restriction

References for 6.11

1. In-vessel vehicular system produced by SPAR and Commissariat A L'Energie Atomique (CEA) under contract to NET

2. Lower Plug Manipulator portion of the Canadian ITER contribution produced by SPAR under contract to CFFTP

3. JET Remote Handling Equipment produced by JET team.

4. SPAR 2500 and Schilling manipulators in DOE sponsored Underground Storage Tank Technology Demonstration at Hanford

5. Mascot produced by ENEA (Italian Nuclear Agency)

6. X beam and STEM produced by Astro Aerospace

7. RD500 produced by CEA

This page intentionally left blank.

Use or disclosure of data
subject to title page restriction

6.12 Safety and Environment

One of the paramount goals of the Prometheus project was to develop design criteria consistent with attaining a high degree of safety and compliance with all current and near term regulations. The approach taken to realize these goals was:

- Safety analysis focused on those aspects of Prometheus which are unique to an IFE reactor (i.e., differ from both a fission reactor and a magnetic fusion reactor).
- Approach and methodology from the ESECOM study[1] were used whenever feasible to allow for comparison of results to MFE.
- Designed Prometheus to meet (at a minimum) existing regulatory criteria.

Many of the safety and environmental analyses which were performed for specific Prometheus subsystems are presented in those sections of the report in which the particular subsystem is discussed. For example, Section 6.8.4 provides a description of the shielding analysis which was performed, while Section 6.7.10 provides a description of the calculation of tritium permeation through the heat exchangers that was completed. Section 6.8.2 discusses both an analysis which was done to determine the effects of dry spot formation on the wet wall and the analyses performed to determine an effective design for dissipating Pb^{203} decay heat following a loss of coolant accident.

Additionally, safety and environmental issues continuously influenced many features of the design, although no specific analysis may have been performed. For example, lead was selected as the first wall coolant because of the fire hazard associated with many of the other candidate metals (e.g., lithium, FLiBe). Also, the Prometheus-H reactor vessel was intentionally set as low as feasible within the reactor building in order to reduce seismic response, although a detailed seismic analysis was not performed. Because of its many beamlines, however, it was impracticable to place the Prometheus-L reactor vessel at a low elevation and additional structural support would have to be provided by a more robust reactor building.

Five areas in which specific safety and environmental assessment were made are:

- Occupational Radiation Exposures
- Off-Site Radiation Exposures
- Off-Site Impacts From Accidents
- Waste Disposal
- Non-Radiological Impacts

Use or disclosure of data
subject to title page restriction

In this section, pertinent safety and environmental regulations from the Nuclear Regulatory Commission (NRC), the Environmental Protection Agency (EPA), the Department of Energy (DOE), and the Occupational Safety and Health Administration (OSHA) are reviewed for applicability to the Prometheus reactor. Due to the ground rule of this study which specified that the plant being analyzed is the tenth of a kind, the NRC's and EPA's regulations were used in most cases, instead of DOE's.

6.12.1 Occupational Radiation Exposures - The Nuclear Regulatory Commission's occupational radiation exposure limits are in the 21 May 1991 revision of 10CFR Part 20 and include the 1977 recommendations of the International Commission on Radiological Protection (ICRP), including those of ICRP Publication 26, and subsequent ICRP publications. The external occupational dose limits are:

Committed Effective Dose Equivalent	5 rem/yr
Lens of the Eye	15 rem/yr
Other Organ, Tissue, or Extremity	50 rem/yr

The 10CFR Part 20, Appendix B, Table 1 places limits on the airborne concentration of radionuclides within the work place. For Prometheus, tritium is anticipated to be the radionuclide of greatest concern during normal operations, and its derived air concentration from Appendix B, Table 1 is 2×10^{-5} μCi/ml. There is no difference between HTO and HT values because 10CFR Part 20 assumes that HT and T_2 will oxidize in the air and/or in the body to HTO.

In discussions with the NRC, it was recommended that, due to the time frame of this study, it would be appropriate to incorporate the 1990 recommendations of the ICRP (Publication 60) for normal operation.[2] Although Publication 60 specifies a maximum occupational dose of 5 rem/yr (consistent with current regulations), it also includes a basic dose limit of 10 rem per 5 years.

The Department of Energy's occupational radiation protection standards are contained in DOE Order 5480.11. As with the NRC's standards, these are based on the 1977 recommendations of the ICRP. Hence, the same annual occupational external dose limits as given above apply.

As with the NRC standard, the DOE requires that occupational doses be maintained as low as is reasonably achievable (ALARA). However, during the design of a facility, the DOE specifies that the use of design objectives which are 20% of the applicable standards will result in designs which are ALARA, without having to perform a "cost-benefit" analysis.

Use or disclosure of data
subject to title page restriction

Additionally, the DOE regulations differ from the NRC's in the derived air concentrations. For tritium, the DOE provides a separate guide for airborne elemental tritium of 5×10^{-1} μCi/ml, in addition to an airborne HTO limit of 2×10^{-5} μCi/ml.

Prometheus has been designed to meet the occupational radiation exposure limits of both agencies and maintain exposures ALARA by not exceeding 20% of the applicable limit, as per DOE guidance.

6.12.1.1 Radiation Zone Definitions - For shielding design and access control purposes, the Prometheus plant has been divided into radiation access zones. Given below is a typical radiation zoning scheme that meets the requirements of the revised 10CFR Part 20. The association of areas to radiation zones is based on the occupancy requirements for each area (e.g., continuous occupancy is required in the Main Control Room, while some areas of the Auxiliary and Reactor Service Building will require daily access, and other areas of the building will only require access for maintenance). The necessity to keep exposures ALARA also factors into the assigning of radiation zones to the various areas (e.g., an area should be reduced to a Zone II from a Zone III if it can be done with a minimum expenditure, even though its occupancy requirements do not require that it be a Zone II).

Rather than perform a cost benefit of the shielding analysis to demonstrate the design is ALARA, the design external exposure limits for Zones II, III, and IV have been reduced to 20% of the applicable 10CFR Part 20 limit. The basis for this approach is the DOE Order 5480.11, Section 9.j.(1)(b), which states:

> External Radiation Exposure. The design objectives for personnel exposure from external sources of radiation in continuously occupied controlled areas are ALARA and not exceeding 0.5 mrem (5 microsieverts) per hour on average. The design objectives for exposure rates for potential exposure to a radiation worker where occupancy is generally not continuous are ALARA and not exceeding 20 percent of the applicable standard ...

These ALARA design objective dose rates for Zones II, III, and IV are given in parenthesis after the 10CFR Part 20 exposure limits.

Zone I: <0.05 mrem/hr - This zone has no restriction on occupancy. Such a zone would represent areas in the plant where radiation due to occupancy on a 40-hours per week, 50-weeks per year basis will not exceed the total effective dose equivalent to individual members of the public limit from 10CFR20.1301 of 100 mrem per year. Most non-employees and visitors to the site will receive considerably less than 100

mrem/yr because of the relatively short time interval during which they are on-site. Examples of Zone I areas include: Site Boundary, Administration Building, Turbine Building, etc.

Zone II: <2.5 mrem/hr (<0.5 mrem/hr ALARA Design Objective) - This zone is restricted to access by radiation workers only. Such a zone would represent areas in the plant continuously occupied by plant radiation workers and authorized visitors on a 40-hours per week, 50-weeks per year basis without exceeding the total effective dose equivalent occupational dose limit from 10CFR20.1101 of 5 rem per year. Examples of Zone II areas include: Main Control Room, Auxiliary and Reactor Service Building corridors, etc.

Zone III: <5 mrem/hr (<1 mrem/hr ALARA Design Objective) - This zone is restricted to access by radiation workers only. Such a zone would represent areas in the plant which could be occupied by plant radiation workers and authorized visitors on a less than 40 hours per week and/or less than 50 weeks per year basis without exceeding the total effective dose equivalent occupational dose limit from 10CFR20.1101 of 5 rem per year. The length of stay in this (and higher zoned areas) would be determined by the actual radiation level in the area, the past radiation history of the person entering, and the nature of the radiation. Examples of Zone III areas include: Auxiliary and Reactor Service Building, etc.

Zone IV: >5 mrem/hr (>1 mrem/hr ALARA Design Objective) - This zone is a restricted, radiation area as defined by 10CFR20.1003. Such a zone would need to be posted with a conspicuous sign(s) bearing the radiation symbol and the words "CAUTION, RADIATION AREA", in accordance with 10CFR20.1902(a). Examples of Zone IV areas include: Containment Building during shutdown, Radwaste System Tank cubicles, Auxiliary and Reactor Service Building valve galleries.

Zone V: >100 mrem/hr - This zone is a restricted, high radiation area as defined by 10CFR20.1003. Such a zone would need to be posted with a conspicuous sign(s) bearing the radiation symbol and the words "CAUTION, HIGH RADIATION AREA", in accordance with 10CFR20.1902(b). Access to areas within this zone would be controlled in accordance with the requirements of 10CFR20.1601. Examples of Zone V areas include: Containment Building during operations, Reactor Vessel area during shutdown.

Zone VI: >500 mrem/hr - This zone is a restricted, very high radiation area as defined by 10CFR20.1003. Such a zone would need to be posted with a conspicuous sign(s) bearing the radiation symbol and the words "GRAVE DANGER, VERY HIGH RADIATION AREA", in accordance with 10CFR20.1902(c). Access to areas within this

Use or disclosure of data subject to title page restriction

zone would be controlled in accordance with the requirements of 10CFR20.1602. Examples of Zone VI areas include: Reactor Vessel area during operations.

Airborne Radioactivity - In addition to the above radiation zoning scheme, if an area is determined to contain, or potentially contain, airborne radioactivity in excess of the 10CFR Part 20, Appendix B derived air concentrations (DAC) (i.e., 2×10^{-5} μCi/ml for tritium), the suffix "A" will be added to its radiation zone designation (e.g., if a Zone III area contains airborne tritium in excess of the DAC, it would be designated as a Zone III-A area). Also, each airborne radioactivity area would need to be posted with a conspicuous sign(s) bearing the radiation symbol and the words "CAUTION, AIRBORNE RADIOACTIVITY AREA", in accordance with 10CFR20.1902(d).

6.12.1.2 In-Plant Radiation Monitoring System

The Prometheus In-Plant Radiation Monitoring System has been designed to inform operations personnel, both locally and in the Main Control Room, of radiation and radioactivity levels throughout the plant and to provide warning when abnormal levels occur in specific areas due to possible equipment malfunction. Some channels of the In-Plant Radiation Monitoring System are designed to Safety Class 1E requirements and can withstand accident environmental conditions. The safety class monitors are required to mitigate the effects of an accident by performing some action (e.g., isolate the Containment, close an exhaust valve). The In-Plant Radiation Monitoring System will consist of the following five subsystems:

- Area Radiation Monitoring System - Will measure the ambient radiation levels at various locations throughout the plant.
- Airborne Radiation Monitoring System - Will measure the airborne concentration of radionuclides at various locations throughout the plant.
- Tritium Airborne Radiation Monitoring System - Will measure the airborne concentration of tritium at various locations throughout the plant.
- Process Monitoring System - Will measure the concentration of radioactive fluids in the various process systems of the plant.
- Process Tritium Monitoring System - Will measure the concentration of tritium in the various process systems of the plant.

The In-Plant Radiation Monitoring System is divided into a safety class portion and a nonsafety-related portion, with all safety class equipment designed in accordance with IEEE 279-1971, IEEE 308-1980, IEEE 323-1983, IEEE 336-1985, IEEE 344-1987, and IEEE 384-1981. Safety class equipment will also be qualified in accordance with NUREG-0588 and Regulatory Guide 1.89 requirements.

Use or disclosure of data
subject to title page restriction

Area Radiation Monitors - Safety class Area Radiation Monitors will include:

- Main Control Complex Area Monitor - To detect ambient levels of radiation in the control complex environment, particularly the Main Control Room.
- Containment Isolation Monitor - To detect increased levels of radiation in the exhaust air and to automatically isolate the ventilation system upon signal actuation.
- Containment Post-Accident Monitors - To detect levels of radiation in the containment during the post-accident period.

Non-safety Area Radiation Monitors will include monitors located in strategic areas of the plant (including the Laser Building and/or the Accelerator Tunnel) to indicate to operations personnel the radiation levels within the plant and to signal, alert, or alarm an unacceptably high level of radiation. On the order of 40 to 50 non-safety Area Radiation Monitors are expected to be installed in Prometheus.

Airborne Radiation Monitors - Safety Class Airborne Radiation Monitors will include:

- Main Control Complex Outside Air Intake Monitors - To detect increased radioactivity in the supply air to the control complex environment.

Non-safety Airborne Radiation Monitors will include monitors located within the plant to detect the presence of excess airborne concentrations of radioactivity either in cubicles, open areas, or ventilation ducts. On the order of 30 to 40 non-safety Airborne Radiation Monitors are expected to be installed in Prometheus.

The Airborne Radiation Monitors will measure particulates and noble gases. The sample is drawn into the monitor and then passes through a moving paper filter which collects particulates. A beta sensitive scintillation detector, aimed at the filter, monitors for particulate radiation. After passing through the filter, the sample is dried and then monitored for radioactive gas content.

Tritium Airborne Radiation Monitors - Safety class Tritium Airborne Radiation Monitors will include:

- Main Control Complex Outside Air Intake Monitors - to detect increased tritium levels in the supply air to the control complex environment.
- Target Factory - To detect increased tritium levels in the exhaust air and to automatically isolate the ventilation system upon signal actuation.

Use or disclosure of data
subject to title page restriction

Non-safety Tritium Airborne Radiation Monitors will be collocated with the non-safety Airborne Radiation Monitors in those areas in which airborne tritium contamination could occur. Prometheus is expected to have on the order of 30 to 40 non-safety Airborne Radiation Monitors installed. The Tritium Airborne Radiation Monitors detect tritium airborne concentration by absorption and isotopic exchange processes.

Process Monitoring System - Both the Process Monitoring System and the Process Tritium Monitoring System are expected to contain radioactivity, as well as normally non-radioactive systems to detect developing equipment failure conditions. Twenty to twenty-five Process Monitors and Process Tritium Monitors are expected to be installed in the Prometheus design.

Process Tritium Monitors are similar to the Effluent Tritium Monitors, which are discussed in Section 6.12.2.3, below.

6.12.2 Off-Site Radiation Exposures - As stated above, the NRC's 21 May 91 revision of 10CFR Part 20 follows the lead of the 1977 recommendations of the ICRP, including those of ICRP Publication 26. For individual members of the general public, 10CFR20.1301 specifies an annual dose limit from normal plant operations of 0.1 rem total effective dose equivalent (TEDE).

In addition to the exposure limits contained in 10CFR Part 20 for nuclear power reactors, the NRC has numerical guides for design objectives and limiting conditions of operation contained in 10CFR Part 50, Appendix I. These limits were not revised to reflect the ICRP 1977 recommendations and remain based on the critical organ concept. The general public individual dose limits from effluents are:

Total Body - Airborne Effluent	5 mrem/yr
Any Organ - Airborne Effluent	15 mrem/yr
Total Body - Liquid Effluent	3 mrem/yr
Any Organ - Liquid Effluent	10 mrem/yr

In order to keep off-site exposures ALARA, 10CFR Part 50, Appendix I requires that all items of reasonably demonstrated technology that can effect reductions in dose to the population within 50 miles of the reactor be included in the design. The values of $1000 per total body man-rem and $1000 per man-thyroid-rem (based on 1977 dollars) should be used in determining whether an item is reasonably achievable.

In 10CFR Part 20, Appendix B, Table 2 places limits on the concentration of radionuclides in liquid and airborne effluents at the boundary of the unrestricted area. For Prometheus, tritium is the radionuclide of greatest concern during normal

Use or disclosure of data
subject to title page restriction

operations. The derived air concentrations for tritium are 1 x 10^{-7} μCi/ml for airborne effluents and 1 x 10^{-3} μCi/ml for effluents to water. As for occupational exposure, there is no distinction between HTO and HT Table 2 values because 10CFR Part 20 assumes that HT and T_2 will oxidize in the air and/or in the body to HTO.

The DOE's radiation protection standards and requirements for the public and the environment are contained in DOE Order 5400.5 and, since they are also based on the 1977 recommendations of the ICRP, the annual dose limit to members of the general public is the same as the NRC's 100 mrem.

As with occupational exposure, the DOE differs from the NRC in the tritium concentration guides. The DOE provides a separate guide for airborne elemental tritium of 2 x 10^{-2} μCi/ml, in addition to an airborne HTO limit of 1 x 10^{-7} μCi/ml. Also, because the NRC reduces its concentration limits by a factor of two so that they will be applicable to age groups other than adults, the DOE liquid tritium concentration guide of 2 x 10^{-3} μCi/ml is twice the NRC's value.

In 40CFR Part 61, "National Emission Standards for Hazardous Air Pollutants" (NESHAP), the Environmental Protection Agency (EPA) presents its regulations, under the Clean Air Act, for emissions of radionuclides. In 40CFR Part 61 sets standards for different categories of facilities, including DOE facilities, NRC-licensed facilities, and uranium fuel cycle facilities. However, when a dose limit is used as the standard, it is usually set at 10 mrem/yr (40CFR61.92 & 61.102) effective dose equivalent. Although the EPA applies NESHAP regulations to DOE facilities, it has suspended them for facilities (such as Prometheus) that are regulated by the NRC.

The EPA's regulations for radionuclides released into surface water are contained in 40CFR141.16, "National Primary Drinking Water Regulations, Mixed Containment Levels for Beta Particles and Photon Radioactivity from Man-Made Radionuclides in Community Water Systems." The dose limit in 40CFR141.16 for the maximum exposed individual is 4 mrem/yr.

Prometheus has been designed to meet the NRC's 10CFR Part 50, Appendix I off-site dose guides for design objectives and limiting conditions of operation, and limit the tritium concentration to the values given in 10CFR Part 20, Appendix B, Table 2. It will also, then, meet the applicable DOE and EPA requirements.

6.12.2.1 Normal Operation Release Estimate—HT vs HTO - The two primary forms of tritium released to the environment from Prometheus are tritiated water vapor (HTO) and tritium-hydrogen gas (HT), with a small amount of tritium gas (T_2). Since

Use or disclosure of data
subject to title page restriction

HTO is approximately 25,000 times more radiotoxic than HT, it is important to know the fraction of the initial release which is HTO, as well as the extent of oxidation of HT to HTO in the open environment and the body, in order to realistically estimate the off-site exposure. However, little data are available regarding the rate of conversion of tritium from its gas form to tritiated water vapor. Two sources of such data are the experimental releases of HT, conducted at the Chalk River Meteorological Field on 26 August 1986 and 10 June 1987[3,4,5] and at the CEA Centre of Bruyere-le-Chatel on 15 October 1986.[6,7] These experiments confirmed that most of the oxidation occurs in the top layer of soil as opposed to in the atmosphere, and that the rate of conversion is slow. Russell and Ogram[5] present a maximum downwind HTO/HT concentration ratio of 3.4×10^{-4}, when pure HT is released.

Nonetheless, discussions with the NRC[2] indicate that because of the difficulty in determining when, where, and to what extent the oxidation of HT to HTO occurs, the NRC would be prone to assume that all tritium releases from the plant, both normal operation and accident conditions, are in the oxide form. As discussed above, this is consistent with revised 10CFR Part 20, Appendix B, which instructs that the HTO tritium annual limits on intake (ALI) and derived air concentrations (DAC) be used for HT and T_2, since "HT and T_2 oxidize in air and in the body to HTO."

With the assumption that all tritium is released in the HTO form, the maximum allowable annual tritium release from Prometheus can be determined from:

$$5\left[\frac{\text{mrem}}{\text{yr}}\right] = \frac{50\left[\frac{\text{mrem}}{\text{yr}}\right]}{1 \times 10^{-7}\left[\frac{\mu\text{Ci}}{\text{ml}}\right]} \bullet Q\left[\frac{\text{Ci}}{\text{yr}}\right] \bullet 1 \times 10^{-5}\left[\frac{\text{sec}}{\text{m}^3}\right] \bullet \frac{10^{-6} \bullet 10^{6}}{3.15 \times 10^{7}}\left[\frac{\text{yr-m}^3\text{-}\mu\text{Ci}}{\text{sec-ml-Ci}}\right]$$

Where:

5 [mrem/yr]	= The 10CFR Part 50, Appendix I whole body limit,
50 [mrem/yr]	= The 10CFR Part 20, limit used to determine DACs,
1×10^{-7} [μCi/ml]	= The 10CFR Part 20, Appendix B, Table 2, HTO DAC,
Q [Ci/yr]	= Annual tritium release, and
1×10^{-5} [sec/m^3]	= Annual average atmospheric dispersion.

All other parameters are units conversion factors.

Solving the above equation gives: $Q = 3.15 \times 10^4$ (Ci/y) = 86.2 (Ci/d). This is well above the daily tritium release design value of 10 [Ci/day] that was used in the Prometheus design (see Section 6.7). With a tritium release of 10 [Ci/day], the annual off-site dose would be less than 1 mrem. Taking credit for some tritium being in its

elemental form will result in a greater maximum allowable annual release, while still maintaining off-site exposures within the 10CFR Part 50, Appendix I limits.

6.12.2.2 Effluent Monitoring System - The Prometheus Effluent Monitoring System measures the radioactivity concentration in the effluent streams from the plant for the determination of off-site releases. This system also actuates alarms and actions which prevent the continued effluent release if either the instantaneous or average release limits are exceeded. The Effluent Monitoring System monitors for particulate, noble gas, and tritium radioactivity at the point of release to the environs. The Effluent Monitoring System will consist of the following subsystems:

- Effluent Monitoring System - Will measure the concentration of radioactive fluids at the various release points of the plant.
- Effluent Tritium Monitoring System - Will measure the concentration of tritium at the various release points of the plant.

The following effluent points are measured for radioactivity:

- Plant Stack
- Containment Ventilation Exhaust
- Auxiliary Building Exhaust
- Target Factory Exhaust
- Laser Building Exhaust
- Accelerator Tunnel Exhaust
- Gaseous Radwaste Effluent
- Liquid Radwaste Effluent

The Effluent Tritium Monitors are composed of individual channels, consisting of a sampling ionization chamber, a check source, and an analyzer. The ionization chamber is ion differentiating so that non-tritium radionuclide emissions of a higher energy producing more energetic primary ions are spectrally differentiated from the weak tritium beta (i.e., 18.6 KeV). A Bremsstrahlung On-Line Monitoring System will be used for tritium monitoring of liquid effluents. Ionization chambers would be adequate for gaseous effluents. This system is comprised of a dual matched GELI detector system with two bremsstrahlung windows, one of gold foil and the other of aluminum foil. By virtue of a subtract mode, the differential signal between the gold-foiled GELI and aluminum-foiled GELI yields the actual tritium bremsstrahlung signal, since all other signals would be registered on both detectors with the same magnitude.

6.12.3 Off-Site Impacts From Accidents - For the purposes of defining the exclusion area of a power reactor, 10CFR Part 100 specifies that for the two hours

Use or disclosure of data subject to title page restriction

immediately following onset of the postulated accident, an individual located at the exclusion area boundary would not receive a whole body dose in excess of 25 rem or a thyroid dose in excess of 300 rem. Likewise, for determining the distance to the boundary of the low population zone, 10CFR Part 100 specifies that for the duration of the postulated accident, an individual located at the low population zone boundary would not exceed the same limits. The postulated radionuclide release assumed for these calculations should be based upon a major accident, hypothesized for purposes of site analysis or postulated from consideration of possible accidental events, that would result in potential hazards not exceeded by those from any accident considered credible.

In addition to the guidance provided in 10CFR Part 100, the NRC has developed Standard Review Plans (NUREG-0800)[8] that describe how the NRC reviews each section of a Safety Analysis Report, including the design basis accident analyses of each system and subsystem. Depending on the expected frequency of occurrence of an accident, NUREG-0800 requires that the calculated off-site exposures be either "within," "well within (i.e., 25%)," or "a small fraction of (i.e., 10%)" 10CFR Part 100 limits.

In DOE Order 6430.1A, "Design Criteria," Section 0200-1.3 "Radiological Siting Guidelines," the DOE provides dose values to be used in the evaluation of design basis accidents. In addition to the whole body and thyroid dose limit (which are the same as the NRC's 10CFR Part 100 limits), Order 6430.1A provides limits for the bone surface (300 rem), the lung (75 rem), and other organs (150 rem). Finally, this Order specifies an effective dose equivalent limit (25 rem) in keeping with the ICRP's 1977 recommendations.

Prometheus was designed to meet the DOE's effective dose equivalent limit of 25 rem for the worst case design basis accidents and will be "well within" or a "small fraction of" this limit for lesser, more frequent design basis accidents. It is not necessary to impose the thyroid dose limit on Prometheus, since radio-iodine will not be a contributor to exposures from a fusion reactor.

6.12.3.1 LSA Determination - The ESECOM study,[1] sponsored by the DOE, is the most comprehensive examination of safety and environmental issues for magnetic fusion energy (MFE) reactors. Recognizing that the current state of development of fusion reactor technology is still in the conceptual design phase and that high levels of uncertainty exist about postulated accident sequences and probabilities, MFE studies could not follow the path taken by the fission reactor community, where extensive (and expensive) PRA accident analyses are conducted during the design phase of each new plant. Instead, the ESECOM study applied a simpler, semi-quantitative approach

to safety analysis of MFE reactors. This same methodology was applied to the Prometheus reactors.

The ESECOM study defined four levels of safety assurance (LSA) to characterize the relative risks of different design concepts. Although the categories are coarse, such classification facilitates comparison of the degree of inherent safety (i.e., passive versus active safety systems) in different IFE designs and, indeed, comparison to MFE designs (e.g., ARIES) and fission reactors. LSA levels are defined as:

Level	Characteristics
1	*Safety is assured by passive mechanisms of release limitations no matter what the accident sequence. The radioactive inventories and materials in such a reactor preclude a fatal release regardless of the reactor's condition.*
2	*Safety is assured by passive mechanisms of release limitations as long as severe reconfiguration of large-scale geometry is avoided, and escalation to fatality-producing reconfigurations from less severe initiating events can plausibly be precluded by passive design features. In such a reactor, natural heat-transfer mechanisms suffice to keep temperatures below those needed–given its radioactivity inventories and material properties–to produce a fatal release unless large-scale geometry is badly distorted.*
3	*Safety is assured by passive mechanisms of release limitations as long as severe violations of small-scale geometry–such as a large break in a major coolant pipe–are avoided, and escalation to fatality-capable violations from less severe initiating events can plausibly be precluded by passive design features. In such a reactor, sufficiency of natural heat-transfer mechanisms to keep temperatures low enough to avoid a fatal release–given the radioactivity inventories and materials properties–can only be assured while the coolant boundary is substantially intact.*
4	*There are credible initiating events that can lead to fatalities without any severe violation of small-scale or large-scale geometry or that can only be prevented from escalating to fatality-capable boundary violations or reconfigurations by means of active safety systems.*

Thus, the LSA categories range from totally passive (LSA = 1) to conditions requiring active safety features (LSA = 4). The ESECOM study also developed the concept of threshold dose release fractions (TDRF) to evaluate the potential hazard of a particular radionuclide appearing in a particular material or form. The TDRF of a radionuclide is

Use or disclosure of data subject to title page restriction

defined as that fraction which must be mobilized to produce an off-site dose equal to some dose limit. For TDRF greater than one, release of all the inventory would not exceed the dose limit.

The threshold dose release (i.e., the release which would result in an off-site individual receiving a dose equivalent to the dose criteria) was determined for Prometheus from the ESECOM data. These are presented on Table 6.12-1. The N^{16} ESECOM

Table 6.12-1 ESECOM[1] Threshold Dose Release (Curies)

	Case 1	Case 2
H^3	2.5×10^8	8.9×10^7
N^{16}	—	—
Al^{28}	1.5×10^{11}	—
Cr^{51}	1.8×10^8	1.9×10^6
Fe^{55}	6.4×10^8	1.1×10^7
W^{187}	2.4×10^7	5.4×10^6
Pb^{203}	3.1×10^7	3.3×10^6
Pb^{209}	2.1×10^9	5.5×10^6
Po^{210}	4.2×10^4	9.6×10^3

threshold release was not determined due to the extremely short half-life of N^{16}. The Prometheus inventories (found in Section 6.4 and 6.7 for tritium and Section 6.8 for the other radionuclides) were compared to the release values and found to be less for all radionuclides (i.e., TDRF > 1.0), with the exception of W^{187} and Pb^{203}.

For example, it has been determined that the Prometheus Po^{210} inventory in the lead coolant amounts to a maximum of 1.6×10^3 Ci. The ESECOM limit for this radionuclide, so as not to exceed an off-site dose (case 1) of 200 rem, is 4.2×10^4 Ci. Thus, the TDRF = $4.2 \times 10^4 / 1.6 \times 10^3 = 26$. Since this is much greater than 1.0, even if all the Po-210 were to become mobilized, the off-site dose would not exceed the regulatory limit. This results in an LSA of one (totally passively safe) for all accidents involving only Po^{210} mobilization.

With respect to the two Prometheus radionuclides with a TDRF of less than one, the following observations are made. The ESECOM W^{187} inventory also exceeded that which would allow classification as an LSA of one. However, ESECOM still classified the SiC reactor system as a nominal LSA of one because of the low inherent mobility of tungsten (an ESECOM mobility category of IV "somewhat volatile"), and the absence of a mechanism for mobilization of the tungsten. Likewise, the W^{187} component of the Prometheus design will be classified as an LSA of one.

Use or disclosure of data
subject to title page restriction

A larger concern is the Pb^{203}, since its inventory exceeds the Threshold Dose Release value and since lead has been classified into a higher mobility category then tungsten (an ESECOM mobility category of III "somewhat to highly volatile"). Also, as discussed in Section 6.8.2, the Prometheus design has had to incorporate features to dissipate the decay heat generated by the Pb^{203} which could be disrupted by a reconfiguration of large-scale geometry. For these reasons, the tentative classification of Pb^{203} as an LSA of one is subject to change, but in any case the highest LSA classification for Pb^{203} would be that of two.

This LSA determination demonstrates the technique of radionuclide "inventory control" where passive safety is assured by limiting amounts of radionuclides below quantities which could exceed off-site dose limits if mobilized. The Prometheus design specifies low activation materials where possible (e.g., SiC structural material, He coolant) and limits amounts of tritium contained in any one place.

6.12.3.2 NRC Compliance - A second evaluation was performed to demonstrate compliance with the above quoted NRC and DOE regulations using the methodology specified by the NRC in various Regulatory Guides, Standard Review Plans, and elsewhere.

Because the radionuclides of interest for this study are not the common radionuclides of interest for a fission reactor, the fission literature does not provide readily available dose conversion factors. Therefore, the dose conversion factors for this evaluation were determined from DOE Order 5400.5 derived concentration guides (DCG) and dose limits. The dose conversion factors which were determined, as well as the DCGs, are provided on Table 6.12-2.

The radionuclide release which will result in a specified off-site dose can be determined from:

$$R\,[Ci] = \frac{D[rem]}{\frac{\chi}{Q}\left[\frac{sec}{m^3}\right] \bullet DCF\left[\frac{rem - m^3}{Ci - sec}\right]}$$

Where:

R [Ci]	=	the NRC threshold dose release,
D [rem]	=	the 10CFR Part 100 dose limit,
χ/Q [sec/m^3]	=	the atmospheric dispersion, and
DCF [(rem-m^3) / (Ci-sec)]	=	the dose conversion factor.

Use or disclosure of data subject to title page restriction

The atmospheric dispersion was determined to be 1.78×10^{-4} [sec/m^3] via the plume meander methodology from Regulatory Guide 1.145 and the meteorological parameters from the ESECOM study (i.e., a site boundary distance of one kilometer, stability class F, and a wind speed of 1 meter/second). The NRC threshold dose release values that were determined are presented in Table 6.12-2. For example, for tritium:

$$4.43 \times 10^{6} = \frac{25}{1.78 \times 10^{-4} \bullet 3.17 \times 10^{-2}}$$

Note that the calculated NRC threshold dose releases are much lower than the ESECOM threshold dose releases. This is due to the different methodology utilized in their determinations and is not contradictory since the NRC allows credit to be taken for other factors such as hold up by the containment.

Table 6.12-2 NRC Compliance Parameters

	Derived Concentration Guides		DCF	NRC Threshold
	Inhalation (mCi/ml)	Immersion (mCi/ml)	(rem-m^3) (Ci-sec)	Dose Release Curies)
H^3 (HTO)	1.0×10^{-7}	Not Given	3.17×10^{-2}	4.43×10^{6}
N^{16}	Not Given	3.0×10^{-9}	1.06×10^{0}	—
Al^{28}	1.5×10^{11}	1.0×10^{-8}	3.17×10^{-1}	4.43×10^{5}
Cr^{51}	5.0×10^{-8}	Not Given	6.34×10^{-2}	2.22×10^{6}
Fe^{55}	5.0×10^{-9}	Not Given	6.34×10^{-1}	2.22×10^{5}
W^{187}	2.0×10^{-8}	Not Given	1.58×10^{-1}	8.89×10^{5}
Pb^{203}	2.0×10^{-8}	Not Given	1.58×10^{-1}	8.89×10^{5}
Pb^{209}	1.0×10^{-7}	Not Given	3.17×10^{-2}	4.43×10^{6}
Po^{210}	1.0×10^{-12}	Not Given	3.17×10^{3}	4.43×10^{1}

6.12.4 Waste Disposal - Waste disposal issues were also investigated, considering both radioactive and hazardous (non-radioactive) waste regulations as applied to Prometheus. The Resource Conservation Recovery Act (RCRA) is the primary Federal statute which governs the regulation of solid and hazardous waste. RCRA is broken into many subtitles. The subtitle particularly pertinent to Prometheus is C: "Hazardous Waste." Subtitle C provides "cradle-to-grave" regulation of hazardous waste and authorizes the EPA to regulate the generation, transportation, treatment, storage, and disposal of hazardous waste. Regulations governing these processes are contained in 40CFR Part 262 (generation), 40CFR Part 264 (treatment, storage, and disposal), 40CFR Part 268 (treatment, and land disposal), and 49CFR Part 170 (transportation).

Use or disclosure of data subject to title page restriction

Low level radioactive waste (LLW) is regulated by the NRC under 10CFR Part 61 "Licensing Requirements for Land Disposal of Radioactive Waste." Depending on the degree of radioactivity, 10CFR 61.55 classifies waste as being Class A, Class B or Class C, with Class A waste being the least radioactive. It is expected that Prometheus, like other proposed IFE reactor plants, along with MFE plants, should produce a much lower level of radioactive waste than the same size fission plants.

"Greater than Class C" waste is waste with radionuclide concentrations which are greater than those allowed by 10CFR Part 61 for disposal in a near surface facility, but which do not meet 10CFR Part 60 definition of high level waste. In a Statement of Consideration, the NRC has stated that all greater than Class C waste is a Federal responsibility and indicates that no permanent disposal facility for this waste will be available for at least 15 to 20 years. In the meantime, the NRC suggests that the Federal government provide limited access to an existing DOE storage facility.

The only Prometheus radionuclide of concern that has specific concentration limits specified in 10CFR61.55, Table 1 or 2 is C^{14}. The 10CFR61.55 specifies that if the C^{14} concentration in waste does not exceed 0.8 Ci/m^3 then the waste is Class A. If the C^{14} concentration is greater than 0.8 Ci/m^3, but less than 8 Ci/m^3, then the waste is Class C. The C^{14} concentration in Prometheus ranges from 0.13 Ci/m^3 after two years of full power operation in the first wall to 0.2 Ci/m^3 after 30 years of full power operation in the blanket. (See Table 6.8.5-2 and related text for explanatory data.) Therefore, the **first wall and blanket can be disposed of as Class A LLW.**

The regulations contained in 10CFR Part 61 were developed by the NRC to address existing LLW concerns and only explicitly address a very limited number of radionuclides. If a fusion reactor design using liquid lead as a coolant becomes a popular power reactor, then the NRC may revise their regulation to address radionuclides which are characteristic of this design (e.g., Pb-205). Reference 9 provides an estimate of what LLW concentration limits could be for radionuclides of interest to fusion reactors, including Pb-205. In determining these limits, Reference 9 utilized the same methodology that the NRC used to determine the 10CFR Part 61 limits. For Pb-205, Table II of Reference 9 gives a concentration limit of 1 x 10^6 Bq/cm^3 (27 Ci/m^3) but does not indicate whether this is a Class A or Class C limit. The maximum Prometheus Pb-205 concentration is 13.2 Ci/m^3 after two years of full power operation, or 198 Ci/m^3 after 30 years of full power operation.

Mixed wastes are wastes which contain both hazardous and radioactive materials. The 10CFR61.2 defines hazardous waste as "those wastes designated as hazardous by EPA regulations in 40CFR Part 261." The 10CFR61.56 states that any radioactive waste "containing hazardous, biological, pathogenic, or infectious material must be

Use or disclosure of data
subject to title page restriction

treated to reduce to the maximum extent practicable the potential hazard from the non-radiological materials." The 40CFR Part 261 considers lead to be an extraction procedure (EP) toxic substance, as per the Extraction Procedure Toxicity Test (40CFR Part 261, Appendix II) and has given lead the hazardous waste number D008 (40CFR261.24, Table I). For Prometheus, the lead coolant will have to be classified as a hazardous material and any radioactive lead which cannot be recycled will have to be disposed of as mixed waste (both radioactive and hazardous).

The Hazardous and Solid Waste Amendments Act of 1984 brought mixed radioactive/hazardous waste into the RCRA universe. Prometheus will need RCRA generator permits for mixed waste under 40CFR Part 262.

6.12.4.1 Waste Volume Estimates - As described in Section 6.8.2, the first wall of Prometheus has been designed to last two years. With the replacement of the first wall, the old wall will have to be disposed of as LLW. The volume of SiC in the first wall is approximately 170 ft^3, assuming a packing fraction of 0.67 (to account for fitting the shaped wall into a disposal container). The amount of first wall to be disposed of is estimated to be 255 ft^3 over two years (or 128 ft^3/yr). For the purpose of this study, a LLW disposal cost of $100 per cubic foot has been assumed.

The amount of lead contained in the first wall coolant system is estimated at 540 ft^3. Because of the high cost of disposal of mixed waste (currently estimated to be $15,000 per cubic foot[10]), it is preferable to keep the original lead as the first wall coolant for the duration of operations (i.e., 30 years). After operations cease, the lead can either be disposed of as mixed waste or recycled into the replacement reactor. With the recycle option, however, the Pb^{205} will continue to increase in concentration due to its extremely long half-life (15 million years).

6.12.5 Non-Radiological Impacts - The Occupational Safety and Health Administration (OSHA) has promulgated a voluminous set of health and safety standards. OSHA's standards, which apply to employee activities in all industries (including the electric utility industry), are codified as 29CFR Part 1910. OSHA's standards for construction activities (including power plant construction) are codified as 29CFR Part 1926. In general, these standards have already been adopted by nationally recognized standards setting organizations and Federal standards in existence in 1971. In addition to complying with these standards, employers are required to maintain records of employee exposure to potentially hazardous materials and report to OSHA periodically work-related deaths, injuries, and illness.

Lead toxicity and exposure are of interest in the Prometheus design, since lead is used as a first wall coolant and protector. The regulations governing occupational

Use or disclosure of data
subject to title page restriction

exposure to airborne lead are defined by OSHA and are contained in 29CFR1910.1025, which defines an action level concentration of 30 $\mu g/m^3$, time weighted average (TWA), based on an 8-hour work day. The action level initiates several requirements, such as exposure monitoring, medical surveillance, and training and education. The permissible exposure limit for lead is defined as 50 $\mu g/m^3$ TWA. If an employee is exposed to lead above the permissible level, a respirator must be worn by the employee. In addition, when the lead level exceeds the permissible exposure limit, warning signs must be posted.

The National Institute for Occupational Safety and Health (NIOSH) has set an Immediately Dangerous to Life or Health (IDLH) level for lead of 700 $\mu g/m^3$. The Control Room personnel (and other critical personnel) will be protected such that the lead levels are below this IDLH value for all credible accidents.

Also of special concern in the Prometheus-L plant is the possibility of exposure of personnel to fluorine in the KrF laser system. The NIOSH has set the time weighted average exposure limit for fluorine at 0.1 ppm (0.2 $\mu g/m^3$), with an IDLH value of 25 ppm. The time weighted average exposure limit for fluorides is set at 5.5 $\mu g/m^3$, with an IDLH value of 500 $\mu g/m^3$.

The Clean Water Act of 1977 established a comprehensive program to regulate pollutant discharges into surface waters of the United States. This program is implemented primarily through the discharge permit program of CWA Section 402, called the National Pollutant Discharge Elimination System (NPDES). The Environmental Protection Agency (EPA) usually delegates to the states the enforcement of the NPDES. Since for this study a particular state has not been identified, a "representative" set of discharge limits is postulated based on 40CFR Part 423.

Detailed analysis of Prometheus for compliance with non-radiological regulations was not performed. However, no "design threatening" problems were found or expected to be found following a future, more comprehensive examination.

6.12.6 Safety and Environment Conclusions - The Prometheus study has identified applicable regulations which must be factored into the design of a commercially viable IFE power plant and demonstrated that they can be met. The ESECOM level of safety assurance methodology was applied to Prometheus in assessing off-site doses due to releases of key radionuclides present in the plant. With the exception of W^{185} and Pb^{203}, the Prometheus inventories allow the plant to be classified as totally passively safe (LSA = 1). The tungsten isotope was also

Use or disclosure of data
subject to title page restriction

identified in the ESECOM study, but not seen as a problem due to its immobility. The lead isotope, however, is unique to Prometheus with its lead coolant, and design features to remove lead afterheat in the event of loss of cooling have been incorporated to address this issue.

In addition to determining the LSA level of Prometheus, compliance with the NRC's accident dose criteria and the NRC's and EPA's normal operational dose criteria were also determined. Environmental, nonradiological EPA regulations such as the Clean Water Act and the Resource Conservation Recovery Act were examined with no "design threatening" problems identified or expected to be identified.

Finally, during the course of the Prometheus study, a number of safety and environmental issues were identified that must be addressed prior to the successful commercial operation of IFE reactors. These issues are identified and discussed in Section 5.3 Key Issues Description. Although some of these safety and environmental issues are a direct result of the Prometheus design (e.g., liquid lead), others are generic to Inertial Fusion Energy (e.g, local dry spots), while still others are generic to all fusion reactors (e.g., tritium). With few exceptions, these safety and environmental issues can be resolved via engineering analysis and design and do not constitute a major obstacle to the successful development of IFE.

References for 6.12

1. J. P. Holdren, Chair, et al., "Report of the Senior Committee on Environmental, Safety, and Economic Aspects of Magnetic Fusion Energy," UCRL-53766, 25 September 1989.

2. Personnel communication with Dr. Donald Cool, Chief, Radiation Protection and Health Effects Branch, Division of Regulatory Applications, Office of Nuclear Regulatory Research, Nuclear Regulatory Commission, 6 October 1991.

3. R. M. Brown, et al., "Field Studies of HT Behavior in the Environment: 1. Dispersion and Oxidation in the Atmosphere," Fusion Technology, Volume 14, Number 2 Part 2B, September 1988.

4. G. L. Ogram, et al., "Field Studies of HT Behavior in the Environment: 1. The Interaction with Soil," Fusion Technology, Volume 14, Number 2 Part 2B, September 1988.

Use or disclosure of data subject to title page restriction

5. S. B. Russell and G.L. Ogram, "Modelling Elemental Tritium Deposition, Conversion and Reemission Using Ontario Hydro's Tritium Dispersion Code," Fusion Technology, Volume 14, Number 2 Part 2B, September 1988.

6. H. Djerassi and W. Gulden, "Overview of the Tritium Release Experiment in France," Fusion Technology, Volume 14, Number 2 Part 2B, September 1988.

7. P. Paillard, et al., "Tritium Release Experiment in France Results Concerning HT/HTO Conversion in the Air and Soil," Fusion Technology, Volume 14, Number 2 Part 2B, September 1988.

8. U.S. Nuclear Regulatory Commission, "Standard Review Plan," NUREG-0800.

9. C. Ponti, "Recycling and Shallow Land Burial as Goals for Fusion Reactor Materials Development," Fusion Technology, Volume 13, January 1988.

10. D. W. Stever, "EPA Regulation of Mixed Waste," Sidley & Austin, Mixed Waste Regulation Conference, June 1991.

Use or disclosure of data subject to title page restriction

6.13 Economics

This section presents an economic assessment (cost analysis) for the Prometheus power plants. The projected costs are developed using the basic groundrules and assumptions discussed in Section 3, together with the parametric performance and cost scaling developed in support of the systems modeling. Efforts have been made to normalize the cost projections across all subsystems, but this is difficult because proposed technologies often correspond to significant extrapolations of present-day hardware. Where possible, costs were normalized using assumptions from recent MFE studies[1-2] to provide a common basis for comparison. Elsewhere, costs were based on the best judgment of technical experts. Economic scaling in the present systems model ICCOMO has evolved over many years. The models were originally developed as part of the STARFIRE reactor design study[3] and were adapted to IFE as part of the HIFSA project[4]. As a result, many of the cost models used here have achieved some level of acceptance within the fusion community. A detailed description of the final cost models is presented in Appendix C.

The program guidelines stated that costs are to be evaluated for a tenth-of-a-kind power plant. The enclosed economic analysis has attempted to conform to this guideline and the rationale for doing so is presented in Appendix C. However, cost scaling models in the systems code are represented in terms of the first commercial unit. This prevents a somewhat arbitrary learning curve cost adjustment from influencing the systems trade studies. Many results in this section are, therefore, presented in the form of relative comparisons in order to avoid confusion in relating them to the tenth unit costs discussed for the baseline design point. In cases where learning curve adjustments have been applied, they are so noted and the assumed learning factor is documented.

The effect of different learning curves on projected cost is shown in Figure 6.13-1. It compares unit cost reduction factors for 90, 80 and 70% learning curves in plants with a single unit per plant to those for plants with 100 units per plant. This figure highlights the significant effect that learning curve assumptions can have on the projected COE for the tenth plant. For example, the cost of the tenth plant reactor vacuum vessel (one per plant) is less than half of its first plant cost assuming an 80% learning curve. On the other hand, the cost of grazing incidence mirrors (60 per plant) will be less than 40% of the first plant cost for the same learning curve assumption. Therefore, experience and judgment were used in applying learning curves to the unit costs with values of 85-90% typically assumed for most systems.

A cost summary for the Prometheus-L and -H tenth-of-a-kind power plants is presented in Table 6.13-1. This table also shows the learning curves assumed for each subsystem. Note that learning curves were used only in the target plant, reactor plant, and driver systems and not to the "standard" balance-of-plant systems.

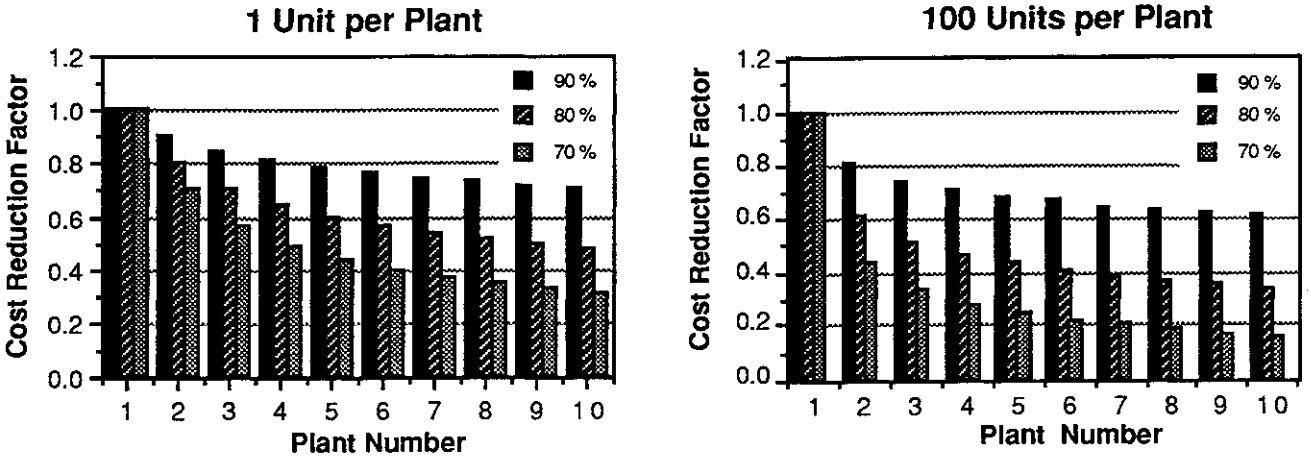

Figure 6.13-1. Unit Cost Reduction Factors for 70, 80 and 90% Learning

Comparing the two cost summaries of Table 6.13-1 shows that the projected COE for the laser-driven plant is ~15% higher than that for the heavy ion linac-driven plant. This is a surprising result for a 1000 MWe power plant since it is contrary to the past perceptions that heavy ion drivers were only attractive for larger units (> 1500 MWe) where the high capital cost of the driver could be distributed over more delivered power. The innovative single beam linac results in a heavy ion driver cost that is nearly identical to that for the laser (~$400M) even though the laser delivers only 4 MJ compared to 7.8 MJ for the heavy ion system. The COE difference is, thus, a direct consequence of ηG which is 21 for the heavy ion compared to only 8 for the laser system. As a result, the reactor and balance-of-plant systems must be larger for the laser driver and this is reflected in their costs which are ~$230M higher for the laser plant. In addition, as discussed in Section 6.3, the projected plant availability is 80.8% for the heavy ion system as compared to 79.4% for the laser which also lowers the heavy ion COE.

A key aspect of this cost difference involves the ~$130M reduction in reactor plant cost for the heavy ion design in spite of a fusion yield of 719 MJ as compared to 497 MJ for the laser system. The design studies indicate that cavity vapor pressure, not target yield, is the determining factor for the design of wetted wall cavities larger than 4 m radius. This permits the use of nearly identical cavity designs for both driver concepts. Cavity vapor pressure and size are directly related for a wetted wall design. This is due to the need to conduct surface heat through the first wall structure and into the coolant while maintaining a suitable surface temperature and cavity vapor pressure.

Use or disclosure of data
subject to title page restriction

Table 6.13-1. Cost Summaries for Prometheus-L and -H Power Plants

COST SUMMARY FOR 972 MWe PROMETHEUS-L DESIGN POINT

1991$ Interest=16.5% Escalation=0.0% Fixed Charge Rate=9.7% Construct Time=6.0 yrs Avail=0.794 LSA=1

		Lrn Crv			Lrn Crv		CYD	NYD
LAND	10.00	None	REACTOR PLANT	700.43		DIRECT COST	2171.67	2171.67
			Equipment	391.82				
STRUCTURES	376.66	None	FW Blanket	157.03	85%	CONSTR SERVICES	245.40	245.40
Site Improvements	21.00		Bulk Shield	203.82	90%			
Reactor Building	106.06		Structure	22.99	85%	ENG - HOME	112.93	112.93
Driver Building	36.52		Vacuum System	4.54	85%			
Turbine Building	57.18		Target Injection	3.44	85%	ENG - FIELD	112.93	112.93
Heat Rejection	11.48		Heat Transfer	198.59	75%			
Auxiliary Power	15.54		Auxiliary Cooling	4.87	85%	OWNER COST	396.44	396.44
Target Manufacturing	46.92		Waste Processing	5.68	None			
Tritium & Waste Proc	46.92		Fuel Handling	48.15	85%	PRCSS CONTGNCY	0.00	0.00
Misc Structures	35.03		Maint Equipment	21.07	85%			
			Reactor I&C	26.60	90%	PRJCT CONTGNCY	445.27	445.27
			Other	3.65	None			
TURBINE PLANT	327.13	None	Spare Parts	0.00		INTEREST	575.66	1107.41
			Contingency	0.00				
ELECTRIC PLANT	165.46	None				ESCALATION	0.00	848.86
			DRIVER	398.28				
MISC PLANT	57.15	None	Front End	10.25	90%	TOTAL COST	4060.29	5440.90
			Discharge Lasers	44.91	90%			
TARGET PLANT	134.94	90%	RAC System	4.65	90%			
			SBS System	1.27	90%	ANNUAL CAPITAL	392.22	891.22
SPCL MATERIALS	1.62	None	Gas Flow System	33.91	80%			
			Optics	106.18	90%	OPERATING COST	94.96	127.25
			Pulsed Power	142.14	90%	Plant O&M	49.71	66.61
			Vacuum System	0.00	90%	Sched Replacemt	24.29	32.55
			I&C	20.00	90%	Target Mfg O&M	12.32	16.51
			Maint Equipment	16.66	85%	Fuel	4.08	5.47
			Misc Equipment	18.31	90%	Decommission	4.56	6.11
			Spare Parts	0.00				
			Contingency	0.00		COST OF ELECT	72.0	150.5

COST SUMMARY FOR 999 MWe PROMETHEUS-H DESIGN POINT

1991$ Interest=16.5% Escalation=0.0% Fixed Charge Rate=9.7% Construct Time=6.0 yrs Avail=0.808 LSA=1

		Lrn Crv			Lrn Crv		CYD	NYD
LAND	10.00	None	REACTOR PLANT	568.34		DIRECT COST	1940.64	1940.64
			Equipment	271.64				
STRUCTURES	322.41	None	FW Blanket	129.62	85%	CONSTR SERVICES	219.29	219.29
Site Improvements	21.00		Bulk Shield	129.58	85%			
Reactor Building	60.88		Structure	6.19	85%	ENG - HOME	100.91	100.91
Driver Building	38.27		Vacuum System	3.51	85%			
Turbine Building	52.79		Target Injection	2.74	85%	ENG - FIELD	100.91	100.91
Heat Rejection	10.60		Heat Transfer	182.70	75%			
Auxiliary Power	14.81		Auxiliary Cooling	3.52	85%	OWNER COST	354.26	354.26
Target Manufacturing	44.47		Waste Processing	5.41	None			
Tritium & Waste Proc	44.47		Fuel Handling	55.38	85%	PRCSS CONTGNCY	0.00	0.00
Misc Structures	35.11		Maint Equipment	19.44	85%			
			Reactor I&C	26.60	90%	PRJCT CONTGNCY	397.90	397.90
			Other	3.65	None			
TURBINE PLANT	282.98	None	Spare Parts	0.00		INTEREST	514.42	989.60
			Contingency	0.00				
ELECTRIC PLANT	151.59	None				ESCALATION	0.00	758.55
			DRIVER	403.11				
MISC PLANT	57.27	None	Ion Source	7.05	90%	TOTAL COST	3628.34	4862.07
			Accelerator Structure	70.84	90%			
TARGET PLANT	143.62	90%	Focusing Magnets	43.25	90%			
			Cryogenic System	8.67	90%	ANNUAL CAPITAL	350.50	796.41
SPCL MATERIALS	1.32	None	Storage Rings	13.05	80%			
			Final Transport	53.72	90%	OPERATING COST	92.52	123.98
			Pulsed Power	150.98	90%	Plant O&M	50.39	67.53
			Vacuum System	9.66	90%	Sched Replacemt	20.17	27.03
			I&C	19.00	90%	Target Mfg O&M	11.80	15.81
			Maint Equipment	19.29	85%	Fuel	5.60	7.50
			Misc Equipment	7.60	90%	Decommission	4.56	6.11
			Spare Parts	0.00				
			Contingency	0.00		COST OF ELECT	62.6	130.0

Use or disclosure of data
subject to title page restriction

The cavity size is actually smaller for the heavy ion system, 4.5 compared to 5 m, due to several factors. The primary factor is the proposed self-pinched, heavy-ion transport channel (see Section 4.3.2). This decouples beam focusing concerns from the cavity pressure environment, permitting relative freedom in choosing a heavy ion cavity operating pressure (100 mtorr compared to < 5 mtorr) for the laser where laser induced gas breakdown is a concern. Fusion power is also reduced for the heavy ion plant which contributes to a smaller cavity. Lastly, the transport channel dramatically reduces the number and size of first wall penetrations—two 2-cm diameter openings compared to sixty ~20 cm diameter openings for the laser. The reactor plant cost reflects these differences. It should be noted that the cost difference could be even larger for the two systems. Cavity vapor pressure limits correspond to a radius of ~3.8 m for the heavy ion system; however, study resources did not permit a detailed assessment of the effects of the higher yield and blanket power density on a cavity with this small a radius.

A final comment involves the cost estimate of the target factory for the two systems. The laser design employs direct drive targets which are envisioned as simple hydrocarbon shells filled with frozen DT. The heavy ion targets are indirect drive with a simple shell suspended in a radiation case that has energy conversion regions at the opposing ends. As discussed in Section 6.4, the costs for the heavy ion target factory are higher than those for the laser system, but only by ~6.4%. This is partially due to the lower repetition rate for the higher yield heavy ion system, 3.54 pps compared to 5.65 pps for the laser. The heavy ion target factory thus manufactures only 63% as many targets per year. However, it should also be noted that concerns about the complexity and cost of heavy ion targets do not appear warranted. The only major difference is the radiation hohlraum. Suspension of the capsule inside the case is a concern, but analyses indicate that a low cost solution might be possible.

Cost sensitivity studies for the Prometheus designs were conducted to assess the relative impact to factors of concern to utilities. Figure 6.13-2 shows how the design benefits from a level of safety assurance of 1 for both the laser and heavy-ion systems. Guidelines for assessing the cost impact of LSA were developed by Holdren[5] and are summarized in Table 6.13-2. The bases for the economic guidelines are discussed in Section 3.5, Economic Guidelines. The factors shown in Table 6.13-2 were used to calculate the data displayed in Figure 6.13-2. This shows that the COE would be ~13% higher for LSA = 4 which is typical of present day nuclear fission plants. However, the story is incomplete because this type of plant would likely employ cheaper cavity and shield structural materials than those used for the Prometheus design.

Use or disclosure of data
subject to title page restriction

Table 6.13-2. Indirect Cost Factors for Different LSA Values

	LSA 1	LSA 2	LSA 3	LSA 4
Construction Services	0.113	0.120	0.128	0.151
Home Office Engineering	0.052	0.052	0.052	0.052
Field Office Engineering	0.052	0.060	0.064	0.087
Owners Cost	0.150	0.150	0.150	0.150
Process Contingency	0	0	0	0
Project Contingency	0.1465	0.173	0.184	0.195
Plant O&M Factor	0.700	0.850	0.952	1.0
Decommissioning (M$/yr)	4.56	9.12	13.68	18.23

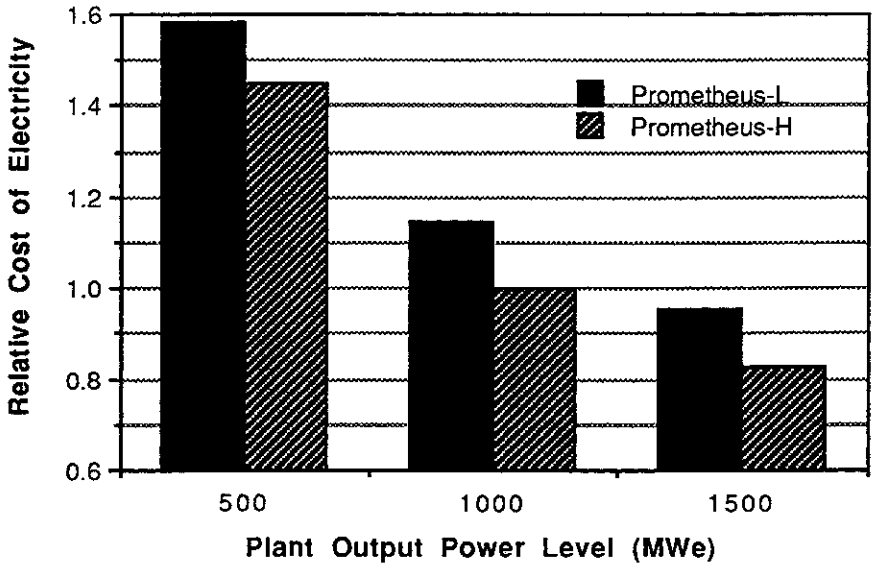

Figure 6.13-2. Change in Prometheus COE for Different LSA Assumptions

Economy of scale is another important economic characteristic of a central station power plant . The projected variation in COE for the Prometheus plants with electric power output is depicted in Figure 6.13-3. This figure indicates the economies of scale for large power plants, however it is interesting to note that the heavy ion system is still significantly better than the laser (~8.9%) at 500 MWe, even though the driver cost is virtually unchanged. This is because of the significant ηG advantage for the heavy ion system. This is a more favorable result than historically expected for the heavy-ion driver and it is a direct outgrowth of the potential cost savings afforded by the innovative, single beam configuration.

Use or disclosure of data
subject to title page restriction

The driver output energy (hence overall driver size, ion energy, etc.) was not reoptimized at each different power level for this study, only the pulse repetition rate was varied. Slightly different results might be expected for an optimized design. However, the conclusions are not expected to change much if the same gain curves are employed. This brings up an important point – there may be more attractive target designs for lower output power plants. Such targets would provide moderate gain at low (1-2 MJ) drive energies that would reduce the required size (and cost) of the driver, possibly leading to more cost attractive 100-500 MWe power plants. This is the subject of one of the critical issues identified by the present study and it is discussed in Section 5.

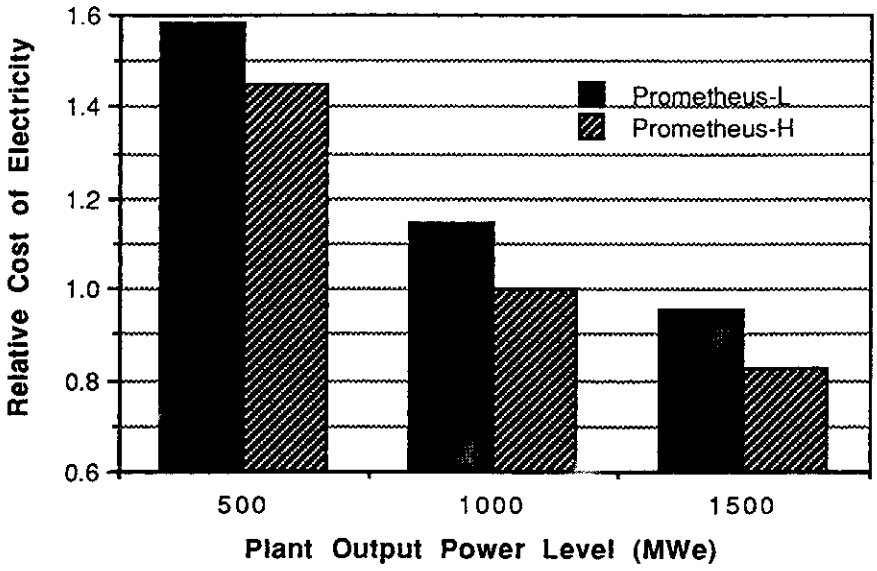

Figure 6.13-3. Change in Prometheus COE for Different Plant Electric Power Outputs

The conclusions of the economic studies are that IFE power plants can be designed and constructed to have reasonable economics to effectively compete with other energy sources. The innovative approaches used in the driver designs have lowered costs for both the laser and the heavy ion driven power plants so that they are now more than competitive with comparable MFE designs. Indeed, if the using community, be it utilities or owners/operators, can effectively use the larger sized plants, then IFE will be a clear winner from the standpoint of more affordable power. The flexibility of the separation of the driver from the reactor chamber offers several advantages including the use of very low activation materials. The low Level of Safety Assurance is also a significant economic benefit. The economic analyses affirm that IFE should be further developed as a future energy source.

Use or disclosure of data
subject to title page restriction

References for 6.13

1. F. Najmabadi, R. W. Conn, et al., "The ARIES_I Tokamak Reactor Study, Final Report,", UCLA-PPG-1323, 1991

2. M.A. Abdou, "FINESSE, A Study of the Issues, Experiments and Facilities for Fusion Nuclear Technology Research & Development," PPG-821, UC LA-ENG-84-30, 1984.

3. C. C. Baker, M. A. Abdou, et al., "STARFIRE - A Commercial Tokamak Fusion Power Plant Study," ANL/FPP-80-1, September 1980.

4. The Heavy-Ion Fusion Systems Assessment (HIFSA) Fusion Technology, 13, No. 2 (1988).

5. J. P. Holdren et. al., "Report of the Senior Committee on Environmental, Safety and Economic Aspects of Magnetic Fusion Energy," LLNL Report URL-53766, 25 September 1989.

Use or disclosure of data
subject to title page restriction

This page intentionally left blank.

TABLE OF CONTENTS – CHAPTER 7

Section	Title	Page
CHAPTER 7	**COMPARISON OF IFE DESIGNS**	7-1
7.1	INTRODUCTION	7-1
7.2	EVALUATION METHODOLOGY	7-2
7.3	COMPARATIVE EVALUATION RESULTS	7-12
7.3.1	Introduction	7-12
7.3.2	Physics Feasibilities of KrF and Heavy ion Inertial Confinement Fusion	7-12
7.3.2.1	KrF Laser IFE Physics Feasibility	7-12
7.3.2.2	Heavy Ion Driver IFE Feasibility	7-13
7.3.2.3	Summary of KrF Laser and Heavy Ion Driver Physics Feasibilities	7-14
7.3.3	Engineering Feasibility	7-16
7.3.4	Economic Comparison and Evaluation	7-18
7.3.5	Safety and Environment	7-21
7.3.6	R&D Requirements	7-23
7.3.7	Overall Evaluation	7-23
	References for 7	7-24

Use or disclosure of data
subject to title page restriction

CHAPTER 7
COMPARISON OF IFE DESIGNS

7.1 Introduction

There are several design and technology options for inertial confinement fusion reactors, e.g. laser or heavy ion drivers, direct or indirect drive targets, and dry or wetted first walls. Comparison among options is sought by decision-makers in order to select or identify options for further research and development (R&D).

A quantitative methodology is a useful tool in comparing and selecting among options. In some cases, the basic information required to perform this quantitative comparison is not available. Therefore, decisions to narrow design and technology options for further R&D must be made based on "expert judgment." Quite often, the experts disagree on their preferred choices, further confusing the decision process. The Prometheus study developed a comparative methodology. In this methodology, some data were not available or did not exist and a "best guess" by technical experts is substituted for such data. Results of the comparative evaluation were analyzed and discussed with experts who attempted to formulate conclusions. One advantage of using this quantitative and comparative methodology was that differences among experts and methods for resolution became clear. Another process advantage is that experts gain insight into important areas of differences among design and technology options. Such insights foster more informed decisions even if the results of the comparative analysis are not clear-cut conclusions.

Section 7.2 presents the highlights of the Evaluation Methodology developed in the Prometheus design study. The methodology has utilized previous work when available, e.g. References 1, 2, and 3. Section 7.3 summarizes the results of applying this methodology to comparisons of Prometheus Laser-Driven and Heavy-Ion Driven reactor designs. An attempt was made to keep the methodology framework general enough to allow future comparisons of other options, e.g. comparing inertial and magnetic fusion reactors.

Use or disclosure of data
subject to title page restriction

7.2 Evaluation Methodology

Design options for power plants constructed today can be compared on economics, safety, and environmental attractiveness. However, fusion is in an early stage of research and development. Data bases are incomplete and success in developing particular design options for subsystems cannot be assured. Designers extrapolate present knowledge to predict fusion performance with varying results. Further, there are substantial differences among proposed design options: probability of success, time, and developmental costs required. Therefore, a prudent evaluation methodology for comparing fusion reactor conceptual designs must account for these differences.

Five major areas were evaluated:

(1) Physics Feasibility
(2) Engineering Feasibility
(3) Economics
(4) Safety and Environment
(5) Research and Development Requirements

Each major area was quantified using a detailed criteria developed for each area. For each criterion, there is an attribute (index) that can be applied and weighting scale devised. Weighted sums of each attribute were evaluated according to a score.

Evaluation results of each reactor design concept gave a numerical score in each of the five evaluation areas. No mixing of the scores for the five evaluation areas was allowed; i.e., the numerical scores are not combined to derive one final composite score. Instead, the comparison among reactor design concepts involved comparative analysis of the scores for the five areas. A panel of knowledgeable experts then interpreted the results in each of the five evaluation areas. The evaluation approach is highlighted in Figure 7-1.

Evaluation results are impacted by the many choices available to designers. For this study, it is very important to distinguish scoring impact between generic and non-generic design choices. For example, selection of low activation structural material is not a necessity, but a designer's choice. Therefore, a reactor concept with low activation materials cannot be compared to a reactor design with high activation structural materials (or vice versa). Evaluations are dictated by different design requirements. A description of the evaluation system for each of the five evaluation areas follows.

Use or disclosure of data
subject to title page restriction

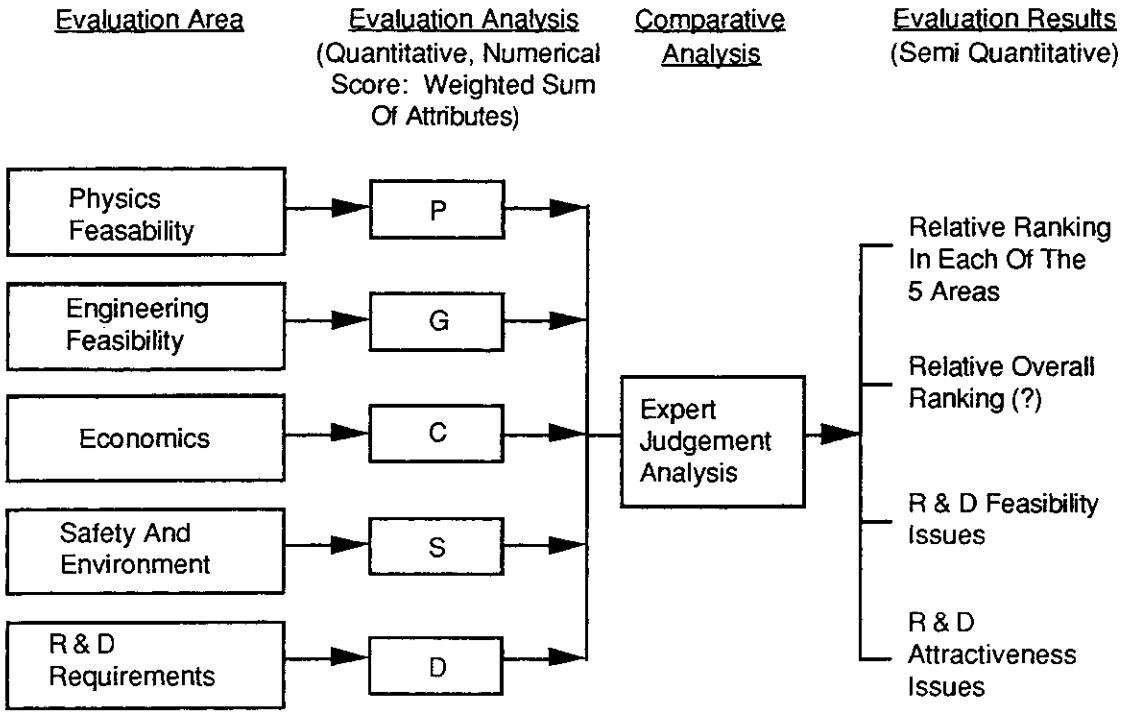

Figure 7-1. Evaluation Methodology Approach

Physics Feasibility - Physics feasibility is clearly a requirement for acceptance of any reactor design concept. However, the required and achievable physics performance goals vary from one reactor concept to another, such as the fusion yield of direct or indirect-driven targets in laser or heavy ion reactors and ß (ratio of plasma-kinetic to magnetic pressure) in magnetic fusion reactors. In IFE reactors, feasibility extends beyond the implosion to cover other physics areas associated with the driver and driver-target coupling.

The study did not attempt to develop a general methodology for comparative evaluation of physics feasibility for all options. Rather, a specific methodology was developed to compare laser and heavy ion-driven reactor physics feasibility. This methodology is presented in Section 7.3.2, together with the application to compare Prometheus-L and H.

Engineering Feasibility - Present conceptual designs are based on extrapolations from present engineering knowledge and experience. Hence, there are uncertainties in the ability to develop conceptual designs that meet study goals. These uncertainties vary between designs, depending on extrapolation and performance optimism. Various design options may be rewarded indirectly through "economics" and "safety and environment" categories of the evaluation criteria. A key purpose of the "engineering feasibility" is to scrutinize, assess, and calibrate each extrapolation and provide a figure of merit. This attempts to balance "questionable rewards" made in other categories of the comparative evaluation. Another key purpose of engineering

Use or disclosure of data subject to title page restriction

feasibility is to assure certain goals must be met (e.g. tritium self-sufficiency) in order for the reactor design concept to be acceptable.

The Engineering Feasibility category has two subcategories:

(1) Ability to achieve design goals
(2) Ultimate potential.

Subcategory (1) provides a measure to account for uncertainties in achieving the design goals. Subcategory (2) provides a measure for comparing the practicality of various designs in ultimately reaching very desirable goals such as inherent safety; low, long term activation; and enhanced energy conversion efficiency.

Figures of merit for Engineering Feasibility, G, are obtained as follows:

$$G = W_a I_a + W_p I_p$$

where

W_a = weighting factor for the "ability to achieve design goals" subcategory
I_a = score for "ability to achieve design goals" subcategory
W_p = weighting factor for the "ultimate potential" subcategory
I_p = score for the "ultimate potential" subcategory

W_a is assigned 60% while W_p is assigned 40% to reflect the notion that the ability to achieve design goals has somewhat higher priority than capabilities to ultimately reach desirable goals.

Each subcategory is further divided into a number of attributes (indices), each has a weight and score. The score for each subcategory is obtained as the weighted sum of the scores for the attributes.

Table 7-1 shows the various indices and assigned weights. A scoring system has been devised so that the maximum score for any given index is 3. Since the sum of the weights for all indices is 1.0, the maximum score for Engineering Feasibility is 3. Table 7-2 shows the scoring system for engineering feasibility.

Economics - A single figure of merit, cost of electricity, was adopted. Use of the cost of electricity as a figure of merit integrates the weighted effects of capital, operating costs, replacement time and frequency, fusion power, thermal power conversion efficiency, and recirculating power requirements.

Use or disclosure of data
subject to title page restriction

Table 7-1 Engineering Feasibility Evaluation

Ability to Meet Design Goals	Weight (0.60) ×
1. Component Fabricability	0.1
First Wall	× 0.35
Blanket	× 0.20
Driver	× 0.15
Beam Transport	× 0.15
Final Optics	× 0.15
2. Subsystem Performance Goals	0.3
Cavity	× 0.4
First Wall Protection	× 0.5
Blanket	× 0.5
Fusion Reaction Support Systems	× 0.6
Driver	× 0.2
Beam Transport	× 0.2
Final Optics	× 0.2
Target Fabrication	× 0.2
Target Injection	× 0.2
3. Tritium Fuel Self-Sufficiency	0.2
4. Reliability Goals	0.1
First Wall	× 0.35
Blanket	× 0.20
Driver	× 0.15
Beam Transport	× 0.15
Final Optics	× 0.15
5. Maintainability	0.1
First Wall	× 0.35
Blanket	× 0.20
Driver	× 0.15
Beam Transport	× 0.15
Final Optics	× 0.15
6. Lifetime Goals	0.1
First Wall	× 0.35
Blanket	× 0.20
Driver	× 0.15
Beam Transport	× 0.15
Final Optics	× 0.15
7. Cost Projections	0.1
Cavity	× 0.25
Driver	× 0.25
Target Manufacture	× 0.25
BOP	× 0.25
Ultimate Potential	**(0.4)** ×
8. Potential for Inherent Safety	0.25
9. Potential for Low, Long-Term Activation	0.25
10. Engineering Simplicity	0.3
Individual System Complexity	× 0.5
Interdependence of Systems/Functions	× 0.5
11. Operating Requirements	0.10
12. Potential for Enhanced Energy Conversion Efficiency	0.10

Use or disclosure of data
subject to title page restriction

Table 7-2 Scoring System for Engineering Feasibility

	Score
Component fabricability	
Existing technology	3
Direct extrapolation of existing technology	2
New technology	1
Subsystem performance goals	
Demonstrated performance in existing facilities	3
Uncertain, but judged to be resolvable with R&D	2
Highly uncertain – may be impossible	1
Ability to achieve tritium fuel self-sufficiency (margin = $\lambda_a - \lambda_r$)	
$\lambda_a - \lambda_r$ > 0.2	3
$\lambda_a - \lambda_r$ > 0.1	2
$\lambda_a - \lambda_r$ < 0.1	1
$\lambda_a - \lambda_r$ < 0.0	0
Reliability goals	
Goals based on extrapolation of relevant data	3
Little data, but confidence in estimates	2
Little confidence in estimates	1
Maintainability	
Maintenance achieved by demonstrated methods	3
Some novel or complex maintenance procedures	2
System availability depends on novel or complex procedures	1
Lifetime goals	
Credible data exists to support lifetime estimate	3
Existing data can be extrapolated to support goal	2
Little or no data to support lifetime estimate	1
Cost projections	
Credible data exists to support cost estimate	3
Existing data can be extrapolated to support estimate	2
Little or no data to support cost estimate	1
Potential for inherent safety (IS)	
No reason inherent safety couldn't be achieved	3
Some sources/pathways may prevent IS	2
Some features of design probably prevents IS	1
Potential for low long-term activation (LTA)	
No sources of LTA	3
Sources of LTA could be eliminated with R&D	2
Sources of LTA inherent to design	1
Engineering simplicity	
Simple design and/or operation	3
Some complex aspects of design and/or operation	2
Highly complex aspects of design and/or operation	1
Operating (e.g., startup-shutdown) requirements	
Response times <hours	3
Response times >hours	2
Off-normal operation puts plant or personnel at risk	1
Potential for enhanced energy conversion efficiency	
Well-defined options exist	3
Some speculative options exist	2
No credible means known to significantly	1
Improve efficiency	

Use or disclosure of data
subject to title page restriction

The "first year" cost of electricity in then-year dollars is defined by the following equation.

$$COE = \frac{\text{Annualized Capital Cost + Yearly Operating Cost}}{\text{Net Power x Plant Availability x Time}}$$

$$COE = \frac{(DC+SPR+CTGY+ID+INT+ESCL)\,FCR + (O\&M+SCR+Fuel)(1+ESC\ Rate)^{Yrs}}{(\text{Thermal Power x Gross Efficiency-Recirculating Power })(Availability)(Hrs/y)}$$

where

COE	=	Cost of Electricity
C	=	Figure-of-Merit for the Economics Evaluation Area
DC	=	Direct Capital Costs
SPR	=	Spare Parts Allowance
CTGY	=	Contingency Allowance
ID	=	Indirect Costs (Constr. Services and Engineering)
INT	=	Interest During Construction
ESCL	=	Escalation During Construction
FCR	=	Fixed Charge Rate
O&M	=	Operations and Maintenance Cost
SCR	=	Scheduled Component Replacement Cost
FUEL	=	Annual Fuel Cost
ESC RATE	=	Annual Escalation Rate
YRS	=	Construction Period

Cost of electricity is the total busbar energy cost for the first year of operation. Total capital investment is equally divided and charged to the annual operating periods through the use of a fixed charge rate. Annual operating costs are also included with appropriate escalation from the year of the estimate (start of construction) to the initial operation date. See Figure 3.5-1 for specific economic guidelines and bases used in this study.

Safety and Environment - The most important incentives for fusion energy development is its potential safety and environmental attractiveness. Therefore, enhancing safety and environment features impact the ultimate acceptance of fusion. The Safety and Environment evaluation area measures the relative safety and environmental attractiveness of each design concepts.

Limited study resources and knowledge preclude performing a complete probabilistic risk assessment to obtain a total risk to the public single figure-of-merit. Therefore, a simpler approach was adopted based on a method developed earlier in BCSS.[3] Three subcategories define the Safety and Environmental area as shown in Figure 7-2 and listed below.

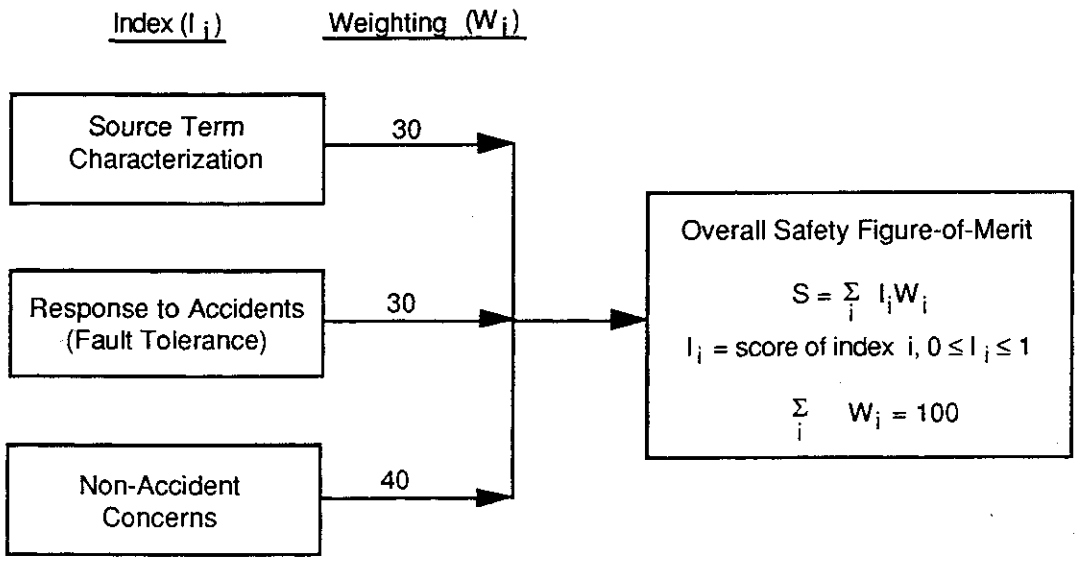

Figure 7-2. Safety and Environment Evaluation Approach

(1) Source Term Characterization (I_1)
(2) Response to Accidents (Fault Tolerance) (I_2)
(3) Non-Accident Concerns (I_3)

The attribute for each subcategory, I_i, is measured on a scale from 0.0 to 1.0 and has a weighting value, W_i. The overall figure of merit (S) for the safety and environmental area for a given reactor design concept is defined as

$$S = \sum_{i=1}^{3} I_i W_i \qquad (7\text{-}1)$$

with

$$\sum_i W_i = 100 \qquad (7\text{-}2)$$

The weights given to each of the three subcategories are shown in Figure 7-2.

Subcategory (1) is a measure of the component of accident risk from the radioactive and chemical source term common to accident initiators. The value of the attribute, I_i, for this subcategory is obtained from the scores of subindices, f_j, for key components of the reactor as:

$$I = \sum_j f_j \omega_j \qquad (7\text{-}3)$$

where $0.0 \le fj \le 1.0$ and $\sum_j \omega_j = 1.0$.

The weights assigned to various reactor components are given in Table 7-3.

Use or disclosure of data
subject to title page restriction

Table 7-3: Safety and Environmental Evaluation Indices and Weights

	ω_j
Source Term Characterization (Score = I_S, W_S = 30%)	
Source Term in Target Factory	0.2
Source Term in the Chamber First Wall	0.2
Source Term in the Breeding Blanket and Shield	0.2
Source Term in the Driver	0.2
Non-radiological Sources (e.g. Fluorine)	0.2
Sum of Weighted Score for Source Term $I_S = \Sigma f_j \omega_j$	---
Response to Accidents (Fault Tolerance) (Score = I_R, W_R = 30%)	
Response to LOCA and LOFA in the Chamber First Wall	0.12
Response to LOCA and LOFA in the Breeding Blanket and Shield	0.12
Response to Beam Pellet Misfire Accident in the Chamber Wall	0.12
Response to Loss of Coolant in the Final Optics or Focusing Magnet Vacuum Pumping System	0.12
Response to LOCA in the Driver System	0.12
Fault Tolerance to Loss of T_2 and D_2 Containers	0.10
Fault Tolerance to Containment Integrity	0.10
Fault Tolerance to Target Factory Integrity	0.10
Fault Tolerance to Driver System	0.10
Sum of Weighted Score for Response to Accidents (Score = IR = $\Sigma \omega_j f_j$)	---
Non-Accident Concern (Score = I_N, W_N = 40%)	
Occupational Exposure (Regular, Maintenance)	0.25
Routine Radioactive Emission Rate	0.25
Waste Disposal (Radiological, Hazardous, Mixed)	0.20
Non-radiological Hazards (Fluorine, Lead)	0.15
Heat Dissipation	0.10
Construction Impacts	0.05
Sum of Weighted Score for Non-Accident Concerns $I_N = \Sigma f_j \omega_j$	---
Overall Safety Figure of Merit = $W_S I_S + W_R I_R + W_N I_N$	---

Subcategory (2) relates to the likelihood and response to accidents. Again, the value of the attribute is obtained as the weighted sum of several indices related to the initiators of specific accidents. The indices, f_j, and weights, ω_j, for this subcategory are shown in Table 7-3. Subcategory (3), Non-Accident Concerns, has indices related to occupational exposure, radioactive emission rate waste disposal, non-radiological hazards, heat dissipation, and construction impact. Each has an assigned weight as shown in Table 7-3.

Research and Development Requirements - An important figure of merit in comparing options is the R&D required of future technology. Developing a complete R&D plan is not within the scope of this study; however, R&D data base requirements for design and construction of a Prometheus experimental power reactor were evaluated and discussed in Chapter 5.

Use or disclosure of data
subject to title page restriction

Three important subcategories comprise the figure of merit for the R&D requirements:

(1) Cost
  (a) Average annual operating cost
  (b) Capital cost of required facilities (new or upgrades)
(2) Time: Total time to complete the R&D
(3) Risk

The relative risk in not resolving key issues is weighted by the potential consequences of negative results.

The overall figure of merit (D) for R&D is written as

$$D = W_c R_c + W_t + R_t + W_r R_r$$

where R_c, R_t, and R_r are the scores for cost, time, and risk, respectively, and W_c, W_t, and W_r are the corresponding weighting factors.

Subcategory (1) – Cost (R_c)

$R_c = 0.5 (A + F)$
A = Score for average annual operating cost
F = Score for capital cost of required facilities

Average Annual Operating Cost	Score A	Capital Cost of Required Facilities*	Score F
> $ 100 M	1	> $500 M	1
$50 - 100 M	2	$200 - 500 M	2
< $50 M	3	< $200 M	3

* Summation for all key issues
* Specific dollar numbers for categories may change depending on the issues included and the purpose of comparison

Subcategory (2) – Time (R_t) - Time is the longest time required to resolve the issues. It is either cumulative time for sequential tasks or the longest time for parallel tasks. The score is according to the following table.

Time Scale	Score R_t
> 30 yr	1
15-30 yr	2
<15 yr	3

Use or disclosure of data subject to title page restriction

Subcategory (3) – Risk (R_r) - The figure of merit, R_r, accounts for the probability of not resolving the key issues and the consequence of negative results. It is written as:

$$R_r = \frac{1}{3n} \sum_{i=1}^{n} P_i C_i$$

where n = number of key issues. Dividing by the Factor 3n ensures the maximum score for R_r is 3. P_i is the probability of not resolving the issue (negative result) and is assigned as follows:

Relative Probability	P_i
Unlikely	3
Even (50/50)	2
Likely	1

C_i is the consequence of not resolving the issue (i.e., of negative results)

Relative Consequence	C_i
Severe Impact	1
Moderate Impact	2
Low impact	3

7.3 Comparative Evaluation Results

7.3.1 Introduction - Evaluation methodologies developed in the previous section compared the two inertial fusion reactor designs: Prometheus-L and Prometheus-H. Comparisons covered the five evaluation areas: physics feasibility, engineering feasibility, economics, safety and environment, and R&D requirements.

Evaluation efforts relied on the quantitative data available from the conceptual design study and other sources wherever possible. However, time and resource limitations precluded complete quantitative analysis. Whenever data was not readily available, "expert judgment" was substituted. Results of the comparative evaluation in each of the five evaluation categories are presented in the following subsections. Subsection 7.3.7 discusses the overall evaluation results.

7.3.2. Physics Feasibilities of KrF and Heavy Ion Inertial Confinement Fusion - The physics feasibilities of both the KrF and the Heavy Ion drivers are described briefly below.

7.3.2.1 KrF Laser IFE Physics Feasibility - Physics feasibility of the KrF Laser Driver has two parts:

(1) Feasibility of efficient laser interaction with the direct drive DT target and its subsequent implosion (which may be beset with a variety of laser-plasma interactions driving Rayleigh Taylor instabilities). Also, efficient conversion of laser light into soft x-rays and the subsequent desired implosion of an indirect-drive DT target.

(2) Feasibility of meeting DT target specifications of photon energies, phase distributions, intensity fluctuations, pulse duration, etc.

Much has been written about Subcategory (1), target interactions and design; however, the Prometheus study has concentrated on Subcategory (2), delivering appropriate laser pulses. Subcategory (2) also includes target fabrication, handling, and delivery methods.

A Prometheus KrF laser driver system is extremely complex with many elements required to perform at specified operating levels for extended periods of time. Laser driver elements are designed and engineered in such a manner as to attain performance levels at or below limits defined by the fundamental physics of the element. To assess the physics feasibility of the laser driver design, it is necessary to analyze the fundamental operating principles behind the crucial elements. Prometheus KrF laser driver physics feasibility criteria is based upon answering the following questions:

Use or disclosure of data
subject to title page restriction

(1) Does the intended operational mode violate fundamental physics relationships?
(2) Can a self-consistent theory be developed which simulates the operation in the ranges of interest?
(3) If a self-consistent theory is developed, are there highly unstable regions in operational phase-space which could produce significant fluctuations or undesired interactions with other systems?
(4) If the device is to be integrated into a subsystem containing several similar or different devices, can an overall self-consistent theory be developed which describes the combined operation of the subsystem?
(5) Using the physics simulations described above, is it possible to define clear operational regimes of acceptable performance to define the functional phase space for the selected devices and subsystems?

Question (1) aside, affirmative answers signify that the fundamental physics are sufficiently understood and advanced simulations are capable of predicting operational behavior. Systems engineering assessments and simulations then evaluate the predicted performance of the overall laser driver system.

7.3.2.2 Heavy Ion Driver IFE Feasibility - As described for the KrF Laser Driver, there are two parts to the physics feasibility of the Heavy Ion Driver:

(1) The physics feasibility of the interaction of the heavy ion beams with the converter plugs to convert the energy efficiently into soft x-rays, together with the physics feasibility of the subsequent uniform implosion of the DT target within the hohlraum.
(2) Feasibility of generating the specified indirect-drive target irradiation conditions of particle energies, beam intensity profiles, directionality, focused beam diameters, pulse durations, etc.

The Prometheus study has concentrated on generating and delivering 4-6 MJ of heavy ion beam energy in 6 ns pulses in <6 mm-diameter focused beams at a 5 Hz rate. Category (2) addresses indirect-drive DT target fabrication and delivery.

Prometheus Heavy Ion Driver design is a complex system composed of bright Pb^{+2} source, ramp gradient accelerator, constant gradient accelerator, storage rings, bunching accelerator, focusing magnets, self-pinched channel generator, and target injection system. Each system element must perform at specified operating levels for a known length of time. Engineering feasibility is described in Section 7.3.3 for the heavy ion driver. To assess the Prometheus Heavy Ion Driver design physics feasibility, it is necessary to analyze fundamental operating principles supporting crucial elements. Typical Prometheus Heavy Ion driver physics feasibility criteria are based upon answering the following questions:

Use or disclosure of data subject to title page restriction

(1) Does the intended operational mode violate fundamental physics relationships?
(2) Can a self-consistent theory be developed which simulates operation in the ranges of interest?
(3) Do the simulations show that the device can actually operate in the region of phase space of interest?
(4) If a self-consistent theory is developed, are there highly unstable regions in operational phase-space which could produce significant fluctuations or undesired interactions with other systems?
(5) If the device is to be integrated into a subsystem containing several similar or different devices, can an overall self-consistent theory be developed which describes the combined operation of the subsystem?
(6) Using the physics simulations described above, is it possible to define clear operational regimes of acceptable performance to define the functional phase space for the selected devices and subsystems?

Question (1) is a sanity check of the fundamental idea behind the device. Question (2) eliminates novel ideas which are not sufficiently mature to be developed into a device at the present time. Question (3) assesses whether or not the range of phase space occupied by the device in operation adequately overlaps the desired performance levels. In general, affirmative answers to Questions (2) through (6) signify that the fundamental physics bases of the devices in question are sufficiently well understood and advanced simulations are capable of predicting operational behavior. Simulations are extremely important since heavy ion drivers must typically be investigated experimentally at full scale, a fact which can make development of heavy ion drivers very expensive. Providing a fundamental physics model for the heavy ion beam propagation, bunching, neutralization, and self-pinched channel formation is well understood. Subsequent systems engineering assessments and corresponding end-to-end system simulations permit evaluation of the predicted performance.

7.3.2.3 Summary of KrF Laser and Heavy Ion Driver Physics Feasibilities – Detailed physics analyses and evaluations of the fundamental elements of both the KrF Laser and Heavy Ion Drivers have revealed that both designs are consistent with known physics (affirmative answer to Question (1) in Sections 7.3.2.1 and 7.3.2.2). There are, however, uncertainties in whether we will be able to operate in the assumed parameter ranges when operating the actual devices. These uncertainties preclude us from guaranteeing that all parts of each driver will work together as a whole to the degree required to meet driver requirements. These uncertainties, in our estimation, can only be resolved by a series of experiments to be performed at a variety of levels. Samples of needed experiments are described elsewhere as Research and Development Experiments related to identified Critical Issues. The bottom line is that there appear to be no show stoppers for either the KrF Laser Driver

Use or disclosure of data
subject to title page restriction

or the Heavy Ion Driver, but some of the required work-arounds could raise the costs of both the laser drivers.

The physics feasibilities of both the KrF Laser and the Heavy Ion Drivers are summarized below in Table 7.3.2-1. The rating system assumes the following ranking:

7-9 = Demonstrated or easily extrapolated from existing systems
4-6 = Physics feasibility highly probable but needs verification
1-3 = Low physics feasibility except in limited parameter range

Table 7.3.2-1. Physics Feasibilities of Laser and Heavy Ion Drivers

No.	Category	Laser	Heavy Ion
1	**Overall Driver**	**5.8**	**6.6**
1a1	Excimer Amplifiers	4	
1a2	Raman Accumulators	7	
1a3	SBS Pulse Compressors	6	
1a4	E/O Pulse Shaping	5	
1a5	Final Focusing	7	
1b1	Injector		7
1b2	Main Accelerator		8
1b3	Storage Rings		5
1b4	Buncher		7
1b5	Beam Transport		6
2	**Beam Transport**	**7.3**	**4.7**
2a1	Excimer Laser Beam Quality Correction	8	
2a2	Image Relaying	8	
2a3	Beam Conditioning	7	
2b1	Transport to Final Focus		7
2b2	Autoneutralized Final Focus		4
2b3	Channel Transport		3
3	**Target/Beam Alignment**	**3.5**	**4.5**
3a1	Laser Beam Alignment/Overlap	4	
3a2	Target Positioning/Sensing	3	
3b1	Positioning on Target		6
3b2	Channel Motion		3
4	**Target/Driver Coupling**	**3.5**	**7**
4a1	Avoiding Rayleigh-Taylor Instabilities	3	
4a2	Efficient Inverse Bremsstrahlung Absorption	4	
4b1	Efficient Conversion in Hohlraum plugs		8
4b2	Generating & Focusing Soft X-rays		6
5	**Target Gain**	**Equal**	**Equal**
Total		**5.025**	**5.7**

Use or disclosure of data
subject to title page restriction

Based upon our assessments, the heavy ion driver irradiating indirect-drive DT targets has a somewhat higher estimated physics feasibility than does the KrF laser driver irradiating direct-drive DT targets. As can be seen in Table 7.3.2-1, the laser driver physics feasibilities associated with Target/Beam Alignment and Target/Driver Coupling suffers considerably compared with the corresponding feasibilities associated with the Heavy Ion Driver. This major difference in target/beam physics feasibilities is due in part to the considerable technical difficulties in illuminating a moving direct-drive target with a 1% uniformity in the middle of a 5-m radius target chamber.

There is a fundamental connection between the "Research and Development Experiments" identified in the Prometheus study and estimates of low driver physics feasibilities. By dealing with the high risk physics issues promptly, the goals of inertial confinement fusion research can be met during the first half of the 21st Century.

7.3.3 Engineering Feasibility - An engineering feasibility evaluation was performed by several experts within the Prometheus team. Each subcategory was scored by the participants, and an arithmetic average was computed. The subcategory scores were then weighted and summed to obtain total scores. The results are shown in Table 7.3.3-1.

As discussed in Section 7.2, engineering feasibility is broken into two categories: ability to meet design goals and ultimate potential. The heavy ion reactor scored higher in both categories. The total scores were 1.87 and 2.04 for the laser and heavy ion reactor, respectively. Below, some of the reasons for the differences are highlighted.

In general, the heavy ion driver was judged to be easier to build and more reliable. Most of the technology is currently available for the accelerator. One of the largest differences shows up in the engineering simplicity attribute, where the heavy ion reactor scores much higher. For the same reasons, cost projections were felt to be more credible for the heavy ion reactor.

Several components of the laser reactor provide uncertainty in fabrication and performance. The final optics appears much more problematic. The large size, vulnerability to the blast effects, and difficulty with shielding lead to lower scores.

Shared cavity design concepts of the two reactors tended to reduce the differences. However, the large number of beamline penetrations for the laser reactor make it considerably less attractive. The smaller size of the heavy ion reactor makes fabrication easier, but uncertainties due to the higher power density offsets this advantage.

Use or disclosure of data
subject to title page restriction

Table 7.3.3-1 Engineering Feasibility Evaluation

	Weight	Net Weight	Laser Score	Weighted Laser Score	Heavy Ion Score	Weighted Heavy Ion Score
Ability to Meet Design Goals	**(0.60)x**					
1. Component Fabricability	0.1					
First Wall	x 0.35	.021	1.375	.029	1.375	.029
Blanket	x 0.20	.012	1.625	.020	1.625	.020
Driver	x 0.15	.009	1.833	.017	2.5	.023
Beam Transport	x 0.15	.009	2.0	.018	2.75	.025
Final Optics	x 0.15	.009	2.333	.021	2.5	.023
2. Subsystem Performance Goals	0.3					
Cavity	x 0.4					
First Wall Protection	x 0.5	.036	1.375	.050	1.5	.054
Blanket	x 0.5	.036	2.375	.086	2.375	.086
Fusion Reaction Support Systems	x 0.6					
Driver	x 0.2	.0216	1.75	.038	2.333	.050
Beam Transport	x 0.2	.0216	2.0	.043	2.167	.047
Final Optics	x 0.2	.0216	1.5	.032	2.167	.047
Target Fabrication	x 0.2	.0216	2.0	.043	1.833	.040
Target Injection	x 0.2	.0216	2.0	.043	1.667	.036
3. Tritium Fuel Self-Sufficiency	0.2	.12	1.5	.18	1.5	.18
4. Reliability Goals	0.1					
First Wall	x 0.35	.021	1.5	.032	1.5	.032
Blanket	x 0.20	.012	1.75	.021	1.75	.021
Driver	x 0.15	.009	1.833	.017	2.5	.023
Beam Transport	x 0.15	.009	1.5	.014	2.5	.023
Final Optics	x 0.15	.009	1.375	.012	2.333	.021
5. Maintainability	0.1					
First Wall	x 0.35	.021	2.0	.042	2.125	.045
Blanket	x 0.20	.012	2.333	.028	2.5	.030
Driver	x 0.15	.009	2.667	.024	2.25	.020
Beam Transport	x 0.15	.009	2.0	.018	2.0	.018
Final Optics	x 0.15	.009	1.667	.015	1.667	.015
6. Lifetime Goals	0.10					
First Wall	x 0.35	.021	1.5	.032	1.5	.032
Blanket	x 0.20	.012	1.75	.021	1.75	.021
Driver	x 0.15	.009	1.5	.014	2.5	.023
Beam Transport	x 0.15	.009	1.5	.014	1.833	.016
Final Optics	x 0.15	.009	1.5	.014	1.5	.014
7. Cost Projections	0.1					
Cavity	x 0.25	.015	1.25	.019	1.25	.019
Driver	x 0.25	.015	1.75	.026	2.333	.035
Target Manufacture	x 0.25	.015	1.833	.028	1.833	.027
BOP	x 0.25	.015	2.375	.036	2.375	.036

Use or disclosure of data
subject to title page restriction

Table 7.3.3-1 Engineering Feasibility Evaluation (Cont.)

	Weight	Net Weight	Laser Score	Weighted Laser Score	Heavy Ion Score	Weighted Heavy Ion Score
Ultimate Potential	**(0.4) x**					
8. Potential for Inherent Safety	0.25	.1	2.7	.270	2.75	.275
9. Potential for Low Long-Term Activation	0.25	.1	2	.200	1.917	.192
10. Engineering Simplicity	0.30					
Individual System Complexity	x 0.5	.06	1.75	.105	2.667	.160
Interdependence of Systems/Functions	x 0.5	.06	1.5	.090	2	.120
11. Operating Requirements	0.1	.04	2	.080	2	.080
12. Potential for Enhanced Energy Conversn Efficiency	0.1	.04	2	.080	2	.080
Totals						
Design Goals				**1.047**		**1.131**
Ultimate Potential				**0.825**		**0.907**
TOTAL				**1.872**		**2.038**

The use of direct vs. indirect drive targets did not lead to large differences in engineering feasibility. The impact of target choice is probably felt more strongly in the physics feasibility.

For both reactor designs, the Engineering Feasibility scoring for safety was very high. The scores for long-term activation were also relatively high, but somewhat lower than for safety. This is due to the presence of Pb and to uncertainties in predicting impurity levels and in the nuclear data.

7.3.4 Economic Comparison and Evaluation - Comparison and evaluation parameters judge the relative economic basis between the two reactor conceptual designs. Eventually this economic parameter will be the only meaningful measure to be used by utilities to judge the relative merit of opposing designs. As the experimental devices and the demonstration plants are developed and operated, the physics and engineering feasibility questions will have all been resolved in a positive or a negative manner. The R&D criteria is a measure to scope the money and effort required to realize the goal of commercial fusion. All other criteria and judgment factors such as safety will eventually be measured and compared in economic terms. A present example is that of an allowance for the decommissioning of the reactor. The plants with the lower environmental risk have a lesser cost factor for the decommissioning effort.

Use or disclosure of data
subject to title page restriction

The criteria to be employed in this present Economic Comparison will be the cost of electricity (COE). This is a meaningful metric in that it combines many aspects of the plant into a single value. The component factors are weighted according to the cost structure employed in the U.S. utilities. The structure of the COE determination is as follows:

$$COE = \frac{[\text{Annualized Capital Cost} + \text{Yearly Operating Cost}]}{\text{Net Power x Plant Availability}}$$

$$COE = \frac{[\text{Annualized Capital Cost} + \text{Yearly Operating Cost}]}{[\text{Thermal Power x Efficiency} - \text{Auxiliary Power}] \times [1\text{-Sched Downtime-MTBFxMTTR}]}$$

This equation combines the effects of the capital costs of the entire plant facility as well as the time it takes to construct the plant. The capital cost emphasizes choice of materials, design optimization, and cost efficient processes. The yearly operating costs include the operating and maintenance staffs, fuel costs, and the maintenance and supply costs. These costs are offset by the production of energy sold to the distribution grid. To generate net power, thermal energy must be produced, thus emphasizing utilization of high quality energy conversion, high gain targets, high neutron and energy multiplication in the blankets, and efficient use of materials. Plant availability stresses minimizing the downtime, both the scheduled and the unscheduled. Reliability and maintainability of future systems is very difficult to predict.

Before the specific COE values are revealed, several comments should be discussed. Although one reactor design concept may show more favorable values of COE over the other concept, there are many competing and generally offsetting factors which should be recognized and considered.

Capital Costs Are Strong Drivers - Drivers, beamlines, power supplies, and reactor cavities are the most influential cost elements. Heavy ion drivers have the deserved reputation of being a very costly item. Our team took an innovative approach to minimize the cost of the heavy ion driver and succeeded in reducing the cost to that of the laser driver. The many laser beamlines required for symmetric illumination also strongly contributed to the cost of the laser plant. The quality of the laser driver power supplies implied a higher cost for the laser system than the heavy ion system. The lower system efficiency of the laser system caused a larger demand for recirculating power and, hence, more thermal power, more reactor plant equipment, more turbine plant equipment, more electric plant equipment, etc. Plant elements with a minor cost influence included the fuel cycle, the target factory, general-purpose buildings, and the shielding. Elements with slight influences were the reactor cavity and remote handling which did not significantly affect either candidate concept.

Use or disclosure of data
subject to title page restriction

Operating Costs Did Not Have a Significant Impact - The level of definition in these studies did not offer any discernible differences in the operating costs between these two conceptual designs. The operating costs for the direct drive targets are nearly equal the indirect target costs. The targets are cheaper but more are required due to the higher repetition rate. An indirect target may be an option for the laser-driven plant but future target designs may significantly impact the performance of the targets which would outweigh the perceived cost differences.

Net Thermal Power Is a Split Decision - The higher gain of the direct drive target tends to favor the laser driver for the same energy level. However, the more efficient LINAC driver better utilizes the available target yields requiring less recirculating power be generated, thus delivering more net energy to the electric grid.

Overall Efficiency Is Credited to the Heavy Ion Driver - The higher system efficiency of the heavy ion LINAC makes better use of the driver energy, holds the size of the other plant equipment to a minimum, and maximizes the plant output for a given level of fusion and thermal plant output. Both reactor concepts have been designed with high temperature primary coolant in order to maximize the thermal efficiency conversion. To improve the efficiency of the KrF driver, the waste heat associated with the KrF gas flow loops was used as an additional source of energy.

Low Auxiliary Power Helps the Efficient Use of Energy - The LINAC has the advantage of requiring less auxiliary power delivered back into the LINAC. All other plant considerations are generally even.

Scheduled Downtimes Are Nearly Equal - It is believed that the Heat Transfer and Transport System, the Turbine Plant Equipment, and the Reactor Cavity are the systems which will require the majority of the scheduled downtime for the plant. The steam generator and the turbines will require routine preventative maintenance. The reactor cavity will have components with limited lifetimes which need periodic replacement. The laser mirrors and optics are designed for long lifetimes and only the final optics may need replacement a few times during the plant lifetime. The heavy ion driver components are designed for life of a plant.

The Unscheduled Downtime Is Determined by the MTBF and MTTR - The Mean Time Between Failures (MTBF) is again driven by the systems mentioned above which have large scheduled downtimes; namely, the Heat Transfer and Transport, Turbine Plant Equipment, and the Reactor Cavity. In addition, the Driver Plant Equipment will contribute to the unscheduled downtime. The laser amplifiers may have some failures, but these can be accommodated without causing a shutdown of the reactor. If a mirror or lens must be replaced, it can be done quickly with a low mean time to repair (MTTR). The LINAC components are more reliable but any failures of the main beamline elements would cause a shutdown of the entire reactor until the element is

Use or disclosure of data
subject to title page restriction

repaired. The net result of scheduled and unscheduled downtime is assessed in inherent availability which slightly favors the heavy ion design.

In summary, factors which contribute toward final economic evaluation are comprised of many issues which are not black and white. Both reactor and driver concepts have advantages and disadvantages as viewed with today's perspective. But technology marches ahead, making twists and turns, driven by market pressures, political maneuvers, and societal influences. Necessity, after all, is the mother of invention. So do not place too much faith in any of the absolute numbers given herein. We believe these studies have suggested some innovative and cost-effective solutions to existing problems, and we believe there are even better solutions yet to be uncovered!

Results of the Economic Evaluation - The Cost of Electricity for the two reactor concepts indicate that the heavy ion-driven reactor would be somewhat more attractive than the KrF laser-driven reactor as shown below:

Reactor Concept	Cost of Electricity
KrF Laser Driven	72.0 mill/kWh
Heavy Ion Driven	62.6 mill/kWh

7.3.5 Safety and Environment - Evaluation criteria falls into three general categories, with a weighting factor assigned to each, as follows: (1) Source Term Characterization (30%), (2) Response to Accident (Fault Tolerance) (30%), and (3) Non-Accident Concerns (40%). With these factors, accident conditions receive substantially more weight in the comparison (60%), than do normal operation factors (40%). Next, each of the three general categories was further divided into subcategories, as indicated on Table 7.3.5-1. As with the general categories, the subcategories were assigned weighting factors.

Each reactor design (laser or heavy ion) was then assigned a relative score for each subcategory. The design that has the least adverse impact for a subcategory is given a score of 1, while the score for the other design is based on how severe its impacts are relative to the least adverse design. For example, if the laser design is judged to have impacts which are twice as severe as the heavy ion design, then the heavy ion is assigned a score of 1, while the laser design is given a .5 score. If both designs are judged to be equal in their impacts of a subcategory, then both are given a score of 1.

Using this methodology, Table 7.3.5-1 presents the results of the safety and environment comparison. A brief rationale for the assignment of the scores is provided for each category. As shown, the laser design is slightly preferred over the heavy ion

Use or disclosure of data
subject to title page restriction

Table 7.3.5-1. Safety and Environment Comparison

Category	WT	L	HI	Rationale
Source Term Characterization	30%			
Source Term in Target Factory	0.2	1.0	1.0	No difference at the level of this study
Source Term in the First Protection Chamber Wall	0.2	1.0	1.0	No difference at the level of this study
Source Term in the Breeding Blanket and Shield	0.2	1.0	1.0	No difference at the level of this study
Source Term in the Driver	0.2	1.0	.83	The heavy ion beam will activate the material in the beam funnel
Non-radiological Sources (Fluorine)	0.2	.75	1.0	The fluorine for the laser has no counterpart in the heavy ion
Total Source Term Characterization:		.95	.97	
Response to Accidents (Fault Tolerance)	30%			
Response to LOCA and LOFA in the First Protection Chamber Wall	12	1.0	1.0	No difference at the level of this study
Response to LOCA and LOFA in the Breeding Blanket and Shield	.12	1.0	1.0	No difference at the level of this study
Response to Beam/Pellet Misfire Accident in the Chamber Wall	.12	1.0	0.9	The loss of one of the two heavy ion beams will have greater effect than the loss of one of the laser's 60 beams
Response to Loss of Coolant in the Final Optics or Focusing Magnet or Vacuum Pumping Systems	.12	1.0	1.0	No difference at the level of this study
LOCA in Driver System	.12	1.0	.83	The loss of one of the two heavy ion beams will have greater effect that the loss of one of the laser's 60 beams
Fault Tolerance to Loss of T_2 and D_2 Containers	0.1	1.0	1.0	No difference at the level of this study
Fault Tolerance to Containment Integrity	0.1	1.0	1.0	No difference at the level of this study
Fault Tolerance to Target Factory Integrity	0.1	1.0	1.0	No difference at the level of this study
Fault Tolerance to Driver System	0.1	1.0	1.0	No difference at the level of this study
Total Response to Accidents:		1.0	.97	
Non-Accident Concerns	40%			
Occupational Exposure (Regular, Maintenance)	.25	1.0	.75	The heavy ion beam will activate the material in the beam tunnel
Routine Radioactive Emission Rate	.25	1.0	1.0	No difference at the level of this study
Waste Disposal (Radiological, Hazardous, Mixed)	.20	1.0	.75	The heavy ion will activate the material in the beam tunnel, causing more waste disposal
Non-Radiological Hazards (Fluorine, Lead)	.15	0.5	1.0	The fluorine for the laser has no counterpart in the heavy ion system
Heat Dissipation	.10	0.9	1.0	A greater amount of power is needed to drive the laser, with a corresponding greater amount of waste heat to be dissipated
Construction Impacts (Environmental)	.05	1.0	.75	The long heavy ion beam tunnel has no laser counterpart
Total Non-Accident Conditions		.92	.88	
Total Safety and Environment Comparison		.95	.93	

Use or disclosure of data
subject to title page restriction

design. However, at the level of this study, the difference is not considered to be significant, and the two designs should be considered to be equal with regard to safety and environment.

7.3.6 R&D Requirements - An R&D assessment has been carried out for Prometheus-L and -H. Because of limitations on time and resources available for this study, the assessment has not attempted to develop comprehensive R&D plans. Rather, the effort was limited to identifying the R&D required to resolve the key technical issues identified for Prometheus. A specific development goal was selected as the ultimate objective of the R&D identified in this effort. This goal is to develop a physics and engineering data base sufficient to construct an IFE Experimental Power Reactor (IEPR). An IEPR is envisioned as a facility in which the basic physics and engineering performance, as well as system integration tests, are carried out. It will have prototypical components and will probably produce several hundred megawatts of fusion power and operate with about one pulse per second and overall availability of about 20-30%.

The R&D assessment focused primarily on critical components unique to IFE: target, driver, and cavity. Some modest R&D has also been identified for the tritium system and safety.

The evaluation methodology for the R&D category requires evaluation of costs (capital and operating), time, and risk. Since a comprehensive R&D assessment was not within the scope of this study, complete data was not available to rigorously follow the evaluation methodology.

The key items of the R&D costs are shown in Table 7.3.6-1. The costs for laser and heavy ion drivers are comparable with the heavy ion reactor concepts having a modest advantage in lower cost. The time it takes to perform the required R&D does not appear to be a significant discriminating factor for the R&D items evaluated in this study.

7.3.7 Overall Evaluation - A summary of the scores for the figures-of-merit of the five evaluation areas is given in Table 7.3.7-1 for the laser-driven and heavy ion-driven reactors. The scores were normalized so that higher numbers mean better scores. Two key conclusions can be made based on the overall evaluation analysis and the scores in Table 7.3.7-1:

(1) The heavy ion-driven reactors appear to have an overall advantage over laser-driven reactors.
(2) However, the differences in scores are not large and future results of R&D could change the overall ranking of the two IFE concepts.

Use or disclosure of data
subject to title page restriction

Table 7.3.6-1. Summary of Key Items of Costs (Capital Plus Operating) of R&D for Laser and Heavy Ion Reactors

Areas Requiring R&D Effort	Laser	Heavy Ion
Cavity	(MS)	(MS)
First Wall Protection	175	175
Blanket	273	273
Shield	60	50
Target and Driver		
Driver	825	805
Target (for both)	235	235
Target (driver-target)	300	200
Tritium	30	30
Safety and Environment (specific items)	20	20
Total (for items shown)	**1918**	**1788**

Table 7.3.7-1 Summary of Scores for the Five Evaluation Areas

	Score*	
Evaluation Area	Laser-Driven	Heavy Ion-Driven
Physics Feasibility (P)	50	57
Engineering Feasibility (G)	85	93
Economics (C)	68	78
Safety and Environment (S)	95	93
R&D Requirements (D)	52	56

*Score normalized so that higher numbers mean better scores.

References for 7

1. M. A. Abdou, P. J. Gierszewski, M. S. Tillack, et al., "Technical Issues and Requirements of Experiments and Facilities for Fusion Nuclear Technology," Nuclear Fusion, Vol. 27, No. 4, 619-688 (1987).

2. M. A. Abdou, et al., "A Study of the Issues and Experiments for Fusion Nuclear Technology," Fusion Technology, (8) 3, pp. 2595-2645, November 1985.

3. "Blanket Comparison and Selection Study," Interim Report, ANL, FPP-83-1(1983), and Final Report, ANL/FPP-84-1 (1984).

Use or disclosure of data
subject to title page restriction

APPENDICES

Use or disclosure of data
subject to title page restriction

APPENDIX A

PROMETHEUS-L BASELINE PARAMETER LIST

PARAMETER CATEGORY	PAGE NO
GENERAL PLANT	A-2
REACTOR CAVITY	A-2
DRIVER SYSTEM	A-4
TARGET	A-5

Use or disclosure of data
subject to title page restriction

PROMETHEUS-L BASELINE PARAMETER LIST

GENERAL PLANT PARAMETERS	VALUE
Net Electric Power (MWe)	972
Gross Electric Power (MWe)	1382
Recirculation Power (MWe)	410
Driver Power (MWe)	349
Auxiliary Power (MWe)	36
Cavity Pumping Power (MWe)	25
Total Thermal Cycle Power (MWt)	3264
Net Thermal Power (MWt)	3049
Blanket (MWt)	1782
First Wall (MWt)	1267
Usable Driver Waste Heat	193
Usable Pumping Waste Heat	22
Thermal Conversion Efficiency (%)	42.3
Recirculating Power Fraction (%)	30
Net System Efficiency (%)	31
Net Thermal Power (MWt) ((1.14x2027)+780-43)	3049
Fusion Power (MW)	2807
Surface Heating Power	780
Neutron Power	2027
Energy Multiplication Ratio	1.14
Power Loss to Shield	-43

REACTOR CAVITY	VALUE
Cavity Radius (m)	5.0
Cavity Cylinder Height (m)	5.0
Total Cavity Height (m)	15.0
FW Surface Area (m^2)	471
Volume (m^3)	916
Total Target Yield (MJ)	497
X-ray (MJ)	31
Debris (MJ)	107
Neutron (MJ)	359
Power	
Surface Heating (MW)	780
Neutrons (MW)	2027
Neutron Source Strength (n/sec)	9.83×10^{20}
FW/Blanket/Shield Characteristic	
TBR	1.2
Power Multiplication	1.14
Nuclear Power (MW) (2027x1.14)	2311

Nuclear Power Distribution	%	MW
First Wall (+Surface Heatg)	21.1	1268
Blanket/Reflector/Plenum	77.1	1782
Vacuum Vessel	0.4	9.2
Shield (concrete)	1.4	32.4

Use or disclosure of data
subject to title page restriction

REACTOR CAVITY (Cont)	VALUE
First Wall System	
Structural Material	SiC
Coolant Channel Wall Thickness (mm)	5.0
Coolant Channel Diameter (cm)	5.0
Mean Fiber Pore Diameter (μm)	50.0
Porosity (%)	10.0
Permeability (m^2)	1.76×10^{-14}
Coolant Media	Liquid Lead
Surface Protection Media	Liq Lead Film
Surface Film Thickness (mm)	0.4-0.6
Inlet Temperature (°C)	375
Outlet Temperature (°C)	525
Delta-T(bulk) (°C)	150
Mass Flow Rate (kg/s)	58,770
Volume Flow Rate (kg/s)	5.65
Coolant Flow Area(cylindrical chamber)	1.1775 (m^2)
Average Velocity (m/s)	4.8
Reynolds Number	1.2×10^6
Frictional Factor	0.02
Coolant Path Length (m)	12.85
Frictional Pressure Drop (MPa)	0.615
Inlet Pressure (top)(MPa)	1.0
Outlet Pressure (bottom)(MPa)	1.385
Pumping Power (85% efficiency)(MW)	4.1
Maximum SiC Temperature (°C)	775
No. Liq Lead Steam Generators	6
No. Liq Lead Pumps	2
Blanket System	
Structural Material	SiC
SiC Min Temperature (°C)	400
SiC Max Temperature (°C)	800
Coolant Media	Helium
Helium Inlet Temperature (°C)	400
Helium Outlet Temperature (°C)	650
Helium Velocity (m/s)	46
Helium Inlet Pressure (MPa)	1.5
Pressure Drop (kPa)	24
Neutron Multiplier	FW Liq Lead Coolant
Breeder Material	Li_2O
Li_20 Min Temperature (°C)	425
Li_20 Max Temperature (°C)	800
Li_2O Theoretical Density Fraction	0.8
Li_2O Density (kg/m^3)	2.01×10^3
Beeder Volume (m^3)	92
Avg Annual Li Burnup (%)	0.5

Use or disclosure of data
subject to title page restriction

REACTOR CAVITY (Cont)	VALUE	
Blanket System (Cont)		
Peak-to-Average Burnup (%)	3	
Tritium Inventory (g)	100	
Tritium Generation Rate (g/day)	362	
BET Surface Area (m^2/kg)	50	Grain
Radius (μm)	10	
Grain Diffusion Coefficient:		
Pre-exponential Factor (m^2/s)	6.81×10^{-7}	
Activation energy (kJ/mol)	84.8	
Purge Composition	He + 0.2%H2	
Amount of Protium in Purge (%)	0.2	
Helium Purge Pressure (MPa)	0.2	
No. Helium Steam Generators	6	
No. Helium Reheaters	6	
No. Helium Recirculators	6	
Vacuum System		
Cavity Pressure @0 °C (mtorr,Pb)	3.0	
Background Gas Density (cm^{-3})	3.5×10^{13}	
No. Vacuum Pumping Ports	3	
No. Vacuum Pumps/Port	10	
Vacuum Pumping Port Diameter (m)	2	
Vacuum Pump Type	Cryogenic	
Vacuum Vessel Material	Ferretic Steel	
Cavity Exhaust (total)	34.7 mg/s	289,900 l/s
	mg/s	l/s
Hydrogen (mg/s)	7.6	126,400
Deuterium	8.16	67,800
Tritium	12.24	67,800
Helium (mg/s)	6.7	27,900

DRIVER SYSTEM	VALUE
Driver Type	KrF Excimer Laser
Target Illumination Scheme	Direct Drive, Symmetric
Amplifier Type	Electric Discharge
Beam Combination Type	Non-Linear Crossed Raman
Pulse Compression TypE	Non-Linear Stimulated Brillouin Scattering
Number of Beams	60
Repetition Rate (pps)	5.65
Driver Output Energy (MJ)	4.0
Single Pulse Efficiency	6.5%
Pulse Power	64%
Discharge Laser	14%
Transport into Raman Cell	98%
Raman Accumulator	88%
Transport into SBS Cell	98%
SBS Cell	88%
Downstream Optics	95%
Single Pulse Input Energy (MJ)	62

Use or disclosure of data
subject to title page restriction

DRIVER SYSTEM (Cont)	VALUE
Driver System Power (MWe)	345
Laser Power (MWe)	344
Gas Flow Power (MWe)	1.5
Driver Overall Efficiency	6.47%
Discharge Lasers (Number)	960
Output Energy (kJ)	5.9
Output Pulse Length (ns)	250
Size (lxwxh, m)	2.0x0.44x0.44
Raman Accumulator Cells (Number)	60
Output Energy (kJ)	81
Output Pulse Length (ns)	250
Size (lxwxh, m)	5.0x1.8x1.8
Stimulated Brillouin Cells (Number)	60
Output Energy (kJ)	70
Output Pulse Length (ns)	5.6
Size (lxwxh, m)	37.5x0.9x0.9
Delay Optics (Number Sets)	60
Pockels Cell (4, wxh)(m)	0.9x0.9
Polarizer Plate (2, wxh)(m)	1.65x0.9
Quarter-Wave Plate (2, wxh)	0.9x0.9
Delay Line Mirror (4, wxh)	0.9x0.9
Downstream Optics (Number Sets)	60
Turning Mirror (2, wxh)(m)	0.97x0.69
Vacuum Interface Mirror (wxh)	0.97x0.69
Turning Mirror (wxh)(m)	0.97x0.69
Pinhole Collimating Mirror	0.97x0.69
Target Focusing Mirror (wxh)	0.97x0.69
Grazing Incidence Mirror	3.95x0.69

TARGET	VALUES
Target Type	Direct Drive Single-Shell
Number of Beams	60
Beam Profile	$\sin^2 x/x^2$
Beam Focus	Initially Tangential
Illumination Nonuniformity	<1%
Driver Output Energy (MJ)	4.0
Target Gain	124
Target Yield (MJ)	497
Neutron Energy (MJ)	359
Debris Energy (MJ)	107
X-ray Energy (MJ)	31
Fusion Power (MW)	2807
Neutron Power (MW)	2027
Surface Heating Power (MW)	780
Final Beam Transport Efficiency (%)	100
Peak Power Pulse Length (ns)	5.6
Repetition Rate (pps)	5.65
Fuel Burnup Fraction	29%
Tritium Throughput (g/day)	1496

Use or disclosure of data
subject to title page restriction

This page intentionally left blank.

APPENDIX B

PROMETHEUS-H BASELINE PARAMETER LIST

PARAMETER CATEGORY	PAGE NO
GENERAL PLANT	B-2
REACTOR CAVITY	B-2
DRIVER SYSTEM	B-4
TARGET	B-6

Use or disclosure of data
subject to title page restriction

PROMETHEUS-H BASELINE PARAMETER LIST

GENERAL PLANT PARAMETERS	VALUE
Net Electric Power (MWe)	999
Gross Electric Power (MWe)	1189
Recirculation Power (MWe)	190
Driver Power (MWe)	137
Auxiliary Power (MWe)	28
Cavity Pumping Power (MWe)	25
Total Thermal Cycle Power (MWt)	2780
Net Thermal Power (MWt)	2759
Blanket (MWt)	1597
First Wall (MWt)	1162
Usable Driver Waste Heat	NA
Usable Pumping Waste Heat	21
Thermal Conversion Efficiency (%)	42.7
Recirculating Power Fraction (%)	16
Net System Efficiency (%)	36
Net Thermal Power (MWt) ((1.14x1818)+725-38)	2759
Fusion Power (MW)	2543
Surface Heating Power	725
Neutron Power	1818
Energy Multiplication Ratio	1.14
Power Loss to Shield	-38

REACTOR CAVITY	VALUE
Cavity Radius (m)	4.5
Cavity Cylinder Height (m)	4.5
Total Cavity Height (m)	13.5
FW Surface Area (m^2)	382
Volume (m^3)	668
Total Target Yield (MJ)	719
X-ray (MJ)	46
Debris (MJ)	159
Neutron (MJ)	514
Power	
Surface Heating (MW)	725
Neutrons (MW)	1818
Neutron Source Strength (n/sec)	8.82×10^{20}
FW/Blanket/Shield Characteristic	
TBR	1.2
Power Multiplication	1.14
Nuclear Power (MW) (1818x1.14)	2073

Use or disclosure of data
subject to title page restriction

REACTOR CAVITY (Cont)	VALUE
Nuclear Power Distribution	
	% MW
First Wall (+Surface Heatg)	21.1 1162
Blanket/Reflector/Plenum	77.1 1598
Vacuum Vessel	0.4 8.3
Shield (concrete)	1.4 29
First Wall System	
Structural Material	SiC
Coolant Channel Wall Thickness (mm)	5.0
Coolant Channel Diameter (cm)	5.0
Mean Fiber Pore Diameter (μm)	50.0
Porosity (%)	10.0
Permeability (m^2)	1.76×10^{-14}
Coolant Media	Liquid Lead
Surface Protection Media	Liq Lead Film
Surface Film Thickness (mm)	0.4-0.6
Inlet Temperature (°C)	375
Outlet Temperature (°C)	525
Delta-T(bulk) (°C)	150
Mass Flow Rate (kg/s)	54,422
Volume Flow Rate (kg/s)	5.21
Coolant Flow Area(cylindrical chamber)	1.1775 (m^2)
Average Velocity (m/s)	4.42
Reynolds Number	1.12×10^6
Frictional Factor	0.02
Coolant Path Length (m)	12.34
Frictional Pressure Drop (MPa)	0.5
Inlet Pressure (top)(MPa)	1.0
Outlet Pressure (bottom)(MPa)	1.5
Pumping Power (85% efficiency)(MW)	3.0
Maximum SiC Temperature (°C)	775
No. Liq Lead Steam Generators	6
No. Liq Lead Pumps	6
Blanket System	
Structural Material	SiC
SiC Min Temperature (°C)	400
SiC Max Temperature (°C)	765
Coolant Media	Helium
Helium Inlet Temperature (°C)	400
Helium Outlet Temperature (°C)	650
Helium Velocity (m/s)	42
Helium Inlet Pressure (MPa)	1.5
Pressure Drop (kPa)	19
Neutron Multiplier	FW Liq Lead Coolant
Breeder Material	Li_2O
Li_20 Min Temperature (°C)	422

Use or disclosure of data
subject to title page restriction

REACTOR CAVITY (Cont)	VALUE
Blanket System (Cont)	
Li_2O Max Temperature (°C)	765
Li_2O Theoretical Density Fraction	0.8
Li_2O Density (kg/m^3)	2.01×10^3
Beeder Volume (m^3)	75
Avg Annual Li Burnup (%)	0.6
Peak-to-Average Burnup (%)	3
Tritium Inventory (g)	100
Tritium Generation Rate (g/day)	362
BET Surface Area (m^2/kg)	50
Grain Radius (μm)	10
Grain Diffusion Coefficient:	
Pre-exponential Factor (m^2/s)	6.81×10^{-7}
Activation energy (kJ/mol)	84.8
Purge Composition	He + 0.2%H2
Amount of Protium in Purge (%)	0.2
Helium Purge Pressure (MPa)	0.2
No. Helium Steam Generators	6
No. Helium Reheaters	6
No. Helium Recirculators	6
Vacuum System	
Cavity Pressure @0 °C (mtorr,Pb)	100
Background Gas Density (cm^{-3})	3.5×10^{15}
No. Vacuum Pumping Ports	4
No. Vacuum Pumps/Port	3
Vacuum Pump Type	Roots Blower
Vacuum Pumping Port Diameter (m)	1
Vacuum Vessel Material	Ferretic Steel
Cavity Exhaust (total)	110.6 mg/s, 48,056 l/s

	mg/s	l/s
Hydrogen (total-all forms)	104.6	47,308
Helium	6.0	748

DRIVER SYSTEM	VALUE
Driver Type	Single Heavy Ion Beam LINAC
Target Illumination Scheme	Indirect Drive, Two Sided
Number of Beams..(12 main + 2 prepulse)	18
Repetition Rate (pps)	3.54
Driver Output Energy (MJ)..(7.0 delivered to target)	7.8
Ion Accelerated	Lead
Charge State	+2
Final Energy (GeV)	4.0
Driver Power (MWe)	137

Use or disclosure of data
subject to title page restriction

PARAMETER SUMMARY SINGLE-BEAM, MASCHKE SCALING
(alpha = 0.2, beta = -0.15, gamma = 0.8

	Injection	Ramped to Fixed Transition	Final Transport	Main Beam Buncher	Main Beam Final Focus	Prepulse Beam Buncher	Prepulse Beam Final Focus
Beam Voltage MV	3	49.73	2000	2000	2000	2000	2000
Beam Radius cm	9.39	9.39	9.39	9.94	15.02	10.50	14.94
Lattice Period m	0.5	1.33	4.85	4.67	3.55	4.50	3.56
Pulse Length ns	15495.0	1639.0	85.3	70.5	17.8	176.4	54.4
Bunch Length m	36.54	15.74	5.13	4.24	1.07	10.61	3.27
Beamlet Current A	14	132	2532	3065	12125	3674	11915
Packing Fraction %	69.0	39.3	18.8	21.5	56.2	24.4	55.5
Magnet Length m	0.344	0.523	0.911	1.00	1.99	1.10	1.98
Magnet Bore Rad cm	15.51	15.51	15.51	16.43	24.81	17.34	24.68
Magnet a/L Ratio	0.273	0.179	0.103	0.099	0.075	0.096	0.076
Core Inner Radius cm	43.0	43.0	43.0	155.44	0	68.0	0
Core Thickness cm	36.9	150.2	7.8	6.46	0	16.2	0
Depressed Tune Deg	8	5.25	3.02	2.59	0.86	2.24	0.87

	Ramped Gradient	Fixed Gradient	Storage Rings	Main Beam Buncher	Main Beam Final Transport	Prepulse Beam Buncher	Prepulse Beam Final Transport
Number Beams	1	1	14	6	6	1	1
Section Lengths m	222.5	1953.9	157.3	84.5	180.0	195.6	180.0
Tunnel Widths m	9.8	9.7	8.1	8.1	8.1	8.1	8.1
Core Volume m^3	906.0	1628.6	0	60.4	0	193.0	0
Pulser Energy MJ	0.13	1.9	0	0.49	0	0.59	0
Number Quadrupoles	300	578	34	18	39	41	37
Quad Lengths cm	40.1	77.0	91.1	94.0	133.4	96.6	141.1
Number Dipoles	0	0	32	0	19	0	20
Dipole Lengths cm	0	0	239.6	0	229.8	0	215.5
Magnet Powers MW	0.9	1.734	0.198	0.054	0.348	0.123	0.342
Driver Efficiency %	70.6	85.0	34.4	20.6			
Z_{ion}	2	A_{ion}	207	E_{ion}	4		
B_{pole}	1.97	N_{beams}	18	$Emit_n$	9.8		
α_s	0.20	β_s	-0.15	γ_s	0.80		
β_F	0.20	f_{Bunch}	2.1%	τ_{TGT}	7.28		
Len_{STND}	30	f_{Bunpp}	4.9%	τ_{PRE}	30		

Use or disclosure of data
subject to title page restriction

TARGET	VALUES
Target Type	Hohlraum
Target Illumination Scheme	Indirect Drive, Two Sided
Driver Output Energy (MJ)	7.8
Final Beam Transport Efficiency.(%)	90
Target Gain	103
Target Yield (MJ)	719
Neutron Energy (MJ)	514
Debris Energy (MJ)	159
X-ray Energy (MJ)	46
Fusion Power (MW)	2543
Neutron Power (MW)	1818
Surface Heating Power (MW)	725
Repetition Rate (pps)	3.54
Fuel Burnup Fraction	32%
Tritium Throughput (g/day)	1248

Use or disclosure of data
subject to title page restriction

APPENDIX C

INERTIAL FUSION ENERGY REACTOR DESIGN STUDIES

COST BASIS

LIST OF PAGES

C-i through C-iii
C-1 through C-41

TABLE OF CONTENTS

Section	Title	Page
Introduction		1
C.1	Developed Economic Study Guidelines	10
C.2	Overall Costing and Economic Methodology	14
C.3	Capital Cost Accounts	17
C.3.1	Land and Land Rights (Account 20)	17
C.3.2	Structures and Site Facilities (Account 21)	17
C.3.2.1	Site Improvements and Facilities (Account 21.01)	17
C.3.2.2	Reactor Building (Account 21.02)	18
C.3.2.3	Driver Building (Account 21.03)	19
C.3.2.4	Turbine Building (Account 21.04)	19
C.3.2.5	Heat Rejection Structures (Account 21.05)	19
C.3.2.6	Auxiliary Building (Account 21.06)	19
C.3.2.7	Target Manufacturing Building (Account 21.07)	20
C.3.2.8	Tritium and Waste Processing Building (Account 21.08)	20
C.3.2.9	Miscellaneous Buildings (Account 21.09)	20
C.3.3	Reactor Plant Equipment (Account 22)	20
C.3.3.1	Reactor Equipment (Account 22.01)	20
C.3.3.1.1	First Wall and Blanket (Account 22.01.01)	21
C.3.3.1.2	Shield and Vacuum Vessel (Account 22.01.02)	24
C.3.3.1.3	Primary Structure (Account 22.01.03)	25
C.3.3.1.4	Reactor Cavity Vacuum (Account 22.01.04)	26
C.3.3.1.5	Target Injection and Tracking (Account 22.01.05)	27
C.3.3.2	Main Heat Transfer and Transport Systems (Account 22.02)	27
C.3.3.3	Auxiliary Cooling System (Account 22.03)	29
C.3.3.4	Radioactive Waste Treatment and Disposal System (Account 23.04)	29
C.3.3.5	Fuel Cycle System (Account 22.05)	29
C.3.3.6	Reactor Plant Maintenance (Account 22.06)	30
C.3.3.7	Reactor Plant Instrumentation and Control (Account 22.07)	30
C.3.3.8	Other Reactor Plant Equipment (Account 22.08)	30
C.3.3.9	Reactor Spare Parts (Account 22.98)	32
C.3.3.10	Contingency (Account 22.99)	32
C.3.4	Turbine Plant Equipment (Account 23)	32
C.3.5	Electric Plant Equipment (Account 24)	33
C.3.6	Miscellaneous Plant Equipment (Account 25)	33
C.3.7	Target Plant Equipment (Account 26)	33
C.3.8	Driver Plant Equipment (Account 27)	34
C.3.9	Special Materials (Account 28)	35
C.3.10	Indirect Cost Accounts (Accounts 91 through 98)	36
C.4	Cost Of Electricity Accounts	37

Use or disclosure of data
subject to title page restriction

TABLE OF CONTENTS (CONT.)

Section	Title	Page
C.4.1	Annual Capital Cost	37
C.4.2	Annual Operating Cost	38
C.4.2.1	Plant O&M Cost	38
C.4.2.2	Scheduled Maintenance Cost	38
C.4.2.3	Target O&M Cost	38
C.4.2.4	Fuel Cost	39
C.4.2.5	Decommissioning Allowance Cost	39
C.4.3	Cost of Electricity Summary	40
References		41

LIST OF FIGURES

Number	Title	Page
C-1	Log Linear Unit Cost Curves	11
C-2	Radial Build of First Wall, Blanket, and Shield Subsystems	22

LIST OF TABLES

Number	Title	Page
C-1	Economic Requirements and Criteria	2
C-2	Commerce Department Gross National Product Implicit Price Level Deflators	2
C-3	Prometheus Plant Cost Accounts	3
C-4	Application of Learning Curve by Cost Account	12
C-5	Site Improvements and Facility Costs	18
C-6	Cost of Materials Used in the FW/B/S Systems	23
C-7	First Wall and Blanket Material Costs	23
C-8	Cost of Shield Materials Comparison	24
C-9	Total Shielding and Vacuum Vessel Costs	25
C-10	Primary Structure Weights and Costs	26
C-11	Main Heat Transfer and Transport System Costs	28
C-12	Reactor Plant Maintenance Equipment Costs	31
C-13	Turbine Plant Cost Estimating Relationships	33
C-14	Target and Target Plant Cost Factors	34
C-15	Driver Plant Equipment Costs	35
C-16	Prometheus Reactor Plant Cost Factors in Constant 1991 Dollars	36
C-17	Cost of Electricity Accounts for the Prometheus Reactor Plants	37

This page intentionally left blank.

INTRODUCTION

The economic basis for the Prometheus IFE Reactor Design Studies is presented in this Appendix C. One of the major tasks of the study was to conduct an economic assessment of the two reactor designs developed. In order to provide compatibility with other fusion and fission reactor design studies, the groundrules and estimating guidelines were established to allow consistency in the study comparisons. The IFE Reactor Study Oversight Committee provided the study team with a recommended set of guidelines[1]. Chapter 3 of the study final report documented all the technical and economic guidelines and recommendations which were implemented. The economic guidelines will be repeated here for completeness.

The analyses and methodologies used herein were outgrowths of reactor design studies conducted in the late 1970s and early 1980s, such as UWMAK and STARFIRE studies. Later studies have built upon those early efforts and have improved the overall methodology. However, realistic economic assessments of a future technology cannot be accomplished with a high degree of fidelity due to the degree of extrapolation over many years. Many tools are used to account for proper modeling of tax structures, depreciation, cost of money, fixed charge rates, and inflation rates. References 2 and 3 have significantly improved these economic models. The latest MFE reactor design studies, the ARIES series, have contributed toward normalization of such economic factors as noted in Reference 4.

Table C-1 presents the economic requirements and criteria employed in the Prometheus IFE Reactor Design Studies. These data have been coordinated with the Oversight Committee (Robert Krakowski), ARIES (Ron Miller), and the other parallel IFE reactor design study[5] (Wayne Meier). The factors used for the plant lifetime, lead time, and general economic and tax factors have generally been proposed by Delene[3] and accepted by the fission and fusion energy community. Delene (and the Oversight Committee) has also recommended the indirect cost factors be adjusted depending upon the LSA factor. A trade study on this factor was discussed in Section 6.13 of the Prometheus final report.

The cost for operations and maintenance cost was adopted from the ARIES study. The magnitude of the scaling coefficient was increased to bring the ARIES 1988$ cost basis to the study guideline of 1991$. As noted in Table C-1, the Gross National Product Implicit Price Level Deflators were used as the basis for inflating/deflating specific cost values. Table C-2 presents specific deflator data from 1980 to 1991.

Decommissioning costs were addressed in the recommended guidelines for the study, namely a range of 0-1 mill/kWh with an LSA dependency. Treatment of these costs were addressed in detail in a subsequent section in this Appendix.

Use or disclosure of data
subject to title page restriction

Table C-1 Economic Requirements and Criteria

Plant Operating Lifetime, yrs		30			
Plant Construction Lead Time, yrs		6			
Contingency Factor, Project and Process		See below, may add risk factor			
Spare Parts Multiplier		1.0 (no spares)			
Constant Year Dollars		1991			
Nominal Year Dollars		1997			
Inflation Rate		.05			
Escalation Rate		.05			
		Average	Tax-Adjusted		
Effective Cost of Money, Nominal Dollars		.1135	.0957		
Effective Cost of Money, Constant Dollars		.0605	.0435		
Fixed Charge Rate, Nominal Dollars		.1638			
Fixed Charge Rate, Constant Dollars		.0966			
Indirect Cost Factors	LSA	1	2	3	4
91 Constr Serv & Equipment	(x TDC)	.113	.120	.128	.151
92 Home Office Engr & Services	(x TDC)	.052	.052	.052	.052
93 Field Office Engr & Services	(x TDC)	.052	.060	.064	.087
94 Owners Cost	(x TDC+91+92+93)	.150	.150	.150	.150
95 Process Contingency	(x TDC+91+92+93+94)	.000	.000	.000	.000
96 Project Contingency	(x TDC+91+92+93+94)	.1465	.173	.184	.195
		Constant $	Nominal $		
97 IDC Factor		.1652	.3178		
98 EDC Factor		-0	.2436		
Operations and Maintenance Cost [$91]		$78.9x(L^*)\ (P_E/1200)^{0.5}$			
LSA Factor, L*		0.7[1]; 0.85[2]; 0.952[3]; 1.0[4]			
Decommissioning Allowance, mill/kWeh		0-1 (LSA-dependent)			
Deuterium Fuel Cost, mill/kWeh		-0.05			
Learning Curve		85-90% on fusion systems, 75-100% on non-fusion systems			
Quantity Assumption		10th of kind commercial plant + Prototype and Demo if applicable			
Other Factors Influencing the Economics					
Plant Availability/Capacity		Value derived from design approach Will use typical MCF values (.75) as a starting value			
Cost Adjustment Factor up to 1991$		Use Gross National Product Implicit Price Level Deflators [1982 Basis]			

Table C-2 Commerce Department Gross National Product Implicit Price Level Deflators (1982 Basis Year)

Year	Annual Deflator	Rate of Change Change
1980	85.7	9.0
1981	94.0	9.7
1982	100.0	6.4
1983	103.9	3.9
1984	107.7	3.7
1985	110.9	3.0
1986	113.8	2.6
1987	117.4	3.2
1988	121.3	3.3
1989	126.3	4.1
1990	131.5	4.1
1991	138.1*	5.0 (assumed 5% Inflation)

Use or disclosure of data
subject to title page restriction

Another of the Oversight Committee's recommendations was the use of common costing accounts[1]. The set given to the two design teams was developed by ARIES. This set was slightly modified for the Prometheus study to include IFE-specific equipment as shown in Table C-3. One of the changes was to incorporate the Target Manufacturing Plant Equipment and the Driver Plant Equipment into separate main Accounts 26 and 27. The Driver Plant Equipment has unique account names for several subaccounts, such as Ion Source or Driver Optics. Other driver accounts are common such as Pulsed Power Systems. Buildings were added in the Structures and Site Facilities Account for these new systems. Most other accounts were suitable with minor changes.

Table C-3 Prometheus Plant Cost Accounts

Number	Title
20.00	Land and Land Rights
20.01	Land and Privilege Acquisition
20.02	Relocation of Bldgs, Util, etc.
21.00	Structures and Site Facilities
21.01	Site Improvements and Facilities
21.01.01	General Yard Improvements
21.01.03	Transportation Access
21.01.02	Waterfront Improvements
21.02	Reactor Building
21.02.01	Basic Building Structures
21.02.02	Building Services
21.02.03	Containment Structures
21.02.04	Architectural
21.03	Driver Building (incl Tunnels/F.Focus/Pwr Supply)
21.03.01	Basic Building Structures
21.03.02	Building Services
21.03.03	Architectural
21.04	Turbine Building
21.04.01	Basic Building Structures
21.04.02	Building Services
21.04.03	Architectural
21.05	Heat Rejection Structures
21.05.01	Intake Structures
21.05.02	Discharge Structures
21.05.03	Unpressurized Intake & Discharge Conduits
21.05.04	Recirculating Structures
21.05.05	Cooling Tower Systems (See 23.03 for Cooling Towers)
21.06	Auxiliary Building
21.06.01	Basic Building Structures
21.06.02	Building Services
21.06.03	Architectural
21.07	Target Manufacturing Building
21.07.01	Basic Building Structures
21.07.02	Building Services
21.07.03	Architectural

Use or disclosure of data subject to title page restriction

Table C-3 Prometheus Plant Cost Accounts (Cont.)

Number	Title
21.08	Tritium and Waste Processing Building
21.08.01	Basic Building Structures
21.08.02	Building Services
21.08.03	Architectural
21.09	Miscellaneous Buildings
21.09.01	Administration Building
21.09.02	Control Room Building
21.09.03	Diesel Generator Building
21.09.04	Service Building
21.09.05	Cryogenics Building
21.09.06	Ventilation Stack
21.09.07	Misc Structures and Building Work
21.98	Spare Parts Allowance
21.99	Contingency Allowance
22.00	Reactor Plant Equipment
22.01	Reactor Equipment
22.01.01	First Wall and Blanket
22.01.01.01	First Wall Material and Structure
22.01.01.02	Blanket Structure and Cooling Tubes
22.01.01.03	Breeding Material
22.01.01.04	Attenuators, Reflectors, and Multipliers
22.01.01.05	Other
22.01.02	Shield and Vacuum Vessel
22.01.02.01	Vacuum Vessel Structure
22.01.02.02	Shielding Material (Bulk and Beamline)
22.01.02.03	Cooling Plumbing
22.01.03	Primary Structure
22.01.03.01	Reactor Support Structure
22.01.03.02	Equipment Support Structure
22.01.03.03	Cavity Support Pedestal
22.01.04	Cavity Vacuum
22.01.04.01	Helium Liquifier-Refrigerators
22.01.04.02	Vacuum Pumps
22.01.04.03	Backing Pumps
22.01.04.04	Vacuum Plumbing
22.01.04.05	Plenum Chamber
22.01.04.06	Other
22.01.05	Target Injection and Tracking
22.01.05.01	Accelerating Tube System
22.01.05.02	Sabot Retrieval System
22.01.05.03	Cryogenic System
22.01.05.04	Target Tracking System
22.01.05.06	Target and Sabot Storage System
22.02	Main Heat Transfer and Transport Systems
22.02.01	Primary Lead Coolant Subsystem
	Pumps and Motor Drives
	Piping
	Heat Exchangers, Steam Generators, Superheaters, Reheaters
	Tanks (Dump, Makeup, Clean-up...)
	Coolant Cleanup and Tritium Extraction System
	Thermal Insulation, Piping, and Equipment

Use or disclosure of data
subject to title page restriction

Table C-3 Prometheus Plant Cost Accounts (Cont.)

Number	Title
	Tritium Extraction
22.02.02	Primary Helium Coolant Subsystem
	Pumps and Motor Drives
	Piping
	Heat Exchangers, Steam Generators, Superheaters, Reheaters
	Tanks (Dump, Makeup, Clean-up...)
	Coolant Cleanup and Tritium Extraction System
	Thermal Insulation, Piping, and Equipment
	Tritium Extraction
22.02.03	Primary Driver Waste Heat Coolant Subsystem
	Pumps and Motor Drives
	Piping
	Heat Exchangers, Steam Generators, Superheaters, Reheaters
	Tanks (Dump, Makeup, Cleanup...)
	Coolant Cleanup and Tritium Extraction System
	Thermal Insulation, Piping, and Equipment
22.02.04	Intermediate Coolant Subsystem (Not Used)
22.02.05	Secondary Coolant Subsystem (Not Used)
22.03	Auxiliary Cooling System
22.03.01	Shield and Structure Cooling Subsystem
	Pumps and Motor Drives
	Piping
	Heat Exchanger Equipment
	Tanks
	Pressurizing Equipment
	Cleanup Equipment
22.03.02	Final Optics and Beamline Cooling Subsystem
	Pumps and Motor Drives
	Piping
	Heat Exchange Equipment
	Tanks
	Pressurizing Equipment
	Cleanup System
22.03.03	Cryogenic Cooling Subsystem
	Helium Liquefier - Refrigerator
	LHe Transfer and Storage
	He Gas Storage
22.03.04	Other Cooling Subsystems
	Pumps and Motor Drives
	Piping
	Heat Exchange Equipment
	Tanks
	Pressurizing Equipment
	Cleanup System
22.04	Radioactive Waste Treatment and Disposal System
22.04.01	Liquid Waste Processing & Equipment Subsystem
22.04.02	Gaseous Wastes & Off-gas Processing Subsystem
22.04.03	Solid Waste Processing Equipment Subsystem
22.05	Fuel Cycle System
22.05.01	Chamber Exhaust Gas Processing (incl Beamlines gases)
22.05.02	Breeder Purge Gas Processing

Use or disclosure of data
subject to title page restriction

Table C-3 Prometheus Plant Cost Accounts (Cont.)

Number	Title
22.05.03	Impurity Processing (Incl Lead Coolant Stream)
22.05.04	Water Processing
22.05.05	Isotope Separation System
22.05.06	Tritium and Deuterium Storage
22.05.07	Atmospheric Tritium Recovery
22.05.08	Waste Products Handling and Storage
22.06	Reactor Plant Maintenance
22.06.01	Reactor Cavity Maintenance Equipment
22.06.02	Hot Cell Maintenance Equipment
22.06.03	Final Optics Maintenance Equipment
22.07	Reactor Plant Instrumentation and Control System
22.07.01	Reactor Instrumentation & Control Equipment
22.07.02	Radiation Monitoring Systems
22.07.03	Isolated Indicating & Recording Systems
22.08	Other Reactor Plant Equipment
22.08.01	Special Heating Systems
22.08.02	Coolant Receiving, Storage and Makeup Systems
22.08.03	Gas Systems
22.08.04	Building Vacuum Systems
22.98	Spare Parts Allowance
22.99	Contingency
23.00	Turbine Plant Equipment
23.01	Turbine-Generators
	Turbine-Generators and Accessories
	Foundations
	Standby-Exciters
	Lubrications Systems
	Gas Systems
	Reheaters
	Shielding
23.02	Main Steam System
23.03	Heat Rejection System
	Water Intake Common Facilities
	Circulating Water Systems
	Cooling Towers
	Other Heat Rejection Systems
23.04	Condensing Systems
	Condensers
	Condensate System
	Gas Removal System
	Turbine By-pass Systems
23.05	Feed Heating System
	Regenerators & Recuporators
	Pumps
	Tanks
23.06	Other Turbine Plant Equipment
	Turbine Auxiliaries
	Auxiliaries Cooling System
	Makeup Treatment System
	Chemical Treatment and Condensate Purification System
	Central Lubrication Service System

Use or disclosure of data
subject to title page restriction

Table C-3 Prometheus Plant Cost Accounts (Cont.)

Number	Title
23.07	Turbine Plant Instrumentation & Control
	Process Instrumentation & Control
	Automatic Monitoring and Control
	Isolated Indicating and Recording Gauges, Meters and Instr
23.98	Spare Parts Allowance
23.99	Contingency
24.00	Electric Plant Equipment
24.01	Switchgear
	Generator Circuits
	Station Service
24.02	Station Service Equipment
	Station Service & Startup Transformers
	Low Voltage Unit Substation & Lighting Transformers
	Battery System
	Diesel Engine Generators
	Gas Turbine Generators
	Motor Generator Sets
24.03	Switchboards, including Heat Tracing
	Main Control Board for Electric Systems
	Auxiliary Power and Signal Boards
24.04	Protective Equipment
	Generating Station Grounding System
	Cathodic Protection
24.05	Electrical Structures and Wiring Containers
	Concrete Cable Tunnels, Trenches and Envelopes
	Cable Trays and Support
	Conduit
	Other Structures
24.06	Power and Control Wiring
	Generator Circuits Wiring
	Station Service Power Wiring
	Control Wiring
	Instrument Wiring
	Containment Penetrations
24.07	Electrical Lighting
	Reactor Building Lighting
	Turbine Building Lighting
	Electric Plant Equipment Building Lighting
	Miscellaneous Plant Equipment Buildings Lighting
	Target Manufacturing Plant Building Lighting
	Driver Building Lighting
	Yard Lighting
24.98	Spare Parts Allowance
24.99	Contingency
25.00	Miscellaneous Plant Equipment
25.01	Transportation and Lifting Equipment
	Cranes, Hoists, Monorails and Conveyers
	Railway
	Roadway Equipment
	Watercraft
	Vehicle Maintenance Equipment

Use or disclosure of data
subject to title page restriction

Table C-3 Prometheus Plant Cost Accounts (Cont.)

Number	Title
25.02	Air and Water Service Systems
	Air Systems (Excl Piping)
	Water Systems (Excl Piping)
	Auxiliary Heating Boilers
25.03	Communications Equipment
	Local Communications Systems
	Signal Systems
25.04	Furnishings and Fixtures
	Safety Equipment
	Shop, Laboratory, and Test Equipment
	Office Equipment and Furnishings
	Change Room Equipment
	Environmental Monitoring Equipment
	Dining Facilities
25.98	Spare Parts Allowance
25.99	Contingency Allowance
26.00	Target Manufacturing Plant Equipment
26.01	Capsule Fabrication
26.02	Indirect Case Fabrication
26.03	Fuel Filling
26.04	Indirect Target Mating
26.05	Target Storage
26.06	Target Manufacturing Plant Instrumentation and Control Equipment
26.07	Target Manufacturing Plant Maintenance Equipment
26.98	Spare Parts Allowance
26.99	Contingency Allowance
27.00	Driver Plant Equipment
Heavy Ion Driver	
27.01	Ion Source/Injector System
27.02	Accelerating Structures
	Insulators, Cores, Structure
27.03	Focusing Magnet System
27.04	Cryogenics and Cooling System
27.05	Storage Rings
27.06	Transport/Final Focus System
Laser Driver	
27.01	Front End System
27.02	Discharge Laser System
27.03	Raman Accumulator System
27.04	Stimulated Brillouin System
27.05	Excimer Gas System
	Gas Flow System
	Gas Conditioning System
27.06	Driver Optics Systems
	Front End Optics
	Discharge Laser Windows
	Discharge Turning Mirrors
	Raman Input Windows
	Raman Secondary Mirrors
	Raman Output Windows
	SBS Polarizer

Use or disclosure of data
subject to title page restriction

Table C-3 Prometheus Plant Cost Accounts (Cont.)

Number	Title
	SBS Quarter-Wave Plate
	SBS Chirper Crystal
	SBS Cell Window
	SBS Cell Mirror
	Vacuum Interface Windows
	Turning Mirrors
	Focusing Mirrors
	Grazing Incidence Mirrors
	Spares
	Mounts
Common Driver Systems	
27.07	Pulsed Power System
27.08	Driver Vacuum System
27.09	Driver Instrumentation & Control Equipment
27.10	Driver Maintenance Equipment
27.11	Miscellaneous Systems
27.98	Spare Parts Allowance
27.99	Contingency Allowance
28.00	Special Materials
	Initial Supply of Special (Non-fuel and Non-structural) Materials, Fluids, Gases and Liquids which require non-standard indirect costing or fixed charge rate accounting.
	Reactor Coolants
	Turbine Working Fluids
	Driver Fluids and Gases
	Reactor Building and Beamline Cover Gases
91.00	Construction Facilities, Equipment and Services
	Temporary Facilities
	Construction Equipment
	Construction Services
92.00	Home Office Engineering and Services
	Systems Engineering
	Management Services
	Quality Assurance
	Safety and Environmental Engineering
93.00	Field Office Engineering and Services
	Construction Management
	Inspection
	Pre-Operational Training
94.00	Owners Cost
	Project Administration
	Staff Training and Plant Startup
	Inventories and Spares Administration
95.00	Process Contingency
96.00	Project Contingency
97.00	Interest During Construction (IDC)
98.00	Escalation During Construction (EDC)

Use or disclosure of data
subject to title page restriction

C.1 DEVELOPED ECONOMIC STUDY GUIDELINES

The Introduction Section discusses many of the important economic guidelines which significantly affect the total capital cost (including the indirect costs) and the cost of electricity. Although there is some controversy on the best technique to represent the ultimate capital and operating cost with a high degree of fidelity, the salient point is that all practitioners should conform to the same, pre-established groundrules to insure valid comparisons between studies.

This section will discuss some of the groundrules which have a higher degree of uncertainty, more controversy, and perhaps, a higher impact on the overall final economic results.

Level of Safety Assurance - The ESECOM study[6] introduced the concept of Level of Safety Assurance (LSA) to describe and categorize varying degrees of safety. The ESECOM study associated costs with those prescribed levels. Delene[3] further proposed additional costs or credits based upon the LSA determination. As noted in Table C-1, the indirect costs are scaled according to the plant LSA values. Delene also recommended scaling direct capital costs according to the LSA values. In the Prometheus studies, only the indirect costs, the O&M costs, and the decommissioning costs were scaled by the LSA values. It was felt that the means to obtain the lower LSA rating depends, in part, upon the selection of certain materials or designs. This decision significantly impacts the direct costs and we could not justify modifying the direct costs depending on the LSA rating. Section 6.13 describes a trade study of varying levels of LSA, with no decrease in the direct capital costs of the plant. In fact, if a plant were judged to have a higher LSA rating, presumably a lower cost of materials and processes would have been utilized, somewhat offsetting the LSA penalties.

Learning Curve - The recommended economic guidelines[1] suggested the use of learning curves to estimate the cost reduction possible with quantity purchases of like components or subsystems. Indeed, this practice has been instituted beginning with the STARFIRE study. The concept is well documented in many industries. However the application in reactor studies has been somewhat inconsistent. In the STARFIRE economic analysis, Waganer attempted to apply differing learning curves to subsystems as appropriate, with some systems having no learning (i.e., 100%) and others which were judged to be labor intensive, to have a high degree of learning (~80%). Since the STARFIRE analyses, other reactor designs have continued to use the technique of learning curves. But the practice has deteriorated with less emphasis on justification and more on a broad-brush treatment, perhaps with a single learning curve value for all accounts. The Oversight Committee recommended the Prometheus study follow the example of ARIES in establishing economic guidelines and indeed many of the guidelines are taken from ARIES study. A rough draft of an ARIES System Studies report[7] indicated the ARIES economic analysis would use a universal learning curve of 75%. If applied to large quantity purchases, a 75% learning curve is

Use or disclosure of data
subject to title page restriction

a very powerful cost reduction technique. For example, the cost of a tenth of a kind would be 38% of the first unit cost and the 100th would be 15% of the first unit cost, see Figure C-1 Only a small portion of documented cases[8] would support such an overall level of cost improvement.

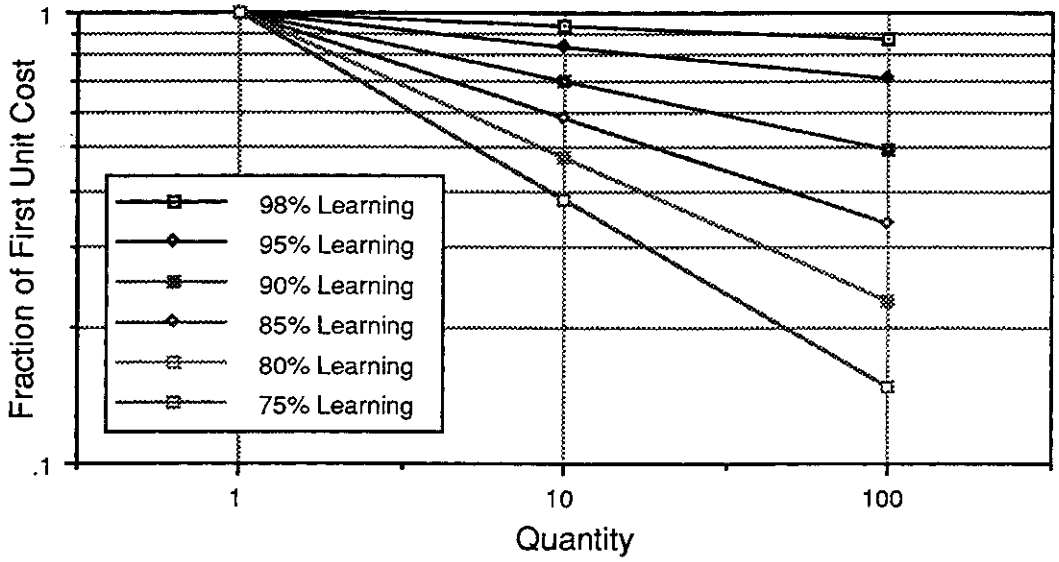

Figure C-1. Log Linear Unit Cost Curves

In the Prometheus economic analysis, it was felt that each system, subsystem, and in some cases, the components must be examined individually to determine which learning curve should be applied. Table C-4 illustrates the learning curves applied to each of the reactor cost accounts. No learning was applied to the Structures and Site Facilities because these would largely constructed on site with local labor. Many of the components would be unique to this site. Some of the interior building systems, i.e., HVAC and lighting fixtures, would experience learning effects, but they would be considered as high quantity purchases from many other construction projects and therefore, any incremental learning effects on this estimate would be negligible.

In the Reactor Plant Equipment, each system and subsystem was viewed independently with regard to the amount of labor (subject to learning) and to materials (weakly influenced by learning). Another factor was if the system would be constructed on-site or off-site in a factory. The quantity to be purchased was used in the learning curve analysis, along with an estimate of how many identical prior units would have been constructed for demonstration units or other purposes. The First Wall and Blanket is estimated to have a 85% learning curve. The Shield is estimated at 90% because an increased percentage of the construction cost would occur at the site location. The Main Heat Transfer and Transport System is estimated at 75% because of the large number of like components, such as pipes, valves, pumps, and storage tanks. Many of these would be new and unique to this application, especially the SiC plumbing within the reactor bulk shield region. The Reactor Radioactive

Use or disclosure of data
subject to title page restriction

Table C-4 Application of Learning Curve by Cost Account

Cost Acct	IFE Reactor Plant Cost Accounts	Lrn Crv
20.00	Land and Land Rights	
21.00	Structures and Site Facilities	
21.01	Site Improvement and Facilities	1.00
21.02	Reactor Building	1.00
21.03	Driver Building	1.00
21.04	Turbine Building	1.00
21.05	Heat Rejection Structures	1.00
21.06	Auxiliary Building	1.00
21.07	Target Manufacturing Building	1.00
21.08	Tritium and Waste Processing Bldg	1.00
21.09	Miscellaneous Buildings	1.00
22.00	Reactor Plant Equipment	
22.01	Reactor Equipment	
22.01.01	First Wall and Blanket	0.85
22.01.02	Shield and Vacuum Vessel	.90/.85
22.01.03	Primary Structure	0.85
22.01.04	Cavity Vacuum	0.85
22.01.05	Target Injection and Tracking	0.85
22.02	Main Heat Transfer and Transport Sys	
22.02.01	Primary Lead Coolant Subsystem	0.75
22.02.02	Primary Helium Coolant Subsystem	0.75
22.02.03	Driver Waste Heat (See Acct 23)	
22.03	Auxiliary Cooling System	
22.03.01	Shield and Structure Cooling Subsystem	0.85
22.03.02	Final Optics and Beamline Cooling Subsys	0.85
22.03.03	Cryogenic Subsystems, Reactor Plant	
22.03.04	Other Cooling Subsystems	
22.04	Radioactive Waste Treatment and Disposal	1.00
22.05	Fuel Cycle System	0.85
22.06	Reactor Plant Maintenance System	0.85
22.07	Reactor Plant Instrumentation and Control	.90
22.08	Other Reactor Plant Equipment	1.00
23.00	Turbine Plant Equipment	1.00
24.00	Electric Plant Equipment	1.00
25.00	Miscellaneous Plant Equipment	1.00
26.00	Target Manufacturing Plant Equipment	0.90
27.00	Driver Plant Equipment	
27.01	Front End System (L)	0.90
	Ion Source/Injector System (HI)	0.90
27.02	Discharge Laser System (L)	0.90
	Accel Modules and Power Supplies (HI)	0.90
27.03	Raman Accumulator System (L)	0.90
	Focusing Magnet System (HI)	0.90
27.04	Stimulated Brillouin System (L)	0.90
	Cryogenics and Cooling Systems (HI)	0.90
27.05	Excimer Gas Flow System (L)	0.80
	Storage Rings (HI)	0.90
27.06	Driver Optics (L)	0.90
	Transport/Final Focus System (HI)	0.90
27.07	Driver Pulsed Power System	0.90
27.08	Driver Vacuum System	0.90
27.09	Driver I&C Equipment	0.90
27.10	Driver Maintenance Equipment	0.85
27.11	Miscellaneous Systems	0.90
28.00	Special Materials	1.00

Use or disclosure of data
subject to title page restriction

Waste Treatment and Disposal system is considered to not have any learning effects. It was felt that this system would continue to evolve throughout the first to the tenth unit and learning curves would be inappropriate.

No learning curve effects are applied to the Turbine Plant Equipment, Electric Plant Equipment, and the Miscellaneous Plant Equipment. The rationale is that these systems are relatively common to other large power plants and any learning effects may be offset with site- and plant-specific effects. The Target Plant Equipment is estimated with a 90% learning curve because this equipment would be unique to this type of IFE plant and a limited degree of learning would be anticipated. The Driver Plant is generally costed with a 90% learning curve. The number of components in this system are generally larger that those present with the other major systems. For the KrF laser driver, there are 960 laser amplifier modules that are coupled into 60 Raman accumulators using 960 sets of comparable optical components. There are 60 beamlines with associated optical elements and support equipment. In the heavy ion driver, there are a large number of like coils, pulse power equipment, vacuum equipment, and storage ring equipment. Even though there will be demonstration or prototype equipment which would represent the first of a kind costs, the cost reduction with a large number of equipment purchases is significant.

Plant Availability/Capacity Factors - The canonical plant availability which has been derived or assumed in most MFE reactor design studies is 75% plus or minus a few percentage points. Our team was fortunate to have SPAR as a subcontractor to specifically examine the factors contributing to availability (or lack of availability). The major plant systems were examined for mean times to failure and mean times to repair. These data, along with the anticipated scheduled maintenance period, were used to determine the plant availability. The results for the laser-driven plant is 79.4% and the heavy ion-driven plant is 80.8%. Section 6.3.3 of the final report explains the methodology and analysis to derive these values. These values are higher than those estimated for MFE reactor power plants, but we believe they are justified due to the simpler and longer-lived IFE first wall and blanket system. Moreover, the two drivers examined in the Prometheus study are highly reliable which also contributes to the higher availability. A new system in the IFE plants which is not present in MFE plants is the Target Manufacturing Plant. Since redundancy is required to assure a constant supply of high quality targets, this plant equipment is specified to have a very high degree of reliability. The net result of the higher plant availability is roughly a 6% lower cost of electricity for an equivalent annual capital cost.

Use or disclosure of data
subject to title page restriction

C.2 OVERALL COSTING AND ECONOMIC METHODOLOGY

Cost of Electricity - The main economic evaluation parameter is the ultimate cost of electricity (COE) as expressed either in constant year dollars or nominal year dollars. Constant year dollars assumes the purchasing power of the dollar remains constant over time, i.e. no inflation. Even with no inflation, there remains a certain cost of capital (~6.05% in the study guideline). In the nominal dollar accounting technique, a nominal inflation rate is assumed (5% per annum) and the cost of money is inflated accordingly.

All the direct capital cost accounts, 20 through 28, were estimated in 1991 dollars. If the cost estimate or cost estimating relationship (CER) were accomplished in a prior year, the data in Table C-2 were used to escalate the cost to 1991 dollars. Spare parts are usually incorporated in the direct costs, but the recommended guidelines specified that the spare parts would be assumed to be zero. The typical indirect cost accounts (91-94) were estimated using the agreed upon percentages shown in Table C-1. The specific values are dependent upon the specific LSA of the power plant designed. Process contingency was assumed to be zero and the project contingency 14.65% of the previous subtotal. And again the percentage value is dependent upon the LSA value. All of these data are in 1991 dollars. This is sometimes referred to as the "Overnight Costs" referring to the plant being constructed in zero time with no interest or escalation charges.

In actual practice, a power plant requires time for construction. A 6-year construction schedule is assumed for Prometheus, which is very optimistic in today's environment. However, it is not inconceivable that future plants could be constructed in this time span. And by the time a tenth identical plant is constructed, it may be the norm. At the end of the construction period the interest on the borrowed money has contributed to the outstanding debt. If inflation is present, then items purchased and wages in the latter stages of the construction period will further increase the cost of the plant due to the effects of escalation. The IDC (Interest During Construction) factor assumes a typical expenditure curve and expected rates of return of capital available from different sources. The IDC factor of 0.1652 accounts for those effects in a constant money scenario. For the nominal dollar case, the IDC factor increases to 0.3178. If there is no inflation, the EDC (Escalation During Construction) is zero, but for a nominal 5% inflation, the EDC factor is 0.2436. See Reference 3 for more discussion on this topic. The above methodology is intended to transform the overnight construction costs in 1991 dollars to those associated with the end of construction and the start of plant operation.

The cost of electricity is usually quoted for the first year of operation. The plant Total Capital Cost is converted into an annual cost by multiplying with a fixed charge rate which accounts for the rate of return on capital and tax law implications. Two different

Use or disclosure of data
subject to title page restriction

Fixed Charge Rates are quoted for either the constant dollar or the nominal dollar accounting. Other annual costs include Operations and Maintenance (Plant O&M), Scheduled Replacement of large components such as the First Wall and Blanket modules, Target Manufacturing O&M, Fuel, and an allowance for the eventual decommissioning of the plant (also LSA dependent). For the constant year dollars, no escalation is applied to the operating costs, whereas for the nominal dollar case, the escalation rate is compounded for the construction period and the result applied to the operating costs.

There are several other factors contributing to the plant COE. The following equation displays the formulation of the COE:

$$\text{COE} = \frac{[\text{Annualized Capital Cost} + \text{Yearly Operating Cost}]}{\text{Net Power} \times \text{Plant Availability}}$$

$$\text{COE} = \frac{[\text{Annualized Capital Cost} + \text{Yearly Operating Cost}]}{[\text{Thermal Power} \times \text{Efficiency} - \text{Auxiliary Power}] \times [1 - \text{Scheduled Downtime} - \text{MTBF} \times \text{MTTR}]}$$

The Annual Costs in the numerator have generally been discussed in the previous paragraphs. More detail on this subject will be discussed in a later section of this appendix. The net electric power output will provide the income source to offset the annual expenses. The nominal output for the Prometheus designs was intended to be 1000 MWe. However, the process to arrive at the net power output is iterative. A nominal fusion power is chosen which in turn causes choices in driver energy, target gain and yield, and plant repetition rate. Meanwhile, the design of the energy collection and transformation systems in the First Wall, Blanket, Main Heat Transport, and Energy Conversion is proceeding. Only after the entire energy system is defined and overall efficiencies are established, can a preliminary new output be estimated. To adjust the net output closer to the desired value, assumptions and designs are modified and the process repeated. In Prometheus, the design for the laser plant achieved 972 MWe and the heavy ion plant achieved 999 MWe.

There is an economy of scale to be considered in scaling the size of the plants. The study was instructed to design and evaluate a 1000 MWe plant, recognizing that the COE would be more favorable if the plant size were larger. In Section 6.13 of the main report this economy of scale is discussed in detail. The COE is presented for plants of 500, 1000, and 1500 MWe. Detailed designs were not developed for these three cases, but the system code performance and cost estimating relationships were developed over a range of size parameter space, thus enabling the trade study.

The net electric power output discussed above is the nominal plant capacity. Over the period of a year, there are some number of scheduled and unscheduled outages which contribute to a loss of productive power output. The Plant Availability factor

Use or disclosure of data
subject to title page restriction

accounts for this decrement in productive output. Section 6.3.3 of the main report discusses this factor. The determined Availability for the Prometheus-L is 79.4% and Prometheus-H is 80.8%.

Costing Basis - The cost basis for the Prometheus Reactor Plants is in 1991 dollars. The design task leaders and the cost analysts developed the cost estimate for today's cost to purchase and install the system. If a cost estimate or cost estimating relationship was developed in a prior year, the estimate was updated to 1991 dollars by applying the appropriate inflation rates shown previously in Table C-2. The level of technology varied somewhat over the plant subsystems. Most of the systems and components were state-of-the-art and were costed thusly. Some systems or components were considered to advance the state-of-the-art. Some judgment was applied to determine what that system would cost today.

The costs reported in this report, principally in Section 6.13 and in this appendix, were based upon data generated within the ICCOMO systems code. Likewise, the cost estimating relationships (CERs) reported in the following sections are those used by the code to generate the cost data. These CERs are based upon the historical or developed cost bases. Many of the CERs use other data generated within the systems code. These data are generated or developed based upon general models within the code for the purposes of trade studies over wide parameter ranges. These general models in the systems code were continuously updated to conform to the most current embodiment of the reactor design approach. However, in the area of the reactor power balance, the systems code was not updated to handle and report the power balance exactly the same manner as the final Ebasco power balance calculations. To do so would have required recomputing all the study's economic trade study results which would have been a formidable task. The reported power balance in the reactor design parameter list reflects the final Ebasco thermal heat balance data; however, the power balance data in the systems code is not identical. Thus, power data taken from the reactor parameter list and used in the CERs to determine system cost will show slight discrepancies as compared to the reported costs.

Use or disclosure of data
subject to title page restriction

C.3 CAPITAL COST ACCOUNTS

The cost accounting format used in the Prometheus design studies conforms to the cost accounts shown in Table C-3. This is very similar to that used by MFE in the most recent design studies, ARIES as well as several other IFE design studies. This format will assist in evaluating the plant systems relative cost impact. This will also allow commonalty in comparison of other alternative design approaches. The accounts reflect all the systems and facilities required to produce busbar electricity.

The following sections will present a brief synopsis of the supporting cost basis for the presented costs. More detail on the content in each account is provided in Table C-3.

C.3.1 Land and Land Rights (Account 20)

The cost of the land, land rights, and relocation of buildings is the major cost in this account. STARFIRE[9] estimated the size of the site to be 1000 acres costing $3.3M in 1980 dollars (~$5.3M in 1991 dollars). This plant site would likely be somewhat larger and siting of power plant have become more complex, both of which would indicate a higher cost would be suggested. ARIES assumed a $10M land cost for their plant. Prometheus is estimated to have similar land cost at $10M; therefore C_{20} = $10M.

C.3.2 Structures and Site Facilities (Account 21)

This account covers all direct costs associated with the physical plant buildings such as the reactor, driver, turbine, electrical equipment, cooling system structures, and site improvements and facilities. All provisions cooling, site access, and security will be provided. The total cost of Structures and Site Facilities, Account 21, is $376.66M for the laser option and $322.41M for the heavy ion option.

C.3.2.1 Site Improvements and Facilities (Account 21.01) - This account encompasses all site improvements and facilities necessary for the complete power plant. This includes the general site improvements including site work, fencing, storm sewer, earth moving equipment, tank and pump foundations, fire protection, and sanitary sewers. Transportation access is provided by highway and railway access, but no waterfront improvement were considered. The STARFIRE[9] and EBTR [10] estimates were $11.15M (1980$), which would convert to $18M in 1991$. HIFSA[11] estimated the site improvements at $17M in 1986$ which would convert to $20.5M in 1991$. ARIES estimated this account at $11.85M in 1990$. It is thought the Site Improvements and Facilities costs would continue to escalate and $21M would be a more appropriate cost estimate for both sites. See Table C-5 for account details.

Use or disclosure of data
subject to title page restriction

Table C-5. Site Improvements and Facilities Costs

Category	Costs, ($ M)
General Site Improvements	
Site Work, Fencing, Storm Sewer	6.70
Earth Moving Equipment	7.00
Tank and Pump Foundations	1.00
Fire Protection	1.40
Sanitary Sewer	1.50
Transportation Access	
Highway	1.40
Railway	1.90
Total Site Improvements and Facilities, $C_{21.01}$ =	21.00

C.3.2.2 Reactor Building (Account 21.02) - The reactor building and other BOP facilities are described in the main report, Section 6.10. Ebasco helped develop these costs contained herein along with comparable estimates from past design studies. The Ebasco cost estimate was from a similar sized fission reactor building. Some design features were modified to account for changes associated with the Prometheus reactor designs. The volume of the Prometheus-L reactor building is roughly similar to STARFIRE[9] and EBTR[10], but the Prometheus-H building is much smaller. The Ebasco cost reference was of a comparable size to the Prometheus-L building design, but it had a free-standing containment structure. The Prometheus building designs use a steel liner inside the concrete building structure which would be a less expensive option. Scaling these data, the cost for the Prometheus-L building would be $106.06M and the smaller heavy ion reactor building would be $60.88M. These may seem low when compared to MFE reactor buildings, but the comparable MFE reactor buildings would include the functions contained in both the IFE reactor buildings and the driver buildings and, in some part, the target manufacturing buildings.

The cost estimating relationships for the reactor building assumed a cost based upon a volume relationship. The radius of the laser reactor building was 43 meters scaled to the ratio of the thermal power to the nominal thermal power of 3091 MW raised to the 0.5 power. The radius of the heavy ion reactor building was normalized to a 31.5 meter radius and using the same thermal power ratio to 3091 MW raised to the 0.3 power. The building height used similar relationship with the coefficients of 71.5 m for the laser reactor building and 64.0 m for the heavy ion reactor building. The differences in the nominal coefficients account for the building differences due to beam enclosure requirements whereas the lower heavy ion scaling coefficient is meant to reflect a weaker dependence of the thermal power in this type of reactor building. The building cost was scaled from the Ebasco estimate by assuming a fixed cost of $25.5M plus a variable cost of $194/m^3.

Use or disclosure of data
subject to title page restriction

Radius, Reactor Bldg = 43.0 x $(P_t/3091)^{.5}$ (Laser)
Height, Reactor Bldg = 71.5 x $(P_t/3091)^{.5}$ (Laser)

Radius, Reactor Bldg = 31.5 x $(P_t/3091)^{.3}$ (Heavy Ion)
Height, Reactor Bldg = 64.0 x $(P_t/3091)^{.3}$ (Heavy Ion)

Volume, Reactor Bldg = π x Radius^2 x Height

Cost, Reactor Building, $C_{22.01}$ = \$194 x volume + \$25.5 M

C.3.2.3 Driver Building (Account 21.03) - The costing basis for the Laser Driver Building for Prometheus-L is similar to the costing basis for the Power Supply Building for STARFIRE[9]. This building is priced on a volume basis with an approximate volume of 415,000 m^3. The escalated cost basis is \$88/m^3 which results in a laser building cost of \$36.52M. The heavy ion driver building is largely below ground building, just sufficiently wide to accommodate both legs of the accelerator. The costing basis is \$120/ft^2 tunnel floor area plus \$50/ft^2 floor area of the above-ground, pulse-forming network (PFN) building. The tunnel floor area is assumed to equal the LINAC length multiplied by five times the maximum induction core radius. The PFN building is assumed to be half the tunnel width. The total cost of the heavy ion beam driver enclosure is \$38.27M.

C.3.2.4 Turbine Building (Account 21.04) - The Turbine Building houses the turbines and all the auxiliary equipment for the turbines. The economic basis is the ARIES cost estimating relationship, C = \$53.9M x $(P_{gross}/1246)^{0.5}$. This results in a cost of \$57.18M for the laser option and \$52.79M for the heavy ion option.

C.3.2.5 Heat Rejection Structures (Account 21.05) - These structures support the heat rejection systems. The main elements in this account are the Intake Structures, the Discharge Structures, the Unpressurized Intake and Discharge Conduits, the Recirculating Structures, and the Cooling Tower Earth Work. The Cooling Towers are not included in this account, rather are covered in Account 23.03, Heat Rejection Systems. The economic basis is the ARIES CER. This results in a cost of \$11.48M for the laser system and \$10.69M for the heavy ion option.

$$C_{21.05} = \$11.48M \times \left(\frac{(\text{Power to Conversion System} - P_{gross})}{1860} \right)^{0.5}.$$

C.3.2.6 Auxiliary Building (Account 21.06) - This building houses the HX pumps, ancillary systems, and maintenance facilities for the Reactor Plant Equipment, including the Hot Cell Facilities. The cost basis is the ARIES[7]. This results in a cost of \$15.54M for the laser option and \$14.81M for the heavy ion option.

$$C_{21.06} = \$15.0M \times \left(\frac{P_{gross}}{1246} \right)^{0.3}.$$

Use or disclosure of data
subject to title page restriction

C.3.2.7 Target Manufacturing Building (Account 21.07) - This building handles the processed DT fuel from the Fuel Processing System and fabricates either the direct drive targets for the laser-driven reactor or the indirect drive targets for the heavy ion-driven reactor. As described in Section 6.4, the Target Manufacturing Building is divided into different zones according to the tritium handling requirements and the cryogenic processes. The nominal cost was derived by Ebasco with appropriate scaling by grams of tritium used/day as recommended by ARIES[7]. This results in a cost of $46.92M for the laser option and $44.92M for the heavy ion option.

$$C_{21.07} = \$47M \times \left(\frac{T_{usage}}{1500}\right)^{0.3}.$$

C.3.2.8 Tritium and Waste Processing Building (Account 21.08) - This building is similar in size and function to the Target Manufacturing Building. Thus the same CER is used to estimate the building cost.

$$C_{21.08} = \$47M \times \left(\frac{T_{usage}}{1500}\right)^{0.3}.$$

C.3.2.9 Miscellaneous Buildings (Account 21.09) - The CER for this category of Miscellaneous Buildings is taken from the ARIES report as

$$C_{21.09} = \$35M \times \left(\frac{P_{net}}{1000}\right)^{0.3}.$$

This results in a cost of $35.03M for the laser option and $35.11M for the heavy ion option.

C.3.3 Reactor Plant Equipment (Account 22)

This account summarizes all the fusion Reactor Plant Equipment (RPE). The systems contained herein are usually designed uniquely designed for the fusion application or have been tailored to accommodate the fusion systems. In the IFE application, this account only encompasses the reactor cavity and its systems, the heat transport and transfer systems, auxiliary cooling, radioactive waste, fuel cycle, reactor plant maintenance, reactor plant I&C and other reactor plant equipment. The functions of the driver and the target manufacturing plant are contained in other accounts at this same level. Because of this separation of function, the costs associated with this account will be less than that associated with the RPE for MFE reactor designs. The total RPE costs for the laser option is $700.43M whereas the heavy ion option is $568.34M. The bulk of this difference is traceable to the larger laser reactor cavity, higher power handled by the laser option systems, and the different beamline shielding approach and requirements. These are explained separately below.

C.3.3.1 Reactor Equipment (Account 22.01) - The costs in the account cover the components of the first wall and blanket, shield and vacuum vessel, primary

Use or disclosure of data
subject to title page restriction

structure, cavity vacuum, and target injection and tracking. These accounts represent all the functions contained within the reactor cavity as a whole to contain the fusion blast and debris, breed the tritium, and convert and capture the fusion energy. Each of these accounts are important and will be discussed separately. The cost of the laser option is $391.82M and the heavy ion option is $271.64M.

C.3.3.1.1 First Wall and Blanket (Account 22.01.01) - The standard approach for estimating this account in most or all fusion reactor design studies is to estimate the volume and mass of each type of material required in subsystem and then multiply by an average cost per unit mass. This average cost accounts for the material cost of the components, assuming for bulk purchases in a mature manufacturing environment. Likewise the labor cost for the fabrication, inspection, assembly, and installation and checkout have been factored into the overall unit cost for the material.

Figure C-2 is a modified version of a figure presented in Section 6.8 which illustrates the radial build of the First Wall/Blanket/Vacuum Vessel/Plena/Shield of the reactor cavity. This figure displays the radial thicknesses assumed, the volumetric density, and the materials used. The geometry of the cavities are right circular cylinders with hemispherical ends. The specific geometry is defined in Section 6.3. Using these data, the cost of each layer of the radial build was estimated. The unit cost of materials used is noted in Table C-6. The fabricated costs for the First Wall, Blanket and Shield have always been a topic of great debate, mainly because the materials are usually exotic, of currently-limited supply, and leading the state-of-the-art in fabrication. Thus the estimated costs involve extrapolation in time, quantity, fabrication methods, supply, and demand. The unit cost values quoted in Table C-6 are representative of those currently quoted by comparable studies and are not considered to be out of the realm of feasibility. The learning curve for this type of construction would be approximately 85%. However it is anticipated that a previous demonstration plant would have been built and learning would have begun with that unit. The cost basis for the unit cost have been assumed for the first commercial unit, thus the cost of the Demo plant (first of a kind) will have to be increased by 1/.85 and the cost computed for the 11th unit (for the 10th commercial plant). The resultant learning curve is 0.6705 for the 10th commercial First Wall and Blanket.

Silicon carbide (SiC) composite material is used to a great extent in the reactor cavity—in the first wall, blanket structure, reflector material, in the plena region as piping for the lead and helium coolants, and in the shield as one of the shielding materials. Several different costs are assumed for this material depending the usage and the fabrication and quality requirements as shown in Table C-6. The high quality SiC material is costed at $400/kg whereas the bulk granular material is $70/kg for neutron multiplier and $20/kg for bulk shield material. Currently SiC can be purchased at prices much lower than $20/kg, but the required level of purity will increase the cost.

Use or disclosure of data
subject to title page restriction

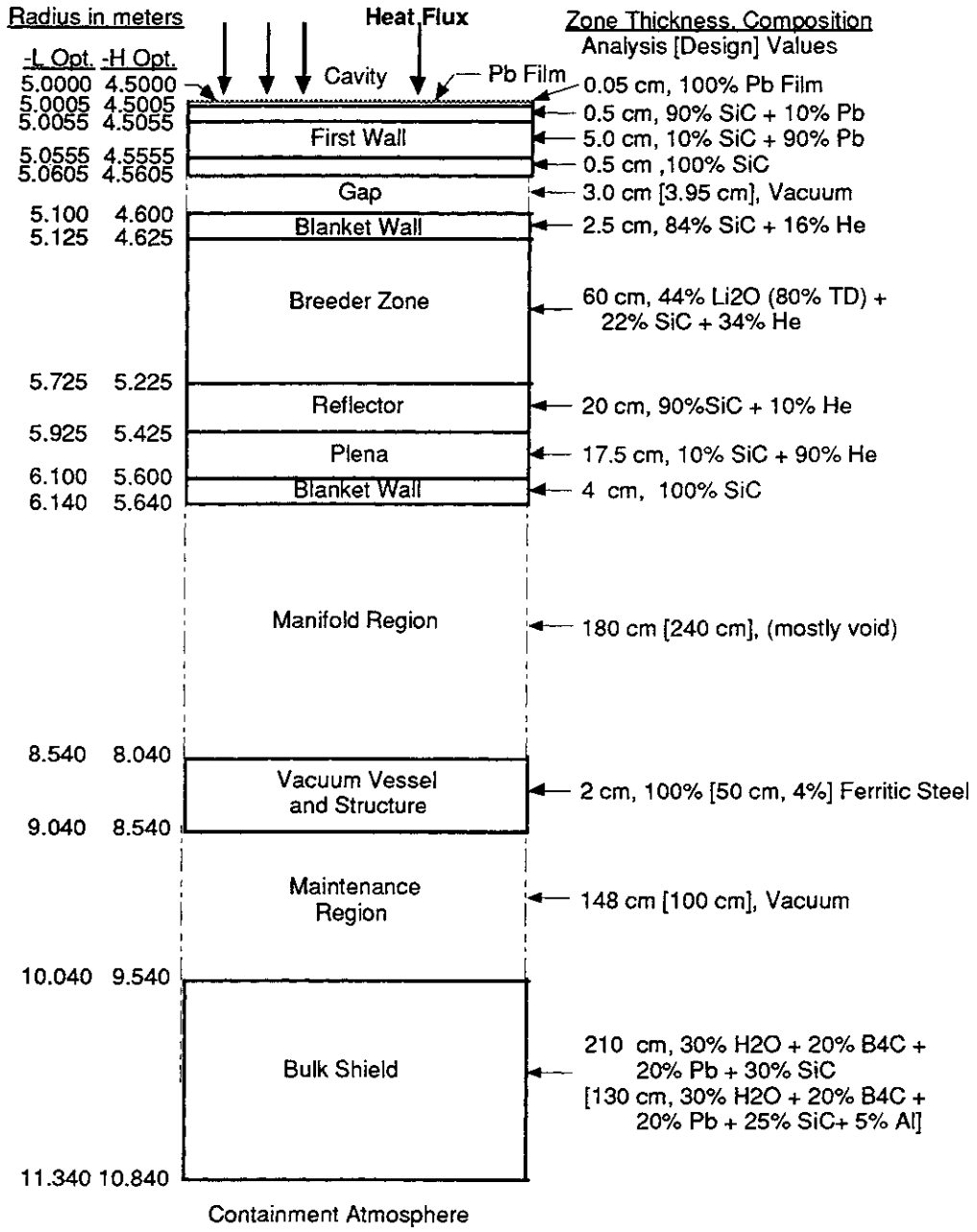

Figure C-2. Radial Build of the First Wall, Blanket, and Shield Subsystems

Use or disclosure of data subject to title page restriction

Table C-6 Cost of Materials Used in the FW/B/S Systems

Material	Special Properties/Usage	Installed Cost, $/kg
SiC	Composite, Structural, Complex/First Wall, Blanket, Headers	400
SiC	Solid Bulk Material/Neutron Reflector	70
SiC	Powdered Bulk Material/Shield Component	20
Li_2O	Pebble-Sized Material/Breeder	210
Pb	Liquid with Low Bi Impurity/Protectant, Coolant, N. Multiplier	2.2
Pb	Solid Granules with Low Bi Impurity/Shield Component	2.2
F. Stl	Structural, Moderate Complexity/Vacuum Vessel, Structure	30
Al	Structural, Moderate Complexity/Shield Structure	30
B_4C	Solid Granules, High Purity/Shield Structure	40
Concrete	High Purity Concrete/Alternate Shield Material	4
Steel	Structural, Low Complexity Liner	15

The ceramic breeding material, Li_2O, also has a nebulous cost basis in that it and other breeding materials have not been used in quantity over a long time period. But this cost data is representative of cost estimates used by other contemporary studies. The cost of lead is significantly higher than current applications, but the need to lower the bismuth impurities will cause the cost increase.

Table C-7 summarizes the material cost of the First Wall and Blanket subsystem for the two reactor concepts. In the Prometheus reactor concepts, the cost of the first wall is a rather insignificant portion of the overall cavity cost. The cost of the blanket is approximately 30 times more expensive than the first wall component. The cost of the silicon carbide in the blanket is the dominate cost element, as it is an expensive material and is used for the structural material, coolant tubes, and plenum region piping. The cost of the breeding material is a moderate cost element. The lesser cost of the heavy ion options is attributable to the smaller cavity radius and height and is roughly proportional to the square of the cavity radius (surface area). If the cavity blanket could be further optimized, the cost of the heavy ion reactor cavity would be reduced.

Table C-7 First Wall and Blanket Material Costs

Component Material		Laser Reactor (M$)	Heavy Ion Reactor (M$)
First Wall			
SiC		5.92	4.81
	Subtotal	5.92	4.81
Blanket			
SiC		118.96	98.38
Li_2O		32.15	26.43
	Subtotal	151.11	124.81
	Total	157.03	129.62

Note: The lead and helium coolants are treated as a special materials and are costed in Account 28.

Use or disclosure of data
subject to title page restriction

C.3.3.1.2 Shield and Vacuum Vessel (Account 22.01.02) - During the conduct of the study, a trade study of two shield approaches were conducted with two different sets of shielding materials. Table C-8 illustrates the materials considered, their densities, and the respective cost per kilogram. The type #1 shield reflects the composite shield approach with aluminum, water, lead, B_4C, and SiC, whereas Type #2 shielding uses concrete and steel. All the materials are carefully graded and selected to assure the proper shielding performance. This selection and quality requirement adds to the material cost. The cost of the concrete is not just the bulk cost of common construction grade concrete. The materials will have to be carefully screened to assure a radiation resistant concrete with a carefully known composition, blended especially for shielding. Other charges are included to forms, scaffolding, equipment charges, labor, finishing costs, and wastage.

Table C-8 Cost of Shield Materials Comparison

			Type #1 Shield, Composite			Type #2 Shield, Concrete		
Material	Density kg/m^3	Cost $/kg	Usage	Mass/Vol kg/m^3	Cost/Vol $/m^3$	Usage	Mass/Vol kg/m^3	Cost/Vol $/m^3$
Alum	2,700	30.0	0.05	135	4,050			
Water	1,000	NC	0.30	300	0			
Lead	11,350	2.2	0.20	2,270	4,994			
B_4C	2,500	40.0	0.20	500	20,000			
SiC	3,200	20.0	0.25	800	16,000			
Concrete	2,240	4.0				0.87	1,948.8	7,795
Steel	7,860	15.0				0.08	628.8	9,432
	Total or Avg.			4,005	45,044		2,577.6	17,227
	Avg. Cost/kg				11.25			6.68

The cost information from Table C-8 indicates that the concrete shield is less expensive than the composite shield on a equal volume basis. However, thicknesses need to be adjusted to have an equally effective shield. As is discussed in Section 6.8.4, the composite bulk shield should be 1.3 meters thick and the concrete would have to be 1.7 meters thick. This would equate to a shielding cost per square meter of $\$14.63/m^2$ for the composite shield and $\$11.35/m^2$ for the concrete shield.

From the data in Table C-8, it was determined that the lesser cost shield would be the concrete option. However due to activation concerns and waste disposal considerations, it was decided the more responsible decision would be to adopt the slightly more expensive, but environmentally attractive, composite material shield option. Table C-9 summarizes the shield and vacuum vessel costs for the two options. As noted in Sections 6.8.4 (Primary Shielding and Beamline Shielding) and 6.5.3 (Common Subsystems), the shielding approach is designed to closely contain the radiation volumes and not allow irradiation access to the large reactor building or

Use or disclosure of data
subject to title page restriction

ancillary equipment. The Bulk Shielding and the Vacuum Vessel costs are influenced by the reactor cavity size of the two options. The much smaller cost for the vacuum port enclosures reflects the reduced vacuum requirements for the heavy ion cavity. The cost of the 60 laser beamline shields is the dominate cost factor. The cost of the heavy ion beamlines is still significant but the HI beamlines are fewer in number and in size than the laser option. If the channel transport concept proves not to be feasible, the cost of heavy ion shielding would increase significantly.

Table C-9 Total Shielding and Vacuum Vessel Costs

Component		Laser Reactor (M$)	Heavy Ion Reactor (M$)
Bulk Shielding		128.55	117.25
Vac Port Enclosure		23.50	6.09
Beamline Shielding		48.34	3.22
	Subtotal	200.39	126.56
Vacuum Vessel		3.43	3.02
	Total	203.82	129.58

Learning curve factors are used to arrive at the data illustrated in Table C-9. Some reduction in the composite shielding costs is expected. The aluminum containment vessel would probably be fabricated in a remote factory and assembled and filled with the composite material at the site. Thus the overall composite learning curve was estimated at 90% with no prior units assumed. Ten units were used for the bulk shield whereas the vacuum port has three enclosures per reactor and the laser has 60 beamlines. The number of purchased units influences the resultant learning factor. The heavy ion reactor has a slightly different number of units of vacuum enclosures and beamlines.

If the shield beamlines were constructed of concrete, it would not be prudent to use a learning curve because the shield would be constructed mostly with on-site labor. This would have nullified any cost advantage for the concrete shield.

The Vacuum Vessel is thought to be constructed with more off-site labor, thus it is costed at ten units and a learning curve of 85%.

C.3.3.1.3 Primary Structure (Account 22.01.03) - This account considers the reactor structure to support the inner wall, blanket, and vacuum vessel as well as the beamline supports and the vacuum pump enclosures. It is assumed the bulk shielding is self-supporting and the cost of any structural function is included in the shielding account, except for the beamline shield supports.

The structure would likely be constructed with either steel or aluminum, both of which would be costed at $30/kg installed, with no prior units and an 85% learning curve

Use or disclosure of data
subject to title page restriction

applied. There was no detailed design developed for these components, so an estimating technique was used. It was assumed the mass of the inner structure between the blanket subsystem to the vacuum vessel would be 1/10 of the supported first wall, blanket, and lead coolant weight. The resultant structure would be approximately 0.123×10^6 kg for the laser option. The structure between the laser reactor vacuum vessel to the bulk shield was also estimated with the same technique, adding the incremental weights of the first wall, blanket, coolant, FW/B structure and vacuum vessel. The vacuum vessel to bulk shield structure would weight 0.155×10^6 kg. In as similar fashion, the resultant weights of the beamline support structure and the vacuum pump enclosure were estimated. Table C-10 summarizes the supported and structural weights and the resultant costs.

Table C-10 Primary Structure Weights and Costs

Components	Supported Wt kg $\times 10^6$	Structural Wt kg $\times 10^6$		Component Cost M $
Laser Option				
Blanket/VV Structure	1.229	0.1229		2.15
VV/Bulk Shield Str	1.425	0.1425		2.71
Beamline Structure	7.175	0.7175		12.55
Vac Pump Encl Str	3.19	0.319		5.58
			Total	22.99
Heavy Ion Option				
Blanket/VV Structure	1.013	0.1013		1.77
VV/Bulk Shield Str	1.287	0.1287		2.25
Beamline Structure	0.410	0.0410		0.72
Vac Pump Encl Str	0.827	0.0827		1.45
			Total	6.19

C.3.3.1.4 Reactor Cavity Vacuum (Account 22.01.04) - This account includes the vacuum system costs for the reactor cavity including the vacuum pumps and all roughing pumps, liquifiers and cooling systems, plenum chambers and ancillary equipment. The cost is based upon the base pressure requirement of the non-condensable cavity atmosphere. The laser system has a lower base pressure (~3 mtorr compared to ~100 mtorr for the HI case) so its vacuum system is more expensive.

	Cavity Pumping		Beamline Pumping
Heavy Ion	\$0.5M x (h_{usage}/2420)	+	2 x \$2.0M x (nbft/7)$^{.5}$
Laser	\$6.0M x (h_{usage}/2420)		

The independent parameters are h_{usage} which is hydrogen usage in g/d and nbft is the number of beams for final transport per cavity side. The system cost for the laser option is \$4.54M and the heavy ion option is \$3.51M.

Use or disclosure of data subject to title page restriction

C.3.3.1.5 Target Injection and Tracking (Account 22.01.05) - This system includes all the injection system costs for the injection acceleration system (either electromagnetic or pneumatic), the timing and tracking system outside the reactor cavity and possibly a tracking system within the reactor cavity. This cost was based upon the HIFSA[11] database of $7.9M for a target injection and tracking system based upon 10 targets per second. The CER is $7.9M x Repetition rate/10 Hz times the learning curve factor for 85% (.8528). The cost of the laser system is estimated at $3.44M for a repetition rate of 5.65 Hz and $2.74M for a repetition rate of 3.5 Hz. The related computer system would not be included in this account.

C.3.3.2 Main Heat Transfer and Transport Systems (Account 22.02) - These systems encompass all the main coolant systems which transport the usable heat from the reactor cavity. Specifically the coolant systems are the liquid lead for the first wall coolant and protectant and the gaseous helium coolant for the blanket. In the case of the laser reactor system, the waste heat from the laser amplifiers is used as supplemental heating for the steam generator (feedwater heating and supplemental heating). The system contained a heat exchanger which transferred the heat from the KrF amplifier gas into a helium coolant, which was used in the main helium coolant system steam generation. The cost for these are treated in Cost Account 23.05. The heavy ion driver systems have high enough efficiency that it was judged not economical to process the lesser amount of waste heat from the heavy ion driver. Intermediate or secondary coolant systems were not used in the Prometheus designs.

As shown in Table C-3, the elements of the heat transfer and transport include pumps and motor drives, piping external to the reactor cavity, heat exchangers, steam generators, superheaters, reheaters, tankage, coolant cleanup, tritium extraction from the coolants, and insulation.

The cost estimating basis for this system is derived from several sources—ARIES[7] (which seems to have some lineage back to STARFIRE[9] and MARS[12]) and some historical data from Ebasco in work they had previously estimated or current estimates on steam generators. The learning curve factor applied to this system was judged to be 75% which represents a system with a high degree of learning (lots of new technology, high labor content in factory conditions, and opportunity for significant improvement). The 75% learning over 10 units reduces the first commercial lot cost to 0.3846 of the estimated cost. The summarized first unit costs and the 10th unit costs are shown in Table C-11.

Ebasco estimated the cost for the first commercial steam generator, sized for the laser system. An average cost was obtained for the first six units used in a single plant, $76.8M for the lead steam generators and $132.6M for the helium steam generators (first lot of commercial units). These were scaled by thermal power raised to the 0.8

Use or disclosure of data
subject to title page restriction

power (per ARIES[7] recommendation) to obtain the costs for the heavy ion system costs.

The cost of the steam-driven helium circulators was estimated by Ebasco for a trade study during the conduct of the Prometheus study. The cost of the laser system was $47.53M with a scaled cost of $43.54M for the heavy ion system (first lot costs). Associated costs of the 108" diameter helium piping was estimated to be $165.59M for the laser system and $151.69M for the heavy ion system. Helium coolant makeup costs from the BCSS[13] study would be $9.88M and $9.05M based upon the scaled thermal power.

Ebasco did not specifically estimate the cost of the lead piping or pumps. The best reference for the lead pumps and piping was that generated by TRW in conjunction with the MARS[12] study and subsequently used in the BCSS[13] study. MARS used $Li_{17}Pb_{83}$ coolant, 2081 MW of thermal power, and four main loops with a flow rate of 22,750 kg/s per loop. The Prometheus lead loops have a lower flow rate of 9229 kg/s. If the TRW data are scaled to 91$, and adjusted for the flow rate to the 0.8 power, the cost for the pumps are $16.73M for the laser and $15.42M for the heavy ion systems. The MARS pipe size was 0.762m whereas the Prometheus size is 0.609 m. If the costs are adjusted to 91$, the thermal power to the 0.8 power, and the pipe size to the 0.85 power, the resultant costs are $63.10M for the laser and $58.88M for the heavy ion.

The lead coolant makeup and cleanup system is estimated at $4.13M for the laser system and $3.34M for the heavy ion system. Table C-11 summarizes all Main Heat Transfer and Transport System costs.

Table C-11 Main Heat Transfer and Transport System Costs

Component	Laser Reactor w/o Learning	Laser Reactor w/ Learning	Heavy Ion Reactor w/o Learning	Heavy Ion Reactor w/ Learning
Primary Lead Coolant System				
Steam Generators	76.80	29.54	71.66	27.56
Pumps	16.73	6.43	15.42	5.93
Piping/Valves	63.10	24.27	58.88	22.65
Coolant Cleanup	4.13	1.59	3.34	1.28
Subtotal	160.76	61.83	149.30	57.42
Primary Helium Coolant System				
Steam Generators	132.60	51.00	121.47	46.72
Pumps	47.53	18.28	43.54	16.74
Piping/Valves	165.59	63.68	151.69	58.34
Coolant Cleanup	9.88	3.80	9.05	3.48
Subtotal	355.60	136.76	325.75	125.28
Total	516.36	198.59	475.05	182.70

Use or disclosure of data subject to title page restriction

C.3.3.3 Auxiliary Cooling System (Account 22.03) - In the Prometheus reactor designs, there are only two major subsystems in the Auxiliary Cooling System. These are the Shield and Structure Cooling Subsystem and the Final Optics and Beamline Cooling Subsystem. Cryogenic Cooling would be a candidate subsystem, but in the Prometheus designs, the costs are contained within the Cavity Vacuum account under the Reactor Equipment, Account 22.01.04. No other requirements exist for cryogenics within the Reactor Plant Equipment. The Driver Plant will need cryogenics, but this is covered under the Driver Plant Equipment.

Both the Shield and Structure Cooling Subsystem and the Final Optics and Beamline Cooling Subsystem were assumed to have learning applied at 85% over 10 units. The basis for the Shield and Structure Cooling Subsystem is the ARIES[7] CER for the Primary or Intermediate Cooling (H_2O) system, which was \$0.103M x $Pth^{0.8}$ x escalation factor. With shield waste heat of 43 MW and 38 MW for the laser and heavy ion cases, this CER yields \$8.36M and \$6.06M. With 85% learning applied, the laser cost is \$1.96M and the heavy ion cost is \$1.77M for Account 22.03.01.

For laser case, the Final Optics and Beamline Cooling system covers the cooling of the 60 composite shield beamline structures and neutron apertures as well as the cooling of the final optics. This is a low grade heat system, not suitable for energy production. This system was not specifically defined, so an allowance of \$5M was allocated for this system (which would equate to \$2.91M after the learning curve factor was applied). The heavy ion beamlines would also be shielded in the two large beamline enclosures. Cryogenic cooling of the final magnets are handled in the driver costs. An allowance of the beamline cooling was assumed to be \$3M before learning and \$1.75M after learning.

The total cost for Account 22.03 is \$4.87M for the laser option and \$3.52M for the heavy ion reactor.

C.3.3.4 Radioactive Waste Treatment and Disposal System (Account 23.04) - This account handles all the liquid, gaseous, and solid waste processing and disposal for the reactor plant equipment. The cost basis for this account is the ARIES[7] study. When scaled for the thermal power handled for the two reactors and the year of the estimate, the cost for the laser reactor was \$5.68M and for the HI option was \$5.41M. No learning curve (LC =1.0) was applied to this account because it was felt this system would continue to evolve from the first commercial unit continuously to the final unit. Continuing regulation and environmental concerns would prevent the benefits of producing a common design over the several units.

C.3.3.5 Fuel Cycle System (Account 22.05) - The cost of the Fuel Cycle System is based upon the flow rate of the hydrogen isotopes used in the fuel cycle. The cost for the deuterium and tritium processing are determined from the tritium flow

Use or disclosure of data
subject to title page restriction

rate. Because the IFE targets are comprised of CH compounds, additional hydrogen flow rates must be handled by the Fuel Cycle System. There is a difference in that the direct drive targets contain only target capsules whereas the indirect targets contain both capsules, radiation cases, and internal support structures. Other compounds and elements are in these targets, such as carbon and lead, but these will be collected in the first wall protectant and disposed of in the Waste Processing System. Only the excess hydrogen will influence the Fuel Cycle System with the heavy ion reactor and indirect target design having a significantly higher hydrogen flow rate. See Section 6.7 for details on the Fuel Cycle System and the estimated flow rates.

The cost estimating relationship used for the Fuel Cycle System is \$20M x (hydrogen usage/2420)$^{0.5}$ + \$60M x (tritium usage/1500)$^{0.5}$ x learning. The usage values are expressed in grams/day. The final costs with 85% learning included are \$48.15M for the laser system and \$55.38M for the heavy ion system. The heavy ion option has a lower tritium flow rate, but the hydrogen flow rate is much higher, which yields a more expensive system.

C.3.3.6 Reactor Plant Maintenance (Account 22.06) - This account covers the Reactor Cavity Maintenance Equipment, the Hot Cell Maintenance Equipment and the Final Optics Maintenance. The maintenance equipment for the driver systems are associated with that major account. SPAR Aerospace estimated the cost of the first commercial system for the laser option to be \$22.7M for the Reactor Building Maintenance and \$13.45M for the Hot Cell Maintenance Equipment for a total of \$36.15M. Table C-12 for details on these costs. Scaling these costs by thermal power raised to the 0.5 exponent yields an estimated cost of \$33.36M for the heavy ion case. Note that the 0.5 exponent only weakly scales the cost to the thermal power. After application of an 85% learning curve, the laser option total cost is \$21.07M and the heavy ion option is \$19.44M.

C.3.3.7 Reactor Plant Instrumentation and Control (Account 22.07) - STARFIRE[9] estimated I&C costs for the Reactor I&C, Monitoring Systems, and Instrumentation and Transducers at \$23.41M which escalates to \$37.69M. ARIES[7] had the identical cost values for their instrumentation and control systems. HIFSA[11] had lower costs, around \$10M which was probably too low. Thus the STARFIRE costs would be adopted with a 90% learning applied. The final cost I&C cost for both reactor plants is estimated at \$26.60M with learning curve effects applied.

C.3.3.8 Other Reactor Plant Equipment (Account 22.08) - This account covers special heating systems, coolant receiving, gas systems and building vacuum systems. No detailed estimates were conducted on these systems and allowances were used in concert with previous estimates. No learning curve effects were used because of the lack of detailed estimates.

Use or disclosure of data
subject to title page restriction

Table C-12 Reactor Plant Maintenance Equipment Costs
First Unit Costs

Item Description	Number		Cost, $ M
Reactor Cavity Maintenance Equipment			
Upper Manipulator	1		2.5
Deployable Heavy Lift Manipulator	1		1.5
Mobile Heavy Duty Manipulator	2 @ $1M		2.0
Bi-arm Manipulators	2 @ $1M		2.0
Small Power Manipulator, 100 kg	4 @ $0.1M		0.4
Helium Steam Generator Robot	1		1.3
Lead Steam Generator Robot	1		1.3
Pump Room Manipulator	1		1.0
Contaminated Lead Manipulator	1		1.0
Viewing Equipment (lights, stems, etc.)			1.0
Measuring Tools			0.5
General Tools			3.0
Flask Handling Buggy			0.5
Crawlers			0.25
Crane Maintenance Equipment			1.0
Strongbacks, Fixtures			1.0
Welding Units	3		0.45
Radiation/contamination Detection Tools			2.0
		Total (Laser)	22.70
Note: Main Cranes, Small Cranes and Transporter are costed in Account 25.01			
Hot Cell Maintenance Equipment			
Bi-arm Manipulator	2 @ 1M		2.0
Payload Manipulator	2 @ 0.1M		0.2
Heavy Duty Manipulator	1		1.0
Flask Handler	1		0.5
Tools			2.0
Assembly Fixtures			3.0
Crane Maintenance Equipment			0.75
Viewing Equipment			0.5
Radiation/contamination Detection Tools			2.0
Decontamination Equipment (incl Tanks)			1.5
		Total (Laser)	13.45
		Total (Laser)	36.15
		Total (Heavy Ion)	33.36*
With Learning		Total (Laser)	21.07
		Total (Heavy Ion)	19.44

* Scaled by thermal power$^{0.5}$

Use or disclosure of data
subject to title page restriction

Special heating equipment will be require to assure the lead coolant can be added and removed from the reactor piping and first wall components. An allowance of $3M is provided for this system.

Coolant Receiving from STARFIRE[9] had been estimated at $0.24M which when escalated would be approximately $0.4M.

Gas Systems will be required due to the CO_2 inert atmosphere in the Reactor Building. The estimated cost would be $0.15M.

The Building Vacuum Systems to provide vacuum to other subsystems requiring vacuum conditions. This does not imply the building is under a vacuum, rather the building is nominally at atmospheric pressure, inerted with CO_2. Detritiated for the Reactor Building is handled under Account 22.05.07. A small allowance of $0.10M is provided for the Reactor Building Vacuum System.

The total cost of the Other Reactor Plant Equipment is $3.65M.

C.3.3.9 Reactor Spare Parts (Account 22.98) - The project recommended guidelines[1] specified that all spare costs should be set to zero for this analysis. Therefore Cost Account 22.98 = $0.0.

C.3.3.10 Contingency (Account 22.99) - The cost contingency for this account is accounted at a higher level, namely Account 96.00. Thus the contingency cost at this level is $0.0.

C.3.4 Turbine Plant Equipment (Account 23)

This account summarizes all the turbine plant equipment (TPE). The account usually parallels the equipment contained in most power plant cost accounts, i.e., turbine generators, main steam, heat rejection, condensing systems, feed heating and other TPE systems. Listed below are the cost estimating relationships for the major systems. The costs are assumed to be mature with no learning curve reductions applied. Ebasco data were used on the accounts 23.1 and 23.3 with the remainder being obtained from the ARIES study cost basis. The nominal costs shown below in Table C-13 differ slightly from that shown in the final cost tabulation. This is due to slight differences in the handling of the power values within the code. The CERs described in the following sections are those used in the code.

Use or disclosure of data
subject to title page restriction

Table C-13 Turbine Plant Cost Estimating Relationships

Account	Cost Relationship	Nominal Costs	
		Laser	Heavy Ion
23.01	140 x (Gross Elect/1400)$^{.7}$	138.74	124.87
23.02	7.73 x (Gross Thermal/2860)	8.82	7.51
23.03	58.68 x ((Gross Ther-Elect)/1860)$^{.8}$	59.37	50.19
23.04	(Condensing is in Heat Rejection Account)		
23.05	12.16 x (Gross Thermal/2860) + 11.13 x (Waste Power recovered/193)	26.28	13.03
23.06	65.85 x (Gross Electric/1000)$^{.6}$	79.96	73.06
23.07	12.6 x (Gross Electric/1000)$^{.3}$	13.88	13.27
	Nominal Total	327.05	281.93
	Reported Total Costs	327.13	282.98

C.3.5 Electric Plant Equipment (Account 24)

The subaccounts in the Electric Plant Equipment include Switchgear, Station Service, Switchboards, Protective Equipment, Electrical Structures and Wiring Containers, Power and Control Wiring and Electrical Wiring. The cost estimating relationship for this account is 71.5 + 67 x (Gross Electric Power/1000). The amount shown in the final cost table is calculated using the internal code power balance which is slightly different from the power balance data calculated by Ebasco which is shown in the data parameter list. The reported Electric Plant Equipment cost for the laser option is $165.46M and the heavy ion version is $151.59M. There were no learning curve cost factors applied to this account.

C.3.6 Miscellaneous Plant Equipment (Account 25)

This account included Transportation and Lifting Equipment, Air and Water Service Systems, Communications Equipment, Furnishings and Fixtures. This account is weakly scaled to the gross electric power. The account cost estimating relationship is 57.1 x (Net Electric Power/1000)$^{.3}$. The costs for the laser version is $57.15M and the heavy ion version is $57.27M. Since the plant design did not exactly iterate on the exact value of 1000 MWe, this cost for the Miscellaneous Plant Equipment varied slightly from one version to the other. There were no learning curve cost factors applied to this account.

C.3.7 Target Plant Equipment (Account 26)

This account included all facilities to manufacture and store the targets used in the reactor plant. The extraction and processing of the fuel elements is contained within and is costed in the reactor plant. Likewise the injection of the targets is also a

Use or disclosure of data
subject to title page restriction

function of the reactor plant. All other target preparation facilities are in this account. This would include capsule fabrication for both the direct and indirect targets and the related fuel filling. The indirect drive target case fabrication will be included in the cost account along with the mating of the fuel capsule, the support structure, and the outer case structure. Facilities will be provided for temporary storage of the target structures sufficient for the inventory needs. Support equipment will include instrumentation, control, and maintenance services. Section 6.4 explains the necessary equipment in more depth.

An approximation of the capital cost of target plant can be developed from the following parameters and the general cost relationship shown in Table C-14.

Table C-14 Target and Target Plant Cost Factors

Target Type	Nominal Capital	Repetition Rate	Reject Fraction	Target Matl Cost	Matl Usage
Laser DD	$127 M	5.65	.02	$0.010	0.75
Laser ID	$157 M	Not Determined	.04	$0.012	0.75
Heavy Ion ID	$182 M	3.54	.05	$0.014	0.75

$$\text{Number Targets / Yr} = \frac{\text{Repetition Rate} \times 3.155 \times 10^7}{(1 - \text{Reject Fraction})}$$

$$\text{Target Factory Cost} = \text{Nominal Capital Cost} \times \left[\frac{\text{Number Targets / Yr}}{10^8}\right]^{.7}$$

The above values determine the first unit cost for a target factory. It is assumed the factory capital cost follows a 90% learning curve (0.7047).

This yields $134.94M for the direct drive laser target factory and $143.62M for the heavy ion indirect drive target factory.

C.3.8 Driver Plant Equipment (Account 27)

This account is unique from other all major accounts in that the drivers are completely different from each other. These unique accounts for the Heavy Ion Driver are the Ion Source and Injector, Accelerating Structures, Focusing Magnet Systems, Cryogenics and Cooling Systems, Storage Rings and Transport and Final Focus Systems. For the Laser Driver, the analogous subsystems are the Front End Systems, the Discharge Laser System, the Raman Accumulator System, the Stimulated Brillouin System, the Excimer Gas Flow System, and the Complete Optics System including the Final Focus and Grazing Incidence Mirrors.

Use or disclosure of data
subject to title page restriction

There are some common types of accounts which support both types of driver systems. These are the Pulsed Power Systems, the Driver Vacuum Systems, the Instrumentation and Control System, Driver Maintenance System, and Miscellaneous Systems.

Learning curves were applied to these accounts. The majority of the accounts are assumed to learn at the rate of 90%. The Laser Gas Flow system is expected to have a higher learning rate of 80% due to the large amount of mechanical equipment in the system. The Heavy Ion Storage Rings is also expected to exhibit a 80% learning also due to the large number of like mechanical and electrical components. The common maintenance account is expected to have an 85% learning curve.

The costs for the Driver Subsystems are noted below in Table C-15. See Table 4.1.2-2 for more detailed cost data on the HI driver and Tables 4.1.1-2, 4.1.1-3, and 4.1.1-4 for the laser driver systems and subsystems.

Table C-15 Driver Plant Equipment Costs

Account No	HI Driver Title	Cost, $ M	Laser Driver Title	Cost, $ M
27.01	Ion Source/Injector	7.05	Front End System	10.25
27.02	Accelerating Struct	70.84	Discharge Lasers	44.91
27.03	Focusing Magnets	43.25	Raman Accelerators	4.65
27.04	Cryogenic System	8.67	SBS Cells	1.27
27.05	Storage Rings	13.05	Gas Flow System	33.91
27.06	Final Transport	53.72	Optics Systems	106.18
27.07	Pulsed Power	150.98	Pulsed Power	142.14
27.08	Driver Vacuum	9.66	Driver Vacuum	0.00
27.09	Driver I&C	19.00	Driver I&C	20.00
27.10	Driver Maintenance	19.29	Driver Maintenance	16.66
27.11	Miscellaneous Systems	7.60	Miscellaneous Systems	18.31
	Totals	403.11	Totals	398.28

C.3.9 Special Materials (Account 28)

This account accrues the costs of the special materials necessary at the start up of the reactor. These are generally fluids or gases which are non-fuel and non-structural. These will only need be purchased at the time of the initial checkout phases and do not need to be acquired during the early phases of the plant construction. The general classes are the reactor coolants (helium and liquid lead), the turbine working fluids, the driver working fluid (KrF gases), and reactor building and laser building cover gases.

Use or disclosure of data
subject to title page restriction

The allowance for the special materials is $1.62M for the laser driver reactor and $1.32M for the heavy ion. The higher cost for the laser is due to the larger size reactor cavity and the inclusion of the KrF gases and the driver beamline cover gas.

C.3.10 Indirect Cost Accounts (Accounts 91 through 98)

The economic guidelines for these accounts were agreed upon by the two contractors and approved by the DOE IFE Reactor Design Study Economics Working Group. The resulting formulations for each indirect cost account are shown in Table C-1. There is a Level of Safety Assurance dependence on each account. Prometheus was assessed to be at the LSA Level One for both reactor types.

Table C-16 summarizes the Indirect Costs for the two Reactor Plant Designs with an LSA rating of one.

Table C-16 Prometheus Reactor Plant Cost Factors in Constant 1991 Dollars LSA = 1

Cost Account		Prometheus-L CYD*		Prometheus-H CYD*	
	Total Direct Cost	2171.67		1940.64	
91	Constr Serv & Equip	245.40		219.29	
92	Home Office Engr & Serv	112.93		100.91	
93	Field Office Engr & Serv	112.93		100.91	
94	Owners Cost	396.44		354.26	
95	Process Contingency	0.00		0.00	
96	Project Contingency	445.27	NYD**	397.90	NYD**
97	Interest During Constr	575.66	1107.41	514.42	989.60
98	Escalation During Constr	0.00	848.68	0.00	758.55
	Total Capital Cost	4060.29	5440.90	3628.34	4862.07

* CYD (Constant 1991 Dollars)
** NYD (Nominal 1997 Dollars)

Use or disclosure of data subject to title page restriction

C.4 COST OF ELECTRICITY ACCOUNTS

The cost of electricity (COE) is defined as the cost of delivering a kilowatt of energy to the busbar. The cost is projected to the first year of operation. The cost elements of the COE are the annualized plant capital cost, annual operations and maintenance (O&M) cost, scheduled replacement cost, target manufacturing O&M cost, fuel cost, and decommissioning cost. The remaining elements which determine the energy production include the plant availability factor and the net plant capacity. Table C-17 summarizes these elements in millions of dollars for both current dollars and nominal year dollars for Prometheus-L and Prometheus-H.

Table C-17 Cost of Electricity Accounts for the Prometheus Reactor Plants

Cost Account		Prometheus-L		Prometheus-H	
		CYD	NYD	CYD	NYD
	Annual Capital	392.22	891.22	350.50	796.41
40-47	Plant O&M	49.71	66.61	50.39	67.53
50	Sched Replacements	24.29	32.55	20.17	27.03
	Target Mfg O&M	12.32	16.51	11.80	15.81
2	Fuel	4.08	5.47	5.60	7.50
	Decommissioning	4.56	6.11	4.56	6.11
Total Annual Operating Costs		94.96	127.25	92.52	123.98
Total Annual Costs		487.18	1018.47	443.02	920.39
Plant Availability Factor, %		79.4	79.4	80.8	80.8
Plant Capacity, MWe		972	972	999	999
Cost of Electricity, mills/kWh		72.0	150.5	62.6	130.0

Each of these elements are discussed in following sections.

C.4.1 Annual Capital Cost

The cost of capital to construct the Prometheus plants are accumulated over the construction period along with the interest charges. The payback of this borrowed capital begins at the initial operating date and continues for the economic lifetime of the plant. These costs are levelized on an annual basis. Fixed charge rates are determined to take into rate of return of capital and the tax law provisions. Section C.2 provides additional information. The constant and nominal fixed charge rates are 0.0966 and 0.1638 respectively. See Table C-2 for the complete economic guidelines. Two different fixed charge rates are provided to account for the constant year dollars or the nominal year dollars. Table C-17 illustrates the annual cost values for the two reactor plants and the two charge rates. Prometheus-L is slightly more expensive by approximately 10% than the heavy-ion version. This effect is largely due to the larger structures, the larger Reactor Plant Equipment, and the larger-sized

Use or disclosure of data
subject to title page restriction

Electric and Plant Equipment for the laser system. The Driver Plant Equipment costs are nearly identical in both cases.

C.4.2 Annual Operating Cost

The summary of the Annual Operating Cost shown in Table C-17 notes that the costs are nearly identical with compensating small factors. Scheduled replacement costs are slightly higher for the laser system but the fuel target costs are more expensive in the case of the heavy ion system. All annual operation costs are estimated in 1991 dollars. The nominal year dollar data is escalated at a 5% annual rate to the initial operating date.

C.4.2.1 Plant O&M Cost - This account includes staff, materials, scheduled and unscheduled activities, and general supplies for the entire reactor plant except for the target plant which has unique maintenance requirement above and beyond those of a typical MFE power plant. For consistency with other fusion reactor design studies, the Economics Working Group recommended[1] the usage of a cost estimating relationship used by ARIES[4] on this project. The equation was escalated from the ARIES 1988$ baseline to Prometheus baseline of 1991$. The Plant O&M cost is defined by $78.9 x LSA factor x $(Pe/1200)^{0.5}$ for the constant year dollars, see Table C-1. This results in similar O&M costs due to the nearly identical plant power outputs. This result is reasonably correct at the level of detail developed in these studies. On a relative basis, it would be expected the laser-driven plant would exhibit a slightly higher O&M plant cost due to more maintenance on the driver and the more involved reactor plant equipment arrangement.

C.4.2.2 Scheduled Maintenance Cost - The costs accrued in this account provide for periodic replacement of significant cost items with a finite and predictable lifetime. In the case of the two Prometheus reactors, the replacement cost of the first wall and the blanket modules were included. The life of the first wall is estimated to be five years and the blanket, ten years. The margin of error on these components are significant, but these values are reasonable estimates for today's technology. The replacement costs of the final mirrors and the grazing incidence metal mirrors were considered for inclusion, but the estimated lifetime ranged from life-of-plant down to 5-10 years. Thus these were not included in this cost category. The plant and target plant O&M cost accounts do include all costs associated with the remaining periodic and periodic maintenance activities.

Since the laser-option first wall and blanket components are more expensive, this is reflected in the higher Scheduled Maintenance cost for the laser option.

C.4.2.3 Target O&M Cost - This account includes staff, materials, scheduled and unscheduled activities, and general supplies associated with the Target Plant. The

Use or disclosure of data
subject to title page restriction

data is based upon the previous work done by Pendergrass[15]. More specific detail is shown in Table 6.4.3-1 regarding the Target Factory O&M cost assumptions and bases. The higher number of the laser direct drive targets required per day slightly offset the individually higher cost of each indirect drive heavy ion target.

C.4.2.4 Fuel Cost - These fuel costs are associated with the manufacturing of the direct drive and indirect drive targets. Included are the material and processing costs of the targets. These cost data are derived from the work of Pendergrass[15] and modified as required for the year of the estimate, the materials used, and the target parameters. See Section 6.4.3 for more specific details. The cost of the fuel materials is $C_{MATL} = C_{MATL_i} \times \left(\frac{E_{Beam}}{3MJ}\right) \times \frac{(N/yr)}{USAGE}$. C_{MATL} is cost of target materials. USAGE is a factor which represents losses in the fabrication process. Both C_{MATL_i} and USAGE data are shown in Table C-14. The cost of the indirect drive, heavy ion target results in a more expensive fuel cost than the direct drive laser target. The difference is not an important factor in the overall annual cost and is not a determining factor in the decision between the two options.

C.4.2.5 Decommissioning Allowance Cost - An allowance will have to be provided for the decommissioning of any power-producing plant. The guideline document for this study[1] recommended the use of a methodology similar to that proposed by NECDB[2] and used by the ARIES project[3,4]. Specific to decommissioning costs, the guidelines recommended a range of costs from 0 to 1 mill/kWh dependent upon the level of safety assurance (LSA) with no specific values given. The cost estimate for ARIES did not explicitly define what values they were using, but Reference 3 estimated a value of 0.5 mill/kWh for ARIES and other fusion plants and 0.8 mill/kWh for an advanced passively safe fission plant. Reference 2 estimated and referenced decommissioning costs for fission plants which ranged from average cost of $166M to $191M in 1991$. The U.S. Council for Energy Awareness[14] assumed the decommissioning cost for a fission plant would be $2100M and a coal plant would be $26M in 1991$. It is anticipated that fusion plants will be more environmentally attractive and entail less decommissioning costs, especially those plants which are designed to achieve low LSA values. On the other hand, the trend is toward providing a higher level of protection for the environment which steadily provides additional cost to any environmental cleanup operations. Thus for this analysis it is estimated that for the LSA = 1 case, approximately $200M in 1991$ will have to be provided for decommissioning. Furthermore, LSA levels of 2, 3, and 4 are estimated at $400M, $600M, and $800M each.

The envisioned method of providing adequate funds for decommissioning a plant is to contribute to a sinking fund from power revenues. This sinking fund will accumulate until the plant's useful lifetime has expired (30-40 years). The Nuclear Energy Cost

Use or disclosure of data
subject to title page restriction

Data Base[2] suggested the accruing interest rate should be assumed to be 2.4%/year real dollars based on long term U.S. Government obligations. If the sinking fund is accruing at the rate of 2.5% per annum for 30 years, an allowance of 0.68 mill/kWh would be adequate for a 1000 MW, LSA = 1 plant operating at 75% availability to accumulate $200M. If the plant LSA were judged to be at higher levels, proportionately higher allowances would need to be provided. For the Prometheus designs, this results in an annual allowance of $4.56M for decommissioning.

C.4.3 Cost of Electricity Summary

The cost of electricity (COE) is the ultimate measure of the viability of a competitive power plant. The design of Prometheus has been optimized to produce a high level of power, long life components, low cost systems, and low operations and maintenance costs. All these elements are combined into the figure of merit called the cost of electricity.

The capital costs for the laser option is roughly 10% higher than the heavy ion option mainly due to the more expensive buildings and reactor plant and the requirement to produce more power to offset a slightly lower plant efficiency. The operating costs for both plants are virtually identical with the heavy ion option having a slight advantage due to the cost of replacement parts. By intent, both power plant were designed to produce nominally 1000 MWe net of electricity. Due to the differences in plant efficiencies, the laser plant must be sized slightly larger to produce the same net output. The final factor is the plant availability which slightly favors the heavy ion plant design. This results in a lower COE for the heavy ion plant (62.6 mills/kWh versus 72.0 mills/kWh). The capital cost is the determining factor in this case.

As is discussed in the main body of the report, this difference should not be viewed as a significant difference. Many of the contributing factors have sizable error bands on the data. New developments are occurring which influence the outcome. If a particular option is selected for further development, significant advances can be obtained. The analyses included in this report attempted to be midway between conservative and optimistic.

The final result is that both Prometheus reactor designs economically compare favorably with existing fossil, fission, and MFE fusion power plants. The economics of inertial fusion power plants will not be the deciding factor for the development of this energy option.

Use or disclosure of data
subject to title page restriction

References for Appendix C

1. Ronald C. Davidson, et. al., "Inertial Confinement Reactor Design Studies Recommended Guidelines", September 1990.

2. "Nuclear Energy Cost Data Base: A Reference Data Base for Nuclear and Coal-Fired Powerplant Power Generation Coat Analysis, "U.S. Department of Energy Report DOE/NE-0095 (September 1988).

3. J. G. Delene, "Updated Comparisons of Economics of Fusion Energy," 9th Topical Meeting on Technology of Fusion Energy (Oakbrook, Illinois, 7-11 October 1990)

4. R. L. Miller, "Options and Optimizations for Tokamak Reactors: ARIES, " 9th Topical Meeting on Technology of Fusion Energy (Oakbrook, Illinois, 7-11 October 1990)

5. W. R. Meier, et al., OSIRIS and SOMBRERO IFE Reactor Design Study Final Report, 1991

6. J. P. Holdren et al., "Report of the Senior Committee on Environmental, Safety, and Economic Aspects of Magnetic Fusion Energy," LLNL Report URL-53766, 25 September 1989.

7. Ronald L. Miller, Robert A. Krakowski, David A. Ehst, ARIES System Study Results (Draft), 15 February 1991.

8. Linda Argote and Dennis Epple, "Learning Curves in Manufacturing," Science, Vol. 247, pg. 920-924, September 1990.

9. C. C. Baker, M. A. Abdou, et al., "STARFIRE - A Commercial Tokamak Fusion Power Plant Study," ANL/FPP-80-1, September 1980.

10. C. G. Bathke, et al, "ELMO Bumpy Torus Reactor and Power Plant Conceptual Design Study," LA-8882-MS, August 1981.

11. D. S. Zuckerman, et al., "Induction LINAC Driven Heavy Ion Fusion System Model," Fusion Technology, Vol. 13, #2, 1986.

12. B. G. Logan, et. al., "Mars, Mirror Advanced Reactor Study," LLNL report UCRL-53480, July 1984.

13. M. A. Abdou, et al., "BCSS, Blanket Comparison and Selection Study," Final Report ANL/FPP/84-1, September 1984

14. "Advanced Design Nuclear Energy Plants: Competitive, Economical Electricity," U.S. Council for Energy Awareness, January 1991.

15. J. H. Pendergrass, et al., "Heavy Ion Fusion Target Cost Model," Fusion Technology, Vol. 13, pg. 375, 1988.

Use or disclosure of data subject to title page restriction

This page intentionally left blank.

McDonnell Douglas Aerospace
P.O. Box 516, St. Louis, Missouri 63166-0516 (314) 232-0232

MCDONNELL DOUGLAS